Faculty of Science and Engineering
Department of Imaging and Applied Physics

An investigation of the relationship between Western Australian nickel laterites' leaching performance and their mineralogical properties

Xiaodong Wang

This thesis is presented for the Degree of
Doctor of Philosophy
of
Curtin University

May 2013

Declaration

To the best of my knowledge and belief this thesis contains no material previously published by any other person except where due acknowledgment has been made.

This thesis contains no material which has been accepted for the award of any other degree or diploma in any university.

Signature: 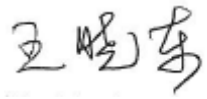

Date: 10th May 2013

Abstract

Sulphide nickel resources are becoming exhausted. However there are vast resources of low grade (<0.8 wt.% Ni) nickel laterites in Western Australia that are currently uneconomic to process. Nickel is associated with iron rich minerals such as goethite and nontronite in these ores. Some ores leach well while other superficially similar ores are acid resistant, leaching slowly with variable percentage of nickel and iron extracted. The differences between these ores have not been well characterised or understood. The investigation of the influences of mineralogy on leaching, the prediction of leaching behaviour and improvements in leaching technology require accurate quantitative phase analysis (QPA). However, the QPA for nontronite, which is an important nickel resource in the Western Australian laterite profile, has proven to be difficult as this clay mineral is always turbostratically disordered.

To facilitate the characterisation of the turbostratically disordered nontronite, two QPA approaches improving both the quantification accuracy and the fitting of its complex X-ray diffraction peak profiles were developed. In the first approach, the envelope fitting in the original PONKCS method (Scarlett & Madsen, 2006) was modified by using spherical harmonics as peak shape modifiers for Pawley phase and independent peak shape descriptions for Peaks phase. The modified PONKCS method resulted in absolute quantitative analysis of nontronite with an error of less than 5 wt.% using laboratory X-ray diffraction data. In the second approach, a supercell model compatible with the Rietveld approach developed by Ufer *et al.* (2004) was translated into TOPAS syntax with a novel calibration method resulting in accurate nontronite quantification with less than 1 wt.% error.

The mineralogical compositions of the Western Australian nickel laterite ore samples characterised by the laboratory X-ray diffraction suggest most samples contain goethite and about half of them also contain nontronite, both of which are known as nickel containing phases. The column leaching rates of the laterite ore samples were assessed by the Kabai (1973) model. An original method similar to the two lines fitting approach (Schwertmann &

Latham, 1986) was used to derive rate constants of slow leaching iron oxides from leaching curves influenced by the accompanying fast leaching nontronite. The correlations between percentage of iron extracted, iron leaching rates versus mineralogical compositions and iron distributions identified a group of oxide type laterite (goethite only) representing the most variable leaching performance. This group of samples were further investigated by synchrotron X-ray diffraction to determine their goethite lattice parameters and by energy dispersive spectroscopy to assess their guest metal substitution levels in goethite. Although positive correlations between goethite lattice parameters and guest metal substitution levels are statistically significant, guest metal substitution cannot fully explain the variation of leaching rate of these samples.

Obviously different goethite morphologies between the fast and the slow leach samples were observed by transmission electron microscopy for the first time. Acicular goethite crystals are prevalent in fast leaching samples while cementations high in iron and silicon were commonly observed in slow leaching samples. These goethite-silica/silicate cementations were confirmed by imaging of energy filtered transmission electron microscopy. The cementation framework could not be fragmented by acid leaching but could be disintegrated by caustic treatment. Acid leaching rates increased by six times by first disintegrating goethite-silica/silicate cementations with caustic. The micro-morphology of goethite-silica/silicate cementation is believed to be the dominant factor for the acid resistance of some laterite ores samples.

The micro-morphological features of goethite-silica/silicate cementation can only be observed by transmission electron microscopy. Pre-treatment of disintegrating the cementation structure of these nickel laterite ores would improve the efficiency of heap leaching and make Western Australian low grade nickel laterites more economical to process.

Acknowledgements

I would like to acknowledge the great contribution from my supervisors Prof. Arie van Riessen, Dr. Robert D. Hart, Curtin University, and Dr. Jian Li, Dr. Robbie G. McDonald, CSIRO Process Science and Engineering. Their enduring guidance has been the most critical for the completion of this thesis and my development as a researcher. I would also like to thank Emeritus Professor Brian O'Connor, who guided me into the field of Powder Diffraction. His insightful advice assisted me and encouraged my efforts in this field.

I benefitted greatly from inspiring discussions with my colleagues Ross Williams, William Rickard, Cat Kelley, Elaine Miller, Mark Paskevicius and other staffs and students at Curtin University. Their knowledge and experience has been extremely helpful in my experiments and data analyses.

My family, and in particular my wife Min (Emily) Xie, have encouraged and supported me emotionally during my study abroad. I am forever indebted to Emily, my most loved, for looking after me for these past four years.

I would like to acknowledge the Endeavour Postgraduate Award from the Department of Industry, Innovation, Science, Research and Tertiary Education, Australia Government for providing the financial support of my Ph.D. program. My case managers Anna Young, Chelsea Berner, and Vanessa Wright in Austraining International are thanked for dealing so professionally with my scholarship. I would also like to thank the Parker Centre CRC and the education program manager Nadine Smith for contributions to my experimental costs and conference travel.

The facilities, scientific and technical assistance of the Centre for Materials Research, Electron Microscopy Facility, and Curtin X-ray Laboratory at Curtin University, the Centre for Microscopy, Characterisation and Analysis at the University of Western Australia, and the Australian Synchrotron are much appreciated. I am grateful to Prof. Martin Saunders for his assistance in EFTEM images acquisition and Principle Beamline Scientist Dr. Justin Kimpton for synchrotron patterns acquisition. Senior diffraction scientist Ian Madsen, Nicola Scarlett, Mark Raven and Dr. Arnt Kern are thanked for their beneficial suggestions.

Contents

List of Figures

List of Tables

List of Abbreviations

AL	Atmospheric pressure Leaching
ASPD	Australian Synchrotron Powder Diffraction Beamline
BET	Brunauer-Emmett-Teller
CIF	Crystallographic Information File
CFSE	Crystal Field Stabilisation Energy
CPD	Commission on Powder Diffraction
CSD	Coherent Scattering Domain
CSIRO	Commonwealth Scientific and Industrial Research Organisation
DCB	Dithionite-Citrate-Bicarbonate
EDS	Energy Dispersive X-ray Spectroscopy
EELS	Electron Energy Loss Spectroscopy
EFTEM	Energy Filtered Transmission Electron Microscopy
EPMA	Electron Probe Microanalysis
FESEM	Field Emission Scanning Electron Microscopy
FP	Fundamental Parameter
FTIR	Fourier Transform Infrared Spectroscopy
FWHM	Full Width at Half Maximum
GUI	Graphic User Interface
HAADF	High-Angle Annular Dark Field image
hkl_Is	Pawley phase
HL	Heap Leaching
HPAL	High Pressure Acid Leaching
HRTEM	High Resolution Transmission Electron Microscopy
ICSD	Inorganic Crystal Structure Database
IUCr	International Union of Crystallography
LOI	Loss On Ignition
LPSD	Linear Position Sensitive Detector
MCD_{hkl}	Mean crystallite dimension perpendicular to hkl plane
NIST	National Institute of Standards and Technology
PDF	Powder Diffraction File
PONKCS	Partial Or No Known Crystal Structure
PV	Pseudo Voigt

PVII	Pearson VII
QPA	Quantitative Phase Analysis
QXRD	Quantitative X-Ray Diffraction
SAED	Selected Area Electron Diffraction
SEM	Scanning Electron Microscopy
SH	Spherical Harmonics
SPV	Split Pseudo Voigt
SPVII	Split Pearson VII
SRM	Standard Reference Materials
STEM	Scanning Transmission Electron Microscopy
str	Crystal structure phase
SXRD	Synchrotron X-Ray Diffraction
TEM	Transmission Electron Microscopy
TOT	Tetrahedral-Octahedral-Tetrahedral
wt.%	Weight percent
XAS	X-Ray Absorption spectroscopy
xo_ls	Peaks phase
XRD	X-Ray Diffraction
XRF	X-Ray Fluorescence spectroscopy
ZM	Unit cell mass in str model, adjustable in hkl_ls or xo_ls models
ZMV	Product of unit cell mass and unit cell volume in str model, adjustable in hkl_ls or xo_ls models

Chapter 1 Introduction

Nickel is a corrosion resistant, lustrous, silvery metal which is used in many industrial and consumer products, including stainless steels, alloys and superalloys, coinage, rechargeable batteries, plating, and chemical catalysis. The most important and main application of nickel is in making stainless steels, nonferrous alloys and superalloys, which are the main materials for infrastructure construction as world-wide urbanisation grows. This application relies upon nickel's ability, when alloyed with other metals, especially iron, to increase the alloy strength, toughness, and corrosion resistance over a wide temperature range. Nickel is essential to the iron and steel industry. The nickel containing steels have played a key role in the development of materials for the auto industry, household appliance industry, and aerospace industry. The products from other minor but broad reaching nickel usage, like rechargeable batteries, fuel cell, and metal coins, impact on everyone's life.

1.1 Nickel demand, price, and production

The last three decades have witnessed a steady growth in world nickel production and consumption (Figure 1-1), mainly driven by the world stainless steel demand and production in emerging economies. Chinese share of global apparent demand[1] of stainless steel increased from 10 % in 2000 to 35 % in 2011. China is also the largest producer of stainless steel with over 30 % average annual increase, from 0.76 million tonne (Mt) in 2001 to 12.6 Mt in 2011, representing 36 % of the world's yearly output (International Stainless Steel Forum, 2012).

The world production of nickel has increased from 0.68 million tonnes in 1983 to about 1.58 million tonnes in 2011 (Mudd, 2010; New, 2011). Nickel demand has recently increased again after global stagnation in 2008 and 2009. Approximately 70 % of nickel is used for stainless steel production. As nickel accounts for 70–80 % of the total stainless steel cost, this use is becoming the main driver for demand and subsequently the nickel price.

[1] The economic term "apparent demand" is the sum of production plus imports minus exports. In contrast, "real demand" also recognises changes in stock level.

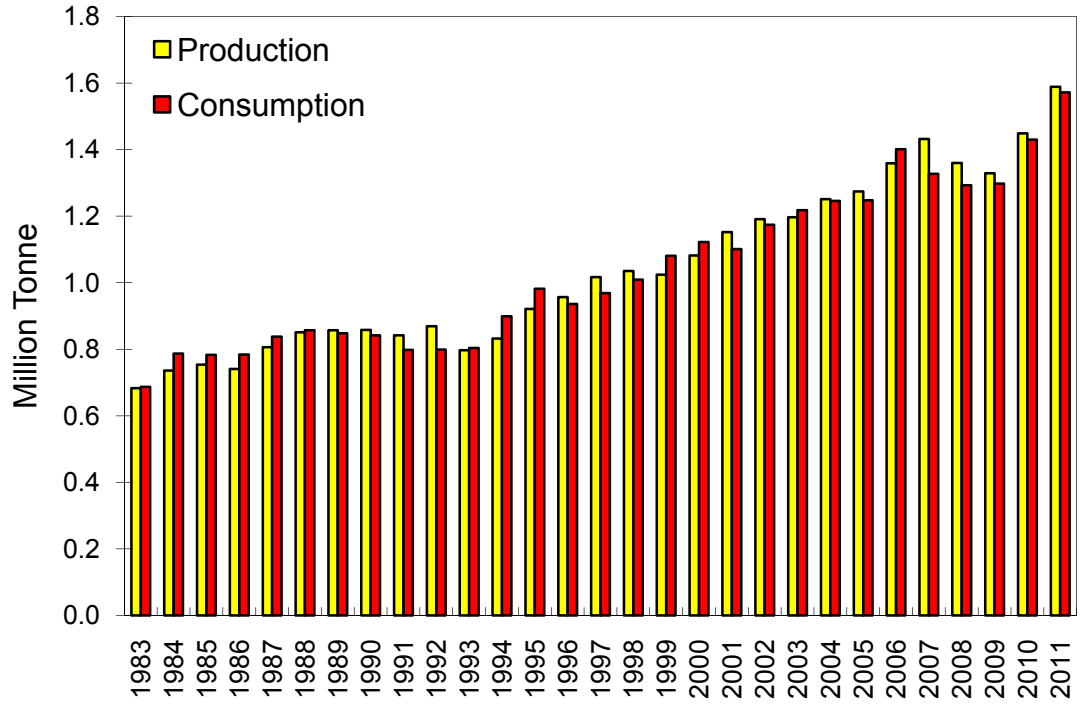

Figure 1-1 World nickel production and consumption from 1983 to 2011 (Mudd, 2010; New, 2011)

Nickel metallurgy is challenging because the average abundance of nickel in the earth crust is low at only 0.0084 wt.% (Kerfoot, 2000, p40); the element is more dispersed than other lower abundance elements, such as copper. Nickel sulphides (28 % of world reserves) and nickel laterite (72 % of world reserves) are the two main ore sources of nickel (Dalvi *et al.*, 2004; Sudol, 2005). Sulphide ores typically have 0.4–2.0 wt.% nickel, while the nickel laterite ore grade varies depending on the deposit profile, location and the weathering conditions but usually contains less than 1 % nickel (Kerfoot, 2000, p41). Nickel can be concentrated pyrometallurgically via oxidative smelting of nickel sulphide in a blast or flash furnace generating nickel matte, followed by several possible refinements to obtain pure nickel metal. It can also be concentrated hydrometallurgically by sulphuric acid leaching (Dyson & Scott, 1976), ammonia leaching (Park *et al.*, 2007; Senaputra *et al.*, 2008), chlorine leaching (Senanayake, 2009), and bioleaching (Watling, 2006), all of which transfer nickel into leachate (Kerfoot, 2000, p45).

The processing options for laterite currently include ammonia leaching of a reduced roast product (de Graaf, 1980; Chander & Sharma, 1981;

Senanayake *et al.*, 2010; Zhai *et al.*, 2010; Zuniga *et al.*, 2010), direct high pressure acid leaching of high grade laterite ores (Whittington & Muir, 2000; Whittington *et al.*, 2003a; Whittington *et al.*, 2003b; Whittington & Johnson, 2005), and assisted by air pressure leaching or heap leaching of low grade laterite ores (McDonald & Whittington, 2008a, b; Agatzini-Leonardou *et al.*, 2009).

Hydrometallurgical concentration of nickel is an energy-efficient process with less exhaust gas emission compared to pyrometallurgical concentration. The hydrometallurgical process control and leachate circulation is also simpler than that of the pyrometallurgical process. Therefore nickel in low grade laterite ores is mainly recovered through the hydrometallurgical process.

1.2 Hydrometallurgical processing of nickel laterite

Nickel laterites are receiving more attention as an important nickel source, and are forming an increasing part of world nickel production due to the large nickel reserves contained in laterite ores and depleting global reserves of nickel sulphide (Singh & Gilkes, 1992; Brand *et al.*, 1998; Gleeson *et al.*, 2003; Dalvi *et al.*, 2004; McDonald & Whittington, 2008a). High pressure acid leaching (HPAL) has been commercialised for higher grade (*e.g.* >1.2 wt.% Ni) laterite ores, with the Canadian-Cuban HPAL operation at Moa Bay in operation for more than 45 years (Sudol, 2005). However, many recent operations commencing in Western Australia have suffered setbacks and been less successful for a range of reasons, including financial and technical deficiencies. These include the Bulong and Cawse operations (suspended), Murrin Murrin (previously Anaconda now Minara, which operates at below name plate capacity), and Ravensthorpe (BHP ceased operations in 2009 but sold the project to First Quantum Minerals who have recommenced production (First Quantum Minerals Ltd., 2011)).

As reserves of higher grade ores are depleted putting lower grade laterite ores through the HPAL process sharply increases the nickel unit cost. Heap leaching technologies thus become more attractive because of their lower capital cost, lower operation and maintenance costs, and less

aggressive leach conditions than HPAL (Taylor, 2007). It should be noted that choosing HPAL or heap leaching methods largely depends on factors ranging from laterite ore grade to nickel market price. Therefore, the introduction of a flexible hybrid route combining both methods may be attractive (Neudorf & Huggins, 2006; Rodriguez & Wedderburn, 2007; Rodriguez, 2008). Column leaching experiments at ambient temperature and pressure are typically used to simulate heap leach conditions prior to embarking on larger scale operations (Agatzini-Leonardou & Dimaki, 1994; Agatzini-Leonardou & Zafiratos, 2004; Elliot *et al.*, 2009; Watling *et al.*, 2011).

1.3 Difficulties with laterite heap leaching in Western Australia

Vast resources of low grade nickel laterites (*i.e.* <0.8 wt.% Ni) in Western Australia are currently uneconomic to process. A major problem for atmospheric heap leaching is that some ores, in particular limonite ores (goethite dominant ores), are often acid resistant leading to low nickel extraction (<50 %) over a time period during which other mineralogically similar ores leach well. As nickel is mainly present in goethite in limonite ores (McDonald & Whittington, 2008a), the goethite reactivity directly affect nickel extraction. The variation in dissolution characteristics between the ores is more obvious at ambient conditions. It is vital to atmospheric and heap leaching technologies to understand these differences. The reason for the extremely diverse nickel extractions of low grade nickel laterite is poorly understood and needs to be further investigated so that leaching rates from all ore types can be improved.

In arid-region laterite ores, nickel is also hosted significantly in nontronite which is an iron-rich smectite clay mineral (Gaudin *et al.*, 2005; McDonald & Whittington, 2008a). Nontronite is not readily quantifiable using full pattern quantitative phase analysis in X-ray diffraction because the phase is often chemically variable, always poorly ordered and not well modelled by the published crystal structure (Scarlett *et al.*, 2008). As a member of the smectite family which are known as swelling clays, nontronite generated from different locations and weathering environments can vary in its chemical composition, with cation substitutions and assorted hydration states causing

variations in its crystal structure. Furthermore, asymmetric non-basal peaks in its X-ray diffraction (XRD) pattern, which are the result of the turbostratic disorder, create problems for line profile fitting and accurate quantitative phase analysis (Moore & Reynolds, 1997, p340). For hydrated nontronite there is no sensible crystallographic information file available in common crystallographic structure databases and without a known structure it is difficult to quantify a phase by the well-developed Rietveld quantitative phase analysis method (Hill & Howard, 1987; Bish & Howard, 1988; O'Connor & Raven, 1988). Hence nontronite is to date the most poorly quantified phase in laterite ores.

1.4 Research proposal

The depletion of nickel sulphide ores along with the substantial reserves of nickel laterite ore available in Western Australia suggest that research to understand these complex lateritic ores that might enable improved recoveries at lower costs would be beneficial.

The research aim of this project is to characterise various natural goethites in Western Australian laterite ores, including crystal morphology, particle dimensions, and degree of substitution of guest metals. In order to develop greater understanding of the properties that impact upon heap leach behaviour, this study will employ micro crystallographic analytical techniques including synchrotron and laboratory X-ray diffraction, transmission electron microscopy and energy dispersive X-ray analysis.

An additional aim of the research is to improve the accuracy of the quantitative XRD analysis for the turbostratically disordered nontronite present in nickel laterite ores.

1.5 Research flow chart

A schematic description of the research program is presented in Figure 1-2. Preliminary column leaching results (conducted by staff in CSIRO Process Science and Engineering, Waterford laboratory) showed that the leaching extractions of limonitic laterite ores in Western Australia vary

dramatically. Detailed ore characterisation, including XRD phase analysis and TEM imaging were conducted for each selected ore.

During the quantitative phase analysis of nontronite rich ores, the lack of a crystal structure model for turbostratically disordered nontronite hindered this characterisation technique. Two calibration based methods, the PONKCS model and the supercell model were developed to quantify the nontronite in nickel laterite ores accurately. The correlation between the ore mineralogy and the leaching rate was then conducted. These findings were verified and further explored by direct TEM imaging and EDS mapping. Factors affecting ore leaching rate were then discussed. A pre-treatment step was proposed and a verification experiment was conducted to test its effect on acid leaching performance.

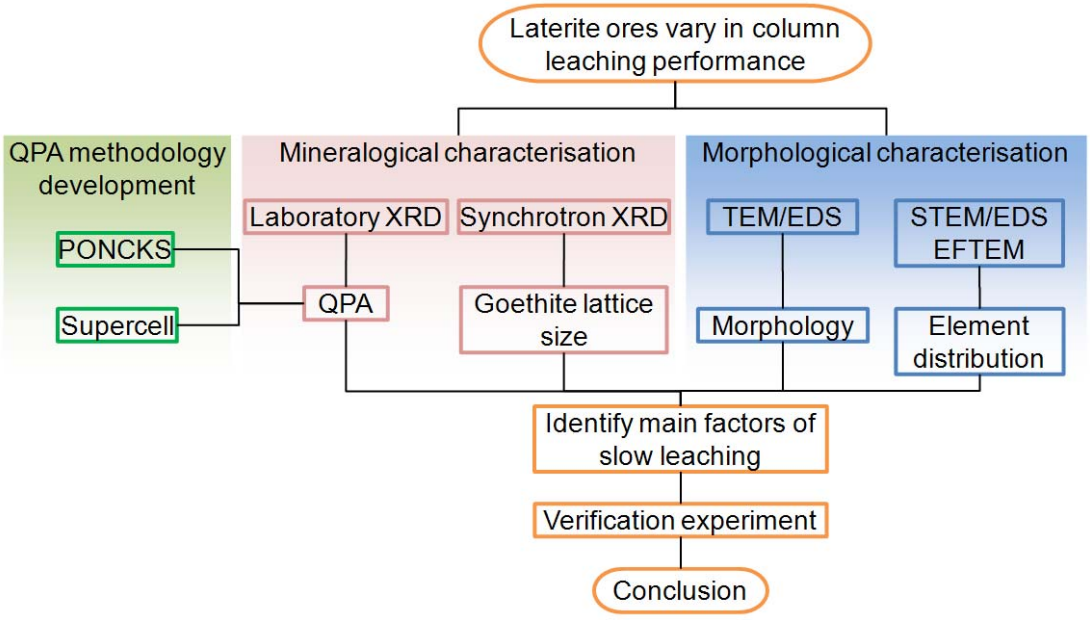

Figure 1-2 Schematic detailing the work flow used during this project

1.6 Thesis organisation

A conventional thesis format has been used. Chapter 2 presents a literature review of nickel laterite ores, pure and substituted goethite (main phase of limonite type laterite), and common heterogenetic dissolution kinetics models. Chapter 3 details the experimental methods and equipment used to characterise ore samples and test their leaching performance.

Chapter 4 and Chapter 5 describe the methodology development of quantitative phase analysis of turbostratically disordered nontronite by using the PONKCS model and the supercell model, respectively.

Chapter 6 contains column leaching rate calculation for all the laterite ore samples studied in this thesis. Their mineralogical compositions and the goethite lattice parameters are also analysed based on their XRD patterns. The averaged metal substitution levels in goethite of these samples are determined from TEM/EDS analysis. A discussion between their leaching rates, their ore mineralogy, and their metal substitution levels is presented.

Chapter 7 present the typical goethite morphologies in samples selected from Chapter 6 with different leaching rates. The details of an accelerated atmospheric leaching experiment for selected ore samples are presented with their TEM imaging and EDS analysis. A new mechanism for the ores leaching performance variation is proposed.

Chapter 8 describes an experiment developed to verify the mechanism proposed in Chapter 7 to enhance the acid leaching rate of the acid-resistant laterite ores.

Chapter 9 contains conclusions made in this study and suggestions for future research.

As this project is linked to a previous project between CSIRO and a commercial partner, the geographical and geological information of the laterite ore samples studied in this thesis and their column leaching data discussed in Chapter 6 cannot be fully disclosed according to the project contract. However, the analysis based on the column leaching data generated within this study will be fully presented.

Chapter 2 Literature review

2.1 Introduction

The currently used leaching technologies and test work required for low grade nickel laterite ores are briefly introduced followed by a review of the literature concerning the mineralogy of nickel laterite ores. Emphasis is given to nontronite and goethite which are the main nickel containing phases in the nickel laterite ores discussed in this thesis. As nontronite is much easier to dissolve with sulphuric acid than goethite, and does not suffer widely variable leaching properties, only the goethite dissolution properties are reviewed. The review of goethite includes details of the different morphologies and their associated dissolution properties and the influence of these properties by elemental substitution. The review of nontronite will focus on the difficulty of characterising this phase by XRD and recent progress in overcoming this limitation.

2.2 Acid Leaching of Laterite Ores

High Pressure Acid Leaching (HPAL) is currently used for all large laterite leaching projects. This process involves dissolving nickel containing minerals with sulphuric acid in an autoclave at high temperature (240–270 °C) and high pressure (3400–5400 kPa) (Georgiou & Papangelakis, 1998; Whittington & Muir, 2000; Dalvi *et al.*, 2004). HPAL provides harsh leaching conditions for laterite ores and is relatively insensitive to ore mineralogy. The main impurity ions, Fe^{3+} and Al^{3+}, in the leachate are rejected as hematite (Eq. 2-1) and jarosite/alunite (Eq. 2-2) in the autoclave and regenerate sulphuric acid for reuse (Dutrizac & Jambor, 2000; Whittington *et al.*, 2003b):

$$2Fe^{3+} + 3H_2O \rightarrow Fe_2O_3\downarrow + 6H^+ \qquad \text{Eq. 2-1}$$

$$3G^{3+} + 2SO_4^{2-} + D^+ + 6H_2O \rightarrow DG_3(SO_4)_2(OH)_6\downarrow + 6H^+ \qquad \text{Eq. 2-2}$$

Where D = H_3O^+, Na^+, and K^+; G = Fe^{3+} and Al^{3+}

However, the hydrolysis of jarosite/alunite waste would release acid and pose environmental issues of acid mine drainage, if not handled properly:

$$DG_3(SO_4)_2(OH)_6 + 3H_2O \rightarrow 3G(OH)_3 + D^+ + 3H^+ + 2SO_4^{2-} \qquad \text{Eq. 2-3}$$

The recent shift in focus from HPAL to Atmospheric Leaching (AL) is largely due to cost considerations. AL involves leaching laterite ores in large tanks with constant agitation to keep solids in suspension and improve solid/liquid contact at ambient or elevated temperatures (< 100 °C). As there is no need for an autoclave the capital and maintenance expenses are significantly reduced. AL can be used as a complementary leaching technology to HPAL. AL is exposed to acid price rises as it requires more concentrated acid to be effective. This is because the acidity of sulphuric acid is the main driving force to dissolve nickel containing minerals in AL and no acid is recovered during the process (Agatzini-Leonardou & Zafiratos, 2004; Arroyo & Neudorf, 2004; Taylor, 2009).

When a lower grade nickel laterite ore is mined, Heap Leaching (HL) is preferred due to its relatively low capital expense. HL is more suitable for small and medium size projects and can serve as a satellite leaching process (or Brownfield development) for a HPAL facility. This approach has been adopted at the Murrin Murrin laterite deposit (Minara Resources Ltd.), Western Australia. However, HL generally has lower nickel extraction, and slower leaching kinetics than HPAL and AL. The efficiency of HL is also largely sensitive to climatic conditions and ore mineralogy (Taylor, 2009; Watling *et al.*, 2011). The leachate from HL, like AL, contains higher levels of iron, which cannot be automatically removed as jarosite, as in HPAL, and requires an additional iron rejection step. Despite these issues, HL is still an attractive technology for nickel extraction from low grade laterites (McDonald & Whittington, 2008a; Wedderburn, 2009, 2010).

2.3 Test work before scaling up to heap leaching

The test work needed prior to setting up a heap leaching plant can be classified into two main areas; the ore leachability and the physical performance of the heap. The former includes the impact of different ore mineralogy on the ore extractive metallurgy, while the latter is mainly concerned with the determination of a range of processing parameters such as particle size distribution, agglomerate strength, heap height etc. (Robertson & van Staden, 2009; Steemson & Smith, 2009).

A bottle roll experiment is usually employed to investigate the leaching performance of an ore, including the maximum achievable extraction and acid consumption. Detailed studies of changes in mineral morphology and phase transformations could be performed at this stage by using a number of characterisation techniques including electron microscopy, X-ray fluorescence spectroscopy and X-ray diffraction (Robertson & van Staden, 2009).

The next experimental stage is column leaching, which simulates the static leaching conditions encountered in heap leaching. The minerals' dissolution kinetics and metal extraction rates can be determined at this stage. A number of leaching considerations, including lixiviant choice, agglomeration parameters, irrigation rate, leachate circulation, and column permeability can be investigated at this stage (Elliot *et al.*, 2009).

If results from the previous stages are promising then a pilot heap leaching plant can be constructed and operated in closed cycle mode using the optimised conditions obtained from column leaching. After validating column leaching results, the processing parameters need to be determined for high-volume production. At this stage assessment of local climatic conditions, heap stability and percolation conditions can be performed before commercial heaps are constructed (van Staden *et al.*, 2009).

2.4 Laterite mineralogy and nickel containing phases

Laterite was named from the Latin word "later" meaning literally "brick" by Dr. Francis Buchanan-Hamilton as brick making was a traditional use for the material. He first described laterite formations in southern India in the early 19th century (Thurston, 1913). The word "laterite" has been used for variably cemented sesquioxide rich soil horizons. It has also been used for any reddish regolith (Helgren & Butzer, 1977).

Laterite in this thesis refers to the upper soil horizon of intensely weathered regolith often found in tropical climates which are rich in iron oxide and poor in silica, while nickel laterite refers to a regolith that contains economically exploitable concentrations of nickel (Gleeson *et al.*, 2003). The nickel content in laterite is relatively low compared to the major element iron.

Other examples of economically exploitable laterites include gold deposits and bauxites (Freyssinet *et al.*, 2005). Laterite covers are thick on the stable areas of the African Shield, the South American Shield, the Australian Shield, and the Indian Shield. Basement rocks are buried under the thick weathered layer and rarely exposed (Tardy, 1997).

Nickel laterites occur in zones of the earth that have experienced prolonged weathering, including rain and ground water leaching of ultramafic dunite or peridotite associated with a variety of geological settings spanning the Precambrian to the Tertiary (Freyssinet *et al.*, 2005). Ultramafic rocks are comprised of dunite, peridotite, pyroxenite, hornblendite, and serpentinite. Serpentine is the most common product of serpentinisation (geological hydrothermal alteration) of olivine in dunite or peridotite. During this process some of the nickel is mobile in solution and some remains in the serpentine, or combines with magnetite, a co-product of serpentinisation (Dalvi *et al.*, 2004). Serpentinisation of protolith helps the weathering of laterite (Brand *et al.*, 1998).

Compared to nickel sulphides, which are generally found hundreds of metres below the surface, nickel laterite deposits typically occur in surface layers from 0 to 40 m in depth (Freyssinet *et al.*, 2005; Sudol, 2005; Agatzini-Leonardou *et al.*, 2009). As shown in Figure 2-1, the laterite profile can be divided into five zones from the surface downwards, pedolith (ferriecrete), limonite, transition (smectite), saprolite, and bedrock (peridotite) (Li, 1999; Crundwell *et al.*, 2011). The transition zone may be missing in some humid geological profiles. Generally the nickel rich minerals are present beneath the ferricrete or pedolith zone and above the peridotite zone, as shown in Figure 2-1. The typical minerals present in nickel laterite are iron oxides, silicates including clay minerals, manganese oxides, and other parent rocks, details of which were summarised recently by Senanayake *et al.* (2011).

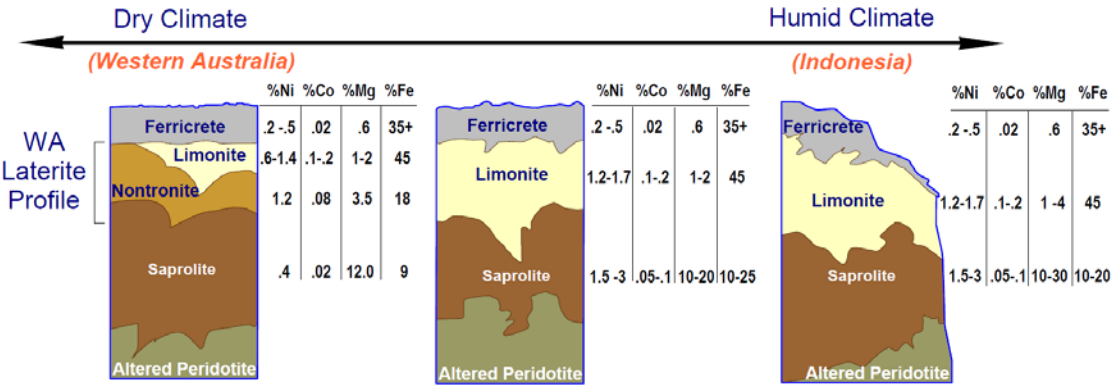

Figure 2-1 Common laterite profiles of dry and wet climate region. (adapted from Dalvi *et al.* (2004))

Laterite profiles also vary significantly from site to site (Elias *et al.*, 1981; Brand *et al.*, 1998; Gleeson *et al.*, 2003; Freyssinet *et al.*, 2005). In terms of their geological formation ages, normally older dry laterites contain lower nickel levels and higher clay contents, and are found in Greece, Albania, and Western Australia. Younger tropical wet deposits with higher nickel and iron oxide contents are found in Cuba, Indonesia and New Caledonia (Whittington & Muir, 2000; Sudol, 2005; Agatzini-Leonardou *et al.*, 2009). The goethite content in laterite profiles from equatorial Cameroon are high both in the topsoil and the deep saprolite layer; while the hematite content increases with depth (Boudeulle & Muller, 1988). Nickel and cobalt were reported to be rich in maghemite, lizardite, and goethite in Yuanjiang laterite deposit in China (Liu *et al.*, 2009; Liu *et al.*, 2010a; Liu *et al.*, 2010b). Nickel was found to be associated with phyllomanganate, goethite, and lizardite in laterite deposits in the Philippines (Fan & Gerson, 2011).

Based on the mineralogy of the main nickel host mineral, nickel laterite ores can be classified into three types: 1) the oxide type, which is dominated by goethite and occasionally manganese oxide in the shallow limonite zone; 2) the clay type, which contains nontronite and saponite in the intermediate smectite zone; 3) the silicate type, which is dominated by saprolite, garnierite and serpentine minerals, like lizardite, antigorite, and greenalite, in the deeper saprolite zone, as shown in Figure 2-1 (a). This laterite classification is widely agreed upon among researchers (Brand *et al.*, 1998; Gleeson *et al.*, 2003; Freyssinet *et al.*, 2005).

In Western Australian nickel laterite profile (Figure 2-1) and more specifically in the nickel laterite profile of the Bulong Complex (Figure 2-2), the transition clay zone (nontronite) contains the highest amounts of nickel, cobalt, and manganese with relatively lower levels of iron than the limonite zone and lower levels of magnesium than the saprolite zone. Thus leaching of the transition zone will result in relatively low amounts of iron and magnesium in the leachate making this zone an economically exploitable deposit (Duyvesteyn *et al.*, 2001). The iron can be partially precipitated out as jarosite returning acid to the HPAL circuit but magnesium stays in solution consuming acid.

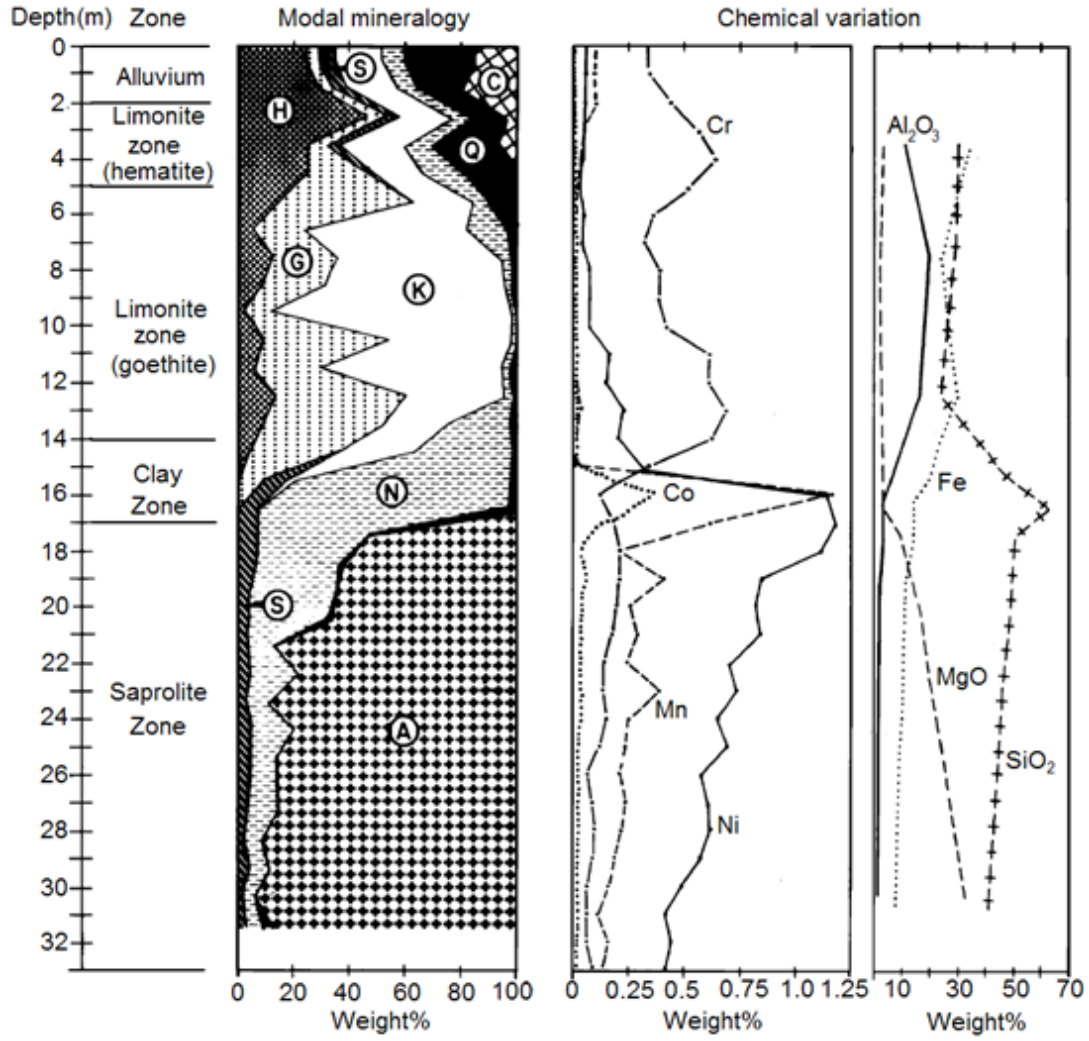

Figure 2-2 Typical mineralogical and chemical profile through the Bulong Laterite Complex in Western Australia. A=antigorite, C=calcite and dolomite, G=goethite, H=hematite, K=kaolin, N=nontronite, Q=quartz, S=spinel (magnetite, chromite and maghemite) (Elias *et al.*, 1981).

2.5 Nontronite

Studies of the high-pressure acid leaching and heap leaching behaviours of nickel laterites are hindered by the inability to quantify nontronite (Scarlett *et al.*, 2008; Elliot *et al.*, 2009). Although it is well known that nontronite is a nickel-bearing mineral in clay type laterite, this phase is not readily quantifiable using the conventional Rietveld full pattern modelling with XRD data because the phase is often poorly ordered and chemically different from published crystal structure data (Gates *et al.*, 2002; Drits *et al.*, 2006).

Nontronite is an iron rich member of the smectite group of clay minerals. The smectite group includes dioctahedral smectites *e.g.* montmorillonite and nontronite, as well as trioctahedral smectites *e.g.* saponite. Figure 2-3 outlines the position of clay minerals in silicate minerals classification. Nesse (2000, p253) also regards the serpentine and chlorite groups as clay minerals. Clay minerals refer to “phyllosilicate minerals and minerals which impart plasticity to clay and which harden upon drying or firing” (Guggenheim *et al.*, 2006).

2.5.1 Structure of phyllosilicate

The structures of phyllosilicate minerals include layers containing tetrahedral and octahedral sheets with 1:1 (Tetrahedral-Octahedral) or 2:1 ratio (Tetrahedral-Octahedral-Tetrahedral sandwich structure). These layers are stacked one on top of another and bonded together either by Van der Waals forces, by interlayer cations, or by another octahedral layer to form the repeating unit structure of the mineral. These three cases are denoted as “TOT”, “TOT-c”, and “TOT-O” structures respectively in Figure 2-3. The latter two cases occur when the layers are negatively charged as a result of substitution of cations with lower valence.

The tetrahedral sheet contains a mesh of six-fold rings made of corner-linked [TO_4] tetrahedra where T could be Si^{4+}, Al^{3+}, and occasionally Fe^{3+} (Figure 2-4 (a)). In order to fit to their corresponding octahedral sheets, the tetrahedra are usually non-regular and normally rotated (within ±30°) around the axis perpendicular to the projected plane shown in Figure 2-4 (a), leading to a non-regular hexagon in the six-fold ring (Moore & Reynolds, 1997, p110).

It's also not uncommon for the tetrahedrons to be tilted with respect to the projected plane. The three basal O^{2-} of $[TO_4]$ tetrahedra are shared by neighbouring tetrahedra; the apical O^{2-} are shared with $[MO_6]$ octahedra in the octahedral sheets to form the TOT layer, where octahedral metal ion M could be Al^{3+}, Fe^{3+}, Mg^{2+} or other transition metal ions. The misfit of the tetrahedral and octahedral sheets and resulting internal stress contribute to the small grain size of clay minerals (Nesse, 2000, p235).

Octahedral sheets consist of two planes of close packing OH^- anions. The octahedral interstices formed from this close packing are normally occupied by trivalent cations to form a dioctahedral sheet *e.g.* gibbsite configuration $Al_2(OH)_6$ (Figure 2-4 (b)) or divalent cations to form a trioctahedral sheet *e.g.* brucite configuration $Mg_3(OH)_6$ (Figure 2-4 (c)). The total cation charge of +6 is the same in both cases and electrical neutrality is achieved on both dioctahedral and trioctahedral sheets (Nesse, 2000, p235). The trioctahedral sheet is formed with edge-linked regular octahedra since all the octahedral sites are the same. However, the octahedra in the dioctahedral sheet are distorted as the vacant octahedral site does not contribute to the Al-O ionic bond therefore the vacant octahedra are larger.

The attachment of tetrahedral sheets to octahedral sheets is conceptually accomplished by replacing the OH^- of the octahedral sheet with the apical O^{2-} of the tetrahedral sheet. Four out of six OH^- of the octahedra in the TOT layer are replaced by tetrahedral O^{2-}, leaving only two OH^- anions (also referred as hydroxyl). The positions of these hydroxyls define the *trans*-octahedral site (two hydroxyls located in the opposite position) and *cis*-octahedral site (two hydroxyls located on one side) (Tsipursky & Drits, 1984; Moore & Reynolds, 1997, p107). There are two configurations of TOT layer: *trans-vacant* and *cis-vacant*, as shown in Figure 2-5, which have been further discussed by Drits *et al.* (2006). Phyllosilicate with a *trans-vacant* TOT layer has a symmetry plane (010) hence is usually described by the monoclinic space group No. 12 (*C*12/*m*1); phyllosilicate with a *cis-vacant* TOT layer does not have any symmetry plane hence is normally described by the monoclinic space group No. 5 (*C*121).

Silicates	Nesosilicates (Orthosilicate)	Garnet group	$A_3E_2(SiO_4)_3$ A= Ca, Fe, Mg, Mn E= Al, Cr, Fe, Mn					
		Olivine	$(Mg,Fe)_2SiO_4$					
		…						
	Sorosilicate (Disilicate)	Epidote group	$Ca_2Al_2(Fe^{3+},Al)OOH(SiO_4)(Si_2O_7)$					
		…						
	Cyclosilicate (Ring Silicate)	Tourmaline	$NaA_3Al_6[Si_6O_{18}](BO_3)_3E_4$ A=Mg,Fe,Li,Al E=O,OH,F					
		…						
	Inosilicates (Chain Silicate)	Orthopyroxene	$(Mg,Fe)_2Si_2O_6$					
		…						
	Phyllosilicates (Layer silicate)	1:1 layer silicate	Serpentine group (trioctahedra, uncharged)		Serpentine	$(Mg,Fe)_3Si_2O_5(OH)_4$		
					Lizardite	$Mg_3Si_2O_5(OH)_4$		
					…			
			Kaolinite group (dioctahedra, uncharged)		kaolinite	$Al_2Si_2O_5(OH)_4$	dickite	nacrite …
					Halloysite	$Al_2Si_2O_5(OH)_4 \cdot 2H_2O$		
		2:1 layer silicate	TOT structure	Talc		$Mg_3Si_4O_{10}(OH)_2$		
				Pyrophyllite		$Al_2(Si_4O_{10})(OH)_2$		
			TOT+c structure	Smectite group (low layer charge)	Nontronite	$Na_{0.3}(Al,Fe)_2(Si,Al,Fe)_4O_{10}(OH)_2 \cdot nH_2O$		
					Montmorillonite	$(Na,Ca)_{0.3}(Al,Mg)_2Si_4O_{10}(OH)_2 \cdot nH_2O$		
					Saponite	$(½Ca,Na)_{0.33}(Mg,Fe)_3(Si,Al)_4O_{10}(OH)_2 \cdot 4H_2O$		
				Illite group (high layer charge)	Illite	$(K,H_3O)(Al,Mg,Fe)_2(Si,Al)_4O_{10}[(OH)_2,(H_2O)]$		
					glauconite	$(K,Na)(Fe,Al,Mg)_2(Si,Al)_4O_{10}(OH)_2$		
					celadonite	$K(Mg,Fe)(Fe,Al)[Si_4O_{10}](OH)_2$		
				Vermiculite		$(Mg,Fe,Al)_3(Al,Si)_4O_{10}(OH)_2 \cdot 4(H_2O)$		
			TOT+O structure	Chlorite group	Chlorite	$(Fe,Mg,Al)_3(Si,Al)_4O_{10}(OH)_2 \cdot (Fe,Mg,Al)_3(OH)_6$		
					Clinochlore	$(Mg,Fe)_2Al(Si_3Al)O_{10}(OH)_2 \cdot (Fe,Mg)_3(OH)_6$		
			TOT+c structure	Mica group	Muscovite	$KAl_2(AlSi_3O_{10})(F,OH)_2$		
				Biotite sub group	Annite	$KFe_3AlSi_3O_{10}(OH)_2$		
					Phlogopite	$KMg_3AlSi_3O_{10}(OH)_2$		
	Tectosilicates (Framework silicate)	Feldspar	Anorthite	$CaAl_2Si_2O_8$				
			Orthoclase	$KAlSi_3O_8$				
			Albite	$NaAlSi_3O_8$				
			Microcline	$KAlSi_3O_8$				

Figure 2-3 The position of nontronite in silicate minerals classification (Nesse, 2000; Guggenheim *et al.*, 2006; Klein *et al.*, 2008). The highlighted minerals are clay minerals. The “TOT”, “TOT+c”, and “TOT+O” indicate the interlayer as none, cations, and hydroxide sheet.

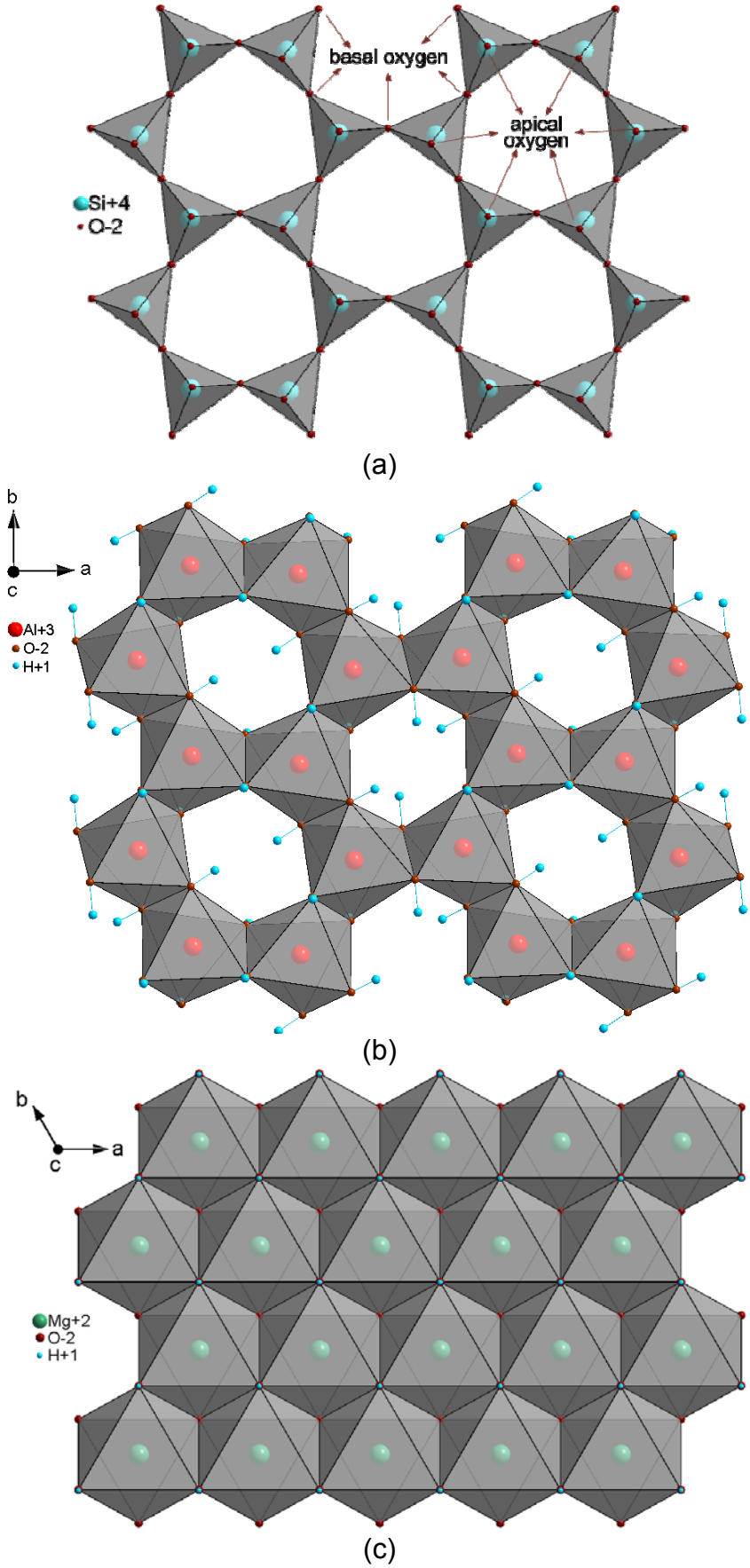

Figure 2-4 Structures of (a) tetrahedral sheet, (b) dioctahedral sheet (gibbsite ICSD# 6162 configuration), (c) trioctahedral sheet (brucite ICSD# 95475 configuration).

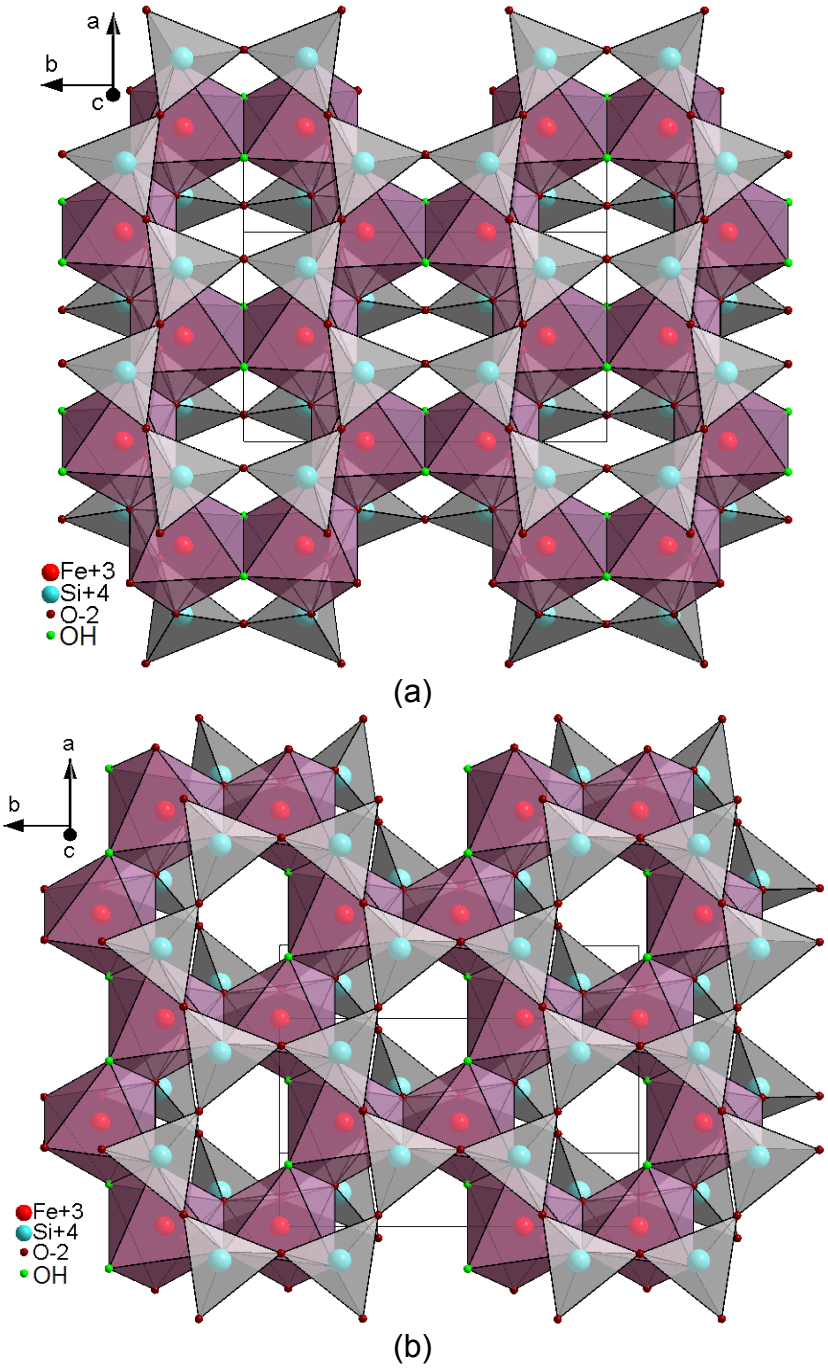

Figure 2-5 Two configurations of TOT layer of (a) trans-vacant and (b) cis-vacant. The projected plane is the a-b plane. The octahedral hydroxyls are highlighted in green. The atom coordinates published by Tsipursky and Drits (1984) were used for this figure.

2.5.2 Turbostratic disorder

Stacking disorder of clay minerals, including rotations and translations of one TOT layer with respect to another, usually occurs at the connection between layers. The systematic rotation (normally 120°) is preferred for clay

minerals with higher charge as the rotated $(\bar{1}31)$ plane coincides with the (200) plane after 120° rotation, providing the lattice upholds the relationship given by Eq. 2-4, which is not uncommon for clay minerals. With this relationship the d-spacing of the $(\bar{2}01)$ plane equals the d-spacing of (130) plane.

$$\mathrm{b} = \mathrm{a}\sqrt{3};\ \ \mathrm{c} * \cos\beta = -\mathrm{a}/3 \qquad \text{Eq. 2-4}$$

here *a*, *b, c* and *β* are unit cell parameters.

The reflections generated from the *hkl* planes mentioned above are not affected by systematic rotation reflections in the XRD pattern (Moore & Reynolds, 1997, p344). The stacking pattern of systematic rotations result in different polytypes of the same layer, such as 1*M*, 2*O*, 2M_1, 3*T etc.* which are detailed in mineralogy textbooks (Klein *et al.*, 2008).

Turbostratic disorder (Figure 2-6) is an unsystematic (random) rotation and translation of the layers and generally occurs for clay minerals with low layer charge (weaker bonds), such as smectite. This figure is exaggerated; in reality a few hundred angstrom translation or half degree rotation is sufficient to produce fully turbostratic diffraction. The 00*l* reflections are not affected as the layers are perfectly parallel to one another. The *hk*0 reflections are affected as the layers are optically incoherent (Moore & Reynolds, 1997, p336), *i.e.* the *hk*0 plane of each layer is normal to different directions (Figure 2-6). Turbostratic disorder effectively turns the mineral into a two-dimensional crystallite, as the periodicity along the *c*-axis is destroyed.

As the small crystallite size in the z-direction (normal to the *a*-*b* plane) of turbostratically disordered clay minerals approaches a single unit cell dimension, the reciprocal space spots become rods along the z*-axis, as Figure 2-7 shows (the shape of spots is the reciprocal of the crystal shape). As the increasing reciprocal vector d* cuts the *hk* rod, the intensity of diffracted beam (represented by the sectional area) increases sharply and decreases slowly, resulting in an asymmetrical non-basal diffraction band.

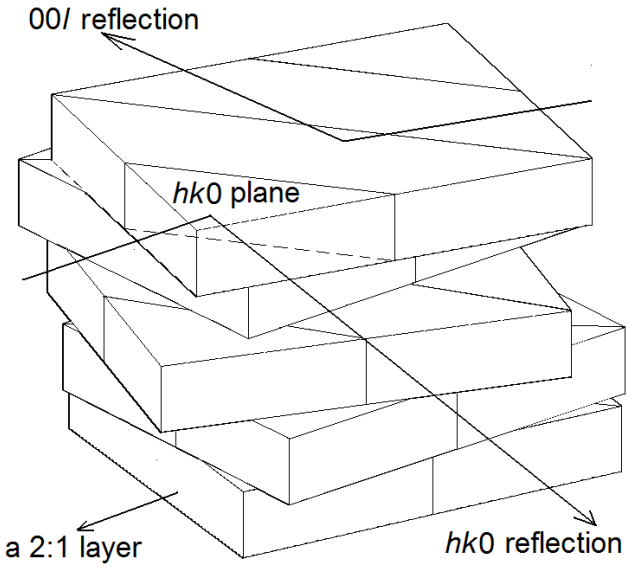

Figure 2-6 Schematic figure of turbostratically disordered 2:1 TOT layer, adapted from Moore & Reynolds (1997, p336).

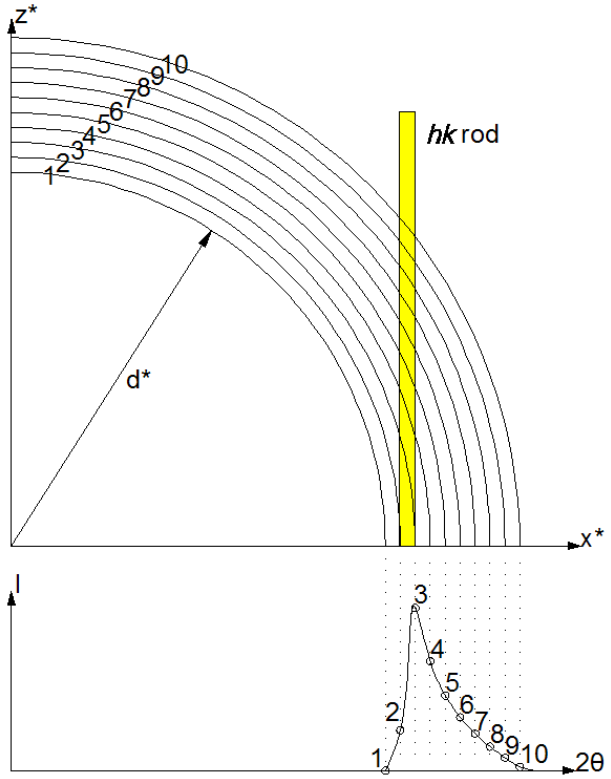

Figure 2-7 The increasing d* spheres in reciprocal space cutting the hk rod causing a asymmetric two-dimensional diffraction band in the XRD pattern, adopted from Moore & Reynolds (1997, p337).

2.5.3 Modelling the nontronite XRD pattern

Both natural and synthetic nontronite are always associated with turbostratic disorder (Gates *et al.*, 2002; Decarreau *et al.*, 2008). As the particles' habit is a small platy morphology, the Coherent Scattering Domain (CSD) size of nontronite in the z-direction is extremely small (Gaudin *et al.*, 2004; Laird, 2006). Therefore, the XRD patterns of nontronite not only demonstrate asymmetric non-basal diffraction bands but also show anisotropic size broadening. The hydration state of nontronite can be double layer hydrated, single layer hydrated, totally dehydrated, or a mixture of these states (Dekov *et al.*, 2007; Scarlett *et al.*, 2011). Conventional full pattern Rietveld refinement assumes crystalline phases have a three dimensional unit cell. It cannot fit the patterns of turbostratically disordered nontronite, which is in the form of two dimensional crystallites.

Taylor and Matulis (1994) described a QPA approach for montmorillonite by calibrating its structure factors from standard mixtures in the Rietveld program SIROQUANT (Taylor, 1991). Bonetto *et al.* (2003) applied a similar approach in FULLPROF (Rodríguez-Carvajal, 1993). Scarlett and Madsen (2006) developed an approach (later called the PONKCS method) which is suitable for quantifying phases with Partial Or No Known Crystal Structure using the Bruker® TOPAS symbolic computation system (Coelho *et al.*, 2011). The method includes two steps: 1) fit the XRD pattern of the unknown phase with either a lattice model (*hkl_ls*) or peaks phase model (*xo_ls*) as well as possible without scaling, since these models have fewer crystallographic constraints than that of structure models (*str*) and are more easily adjusted to match the experimental pattern; 2) use the Rietveld quantification equation to calibrate the ZMV factor (product of unit cell mass and volume) of the unknown phase model built in step 1 from a standard mixture pattern (or preferably multiple standard mixture patterns) of the unknown phase and an internal standard with known weight ratio.

Ufer *et al.* (2004) created a more physically based supercell model to describe the nature of the asymmetric non-basal diffraction bands. To stay compatible with the usual Rietveld modelling, the aperiodic structure along the stacking direction is modelled by a periodic supercell with the *c*-axis

length about 9 times longer. The approach calculates the non-basal reflections from the supercell but calculates the basal reflections with a subcell. Ufer *et al.* (2008) later demonstrated the viability of this approach by confirming the accuracy of a quantitative analysis of nontronite rich bentonite samples using this model.

2.6 Goethite

2.6.1 Importance of goethite leachability

In hydrometallurgy, the efficiency of an extraction process depends upon the ore leachability. The extraction of a substituted element is often controlled by the host mineral's structure (Kumar *et al.*, 1993; Cornell & Schwertmann, 1996, p267). Understanding the occurrence mode of guest elements[2] is important for predicting their leaching rate. The leachability of guest elements follows the sequence: sorption > occlusion or intergrowth > structural substitution (Kumar *et al.*, 1990). A number of researchers have reported that in laterites nickel associates with the goethite phase (Georgiou & Papangelakis, 1998; Beukes *et al.*, 2000). Nickel has been found to substitute for iron in the goethite crystal structure in oxide laterite ores (Trolard *et al.*, 1995; Georgiou & Papangelakis, 1998; Beukes *et al.*, 2000; Manceau *et al.*, 2000; Gleeson *et al.*, 2003; Yongue-Fouateu *et al.*, 2006). The leaching of nickel from goethite therefore requires complete dissolution of this phase. Consequently, the extraction of nickel from limonitic ores is highly dependent upon goethite leachability. Unfortunately, natural samples of goethite show very diverse leachabilities (Schwertmann, 1991). Reviews of previous findings in this area suggest goethite's crystal structure, crystallinity, isomorphous substitution, microscopic morphology, and other materials it is associated with all contribute towards determining its leachability and these are reviewed below. Investigating the relationship between these aspects and the goethite dissolution characteristics is crucial to understanding Western Australian laterite heap leaching performance.

[2] The guest elements can exist on a host phase in three different modes: sorption as another phase, occlusion or intergrowth with the host phase, or structural substitution into the crystal structure of the host phase (Kumar *et al.*, 1990).

2.6.2 Goethite crystal structure

In earlier literature, the goethite (α-FeOOH) crystal structure has been described using both the space group No. 62 non-standard Pbnm and standard Pnma settings. Pnma is related to Pbnm by switching axes (*a*, *b*, *c*) to (*c'*, *a'*, *b'*) using the axes-rotation transformation, as shown in Figure 2-8. The Pnma setting for the goethite crystal structure was reported as early as 1963 (Inouye *et al.*, 1972). However, most of the literature concerning goethite including the ICDD PDF-4+2011 database (new primary PDF card 04-015-2895) has used the Pbnm crystal axis configuration. For the Pbnm setting, the long axis of the acicular goethite is known as the [001] direction (c-axis positive direction). To remain consistent with the bulk of the available literature, the Pbnm setting was chosen to describe the goethite lattice in this thesis and in the following discussions of the literature care has been taken to convert data to the Pbnm space group where appropriate so that correct comparisons can be made.

Goethite is isostructural with diaspore (α-AlOOH) and has an orthorhombic unit cell with a = 4.5979(2) Å, b = 9.9510(5) Å, c = 3.0178(1) Å in the Pbnm space group (245057-ICSD). The lattice parameters for pure goethite reported by different researchers and PDF entries are the same within 1 % (Inouye *et al.*, 1972; Goss, 1987; Cornell & Schwertmann, 1996, p14, p26; Barthelmy, 1997-2009). As shown in Figure 2-8, anions O^{2-} and OH^{-} are hcp (hexagonal close packed) stacked upright along the [100] direction with half of the octahedral interstices occupied by Fe^{3+} cations. These cations fill the double rows separated by double empty rows along the [001] direction in each layer, creating tunnels along the c-axis (Cornell & Schwertmann, 1996). The hydrogen bonds are also shown as dashed lines in Figure 2-8.

Goethite is easily dehydrated and transforms to hematite when it is heated above 220°C (Walter *et al.*, 2001). The stoichiometric water in the goethite structure is approximately 10.1 wt.%, although many TG-DTA results show higher weight losses indicating the presence of non-structural water often adsorbs on goethite samples. The thermal phase change of natural goethite has been extensively studied and laterite pre-roasting has been

proven to be an effective way of increasing its acid dissolution rate although the process is energy intensive (Landers & Gilkes, 2007; Landers *et al.*, 2009a, b; Landers, 2010; Landers *et al.*, 2011). The most important feature of the goethite structure for acid dissolution is the position of the surface hydroxyl, which reacts with protons, according to the surface coordination model. There are three different hydroxyl sites as described by Russell *et al.* (1974), which are marked as 'A', 'B' and 'C' in Figure 2-8. 'A' and 'C' site hydroxyls arise from protonation, while 'B' represents structural hydroxyl. Only the 'A' site hydroxyls of these three types coordinate to a single ferric ion and can form hydrogen bonds with each other. Casey *et al.* (1996) described the detail of the Fe octahedron detachment (part of the dissolution process) according to the classification of surface hydroxyls with respect to their coordinated ferric ions and provided a hypothesis linking the dissolution rate order with iron valence.

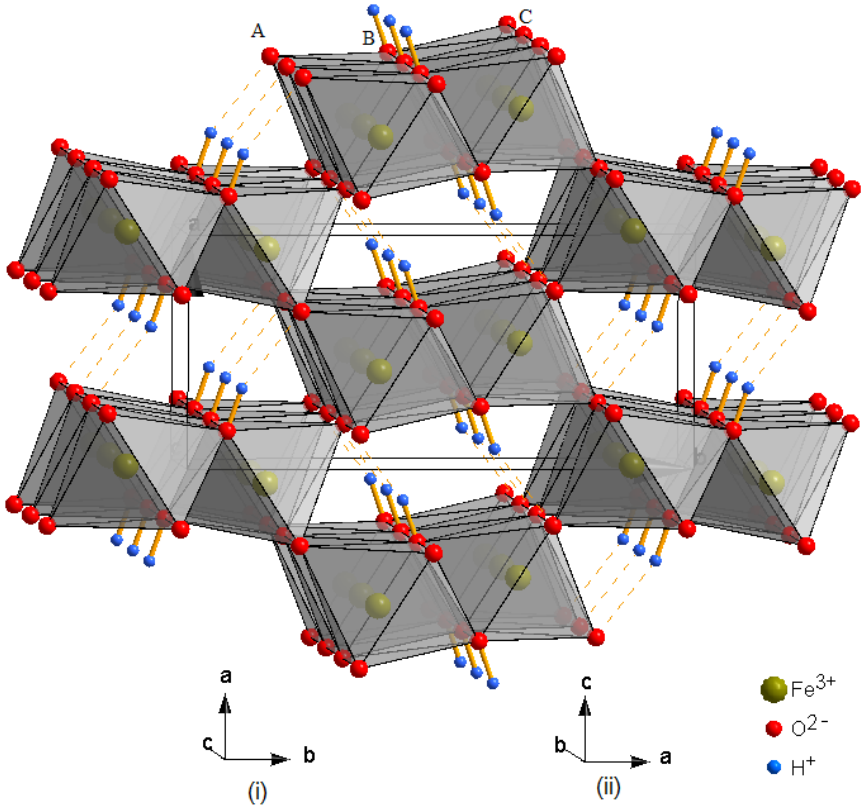

Figure 2-8. Goethite crystal structure drawn from crystallographic information file FIZ-ICSD 245057 shows the double $[FeO_3(OH)_3]$ octahedral chains along the direction perpendicular to the paper plane and the three different hydroxyl sites: A, B, C (Russell *et al.*, 1974) in (i) space group Pbnm and (ii) space group Pnma.

2.6.3 Goethite morphology

Goethite displays several morphologies; the acicular, also known as the lath shape, is by far the most common but it can be associated with others including twinned crystals, hexagons, bipyramids, cubes and thin rods within the same sample (Cornell & Schwertmann, 1996). Twinned crystals possessing further morphologies of; cruciform, star, chunky, dendritic and incomplete twins as well as contact twins have been observed in TEM studies (Atkinson *et al.*, 1968; Cornell *et al.*, 1974; Sidhu *et al.*, 1981; Cornell *et al.*, 1983; Schwertmann & Murad, 1983; van der Woude *et al.*, 1984; Cornell & Giovanoli, 1985; Schwertmann *et al.*, 1985; Cornell & Giovanoli, 1986; Cornell & Schwertmann, 1996, p60-70).

The dimensions of synthetic goethite crystals depend on the conditions of the parent solution these are formed in. The length of acicular goethite has been observed to range from 0.05 μm to 2.5 μm, with widths from 0.01 μm to 0.2 μm. Usually acicular crystals and twinned crystals are present together, with twinned crystals usually 2-4 times larger than the former but in lesser quantities, as twin nuclei occur less frequently than acicular nuclei (Atkinson *et al.*, 1968; Cornell *et al.*, 1974; Sidhu *et al.*, 1981; Cornell *et al.*, 1983; Schwertmann & Murad, 1983; Cornell & Giovanoli, 1985; Schwertmann *et al.*, 1985; Cornell & Giovanoli, 1986). The thickness of goethite crystals is usually less than 1 μm (Cornell *et al.*, 1983; Schwertmann *et al.*, 1985). Although the fine-grained goethite (< 0.1 μm) is thermodynamically unstable compared to hematite of the same size, the phase transformation kinetics are slow allowing goethite to be the common phase in recently formed soils (Goss, 1987).

Although acicular shaped goethite is the most commonly occurring, all the other goethite morphologies described above can be found in natural laterite samples. It is not uncommon for natural goethite crystals with low aspect ratios to be found (Boudeulle & Muller, 1988; Singh & Gilkes, 1992). Other minerals associated with natural goethite and their affinity is also important in understanding natural goethite leaching behaviour. For example, the rounded or quasi-rounded Al-goethite particles (about 50 nm in diameter) from South Australia are closely aggregated with fine grained kaolinite

particles, which are the alteration product of natural weathering (Fordham & Norrish, 1979, 1983). The intimacy of iron oxide and clay particles has also been observed in fragipan bonding of silica and iron oxides in soil samples from Italy (Marsan & Torrent, 1989) and India (Das *et al.*, 2010).

2.6.3.1 Acicular goethite morphology

The acicular model of goethite morphology progressively evolved as understanding accumulated from samples synthesised under different conditions. The cuboid model of synthetic acicular goethite crystals, Figure 2-9(i) was first assumed to be due to the frequent observation of [100] zone electron diffraction patterns with particles found to lay preferentially on the (100) plane (Atkinson *et al.*, 1968; Cornell *et al.*, 1974; Cornell *et al.*, 1975; Cornell *et al.*, 1976; Cornell *et al.*, 1983; Boudeulle & Muller, 1988; Kumar *et al.*, 1990). Therefore the (100), (010) and (001) planes were considered the predominant faces or crystal form with a rectangular cross section perpendicular to the [001] direction (acicular long axis). Based on this model, the dissolution mechanism of goethite in hydrochloric acid was developed to explain the anisotropic acid attack. Preferential dissolution of the (001) face was explained as due to the higher number of singly coordinated hydroxyls on that face and to open tunnels which made proton access to the hydroxyl site easier (Cornell *et al.*, 1974).

Many structural details can be observed in larger acicular crystals. Unequal length and width but equal height domains along the [001] direction can be observed in goethite particles (Cornell *et al.*, 1974; Cornell *et al.*, 1983), resulting in crystals with serrated ends (Schwertmann *et al.*, 1985). These substructures of domains, also known as intergrowths, are observed as unequally spaced parallel fissures on the (100) face and are more apparent after acid attack (Cornell *et al.*, 1974; Cornell *et al.*, 1983; Cornell & Giovanoli, 1986; Kumar *et al.*, 1993). Cornell *et al.* (1983) originally claimed there were no dislocations or structural imperfections in domain boundaries, with High Resolution TEM (HRTEM) imaging showing atoms having highly coherent arrangements at domain boundaries and between twin planes without significant dislocations. However, in later work Cornell and Giovanoli (1986) demonstrated the slight mismatch between domains may rise from a

series of widely spaced dislocations, which are vulnerable to acid attack and can develop into fissures along the [001] direction.

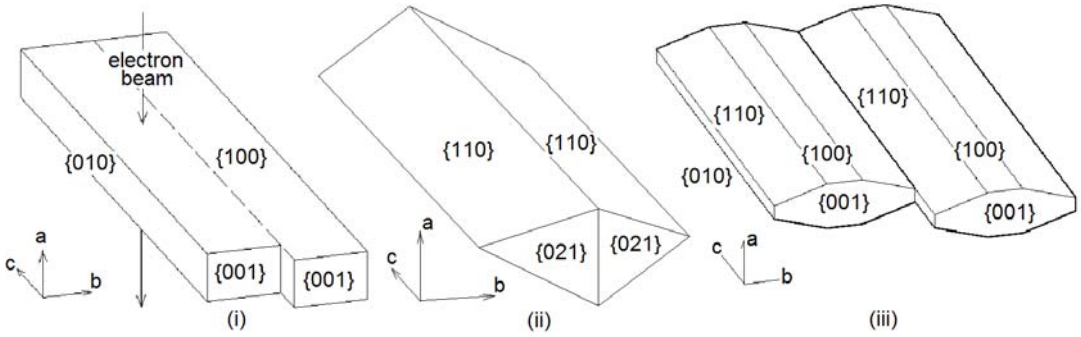

Figure 2-9. (i) Cuboid model of synthetic acicular goethite, with unequal width and length sub-domains (adapted from Cornell *et al.* (1974)); (ii) well grown goethite crystal with the (110) face as the predominant crystal face and (021) plane at the end of the crystal (adapted from Venema *et al.* (1996) and Weidler *et al.* (1996)); (iii) multi-domain crystal lying on the (100) face gives rise to [100] zone diffraction pattern (adapted from Cornell & Giovanoli (1986)).

TEM micrographs of ultrathin cross sections of acicular goethite perpendicular to the *c*-axis show botryoidal shapes for natural goethite (Smith & Eggleton, 1983) and diamond shapes for synthetic samples grown from both acid solutions and alkaline solutions (Schwertmann, 1984b; van der Woude *et al.*, 1984). Multiple domains and their boundaries parallel to the *c*-axis in spindle shaped goethite crystals grown under high pH conditions (Cornell & Giovanoli, 1986) suggest that the (110) face is the predominant crystal face. Thus the closing forms of the acicular goethite crystal should be (110) with (021) at the ends of the crystal, as illustrated in Figure 2-9(ii). A monograph authored by Cornell and Schwertmann (1996, p59) describes many possible forms of well-developed goethite crystals. Another schematic representation of acicular goethite crystals is provided by Cornell (1986) as Figure 2-9(iii); this keeps the (100), (010) and (001) faces but incorporates an additional (110) face as the main form. Multi-domain crystals still lie on the (100) face leading to the [100] zone electron diffraction patterns observed.

2.6.3.2 Twinned goethite morphology

There are two types of twinned goethite forms: epitaxial and homogeneous. Epitaxial goethite refers to the epitaxial growth of goethite

sections (or arms) on hematite (hexagonal system) planar or prismatic nuclei, due to the closely comparable interplanar spacings of the two structures (Atkinson *et al.*, 1968; Goss, 1987; Cornell & Schwertmann, 1996, p27). The [100] direction of epitaxial goethite aligns with the [0001] direction of the hematite nucleus; each section of goethite growth along the [001] direction aligns with one of the six hematite hexagonal directions ($[10\bar{1}0]$, $[01\bar{1}0]$, $[\bar{1}100]$, $[\bar{1}010]$, $[0\bar{1}10]$, and $[1\bar{1}00]$), leading to the formation of epitaxial star-shape twins. Therefore each twin outgrowth can be regarded as an acicular goethite crystal which also contains substructural domains (Atkinson *et al.*, 1968). Goethite epitaxial growth on kaolinite is also observed in Cameroon laterite ore samples from TEM imaging and Selected Area Electron Diffraction (SAED) patterns. The ternary symmetry of the kaolinite sheet allows goethite epitaxy in three equivalent directions at 120° to each other. This also facilitates epitaxial goethite (021) twinning or star-shape goethite formation (Boudeulle & Muller, 1988).

Synthetic growth conditions including pH, temperature, $[Fe^{3+}]$ and suspension concentration have a major impact on the goethite morphology (Cornell & Giovanoli, 1985). The morphology of homogeneous twinned crystals includes twin pieces, star-shape twins and dendritic twins, all of which can be synthesised through the hydrothermal route (Cornell & Giovanoli, 1985). The resulting twinned piece goethite morphology resembles acicular crystals with a width up to 0.15 μm. According to the goethite unit cell dimensions, the twin plane of star-shaped crystals is the (021) plane. The angle between two sections is $2\tan^{-1}(b/2c) = 117.48°$, which is close to 120° (Atkinson *et al.*, 1968; Cornell & Schwertmann, 1996, p68). These star-shaped twins are usually described as pseudo-hexagonal and regarded as composites of three acicular crystals rotated by 120° relative to each other about a central point. Star shaped goethite is also present in natural samples (Boudeulle & Muller, 1988). Dendritic crystals consist of a wide central crystal with one or more outgrowths (Cornell *et al.*, 1983; Cornell & Giovanoli, 1985). Other twinned crystal morphologies have incomplete or irregular shapes with one or more sectors under-developed or totally absent, similar to Cornell's (1983) finding of contact twin goethite.

2.6.4 Acid dissolution of goethite

2.6.4.1 Metal oxide dissolution mechanism

Three groups of factors determine oxide dissolution rates in acid solutions namely system conditions, solution composition, and solid oxide properties (Figure 2-10). Some kinetic models have been developed that focus on the variables defined for the first two groups (Cornell & Schwertmann, 1996). However, it is difficult to link the third group (solids properties such as crystal size, morphology, surface area) to dissolution rates, as the variations of crystal structure, degree of crystallinity (crystal order or perfection), crystalline face areas, the presence of various disorders and defects, the presence of guest ions and the interactions of these factors are difficult to incorporate into the models. Some considerations regarding the effects of defects on dissolution rate are summarised by Schott *et al.* (1989).

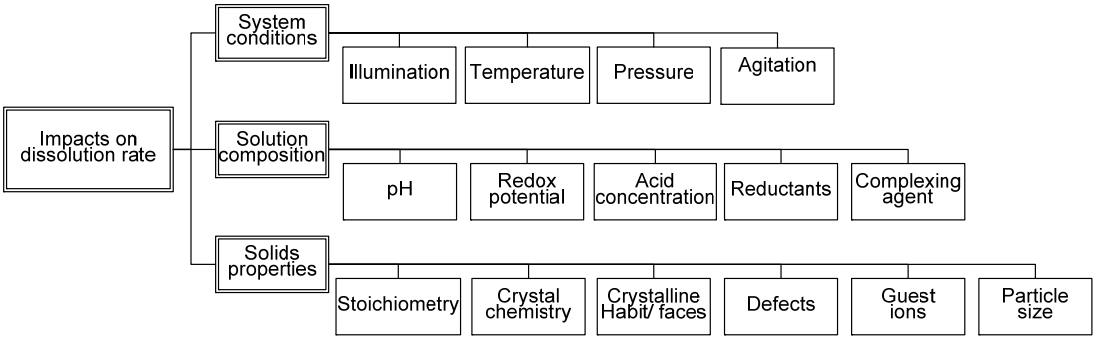

Figure 2-10 Factors influencing solids dissolution rate in liquid after Schott *et al.* (1989)

The dissolution of metal oxides in aqueous acid solutions is usually described using adsorption theory and electrochemical theory (Gorichev & Kipriyanov, 1984; Chiarizia & Horwitz, 1991; Cornell & Schwertmann, 1996, p267-268). In adsorption theory, protonation, complexation, and reduction are the three major dissolution mechanisms. The protonation dissolution process for goethite is interpreted as adsorption of a proton on a surface oxygen or hydroxyl followed by detachment of hydrated ferric ions $Fe(H_2O)_n^{3+}$. Casey *et al.* (1996) broke down the goethite dissolution process into monatomic detachment steps. This paper equated the order of adsorbed $[H^+]$ of a steady-state rate law (Wieland *et al.*, 1988; Ganor *et al.*, 1995) to the

metal valence, which is supported by experiments (Wieland *et al.*, 1988; Guy & Schott, 1989; Stumm & Wollast, 1990; Ludwig & Casey, 1996). However, the rate order 'n' for the $[H^+]$ in liquid is proposed to be within the range 0 to 1 (Cornell *et al.*, 1976; Cornell & Schwertmann, 1996, p271).

The dissolution rate of the protonation mechanism is extremely low compared with complexation or reduction mechanisms. Reductive dissolution of both natural (Surana & Warren, 1969) and synthetic goethite (Torrent *et al.*, 1987) largely promotes the dissolution rate.

Complexation dissolution processes involve three steps: ligand adsorption, metal detachment, and proton adsorption or surface restoration. The polarisation of Fe-ligand bonds weaken the internal Fe-O bonds, which subsequently break when the complex detaches. Hydrogen ions and anionic ligands promote the adsorption of each other at the oxide surface; for example, adsorption of chlorine ions onto the goethite surface neutralises surface positive charge enabling a hydrogen ion to adsorb more easily (Cornell *et al.*, 1976). On the other hand, protonation of the ligand in liquid phase decreases the adsorption capacity of the protonated ligand. Hence a maximum value for the complexation dissolution rate versus pH can be observed (Cornell & Schwertmann, 1996, p272-273). The formation of iron complexes with organic, acid radical, or anionic ligands can either facilitate or retard dissolution (Cornell *et al.*, 1976; Zinder *et al.*, 1986; Chiarizia & Horwitz, 1991; Schwertmann, 1991; Cornell & Schwertmann, 1996, p287).

Reduction boosts oxide dissolution because ferrous coordination spheres are less stable than ferric coordination spheres, since ferrous ions possess lower charge and a larger radius than ferric ions. Ferrous ions are also autocatalytic for the dissolution of ferric iron. Reduction involves electron transfer from a reductant to surface Fe^{3+}, involving pathways that are difficult to confirm. Zinder *et al.* (1986) suggested the pathway could be adsorbed reductant and/or dissolved ferrous ions. When an electron donor and ligand are simultaneously present, the rate of reductive dissolution is a function of both pH and the concentration of the ligand, since pH influences the oxide surface charge and therefore adsorption of the ligand. Fischer (1987) observed that the dissolution rate is an exponential function of E_h (redox

potential) and explained the faster reductive dissolution as due to an increase of electron activity as the redox potential decreases. A recent review (Senanayake *et al.*, 2011) of the reductive leaching of nickel, cobalt, and manganese from both synthetic goethite and limonitic laterite ores compared the effect of all the common reductants used in the literature including $S_2O_4^{2-}$, $S_2O_3^{2-}$, $H_2C_2O_4$, SO_2, Cu^+, Fe, Fe^{2+}, and Cl^- *etc.* The complexation of the anions with metals and the effect of the cations as transfer media for the reductants were highlighted as the reasons for leaching beneficiation. A further complication is that reaction conditions *in situ* and *in vitro* are different so that the laboratory results should be carefully reviewed when applied to heap leaching. In order to investigate the effect of a particular reagent, the concentration change of this reagent should be sufficiently low throughout the whole dissolution process; continuous agitation should be intensive enough to remove the consideration of the effect of diffusion rate of this reagent and the product on dissolution (Cornell & Schwertmann, 1996, p268-269).

Traditionally, reduction and complexation have not found wide application in heap leaching due to the additional cost of the reagents and the investment required in dealing with variations to downstream purification processes. However, several patent documents demonstrate that the industry has managed to apply reduction and complexation at low cost (Harris *et al.*, 2006a; Harris *et al.*, 2006b; Steyl *et al.*, 2008). An improved leaching process using hypersaline or brine water to leach nickeliferous oxide ore was claimed by BHP Billiton (Liu, 2006; Liu & Reynolds, 2009). Significant improvement in nickel (~4-5 times more) and iron (6-7 times more) extractions were found using 40 g/L sulphuric acid in brine water (total dissolved salt, 140 g/L), compared to the same acid strength with no salt present. This is due to the complexation of iron with chloride. Using 10 g/L of sodium metabisulphite ($Na_2S_2O_5$) as a reducing agent in leaching solutions improved the extraction of nickel by 10 % and of cobalt by 200 % (Purkiss, 2004). Using sulphur as a reductant has advantages because it can be reasonably easily recycled (Kittelty, 2008; Roche & Prasad, 2009). Sulfurous and ferrous lixiviants generated from primary heaps, which were rich in saprolite, sulphide, and laterite were also applied to increase dissolution rate

and ultimate recoveries of secondary heaps which mostly contain limonitic laterite (Andreazza, 2007; Moroney, 2007). The idea of mixing these two type of ores into one heap and leaching them together has been examined on other occasions (Moroney *et al.*, 2009). Despite these industrial applications of reductive and complex leaching, protonation dissolution is still the main leaching mechanism for low grade laterite heap leaching, and the difference between the leaching properties of laterite ores is more obvious when this is the primary mechanism.

2.6.4.2 Dissolution kinetics and rate laws

The target of kinetic analysis and the subsequent calculation involved is to provide a good phenomenological description of dissolution curves. The equation which best fits phase transformation data can suggest a reaction mechanism in conjunction with independent micro-morphology evidence. When the reaction mechanism is well defined, the effect of different experimental and environmental conditions on the transformation can be predicted (Goss, 1987). The driving force for solid ion dispersion into liquid is the extent of undersaturation with respect to the solid (Cornell & Schwertmann, 2003, p298). Oxide and hydroxide dissolution processes can be broken down into several steps including metal-oxide bond breakage, diffusion within the surface layer, and diffusion into the liquid phase. Normally, rate models and rate laws based on this process attempt to simulate the rate of the controlling or rate-determining step (Hixson & Crowell, 1931; Cornell & Schwertmann, 1996, p268).

The kinetic models most suitable for iron oxide dissolution are discussed in Section 12.3 of the second edition of “Iron Oxides” (Cornell & Schwertmann, 2003). However, the description in that section contains incorrect equations and description errors. For example: the kinetic model equations “3D diffusion for a sphere” and “Kabai” in Table 12.2 on page 305 are incorrect; the parameter *m* of the C&C1976 model written as “dissolved mass” should be “undissolved mass”; a negative sign is missing in equation (12.16); the exponent ‘a’ was wrongly positioned as the product in equation (12.17); and “dissolved” in third last line on page 325 should be “undissolved”. The relationships between these kinetic models were not discussed in the

Cornell & Schwertmann iron oxide monograph. This deficiency has been rectified below where the commonly used models are summarised and their relationships highlighted.

The established model equations and their corresponding normalised curves describing dissolution kinetics are listed in Table 2-1 and Figure 2-11. Many of these are not only suitable for solids dissolution in liquids but also work for solids-gaseous reduction (Koga & Harrison, 1984) and thermal decomposition of solids (Giovanoli & Brütsch, 1975). Some of these models are general kinetics descriptions of the process or part of the process of isothermal solid phase change and were developed in the context of solids nucleation and growth (Harrison, 1969, p392). A comprehensive review of these kinetic expressions by Brown *et al.* (1980) outlined their physical background and derivation. Most of these models have been derived from surface area change during dissolution; the electrochemical models summarised by Gorichev (1984) are not included here. The "Gorichev" surface area model and "linear" model were added to Table 2-1. The "C&C1976" model (Christoffersen & Christoffersen, 1976) previously present in its differential form in the Section 12.3 of the second edition of "Iron Oxides" is converted to its integration form here to align it with other kinetic models and facilitate comparison with other models.

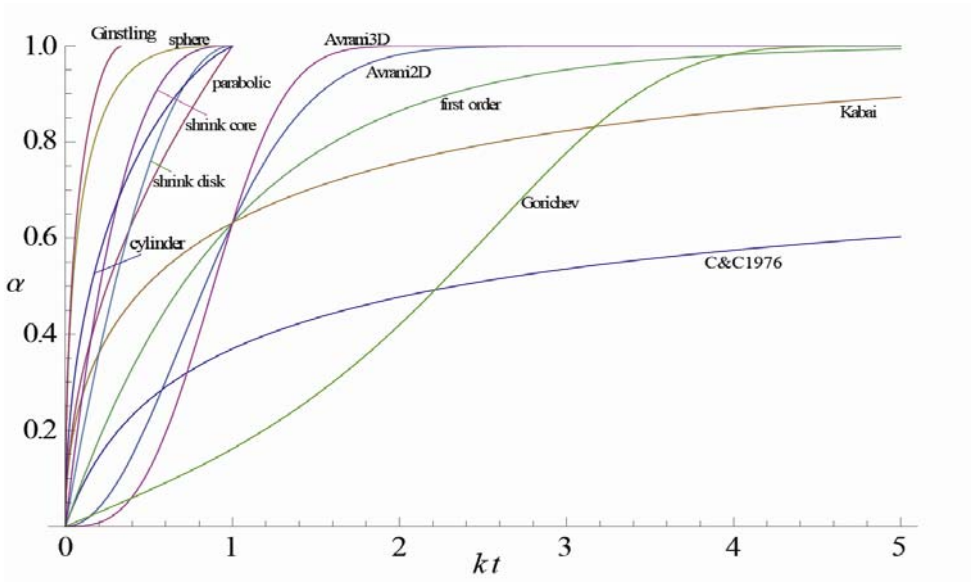

Figure 2-11. Normalised curves for the common dissolution kinetics models, with descriptions in Table 2-1. The abscissa is the product of rate constant '*k*' and dissolution time '*t*'; the vertical ordinate '*α*' represents the dissolved fraction of solids.

Table 2-1 Equations, curve shape type and descriptions of common dissolution kinetics models extended from Cornell & Schwertmann (2003, p305)

Labels in Figure 2-11	Model Equation	Shape Type	Descriptions & Reference
Gorichev†	$\mathrm{ArcSinh}\left[-\frac{\ln(1-\alpha)}{\mathrm{A}}\right] = kt$	Infinite approaching $\alpha = 1$, Double sigmoid ($\mathrm{A} < 1/2$); Decelerative ($\mathrm{A} \geq 1/2$).	Gorichev model (Gorichev & Kipriyanov, 1984)
Kabai†	$[-\ln(1-\alpha)]^{\frac{1}{\mathrm{a}}} = kt$	Infinite approaching $\alpha = 1$, Sigmoid (a > 1); Decelerative (0 < a ≤ 1).	Kabai model (Kabai, 1973)
first order	$-\ln(1-\alpha) = kt$	Infinite approaching $\alpha = 1$, Decelerative	Random nucleation (Noyes & Whitney, 1897)
Avrami2D	$[-\ln(1-\alpha)]^{\frac{1}{2}} = kt$	Infinite approaching $\alpha = 1$, Sigmoidal	Two dimensional random nucleation (Avrami-Erofejev)
Avrami3D	$[-\ln(1-\alpha)]^{\frac{1}{3}} = kt$	Infinite approaching $\alpha = 1$, Sigmoidal	Three dimensional random nucleation (Avrami-Erofejev) (Harrison, 1969)
C&C1976† (γ > 1)	$\frac{1-(1-\alpha)^{1-\gamma}}{1-\gamma} = kt$	Infinite approaching $\alpha = 1$. Decelerative	(Christoffersen & Christoffersen, 1976)
C&C1976† (0 < γ < 1)	$1-(1-\alpha)^{1-\gamma} = (1-\gamma)kt$	$\alpha = 1$ achieved at $kt = \frac{1}{1-\gamma}$. Decelerative	(Christoffersen & Christoffersen, 1976)
shrinking disk	$1-(1-\alpha)^{\frac{1}{2}} = kt$	$\alpha = 1$ achieved at $kt = 1$. Decelerative	Phase boundary control, geometrically shrinking disk (Habashi, 1970)
shrinking core	$1-(1-\alpha)^{\frac{1}{3}} = kt$	$\alpha = 1$ achieved at $kt = 1$. Decelerative	Phase boundary control, geometrically shrinking core (cube root model) (Levenspiel, 1999)
linear	$\alpha = kt$	$\alpha = 1$ achieved at $kt = 1$. Constant	Diffusion of fluidal reactant to spherical solid surface (Levenspiel, 1999)
parabolic	$\alpha^2 = kt$	$\alpha = 1$ achieved at $kt = 1$. Decelerative	One dimensional diffusion for a plate (Wagner, 1933)
cylinder	$(1-\alpha)\ln(1-\alpha)+\alpha = kt$	$\alpha = 1$ achieved at $kt = 1$. Decelerative	Two dimensional diffusion for a cylinder (Holt *et al.*, 1962)
sphere	$\left[1-(1-\alpha)^{\frac{1}{3}}\right]^2 = kt$	$\alpha = 1$ achieved at $kt = 1$. Decelerative	Three dimensional diffusion for a sphere (Jander, 1927)
Ginstling	$\left(1-\frac{2}{3}\alpha\right)-(1-\alpha)^{\frac{2}{3}} = kt$	$\alpha = 1$ achieved at $kt = \frac{1}{3}$. Decelerative	Three dimensional diffusion (Ginstling & Brounshtein, 1950)

† Models employ an extra parameter other than the rate constant *k*. The rate constant, *k* is inversely proportional to reaction time, *t* and acts as an indicator of dissolution rate.

The “first order” model typically assumes the dissolution rate is directly proportional to the amount of oxide remaining. Mathematical transformation shows the rate constant *k* is directly proportional to the dissolution rate at half dissolution ($\mathrm{d}\alpha/\mathrm{d}t|_{\alpha=0.5}$), and inversely proportional to the half dissolution time ($t_{0.5}$); both parameters are experimentally obtainable and serve as good indicators in assessing the rate constant *k* (Eq. 2-5).

$$\ln 2 = k\, t_{0.5}; \quad \left.\frac{\mathrm{d}\alpha}{\mathrm{d}t}\right|_{\alpha=0.5} = 0.5\, k \qquad \text{Eq. 2-5}$$

The “Kabai” model is a more general form of the “first order” model and the Avrami-Erofejev equations (Kabai, 1973). Depending on the value of ‘a’ (constant of average order), the Kabai equation can be reduced to either the first order equation (a = 1) or Avrami-Erofejev equations (a = 2, 3), as shown in Figure 2-12. The authors claiming that the Avrami-Erofejev model fits their experimental data better than the Kabai equation may not be aware that the Kabai equation has a higher degree of freedom than the other two models (Cornell & Giovanoli, 1993; Cornell & Schwertmann, 2003, p330). The dissolution curves published in these papers were digitised and refitted with both models using Wolfram® *Mathematica* v8.0.4. The results indicate that the Kabai model fits the data better than the Avrami-Erofejev equations (see Appendix 1). The “Kabai” model describes sigmoid shaped dissolution curves well (Kabai, 1973; Gorichev & Kipriyanov, 1984). For a > 1, it gives a sigmoidal curve with zero initial dissolution rate; for a < 1, it displays as a deceleration model with infinite initial dissolution rate; for a = 1 (first order law), it has a finite initial dissolution rate. The parameter ‘a’ is a function only of the nature of the solid phase and directly proportional to the reaction activation energy. It is independent of solid size and specific surface area. The Kabai equation is normally arranged into double logarithmic form *i.e.* the linear form (Eq. 2-6). If experimental data are plotted as a $\ln[-\ln(1-\alpha)]$ vs. $\ln t$ graph, the slope is described by the “constant of average order” ‘a’, and intercept by ‘alnk’. Therefore both ‘a’ and ‘k’ can be extracted from linear least squares fitting of the experiment data.

$$\ln[-\ln(1-\alpha)] = \mathrm{alnk} + \mathrm{alnt} \qquad \text{Eq. 2-6}$$

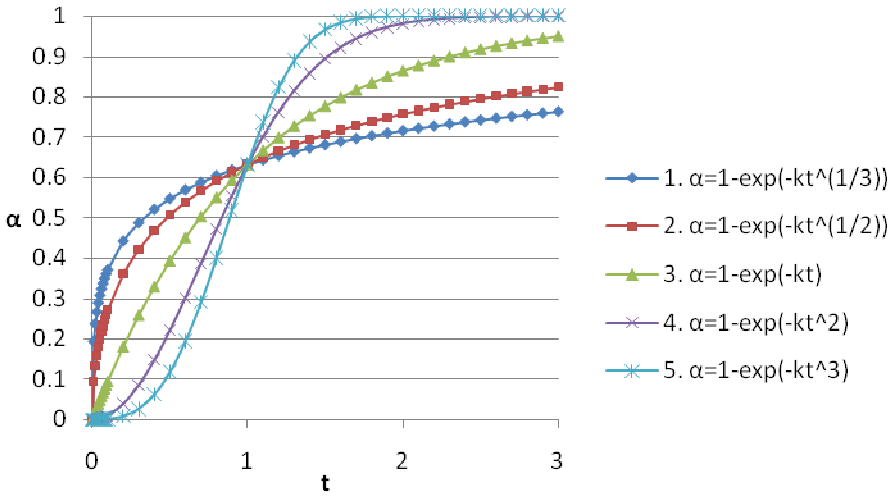

Figure 2-12 Effect of the "constant of average order" (a) to the shape of the Kabai model kinetics curve $\alpha = 1 - e^{-kt^a}$ (assume k = 1)

The form of Kabai equation is the same as the Johnson-Mehl-Avrami (JMA) equation widely used in thermoanalysis and phase transformation kinetics (Avrami, 1939, 1940, 1941). The relationships between apparent experimental indicators (the dissolution rate at half dissolution ($d\alpha/dt|_{\alpha=0.5}$), half dissolution time ($t_{0.5}$) and the model parameters 'a' and 'k' for Kabai model are given in Eq. 2-7

$$(\ln 2)^{\frac{1}{a}} = k\, t_{0.5}; \quad \left.\frac{d\alpha}{dt}\right|_{\alpha=0.5} = \frac{a\,k}{2}(\ln 2)^{\frac{a-1}{a}} \qquad \text{Eq. 2-7}$$

Comparing Eq. 2-5 and Eq. 2-7, the direct proportional relationship between 'k', $d\alpha/dt|_{\alpha=0.5}$, and ($t_{0.5}$) is preserved in the Kabai model, although the coefficients are modulated by "constant of average order" 'a', which should be a constant in a particular experiment. The relationship Eq. 2-7 provides a simple way of calculating model parameters 'a' and 'k' from the apparent experimental indicators $d\alpha/dt|_{\alpha=0.5}$ and ($t_{0.5}$). The initial stage where increasing dissolution rate is indicated by the sigmoidal curves has been attributed to surface area increases by preferential dissolution of domain boundaries (Schwertmann, 1984b; Schwertmann *et al.*, 1985; Schwertmann, 1991; Cornell & Schwertmann, 1996, p294) or surface pitting formation (Surana & Warren, 1969; Warren & Roach, 1971). The existence of an induction time must also be taken into account when plotting the data

according to the equations of the shrinking core model (Chiarizia & Horwitz, 1991).

Strictly speaking, the “linear”, “Ginstling”, and “shrinking core” models were all derived from the spherical shrinking core model with different rate controlling steps. These rate controlling steps can be diffusion of fluid reactant to the surface of solids, diffusion of fluid reactant through the blanket of reaction products (also referred to as the ash layer) to the surface of unreacted core, or the chemical reaction on the unreacted core (Habashi, 1970, p134; Wadsworth, 1979, p148; Levenspiel, 1999, p570). Because of the common physical background, these three models were linearly summed followed by a multi-linear regression to determine the controlling mechanism for acid leaching of porous particles with complex morphology (Nazemi *et al.*, 2011). It should be noted that the naming of these models can differ from author to author; for example Senanayake *et al.* (2011) referred to the “Ginstling” model in Table 2-1 as the “shrinking core” model and the “shrinking core” in Table 2-1 as “shrinking sphere” model. However, the physical background and hypothesis these models were derived from is clear. The naming of models adopted in this thesis follows the convention of Cornell and Schwertmann (2003).

The “shrinking core” model (also called cube root law) describes a special case where the shape of shrinking particles is preserved and solution concentration change is negligible (Hixson & Crowell, 1931). Although the “shrinking core” model is derived from a shrinking sphere or cubic particle model, it has also successfully simulated synthetic acicular goethite dissolution data (Cornell *et al.*, 1975; Chiarizia & Horwitz, 1991). Shape-preserving dissolution has been observed by many researchers (Atkinson *et al.*, 1968; Cornell *et al.*, 1974; Sidhu *et al.*, 1981). The necessary condition for shape-preserving dissolution is that the ratio of dissolution rate with respect to each crystalline face is equal to the original aspect ratio. The “shrinking disk” model is a derivation of the “shrinking core” model.

The differential form of the “C&C1976” model is equivalent to four integration forms shown in Table 2-1, according to a range of γ values:

$$\frac{J}{m_0} = k\left(\frac{m}{m_0}\right)^{\gamma} \Leftrightarrow \begin{cases} \gamma = 0, \quad \alpha = kt \quad \text{linear} \\ 0 < \gamma < 1, \quad 1-(1-\alpha)^{1-\gamma} = k(1-\gamma)t \quad \text{shrinking core or disk} \\ \gamma = 1, \quad -\ln(1-\alpha) = kt \quad \text{first order} \\ \gamma > 1, \quad \dfrac{1-(1-\alpha)^{1-\gamma}}{1-\gamma} = kt \quad C\&C1976\ (\gamma > 1) \end{cases} \qquad \text{Eq. 2-8}$$

where J is dissolution rate (mol/min), m_0 is the initial amount of solid (mol), m is the undissolved solids amount (mol) at time t (min), γ is the exponent describing the remaining solids dependency of reaction rate (the parameter γ varies with respect to the crystal structure, the particle size distribution, or sample phase heterogeneity), k is the rate constant (min^{-1}), and α is the degree of dissolution (Boudreau & Ruddick, 1991; Postma, 1993; Larsen & Postma, 2001; Larsen *et al.*, 2006).

The “C&C1976” model formula for the case 0 < γ < 1 looks the same as that for γ > 1. However, these are regarded as different models as the former case describes a dissolution curve in which total dissolution (α = 1) could be achieved at finite time kt = 1/(1 - γ), while the curve of the latter case approaching the total dissolution with infinite time. The “C&C1976” model reduces to a “linear” model if γ = 0, “shrinking disk” model if γ = 1/2, “shrinking core” model if γ = 2/3, “first order” model if γ = 1. This explains why Houben (2003) found his iron oxide dissolution experiment could be fitted with either the linear model or the “C&C1976” model. This model has been proven to be suitable for many dissolution experiments (Christoffersen & Christoffersen, 1976; Postma, 1993; Larsen & Postma, 2001; Houben, 2003; Larsen *et al.*, 2006).

Gorichev (1984) and references within considered the reaction site formation (nucleation) rate and the first order oxide dissolution (growth) rate separately and found the hyperbolic sine function was able to describe the dissolution kinetics. The “Gorichev” model is a compound function, from which a linear form cannot be analytically deduced.

There are also acceleration models. For example, the power increase $\alpha = kt^n$ and exponent increase $\alpha = e^{kt}-1$ models were used to simulate the dissolution rate for the first 5 % of goethite dissolution, during which varying

acid concentration is considered negligible (Surana & Warren, 1969; Warren & Roach, 1971).

The relationship between these models can be shown in a schematic diagram (Figure 2-13). The “C&C1976” model, “Kabai” model, and “Gorichev” model are more flexible for data fitting because these have an additional refinable parameter other than rate constant ‘*k*’. With the help of the normalised curves (Figure 2-11), these models can be classified into two groups according to the way complete dissolution (α = 1) is achieved. The first six models in Table 2-1 approach full dissolution at infinite time, while the other models achieve full dissolution after finite time. It should be noted that the curves of “C&C1976” models are always decelerative, which means these are not suitable for reproducing sigmoidal experimental curves.

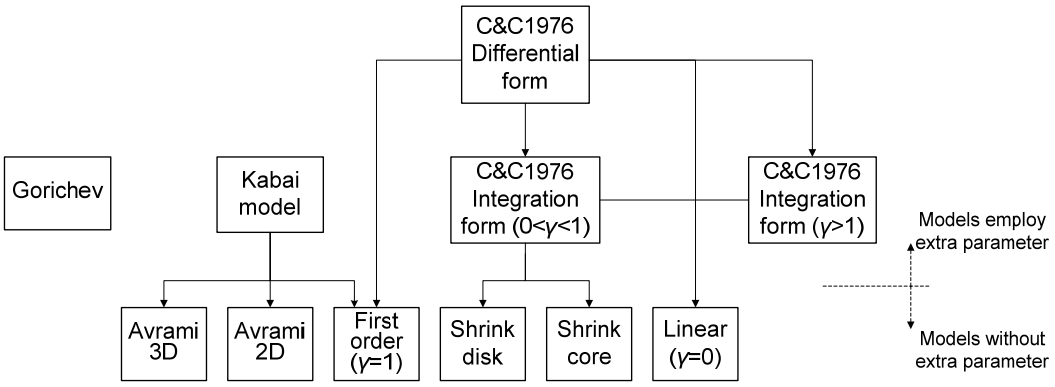

Figure 2-13. Relationships of common kinetic models shown in Table 2-1. The models in the first two rows, which use an additional parameter other than the rate constant, have more degrees of freedom for data fitting.

All of the dissolution models are designed for surface controlled dissolution reactions, suggesting the speed of reactant transportation or product diffusion is high enough that neither will be the rate determining step. This can only occur when the system is agitated, which is not the case for heap leaching. Finally, it is well recognised that the rate law determined from the experimental data does not necessarily mean the theory behind the rate law is valid for that experiment (Cornell *et al.*, 1975).

2.6.4.3 Preference of specific goethite crystal faces to dissolution

Surface area and crystal morphology are two important factors affecting the dissolution rate of goethite. The former determines the solid/solution interface of a reaction, which roughly decides how many Fe^{3+} ions react simultaneously. Cornell *et al.* (1975) found the “shrinking core” model (Hixson & Crowell, 1931) fitted the decreasing goethite dissolution curves very well. Cornell *et al.* (1974) also claimed that the goethite (001) surface planes (both ends of acicular goethite crystals) are the most leachable planes, confirmed by TEM imaging of the replicas of partially leached particles. The goethite anisotropic dissolution property suggests, beside specific surface area, the crystal dissolution rates are also related to particle morphology. Although acicular goethite has a high surface area compared to other goethite forms, its dissolution rate is lower than the others, believed to be due to the small area fraction of the (001) planes relative to the rest of the crystal.

The differences in the leachability of different goethite crystal planes result from the difference of hydroxyl distributions on each plane (Cornell *et al.*, 1974). The number of coordinated ferric ions of surface hydroxyl ranges from 1 to 3, and only the singly coordinated hydroxyls are able to be protonated. The (021) surface has a high density of singly coordinated hydroxyls (Barrón & Torrent, 1996), hence the end plane of goethite acicular crystals leaches faster than others. Both the (001) plane in Figure 2-9(i) and (021) plane in Figure 2-9(ii) refer to the end plane of goethite acicular crystals. The structural channels along the *c*-axis make proton access to surface hydroxyls easier facilitating preferential dissolution. Twinned crystals, especially those with hematite cores, are more vulnerable to acid dissolution because hematite was found to dissolves more easily than goethite (Sidhu *et al.*, 1981) and increases the exposed goethite surface area. Anisotropic acid dissolution of acicular goethite particles, which retains the aspect ratio, has also been described by Cornell *et al.* (1974).

Another feature of acicular goethite particle dissolution is the preferential dissolution of the intra-crystal domain boundary. The domain boundaries of multidomain goethite crystals are high-energy regions and vulnerable to preferential acid attack during the initial stages (Schulze & Schwertmann,

1984; Schwertmann, 1984b; Kumar *et al.*, 1990; Kumar *et al.*, 1993). Rhombic holes parallel to the (011) plane are formed, leading to an increased surface area and subsequently increase in the rate of acid dissolution. This may explain the sigmoid dissolution curves that are often observed. Schwertmann *et al.* (1985) fitted sigmoid dissolution curves using Kabai's law, and successfully generated dissolution rate constants '*k*' and structure indicators 'a'.

2.6.5 Substituted goethite and their leaching performance

Goethite is well known for its ability to incorporate a wide range of guest elements into its crystal structure (Singh & Gilkes, 1992). The maximum amount of guest element incorporated into the structure is dependent on the ion species and the conditions of the goethite formation (Cornell & Schwertmann, 2003). As a result of the incorporation of guest elements, goethite changes its chemical, physical and mineralogical properties.

Guest element substitutions can increase the crystallinity (structural order) of the host goethite structure. Cornell (1988) found that guest elements slow down the ferrihydrite to goethite transformation rate in the order: Zn ≥ Cu >> Ni > Co >> Mn, and slower goethite growth rate may lead to higher goethite crystallinity.

The guest elements influence goethite dissolution performance indirectly by altering the size of the goethite CSD, structural disorder, surface area, and morphology. Kumar *et al.* (1990) examined the multilinear correlations between goethite dissolution rate and its physico-chemical properties and inferred that the goethite dissolution rate is positively linked to the variation of CSD size calculated from different reflections and the structural disorder. The ratios of iron to copper, cobalt, and nickel in leachate were found to remain constant during sulphuric acid leaching, indicating congruent dissolution between iron and these guest metals. In comparison the H_2SO_4-H_2SO_3 mixture was reported to preferentially leach nickel and cobalt over iron and copper (Khalafalla & Pahlman, 1981).

Goethite unit cell parameters are sensitive to guest cation substitution. The theory that unit cell parameters of a solid solution series change linearly

with the composition between those of pure end members was proposed by Vegard and Dale (1928) has become known as Vegard's law. Pabst (1976) later argued that it is the unit cell volume additivity rather than the unit cell dimensions additivity (Vegard's law) that best approximates the relations in certain mixed-crystal series. The linear relations are widely used to estimate guest ion concentration in goethite from the lattice dimensions. Schulze (1984) established a linear relationship in goethite (using Vegard's Law) based on 81 known aluminium substituted samples. For other ion substitutions (Cd, Zn, Pb, Cu, Ni, Co) the *b*-dimension is reported to be more sensitive than the *c*-dimension. Gerth (1990) found that the gradient of the *b*-dimension change versus guest atom substitution level is proportional to the guest cation radii.

As pointed out in Section 2.6.1, guest elements can also adsorb on goethite crystals and potentially form a separate phase. Cornell *et al.* (1992) found that nickel can adsorb on Ni-goethite crystals. Quin *et al.* (1988) observed that phosphorus and silicon are more likely to adsorb on goethite crystals than substitute into the goethite structure. The adsorption of copper, nickel, and cobalt on goethite has been shown to have no impact on particle morphology; copper can be more easily adsorbed on goethite than nickel and cobalt (Kumar *et al.*, 1990). The crystal field stabilisation energy (CFSE) and valency to ionic radius ratio may explain the occurrence mode of guest elements. Elements such as nickel with higher CFSE than cobalt or copper tend to form a separate phase rather than substitute into goethite from Kumar *et al*. (1990)'s co-precipitation experiments.

Different views have been expressed about which elements occur in or associate with goethites in nickel laterites. These elements include aluminium, cobalt, nickel, chromium, silicon, and manganese. (Fordham & Norrish, 1979, 1983; Landers *et al.*, 2009b; Watling *et al.*, 2011). Although they are the main focus of the following review, other minor elements are also discussed. The effects of the metal substitution on goethite formation, morphological and crystallographic properties, and dissolution rates obtained from the literature are discussed in detail below. The properties and isomorphous metal substitutions of Western Australian iron oxides as well as their dissolution

kinetics has been reviewed by Gilkes and colleagues, but these reports mainly focus on the effect of aluminium substitution on dissolution properties (Anand & Gilkes, 1987b, a; Singh & Gilkes, 1992). As single element substituted natural goethite cannot be confirmed to exist, researchers obtain data from single metal substituted goethite from synthetic samples.

2.6.5.1 Aluminium

The impact of aluminium substitution in goethite has been studied in detail and is especially important in soil science. Increasing aluminium substitution makes the goethite crystals shorter and lenticular with lower aspect ratio and fewer intra-crystal domains as well as improving crystal order, which is believed to be due to the reduced Al-goethite growth rate (Fey & Dixon, 1981; Schulze & Schwertmann, 1984, 1987; Cornell & Schwertmann, 2003, p44; Sudakar *et al.*, 2004). These observations could also be partially due to the slow ferrihydrite to goethite phase transformation during Al-goethite synthesis (Lewis & Schwertmann, 1979a, b; Schwertmann, 1984b) and the limited aging time applied in goethite synthesis experiments.

High aluminium substitution in the goethite structure can be achieved because goethite is isomorphous with diaspore (α-AlOOH). Al-goethite is essentially a solid solution between the iron end member goethite and the aluminium end member diaspore. The aluminium substitution level in goethite co-precipitated with Al^{3+} is normally higher with slower goethite growth rate for lower [OH^-] and higher [Al^{3+}] in the original solution (Lewis & Schwertmann, 1979b, a; Ruan & Gilkes, 1995b). Aluminium can substitute for iron up to 33.3 mol.% (Thiel, 1963; Schulze, 1984; Scheinost *et al.*, 1999; Manceau *et al.*, 2000). However, Fey (1981) and references therein argued this miscibility limit is only valid for Al-goethite generated from alkaline solutions; the goethite synthesised from the ferrous oxidation route achieved 36 mol.% aluminium substitution. As much as 47 mol.% aluminium substitution has been reported for goethite synthesised from sulphate solutions (Bronevoi & Furmakova, 1975). With greater levels of aluminium substitution for iron the goethite would gradually change to the diaspore structure with shorter and stronger hydrogen bonds, which has been verified

by the shift of the hydroxyl bonding vibration to higher frequency in IR spectra (Fey & Dixon, 1981).

Vegard's law was successfully applied to Al-substituted goethite (also called Al-goethite in literature). As the ionic radius of Al^{3+} (53.5 pm) is 17 % smaller than that of the Fe^{3+} cation (64.5 pm) (Shannon, 1976), the substitution of aluminium for iron should shrink the goethite unit cell in three dimensions. Although the relationship between lattice parameters and the (111) interplanar spacing (d_{111}) is not linear, the d_{111} value does decrease with increasing aluminium substitution and has often been plotted linearly to estimate aluminium substitution levels (Norrish & Taylor, 1961; Thiel, 1963; Jónás & Solymár, 1970; Lewis & Schwertmann, 1979a; Fey & Dixon, 1981; Goodman & Lewis, 1981; Fitzpatrick & Schwertmann, 1982). The linear relationship of lattice parameters and aluminium substitution levels was summarised by Schulze (1984) and was later extended to the full goethite-diaspore system with the assistance of Rietveld refinement methods (Hill & Howard, 1987; Bish & Howard, 1988; O'Connor & Raven, 1988) using both laboratory X-ray data (Fazey *et al.*, 1991) and neutron diffraction data (Li *et al.*, 2006). The lattice parameters of 127 Al-goethite samples and their aluminium substitution levels are summarised in Figure 2-14. As well as synthetic samples, Schwertmann (1994) developed the relationships between aluminium substitution level and lattice parameter changes from 84 naturally occurring goethite samples.

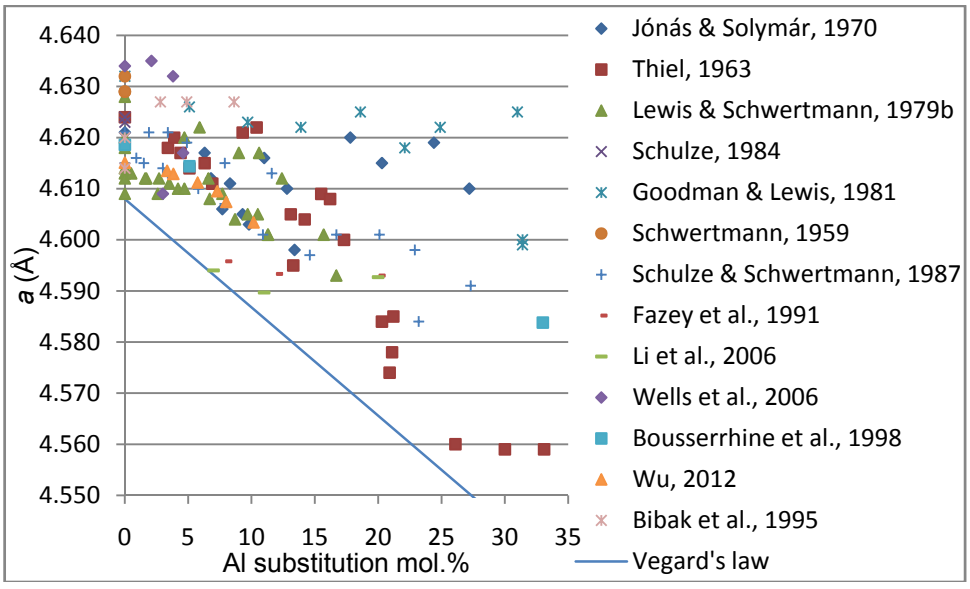

(a)

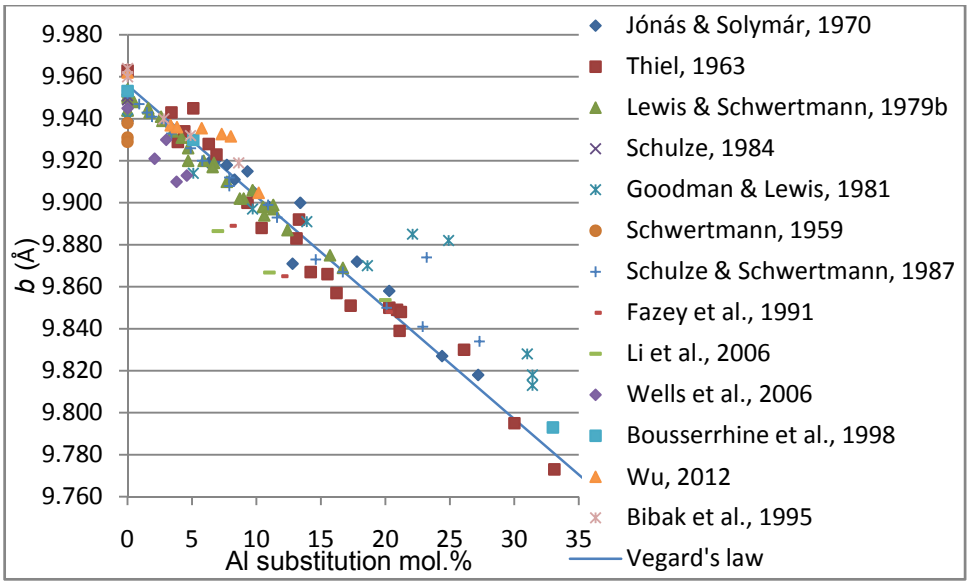

(b)

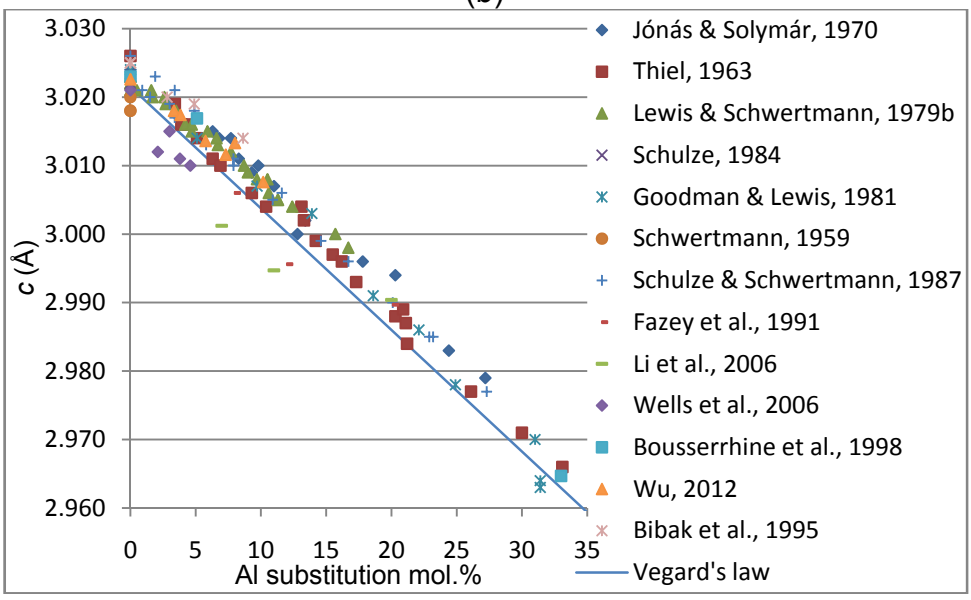

(c)

Figure 2-14 The unit cell dimensions of Al-goethite samples versus Al substitution level for (a) the a-dimension, (b) the b-dimension and (c) the c-dimension. The lattice parameters of goethite samples synthesised by Jónás & Solymár (1970) and Thiel (1963) were refined from their reported d-spacing d_{130}, d_{021}, d_{111}, and d_{140}, with Microsoft® Excel Solver and are slightly different from the calculation of Schulze (1984) but show better linearity. The straight lines represent Vegard's law connecting the two end members of this series: goethite (PDF# 00-029-0713) and diaspore (PDF# 00-005-0355).

As shown in Figure 2-14, the aluminium substitution level in goethite correlates more linearly with lattice parameter *c* than *b*, while *a* is the most variable lattice parameter (Fey & Dixon, 1981; Schulze, 1984; Schulze &

Schwertmann, 1984; Fazey *et al.*, 1991; Li *et al.*, 2006). The lattice parameters may be affected differently because the parallelogram channel gaps along the *a*-direction (Figure 2-8) may yield to distortion and accommodate Fe-octahedron shrinkage in the *a*- and *b*-directions better than in the *c*-direction. The fact that *a*-dimension does not follow Vegard's law has been also attributed to structural disorder in both synthetic goethite (Schulze, 1984; Gasser *et al.*, 1996) and natural goethite (Schwertmann & Carlson, 1994). At low synthesis temperatures, goethite structural disorder would be more obvious inducing a larger "Δa" (the differences between observed lattice parameter 'a' and the 'a' estimated from Vegard law) (Schulze & Schwertmann, 1987; Schwertmann & Carlson, 1994). Fey and Dixon (1981) found that Al-goethite samples dehydrated at 110 °C in vacuum have d_{111} closer to Vegard's law. They also suggested that the hydration of Al-goethites during synthesis procedures might be responsible for the *a*-axis length deviation from Vegard's law. According to multi-parameter regression studies by Schwertmann (1984b) and Schulze and Schwertmann (1984), aluminium substitution level and the structural disorder are the two main factors affecting Al-goethite properties. Increasing aluminium substitution decreases the unit cell parameter and acid dissolution rate, and increases goethite dehydroxylation temperature. Structural disorder induced by synthesis has the opposite effect on these properties. The negative impact of aluminium substitution on goethite dissolution rates has also been confirmed from HCl complexation dissolution (Bibak *et al.*, 1995; Ruan & Gilkes, 1995a), H_2SO_4 protonisation dissolution (Norrish & Taylor, 1961), DCB (citrate-bicarbonate-dithionite) reductive dissolution (Jeanroy *et al.*, 1991), and bio-reductive dissolution (Bousserrhine *et al.*, 1998).

However, the acid resistance effect of aluminium substitution was not obvious in Al-goethite synthesised in high pH conditions (Lim-Nunez & Gilkes, 1987), which can be explained with the finding (Schulze & Schwertmann, 1984; Schwertmann, 1984b) that goethite synthesised under high OH^- concentrations, *e.g.* 2 M $[OH^-]$ in the work of Lim-Nunez and Gilkes (1987), is less ordered and has higher in defects compared to goethite synthesised in low OH^- concentrations, *e.g.* 0.3 M $[OH^-]$ (Schulze & Schwertmann, 1984).

Lewis and Schwertmann (1979a) claimed the induced structural defects in Al-goethite might be also due to their relatively high [OH^-] synthesis environment, *i.e.* 1 M [OH^-]. A recent report studying the acid leaching of some goethite dominated limonitic laterite ores from Western Australia suggested aluminium substitution was not the only factor contributing to the poor nickel extraction (Watling *et al.*, 2011). The formation conditions influence the goethite crystallinity and defects which in turn affect goethite dissolution rates.

Another important structural parameter describing goethite morphology is the size of the mean crystallite dimension (MCD) also referred to as the coherent scattering domain (CSD), which can be measured by its inverse relationship to the XRD line broadening. This parameter is usually smaller than the directly observed goethite crystal size from TEM imaging as unsubstituted goethite is very likely to develop intra-crystal domains along the [001] direction. As the aluminium substitution level increases, these domains gradually merge to form a single domain crystal, leading to an increased MCD. However, as the overall goethite crystal size decreases with aluminium substitution (pointed out in the first paragraph of this section), the MCD will again decrease when the aluminium substitution level approaches the substitution limit (Fey & Dixon, 1981; Schwertmann, 1984b; Schulze & Schwertmann, 1987; Torrent *et al.*, 1987; Wells *et al.*, 2006). Other authors who claimed MCD decreases with aluminium substitution may have ignored the lower Al-goethite growth rate and failed to wait until crystals were fully developed before characterisation was undertaken (Goodman & Lewis, 1981; Ruan & Gilkes, 1995b).

Intra-crystal domain boundaries are seldom present in Al-goethite, making the crystal more homogeneous (Schulze & Schwertmann, 1984; Schwertmann, 1984b) which has been confirmed by HRTEM images published by Mann *et al.* (1985). Goethite domain boundaries are high energy sites for guest ion adsorption and are vulnerable to acid attack; lack of these domain boundaries would result in low leachability of these Al-goethite crystals. The half dissolution time of 8 mol.% substituted Al-goethite (63 days) is much greater than that of pure goethite (8 days) (Schwertmann *et al.*, 1989). As the structure of Al-goethite becomes more homogeneous, its

dissolution curve becomes less sigmoidal; also a better fitting with the first order rate law can be achieved (Schwertmann, 1984b). The increased crystalline order of Al-goethite is controlled by the reduced crystal growth rate during precipitation. The congruent dissolution of aluminium with iron is revealed by their half dissolution times which indicates that aluminium is uniformly distributed throughout the goethite. Although Fey and Dixon (1981) and Schwertmann (1984a) gave different explanations for the double DTA dehydroxylation peak of Al-goethite with higher phase change temperatures, they agreed that this phenomenon suggested greater thermal stability and better ordering of the Al-goethite crystals.

2.6.5.2 Cobalt

The Co^{2+} substituted goethite and Co^{3+} substituted goethite prepared by different chemical routes were found to expand and contract the goethite unit cell, respectively (Pozas *et al.*, 2004a; Pozas *et al.*, 2004b). Cornell & Giovanoli (1989) proposed that Co^{2+} may have been oxidised by Fe^{3+} in goethite for low Co/Fe ratios. Similar to Al-goethite, the goethite unit cell contracts with Co^{3+} substitution, and again the reduction of the *c*-axis is greater than that observed for the *b*-axis (Iwasaki & Yamamura, 2002). This unit cell contraction indicates that it is the Co^{3+} ion (high spin state[3] 0.63 Å) rather than Co^{2+} ion (high spin state 0.74 Å) substituting for the Fe^{3+} ion (high spin state 0.65 Å) in the goethite structure. However, Cornell and Giovanoli (1989) believed the Co^{3+} is in a low spin state, with an even smaller radius of 0.53 Å in Co^{3+} complexes and compounds due to its high charge-induced strong crystal field. Pozas *et al.* (2004a) investigated the pH effect on cobalt

[3] The radius of octahedrally coordinated central transition metal (usually Cr, Mn, Fe, Co, Ni *etc.*) ions is affected by its spin state (outermost electron configuration). The d10 orbit of central transition metals usually splits into two energy levels under octahedral coordinated crystal field: t_{2g}^6 and e_g^4. The low spin state is formed when the t_{2g} orbits are filled before the e_g orbits. The high spin state is formed when the d orbits are filled by electrons with same spin direction first. Strong crystal fields induce a large energy split between t_{2g} and e_g orbits and favour low spin. Transition metal ions of high spin state are always larger than those of low spin state (Shannon, 1976; Atkins & Shriver, 2006, pp. 227–236).

valency in the goethite structure and concluded that higher pH favours the oxidation of Co^{2+} to Co^{3+}, as confirmed by IR, XPS, and EELS.

Cornell and Giovanoli (1989) reported the maximum cobalt substitution into the goethite structure as 7 mol.% from the ferrihydrite transformation route while 10 mol.% substitution has been reported in more recent publications (Gerth, 1990; Gasser *et al.*, 1996; Pozas *et al.*, 2004a; Alvarez *et al.*, 2008). Spinel phases such as Fe_3O_4 and $CoFe_2O_4$ were observed for cobalt content approaching 16 mol.% (Iwasaki & Yamamura, 2002).

While 2 wt.% Co substitution had minimal impact on goethite morphology (Kumar *et al.*, 1990), increasing levels of cobalt substitution elongated the goethite crystals in the *c*-direction but shortened it in the *b*-direction, changing the aspect ratio from 4 to 25 and producing whisker-like crystals with curvature possibly due to accumulated strain (Cornell & Giovanoli, 1989; Iwasaki & Yamamura, 2002; Sudakar *et al.*, 2004; Krehula & Musić, 2008). This effect is partially attributed to the exclusive adsorption of OH^- on (*hk*0) side-planes, which block $Fe(OH)_4^-$ precipitation on these planes; the goethite formation rate constant '*k*' derived from the first order law decreases with increasing cobalt incorporation. Another reason could be the shrinkage of unit parameter *c* which result in a mismatch between (*hk*0) planes and incoming $Fe(OH)_4^-$ complexes during precipitation (Iwasaki & Yamamura, 2002). Cornell and Giovanoli (1989) compared the products of different cobalt concentrations and pH conditions ranging from 9 to 12 and concluded that cobalt retards the ferrihydrite to goethite transformation and favours magnetite or hematite formation.

However, Kumar *et al.* (1990) believe the chemical nature of Co^{3+} acts as a major controlling factor in cobalt substitution. Despite the shrinkage of the unit cell of Co-goethite (which differs from expanding unit cell observed by Pozas *et al.*, (2004a)), they suggest the lower CFSE of Co^{2+} allows its substitution into the goethite structure, confirmed by the congruent leaching of cobalt with iron in sulphuric acid; with the Fe/Co ratio in the solid almost the same as in the leachate. Burns (1976) believe high level cobalt substitution in goethite structure is discouraged by the crystal structure

difference between heterogenite (CoOOH, trigonal or hexagonal) and goethite (FeOOH, orthorhombic).

Increasing the amount of cobalt substitution reduces crystal size, increases the specific surface area of Co-goethite, and increases the Co-goethite dissolution rate (Kumar *et al.*, 1990; Kumar *et al.*, 1993; Gasser *et al.*, 1996; Alvarez *et al.*, 2008). A weaker Co^{3+}-O bond than the Fe^{3+}-O bond results in lower activation energy than that of pure goethite, which also contributes to the faster leaching of Co-goethite (Alvarez *et al.*, 2008). Incorporation of low amounts (~2.4 wt.%) of nickel, cobalt or copper were all found to increase goethite dissolution rate (normalised according to the specific surface area) compared to pure goethite (Lim-Nunez & Gilkes, 1987; Kumar *et al.*, 1990; Schwertmann, 1991). Co-goethite dissolution rates in sulphuric acid were found to be strongly correlated with its MCD_{110} and MCD_{111} sizes and the XRD intensity ratio I_{110}/I_{111}, both of which point to disorder of the goethite structure (Kumar *et al.*, 1990).

The effect of cobalt substitution on the reductive leaching rate of goethite is controversial. Cobalt is reported to be preferentially leached by sulphurous acid (Khalafalla & Pahlman, 1981; Kumar *et al.*, 1990). Kumar *et al.* (1993) later reported the contradictory result that cobalt substitution decreases both the iron and cobalt dissolution rates. Similar findings of slower dissolution rates were also made when using Dithionite-Citrate-Bicarbonate (DCB) dissolution (Gasser *et al.*, 1996).

Kumar *et al.* (1993) proposed the goethite dissolution mechanism as an interface reaction controlled according to activation energies calculated from the dependency of reaction rate on temperature. Cobalt incorporation did not appear to change the reaction mechanism of goethite. The factors contributing to a decreased iron dissolution rate by cobalt incorporation were suggested to be either cobalt interface obstruction or retardation of electrical potential induced by cobalt dissolution. As with the dissolution in sulphuric acid (Kumar *et al.*, 1990), iron and cobalt dissolution in sulphurous acid were congruent (Kumar *et al.*, 1993; Alvarez *et al.*, 2008).

2.6.5.3 Copper

The co-precipitation of Cu^{2+} ions with ferrihydrite slow down its transformation rate to goethite and completely hinder the formation of goethite for high Cu^{2+} concentrations (>2.5 mol.%) (Inouye *et al.*, 1972; Kumar *et al.*, 1990). The copper substitution level in goethite was later reported to be close to 3 mol.% (Bibak *et al.*, 1995; Krehula & Musić, 2007). Doping Cu^{2+} ions into ferrihydrite favours the formation of hematite and star shaped goethite and twin goethite epitaxial growth from a hematite core (Kumar *et al.*, 1990; Kaur *et al.*, 2009b). Inouye *et al.* (1972) reported that Cu-goethite needles have a lower aspect ratio compared to pure goethite, while later work reported a higher aspect ratio for Cu-goethite than pure goethite (Kumar *et al.*, 1990; Bibak *et al.*, 1995; Krehula & Musić, 2007; Kaur *et al.*, 2009b). All of the authors agreed that Cu^{2+} substitution increased the specific surface area except for Kaur *et al.* (2009b).

Substitution of Cu^{2+} ions affects the goethite unit cell parameters anisotropically. Copper substitution induced lattice distortion occurs mainly in the *a*-*b* plane and is not apparent in the *c*-direction (Inouye *et al.*, 1972). The *b* dimension increases while the *a* dimension decreases, although the incorporated Cu^{2+} ions (radius 0.72 Å) are larger than Fe^{3+} ions (high spin state 0.65 Å). This was explained by the *a*-dimension being particularly vulnerable to Jahn-Teller distortion associated with the d^9 electron structure $t_{2g}^6 e_g^3$ of Cu^{2+} ions (Gerth, 1990). The relaxation of the nearest iron and oxygen shells of the substituted Cu^{2+} ion and the compliance of interpolyhedral angles of corner sharing octahedral structure prevent EXAFS being able to detect any steric effect (Manceau *et al.*, 2000). The *c*-dimension is not sensitive to cupric ion substitution (Gerth, 1990). Kaur *et al.* (2009b) reported conflicting results; namely that copper substitution increases the goethite unit cell dimensions in all directions.

Copper substitution favours goethite dehydration and transformation to hematite based on the endothermic peak of the DTA curve of Cu-goethite decreasing from 300 °C to 285 °C. The imperfect goethite structure due to copper doping is thought to be responsible for the broadening of the dehydration endotherm (Inouye *et al.*, 1972).

The colourless Cu^{+} ion is very easily oxidised to the blue Cu^{2+} ion by hydroxide anions in solution. The catalytic effect of cuprous ions during sulphurous acid leaching promotes iron dissolution from goethite (Warren & Hay, 1975; Byerley *et al.*, 1979). Copper leaches slower than iron from Cu^{2+} co-precipitated samples during sulphuric acid leaching (Kumar *et al.*, 1990). Bibak *et al.* (1995) also reported that copper substitution increases the goethite stability to acid leaching. Kaur *et al.* (2009b) reported a conflicting result that copper substitution increased the goethite leaching rate in hydrochloric acid. However, it is not clear that the copper substituted materials tested by the different groups are comparable.

2.6.5.4 Chromium

The weathering of chromites and pyroxenes in ultramafic rock releases Fe^{2+} and Cr^{3+}, which can recombine to form Cr-containing ferric oxides (Nahon & Colin, 1982; Schellmann, 1983). The transformation of ferrihydrite to goethite was retarded by Cr^{3+} ion in a Cr^{3+}, Fe^{3+} co-precipitation experiment, which was supported by the increasing ratio between oxalic acid dissoluble iron and total iron of the transformed product (Schwertmann *et al.*, 1989). The maximum chromium substitution level in synthetic goethite is reported as 14 mol.% by Lim-Nunez and Gilkes (1987).

Schwertmann *et al.* (1989) reported that the unit cell dimensions of Cr-goethite reduced with increasing chromium substitution with changes following Vegard's Law except for lattice parameter *b*. As with Al-goethite, the length of the *c*-axis exhibited the best linearity with chromium substitution level, possibly because this direction is perpendicular to the H-bonds which are in the *a*-*b* plane of the goethite structure. The unit cell shrinkage and the agreement with Vegard's law for the *c*-axis of Cr-goethite were also reported by Sileo *et al.* (2004). The radius difference between Cr^{3+} (0.62 Å) and Fe^{3+} (0.65 Å) is not as large as between Al^{3+} (0.54 Å) and Fe^{3+} hence the peak shifts in the XRD pattern are not as obvious as with Al-goethite. Nevertheless, the shortening of M-OH bond length was verified by the shift of the corresponding vibrational peak to a higher frequency in the Infra-Red spectrum (Schwertmann *et al.*, 1989).

The similar local structure of substituted Cr^{3+} to that of Fe^{3+} in synthetic goethite was confirmed by EXAFS spectra, which confirmed similar distances of Cr-O and Cr-Fe to Fe-O and Fe-Fe in pure goethite (Manceau *et al.*, 2000; Singh *et al.*, 2002). The $Cr(OH_{0.5})_6$ octahedron is more symmetric than the $FeO_3(OH)_3$ octahedron that contains two distinct sets of ligands (Sileo *et al.*, 2004). With less than 5 % difference in the ionic radius of Cr^{3+} and Fe^{3+} these form isomorphous oxyhydroxides. The chromium end member is known as bracewellite (CrOOH, Pbnm, *a* = 4.492(3) Å, *b* = 9.860(5) Å, *c* = 2.974(2) Å) (Milton *et al.*, 1976). Consequently, *α*-(Fe,Cr)OOH may form an isomorphous substitution series (Schwertmann *et al.*, 1989). However, heterogeneously distributed chromium substitution within goethite has also been reported (Suzuki *et al.*, 2004).

Goethite morphology is also altered by chromium substitution. The crystal size of Cr-goethite was reported to decrease with increasing chromium substitution (0–10.14 mol.%), demonstrated by TEM, XRD, and Mössbauer spectroscopy (Balasubramanian *et al.*, 2002), and confirmed by Sileo *et al.* (2004), Suzuki *et al.* (2004) and Sudakar *et al.* (2004). The Cr-goethite MCD_{110} decreased while MCD_{020} remained constant if the chromium substitution level was over 7 mol.%. This suggests that the width of goethite particle does not change while the crystal becomes thinner, and this has been confirmed by TEM (Schwertmann *et al.*, 1989). Cr-goethite crystals were also reported to be wider than pure goethite with well formed (100) faces, whereas the (001) and (010) faces were narrower (Krehula & Musić, 2009; Kaur *et al.*, 2010). All the above authors agreed that Cr-goethite crystals are platier than pure goethite crystals.

Chromium substitution increases the chemical stability of goethite. The protective corrosion layer that forms on some steels and alloys is Cr-goethite (Cook *et al.*, 1999; Cook, 2004). The half dissolution time in 6 M HCl at 25˚C of 7.8 mol.% Cr-goethite (660 days) is much longer than that of pure goethite (8 days) and 7.9 mol.% Al-goethite (63 days) (Schwertmann *et al.*, 1989). However, Cr-goethite was reported to dissolve faster than Al-goethite in bacterial reductive dissolution and DCB dissolution (Bousserrhine *et al.*, 1999). The dissolution rate of Cr-goethite was found to significantly decrease

with increasing amount of chromium substitution in the range of 0–10 mol.% but remained constant in the 10–14 mol% range (Lim-Nunez & Gilkes, 1987). The Kabai rate constant for Cr-goethite was about one fifth that for pure goethite (Kaur *et al.*, 2010). The percentage of nickel extracted from goethite rich nickel laterite ores from Western Australia was found to be inversely, but weakly, correlated with the amount of chromium substitution in goethite (Watling *et al.*, 2011).

The chemical stability of Cr-goethite may be attributed to the crystal morphology. As mentioned in Section 2.6.4.3, the goethite (001) face dissolves faster than the (010) or (001) face (Cornell *et al.*, 1974). As Cr-goethite tends to be a broader lath-shaped crystal, it should have a smaller proportion of the fast leaching (001) face (Kaur *et al.*, 2010). Schwertmann (1991) also commented that CrOOH has shorter H-bonds which make the Cr-O bond more covalent, and therefore harder to break and detach.

2.6.5.5 Manganese

Generally in oxidising environments, manganese is likely to form separate or intergrown phyllomanganate and tectomanganates such as lithiophorite, birnessite, and asbolane, rather than substituting into the goethite structure to form a solid solution (Manceau *et al.*, 2000). Manganese oxides also geochemically associate with cobalt because the soluble Co^{2+} is likely to be oxidised to insoluble Co^{3+} ion by Mn^{3+}/Mn^{4+}. These materials can also host nickel (Manceau *et al.*, 2000; Georgiou & Papangelakis, 2004).

The transformation from ferrihydrite to goethite was reported to be unaffected by the presence of Mn^{2+} (Cornell, 1988), while Mn^{3+} hinders this transformation (Cornell & Giovanoli, 1987a). Higher (>18 mol.%) Mn^{2+} co-precipitation with ferrihydrite resulted in the spinel mineral jacobsite ($MnFe_2O_4$) forming as an impurity phase (Cornell, 1988; Sileo *et al.*, 2001). Manganese in goethite is predominantly trivalent regardless of whether the samples are derived from Mn^{2+} or Mn^{3+} solutions (Stiers & Schwertmann, 1985; Scheinost *et al.*, 2001). The maximum manganese substitution level in goethite is reported as 15.3 mol.% (Stiers & Schwertmann, 1985; Cornell & Giovanoli, 1987a; Singh *et al.*, 2002; Wells *et al.*, 2006). However, Ebinger

and Schulze (1989) observed different Mn^{3+} substitution levels in goethite by applying the Vegard's law to *c*-axis (34 mol.%) and *b*-axis (14 mol.%) for the goethite and groutite (α-MnOOH, Pbnm, *a* = 4.56 Å, *b* = 10.70 Å, *c* = 2.87 Å) solid solution series. The inconsistent changes of *c*-axis and *b*-axis is believed due to the Jahn–Teller distortion in Mn^{3+} octahedra (Stiers & Schwertmann, 1985).

The substitution of Mn^{3+} in goethite results in contraction of the goethite unit cell along the *a*- and *c*-direction but expansion in *b*-direction (Stiers & Schwertmann, 1985; Alvarez *et al.*, 2005; Wells *et al.*, 2006; Campo *et al.*, 2008; Mejía Gómez *et al.*, 2009). These unit cell changes approach the lattice parameters of groutite (Glasser & Ingram, 1968) with the same space group and similar atom coordinates (Ebinger & Schulze, 1989). The ionic radius of Mn^{3+} (high spin 0.65 Å) is the same as Fe^{3+} (high spin 0.65 Å) (Shannon, 1976); the unit cell change of Mn-goethite is regarded as an effect of the d^4 electron configuration of Mn^{3+} which undergoes a large static Jahn–Teller distortion of the $[Mn(O,OH)_6]$ octahedron (Gasser *et al.*, 1999; Scheinost *et al.*, 2001; Singh *et al.*, 2002; Alvarez *et al.*, 2006; Campo *et al.*, 2008).

Acicular Mn-goethite (15.3 mol.%) consists of well-developed high aspect ratio euhedral crystals often terminating with distinct (021) faces (Cornell & Giovanoli, 1987a; Alvarez *et al.*, 2005; Wells *et al.*, 2006). Twinned dendritic, or star-shaped Mn-goethite is frequently formed from high Mn^{3+} concentration conditions (Cornell & Giovanoli, 1987a; Krehula & Musić, 2006). The incorporation of Mn^{3+} induces $[MnO_6]$ octahedral distortion and inhibits lateral development of double chains of $[Fe,MnO_6]$ octahedrons in the *b*-direction by weakening the H bonds (Wells *et al.*, 2006). Stiers and Schwertmann (1985) reported the goethite domains gradually merge as manganese substitution increases and the CSD size increases preferentially in the *a*-direction.

Mn-goethite generally dissolves faster in HCl than pure goethite (Schwertmann, 1991), although the decreased rate for manganese substitution in the range 3–8 mol.% was also reported (Lim-Nunez & Gilkes, 1987). In contrast, the Mn-goethite dissolution rate in HCl increase for

manganese substitution concentrations below 8.3 mol.% (Alvarez *et al.*, 2006). The Mn-goethite dissolution rate in HCl was also reported to be slower than Co-goethite for the same amount of metal substitution (Alvarez *et al.*, 2008). Mn-goethite dissolution was reported to be slower than pure goethite during reductive dissolution; either bacterial or DCB reduction (Bousserrhine *et al.*, 1999). The congruency of manganese release with iron suggested that manganese was uniformly distributed in the goethite (Lim-Nunez & Gilkes, 1987). However, Gasser *et al.* (1999) reported manganese to have higher concentration in the goethite crystal core and lower concentration at the needle tip from TEM/EDS mapping.

2.6.5.6 Nickel

Nickel substitution in goethite appears to be the major source of nickel in oxidised laterite ores (Manceau *et al.*, 2000). The presence of Ni^{2+} retards the ferrihydrite to goethite transformation more than Co^{2+}, Mn^{2+}, and Pb^{2+} at the same concentration possibly because the higher covalence of bonds formed with Ni^{2+} makes it easier to coordinate with O^{2-} or OH^{-} in ferrihydrite (Cornell, 1988; Cornell *et al.*, 1992; Ford *et al.*, 1999). The spinel phase trevorite ($NiFe_2O_4$) or metallic nickel were found to form when the initial Ni/Fe ratio was higher than 0.1 (Krehula *et al.*, 2005) or the Ni^{2+} concentration was higher than 13 mol.% (Cornell *et al.*, 1992).

The upper limit of nickel substitution in goethite through the alkaline solution ageing approach was reported as 5.5 mol.% by Cornell *et al.* (1992) and Krehula *et al.* (2005) and 6–7 mol.% by Gerth (1990). This substitution maximum is not affected by simultaneous 7 mol.% cobalt or 8 mol.% manganese substitutions, probably because these were separated by host Fe^{3+} cations (Cornell *et al.*, 1992). The maximum substitution of nickel in goethite is relatively low as a proton is required to balance the ionic charge when the bivalent Ni^{2+} substitutes for trivalent Fe^{3+} (Carvalho-e-Silva *et al.*, 2003). Schellmann (1983) claimed that Si^{4+} could also balance the positive charge deficiency from Ni^{2+} substitution for Fe^{3+} in goethite. Kumar *et al.* (1990) claimed that nickel is more likely to coordinate with O^{2-} or OH^{-} (adsorb

on a solid surface) rather than substitute into the goethite structure as Ni^{2+} has a higher CFSE than Cu^{2+} or Co^{2+}.

The $[NiO_2(OH)_4]$ octahedron of Ni-goethite is larger than the normal $[FeO_3(OH)_3]$ octahedron of pure goethite (Carvalho-e-Silva *et al.*, 2003). The Ni-Ni distance between central cations of octahedra with corner linkage was also larger than the normal Fe-Fe distance in the same direction, which is consistent with the larger ionic radius of Ni^{2+} (0.69 Å) than Fe^{3+} (high spin 0.65 Å) (Shannon, 1976). The longer bond lengths suggested nickel incorporation causes breakage of the goethite structural hydrogen bond and twists the connection between the double chains (Carvalho-e-Silva *et al.*, 2003). Although the first oxygen sphere of the nickel site was dilated, the Ni-Fe distance was shorter than Fe-Fe in pure goethite (Manceau *et al.*, 2000; Singh *et al.*, 2002), which suggests the nickel site contracted in the *b*-*c* plane and expanded in *a*-*b* plane, reducing the octahedral distortion of pure goethite. Nickel substitution resulted in a slight increase of the *b* lattice parameter from 9.960 Å to 9.975 Å (~5.5 mol.% Ni/(Ni+Fe)) (Gerth, 1990; Cornell *et al.*, 1992; Wells *et al.*, 2006), while the *a*- and *c*-dimension were almost unchanged (Gerth, 1990; Wells & Gilkes, 1998).

The length of lath shaped Ni-goethite crystals was reported to be 0.3 to 1 μm for 5.5 mol.% nickel substitution (Cornell *et al.*, 1992) and 0.5 to 2 μm for 3.2 mol.% nickel substitution (de Carvalho-e-Silva *et al.*, 2002) from TEM imaging. Krehula *et al.* (2005) reported smaller Ni-goethite crystals developed with increasing nickel substitution based on XRD line broadening measurements, which has been also reported by Wells and Gilkes (1998) though this effect was not observed in later work (Wells *et al.*, 2006). The effect of nickel substitution on goethite morphology has also been suggested to be insignificant (Sudakar *et al.*, 2004).

The effect of nickel incorporation into goethite between ~2–4 mol.% was not found to have significant impact on the dissolution rate in HCl (Lim-Nunez & Gilkes, 1987). Incorporation of small concentrations (~2.4 wt.%) of nickel, cobalt and copper has been found to increase goethite dissolution rate in sulphuric acid. (Kumar *et al.*, 1990). Nickel was more leachable from goethite than cobalt and copper. Nickel was also reported to be concentrated near the

surface of goethite based on incongruent release of nickel and iron (Wells & Gilkes, 1998).

Nickel co-precipitated goethite and nickel adsorbed samples have similar dissolution curves (Kumar *et al.*, 1990). Kumar *et al.* (1990) suggested that stronger Ni-OH bonds due to relatively high crystal field stabilisation energy (CFSE) of Ni^{2+} may encourage surface-induced precipitation, and suppress structural incorporation into Ni-goethite. This structural configuration may be responsible for selective leaching of nickel (lower value of Fe/Ni in leachate) (Kumar *et al.*, 1990). The preferential release of nickel over iron suggested non-uniform nickel distribution in synthetic Ni-goethite and/or that nickel could also adsorb on co-precipitated Ni-goethite (Cornell *et al.*, 1992).

2.6.5.7 Phosphorus

The presence of phosphorus in goethite has been studied extensively due to its importance in agriculture and its deleterious effects in steelmaking. Small amounts of phosphorus makes steel brittle and subsequently iron ores with levels greater than 0.075 wt.% concentration attract a penalty pricing which increases with increasing phosphorus content (Cheng *et al.*, 1999).

Phosphate adsorption retards the ferrihydrite to goethite transformation but favours hematite formation (Schwertmann, 1966, 1991; Kandori *et al.*, 1992; Shaw *et al.*, 2005). Goethite synthesised from high phosphate concentration environments demonstrates star-shaped and twinned crystals due to the preferential phosphate adsorption by singly coordinated OH groups located on terminal (021) faces relative to prismatic (110) arm faces (Barrón *et al.*, 1997; Gálvez *et al.*, 1999; Shaw *et al.*, 2005). Quin *et al.* (1988) attempted to co-precipitate phosphorus with ferrihydrite and then convert the product to goethite. The results suggest phosphorus did not substitute into the goethite structure but adsorbed onto goethite crystals, limiting goethite growth. Low phosphorus concentrations (<6.8 mol.%) resulted in poorly ordered goethite, while higher concentrations resulted in non-crystalline products.

Although phosphorus in apatite and svanbergite was effectively removed from iron ores using acid leaching (Zhang & Muhammed, 1989; Cheng *et al.*,

1999), bioleaching (Wang *et al.*, 2010), direct smelting (Li *et al.*, 2011), and gas reduction (Tang *et al.*, 2010), some phosphorus remained and was much harder to remove. This remaining phosphorus was believed to be present as a solid solution in goethite (Morris, 1998). However, the size and valency of phosphorus are not suitable for its structural substitution in goethite and surface adsorption is more likely to occur (Parfitt & Atkinson, 1976; Quin *et al.*, 1988; Cheng *et al.*, 1999). Although silicon, phosphorus, and aluminium were confirmed to be closely associated with (and occluded in) some natural goethites by EPMA mapping, the structural substitution of phosphorus in goethite has not been confirmed using TEM (MacRae *et al.*, 2011). The occlusion of phosphate-goethite was also observed in a phosphate-ferrihydrite co-precipitation experiment (Gálvez *et al.*, 1999). Torrent and Barrón (1990) found that the amount of non-extractable phosphorus was closely related to goethite crystal morphology. Multidomain laths retain more phosphorus than monodomain crystals; the presence of V-shaped interdomain grooves (determined by (110) or the (110) and (100) faces of contiguous domains) and the slit-shaped macropores between the domains may provide sites where phosphorus is strongly bonded (Torrent & Barrón, 1990). Research to determine the location of phosphorus in goethite is still the object of significant efforts.

2.6.5.8 Silicon

Silicate species strongly hinder the nucleation and growth rate of goethite (Karim, 1984; Schwertmann, 1991). The presence of silicon in solution during precipitation of iron oxides delays the transformation of ferrihydrite to goethite and promotes the formation of hematite over goethite (Cornell *et al.*, 1987; Mejía Gómez *et al.*, 2011). Complete transformation from ferrihydrite or lepidocrocite to goethite in the presence of high concentrations of silicate species can take longer than several months (Schwertmann & Taylor, 1972a, b). Slow goethite growth results in the formation of large monodomain crystals normally several hundreds of nanometers across, and perpendicular to the [001] direction (Schwertmann & Taylor, 1972a, b; Cornell *et al.*, 1987; Glasauer *et al.*, 1999). These large goethite crystals were less acicular than normal goethite, as silicate species

preferentially adsorbed on goethite tips and retarded growth in the [001] direction, resulting in a clear diamond tip, *i.e.* (021) crystal habit (Cornell & Giovanoli, 1987b; Cornell *et al.*, 1987; Quin *et al.*, 1988; Glasauer *et al.*, 1999).

Isodimensional and twin goethite with low aspect ratio have been formed by sample ageing for up to two years (Schwertmann & Taylor, 1972a; Glasauer *et al.*, 1999). Those authors who claimed smaller or poorly crystalline goethite formed in the presence of silicate still followed pure goethite synthesis procedures (with short ageing time of less than a month) and hence failed to allow the goethite particle morphologies to fully develop (Quin *et al.*, 1988; Kandori *et al.*, 1992; Kwon *et al.*, 2007a; Kwon *et al.*, 2007b; Mejía Gómez *et al.*, 2011). Natural goethite forms on geological time scales therefore only goethite synthesis experiments with long term ageing can approach simulation of the formation of natural goethite.

Silicon is regarded as being difficult to incorporate into the goethite structure (Cornell *et al.*, 1987; Quin *et al.*, 1988; Mejía Gómez *et al.*, 2011). The Fe-O-Si bond in Fourier Transform Infrared Spectroscopy (FTIR) data and the [FeO_6] octahedral linkage distortion in Extended X-ray Absorption Fine Structure (EXAFS) data reported by Kwon *et al.* (2007a; 2007b) could arise from chemical bonding at the goethite surface (Hiemstra *et al.*, 2007). Goethite and silicate co-precipitation experiments (Glasauer *et al.*, 1999), silicon adsorption on goethite surface tests (Torrent *et al.*, 1992; Gerth *et al.*, 1993), and the characterisation of natural goethite morphologies (Smith & Eggleton, 1983) all suggested that silicon is either adsorbed on the goethite surface or located at goethite domain boundaries.

2.6.5.9 General effects of metal substitution in goethite

Metal substitution in the goethite structure is usually verified by changes in the goethite lattice dimensions. The effect of different metal substitution on goethite lattice parameters and dissolution properties is highly variable. Nickel and cobalt are often associated with goethite in lateritic ores, along with aluminium, chromium and manganese (Golightly, 1979; Trolard *et al.*, 1995; Brand *et al.*, 1998; Georgiou & Papangelakis, 1998; Beukes *et al.*,

2000; Georgiou & Papangelakis, 2004; Yongue-Fouateu *et al.*, 2006; Andersen *et al.*, 2009).

Studies of element substitution for aluminium, cobalt, copper, chromium, manganese, and nickel have primarily been carried out on synthetic goethite. The maximum substitution levels of these guest metal ions in goethite are usually achieved in high alkaline conditions and may not represent the natural soil conditions. The linear correlations between the metal substitution levels and the lattice parameters (Vegard's Law) were generally found to exist for these metals. The plots of goethite lattice parameters versus molar percentage of the metals substituted in goethite M/(Fe+M) are shown in Figure 2-15. The linear fitting of these plots and the corresponding references are listed in Table 2-2. Note that two groups of Co-goethite data from Pozas *et al.* (2004a) and Núñez *et al.* (2003) have been excluded as these are not consistent with the rest of the data points. The discrepancy is believed to be caused by different Co-goethites synthetic routes, namely use of Fe^{2+} oxidisation rather than Fe^{3+} co-precipitation which was the preferred route of other researchers (Cornell & Giovanoli, 1989; Gerth, 1990; Gasser *et al.*, 1996; Pozas *et al.*, 2004a; Alvarez *et al.*, 2008).

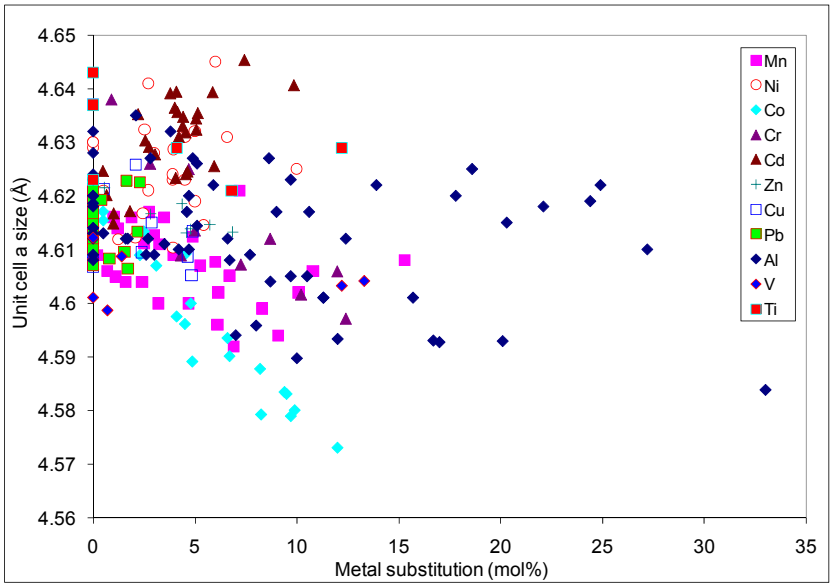

(a)

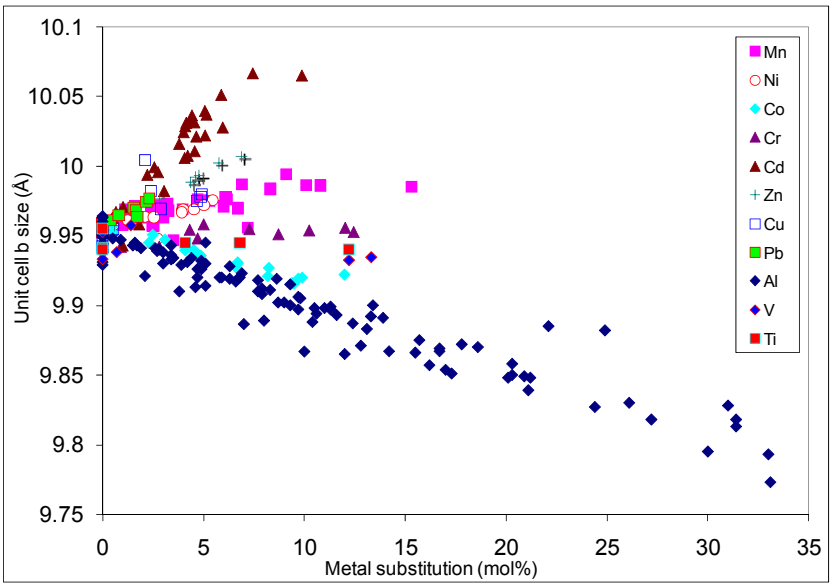

(b)

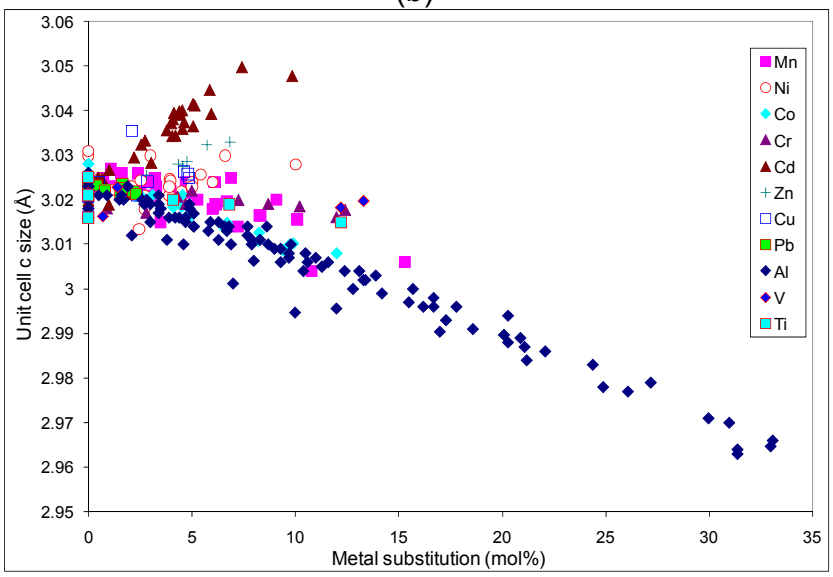

(c)

Figure 2-15 Change of goethite lattice parameter a (a), b (b) and c (c) with amount of metal substitution.

Vegard's Law cannot be applied to all the lattice dimensions of substituted goethite. The *a*-axis length can tolerate goethite structural distortions and therefore does not show good linearity versus the amount of guest metal substitution. The statistical significance of linear correlations have been found (95% confidence level) for lattice parameters *a*, *b* and *c* for aluminium, cobalt and manganese, for *a* and *c* parameters for chromium, for *a* and *b* parameters for nickel and for the *b* parameter for copper. All these metal substitutions were found to be linearly correlated to the change of *b*-axis length except for chromium substitution, which linearly correlates with

lattice parameters *a* and *c*, but not *b* (Schwertmann *et al.*, 1989). The Cr-goethite lattice parameters reported by Wells *et al.* (2006) were excluded as these largely deviate from data in other reports.

Alvareze *et al.* (2007) demonstrated that aluminium has greater influence on the change of goethite lattice parameters than manganese, when simultaneously substituted. All lattice parameters increased with decreasing aluminium and increasing manganese levels. This trend is similar to aluminium only substitution, but different to manganese only substitution, which resulted in an increase in *b* and decreased *a* and *c*.

In the di-, tri- and tetra-metal substitution of cadmium, chromium, lead and zinc into synthetic goethite, the change of unit cell parameters is far more complicated than the single elemental substitutions. No direct relationship between change of lattice parameters and the amount of total metal substitution can be found in the work of Kaur *et al.* (2009a). In the di-metal substitution system, the expansion of the goethite unit cell was greatest if zinc was the co-metal of substitution, and become progressively smaller in the order for co-metals cadmium, chromium and lead. The expansion of the unit cell was observed for all tri- and tetra- metal substitutions in goethite. However, it was impossible to distinguish the effect of individual metals. With substitution of any combination of three metals (Cd, Cr, Pb or Zn) or all four of these, with total metal substitution of 5.6–8.7 mol.%, the expansions of the goethite unit cell were very similar. The general impacts of metal substitution on goethite morphology and dissolution rate detailed in Section 2.6.5 is briefly summarised in Table 2-3 along with the main references.

Table 2-2 Linear fitting of M-goethite lattice parameters with metal substitution level

Substituted metal (M)	Linear fitting of *a*	R^2	Linear fitting of *b*	R^2	Linear fitting of *c*	R^2	Maximum substitution (mol.%)	No. data points	References
Al	y = -0.001x + 4.6196	0.4044	y = -0.0045x + 9.9471	0.9221	y = -0.0017x + 3.0231	0.9688	33.1	127	(Thiel, 1963; Jónás & Solymár, 1970; Goodman & Lewis, 1981; Schulze, 1984; Schulze & Schwertmann, 1987; Fazey *et al.*, 1991; Bousserrhine *et al.*, 1998; Li *et al.*, 2006; Wells *et al.*, 2006; Wu, 2012)
Co*	y = -0.0039x + 4.6171	0.8224	y = -0.0034x + 9.9532	0.8354	y = -0.0012x + 3.0224	0.6573	12	15	(Gerth, 1990; Kumar *et al.*, 1990; Bousserrhine *et al.*, 1999; Alvarez *et al.*, 2008)
Cr	y = -0.0011x + 4.6181	0.6365	y = -0.0004x + 9.9599 ‡y= -0.0003x + 9.9564	0.9696 0.6666	y = -0.0005x + 3.0244	0.9354	14	25	(Lim-Nunez & Gilkes, 1987; Schwertmann *et al.*, 1989; Bousserrhine *et al.*, 1999; Sileo *et al.*, 2004)
Cu	y = -0.0029x + 4.6233	0.5984	y = 0.0051x + 9.9567	0.6518	y = 0.0005x + 3.0220	0.1426	4.88	10	(Gerth, 1990; Kumar *et al.*, 1990; Bibak *et al.*, 1995)
Mn	y = -0.0007x + 4.6094	0.6647	y = 0.0079x + 9.9357	0.9378	y = -0.0017x + 3.0272	0.9219	47†	66	(Stiers & Schwertmann, 1985; Vandenberghe *et al.*, 1986; Ebinger & Schulze, 1990; Vempati *et al.*, 1995; Ford *et al.*, 1997; Bousserrhine *et al.*, 1999; Scheinost *et al.*, 2001; Sileo *et al.*, 2001; Alvarez *et al.*, 2005; Alvarez *et al.*, 2006; Wells *et al.*, 2006)
Ni	y = 0.0022x + 4.6151	0.1593	y = 0.0029x + 9.9550	0.3730	y =0.0004x + 3.0229	0.0764	10	27	(Gerth, 1990; Wells & Gilkes, 1998; de Carvalho-e-Silva *et al.*, 2002; Wells *et al.*, 2006)

* Only Co^{3+}-goethite data was calculated. Co^{2+} expands goethite unit cell when precipitation with Fe^{2+} (Núñez *et al.*, 2003; Pozas *et al.*, 2004a).

† Full goethite-groutite solid solution series has been proposed (Stiers & Schwertmann, 1985; Ebinger & Schulze, 1990; Scheinost *et al.*, 2001).

‡ The linear relationship of *b*-axis length and metal substitution level was fitted with two lines (Schwertmann *et al.*, 1989).

Table 2-3 The impact of metal substitution on goethite crystal morphology (TEM, MCD) and surface area

Substituted metal	TEM crystal width	TEM crystal length	TEM crystal domain size	MCD_{110}	MCD_{111}	Acid dissolution rate	Surface area	Reference
Al	Increase	Decrease	Increase	Increase	Increase	Decrease	Variable depending on synthetic methods	(Schulze & Schwertmann, 1984; Schwertmann, 1984b; Schulze & Schwertmann, 1987; Wells *et al.*, 2006)
Mn	Narrower	Decrease	-	-	-	Increase	Increase	(Alvarez *et al.*, 2006; Wells *et al.*, 2006)
Ni	Narrower	Decrease	Decrease	Decrease	-	Increase	Increase	(Kumar *et al.*, 1990; Wells *et al.*, 2006)
Co	Narrower	Decrease	Decrease	Decrease	-	Increase	Increase	(Kumar *et al.*, 1990; Gasser *et al.*, 1996; Pozas *et al.*, 2004a; Alvarez *et al.*, 2008)
Cr	Increase	Decrease	-	-	-	Decrease	Decrease	(Schwertmann *et al.*, 1989; Rao & Sastri, 1996; Wells *et al.*, 2006)
Cu	-	Decrease	-	Increase	Increase	Increase	Increase	(Kumar *et al.*, 1990; Kaur *et al.*, 2009b)

2.7 Summary

Goethite and nontronite are main nickel containing minerals for oxide type nickel laterite ore and clay type nickel laterite ore, respectively. In order to fulfil the research objectives stated in Section 1.4, the goethite crystal structure, morphology, acid dissolution mechanisms, and the effect of guest metal substitutions on these properties were reviewed. This published data will be compared with the results observed from characterisation of Western Australian nickel laterite ores in an attempt to explain the variation of the laterite leaching performances in the following chapters. The nature of turbostratic disorder and the crystal structure and chemistry of nontronite was also reviewed. This information will contribute to the understanding of difficulties of fitting nontronite XRD patterns and developing better models for the quantitative phase analysis of this mineral.

Chapter 3 Materials and Methods

This chapter covers details of the materials, equipment and techniques used in this study to characterise laterite ore samples and test their leaching performance. Brief details of the principles behind the techniques are additionally included where appropriate.

3.1 Materials

3.1.1 Laterite samples

Fifty two nickel containing laterite ore samples were collected from four mine pits in the Yilgarn Craton, Western Australia (Elias *et al.*, 1981). Further details of sample locations and their geological profile are confidential under a project agreement requested by the mine owner. The samples from the four pits were labelled as A1 – A17, B1 – B20, C1 – C10, and D1 – D5. The masses of these samples ranged from 200 g to 500 g. The particle size of the supplied laterite ore samples was less than 2 cm. The samples were mainly yellow to brown although grey and greenish samples were also observed.

3.1.2 Nontronite samples

In order to better characterise the nontronite present in the 52 laterite samples, a nontronite rich material (greenish with mottled stains ~500 g), known as Bulong nontronite was collected from the same region as the other samples. The nontronite models used in Quantitative X-Ray Diffraction (QXRD) for these laterite samples were derived for the nontronite purified from this material (Chapter 4 and Chapter 5).

A nontronite standard, NAu-1, was supplied by Mr. Mark Raven (CSIRO Land and Water, Adelaide). This Australian nontronite standard was mined in Port Lincoln, South Australia with a full characterisation reported by Keeling *et al.* (2000). This nontronite standard has been used in several previous studies (Gates *et al.*, 2002; Kim *et al.*, 2004; O'Reilly *et al.*, 2006; Scarlett *et al.*, 2011).

3.1.3 Other materials

Other materials used to assist the analysis of the laterite samples and to facilitate the experiments included in this study are detailed in Table 3-1.

Table 3-1 Standards and materials used in this project

Material	Chemical formula	Manufactory/ supplier	Experimental application
synthetic goethite	FeO(OH)	Synergy Pigment Australia Pty. Ltd.	Simulation of laterite samples; Pure goethite standard.
quartz	SiO_2	Cook Industrial Minerals Pty. Ltd.	Simulation of laterite samples;
calcium fluorite	CaF_2	Sigma-Aldrich Pty. Ltd.	Internal standard for XRD
corundum	Al_2O_3	Praxair Surface Technologies, Inc.	Internal standard for XRD
lanthanum hexaboride	LaB_6	NIST Standard Reference Material 660b	XRD line profile characterisation standard for goniometer calibration
sintered corundum	Al_2O_3	NIST Standard Reference Material 1976	XRD instrumental calibration standard
potassium hydroxide	KOH	Sigma-Aldrich Pty. Ltd.	Caustic digestion of laterite ore samples
lithium chloride	LiCl	Sigma-Aldrich Pty. Ltd.	To disperse nontronite clays and purify them
calcium chloride	$CaCl_2$	Sigma-Aldrich Pty. Ltd.	To disperse nontronite clays and purify them
sulphuric acid	H_2SO_4	Sigma-Aldrich Pty. Ltd.	Acid leaching of laterite ore samples
deionised water	H_2O	Department of Imaging and Applied Physics; CSIRO Waterford laboratory	Assist washing the residuals from leaching or digestion; Powder samples dispersed by DI water for TEM imaging
Milli-Q® water	H_2O	Produced by Milli-Q® Plus 185 water purifier (> 18MΩcm)	Nontronite clay dispersion and separation
ethanol absolute	C_2H_5OH	VMR International S.A.S	Assist micronising of powder samples for QXRD

3.2 Experimental methods

Mineralogical characterisation, phase composition and elemental analyses of the ore samples were conducted by a combination of powder X-ray Diffraction (XRD) (both laboratory based and synchrotron radiation),

Inductively Coupled Plasma Optical Emission Spectrometry (ICP-OES) and electron microscopy techniques including: Scanning Electron Microscopy (SEM), Transmission Electron Microscopy (TEM), Scanning TEM (STEM), Energy Dispersive Spectroscopy (EDS), Electron Energy Loss Spectroscopy (EELS) and Energy Filtered TEM (EFTEM). These analytical techniques were also used to re-survey the leached or digested residues at various stages of the process.

The leachability of the ore samples was tested by column leaching in ambient conditions and atmospheric pressure leaching with elevated temperatures.

3.2.1 General sample preparation

Due to the heterogeneous phase content and the differences in morphology of the natural laterite ore samples, it was necessary to split the sample to ensure representative sub-samples were available for analysis. A manual riffle splitter was used to subdivide the laterite ore samples into 100 g aliquots to ensure a uniform and consistent sampling from the bulk supply.

The 100 g subsamples were crushed using a Rocklabs® vibration crusher for 10 seconds to reduce the particle size of ore samples to less than 1 mm. This procedure effectively converts the ore samples into a homogenous powder. A tungsten carbide ring mill was used in the vibration crusher to ensure there was no iron contamination during this size reduction process. Long milling times were avoided to eliminate concerns that milling may alter the samples, *e.g.* elevated temperature caused by milling might dehydrate the goethite phase in the laterite samples. The mineral phases were assumed to be evenly distributed in the milled powder so the subsequent subsamples for characterisations were obtained by randomly sampling from the milled powder.

3.2.2 Inductively coupled plasma optical emission spectroscopy

Inductively Coupled Plasma Optical Emission Spectroscopy (ICP-OES) is a common analytical technique used for determination of the elemental composition of samples. It is an emission spectroscopy that uses the

inductively coupled plasma to excite ions in samples which emit electromagnetic radiation at wavelengths characteristic of each element present. The intensity of this emission is indicative of the concentration of the element in the sample (Brenner & Zander, 2000).

ICP-OES analysis of the laterite ore samples as well as various leach and digestion residues was carried out at the CSIRO Process Science and Engineering, Waterford laboratory (http://www.csiro.au/Portals/About-CSIRO/Where-we-are/Western-Australia/Waterford.aspx). The solids were analysed after digestion in Sigma Chemicals 12:22 lithium borate flux and dissolution in deionised water.

3.2.3 X-ray diffraction

X-ray diffraction is a non-destructive technique for phase identification and quantitative analysis, which is used extensively in this research to examine the mineralogical composition of laterite ore samples and their dissolution residues. This technique is based on the relationship between the interference of coherently scattered X-ray waves by the electrons in crystal unit cells and the crystal interplanar spacing with specific incident X-ray wavelength.

This constructive interference is expressed by Bragg's law:

$$n\lambda = 2d\sin\theta \qquad \text{Eq. 3-1}$$

where:

n = integer determined by the reflection order
λ = X-ray wavelength
d = interplanar distance
θ = half diffraction angle.

An XRD pattern is formed by plotting the diffracted intensity with respect to diffraction angle over the range of interest. The scattering angles (2θ peak positions) and the relative intensities of the Bragg peaks (*d-I* list) can be compared to known phases recorded in powder diffraction databases for phase identification (Hanawalt, 1986; Hanawalt & Rinn, 1986; Hanawalt *et al.*, 1986). With the application of an appropriate (non-overlapping, similar mass

absorption coefficient) internal standard, the relative intensities of the phases can be used to determine the absolute phase concentration in powder samples (Bish & Howard, 1988; O'Connor & Raven, 1988; Madsen *et al.*, 2011).

Micro-structural information, *e.g.* micro-strain and coherently scattering domain (CSD) size can also be determined after deconvolving the instrumental broadening from the measured peak profiles, which is also known as the fundamental parameters approach (Klug & Alexander, 1974, p290; Cheary & Coelho, 1992; Cheary *et al.*, 2004). The information contained within XRD patterns can be extracted with the assistance of modelling software using the Rietveld method (Rietveld, 1967, 1969) and fundamental parameter approach (Cheary & Coelho, 1992; Cheary *et al.*, 2004). XRD patterns can be generated using a laboratory based X-ray diffractometer or with a high intensity monochromatic synchrotron X-ray source.

3.2.3.1 Specimen preparation

The powder diffraction method requires samples to have small particle size, ideally less than 10 μm, to ensure sufficient grains are sampled within the limited sample volume illuminated by X-ray so that a reproducible diffraction pattern is obtained. Small particle size also helps to reduce micro-absorption effects where phases within the sample have different absorption coefficients for the wavelength of the radiation (Madsen & Scarlett, 2008).

The internal standard method (Hill & Howard, 1987) was employed to determine the absolute concentration of each phase. Calcium fluorite (CaF_2) was used to avoid peak overlaps and large deviations in absorption coefficients for minerals in the sample when using CuKα radiation as the CaF_2 absorption coefficient lies in between those of iron oxides and quartz; for CoKα radiation corundum (Al_2O_3) was used as the internal standard to avoid the high absorption of calcium at this wavelength.

To ensure both the particle size reduction (<10 μm) and adequate mixing of the internal standard, 3 g of powder sample were micronized with 0.333 g internal standard for 5 minutes using a McCrone® Micronising Mill with

sintered alumina grinding media and 10 mL ethanol as grinding aids to give 10 wt.% spiked slurry, which was then oven dried at 70°C. For laboratory XRD analysis, the dried powders were side-loaded into plastic sample holders (25 mm diameter round plate sample area) against a frosted glass slide to alleviate preferred orientation effects (Kleeberg *et al.*, 2008). The top of the sample holders were screeded to ensure correct sample height and to minimise specimen displacement errors.

For synchrotron sample preparation, the dried powder samples were packed into 0.3 mm outer diameter (wall thickness 0.01 mm) borosilicate low-background capillaries (Charles Supper, Massachusetts, USA). An ultrasonic bath was utilised to encourage dense packing of the powder before the capillaries were sealed by melting the glass.

3.2.3.2 Laboratory based XRD

A Bruker® D8 Advance (CuKα radiation) and a D8 Discover (CoKα radiation) X-ray diffractometers were used to collect the XRD patterns of laterite ore samples with slightly different beam path and settings, as summarised in Table 3-2.

Table 3-2 Settings for both Bruker D8 diffractometers

Goniometer parameters	D8 Advance	D8 Discovery
Radiation	Cu	Co
Filters	Ni filter to eliminate CuKβ	Fe filter to eliminate CoKβ
X-ray tube operating voltage	40 kV	35 kV
X-ray tube operating current	40 mA	40 mA
Filament length	12 mm	12 mm
LPSD (angular coverage)	LynxEye PSD (3° 2θ)	LynxEye PSD (3° 2θ)
Number of strip channels used	177	153
Detector discriminator window†	0.05 V	0.14 V
Goniometer radii	250 mm	217.5 mm
Sample length in equatorial plane	25 mm	25 mm
Receiving slit length	17 mm	17 mm
Fixed divergence slit angle	0.3°	0.3°
Primary Soller slit angle	2.5°	2.5°
Secondary Soller slit angle	2.5°	2.5°
Sample spinning speed	30 rpm	15 rpm

† The energy discriminator window of the LynxEye detector was tightened to 1/3 of the normal width to minimise Fe fluorescence when using CuKα radiation for iron rich laterite samples.

To measure all the diffraction peaks for the clay minerals in the laterite samples, XRD patterns on the D8 Advance were collected from 3° 2θ with a knife edge collimator on the primary arm to block most of the low angle air scattering. The instrumental geometry was carefully measured to ensure the primary beam footprint did not exceed the sample stage at this starting angle nor was blocked by the knife edge. The XRD patterns collected on the D8 Discover, using Co radiation, started from 5° 2θ without a knife edge collimator as this diffractometer was primarily used for iron rich samples with low or no clay content. For both diffractometers the step size was 0.01 or 0.02° 2θ with a dwell time 0.5 or 1 second per step. As multiple silicon strips of the LynxEye detector were used to collect data covering 3° 2θ of the pattern simultaneously, the dwell time per step is effectively multiple times of the set dwell time (Dąbrowski *et al.*, 2003), when compared with a conventional scintillator detector.

The diffractometer characterisation including zero error, X-ray emission profiles, Kβ residues, and the stability of both diffractometers were determined with NIST SRM 1976 (corundum plate), and an example is presented in Appendix 2.

3.2.3.3 Characterisation of internal standard

The internal standard method (Bish & Howard, 1988) was used in the QXRD analysis of nickel laterite ore samples as it allows the absolute weight percentages of each phase to be calculated (Madsen & Scarlett, 2008, p318). Also by using an internal standard with known lattice parameters, the random experimental deviations, such as sample displacement in laboratory XRD and capillary displacement in synchrotron XRD, could also be assessed (Allmann, 2008, p127).

The lattice parameters of the internal standard itself were accurately measured first in the presence of a standard reference material with certified lattice parameters. The two internal standards used in this thesis, calcium fluorite and corundum, were mixed with NIST SRM 660a LaB_6 using a micronising mill (Section 3.2.3.1). The XRD pattern of this mixture was analysed by Rietveld fitting (Figure 3-1) with the certified lattice parameter of NIST SRM 660a fixed but the sample displacement error and goniometer

zero error refinable. The calculated lattice parameters of calcium fluorite and corundum, which are used as internal standards with the laterite ore samples are listed in Table 3-3. The two internal standards were then used in QPA of laterite ore samples and assumed to be 100% crystalline.

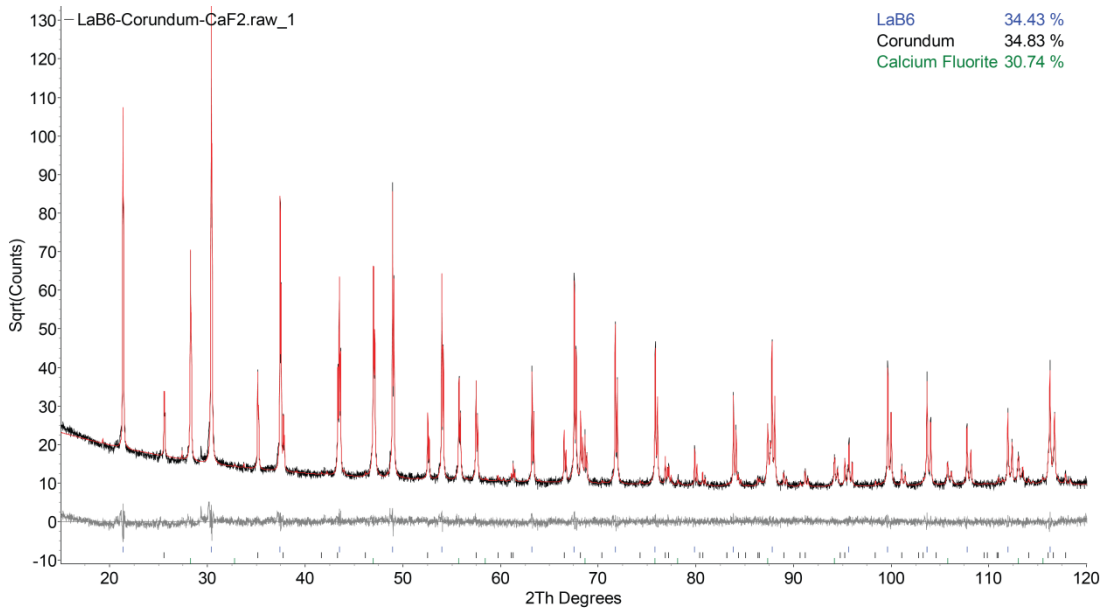

Figure 3-1 Lattice parameters measurement of corundum and calcium fluorite using NIST SRM 660a LaB6 as the internal standard. This fitting achieved Rwp 8.7 and GOF 1.4.

Table 3-3 Lattice parameters of calcium fluorite and corundum

	Lattice parameters	
	a (Å)	*c* (Å)
Calcium Fluorite (CaF_2)	5.46461(3)	-
Corundum (Al_2O_3)	4.75939(4)	12.9930(2)

3.2.3.4 Synchrotron XRD

The synchrotron patterns were collected at the Australian Synchrotron Powder Diffraction (ASPD) Beamline (Wallwork *et al.*, 2007) with Debye-Scherrer geometry using a MYTHEN microstrip detector system comprised of 16 detector modules enabling simultaneous collection of X-rays (Schmitt *et al.*, 2003), as shown in Figure 3-2. One module covers a range of approximately 4.8° 2θ with an approximate 0.2° 2θ gap between adjacent modules. The configuration at the ASPD has pixel spacing approximately

0.00375° 2θ and resulted in a total collection angle of approximately 80° 2θ. Due to the gaps between modules, a second histogram for each sample was collected after shifting the detector 0.5° 2θ. Each histogram was collected for 450 seconds. The two histograms were spliced by the program DataPro v2.7 beta (Gu, 2011), taking into account the beam intensity attenuation via the ion chamber counts, before the diffraction data analyses. The combined patterns spanned 1.2° to 81° 2θ covering d-values from 0.77 to 40 Å using approximately 1 Å radiation and a parallel beam of 2 mm x 0.5 mm. The capillaries were spun at 15 rpm during data collection. The spinner incorporated a motorised goniometer head with image capture and processing software which automatically aligns capillary eucentric positions reproducibly in the order of 10 μm. Other instrumental settings are summarised in Table 3-4.

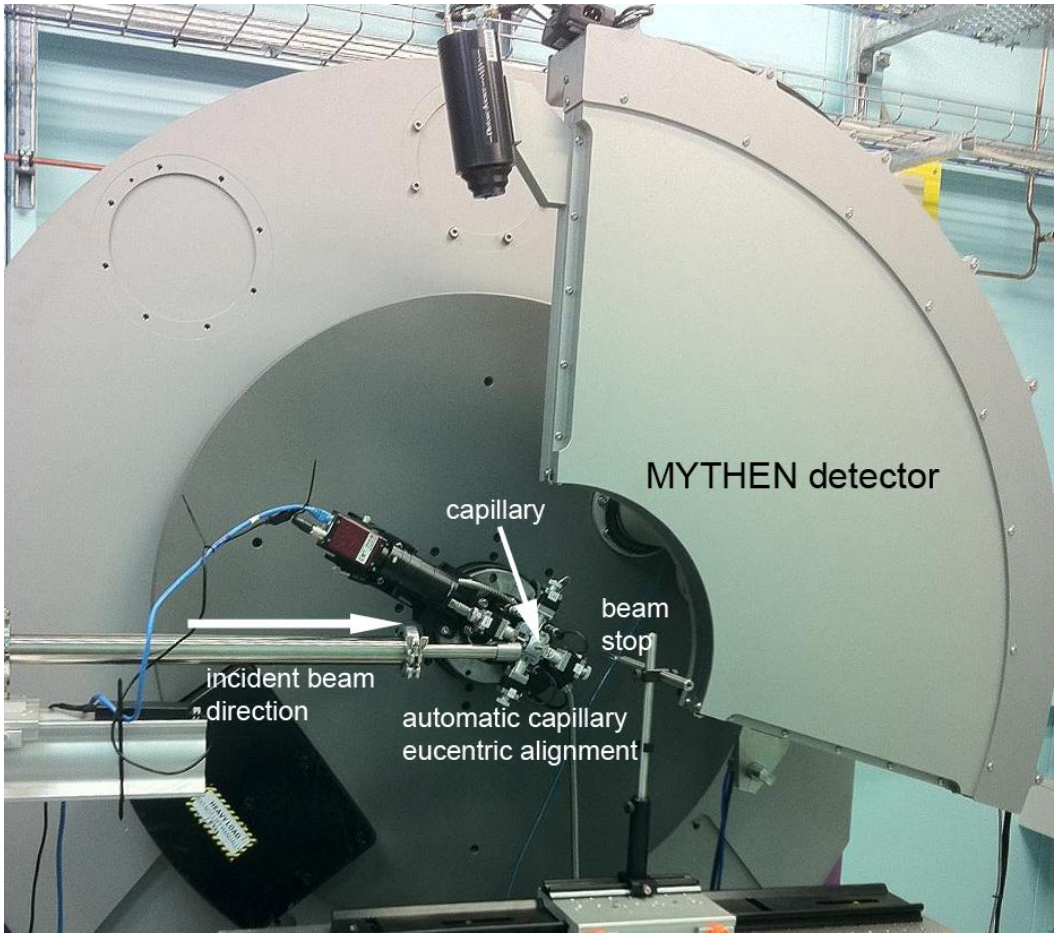

Figure 3-2 The Debye-Scherrer configuration at the ASPD

Table 3-4 Diffractometer parameters of the ASPD

Parameter	Value
Radiation wavelength	0.999047 Å (approx. 12.396 keV)
Source	Bending magnet on a 3 GeV synchrotron
Detector	Mythen II microstrip detector
Monochromator	Si (111) flat crystal pair
Goniometer radii	761.2 mm
Source size	2 mm wide, 0.5 mm high
Take off angle	1.2° 2θ

The instrumental characterisation including accurate wavelength, zero error, and instrumental convolutions of this configuration were determined with NIST SRM 660b (LaB_6) diluted with diamond powder 1:9 by weight. Details of these procedures are available in Appendix 3.

3.2.3.5 Capillary displacement

For synchrotron XRD patterns collected in Debye-Scherrer geometry, the capillary displacement which causes the pattern to shift can be examined using an internal standard method. As CaF_2 from the same container is used as the internal standard for all the nickel laterite ore samples the peak positions of CaF_2 should not vary from sample to sample. However, the variation of the CaF_2 peak positions observed in synchrotron patterns was up to 0.004° 2θ (Figure 3-3), which is larger than the Mythen detector step size of 0.00375° 2θ (Section 3.2.3.4) and cannot result from the fluctuation of photons counted by detector pixels. These variations probably result from the different capillary positions for each pattern. A capillary displacement macro shown in Appendix 5 was used to account for this experimental deviation.

The capillary positions refined by the TOPAS macro (Appendix 5) are shown in Figure 3-4. Compared with the capillary cross section dimension, the displacement is not substantial but appreciable and calculable using the internal standard spike and capillary displacement macro. The maximum displacement is in the order of 10 μm, consistent with the motorised auto-alignment goniometer head specification (Section 3.2.3.4).

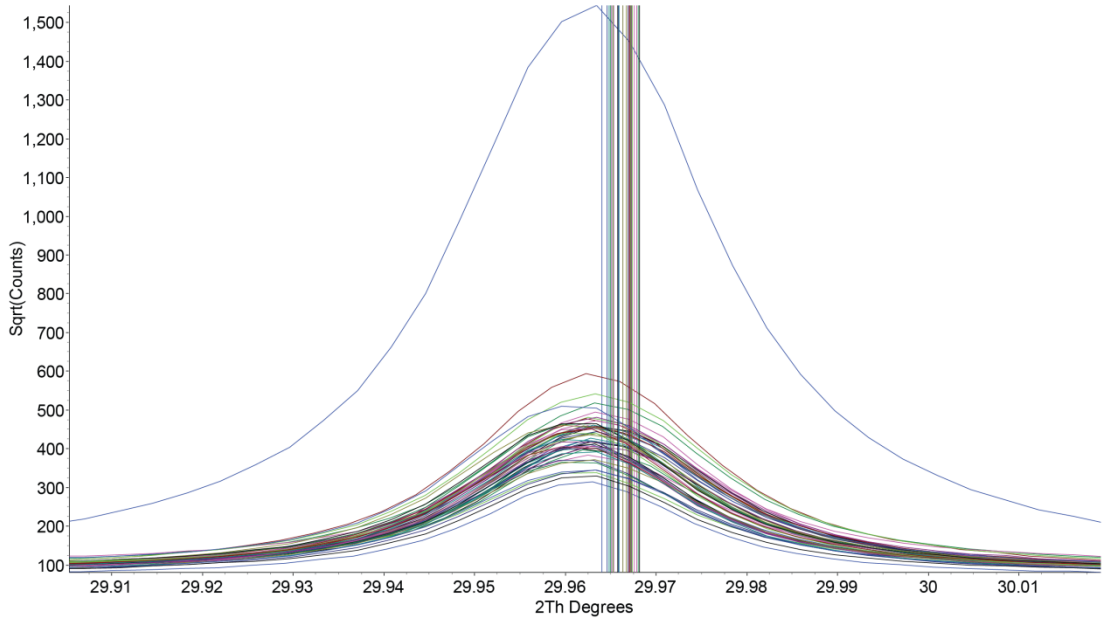

Figure 3-3 The variations of CaF_2 220 peak position derived from pseudo-Voigt peak fitting to the XRD patterns of the 52 CaF_2 spiked laterite ore samples. The zero error (-0.001772471° 2θ) calculated from synchrotron instrumental characterisation (Appendix 3) is applied. The large peak is from the pure CaF_2 pattern.

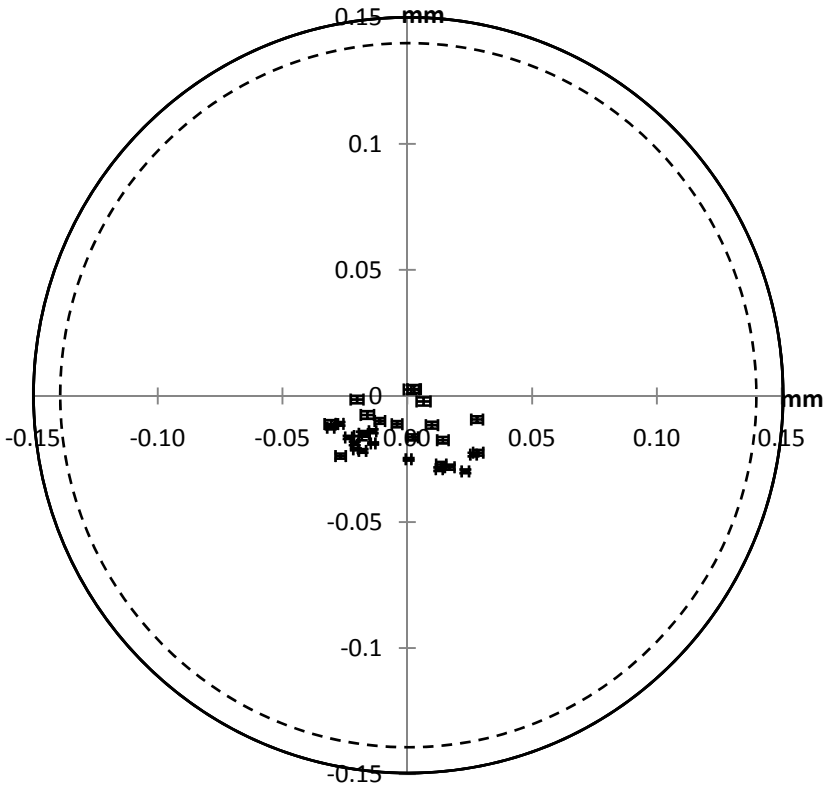

Figure 3-4 The refined displacement of capillary spinning centre with refinement errors, compared with the dimension of the capillary (Section 3.2.3.4). The solid line circle indicates the outer wall and dash line circle, the inner wall.

3.2.3.6 Phase identification

Crystalline phases of the laboratory XRD patterns were identified using Bruker® Diffrac.EVA v2.1 software to search the ICDD® Powder Diffraction File database (PDF-4+ 2011 RDB v4.1102). The spliced synchrotron XRD patterns (.xye file) were converted to raw files by the Bruker® FileExchange program before phase identification using EVA. It should be noted that the step size of the spliced synchrotron XRD patterns is not constant, so these should be treated as variable step patterns when converting file formats otherwise the step size of the resultant patterns is not correct.

Peak positions and relative peak intensities were used to confirm the search/match results. Pattern quality and phase chemistry were also checked to ensure the selection of sensible phases. The crystal structures of the identified phases were exported from the ICDD® DDView+ software, which incorporates the Linus Pauling File (LPF) database, in crystallographic information file (.cif) format.

3.2.3.7 Quantitative analysis and lattice parameter measurement

Bruker® TOPAS v4.2 was used to perform Rietveld quantitative analyses for both laboratory data and synchrotron data. The instrument parameters in Table 3-2 were used to assess instrumental contributions to the line broadening using the fundamental parameters approach. The instrumental convolutions parameterised in Appendix 3 were used to represent the instrumental contribution to line broadening of synchrotron data. The Lorentz-Polarisation factor was set to 0 for laboratory XRD data analysis as no monochromator was used, and set to 90 for the entirely polarised beam in synchrotron data analysis.

Although low background capillaries were utilised, the glass contribution to the background is still obvious in the synchrotron patterns. Two methods were developed to separate the capillary contribution from the measured pattern, which are detailed in Appendix 4. The low angle high background due to residual air scattering in laboratory XRD patterns and the small angle scattering (SAX) effect in synchrotron patterns were modelled mathematically and are also detailed in Appendix 4.

Quantitative phase analyses of laterite ore samples and their corresponding leaching residues are based on laboratory XRD patterns, since much higher sample volumes were examined compared to the small amount of powder in capillaries for synchrotron XRD. The lattice parameters of goethite in laterite samples were derived from synchrotron patterns which have much higher angular resolution than that of laboratory data.

The lattice parameters of internal standards were defined after the instrument was characterised. The result was fixed in the subsequent analysis of the spiked samples, with the sample displacement of laboratory data and capillary displacement of synchrotron data refined, as summarised in Table 3-5.

Table 3-5 Parameters refined during XRD pattern fitting

	Laboratory patterns			Synchrotron patterns		
Parameter	Global	Internal standard	Sample phases	Global	Internal standard	Sample phases
Background[1]	Y			Y		
Zero error[2]	predefined			predefined		
Sample displacement	Y			Y[3]		
Scale		Y	Y		Y	Y
Lattice parameters		predefined	Y		predefined	Y
Crystallite size (LVol-IB)		Y	Y		Y	Y

[1] Background modelling is detailed in Appendix 4;

[2] The zero error was predefined based on the peak position of the Standard Reference Materials (Appendix 2, Appendix 3);

[3] The capillary displacement correction in Deybe-Scherrer geometry is detailed in Appendix 5.

The crystallite sizes were determined by the LVol-IB method (volume weighted column height calculated from the integral breadth). This method provides a good measure of the volume weighted average crystallite size (David *et al.*, 2010). The crystallite size extracted from XRD cannot be directly compared with particle size observed from TEM because the latter is a number weighted mean (Rawle, 2008). In addition each mode of measurement (XRD, TEM) will impose its own bias on the measurement of

particle/crystallite size. Particles can also be polycrystalline, which lead to a larger “particle size” than “crystallite size” in same sample.

3.2.4 Transmission electron microscopy

Small sub-samples of the feed ores and their leach or digestion residues were placed in deionised water and ultrasonically agitated for 10 minutes to disperse the particles. A drop of the suspension for each sample was air dried on carbon film supported by 3 mm diameter 200 mesh copper grids.

Transmission electron microscopy (TEM) is a common imaging technique used to investigate the microstructure and morphology of mineral particles. TEM imaging was conducted using a JEOL 2011 equipped with LaB_6 filament operated at 200 kV in the Centre for Materials Research at Curtin University and a JEOL 3000F Field Emission Gun TEM operated at 300 kV in the Centre for Microscopy, Characterisation and Analysis (CMCA) at the University of Western Australia. Both microscopes were equipped with Gatan® digital cameras for particle morphology imaging.

3.2.4.1 Energy dispersive X-ray spectroscopy

Energy Dispersive X-ray Spectroscopy (EDS) provides elemental analysis of selected sample regions during TEM investigations. The interaction between the beam electrons and different orbital shell electrons of the elements within the sample causes X-rays to be emitted with energies characteristic of the element which can then be detected. The characteristic X-rays were used to determine elements and the relative intensities were used to quantify the elemental percentage in the sample area surveyed. The electron beam can be directed onto specific areas of a sample allowing elemental spectra to be obtained from minor sample features of interest or individual particles, if the sample is well dispersed. Since the sample thickness is on the nanometre scale, the interaction volume of the TEM sample being investigated is almost equal to the volume illuminated by the electron beam (Cliff & Lorimer, 1975).

Both TEM instruments used were equipped with an Oxford Instruments® 200 energy dispersive X-ray spectrometer (EDS) for elemental analyses. Quantitative analysis of the EDS spectra collected at 3500-7000 counts per

second for 100 live seconds was performed using Oxford Instruments® INCA-Analyser software based on the methods of Cliff & Lorimer (1975) and Jepson & Rowse (1975). EDS spectra were also collected from carbon film adjacent to the target particles to assess the silicon level in the carbon supporting film. Oxygen was calculated stoichiometrically.

3.2.4.2 Selected Area Electron Diffraction

The camera length for Selected Area Electron Diffraction (SAED) was calibrated by an evaporated aluminium film standard (Ted Pella Inc. CAT# 619). A 2D diffraction pattern analysis tool FIT2D (Hammersley, 1997, 1998) was used to measure the pixel dimensions of diffraction rings.

3.2.4.3 HAADF imaging in STEM mode and EDS mapping

By scanning a converged electron probe, the signals from the sample could be localised in a small area. The forward scattered electrons out to high angle were collected by a High-Angle Annular Dark-Field (HAADF) detector to form images, when the TEM is operated in Scanning Transmission Electron Microscopy (STEM) mode. At the same time as the HAADF image was being collected, the characteristic X-rays emitted from excited sample atoms could be collected by the EDS detector and used to map the location of elements within sample.

The JEOL 3000F TEM in CMCA was also operated in STEM mode and the HAADF detector was used to image the laterite particles. The Oxford Instruments® 200 EDS was used to map the elemental locations in the sample area of interest.

3.2.4.4 EELS and EFTEM

The Electron Energy-Loss Spectrometry (EELS) system attached to the JEOL 3000F TEM was used to record the energy distribution of electrons transmitted through the specimen which have suffered inelastic collisions leading to an energy loss which is characteristic of the elements present and their bonding environment (Williams & Carter, 2009, p679). A magnetic-prism in the post-column Gatan® image filter disperses the electrons according to their energies on the dispersion plane since electrons with different velocities deflect differently in the magnetic field. Plotting electron intensity versus their

energy loss generates an EELS spectrum, which was used to qualitatively assess the elemental composition in the illuminated sample area. An Energy-Filtered TEM (EFTEM) image could be generated by choosing only those electrons with energy loss right at the absorption edge of a specific element detected from the EELS spectrum, with appropriate background subtraction. The magnetic prism/energy filter is a highly sensitive device with an energy resolution less than 1 eV, even when the electron-beam energy is as high as 300 KeV. The relative sample thickness 't/λ' was assessed by comparison of the unfiltered TEM image and the image formed with elastic electrons (t = sample thickness, λ = inelastic mean free path in samples). Ideal samples for EFTEM imaging should have a relative sample thickness of around 0.8. Most of the particles in laterite ore samples were much thicker than this requirement; thin particles were deliberately selected for EFTEM imaging.

3.2.5 Nontronite separation and purification

The Bulong nontronite clay described in Section 3.1.2 was crushed to powder (<1 mm) using a Rocklabs® model 1A ring mill. A sample of 100 g was transferred to a 500 mL cylinder, soaked with deionised water and shaken vigorously. The cylinder was left standing until the particles settled and the clear supernatant was decanted. The powder was washed with deionised water in this way several times until the solids started to form a gel (the particles at this time do not settle under gravity as the total dissolved salt level of the liquid has now decreased). The pulp was further diluted by deionised water into 5 x 500 mL cylinders, allowed to settle under gravity for 1 hour and the supernatant greenish suspensions were collected in a large beaker and dried at 70 °C. After the water had evaporated the residual powder remained as hard green aggregates which were hand crushed using an agate mortar and pestle until the powder passed through a 100 mesh sieve (150 μm opening size).

The NAu-1 nontronite standard (Section 3.1.2) was used as a reference for chemical assay. The NAu-1 nontronite standard was received as bright green rocks. Dark stains indicating impurities in the nontronite rock were carefully removed using a scalpel and the nontronite crumbs were hand

milled to powder with an agate mortar and pestle and passed through a 100 mesh sieve.

The enriched Bulong nontronite powder and the NAu-1 powder were further purified to remove kaolinite using a high-speed centrifuge. Five grams of each subsample was soaked and agitated in 1 L, 0.02 M LiCl solution in rolling plastic bottles for 48 hours to disperse the nontronite Tetrahedral-Octahedral-Tetrahedral (TOT) layers through hydration of the interlayer cations. The resulting suspensions were centrifuged using Heraeus® Multifuge 3S-R centrifuge with a fixed-angle rotor (Figure 3-5) to separate the clays from exchanged LiCl solutions, which were collected and referred to as the "1st cation exchange liquor". The interlayer cations of the settled clays were exchanged by Li^+ using the above method for a second time to ensure the resultant clays were predominantly Li-saturated. Milli-Q® water was used to wash and disperse the Li-saturated clays, which were then centrifuged to collect the supernatant suspensions containing clay fractions less than 0.2 μm in large beakers. The suspensions were flocculated with $CaCl_2$ and settled overnight before the clear supernatants were decanted. The residual $CaCl_2$ solution was removed by centrifuging the mixture. The Ca^{2+} saturation was repeated and the excess $CaCl_2$ was washed with Milli-Q® water and centrifuged repeatedly until the supernatant become turbid. The settled clays were collected and oven-dried at 70 °C. The dried solids were hand crushed with an agate mortar and pestle. The sieved powder (100 mesh) is referred to as purified Bulong nontronite and purified NAu-1 nontronite.

Figure 3-5 Heraeus® #3334 fixed angle rotor with one of the polycarbonate tubes.

3.2.6 Column leaching

In order to simulate heap leaching conditions and characterise the performance factors of the laterite ores of interest to industry, *e.g.* percentage of nickel extractable and sulphuric acid consumptions, the column leaching data for laterite ores (Section 3.1.1) were collected by staff at CSIRO's Process Science and Engineering, Waterford laboratory.

The column leaching conditions are briefly detailed here. Ores (12 kg) were conditioned with 240 g of sulphuric acid (equivalent to 20 kg of acid/t) in a rotating drum, and water was added as required to bind fine particles into competent agglomerates that would increase the liquid permeability and withstand the effects of leaching over a prolonged period. The agglomerates were loaded into columns (150 mm internal diameter; ore bed approximately 1 m high). The columns were irrigated with acidic solution containing 200 g/L of H_2SO_4 at a rate of 10 L/h/m^2 without solution recycle. The leachate from each column was sampled daily and analysed by ICP to determine the concentration of iron, nickel, cobalt, magnesium, calcium, aluminium, and sodium. The leaching was stopped when no significant increase of iron and nickel concentrations were observed. The leaching period generally spanned from 200 to 260 days.

3.2.7 Atmospheric leaching of laterite ores

Four selected limonitic laterite ore samples were extracted using sulphuric acid at 95 °C in a Parr 1 gallon titanium autoclave. The autoclave leaching system is shown in Figure 3-6. Ore samples weighing 200 g were mixed with sulphuric acid with weight ratio 1:1 (1:2 for sample A15 and B11) in total 2 L slurry and were leached for 9 hours (16 hours for sample A15 and B11). A stirring speed of 500 rpm was applied using a dual pitch six bladed impeller. Pulps were sampled from the autoclave via an actuated sampling valve and cooled sample cylinder at selected reaction times. The primary filtrate was collected through a 47 mm 0.45 µm Supor® membrane. The solids were repulped and washed several times, and dried overnight at 110 °C. The primary filtrate and dried solids were analysed by ICP-OES to determine leaching rates. The Solver tool in Microsoft® Excel was used to

refine the solid to liquid ratio in the autoclave to optimise mass balances based on ICP-OES assay for both filtrate and solids. The weight losses of the solids during acid leaching were calculated from the derived solid to liquid ratio. The solids were also examined by Synchrotron X-Ray Diffraction (SXRD) and laboratory-based Quantitative X-Ray Diffraction (QXRD) for phase identification and phase quantification.

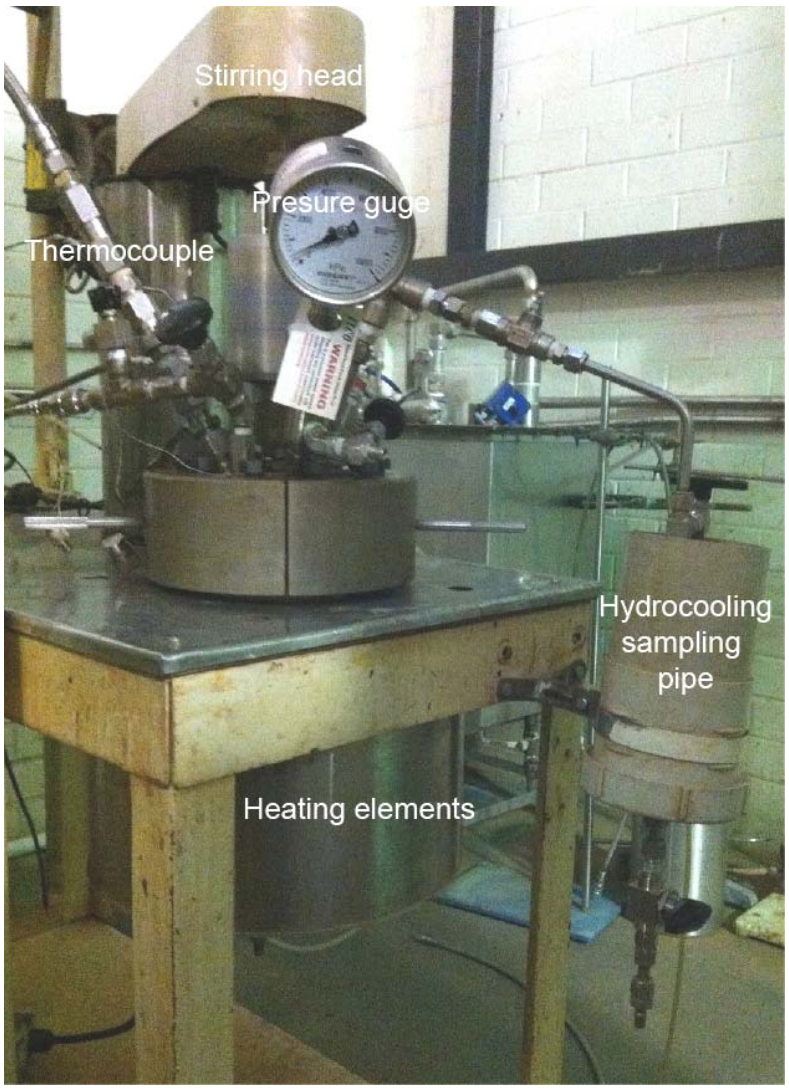

Figure 3-6 Autoclave leaching system used in this study. This system was mainly operated by associate supervisor Dr. Robbie McDonald with assistance from the author of this thesis.

3.2.8 Caustic digestion of the atmospheric leaching residues

In order to concentrate the iron oxides for preparation of samples for TEM imaging, 1 g of the atmospheric leaching residues of laterite sample were digested with 100 mL 5 M potassium hydroxide in a covered Teflon beaker placed in a boiling water bath (85 °C) for 1.5 hours. Magnetic stirring at approximately 200 rpm was conducted during the caustic digestion. The residual solids were filtered using a 47 mm 0.45 μm Supor® membrane then washed by dispersing in 100 mL deionised water twice and filtered again.

3.2.9 Caustic pre-treatment of the laterite ores

Potassium hydroxide caustic pre-treatment of the acid resistant laterite samples was conducted in a Parr 5 gallon 316 stainless autoclave at 95 °C with 450 rpm stirring using a dual pitch blade impeller for 5.5 hours. The solid to liquid ratio (100 mL/g) and the KOH concentration (5 M) were the same as those used in Section 3.2.8. Pulps were taken from the autoclave at the end of the digestion and the pregnant liquor was collected via pressure filter through 330 mm Hollingsworth and Vose Blended Water System Sheets. The mass of the filter paper before use and after drying were recorded to assess the amount of residues attached on the filter paper. The solids were dispersed and washed several times before being dried overnight at 70 °C. The pregnant liquor and the dried solids were analysed by ICP-OES and QXRD.

Chapter 4 The PONKCS method with peak shape modifiers for the quantification of nontronite

4.1 Introduction

This chapter describes a modified Partially Or No Known Crystal Structure (PONKCS) method which takes advantage of the TOPAS diffraction peak profile description tools to quantitatively characterise the turbostratically disordered nontronite clay in Bulong laterite ore samples through XRD techniques. Peak shape modifiers were used with the PONKCS method to achieve better modelling of the anisotropic broadening and asymmetric diffraction peaks of the nontronite. This approach also reduces the number of *hkl* reflections required to form an "envelope fitting" for the complex peak shape of the "unknown phase", reducing the calculation time and increasing the model stability.

This chapter is based on the paper:

Wang, X., Li, J., Hart, R. D., van Riessen, A. & McDonald, R. G. (2011). Quantitative X-ray diffraction phase analysis of poorly ordered nontronite clay in nickel laterites. Journal of Applied Crystallography, 44(5), pp.902–910. DOI: 10.1107/s0021889811027786.

Note: Values in tables are displayed with their uncertainty in adjacent parentheses. Uncertainties are calculated as the estimated standard deviation of the least significant figure of the measured value. This methodology is used throughout this thesis unless otherwise stated.

4.2 Difficulties with quantitative phase analysis of nontronite

Nontronite is a major nickel containing phase in the smectite zone of the laterite profile (Gaudin *et al.*, 2005; McDonald & Whittington, 2008a). Accurate QPA of this phase in laterite ores is important for mining companies who need this information to decide the value of target ore bodies and what metallurgical processes to adopt. However, studies of the high-pressure acid leaching and heap leaching behaviours of these ores are hindered by inadequate quantification of the mineral phases present (Scarlett *et al.*, 2008;

Elliot *et al.*, 2009). Nontronite is not readily quantifiable using the conventional Rietveld QPA approach because this phase has several hydration states and is often chemically variable. Most importantly, nontronite is always turbostratically disordered.

As a swelling smectite, the 001 basal reflection for nontronite is located between d-spacing of 9.7 Å and 15 Å owing to the variable *c*-length caused by interlayer cation hydration. Dehydrated nontronite has the shortest *c*-length with an 001 reflection around 9.7 Å; single layer hydrated nontronite has 4 H_2O molecules coordinated with interlayer cations in a plane parallel to the *a*-*b* plane and an 001 reflection around 12.8 Å; double layer hydrated nontronite has 6 H_2O molecules coordinated with interlayer cations in an octahedron with 2 planes parallel to the *a*-*b* plane and an 001 reflection around 15 Å (Eggleton, 1977; Besson *et al.*, 1983; Tsipursky & Drits, 1984; Bayliss, 1989; Keeling *et al.*, 2000; Dekov *et al.*, 2007; Ufer *et al.*, 2008). For hydrated nontronite there is no crystallographic information file (CIF) available in the ICSD. A typical formula for nontronite is $\mathrm{E_x(Fe,Al,Mg)_2^{VI}(Si,Al)_4^{IV}O_{10}(OH)_2 \cdot nH_2O}$, where VI and IV represent octahedral and tetrahedral sites, respectively and E represent exchangeable interlayer cations normally Na^+, K^+ Mg^{2+}, Ca^{2+} (Keeling *et al.*, 2000; Whittington *et al.*, 2003a; Scarlett *et al.*, 2008). Nontronite can vary in its chemical composition with cation substitutions in octahedral, tetrahedral, and interlayer sites causing variations from published crystal structures. This makes it impossible to find a universal structure model suitable for nontronite from different locations. The asymmetric non-basal reflection bands often present in the smectite XRD pattern are attributed to the turbostratic disorder of the TOT layers which destroys the periodicity in the *c*-direction and essentially forming two dimensional crystallites (Moore & Reynolds, 1997, p340). It is difficult for conventional Rietveld code (Hill & Howard, 1987; Bish & Howard, 1988; O'Connor & Raven, 1988) to calculate the XRD pattern of two dimensional materials.

Bruker® DIFFRAC^{plus} TOPAS software (Bruker AXS, 2009) provides three levels of 'fit objects': (1) structural models containing space group, unit cell dimensions, and atomic species and their positions in the unit cell; (2)

lattice models (Pawley phase or Le Bail phase) specifying space group, lattice dimensions and empirical peak intensities; and (3) peaks phase models, which include a group of related peak positions and peak areas. Fewer crystallographic relationships are used by the latter than the former. Only structural models are normally used for conventional Rietveld QPA. Scarlett & Madsen (2006) introduced the PONKCS method which uses a lattice model to quantify phases with complex XRD patterns. Scarlett *et al.* (2008) used a peaks phase model to quantify the nontronite content of laterite ores during pressure acid leaching. However, currently neither model fits the nontronite asymmetric non-basal reflection bands or anisotropic peak broadening because the models largely rely on "envelope fitting" using isotropic peak shapes.

4.3 "Envelope fitting" in original PONKCS method

Rietveld quantitative phase analysis for turbostratically disordered montmorillonite using a *hkl* file with empirical structure factors for selected *hkl* reflections was demonstrated by Taylor and Matulis (1994) using the Rietveld program SIROQUANT (Taylor, 1991). Bonetto *et al.* (2003) applied a similar approach in the software package FULLPROF (Rodríguez-Carvajal, 1993). This method can be regarded as a precursor of the PONKCS method but has distinct differences. The empirical structure factors Taylor and Matulis (1994) used to fit the montmorillonite experimental XRD pattern were modified from the structure factors derived from an approximate montmorillonite crystal structure. As the sum of the structure factors squared ($\Sigma_{hkl}|F|^2$) was kept unchanged during the modification, the *hkl* file did not require further calibration. However, this also limited the application of this method, *i.e.* the target phases must have a known approximate crystal structure to start from. Some highlights of this method which inspired later developments are: 1) anisotropic peak widths were applied to basal and non-basal reflections differently; 2) the number of *hkl* reflections was reduced by selecting the important ones, to improve the model efficiency; 3) a supercell was used to generate enough reflections in asymmetric non-basal *hk* bands, (although the origin of the asymmetric bands was wrongly assigned to '*a*' and '*b*' axes).

The PONKCS method introduced by Scarlett and Madsen (2006) expanded the "*hkl* file" method to any phase with Partial Or No Known Crystal Structure, *i.e.* an approximate crystal structure of the target phase is no longer required. Instead of modifying the structure factors in the "*hkl* file", the PONKCS method used arbitrary scaled intensities to fit the experimental XRD pattern followed by calibration of the ZMV factor (product of unit cell mass "ZM" and unit cell volume "V") of the model using standard mixtures with known weight ratios.

The PONKCS method (Scarlett & Madsen, 2006) replaced the anisotropic peak shape descriptions with a method called "envelope fitting" (Kern, 2011), which uses a sum of unlimited *hkl* reflections to fit the complex pattern. The "envelope fitting" works well for some patterns, *e.g.* the silica flour pattern from the International Union of Crystallography (IUCr) Commission on Powder Diffraction (CPD) round robin (Madsen, 1999), as shown in Figure 4-1, but does not work well for more complex phases, such as turbostratically disordered smectite, as shown in Figure 4-2. The asymmetric non-basal reflection bands at 64° 2θ and 41° 2θ were fitted by "envelope fitting", while the asymmetric non-basal reflection bands from 23° 2θ to 34° 2θ were not. This is because the anisotropic peak shape description was not adopted by the original PONKCS method which used the "envelope fitting" approach.

Another problem with using an unlimited number of *hkl* reflections in "envelope fitting" becomes obvious when the lattice parameters of the PONKCS model (Pawley phase) are refined later during the model application. As the individual reflections in the "envelope fitting" family may not come from same zone axis, if the lattice parameters change these reflections may shift in opposite directions and deform the overall "envelope" shape. In extreme cases, reflections with fixed intensity may shift to an adjacent "trough", resulting in fitting errors, as demonstrated in Figure 4-3.

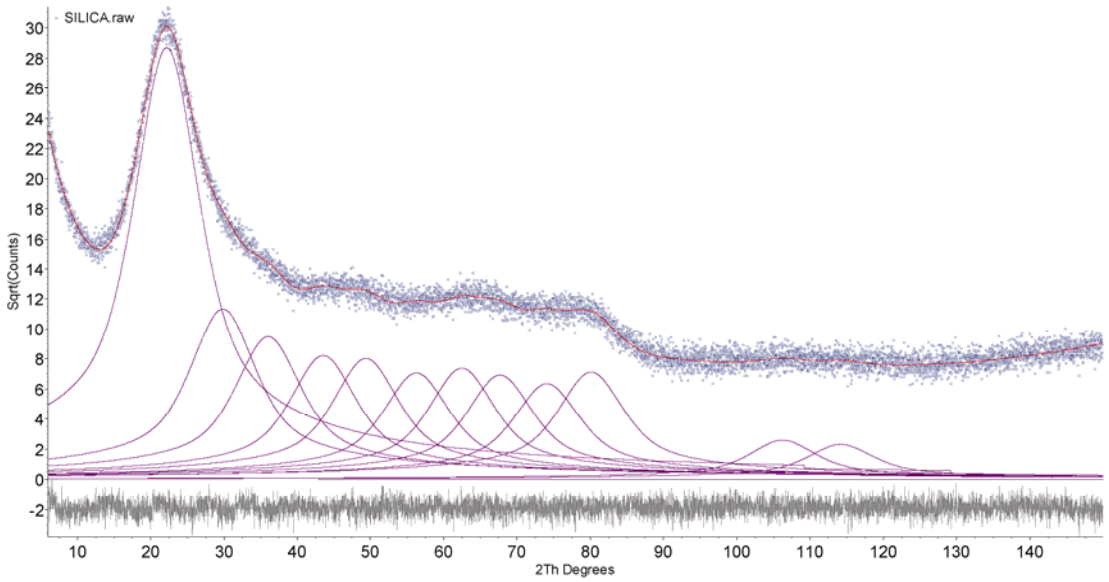

Figure 4-1 Good fitting achieved with peaks phase of 13 Pseudo-Voigt peaks with isotropic peak shape to simulate a silica flour pattern from IUCr CPD round robin on the determination of quantitative phase abundance from diffraction data (Madsen *et al.*, 2001; Scarlett *et al.*, 2002; Madsen *et al.*, 2011)

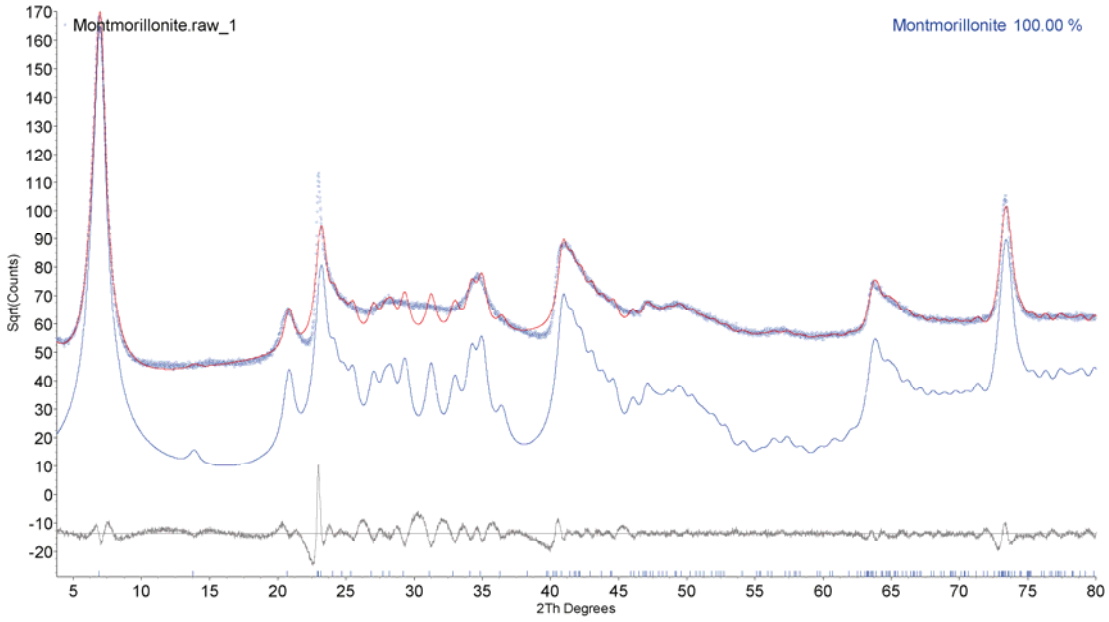

Figure 4-2 The fitting of the montmorillonite pattern (variable divergent slit, CoKα, raw data from Mr. Mark Raven, CSIRO Land and Water) with Pawley phase of isotropic peak broadening (87 non zero reflections generated).

Therefore, it is necessary to use selected reflections and incorporate anisotropic peak shape modifiers into the PONKCS method to better fit and quantify phases with complex patterns *e.g.* anisotropic peak broadening and

asymmetric peak shape. Using flexible peaks shape description tools in TOPAS, a simple modification of the original PONKCS method could be made to achieve this goal. In the rest of this chapter, the PONKCS models were developed from two-phase mixtures, and independently verified using data collected from three phase mixture samples.

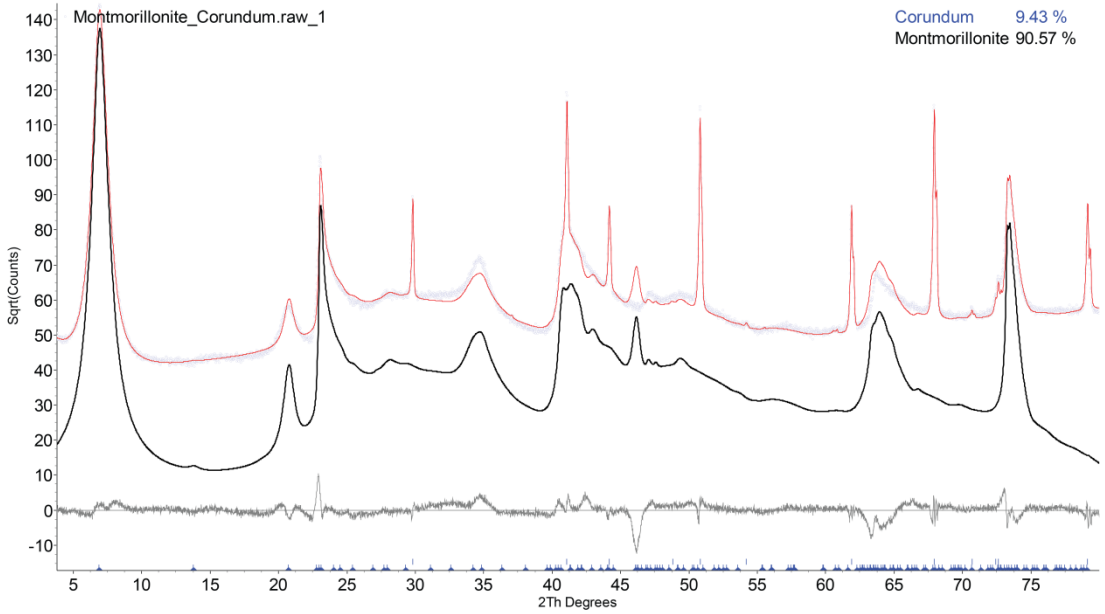

Figure 4-3 The ill-fitting of a mixed montmorillonite-corundum pattern (variable divergent slit, CoKα, raw data from Mr. Mark Raven, CSIRO Land and Water) at 46° 2θ results from a change of lattice parameters which deform the adjacent “envelope fitting”. The figure is drawn by TOPAS V4.2 where squared counts are displayed on square root projection of the y-axis.

4.4 Sample preparation and characterisation

The Bulong nontronite (Section 3.1.2) was enriched using a gravity settling separation method. The powder sample was thoroughly washed with deionised water until the particles were well dispersed and then allowed to settle in a glass cylinder for 1 hour. This settling time was calculated using Stokes’s law based on complete settling of 10 μm (equivalent spherical diameter) clinochlore (2.65 g cm^{-3}) and 30 μm quartz (2.62 g cm^{-3}), as these were the main impurities found in the original nontronite sample, as shown in Figure 4-4. The following clay collection procedures are the same as those described in Section 3.2.5. After this enrichment, the sample was confirmed

by XRD phase identification (XRD details below) to be predominantly nontronite with a minor amount of quartz and kaolinite (Figure 4-5).

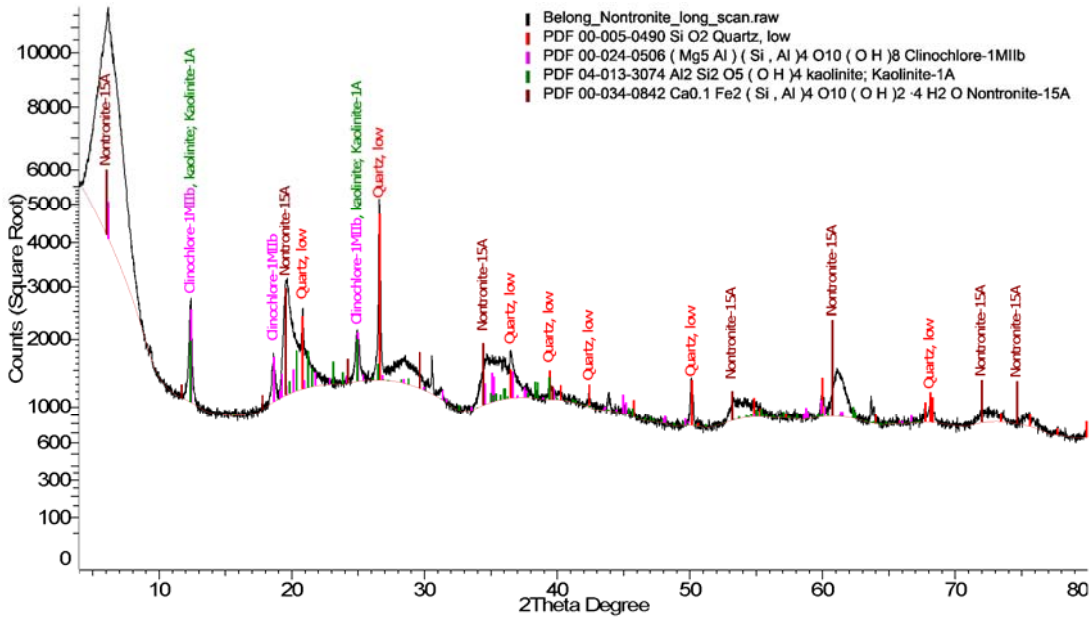

Figure 4-4 Phase identification of the Bulong nontronite from CuKα XRD data showing clinochlore and quartz as major impurities. The figure is drawn by Bruker® DIFFRAC.EVA V2.1 where original counts are displayed on the square root projection of y-axis.

The enriched sample was milled in ethanol using a McCrone® Micronising Mill, oven dried at 70 °C, and side loaded into an XRD holder to minimise preferred orientation. The XRD pattern of the enriched nontronite sample was obtained using a Bruker D8 Advance diffractometer with CuKα radiation. The data were collected from 3 to 100° 2θ with a step size 0.02° 2θ at 1.5 second per step. Other scan setting details are provided in Section 3.2.3. The chemical composition of the Bulong nontronite was determined by inductively coupled plasma optical emission spectrometry (ICP-OES) after fusion with Sigma Chemicals 12:22 lithium borate flux and dissolution in water.

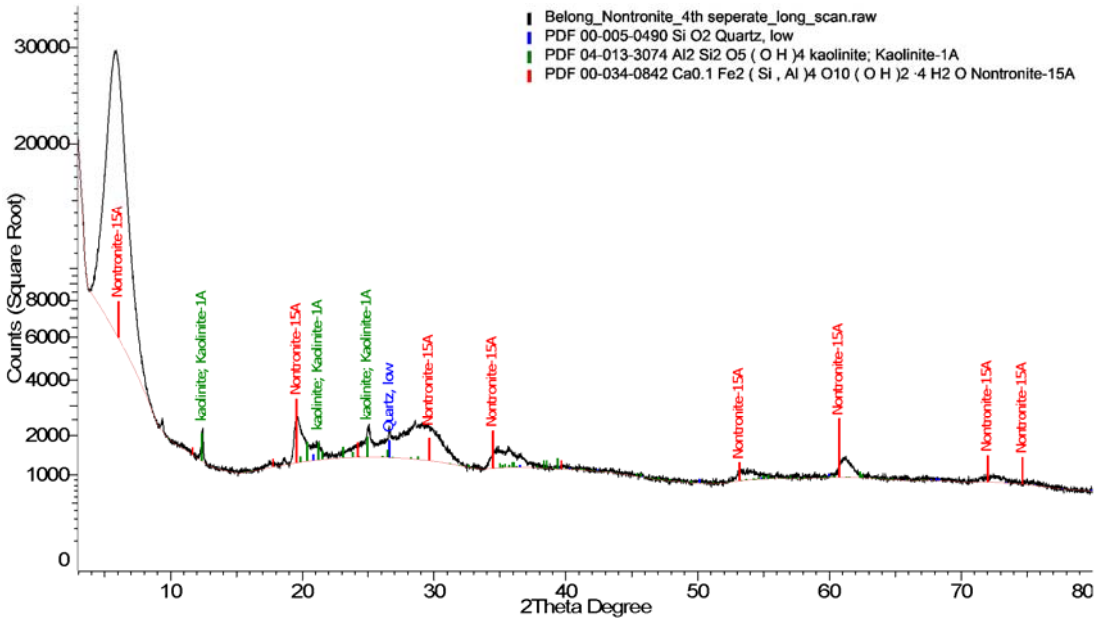

Figure 4-5 Phase identification of CuKα XRD pattern of enriched Bulong nontronite showing minor amounts of kaolinite and quartz still exist after settling separation. The figure is drawn by Bruker® DIFFRAC.EVA V2.1 where original counts are displayed on the square root projection of y-axis.

Five standard mixtures of enriched nontronite and CaF_2 (weight ratios 1:9, 3:7, 5:5, 7:3, 9:1) were used to calibrate the ZMV factors of the Pawley phase and peaks phase models. Calcium fluorite (CaF_2, Sigma–Aldrich, assay > 99.5 wt.%) powder was used as an internal standard. The five standard mixtures were mixed in ethanol using a McCrone® micronizer, oven dried at 70 °C, and gently ground in an agate mortar and pestle before side loading into a plastic XRD sample holder. The scanning conditions were the same as those used for the enriched nontronite sample.

Six independent mixtures of quartz, goethite and the enriched Bulong nontronite simulating various common phase compositions of Western Australian nickel laterite (Elias *et al.*, 1981; Singh & Gilkes, 1992; Landers *et al.*, 2009b) were used to test the accuracy of the nontronite PONKCS models. The synthetic mixtures were also mixed using a McCrone® micronizer. The detailed weight ratios are shown in Table 4-1. The quartz (Cook Industrial Minerals Pty Ltd) and goethite (Synergy Pigments Australia Pty Ltd) used in these synthetic laterites were verified to be pure phases and their lattice

parameters were predetermined with 2θ correction (zero error and sample displacement error) by an internal standard method (McCusker *et al.*, 1999).

4.5 The modified PONKCS method

Bruker® DIFFRAC^{plus} TOPAS v4.2 software was used as the exclusive tool for the whole powder pattern fitting (WPPF), iterative least-squares indexing (LSI indexing), lattice parameter search (LP search), whole powder pattern decomposition (WPPD) and Rietveld quantitative analysis. A flow chart describing the processes of four possible routes of applying the modified PONKCS method to Bulong nontronite is shown in Figure 4-6. The two main stages, indicated as “Build Pawley phase model” and “Calibrate ZMV factor”, are detailed below (‘ZM’ refers to the mass and ‘V’ refers to the volume of the unit cell). The route for using the peak phase group method for nontronite phase quantification is also demonstrated.

Table 4-1 Quantitative results of six synthetic mixtures of goethite (Goe), quartz (Qrt) and nontronite (Nont). Figures in brackets for quantitative results represent the 1σ uncertainty on the last decimal place.

Weighed wt.%‡			SH† assisted P3 Pawley phase model calculated wt.%			SH assisted C2/m Pawley phase model calculated wt.%			peaks phase group calculated wt.%		
Nont	Goe	Qrt	Nont	Goe	Qrt	Nont	Goe	Qrt	Nont	Goe	Qrt
10.03(1)	70.13(2)	19.84(1)	12.6(6)	67.0(5)	20.5(2)	12.5(1)	67.4(2)	20.1(1)	12.6(5)	66.8(2)	20.5(1)
15.07(1)	55.02(2)	29.91(1)	18.1(8)	50.0(5)	31.9(3)	17.6(4)	50.4(2)	32.0(2)	16.1(7)	51.0(1)	32.8(1)
19.96(1)	39.96(2)	40.08(2)	20.3(5)	37.7(3)	42.1(3)	21.5(8)	37.2(4)	41.3(4)	20.1(8)	37.6(1)	42.4(1)
30.02(1)	20.08(1)	49.90(2)	26.6(4)	19.1(1)	54.3(3)	26.8(3)	19.3(1)	53.9(2)	25(1)	19.7(1)	55.6(2)
34.97(1)	50.01(2)	15.02(1)	36.3(7)	47.2(5)	16.5(2)	37.3(5)	46.6(4)	16.1(1)	35(1)	48.4(2)	17.0(1)
49.97(2)	24.92(1)	25.11(1)	47.2(7)	24.3(4)	28.6(4)	50.8(5)	22.6(2)	26.6(3)	43(1)	26.3(2)	31.2(2)

† Spherical Harmonics series (SH)

‡ The uncertainties associated with the weighed samples wt.% arise from reproducibility figures provided by the manufacturer of the balance.

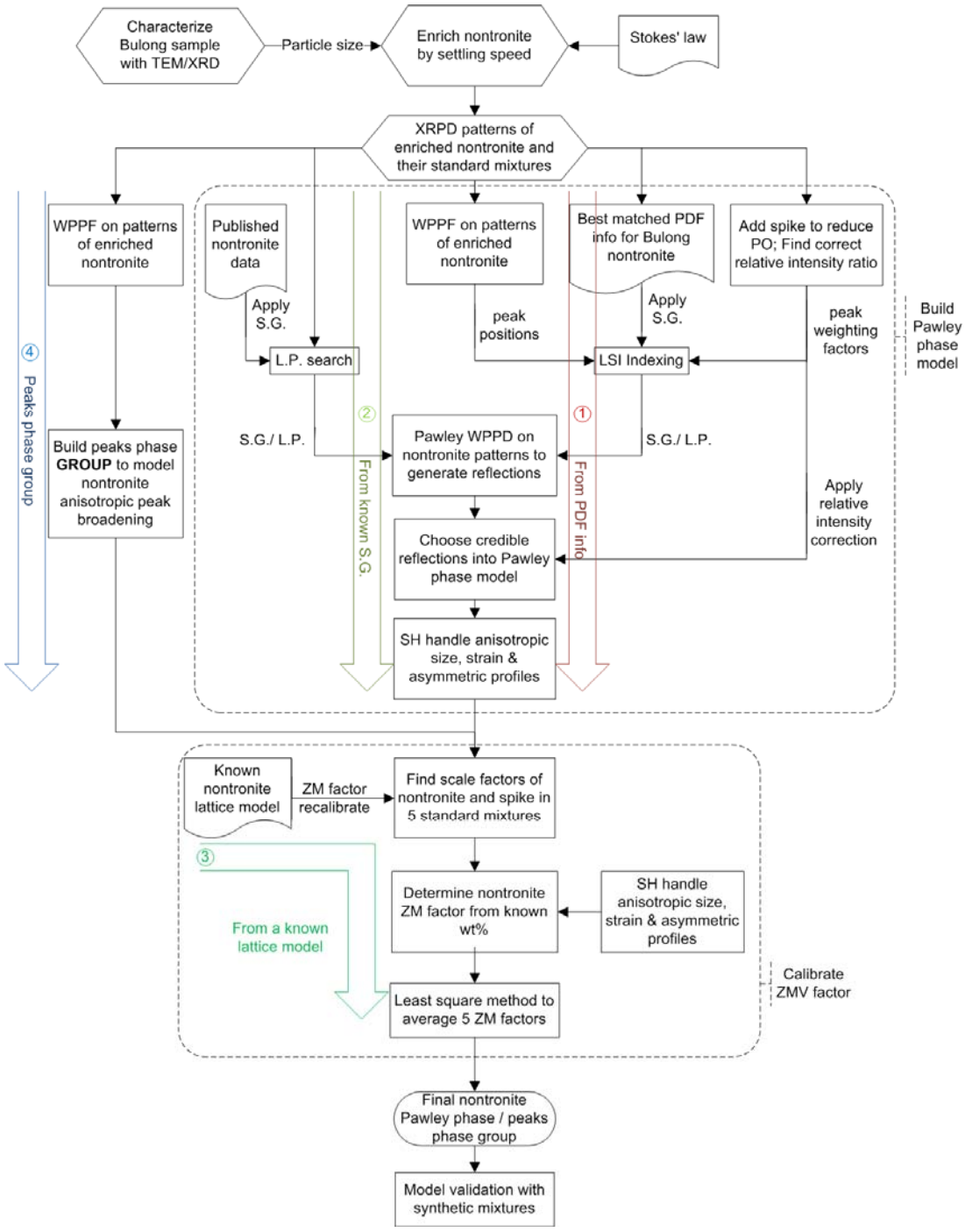

Figure 4-6 Flow chart for applying the modified PONKCS method to Bulong nontronite, outlining the two major stages: “Build Pawley phase model” and “Calibrate ZMV factor”. The PONKCS process can start from the best matched PDF information ①; from a specified space group ②; or recalibrate the ZM factor of a known lattice model ③. The peaks phase group route ④ bypasses the difficulties associated with indexing a complex pattern. L.P. denotes lattice parameter, LSI least-squares indexing, S.G. space group and PO preferred orientation.

4.5.1 Building the lattice models

Two routes for building the Pawley phase model are demonstrated in the first stage. As indicated in route ① in Figure 4-6, one Pawley phase model was developed using a hexagonal P3 space group according to PDF card 00-034-0842 (Eggleton, 1977), which was found to give the best match with the Bulong nontronite XRD pattern. This PDF card was used as the main reference in this route, as the deficiency of nontronite reflections, captured by Split Pseudo-Voigt (SPV) peaks from WPPF of the nontronite pattern, made it difficult to just use LSI indexing to determine a credible space group. The extent of preferred orientation for a set of patterns of the enriched Bulong nontronite mixed with varying amounts of CaF_2 was assessed by comparing basal and non-basal reflection intensities. This set of standard mixtures was also used to later calibrate the ZMV factor. The nearest randomly orientated nontronite pattern was assumed to be the one with the largest non-basal to basal reflection intensities ratio, *i.e.* $I_{d=4.5}/I_{d=15}$. LSI indexing of the captured reflections with weighting factors from the intensities of the nearest randomly orientated patterns was used to determine the lattice parameters with indexing that best agreed with PDF card 00-034-0842.

Another Pawley phase model was developed based on the monoclinic C2/m space group (Besson *et al.*, 1983; Tsipursky & Drits, 1984). As demonstrated in the central route ② of Figure 4-6, an LP search in the monoclinic crystal system was used to find the most suitable lattice parameters from the whole measured pattern. The LP search is a Monte Carlo-based WPPD approach, which was designed to avoid the difficulties associated with extracting reflection d-values from complex patterns (Bruker AXS, 2009). Unit-cell dimensions with the lowest R_{wp} (weighted pattern fitting indicator) were chosen after multi-cycle refinements (150 cycles with refinement allowed to continue beyond the set convergence conditions).

The two routes described above generate two different sets of space groups and lattice parameters. The nontronite *hkl* reflection positions, their intensities and associated errors were generated for these two space groups and sets of lattice parameters by Pawley WPPD. Note that the scale factor

and preferred orientation correction were not (and should not) be used during Pawley WPPD, as the net intensities should be generated without any scale. This differs from the “envelope fitting” approach which adopts all the reflections generated by Pawley fitting in the PONKCS model; here only reflections with intensity error lower than the intensity value were adopted in the Pawley phase model. This reduction in reflections was gradually achieved over several cycles of deleting reflections and re-fitting the new model. The relative intensities of the reflections in the enriched nontronite pattern are often affected by sample preferred orientation. Therefore, the intensities of each reflection were corrected by the intensity ratio from the nearest randomly orientated nontronite pattern. This means that the *hkl* reflections in the final nontronite Pawley phase model were built from two sources: the enriched nontronite pattern with more reflection details and the nearest randomly orientated nontronite pattern (spiked) with correct intensity ratios. The intensities were thereafter fixed for further model development.

A further addition to the original PONKCS method was the use of peak shape modifiers. User-defined convolutions were used to model the asymmetric nontronite peaks after the *hkl* reflections were determined above. The asymmetry and FWHM of the nontronite peaks are *hkl* dependent (anisotropic), therefore spherical harmonics (SH) were employed to represent the asymmetric peak shape factor using “circles” convolution (Bruker AXS, 2009) to fit the nontronite pattern. Spherical harmonics (SH), which are two-dimensional anisotropic functions in a series of directions in spherical coordinates, or of hkl indices in lattice space, were introduced into XRD analysis by Järvinen (1993) to model the particle direction distribution (preferred orientation) of powder samples. Anisotropic crystal size and strain were also represented by another two SH functions in Lorentzian and Gaussian convolutions. Once determined, the SH coefficients of the asymmetric peak shapes were fixed, leaving the SH coefficients for anisotropic size and strain refinable.

4.5.2 Building the peaks phase group model

A peaks phase group model was also developed to quantify nontronite, as indicated in route ④ in Figure 4-6. This approach was modified from the method of Scarlett & Madsen (2006), who successfully quantified corundum with a single peaks phase containing multiple reflections (characterised by peak position and reflection intensity). Confined to a uniform peak shape, a single peaks phase cannot be readily fitted to the complex nontronite pattern, especially the asymmetric peak shapes (Scarlett *et al.*, 2008). To avoid this restriction, multiple peaks phases were used as a group in which each peaks phase fits one peak so that individual peak shape parameters can be assigned; however, the scale factors of these peaks phases were constrained to be a single refinable parameter so these could be scaled together. The SPV peak shape parameters of reflections at the same 2θ were also constrained when multiple nontronite patterns were fitted simultaneously so that the peak shapes are consistent across all nontronite patterns. The positions and intensities of the peaks phase group were determined from WPPF using SPV profiles. An example of the TOPAS input file of the peaks phase group and for comparison an example file for a single peaks phase are presented in Figure 4-7.

```
xdd
...
local scnon 0.41846
...
xo_Is
 xo 6.104790811 I 115.4687813
 scale = scnon;
 MVW(95.642, 1, 3.523)
 peak_type spv
 spv_h1 spvh11 1.00791
 spv_h2 spvh21 0.78480
 spv_l1 spvl11 0.23418
 spv_l2 spvl21 0.97883
xo_Is
 xo 19.40674557 I 44.84893134
 scale = scnon;
 MVW(95.642, 1, 3.523)
 peak_type spv
 spv_h1 spvh12 0.00097
 spv_h2 spvh22 1.86912
 spv_l1 spvl12 5.55111
 spv_l2 spvl22 5.55111
xo_Is
...
xo_Is
...
xo_Is
...
```

(a)

```
xdd
...
xo_Is
 scale @ 0.94754051e-005
 MVW(873.126, 1, 9.306)
 CS_L(csnon, 5)
 peak_type spv
  spv_h1 spvh1 0.9894871611
  spv_h2 spvh2 0.6893253884
  spv_l1 spvl1 0.9922982526
  spv_l2 spvl2 0.8166360062

 xo 6.316892362 I 54.91786578
 xo 19.48884436 I 70.49308065
 xo 26.23335212 I 543.6069451
 ...
```

(b)

Figure 4-7 (a) An example of a peaks phase group in TOPAS syntax, which fit nontronite anisotropic peak broadening independently, with a single scale factor refinable. 'xo' = peak position (° 2θ); 'I' = reflection intensity. The FWHM on the left (spv_h1) and right sides (spv_h2) and the Lorentzian fractions on the left (spv_l1) and right sides (spv_l2) were constrained when multiple patterns were fitted simultaneously. (b) A single peaks phase model from original PONKCS method (Scarlett & Madsen, 2006), which is restricted to a uniform peak profile.

4.5.3 Calibrating the ZMV factor

The procedure used to obtain the ZM factor was essentially the same as that used by Scarlett & Madsen (2006) except the results of multiple standard mixtures were used and averaged. Rietveld errors reported in the TOPAS program only give an estimate of the precision of the refinement process. In order to account for other possible errors, the patterns of five standard mixtures described in Section 4.4 were fitted simultaneously to extract scale factors for both phases. A single set of nontronite lattice parameters was refined for five patterns, while the lattice parameters of the CaF_2 spike were predefined and fixed. The same SH coefficients were used for asymmetric

peak shape for each pattern, while the SH for anisotropic crystal size and strain were allowed to refine separately. According to quantitative Rietveld theory (Hill & Howard, 1987; Bish & Howard, 1988; O'Connor & Raven, 1988), the factor for nontronite (non) are determined from the weight ratio, the refined scale factors and the ZMV factor of the internal standard (Scarlett & Madsen, 2006):

$$\mathrm{ZM_{non}} = \frac{\mathrm{W_{non}}}{\mathrm{W_{CaF_2}}} \cdot \frac{\mathrm{S_{CaF_2}}}{\mathrm{S_{non}}} \cdot \frac{\mathrm{ZMV_{CaF_2}}}{\mathrm{V_{non}}} \qquad \text{Eq. 4-1}$$

Here ZM, V, S and W refer to the ZM factor (unit-cell mass), unit-cell volume, scale factor and weight percentage of each phase described by the subscript.

The ZM values generated from the five standard mixtures were slightly different. A least-squares method was adopted to effectively average the results by adjusting a single nontronite ZM value to minimise the quadratic sum of the differences between calculated and weighed weight percentages for the five standard mixtures. The uncertainty of the calibrated ZM factor was calculated from the refined scale factors of individual standard mixtures.

The ZM factor and corresponding reflection intensities were not scaled to match the real nontronite density because this does not affect quantification (Scarlett & Madsen, 2006). The difference between the final nontronite Pawley phase model developed in this study and that described by Scarlett & Madsen (2006) is that the anisotropic crystal size and strain were represented by SH functions in Lorentzian and Gaussian convolutions, respectively, and the asymmetric peak shape was fitted by a SH function in “circles” convolutions (Bruker AXS, 2009). A March model correction for preferred orientation was used for the five standard mixture patterns.

The ZMV factor calibration for the peaks phase group was the same as described above. The calculated ZMV factor was evenly allocated to each peaks phase, since the nontronite phase concentration was represented by the sum of the weight percentage of all the peaks phases. As no lattice information is used in the peaks phase model, the unit-cell volume is not known; hence the ZM factor cannot be separated from the ZMV factor.

4.6 Results and discussion

The two lattice models and one peaks phase group model were compared by validation with the six independent mixtures of quartz, goethite and the enriched Bulong nontronite, described in Section 4.4.

4.6.1 Chemical analysis

The elemental composition of Bulong nontronite determined by ICP-OES is shown in Table 4-2. Bulong nontronite is higher in magnesium and nickel and lower in Fe and Ca than the two standard nontronite samples NAu-1 and NAu-2 from Port Lincoln, South Australia (Keeling *et al.*, 2000; Gates *et al.*, 2002). The differences in the cation substitutions make the unit-cell mass, and therefore the ZMV factor, different. A feature of the PONKCS method is that, if there is any amorphous content in the enriched unknown phase, it will be included with this phase. The more amorphous material there is, the higher the calibrated ZM factor will be as the total mass of the amorphous content and the target unknown phase are divided by the smaller scale factor of the lower peak intensity of the unknown phase.

Table 4-2 ICP-OES results of major element weight percentage of Bulong nontronite and the nontronite standards from the Clay Mineral Society (ignited at 1050 °C).

	SiO_2	Al_2O_3	Fe_2O_3	MgO	CaO	Na_2O	NiO	CoO	TiO_2	K_2O	Total
Bulong nontronite	56.14	10.28	25.50	3.50	0.33	1.04	2.52	0.07	-	-	99.4
NAu-1[†]	51.36	8.15	35.94	0.19	3.57	0.03	-	-	0.02	0.01	99.5
NAu-2[†]	56.18	3.11	37.85	0.26	2.34	0.14	-	-	0.02	0.01	99.9

[†] Data from Keeling *et al.* (2000).

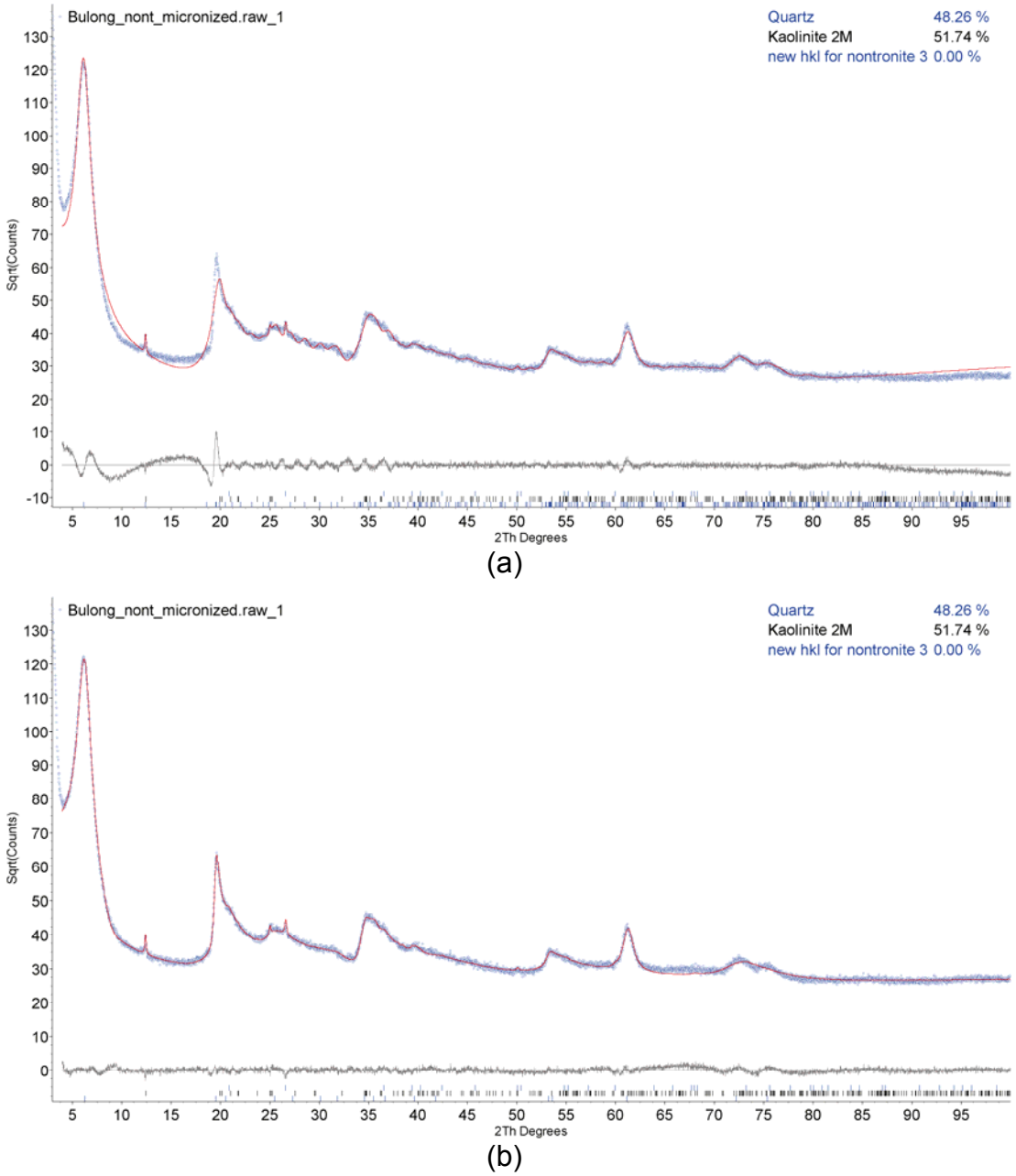

Figure 4-8 The fitting of Bulong nontronite pattern with (a) Pawley phase of isotropic peak broadening (101 non zero reflections generated), GOF 3.12, and (b) Pawley phase of just 17 peaks with anisotropic peak shape modifiers, GOF 1.51. Note the quantification result captured was not included in nontronite as the ZMV factor has not been calibrated yet.

4.6.2 SH-assisted convolutions in the lattice model

The merits of using SH-assisted convolutions in the Pawley phase model are shown by the comparison in Figure 4-8. The nontronite asymmetric peak at 20° 2θ does not fit well even with 101 non-zero reflections ("envelope

fitting" approach) without the help of SH-assisted convolutions (peak shape modifier). If SH-assisted convolutions were used the whole nontronite pattern can be well described with only 17 reflections, especially the asymmetric peak at 20° 2θ. The difference plots and the goodness of fit (GOF) suggest that the anisotropic peak broadening and asymmetric peaks of the nontronite pattern were successfully fitted by SH-assisted convolutions. These convolutions also enabled the Pawley phase model to fit the observed pattern better during Pawley WPPD. As with the structure refinement strategy described by McCusker *et al.* (1999), it is critical to follow the refinement strategy for SH illustrated in Figure 4-9, otherwise too many parameters, often too far from correct starting values, can lead to refinement divergence. For the same reason, only second order SHs were used for each convolution. The quantitative results of the original and modified Pawley phase models in both space groups are compared in Figure 4-10 and Figure 4-11. It is clear that the SH-assisted convolutions and proper refinement strategy improved the fitting and QPA accuracy. The QPA results from the two Pawley phase models based on the two space groups were similar, suggesting that the phase abundance analysis is independent of crystallographic symmetry as long as the fitting is good.

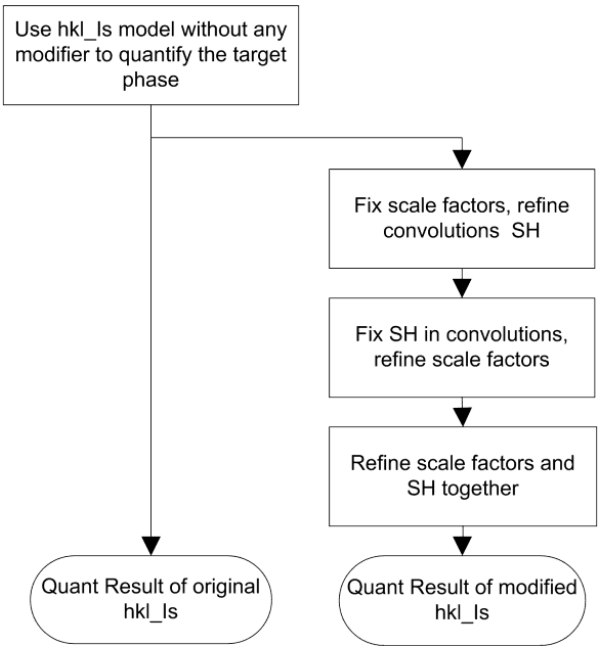

Figure 4-9 Refinement strategy applied when using SH as convolution coefficients.

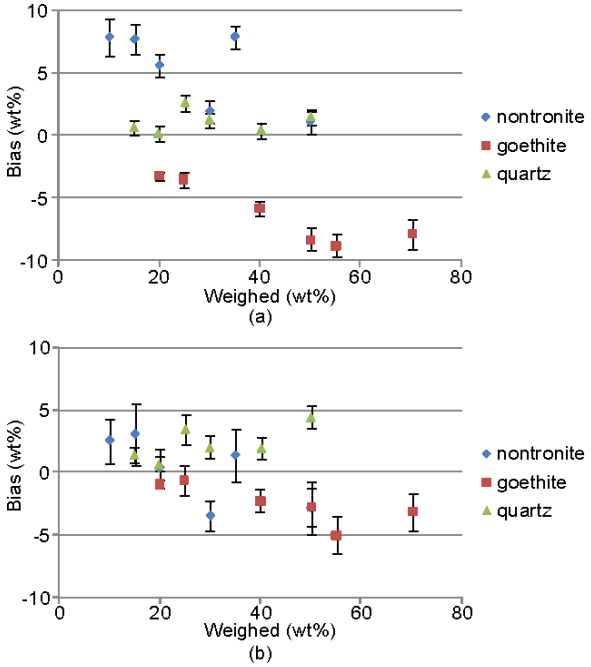

Figure 4-10 Bias of the PONKCS quantification results of synthetic mixtures from the actual values, using the P3 space group Pawley phase model without (a) and with (b) SH-assisted convolutions. The bias of results with SH-assisted convolution is smaller than those without. Error bars represent ±3σ.

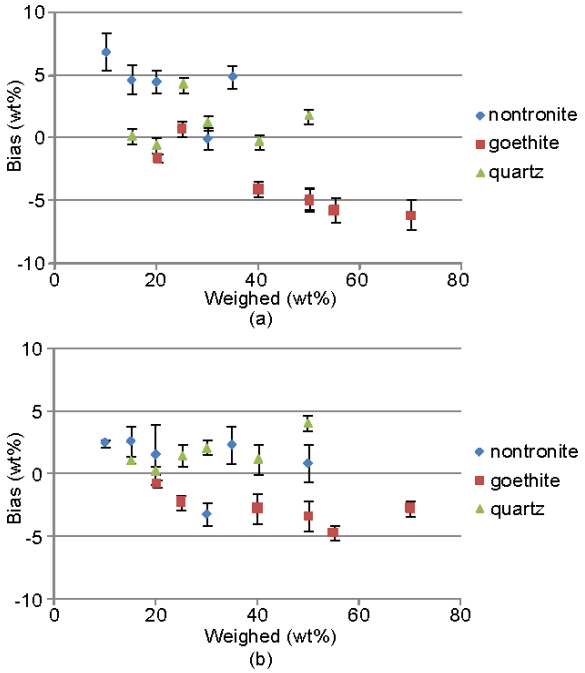

Figure 4-11 Bias of the PONKCS quantification results of synthetic mixtures from the actual values, using the C2/m space group Pawley phase model without (a) and with (b) SH-assisted convolutions. The bias of results with SH-assisted convolution is smaller than those without. Error bars represent ±3σ.

4.6.3 Nontronite quantification by peaks phase group model

Similar to other QPA approaches, such as the multiple-line Reference-Intensity-Ratio (RIR) method or the Mean-Normalised Intensity (MNI) method (Li *et al.*, 1994), the peaks phase model is independent of crystallographic properties and only considers peak fitting. However, the nontronite pattern contains various peak shapes, including a major sharp peak at low angle, asymmetric peaks due to turbostratic disorder and broad humps. As shown in Figure 4-12, a single peaks phase cannot fit this complex pattern as it is restricted by a uniform peak shape. Multiple peak phases which contain anisotropic peak asymmetry and broadening have to be used to fit the complex nontronite pattern. The comparison of quantification results using a single peaks phase and a peaks phase group is shown in Figure 4-13, and again demonstrate the benefit to more accurate quantitative analysis obtained from better fitting of the nontronite pattern.

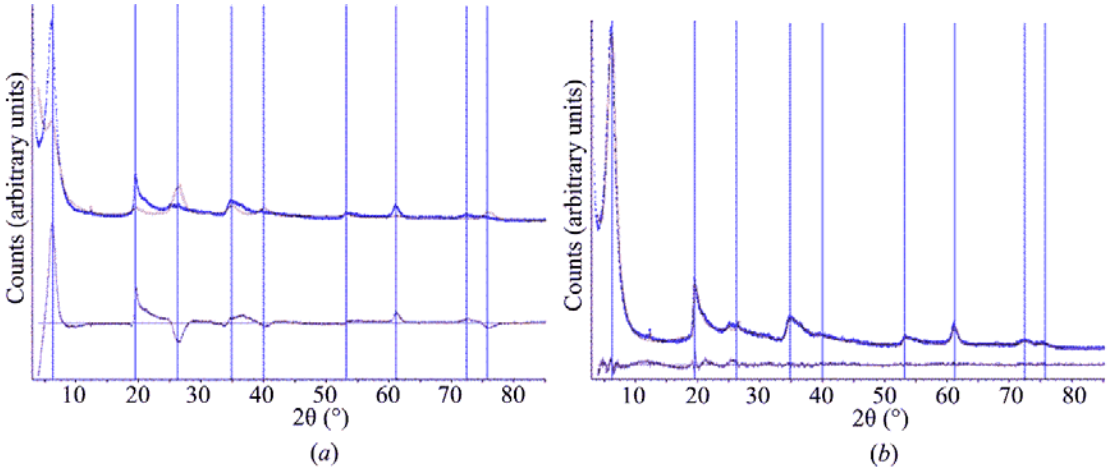

Figure 4-12 (a) A single peaks phase with uniform peak shape cannot fit the complex nontronite pattern. (b) A peaks phase group with individual peak shape improves the fitting of the nontronite pattern. Both models use the same set of peak positions and intensities. Both fits started from 3.98° 2θ to avoid the background at low angles due to air scattering.

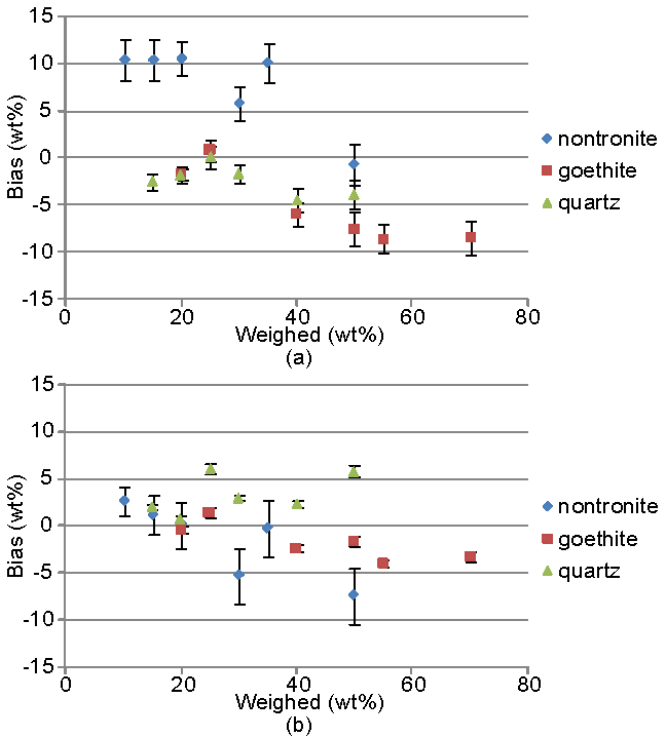

Figure 4-13 Bias of the PONKCS quantification results of synthetic mixtures from actual values, using (a) a single peaks phase and (b) a peaks phase group. The bias of the latter is smaller than those of the former. Error bars represent ±3σ.

4.6.4 Quantification results of all models

According to the ZM calibration procedures described in Section 4.5.3, the calibrated ZM factor for the nontronite Pawley phase based on space group *C*2/*m* is 0.99(1); the ZM factor for the Pawley phase based on space group *P*3 is 1.46(3). These calibrated ZM factors are directly proportional to the intensities assigned to each reflection in the Pawley phase, hence are not comparable. The final quantitative results for the six synthetic mixtures of quartz, goethite and nontronite using the two new Pawley phase models and the peaks phase group model are shown in Table 4-1, and Figure 4-10(b), Figure 4-11(b) and Figure 4-13(b). TOPAS does not consider the uncertainty of the ZM factor of the Pawley phase; therefore the uncertainties of the calibrated ZM factors were propagated to the final quantification results manually according to the Rietveld quantification relationship of the phase scale and phase ZM factors. The final uncertainties of the phase concentrations are shown by the figures in brackets in Table 4-1.

The results of the peaks phase group model were inferior to those of the Pawley phase model, because the peaks phase group model or single peaks phase model intrinsically do not allow preferred orientation correction once the peak intensities are defined and fixed, whereas for both Pawley phase models the preferred orientation effect was corrected during refinement.

The preferred orientation effect also explains why the nontronite quantitative results using a peaks phase group in Figure 4-13(b) showed a trend of increased underestimation of nontronite. The extent of the preferred orientation for front loaded samples increases with the nontronite content. Additionally, as goethite is a heavy absorber and quartz is a light absorber when using CuKα radiation, increased microabsorption effects are also expected to lead to overestimation of quartz content and underestimation of goethite content.

Ideally, nontronite should be enriched from an unknown sample to develop either lattice or peaks phase group models. However, examination of the XRD patterns of nontronite samples obtained from other major nickel laterite projects in Western Australia suggest that the diffraction patterns do not differ greatly and that the models built are useful across various drill holes, pits and mine sites. The XRD pattern of the Bulong nontronite described in this thesis is similar to that of NAu-1 (Keeling *et al.*, 2000). Taylor & Matulis (1994) using SIROQUANT software (Taylor, 1991) claimed that a montmorillonite *hkl* file could be used to quantify montmorillonite samples from other locations. Nevertheless, building individual lattice models and calibrating ZM factors for target phases are always encouraged, because of the variation of cation substitutions, interlayer exchangeable cations and possible amorphous content in actual samples.

4.7 Conclusion

In this chapter, two models were developed with the modified PONKCS method and were used to successfully quantify Bulong nontronite enriched from a laterite ore. The partially known crystal structure was represented by two Pawley phase lattice models, with spherical harmonics assisted

convolutions as peak shape modifiers, and a peaks phase group model with individual peak shape description.

(a) According to the availability of crystallographic information of the target phase, the PONKCS process as illustrated in Figure 4-1 can start from a best matched PDF information, from a published space group, or from a known lattice model only requiring recalibration of the ZM factor.

(b) The use of spherical harmonics as peak shape modifiers in the Pawley phase successfully reproduced asymmetric peaks of the complex nontronite pattern both in Pawley whole powder pattern decomposition and in Rietveld quantification after *hkl* reflections were defined for the Pawley phase model. A refinement strategy needs be applied to avoid parameter divergence when using SH assisted convolutions for the first time (without correct starting value) in the Pawley phase model.

(c) The quantification result of an unknown phase using a Pawley phase model is essentially independent of the model's crystallographic properties (space group, reflection indices) as long as a good fit is achieved.

(d) A peaks phase group can be used to fit a pattern containing anisotropically broadened reflections. This approach bypasses the difficulties associated with indexing complex patterns in the Pawley phase route but suffers from an inability to correct for preferred orientation effects.

(e) All Pawley phase models and peaks phase group models produced acceptable accuracy and consistency with the quantification results of independently synthesised nickel laterite standards and can be generally applied to quantitative phase analyses of nontronite in laterites.

(f) Different from the original PONKCS method using the "envelope fitting" approach, this chapter demonstrated that fewer reflections with peak shape modifiers could achieve better fitting of the complex nontronite pattern and accurately quantify nontronite in multiple phase mixtures. The unstable refinement problem described in Section 4.3 could also be minimised as fewer reflections are used to fit the peaks. The methods used to develop the modified models should be applicable to quantitative phase analyses of other partial or no known crystal structure phases with complex XRD patterns.

Chapter 5 Supercell model for nontronite quantification

5.1 Introduction

A structural model using a supercell was built in the Bruker® TOPAS symbolic computation system (Coelho *et al.*, 2011) for the quantitative XRD analysis of turbostratically disordered nontronite. A novel calibration approach for determining the ZM factor for the nontronite supercell model was also developed within TOPAS using the PONKCS concept. This approach achieves improved accuracy of the nontronite quantitative analysis result compared with the PONKCS approach, largely because the physically based description of turbostratic disorder requires fewer refinable parameters than the PONKCS approach. The drawbacks and limitations of the supercell approach and a comparison of different methods are also discussed.

This chapter is based on the publication:

Wang, X., Hart, R. D., Li, J., McDonald, R. G., & van Riessen, A. (2012). Quantitative analysis of turbostratically disordered nontronite with a supercell model calibrated by the PONKCS method. Journal of Applied Crystallography 45(6), pp.1295-1302. DOI: 10.1107/S0021889812040484.

5.2 Describing turbostratic disorder using Debye equation

The Rietveld method by its nature can only describe powder diffraction patterns of crystals with well defined unit cells (Young, 1995, p12). As discussed in Section 2.5.2, turbostratically disordered smectite does not have periodicity in the *c*-direction, therefore this mineral does not have a well defined three dimensional unit cell and its XRD pattern cannot be successfully modelled by the Rietveld method.

In contrast with Bragg's law, the Debye equation (Eq. 5-1) does not assume translational symmetry and directly calculates the scattering X-ray intensity of every pair of atoms. It is more suitable for nanocrystals, defect rich crystals, and disordered crystals. The Debye equation has been applied to crystallites composed of a few turbostratic layers and a more specific formalism has been derived (Warren, 1941; Warren & Bodenstein, 1965,

1966). In these disordered systems, each layer was regarded as a 2 dimensional crystallite and arranged at an equal interlayer spacing parallel to the next layer but with random translation and rotation about the perpendicular axis. Only two dimensional *hk* bands due to the intralayer interference and 00*l* basal peaks due to interlayer interference can be observed based on this system. All the other general *hkl* reflections are suppressed completely by the random translation and rotation of each layer. These two sets of reflections were treated differently, *i.e.* the basal reflections were calculated with the Rietveld equation and Bragg's law, while the non-basal *hk* bands were calculated using the Debye equation (Warren, 1941; Warren & Bodenstein, 1965, 1966).

$$I(s) = \frac{1}{\mathrm{N}} \sum_{i} \sum_{\mathrm{j}} f_i f_j \frac{\sin\left(2\pi \cdot s \cdot r_{ij}\right)}{2\pi \cdot s \cdot r_{ij}} \qquad \text{Eq. 5-1}$$

where

$I(s)$: Scattered X-ray intensity;

$s = \frac{2\,\mathrm{Sin}\theta}{\lambda}$: Modulus of the scattering vector;

r_{ij}: Distance between two atoms i and j

N: Total number of atoms;

f_i, f_j: Atomic scattering factor of two atoms i and j at diffraction angle θ.

This approach was later applied to any number of turbostratically stacked layers and a special and simple formalism was derived (Yang & Frindt, 1996). The non-basal diffraction bands generated from intralayer interference is still calculated with the regular Debye equation, while the basal reflections from interlayer interference are simplified as interference between sheets of uniform continuous electron density. An analytical expression for the latter part was deduced and is suitable for calculation of the basal reflection of crystallites consisting of any number of layers. By calculating the basal reflections (I_{inter}) and non-basal reflections (I_{intra}) separately, as shown in Eq. 5-2, the amount of computation required was largely reduced. This formalism was then used to simulate XRD patterns of

turbostratic layered systems and matched well with measured patterns (Yang & Frindt, 1996; Ufer *et al.*, 2004).

$$\begin{cases} I(s) = I_{\mathrm{intra}}(s) + I_{\mathrm{inter}}(s) \\ I_{\mathrm{intra}}(s) = \dfrac{1}{\mathrm{N}} \displaystyle\sum_i \sum_j f_i f_j \frac{\sin(2\pi \cdot s \cdot r_{ij})}{2\pi \cdot s \cdot r_{ij}} \\ I_{\mathrm{inter}}(s) = \dfrac{1}{\mathrm{MD}\pi s^2} \displaystyle\sum_{\mathrm{n}=1}^{\mathrm{M}-1} (\mathrm{M}-\mathrm{n}) \sum_{i=1}^{\mathrm{N_{sub}}} \sum_{j=1}^{\mathrm{N_{sub}}} \mathrm{D}_i \mathrm{D}_j f_i f_j \cos\left[2\pi s(\mathrm{n}c + \mathrm{d}_i + \mathrm{d}_j)\right] \end{cases} \quad \text{Eq. 5-2}$$

where

$\mathrm{N_{sub}}$: number of sublayers of one layer,

M: number of layers,

D: number of unit cells per layer area,

D_i and D_j: atomic layer densities of the sublayers i and j,

d_i and d_j: relative position of the sublayers i and j in the layer package,

c: lattice parameter.

5.3 Describing turbostratic disorder using the supercell approach

The main drawback of using the Debye equation is the large amount of computation involved because all the combinations of every two atoms in the atom cluster need to be calculated. The amount of computation increases with the square of the number of atoms, therefore the Debye equation is very computation-intensive for a large crystal. Although Eq. 5-2 could be used to simulate patterns it is still not suitable for pattern refinement where multiple cycles of pattern calculation are required.

The layer translation in turbostratically disordered material could be explicitly constructed in a supercell, which contains several layers with specified shifts. The XRD pattern of such a supercell model calculated with the Rietveld peak intensity equation (Young, 1995, p4) and Bragg equation still showed large deviations from the simulated pattern calculated from the simplified Debye equation Eq. 5-2, which is known to be similar to the experimentally measured XRD patterns (Ufer *et al.*, 2004). In order to achieve “random” translation, multiple Rietveld calculations of the supercell

with layer shifts randomly changed have to be averaged to match the Debye equation Eq. 5-2 simulation. However, the computational burden of this approach is too large to be used for Rietveld refinement (Ufer *et al.*, 2004).

The separate calculation of basal and non-basal reflections used in the simplified Debye equation Eq. 5-2 was then adopted in the supercell approach by Ufer *et al.* (2004). The *hk* non-basal bands were calculated from the supercell, while the 00*l* basal reflections were calculated from the original unit cell (subcell). As only the *hk* bands were generated from the supercell, the number of layers built into the supercell could be reduced to one, *i.e.* the "one layer case" (Ufer *et al.*, 2004). By calculating these two types of reflections separately, the computation time of one calculation was reduced to the order of minutes (Ufer *et al.*, 2004). This approach generated similar turbostratic patterns to those obtained from using the simplified Debye equation (Eq. 5-2) but using Rietveld compatible description within short calculation times suitable for multiple cycle refinement. The supercell model describing turbostratic smectite was first implemented in the Rietveld analysis program BGMN (Bergmann & Kleeberg, 1998). This supercell model was later demonstrated to be able to accurately quantify nontronite content in high smectite content bentonite samples (~70 wt.%), assisted by the measurement of the Cation Exchange Capacity (CEC) for interlayer cations using Cu triethylenetetramine (Ufer *et al.*, 2008). The supercell model for nontronite-15A written in BGMN syntax (http://www.bgmn.de/download-structures.html) is shown in Appendix 6.

5.4 Supercell model in TOPAS symbolic computation system

The supercell model is platform transparent and has been used in another Rietveld code, MAUD (Lutterotti *et al.*, 1999) to facilitate quantitative texture analysis of montmorillonite and opal in uniaxially pressed samples (Lutterotti *et al.*, 2009; Chateigner *et al.*, 2010).

The "one layer case" supercell structure in BGMN syntax was built in the TOPAS symbolic computation system (Appendix 6) and illustrated in Figure 5-1 (Wang *et al.*, 2011). The TOT layer atom coordinates were adopted from the *cis*-vacant nontronite structure model solved by Tsipursky and Drits

(1984). The main model components including the lattice setting for subcell and supercell, the scaling and removal of redundant basal reflections, and interlayer hydrated cation defined by a rigid body were all the same as those defined in the original supercell model shown in Appendix 6. However, several adaptations were made to make it suitable for Bulong nontronite. The Brindley microabsorption correction in the original supercell model was omitted as this correction requires spherical particles (Brindley, 1945; Madsen *et al.*, 2001), while nontronite particles are platy. The TOT layer cation sites and their occupancies were based on the chemical formula determined from ICP elemental data of purified Bulong nontronite powders. The ratio of the interlayer cation occupancies was based on the molar ratio of major exchangeable cations from the ICP assay of the first cation exchange liquor. The translation coordinates of the interlayer cation octahedron were linked with the subcell lattice parameters; therefore the interlayer hydrated cation octahedron is always placed at the centre of the subcell with two of the H_2O planes parallel to the *a*-*b* plane if the lattice parameters are refined later.

Effectively, the *c*-axis length of the “one layer case” supercell model is 9 times larger than the *c*-axis length of the subcell. The supercell consists of only 1 TOT layer. This supercell layer number (9) was recommended in the original BGMN structure. According to Ufer *et al.* (2004), a 9 layer supercell model is sufficient to reproduce smooth *hk* bands with reasonable computation time. To some extent, the approach of multiplying the unit cell dimensions coincides with the model used by Taylor and Matulis (1994), where the *a*- and *b*-axes were doubled in order to generate more reflections, but that approach was not physically based.

This model was built entirely on the basis of the chemical assay and is referred to as the ‘uncalibrated supercell model’. Good fitting to the measured XRD pattern of Bulong nontronite was achieved, as shown in Figure 5-2. The quantitative analysis result for nontronite using the supercell model was not sensitive to variation of cation occupancy in the TOT layer, as Ufer *et al.* (2008) described. However, the systematic bias of the quantitative result from the supercell model suggests it requires calibration in order to be used for quantitative nontronite phase abundance analysis (Wang *et al.*, 2011).

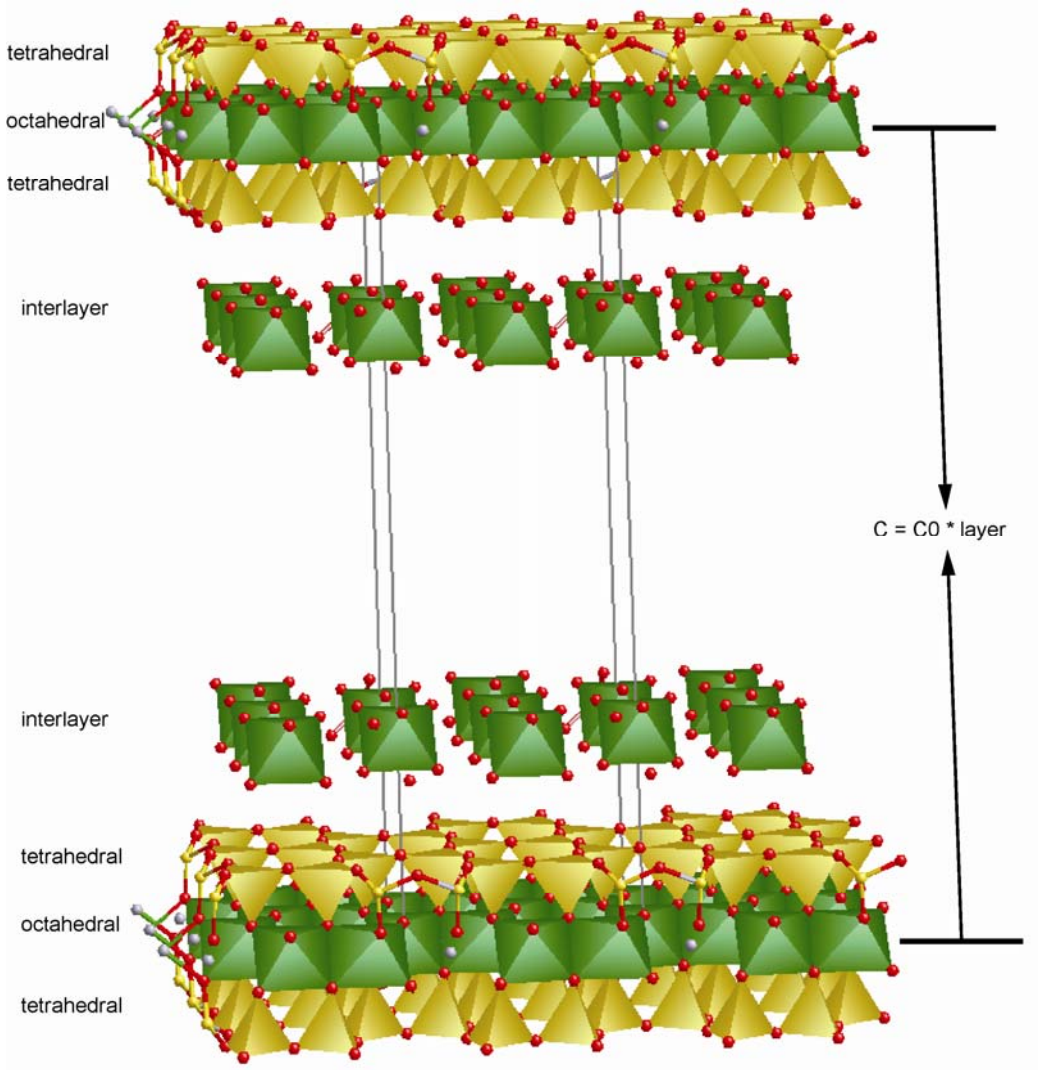

Figure 5-1 Nontronite supercell model drawn by the TOPAS rigid-body editor. The interlayer hydrated cations were calculated twice in the supercell. The c-direction length of the supercell ‘c’ is ‘layer’ times longer than that of subcell ‘c0’. The model where ‘layer’ = 2 is illustrated; a ‘layer’ = 9 model was used in calculation. Note: there is only one TOT layer in the supercell but two interlayers.

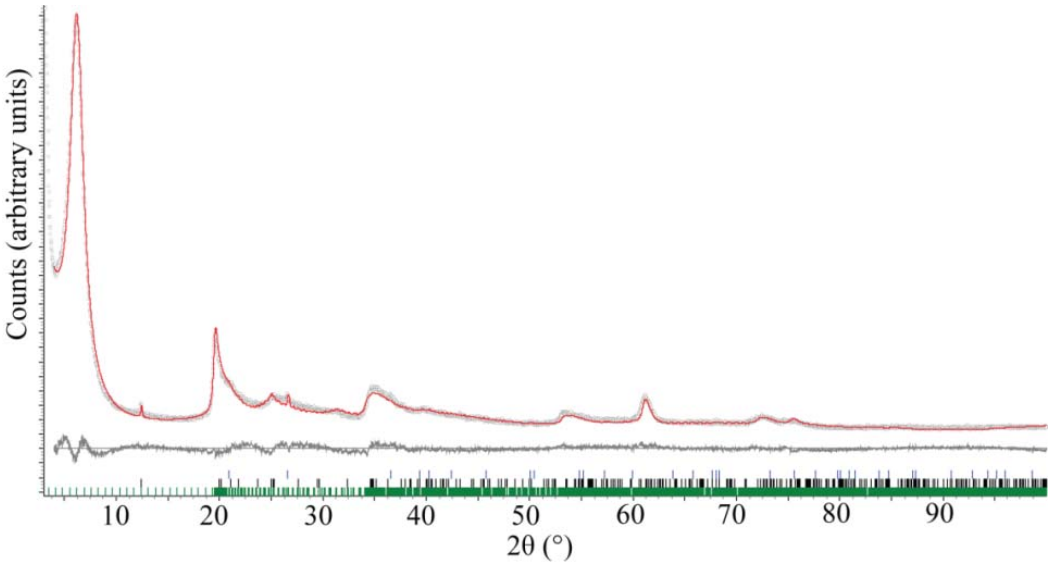

Figure 5-2 Excellent fitting achieved using the supercell structure model in the TOPAS syntax. Low amounts of quartz and kaolinite residue are present in the enriched nontronite pattern. The bottom row of markers corresponds to the nontronite supercell model.

5.5 Calibration of supercell model based on PONKCS concept

The core concept of the PONKCS method is calibrating a QPA model based on the target phase described by this model. However, previous PONKCS calibration approaches only worked for the Pawley phase model and peaks phase model (Chapter 4). The PONKCS method cannot be directly used to calibrate a structural model. The reason for this can be explained by comparing these models (Figure 5-3).

The peaks phase model (*xo_Is*) describes the XRD pattern directly with peak positions, peak shapes, and peak intensities as its model parameters. Another model parameter, the ZMV factor, is used to calculate the weight percentage of this phase. These two sets of parameters are independent. Therefore a PONKCS model can be built on peaks phase by first adjusting the peak positions, shapes, and intensities to fit the experimental XRD pattern of the target phase, and then assigning a ZMV factor based on the intensity ratio of the target phase and internal standard of known ratio (standard mixture).

The peak positions and peak shapes of the Pawley phase model (*hkl_Is*) are no longer model parameters but are determined by lattice parameters

and size and strain parameters. However, the ZM factor of a Pawley phase model is still an independent model parameter. A PONKCS model could also be built by first adjusting the model parameters to fit the experimental XRD pattern of the target phase, and then assigning a ZM factor based on the intensity ratio of the target phase and internal standard with known ratio (standard mixture).

Both ZM and V factors of the structural models (*str*) are not model parameters. They are determined by the atoms and their occupancies. Therefore the ZM factor cannot be directly assigned. Once the atom occupancies are assigned according to chemical assay, the ZM factor is known. The ZM factor of a structural model can only be calibrated by adjusting atom occupancies.

A typical turbostratic nontronite pattern (Figure 5-2) cannot support the refinement of all the atom occupancies in the supercell model. Only the most critical atom occupancies should be refined in the calibration. In fact, the ZM factor of a supercell model is sensitive to the interlayer cation occupancies. There are three reasons why the ZM factor is linked to cation occupancies. First, the stoichiometry numbers of the TOT layer are fixed to 4 and 8 in 2:1 smectite minerals (if octahedral vacancy is ignored), while the interlayer cation occupancy is variable. Second, the interlayer cation is coordinated with 6 water molecules in double layer hydrated nontronite, hence any variation of interlayer cation occupancy would affect the coordinated water occupancy as well, which further affects the unit cell mass. Third, as the supercell model has a doubled interlayer, as shown in Figure 5-1, then any variation of the interlayer cations will be doubled by the supercell model. Therefore a coefficient for the interlayer cation occupancies should be calibrated from a starting value of 0.5.

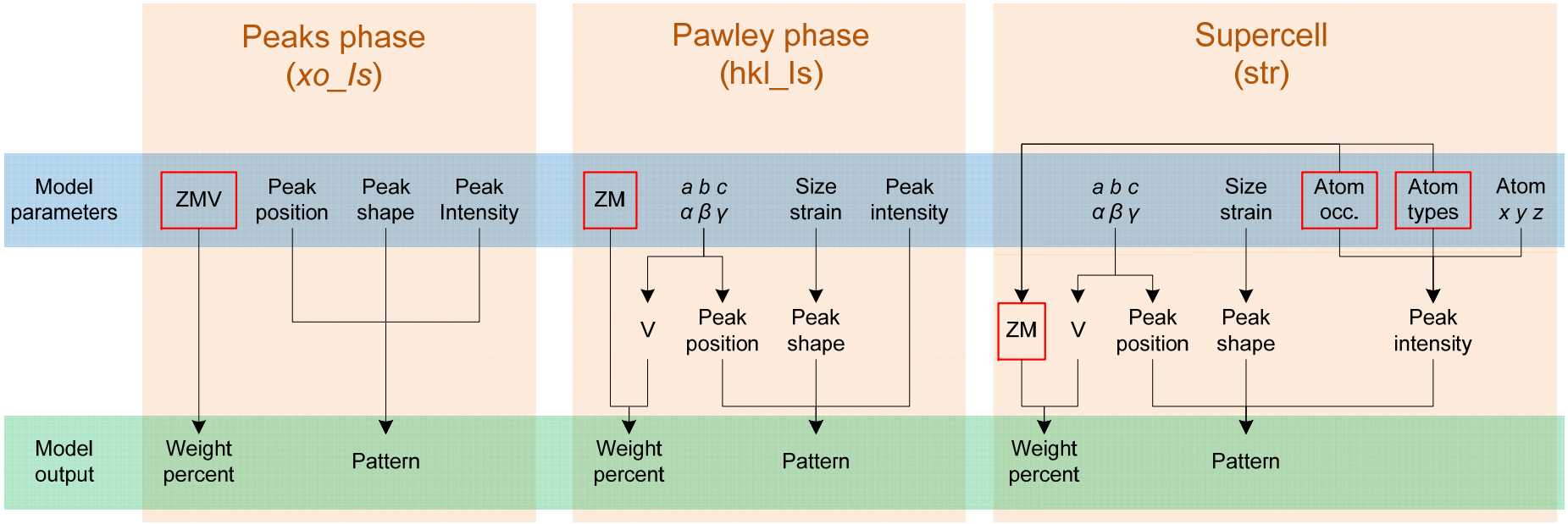

Figure 5-3 Comparison of the three kinds of TOPAS fit objects: the peaks phase (*xo_ls*), the Pawley phase (*hkl_ls*) and the structural model (*str*). The relationships between model parameters and model outputs are shown.

The calibration of a supercell model involves two refinements of the XRD pattern of standard mixtures. A normal refinement with the uncalibrated nontronite supercell model and the structural model of the internal standard (CaF_2 is used in this study) was performed first to achieve a best fit to the patterns of the standard mixtures. The scale factors and lattice parameters of the internal standard (CaF_2) were determined from this refinement. These CaF_2 parameters were then fixed for a 'second refinement', in which the Rietveld quantitative formula was used in a reverse manner for supercell model calibration. In contrast to measuring the interlayer cation occupancy with the CEC method (Ufer *et al.*, 2008), the weighed percentages of components in standard mixtures were used to refine the lattice parameters and the coefficient for the nontronite interlayer cation occupancies, as shown in the input file in TOPAS syntax (Figure 5-4).

```
1 xdd ...
2 str
3  prm cmCaF2 = Get (cell_mass);
4  prm cvCaF2 = Get (cell_volume);
5  phase_name "Calcium Fluorite"
6  MVW(312.300, 163.213, 10.259)
7  scale !scCaF2 0.00554598749
8  Cubic(!afluorite 5.464 min 5.45 max 5.49)
9  ...
10 str
11  prm interlayer 0.5
12  prm pNa = interlayer 0.717;: 0.314 min 0
13  prm pMgI = interlayer 0.287;: 0.126 min 0
14  prm pH2O = pNa+pMgI;: 0.441 min 0 'interlayer H2O
15  prm !layer 9 'layer: supercell factor for elongation in 'c' direction
16  prm cnon 15.61679 min 14 max 15.8 'subcell c
17  scale = cmCaF2 cvCaF2 scCaF2/Get (cell_ mass)/Get (cell_ volume)/O.1*0.9;: 8.1 e-006
18  phase_name "Bulong_ supercell"
19  MVW(999.686, 6620.837, 89.741)
20  a anon 5.255 min 5.25 max 5.35
21  b !bnon 9.095 min 9.1 max 9.2
22  c = layer * cnon; 'supercell c
23  be benon 99.814
24  ...
```

Figure 5-4 Instead of refining the scale factor of the supercell model, the Rietveld quantification equation is used in a reverse manner by inputting the known weight ratio of nontronite and internal standard.

Only the unit cell mass and unit cell volume are refinable in line 17 in Figure 5-4. The TOPAS program will refine the coefficient of the interlayer

cation occupancy to achieve a correct value for the scale factor to match with the measured XRD pattern of standard mixtures. As the intensities of nontronite pattern are used to determine the interlayer coefficient, this approach is expected to be more accurate with nontronite-rich standard mixtures, in which the nontronite scale factors are less correlated with the background.

5.6 Sample preparation and experimental verification

5.6.1 Nontronite enrichment and purification

The enrichment and purification procedures for the Bulong nontronite and the nontronite standard NAu-1 (Section 3.1.2) was described in Section 3.2.5 and are referred to as 'purified Bulong nontronite' and 'purified NAu-1 nontronite', respectively. The chemical compositions of the first cation exchange liquors were determined by ICP-OES (Section 3.2.2) to estimate the species and amounts of interlayer cations for both Bulong nontronite and the NAu-1 standard. Both purified Ca-saturated nontronite powders were also analysed by ICP-OES after high temperature fusion with Sigma Chemicals 12:22 lithium borate flux and dissolution in deionised water.

5.6.2 Bulong nontronite chemical formula

The approach adopted for calculation of the Bulong nontronite structural formula was the same as that reported for NAu-1 (Keeling *et al.*, 2000). The equations for determining the 2:1 phyllosilicate chemical formula as described in CLAYFORM (Bodine, 1987) were rewritten in Microsoft® Excel. The chemical formula of Bulong nontronite was generated based on 22 equivalent oxygen atoms using the ICP results of purified Ca-saturated Bulong nontronite.

5.6.3 Standard mixtures and synthetic laterites

In order to calibrate the supercell models, the enriched Bulong nontronite was mixed with 10, 30 and 50 wt.% calcium fluorite (Section 3.1.3) using a McCrone® micronising mill to prepare three standard mixtures. Fluorite was chosen because its mass absorption coefficient is close to that of nontronite

at the 1 Å X-ray wavelength used to collect the synchrotron XRD data. The following preparation procedures were the same as those described in Section 4.4. Six independent synthetic limonitic laterites were prepared by mixing Bulong nontronite with goethite and quartz to simulate various common phase compositions of Western Australian nickel laterite (Elias *et al.*, 1981; Singh & Gilkes, 1992; Landers *et al.*, 2009b). Details of the weight ratios are shown in Table 5-1. The mixing method was the same as used in Section 4.4.

Table 5-1 The weighed compositions and the quantification results of six synthetic mixtures of goethite (Goe), quartz (Qtz) and nontronite (Nont). Figures in brackets represent the 1σ uncertainty on the last decimal place.

Sample	Weighed wt.% of synthetic laterites			Calculated wt.% by uncalibrated supercell			Calculated wt.% by calibrated supercell		
	Nont	Goe	Qtz	Nont	Goe	Qtz	Nont	Goe	Qtz
NGQ1	10.03	70.13	19.84	8.7(4)	70.4(4)	20.9(1)	9.3(3)	70.0(2)	20.78(10)
NGQ2	15.07	55.02	29.91	19.8(4)	51.5(3)	28.7(2)	14.2(2)	55.17(17)	30.59(11)
NGQ3	19.96	39.96	40.08	24.4(1)	37.45(6)	38.1(1)	19.71(19)	39.84(11)	40.45(11)
NGQ4	30.02	20.08	49.90	35.2(1)	18.58(5)	46.2(2)	30.09(17)	20.20(7)	49.71(13)
NGQ5	34.97	50.01	15.02	38.8(3)	46.5(2)	14.6(1)	35.06(18)	49.44(14)	15.50(7)
NGQ6	49.97	24.92	25.11	55.5(2)	22.1(1)	22.4(1)	50.36(15)	24.94(9)	24.70(10)

5.6.4 Synchrotron X-ray diffraction

The purified Bulong and NAu-1 nontronite samples, three standard mixtures, and six synthetic laterites were loaded into capillaries (Section 3.2.3.1) for synchrotron diffraction measurements. The capillaries were agitated in an ultrasonic bath to assist powder loading and promote random orientation of the particles. Synchrotron X-ray powder diffraction patterns of all samples were collected on the Powder Diffraction Beamline (10-BM-1) at the Australian Synchrotron (Section 3.2.3.4). The wavelength was set to 1 Å and determined to be 0.999047 Å using a NIST Standard Reference Material 660b LaB_6 diluted with diamond powder (weight ratio 1:9). This standard was also used to obtain the instrumental profile of the beamline under the experimental settings employed, which are detailed in Appendix 3.

5.6.5 Applying PONKCS calibration on the supercell model

The instrumental convolutions, zero error of the goniometer were also determined from the NIST Standard Reference Material 660b LaB_6. The capillary background was modelled from the pattern of an empty capillary using a peaks phase group, which is essentially a group of peaks (*xo_Is*) with the peak shape modifier described individually and scale factors linked and refinable (Wang *et al.*, 2011). A zero-order Chebyshev background was used to minimise the correlation between the Chebyshev background and nontronite Bragg humps. A background function *fit_obj* = *a*/(X-*b*) (*a*, *b* refinable) was used to fit the low-angle high background prior to the nontronite 001 basal reflection (Appendix 4); the fitting was much closer to the experimental pattern than that achieved by the conventional *One_on_X* macro, which uses the basic inverse proportion function *fit_obj* = *a*/X (Bruker AXS, 2009).

The supercell model calibration procedures planned in Section 5.5 were performed on the three standard mixtures. The coefficient of interlayer cation occupancy and the lattice parameters of Bulong nontronite used in the final Bulong nontronite supercell model were determined by arithmetically averaging their refined values from the 'second refinement' for all three standard mixtures. These parameters were fixed in the final supercell model used for the quantitative analysis of nontronite in the synthetic laterite mixtures.

5.7 Results and discussions

5.7.1 Bulong nontronite formula

The ICP assays for the first cation exchange liquor and the purified Ca-saturated Bulong and NAu-1 nontronites are shown in Table 5-2. The exchangeable cations for the two nontronites are quite different. Calcium is the dominant interlayer exchangeable cation for NAu-1, while for Bulong nontronite it is sodium. The ICP results for the purified NAu-1 sample matches that previously reported (Keeling *et al.*, 2000). The ICP analysis of the purified Bulong nontronite confirms that nickel is not present as an exchangeable cation but is fixed within the octahedral layer. The structural

formula of Bulong nontronite calculated as described in Section 5.6.2 is $M_{1.29}^{+}[Si_{7.33}^{4+}Al_{0.67}^{3+}][Al_{0.95}^{3+}Fe_{2.40}^{3+}Ni_{0.26}^{2+}Co_{0.01}^{2+}Mg_{0.26}^{2+}Cr_{0.09}^{3+}]O_{20}(OH)_4$, where M^+ represents monovalent cations.

Table 5-2 ICP results of the "1st cation exchange liquor" and the purified powders for both Bulong nontronite and NAu-1 nontronite standard.

Sample		Exchangeable cation fraction (mg/g)									
		Co	Fe	Ni	Mg	Al	Si	Na	Ca	K	Cr
1st cation exchange liquor	NAu-1	<0.04	<0.04	<0.04	1.03	<0.04	0.58	1.12	3.02	<0.04	<0.04
	Bulong	<0.04	<0.04	<0.04	1.94	<0.04	0.30	4.58	0.10	<0.04	<0.04
		Elemental concentration (wt.%)									
		CoO	Fe_2O_3	NiO	MgO	Al_2O_3	SiO_2	Na_2O	CaO	K_2O	Cr_2O_3
purified powder	NAu-1	-	36.0	0.022	0.270	8.02	50.9	0.020	4.72	0.091	0.019
	Bulong	0.060	24.4	2.52	1.361	10.57	56.2	0.107	4.47	0.099	0.849

5.7.2 Uncalibrated supercell model

An uncalibrated supercell model (atom occupancies solely determined from chemical assay) usually gives rise to inaccurate quantitative results, although good fitting for a nontronite pattern can be achieved, as shown in Figure 5-5.

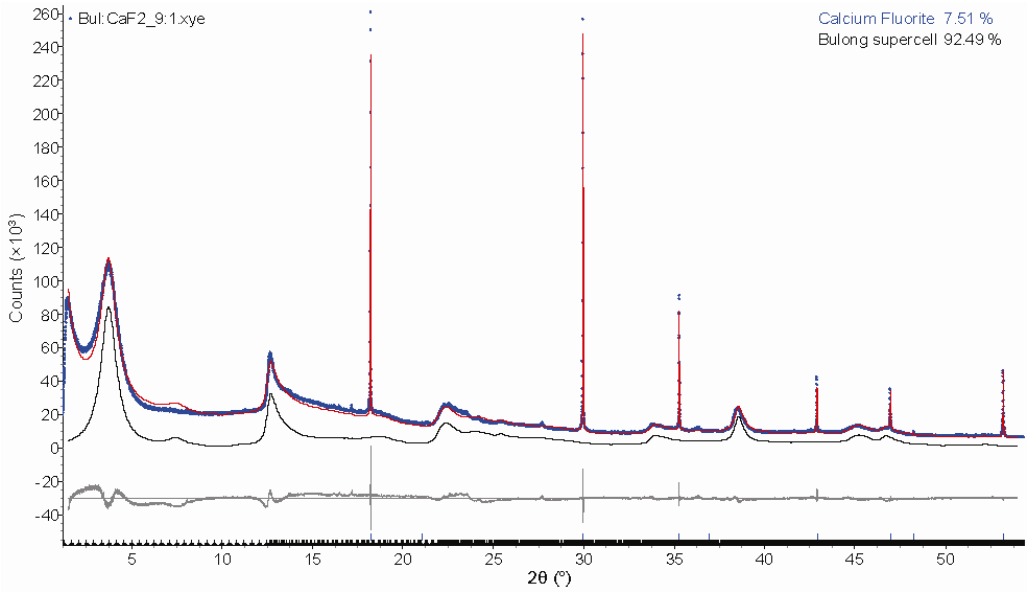

Figure 5-5 Fitting of the asymmetric non-basal diffraction band using the uncalibrated supercell model. The quantitative results show an overestimation for the Bulong nontronite in this 9:1 mixture with CaF_2. The nontronite curve is highlighted.

The inaccurate quantitative results may be due to the error associated with the chemical assay, or the deviation between the real atom positions of Bulong nontronite and the published structure (Tsipursky & Drits, 1984). The uncalibrated supercell model resulted in quantitative discrepancies of more than 5 wt.% for the synthetic laterite samples, as shown in Table 5-1 and Figure 5-6a. Nontronite concentrations are systematically overestimated except for the sample with lowest nontronite concentration, for which the wide Bragg peak may have been strongly correlated with the background.

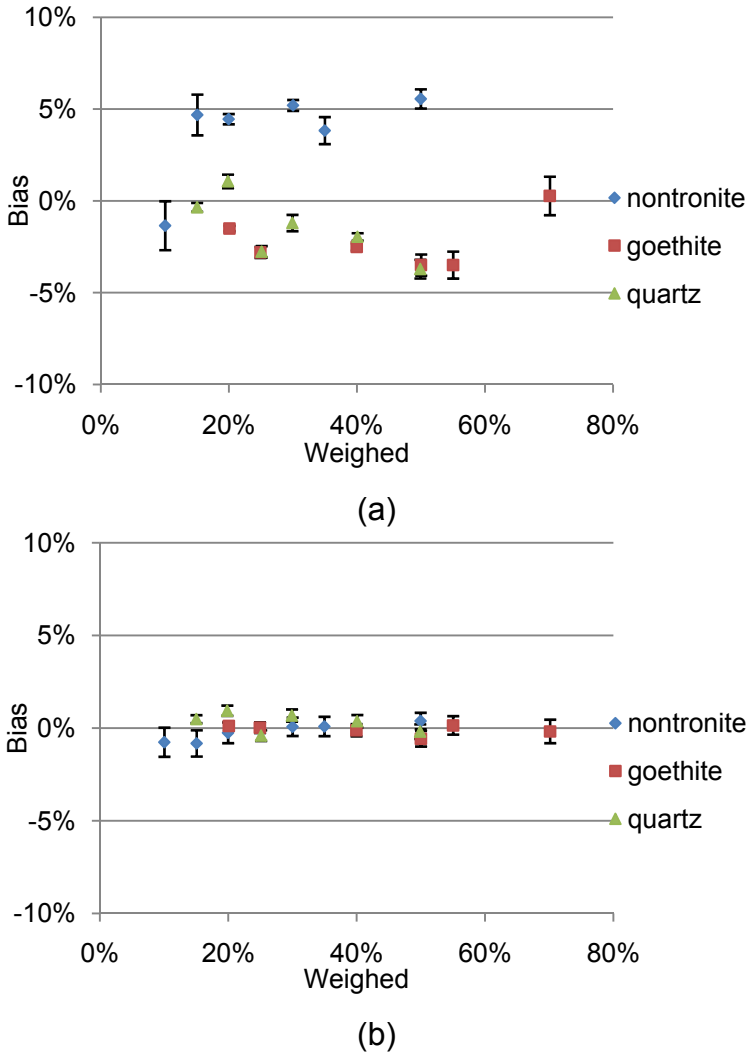

Figure 5-6 Bias plot between the weighed percentage of each phase and the quantitative XRD results for synthetic laterite ores using (a) uncalibrated supercell model and (b) calibrated supercell model.

5.7.3 Calibrated supercell model

The calibrated coefficient of the interlayer cation occupancies derived from the three standard mixtures was 0.398(6), which corresponds to a ZM factor of 980 atomic mass units in the supercell model for Bulong nontronite. The lattice parameters of Bulong nontronite in the final Bulong nontronite supercell model are averaged from three standard mixtures and correspond to a unit cell volume of 6637 $Å^3$. The product of the calibrated unit-cell mass and volume plays the same role as the calibrated ZMV factor in the PONKCS method (Wang *et al.*, 2011). The calibrated coefficient for the interlayer cation occupancies does not have a physical meaning but is simply a factor for adjusting the unit cell mass to achieve the correct weight percentages. This calibration constant also absorbs residual sample-related effects such as microabsorption (Madsen *et al.*, 2011) and other systematic errors, such as structural deviation and residual preferred orientation in Debye-Scherrer geometry.

The quantitative results for the synthetic laterite samples using the calibrated supercell model are shown in Table 5-1. The use of this model reduced the bias from the known weighed values to within 1 wt.% (Figure 5-6b). This result demonstrates the advantage of using a crystallographic structure-based model for the quantitative analysis of turbostratically disordered clay minerals, compared with the accuracy level achieved by the PONKCS model in Chapter 4. Only four refinable parameters relating to the size and strain broadening of the basal and non-basal diffraction peaks were required. In contrast, for the modified PONKCS approach 12 parameters were required for the use of spherical harmonics to reproduce anisotropic size/strain broadening and associated asymmetries (three second-order spherical harmonics in the C2/m space group). The larger number of parameters refined in the PONKCS Pawley model may lead to parameter correlations that impact on scale factor calculations and prevent accurate phase quantification being achieved.

The calibration method used here for the supercell model for nontronite quantitative analysis was derived from the core idea of the PONKCS approach, which uses the target material to calibrate the quantitative X-ray

diffraction (QXRD) model. Hence this approach should be regarded as a calibration-based method. The previous PONKCS method calibrates peaks phase (*xo_ls*) or Pawley phase (*hkl_ls*) models; the approach described in this chapter extends the PONKCS method to calibrate structural (*str*) models. It should be noted that, although the interlayer cation occupancies in the nontronite supercell model were refined during the calibration, this approach is purely to facilitate quantitative analysis and should not be considered as a structure solution. An approach similar to that used by Manceau *et al.* (1998) is recommended for determination of the nontronite crystal structure.

The supercell model requires significantly more effort than the PONKCS method. Building the supercell model requires chemical data for the purified nontronite to determine the substituted metal cations and their occupancies, while the PONKCS approach only requires the target phase to be enriched. The PONKCS method is useful for any phase with an unknown or partially known crystal structure, while the supercell model approach is only applicable to the turbostratically disordered clay minerals. Another drawback of the supercell approach is that the refinement is time consuming as 9 times more reflections are included in the calculation in each refinement step (for this case where “layer = 9” in the supercell structure shown in Appendix 6). For example, refining 5 patterns (5000 data points each) using the PONKCS *hkl* model took 21.7 seconds for an Intel® Core™ 2 Quad Processor Q9400 (2.66 GHz). However, refining the same data set using the supercell model took 203.9 seconds for same CPU. On the other hand, the diffraction peaks used to define the Pawley phase in the PONKCS approach can be selectively deleted, as stated in Chapter 4, reducing the calculation time. If the QXRD accuracy of the PONKCS approach is acceptable then it is the most direct and effective method for mining and metallurgy industries to perform quantitative mineralogy, especially where large numbers of related samples are to be analysed.

5.8 Conclusions

Several methods used for the quantitative analysis of turbostratic smectite are compared in Table 5-3. The method used by Taylor and Matulis

(1994) and Bonetto *et al.* (2003) is based on fine tuning structural factors calculated from the standard structural model therefore is limited to phases with known approximate structural models. The PONKCS method used by Scarlett & Madsen (2006) and Wang *et al.* (2011) based on peaks phase and Pawley phase models have much wider application. Any phase contributing recognisable Bragg peaks in an XRD pattern could be quantified with the PONKCS method. Ufer *et al.* (2004) developed a Rietveld compatible supercell model to physically describe turbostratic disorder. The approach described in this chapter combines PONKCS calibration with the supercell model to achieve more accurate quantification of turbostratically disordered smectite.

The TOPAS symbolic computation system provided an ideal platform to develop a novel structural model calibration approach for the interlayer cation occupancies in the nontronite supercell model using the patterns of standard mixtures with known weight ratios. The new calibrated supercell model was able to achieve quantitative analysis of nontronite in synthetic laterites to within 1 wt.% of the weighed values.

This supercell calibration approach is aimed at quantitative analysis and should not be regarded as providing a structure solution. Although improved quantitative results were obtained, the time-consuming refinement, the need to chemically assay the pure target phase and the limitation to handling turbostratically disordered clay minerals make the supercell model less attractive than the PONKCS approach for mining and metallurgy industries that demand rapid, and often just comparative, mineralogical data.

Table 5-3 Comparison of approaches used for turbostratic disordered smectite quantification

	Taylor and Matulis (1994)	Bonetto *et al.* (2003)	Scarlett and Madsen (2006)	Wang *et al.* (2011)	Ufer *et al*. (2004)	Wang *et al.* (2012)
Platform	SIROQUANT	FULLPROF	TOPAS	TOPAS	BGMN	TOPAS
Approach	Modify $\|F\|^2$ from standard structure model	Modify $\|F\|^2$ from standard structure model	Fit the pattern with "envelop fitting"	Fit the pattern with selected *hkl*s & peak shape modifiers	use supercell model to fit the pattern	use supercell model to fit the pattern
Calibration required?	No	No	Calibrate ZMV factor with standard mixtures	Calibrate ZMV factor with standard mixtures	Chemical Assay & CEC measurement	Calibrate ZMV factor with standard mixtures
Application field	Disordered phase with known structure model	Disordered phase with known structure model	Phases with Partially or No known Crystal Structure	Phases with Partially or No known Crystal Structure	Turbostratically disordered clay minerals	Turbostratically disordered clay minerals
Supercell	Lengths of '*a*', '*b*' axis doubled. No physical meaning.	Lengths of '*a*', '*b*' axis doubled. No physical meaning.	No	No	Lengths of '*c*' axis elongated 9 times to simulate turbostratic disorder	Lengths of '*c*' axis elongated 9 times to simulate turbostratic disorder
Selective hkl peaks	470 reflections reduced to 50	Yes	No	Yes	No, generated by structural model	No, generated by structural model
Anisotropic peak shape	Different FWHM for 00*l* and *hk*0 reflections	Different FWHM for 00*l* and *hk*0 reflections	No	Spherical harmonics function for anisotropic peak shapes	Reproduced by supercell model	Reproduced by supercell model
Preferred orientation	March Model	March Model	March Model	March Model or Spherical harmonics	No	March Model

Chapter 6 Correlations between laterite leaching performance and their mineralogical characteristics

6.1 Introduction

The leaching rates for previously obtained column leach tests using the 52 Western Australian nickel laterite ore samples were derived by fitting their leaching curves (percentages of leached iron and nickel versus leaching time) with an empirical dissolution model, *e.g.* Kabai model (Section 2.6.4.2). The model and their parameters are usually applied to single phase systems, from which the model was established. However, the use of the model for natural multiphase iron oxides samples is not uncommon (Schwertmann & Latham, 1986; Schwertmann *et al.*, 1987; Landers & Gilkes, 2007).

The PONKCS methods (Chapter 4) and the supercell approach (Chapter 5) were applied to assist with the accurate quantitative phase analysis and profile fitting. The mineralogical compositions of these nickel laterite ores are assessed from their laboratory XRD patterns. The guest metal substitution into the goethite crystal structure, the major nickel containing phase, may cause changes in its unit cell dimensions, which are measured from their synchrotron XRD patterns. The averaged metal substitution levels in goethite of the studied ore samples are determined from TEM/EDS analysis. The correlations between their leaching rates, ore mineralogy, and guest metal substitution levels are discussed.

6.2 Nickel and iron final extractions

The column leaching tests were carried out as described in Section 3.2.6. In most cases sample leaching was stopped after the percentage of iron extracted no longer increased significantly. The final iron versus nickel extractions of the 52 laterite ore samples are shown and compared in Figure 6-1. The final extractions of these ore samples vary greatly; *e.g.* samples A15 and B11 are the least leached ores only releasing about 2 % and 8 % of nickel after 126 and 175 days of acid leaching, respectively. Samples D2 and D3 are the most completely leached ores with nickel almost completely extracted after 256 and 174 days of acid leaching, respectively.

The distribution plot for the Ni/Fe extraction ratios of the 52 nickel laterite ore samples (Figure 6-2) indicates that nickel extractions are generally higher than iron extractions. This suggests nickel and iron are located in different phases with different leachabilities, *e.g.* nontronite and goethite, as shown by the most outstanding samples A8 and A10. Their mineralogical compositions before acid leaching (Table 6-1) show they contain both nontronite (Ni/Fe weight ratio ~10 %, Chapter 5), and iron oxide phases (Ni/Fe weight ratio ~1 %, Chapter 7). Nontronite was totally dissolved from these two samples after acid leaching while part of the iron oxides (hematite and maghemite) still remains, as indicated by the qualitative and quantitative phase analysis of the leaching residuals of ore sample A8 and A10 in Figure 6-3 and Table 6-1. The different leachibilities of nontronite and iron oxides produce higher nickel extractions than iron extractions. Most of these samples have 40–85 % iron extracted and 50–90 % nickel extracted. However, the laterite ore samples responsible for the most variability of final iron and nickel extractions (A15, B11, C6, A4, D5, A5, D4, A16, C10, A17, A3, A2, B3, B4, D3, and D2) have Ni/Fe extraction ratios of approximately 1 (along the dashed line in Figure 6-1), which suggests that nickel and iron are mainly hosted in the same phase in these samples. Further study of the variability of the leaching performances of the laterite ores should focus on these samples.

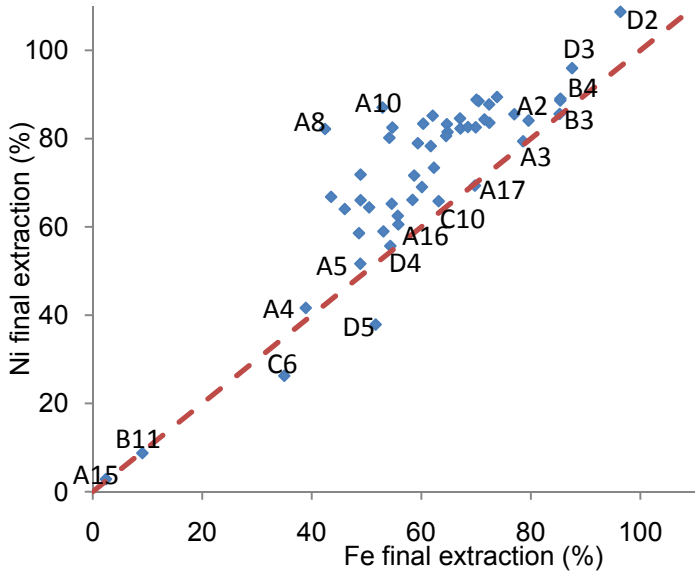

Figure 6-1 Comparison of Ni and Fe final extractions from the 52 laterite ore samples. The dashed line indicates equivalent Fe and Ni final extractions. The >100% Ni extraction for D2 may have arisen from variations of Ni content in the D2 feed ore.

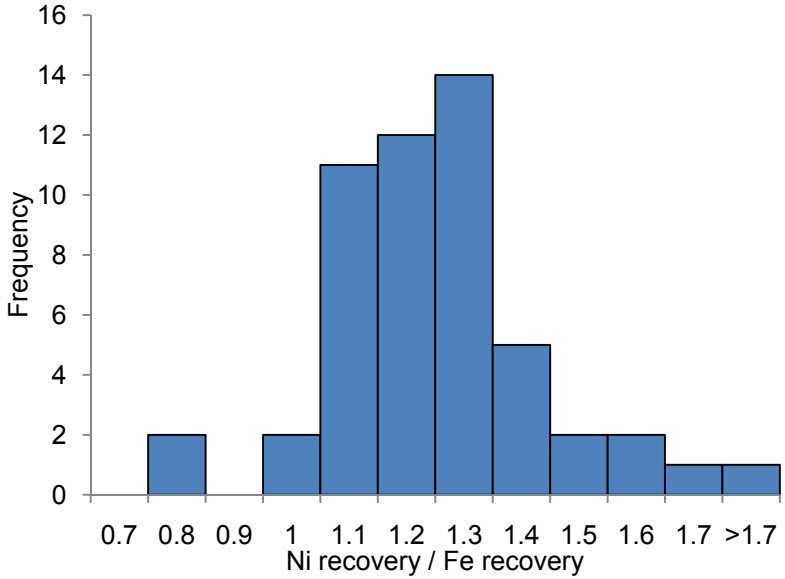

Figure 6-2 The distribution of the Ni/Fe final extraction ratio from Figure 6-1.

Table 6-1 Quantitative phase analysis of ore A8 and A10 before and after column leaching

Sample	Goethite	Quartz	Hematite	Maghemite	Nontronite	Clinochlore	Opal	Talc	Amorphous
A8 feed	8.7(4)	8.1(2)	10.8(3)	7.5(2)	28.9(8)	5.1(5)	18.9(7)	3.1(3)	9(2)
A8 residue	-	11.7(2)	11.7(3)	11.5(2)	-	-	27.7(4)	-	37(1)
A10 feed	13.1(4)	8.2(1)	10.3(2)	12.6(2)	20.1(6)	3.7(5)	25.4(7)	2.5(2)	4(1)
A10 residue	-	10.6(2)	14.7(3)	6.0(3)	-	-	26.0(6)	5.3(4)	37(1)

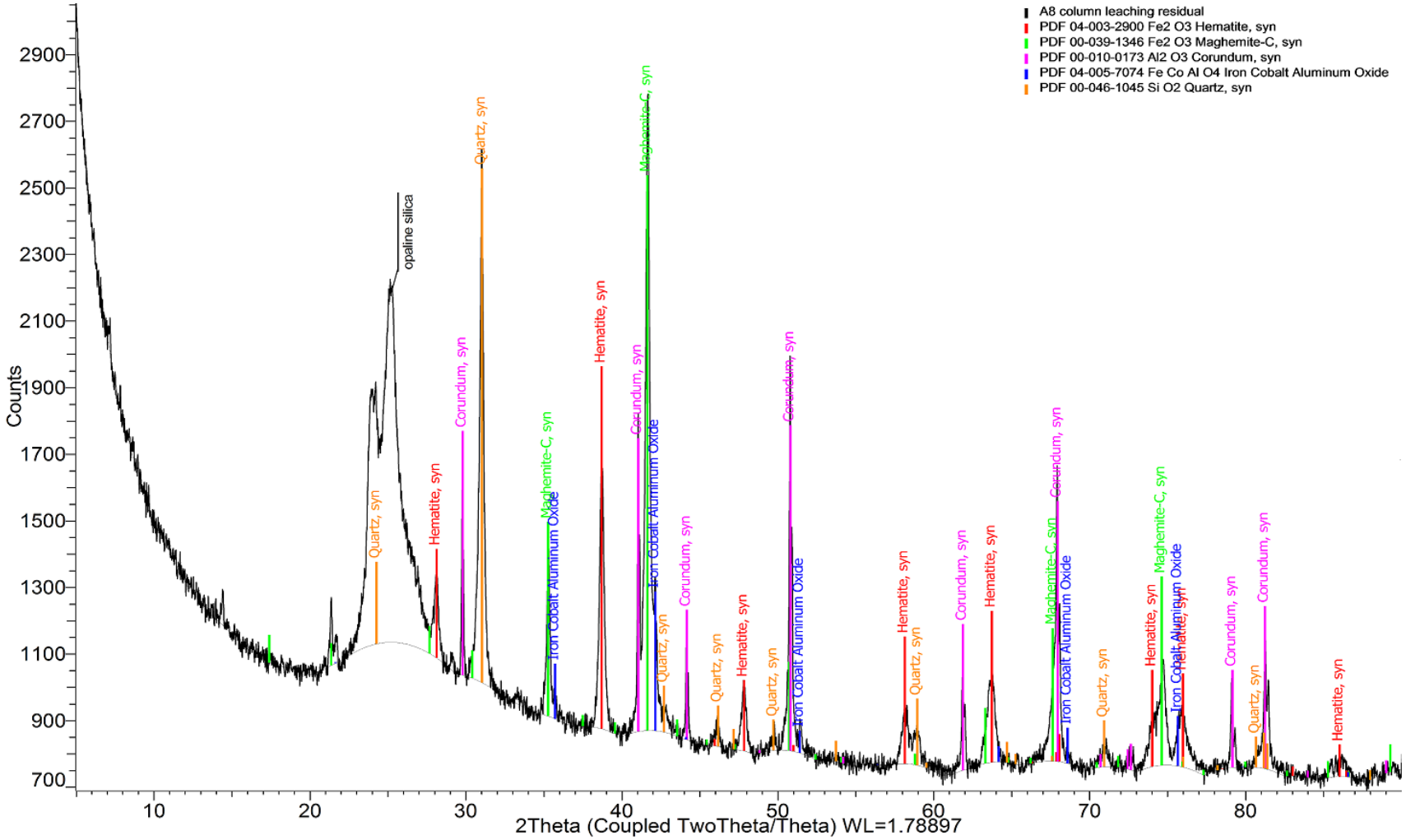
A8 column leaching residual
PDF 04-003-2900 Fe2 O3 Hematite, syn
PDF 00-039-1346 Fe2 O3 Maghemite-C, syn
PDF 00-010-0173 Al2 O3 Corundum, syn
PDF 04-005-7074 Fe Co Al O4 Iron Cobalt Aluminum Oxide
PDF 00-046-1045 Si O2 Quartz, syn
Counts
2900
2700
2500
2300
2100
1900
1700
1500
1300
1100
900
700
10
20
30
40
50
60
70
80
2Theta (Coupled TwoTheta/Theta) WL=1.78897
opaline silica
Quartz, syn
Hematite, syn
Corundum, syn
Maghemite-C, syn
Iron Cobalt Aluminum Oxide

(a)

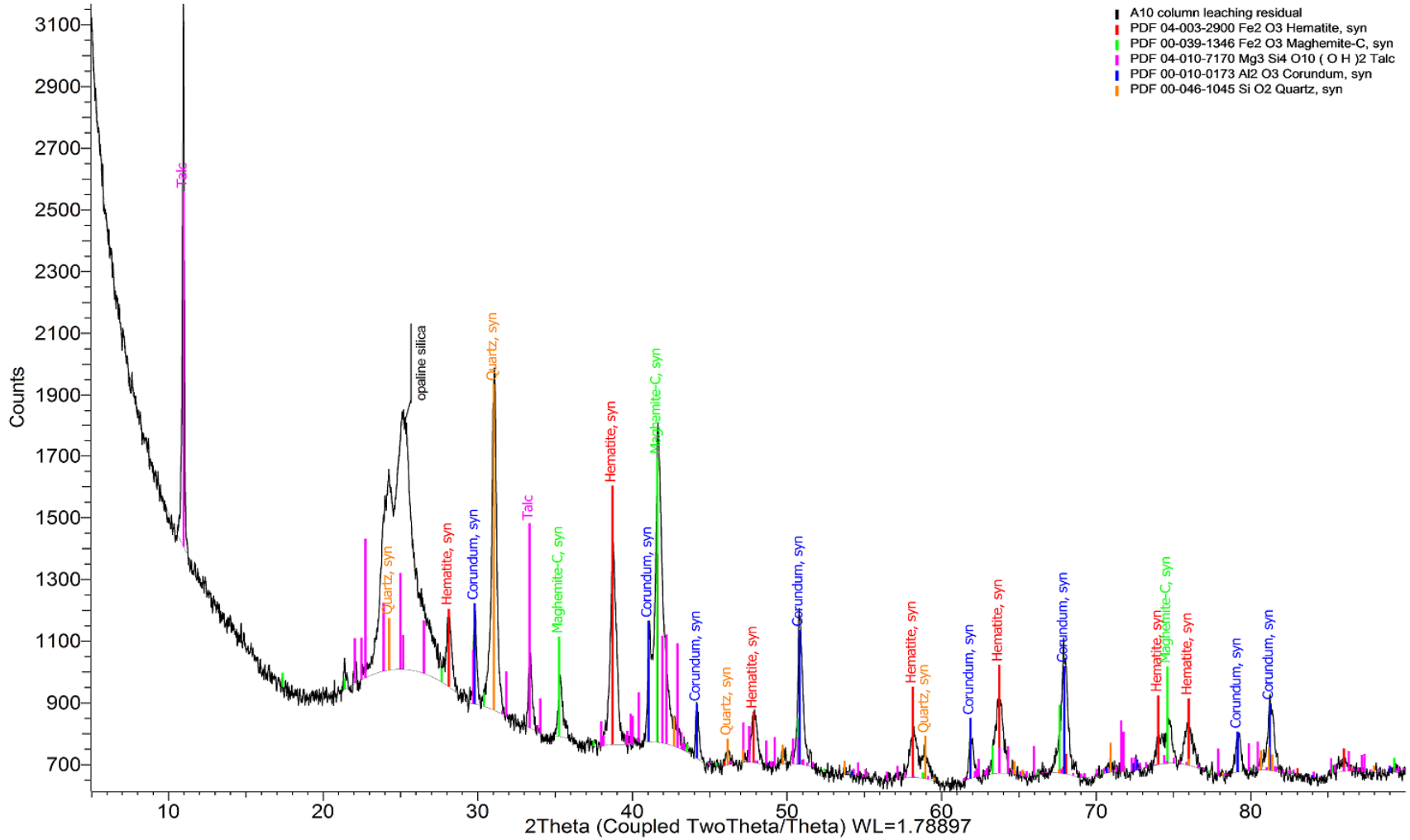

(b)

Figure 6-3 Phase identification of ore leaching residues of (a) A8 and (b) A10, corundum was used as internal standard. WL: wavelength (Å).

6.3 Column leaching rate

For heap leaching, the rate at which metal is extracted is more important than the final extraction when trying to ascertain ore leachability. For example, although sample D2 gave the highest nickel extraction (109 %), it required nearly three times the leaching time (266 days) than sample D1 (66 % extraction, 97 days). The additional acid consumption required for sample D2 may not justify the additional nickel extracted. As a relatively minor amount of nickel is normally distributed in the hosting phase like goethite and nontronite in laterite ores (Section 2.4), the major metal of the hosting phase, iron, was chosen for leaching rate analysis. To better appreciate the variations in both the final extractions and the leaching rates via the shape of these iron leaching curves, eight extremes are compared in Figure 6-4. It is apparent that sample D2 with higher final extraction has a lower initial leaching rate than sample A1; samples with different leaching rates can converge to similar final extractions (A6, C5); samples with similar initial leaching curves can diverge significantly at the later stages of leaching (A4, C6); and the most poorly leached samples may release less than 10 % of their iron content (A15, B11).

In order to quantify the iron and nickel leaching rates from the column leaching experiments, the rate constants k (day^{-1}) of the ores were derived from the fitting of the iron and nickel leaching curves with a heterogeneous chemical reaction model, the Kabai model (Section 2.6.4.2). The Kabai model has been widely used to determine the leaching rate of laterite ore samples (Schwertmann & Latham, 1986; Singh & Gilkes, 1992; Landers & Gilkes, 2007).

The Kabai model can be rearranged into a linear form (right side of Eq. 6-1). If a leaching experiment follows the Kabai model, the data points on the leaching curve (α versus t) should form a straight line when plotted as $\ln[-\ln(1-\alpha)]$ versus $\ln(t)$. The slope is the "constant of average order a" and the y-intercept is "$\mathrm{a}\ln(k)$", from which the rate constant k can be derived.

$$\alpha = 1 - \mathrm{e}^{-(kt)^{\mathrm{a}}} \Leftrightarrow \ln[-\ln(1-\alpha)] = \mathrm{a}\ln(k) + \mathrm{a}\ln(t) \qquad \text{Eq. 6-1}$$

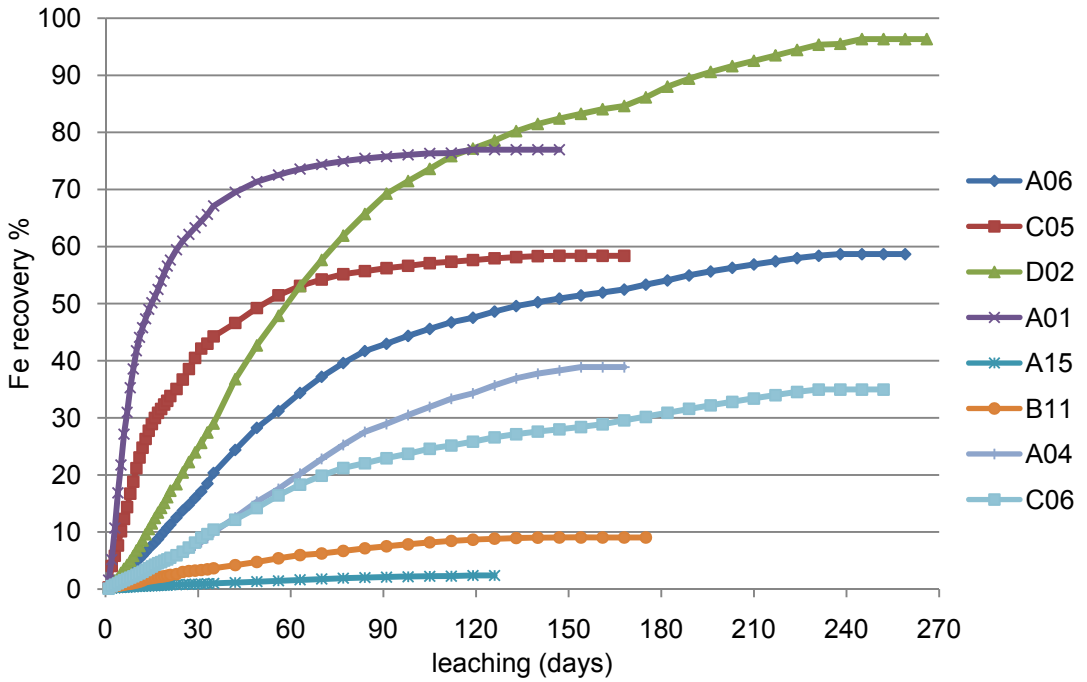

Figure 6-4 Selection of eight Fe leaching curves representing extremes of Fe final extractions and leaching rates.

The $\ln[-\ln(1-\alpha)]$ versus $\ln(t)$ plot can be also used to examine the congruency of iron extraction from different phases. If iron in all the ferruginous phases were congruently leached, the leaching data in this plot would form a straight line. On the other hand if the leaching data plot systematically deviates from a straight line, the iron leaching could be regarded as incongruent leaching from at least two phases, suggesting the two-line fitting practice should be adopted (Schwertmann & Latham, 1986).

The iron and nickel leaching data of the 52 nickel laterite ore samples in this study were plotted as $\ln[-\ln(1-\alpha)]$ versus $\ln(t)$ in Appendix 7. About half of these curves require two-line fitting. It should be noted that the "break point" for both nickel and iron plots are at same time, $\ln(t)$, for most samples, which suggests that the fast leaching nontronite and the slow leaching iron oxides are the major iron and nickel host phases in these samples. It should be noted that leaching profiles that do not conform to the normal Kabai curve could also be due to uneven leaching of the solids in the column. So this is not the only interpretation. The link to the different behaviours of two ferruginous phases will be supported by the quantitative phase analysis results of these ore samples later in this chapter.

An example of the iron leaching curve is shown in Figure 6-5. Of the major iron containing phases in laterite ores, nontronite is a poorly crystalline iron rich smectite clay mineral and is readily dissolved by acid, while iron oxides tend to be more acid resistant (McDonald & Whittington, 2008a). Therefore nontronite dissolution should be the dominant contributor to the earlier stage of the iron leaching curves. After nontronite dissolution, the remaining iron leaching from iron oxides would exhibit a slow leaching rate.

Upon close consideration it would appear that the above practice is problematic. The vertical position of the second fitting line is affected by the background iron level leached from nontronite. For example, if only 10 % iron was extracted from goethite from the 40th day to the 200th day, it will be plotted as 50 % to 55 % of iron extracted during this period for goethite and nontronite mixture containing equal amounts of iron. This overestimates the iron leaching rate if the Kabai model is used to fit data in this range. In other words, this two-line fitting practice does not correctly separate the iron leaching rates of two incongruently dissolving phases. It is necessary to plot the iron leaching data from iron oxides on an independent y axis.

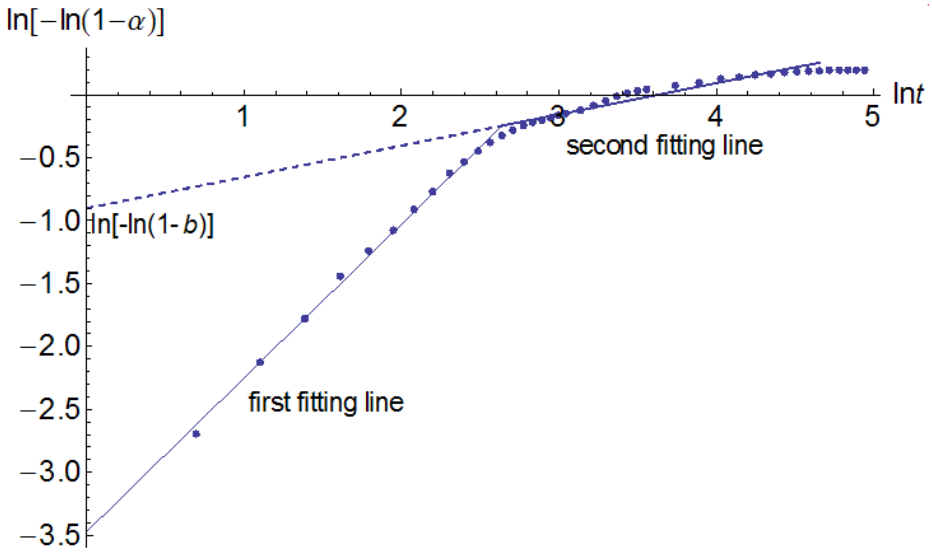

Figure 6-5 Fe leaching data for sample C1 fitted by two lines with distinctly different gradients. Based on Schwertmann and Latham's method (1986) the first fitted line can be attributed to the relatively fast Fe extraction from nontronite and the second fitted line from Fe leaching from iron oxides.

To estimate correct iron leaching rates for the iron oxides, the proportion of iron extracted from nontronite, noted as b (0 < b < 1), should be subtracted from the backend iron leaching data corresponding to the second fitted line in Figure 6-5, noted as a_{i} (b < a_{i} < 1). Then the difference $a_{\mathrm{i}} - b$ can be normalised according to the proportion of iron in iron oxides, $1 - b$. The background iron level b may be roughly assessed from the y-intercept by extrapolating the second fitted line back to ln(*t*) = 0 (Figure 6-5). The dissolution data $(a_{\mathrm{i}} - b)/(1 - b)$ separated from the contribution of nontronite dissolution can now be fitted with the non-linear "Kabai" equation (left side of Eq. 6-1) again in α versus t plot to determine the rate constant '*k*' for iron leaching from iron oxides. The data processing was performed in Wolfram® *Mathematica* v8.0.4 and one example is shown in Appendix 8. The rate constant '*k*' and the constant of average order 'a' of both iron and nickel leaching data for these ores are also reported in Appendix 8.

6.4 Correlation between iron and nickel final extractions and sample mineralogy

The mineralogical properties of all the 52 laterite ore samples were measured by both laboratory XRD and synchrotron XRD (Section 3.2.3). The goethite lattice parameters in these samples were measured from the synchrotron XRD patterns, which have better signal to noise ratio and better angular resolution than laboratory XRD. The quantitative phase analyses were derived from laboratory XRD which examined a larger sample volume.

The mineralogical compositions of the 52 nickel laterite ore samples assessed from their laboratory XRD patterns are given in Table 6-2. The results are consistent with analytical elemental data (Section 3.2.2). Most samples contain goethite. Around half of them are also accompanied with nontronite, which can be considered as limonite-smectite laterite blends. The rest of the samples free from nontronite can be regarded as oxide type (limonitic) laterite ores (Section 2.4). The negative amorphous content in Table 6-2 maybe result from overestimation of quartz or opaline silica (low absorber for CuKα radiation) due to microabsorption (Madsen *et al.*, 2013, p306). This indicates these samples have little if any amorphous content.

Table 6-2 Mineralogical composition of 52 nickel laterite ore samples from Western Australia assessed by QXRD.

Sample	goe	qtz	hem	mght	non	clino	liza	kao	opal	talc	mgns	hal	chamo	albt	lithi	gbst	domt	amor
A1	6.8(4)	4.0(1)	1.1(1)	3.9(1)	57.3(5)	12.9(4)			14.5(5)									-1(1)
A2	3.6(2)	10.7(1)		3.4(1)	17.8(4)	8.6(3)			61.5(5)									-6(1)
A3	9.4(4)	11.5(2)	1.2(1)	2.91(9)	26.7(5)				40.5(5)									8(1)
A4	60.7(2)	33.0(1)	2.9(1)															3.3(7)
A5	29.0(3)	48.6(3)	8.4(2)	6.2(2)			2.2(3)	2.7(4)										3(1)
A6	41.1(2)	39.0(2)	4.0(1)	4.3(1)		2.3(4)												9.3(8)
A7	7.2(2)	85.3(4)	1.17(8)	2.37(9)		2.6(3)		0.8(3)										0.6(8)
A8	8.7(4)	8.1(2)	10.8(3)	7.5(2)	28.9(8)	5.1(5)			18.9(7)	3.1(3)								9(2)
A9	13.7(3)	8.3(1)	10.2(2)	11.3(1)	23.4(4)				26.8(5)	4.0(2)								2(1)
A10	13.1(4)	8.2(1)	10.3(2)	12.6(2)	20.1(6)	3.7(5)			25.4(7)	2.5(2)								4(1)
A11	10.6(5)	1.08(7)	4.9(2)	4.0(2)	63.2(8)	2.6(8)				6.1(6)								1(1)
A12	10.8(4)	6.6(2)	4.1(2)	4.4(2)	64(1)	2(1)				7.8(3)								1(1)
A13	7.3(4)	0.71(8)	5.4(1)	2.08(7)	60.4(7)	3.5(6)			15.9(7)	7.9(4)								-3(1)
A14	17.2(3)	64.5(4)		7.3(1)		6.3(5)	2.8(4)				4.5(1)							-2(1)
A15	51.5(3)	36.9(2)		1.2(1)				6.5(6)										3.9(9)
A16	28.7(2)	66.2(2)		5.15(6)							1.6(1)							-1.7(7)
A17	15.2(2)	84.2(2)		3.22(6)														-2.6(7)
B1	24.6(5)	2.9(1)	2.1(1)	4.1(2)	34.2(7)	2(1)			27.3(7)									3(2)
B2	14.2(6)	15.9(4)	1.8(2)	9.2(3)		25.3(9)	8.1(7)											25(2)
B3		2.5(1)			48(1)	11(2)		17.3(7)						22.1(6)				0(2)
B4	8.9(6)	1.3(1)		1.4(2)	15.8(9)	31(1)			18(1)	5.0(4)				16.0(6)				2(2)
B5	19.2(4)	30.7(4)	5.5(1)	4.1(1)	34.4(8)	8.2(9)	1.5(2)											-3(2)
B6	18.2(5)	23.1(4)	6.0(3)	7.6(3)		22.2(8)	6.7(5)	7.2(8)										9(2)
B7	12.9(5)	0.83(6)			50(2)	2.9(6)		31(1)										2(3)
B8	22.5(3)	35.4(2)	6.5(2)	10.3(1)		7.5(4)				1.6(2)								16.3(8)
B9	13.9(3)	73.5(3)	4.6(1)	7.1(1)		5.5(4)												-4.6(9)
B10	26.0(3)	34.4(3)	13.5(2)	9.4(1)		9.5(5)	1.1(2)			3.4(2)								2.7(9)
B11	43.0(3)	7.04(9)		7.66(9)	12.2(5)			10.8(3)										19.3(8)

Sample	goe	qtz	hem	mght	non	clino	liza	kao	opal	talc	mgns	hal	chamo	albt	lithi	gbst	domt	amor
B12	6.9(4)	2.9(1)	0.7(1)	11.3(2)	43.3(9)	4.7(8)			17.7(8)								4.0(2)	9(2)
B13	19.6(4)	5.1(2)	1.0(1)	14.2(2)	51.6(7)	6.3(7)												2(2)
B14	5.45(3)	2.3(1)	1.5(1)	12.9(3)	48.0(7)	14.2(6)	3.6(4)											12(2)
B15	8.1(5)	1.3(1)	3.8(2)	10.7(2)	24.3(9)	13.7(8)	8.5(6)	6.4(6)	21.5(9)				2.9(2)					-1(2)
B16	9.2(5)	6.0(2)	3.1(2)	9.9(2)	22.2(8)	11.5(7)			38.4(7)									0(2)
B17	4.4(5)	31.4(6)		0.8(1)	29.7(8)	15.3(9)				8.1(4)								10(2)
B18	19.4(4)	24.4(3)	2.5(1)	6.4(1)		7.1(3)	3.1(6)	10.9(4)		11.9(4)								14(1)
B19	7.7(3)	2.7(1)	3.4(1)	8.2(2)	35.2(5)	10.7(5)				6.3(3)			17.3(5)					8(1)
B20	13.4(4)	3.5(1)	7.8(2)	13.5(2)	11.3(6)	7.4(5)			23.6(8)	6.1(5)								13(2)
C1	9.4(5)	0.9(1)	1.2(1)	3.0(1)	52.1(9)	9.7(9)			17.8(6)									6(2)
C2	18.7(3)	43.5(4)	2.0(1)	2.04(8)	19.4(5)	3.3(4)				2.8(2)								8(1)
C3	9.7(3)	55.6(7)	0.6(1)	0.97(8)	20.9(7)			0.9(7)										11(1)
C4	9.6(2)	77.3(3)	1.2(1)	1.08(9)							14.5(2)							-3.7(9)
C5	6.4(2)	36.5(2)	0.48(8)	0.83(7)	20.6(3)						28.5(2)							6.6(7)
C6	56.8(4)	7.2(1)	10.2(3)	2.7(1)				17.2(5)				0.71(8)						5(1)
C7	13.7(6)	55.1(9)	0.6(2)	1.1(2)	19(1)		8.2(3)	2.1(6)										0(2)
C8	15.0(4)	56.5(4)	2.1(2)	4.0(1)			4.2(2)	4.2(4)										14(1)
C9	6.0(2)	53.8(4)	0.7(1)	1.0(1)	13.0(5)		2.4(1)				27.2(2)							-5(1)
C10	14.1(3)	36.6(3)	1.0(1)	2.7(1)	41.6(5)	3.2(4)												1(1)
D1	68.4(7)	0.31(9)		9.9(2)				5(1)				2.11(8)						15(1)
D2	58.0(5)	7.4(1)		0.5(1)	18.2(7)													16(1)
D3	12.8(5)	71.0(2)		2.4(2)			2(2)											12(3)
D4	74.1(5)	0.5(1)		4.8(1)				5.0(4)				1.54(6)			0.7(3)	3.8(3)		10(1)
D5	69.0(5)	0.6(1)		3.3(1)				19.5(5)				1.77(6)			1.5(2)	0.7(3)		4(1)

Key to the mineral phases: goe – goethite, qtz – quartz, hem – hematite, mght – maghemite, non – nontronite, clino – clinochlore, liza – lizardite, kao – kaolinite, opal – opaline silica (modelled with cristobalite structure), talc – talc, mgns – magnesite, hal – halite, chamo – chamosite, albt – albite, lithi – lithiophorite, gbst – gibbsite, domt – dolomite, amor – the difference between unity and the percentage of all the crystalline phases scaled by the known percentage of internal standard. It contains amorphous phases and non-diffracting parts of crystals (Jordan *et al.*, 1990). The figure in brackets is the Rietveld quantification error for the last decimal place. The Goodness of Fit (GOF) of these QXRD analyses range from 1.2 to 3.7, with a mean of 2.2.

It should be noted from Table 6-2 that nearly all the samples demonstrated two-line feature in Appendix 7 are limonite-smectite laterite blends, which suggest the deduction in Section 6.3 has physical bases.

As these nickel laterite ore samples were leached with identical sulphuric acid concentrations (Section 3.2.6), the differences in their iron and nickel final extractions (Figure 6-1) are likely to relate to differences in their mineralogy. The plots of the iron and nickel final extractions from these ore samples versus their goethite percentages (Table 6-2) shown in Figure 6-6a and Figure 6-6b demonstrate that the goethite rich ores (in dashed circles) have high variations of both iron and nickel final extraction. In contrast, less variation of the iron and especially the nickel final extraction were found in ores containing lower amount of goethite. The plots of the iron and nickel final extractions of these ores versus their nontronite contents (Table 6-2) shown in Figure 6-6c and Figure 6-6d suggest that the laterite ore samples that contains higher amount of nontronite have more consistent nickel and iron final extractions than those samples with less nontronite. In these 52 nickel laterite ore samples, the oxide type laterite ores (high in goethite) and the clay type laterite ores (high in nontronite) are generally complementary. It should be noted that the group of samples in the dashed circle in Figure 6-6 (high in goethite content) are almost located along the dashed line in Figure 6-1. The large variations of iron and nickel final extractions are mainly associated with these oxide type laterite ores, which should be the focus of the rest of this study.

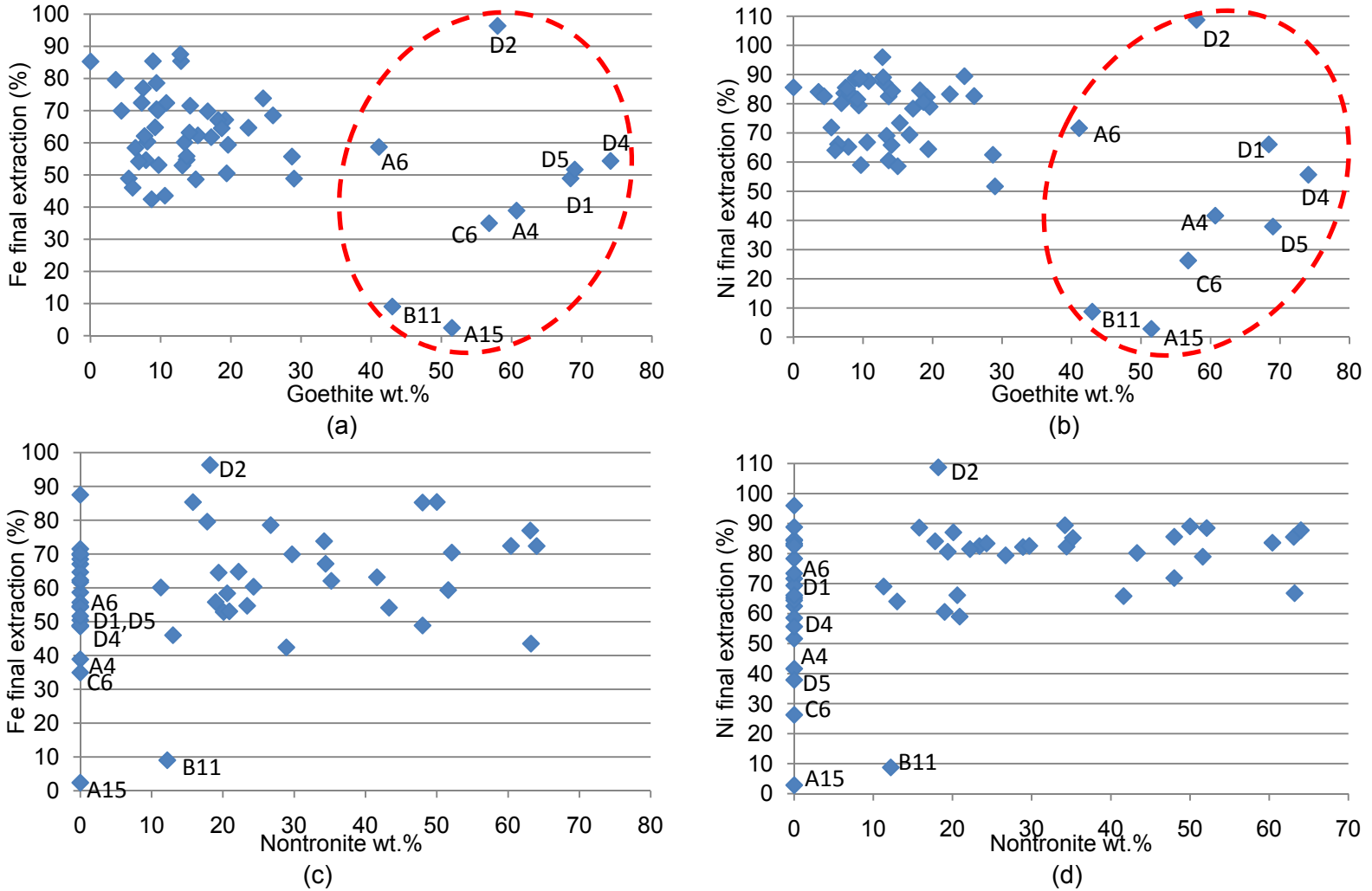

Figure 6-6 The correlations between Fe and Ni final extractions versus the goethite and nontronite weight percentages.

6.5 Correlation between the proportion of iron in goethite and the iron leaching rate from iron oxides

As the iron extraction data is always normalised according to the original iron content in the feed ore samples, these should not be affected by nonferrous phases, which dilute the goethite fraction but do not contribute to the iron leaching. For example, if a pure goethite is mixed with quartz (inert in acid leaching) at 1:1 ratio, the acid leaching curve of this sample, including the final extraction and the derived leaching rate, should not change but the goethite phase fraction of this sample would decrease from 100 wt.% to 50 wt.%. Hence this sample would be plotted at a different point in Figure 6-6, in which the goethite phase fraction of the ore sample was used as the abscissa. To eliminate this problem, only the iron containing phases should be considered.

Four major iron containing phases, goethite, hematite, maghemite and nontronite were identified from the mineralogy of these laterite ores (Table 6-2). The iron distribution in these four phases were then determined (Table 6-3) from the QXRD results. It should be noted that iron can substitute in other phases, *e.g.* kaolinite (Hart *et al.*, 2002), but the amount of iron in these phase is insignificant compared to that of iron oxides. The iron distributions in these four phases (Figure 6-7) suggest that most of the iron is not present in hematite or maghemite but rich in goethite and nontronite for the majority of samples. In order to compare the leaching properties of oxide type laterite ores, the iron column leaching rates from iron oxides (Appendix 8) were plotted against the “Proportion of Fe in goethite” in Figure 6-8. Samples with more iron in goethite show more variable iron leaching rate. The iron leaching rates of samples D3 and A16 are more than 100 times greater than those of samples B11 and A15. This indicates that the goethite in different samples leaches differently. It should be noted that the oxide type laterite ore samples in the dashed box of Figure 6-8 not only counted the goethite rich samples in the dashed circle of Figure 6-6 (A15, B11, C6, A4, D1, D4, D5, A6, and D2) but also recognised samples D3, A16, A17 as oxide type laterite ores, which were diluted by quartz (Table 6-2). This group of samples, in which iron is mostly located in goethite, will be the main focus in the rest of this study.

Table 6-3 Proportion of Fe in the four major phases of the 52 nickel laterite ore samples.

Sample	%Fe in goethite	%Fe in hematite	%Fe in maghemite	%Fe in nontronite
A1	19(1)	3.3(3)	11.8(3)	66.3(9)
A2	24(1)	0	25.3(9)	50(1)
A3	37(2)	5.3(5)	12.8(5)	45(1)
A4	95.0(5)	5.0(2)	0	0
A5	64.1(9)	20.7(5)	15.2(5)	0
A6	81.7(6)	8.8(2)	9.5(2)	0
A7	65(2)	11.7(8)	23.7(9)	0
A8	21(1)	29.1(9)	20.2(6)	29.7(9)
A9	28.8(7)	23.9(5)	26.4(3)	20.9(4)
A10	27.8(9)	24.3(6)	29.8(6)	18.1(6)
A11	22(1)	11.5(5)	9.4(5)	57(1)
A12	22.8(9)	9.6(5)	10.3(5)	57(1)
A13	18(1)	15.6(3)	5.6(2)	62(1)
A14	68(1)	0	32.1(6)	0
A15	97.5(8)	0	2.5(2)	0
A16	83.4(8)	0	16.6(2)	0
A17	81(1)	0	19.1(4)	0
B1	53(1)	5.1(3)	9.9(5)	31.6(8)
B2	54(3)	7.6(9)	39(2)	0
B3	0	0	0	100(3)
B4	52(4)	0	9(1)	39(3)
B5	43(1)	13.8(3)	10.3(3)	32.9(9)
B6	55(2)	20(1)	25(1)	0
B7	38(2)	0	0	62(3)
B8	54.6(9)	17.6(6)	27.8(4)	0
B9	52(1)	19.1(4)	29.2(5)	0
B10	50.5(7)	29.2(5)	20.3(3)	0
B11	75.8(7)	0	15.0(2)	9.1(4)
B12	18(1)	2.0(3)	32.5(8)	48(1)
B13	33.5(8)	1.9(2)	27.0(5)	37.5(6)
B14	13.0(2)	4.0(3)	34.3(9)	48.7(9)
B15	23(2)	12.2(7)	34(1)	30(1)
B16	28(2)	10.4(7)	33(1)	29(1)
B17	25(3)	0	5.0(6)	70(3)
B18	66(2)	9.5(4)	24.3(5)	0
B19	21.6(9)	10.6(3)	25.7(7)	42.1(8)
B20	32(1)	20.7(6)	35.8(7)	11.5(6)
C1	26(1)	3.7(3)	9.2(3)	61(2)
C2	59(1)	7.1(4)	7.2(3)	26.2(8)
C3	48(2)	3.3(6)	5.3(5)	44(2)
C4	79(2)	11.0(9)	9.9(8)	0
C5	39(1)	3.2(5)	5.6(5)	53(1)
C6	79.8(8)	16.0(5)	4.2(2)	0
C7	58(3)	2.8(9)	5(1)	34(2)
C8	69(2)	11(1)	20.4(7)	0
C9	45(2)	5.8(8)	8.3(9)	41(2)
C10	39.3(9)	3.1(3)	8.4(3)	49.3(8)
D1	86(1)	0	13.9(3)	0
D2	87(1)	0	0.8(2)	11.7(5)
D3	83(4)	0	17(2)	0
D4	93.3(9)	0	6.7(1)	0
D5	95(1)	0	5.1(2)	0

The figure in brackets is the error for the last decimal place, propagated from the Rietveld quantification errors in Table 6-2.

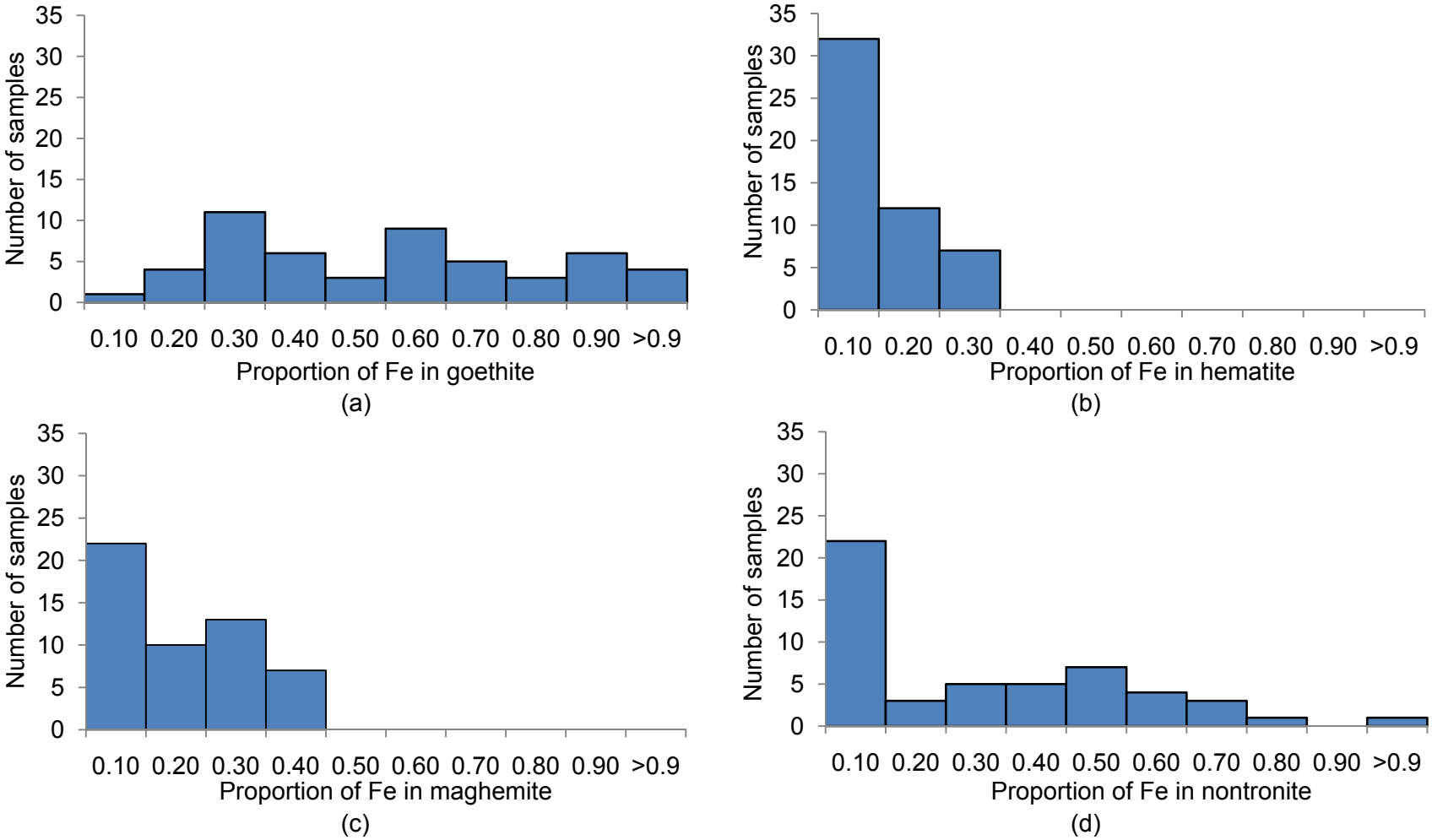

Figure 6-7 Histograms of the Fe distribution in the four major Fe containing phases of the 52 laterite samples.

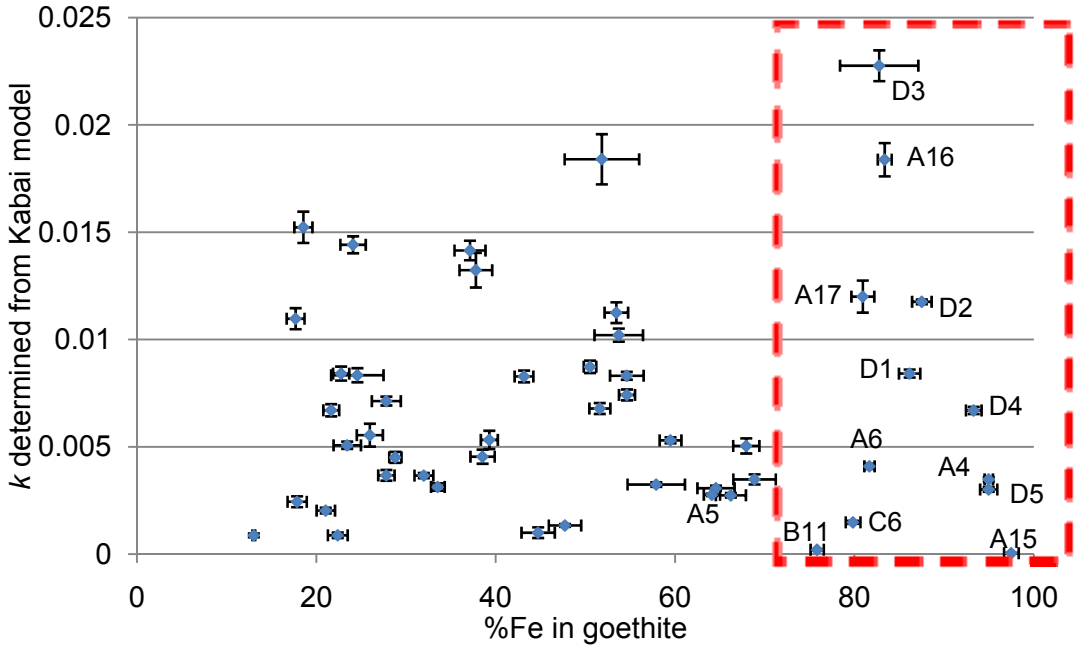

Figure 6-8 Plot of the proportion of Fe in goethite with the rate constant 'k' of the nonlinear Kabai fittings to Fe extracted from iron oxides. Dashed box highlights samples with more than 70 % Fe located in goethite.

6.6 XRD peak profile analyses of goethite in laterites ores

The above analyses suggest that goethite is strongly influencing the variability of acid leaching performance of the laterite ore samples. If this assumption is correct then investigating the crystallographic properties of goethite may provide a better understanding of why this is the case.

6.6.1 Goethite peak positions and Full Width at Half Maximum

Not all the goethite diffraction peaks are detectable in the synchrotron XRD patterns of the nickel laterite ore samples. Peak visibility is dependent on the goethite concentration and the coexistence of phases with overlapping peaks. The peak positions and the Full Width at Half Maximum (FWHM) of eight major goethite peaks were extracted by pseudo-Voigt peak fittings from the XRD patterns in the d-spacing range from 5.72 to 1.46 Å (10° to 40° 2θ at wavelength of 0.999047 Å) and these are listed in Table 6-4. A typical goethite peak fitting is shown in Figure 6-9. The capillary background modelling detailed in Appendix 4 is used. The correlation between the XRD peak positions of goethite in these laterite ores and their column leaching

rates expressed by the *k* value from Kabai model fitting (Appendix 8) is shown in Figure 6-10.

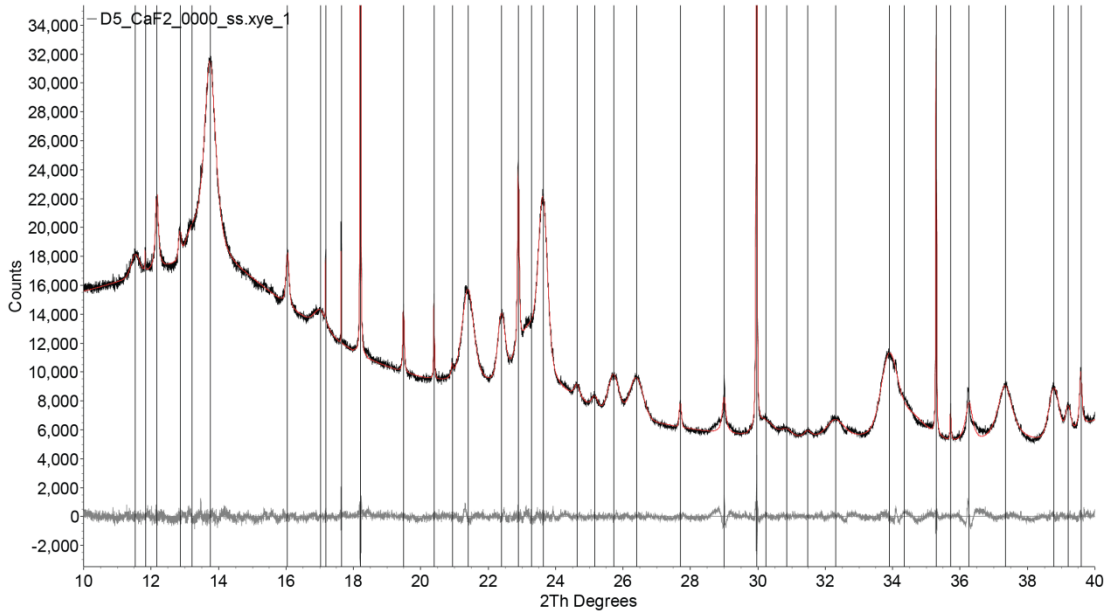

Figure 6-9 Goethite peak positions and peak FWHM of sample D5 are selected from the pseudo-Voigt peak fittings of its synchrotron XRD pattern.

It is apparent that the data points are all located in the left lower corner of the charts in Figure 6-10, suggesting that goethite with XRD peaks shifted to higher angles tends to leach slower, although not exclusively. It should be noted the group of oxide type laterite ore samples identified in the dashed box of Figure 6-8 generally demonstrate an increasing leaching rate with decreasing 2θ peak position, except samples A4, A6, A15 (red dots in Figure 6-10). The goethite 110 reflection does not show this trend because this peak is affected by the adjacent hump of opaline silica (Table 6-2) as shown in Figure 6-11. The samples shown in Figure 6-11 were not used to form Figure 6-10a, but a minor amount of opaline silica may still exist in the samples in Figure 6-10a and cause the goethite peak to effectively shift to higher angle if single peak fitting is used to extract peak positions. Opaline silica is also reported in WA nickel laterite ores by Watling *et al.* (2011).

Neither the plots of goethite peak FWHMs against the iron leaching rate constants nor their associated correlation coefficients in Appendix 9 provide a clear trend for the variability in iron leaching from these ores.

Table 6-4 Goethite peak positions and FWHMs available from the synchrotron XRD patterns of the laterite ores samples

sample	110		130		021		111		140		211		221		151	
	Position	FWHM	Position	FWHM	Position	FWHM	Position	FWHM	Position	FWHM	Position	FWHM	Position	FWHM	Position	FWHM
A1	-	-	21.322(3)	0.166(8)	22.274(2)	0.196(9)	-	-	-	-	-	-	-	-	-	-
A4	13.7304(7)	0.314(3)	21.3681(7)	0.284(3)	22.3369(9)	0.211(4)	23.576(1)	0.278(3)	26.357(2)	0.373(50	32.234(3)	0.37(1)	33.811(2)	0.380(5)	37.280(1)	0.366(4)
A5	13.6985(9)	0.258(4)	-	-	22.277(1)	0.163(5)	23.512(2)	0.234(3)	26.321(4)	0.22(1)			33.737(2)	0.323(6)	37.197(1)	0.228(6)
A6	13.7151(8)	0.297(3)	-	-	22.3192(9)	0.175(4)	23.559(2)	0.229(4)	26.330(2)	0.353(5)	32.207(3)	0.29(1)	33.794(1)	0.304(4)	37.260(1)	0.283(4)
A7	13.66(1)	0.56(6)	-	-	-	-	23.496(2)	0.32(1)	-	-	-	-	33.711(7)	0.49(3)	-	-
A14	13.693(6)	0.45(2)	21.340(4)	0.38(1)	22.279(3)	0.24(1)	23.521(2)	0.332(7)	-	-	-	-	33.734(6)	0.40(2)	37.247(2)	0.256(8)
A15	13.7434(5)	0.167(2)	21.3955(6)	0.182(3)	22.3254(8)	0.137(4)	23.5657(7)	0.193(3)	26.386(1)	0.172(5)	32.230(2)	0.239(8)	33.8203(9)	0.248(4)	37.2800(9)	0.215(4)
A16	13.746(6)	0.41(1)	21.359(2)	0.387(9)	22.336(3)	0.28(1)	23.521(2)	0.423(6)	26.315(6)	0.47(2)	-	-	33.80(2)	0.51(3)	37.282(4)	0.52(2)
A17	13.708(4)	0.47(1)	21.344(3)	0.41(1)	22.302(4)	0.30(2)	23.512(2)	0.393(8)	-	-	-	-	33.78(1)	0.49(2)	37.213(4)	0.43(1)
B5	13.662(4)	0.80(2)	-	-	22.303(3)	0.30(1)	23.514(2)	0.413(7)	-	-	-	-	33.770(4)	0.41(1)	37.238(3)	0.38(1)
B6	13.677(2)	0.261(9)	-	-	22.271(3)	0.178(7)	23.518(4)	0.222(5)	-	-	-	-	33.701(4)	0.39(2)	37.276(2)	0.246(6)
B7	13.735(2)	0.343(5)	21.404(2)	0.237(6)	-	-	23.597(1)	0.195(7)	26.398(3)	0.28(1)	32.263(4)	0.21(1)	33.825(2)	0.307(7)	37.330(2)	0.222(7)
B8	13.712(3)	0.44(1)	-	-	22.315(3)	0.243(8)	23.552(2)	0.329(5)	-	-	-	-	33.803(4)	0.46(1)	37.243(3)	0.44(1)
B9	13.712(3)	0.35(1)	-	-	22.298(3)	0.22(1)	23.539(3)	0.293(7)	-	-	-	-	33.786(4)	0.45(2)	37.211(4)	0.35(1)
B10	13.693(3)	0.47(1)	-	-	22.288(2)	0.186(9)	23.530(2)	0.298(6)	-	-	-	-	33.769(4)	0.44(2)	37.203(3)	0.320(9)
B11	13.7696(5)	0.232(2)	21.431(1)	0.377(3)	22.420(2)	0.291(7)	23.658(1)	0.27(1)	26.463(2)	0.395(7)	32.327(4)	0.38(2)	33.92(1)	0.39(4)	37.418(2)	0.50(1)
B12	-	-	21.324(2)	0.163(6)	22.281(2)	0.11(1)	23.597(2)	0.188(8)	26.336(2)	0.097(7)	-	-	-	-	37.170(5)	0.24(1)
B13	-	-	-	-	22.286(1)	0.112(5)	23.5953(9)	0.164(4)	-	-	-	-	-	-	-	-
C2	13.707(9)	0.55(2)	21.342(2)	0.299(6)	22.291(3)	0.228(9)	23.546(2)	0.311(7)	-	-	-	-	33.764(4)	0.36(5)	37.247(3)	0.42(1)
C3	13.68(2)	0.56(5)	21.327(4)	0.36(1)	22.286(5)	0.27(2)	23.502(2)	0.298(8)	26.29(1)	0.44(5)	-	-	33.728(7)	0.37(3)	37.203(5)	0.27(2)
C4	-	-	21.323(5)	0.36(2)	22.309(7)	0.27(3)	23.493(3)	0.274(8)	-	-	-	-	33.775(9)	0.47(3)	37.24(1)	0.40(5)
C6	13.7605(7)	0.299(2)	-	-	22.416(2)	0.275(5)	23.6388(8)	0.291(2)	26.414(2)	0.466(6)	32.299(4)	0.41(5)	33.900(2)	0.50(7)	37.386(3)	0.51(1)
C7	13.701(7)	0.47(2)	21.350(4)	0.32(1)	22.292(4)	0.24(1)	23.513(2)	0.296(8)	-	-	-	-	33.761(6)	0.33(3)	37.179(2)	0.191(6)
C8	13.64(2)	0.91(4)	-	-	-	-	-	-	-	-	-	-	-	-	37.294(3)	0.131(8)
C9	13.562(9)	0.69(2)	-	-	-	-	23.482(3)	0.37(1)	-	-	-	-	33.750(8)	0.40(2)	37.24(2)	0.21(5)
D1	13.7205(9)	0.463(4)	21.379(1)	0.436(5)	22.342(1)	0.250(5)	23.5920(9)	0.333(9)	26.362(3)	0.450(7)	32.237(5)	0.47(4)	33.812(4)	0.53(3)	37.291(3)	0.50(2)
D2	13.7194(5)	0.198(2)	21.3744(6)	0.197(3)	22.3086(7)	0.144(3)	23.5458(4)	0.184(2)	26.361(1)	0.199(4)	32.199(2)	0.251(7)	33.7910(7)	0.256(3)	37.2507(7)	0.223(3)
D3	13.716(7)	0.39(2)	21.337(5)	0.37(2)	22.271(9)	0.25(3)	23.506(5)	0.328(9)	-	-	-	-	33.71(1)	0.31(6)	37.239(5)	0.32(2)
D4	13.743(9)	0.416(3)	21.383(1)	0.401(4)	22.373(2)	0.254(5)	23.615(1)	0.341(4)	26.369(5)	0.52(1)	32.269(5)	0.67(2)	33.825(6)	0.40(2)	37.308(2)	0.491(7)
D5	13.752(2)	0.416(4)	21.404(1)	0.420(4)	22.398(2)	0.249(4)	23.631(1)	0.318(5)	26.401(4)	0.471(9)	32.303(7)	0.78(7)	33.893(2)	0.53(2)	37.338(2)	0.566(8)

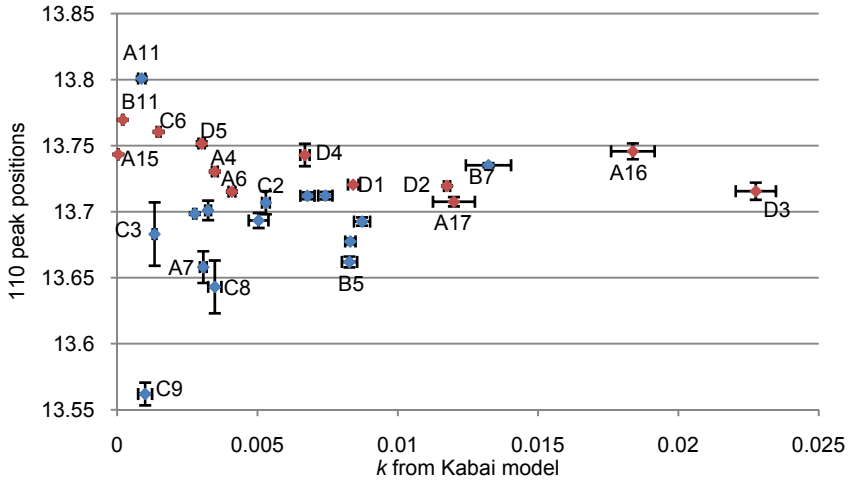
110 peak positions
13.85
13.8
13.75
13.7
13.65
13.6
13.55
A11
B11
C6
D5
A15
A4
D4
A6
C2
D1
D2
B7
A16
D3
C3
A17
A7
C8
B5
C9
0
0.005
0.01
0.015
0.02
0.025
k from Kabai model

(a)

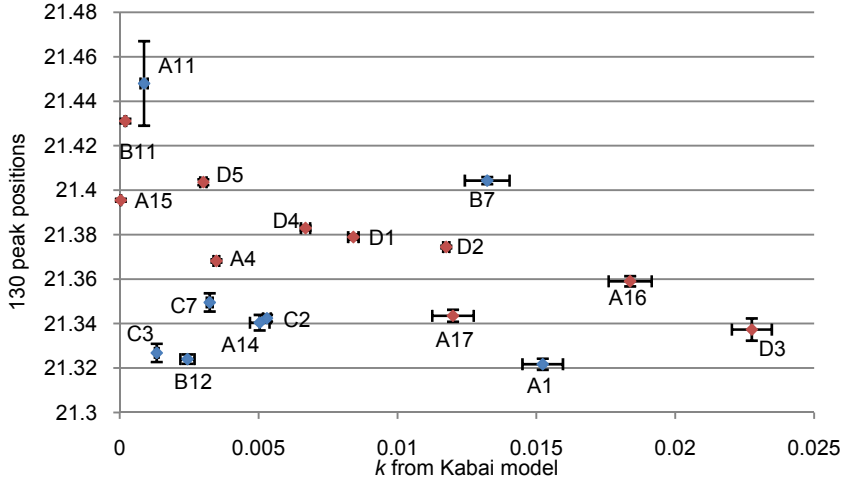
130 peak positions
21.48
21.46
21.44
21.42
21.4
21.38
21.36
21.34
21.32
21.3
A11
B11
D5
A15
B7
D4
D1
D2
A4
A16
C7
C2
C3
A14
A17
D3
B12
A1
0
0.005
0.01
0.015
0.02
0.025
k from Kabai model

(b)

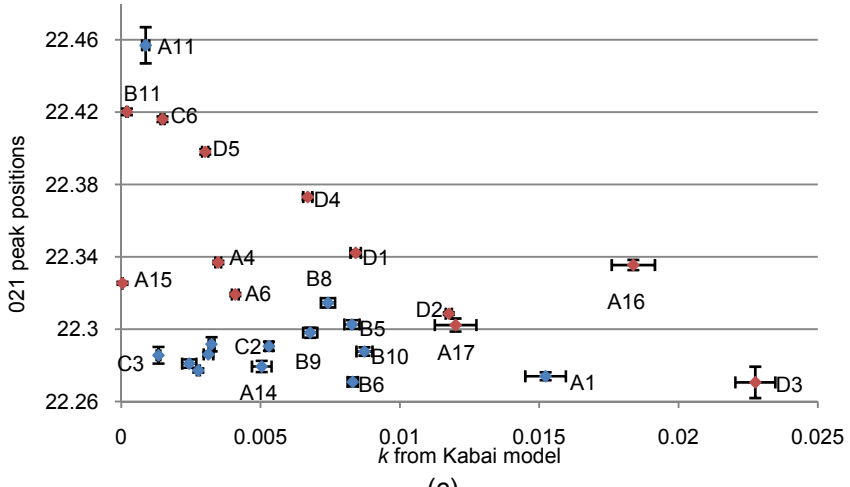
021 peak positions
22.46
22.42
22.38
22.34
22.3
22.26
A11
B11
C6
D5
D4
A4
D1
A15
A6
B8
A16
D2
B5
C2
A17
C3
B9
B10
A14
B6
A1
D3
0
0.005
0.01
0.015
0.02
0.025
k from Kabai model

(c)

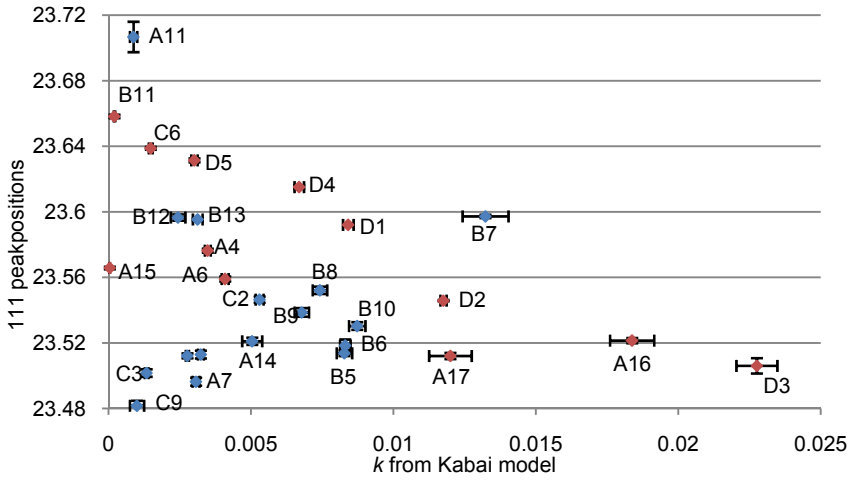
111 peakpositions
23.72
23.68
23.64
23.6
23.56
23.52
23.48
A11
B11
C6
D5
D4
B12
B13
D1
B7
A4
A15
A6
B8
C2
D2
B9
B10
B6
A14
C3
A7
B5
A17
A16
D3
C9
0
0.005
0.01
0.015
0.02
0.025
k from Kabai model

(d)

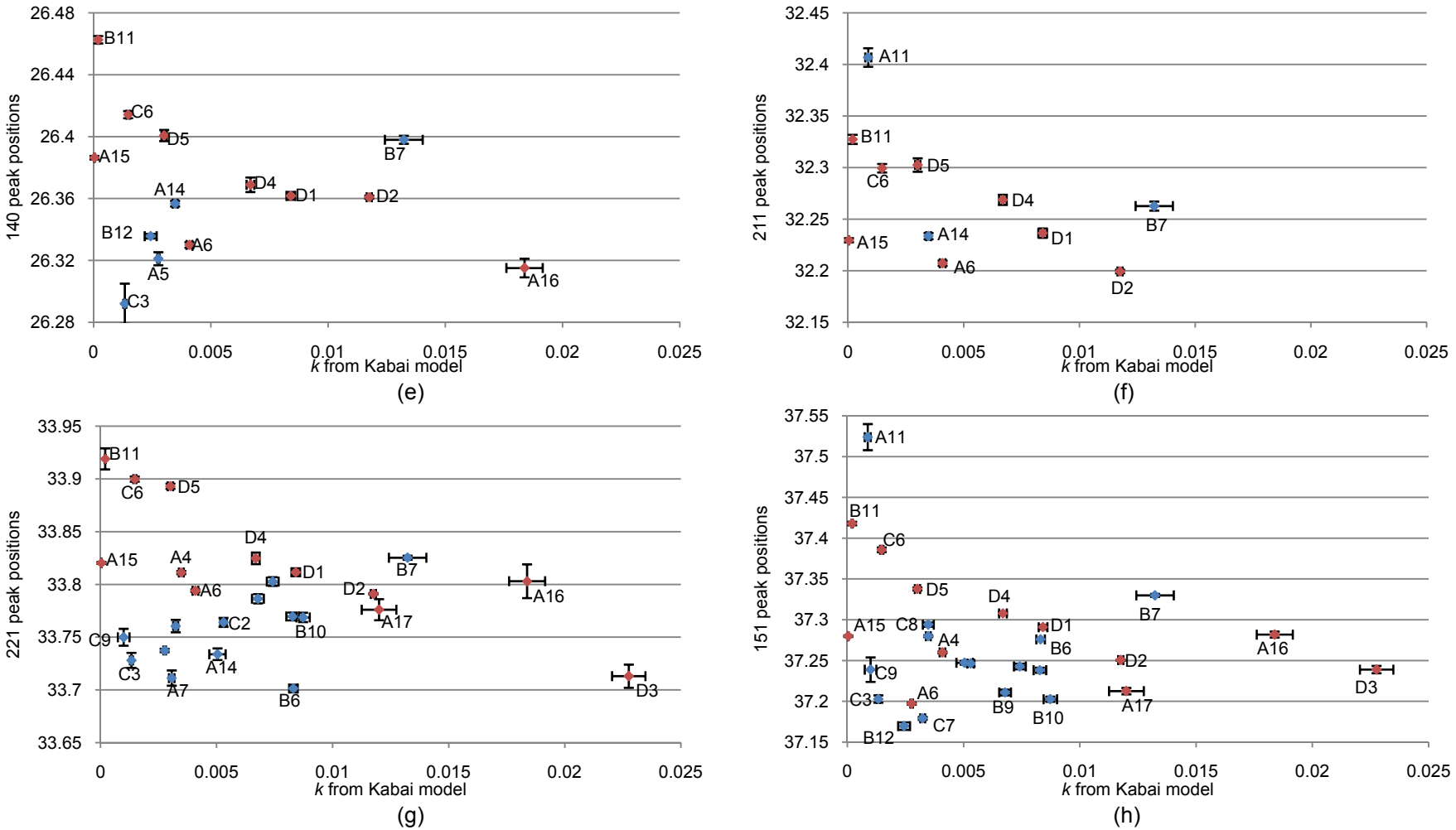

Figure 6-10 The correlation between laterite ore column leaching rates (Appendix 8) and goethite XRD peak positions. Samples highlighted in red are those identified in the dashed box of Figure 6-8.

6.6.2 Lattice parameters of goethite in nickel laterite ore samples

The goethite lattice parameters were calculated by whole pattern Rietveld fitting for the synchrotron pattern of each sample, taking into account all the goethite peaks from 5 Å to 0.77 Å. The lattice parameter of the internal standard (calcium fluorite) was fixed with the capillary displacement refined (Section 3.2.3.5). A typical Rietveld fitting of the synchrotron pattern is shown in Figure 6-12. The lattice parameters and the coherent scattering domain (CSD) size measured by Integral Breadth based Volume weighted mean column Lengths (LVol-IB) (Section 3.2.3.7) are listed in Table 6-5.

Table 6-5 Goethite lattice parameters determined from synchrotron XRD patterns of nickel laterite ore samples.

Sample	*a* (Å)	*b* (Å)	*c* (Å)	LVol-IB (nm)
A4	4.6028(1)	9.9566(2)	3.01498(7)	12.7(2)
A5	4.6125(2)	9.9777(3)	3.0232(1)	14.2(4)
A6	4.6051(2)	9.9623(3)	3.0175(1)	15.2(4)
A7	4.6095(6)	9.9902(9)	3.0215(3)	11.9(7)
A11	4.574(1)	9.933(2)	2.9970(6)	12(2)
A12	4.588(2)	9.948(3)	3.0170(8)	9(1)
A14	4.6070(5)	9.9782(9)	3.0213(3)	12.2(8)
A15	4.60094(9)	9.9535(2)	3.01754(5)	19.4(3)
A16	4.6031(3)	9.9621(6)	3.0155(2)	10.4(3)
A17	4.6067(3)	9.9789(6)	3.0192(2)	11.0(3)
B1	4.5948(4)	9.963(1)	3.0212(4)	9.8(4)
B2	4.618(1)	9.973(2)	3.0205(6)	13(2)
B5	4.6073(4)	9.9807(9)	3.0181(3)	10.8(4)
B6	4.6208(6)	9.979(1)	3.0235(3)	12.5(7)
B7	4.6049(4)	9.9434(6)	3.0106(2)	17(1)
B8	4.6054(4)	9.9762(7)	3.0170(2)	11.9(5)
B9	4.60670	9.9829(7)	3.0189(2)	12.4(4)
B10	4.6106(4)	9.9810(7)	3.0204(2)	12.6(6)
B11	4.5928(2)	9.9191(3)	3.0057(1)	12.7(3)
B13	4.6003(7)	9.943(1)	3.0156(3)	12(1)
C3	4.6070(6)	9.984(1)	3.0204(3)	12.1(9)
C5	4.6008(9)	9.971(2)	3.0219(4)	12(1)
C6	4.5935(2)	9.9300(3)	3.0077(1)	11.9(2)
C7	4.6030(7)	9.984(1)	3.0198(3)	13(1)
C8	4.596(2)	9.959(3)	3.0315(8)	9(1)
C9	4.6104(9)	9.976(2)	3.0215(5)	11(1)
D1	4.6060(2)	9.9571(4)	3.0130(1)	9.8(2)
D2	4.60681(9)	9.9608(2)	3.01927(5)	13.4(8)
D3	4.6072(7)	9.977(1)	3.0220(4)	11.3(9)
D4	4.599(2)	9.9518(4)	3.0088(1)	10.2(2)
D5	4.5998(2)	9.9388(4)	3.0075(1)	9.8(2)

The figure in brackets is the error associated with Rietveld fitting results in the last decimal place.

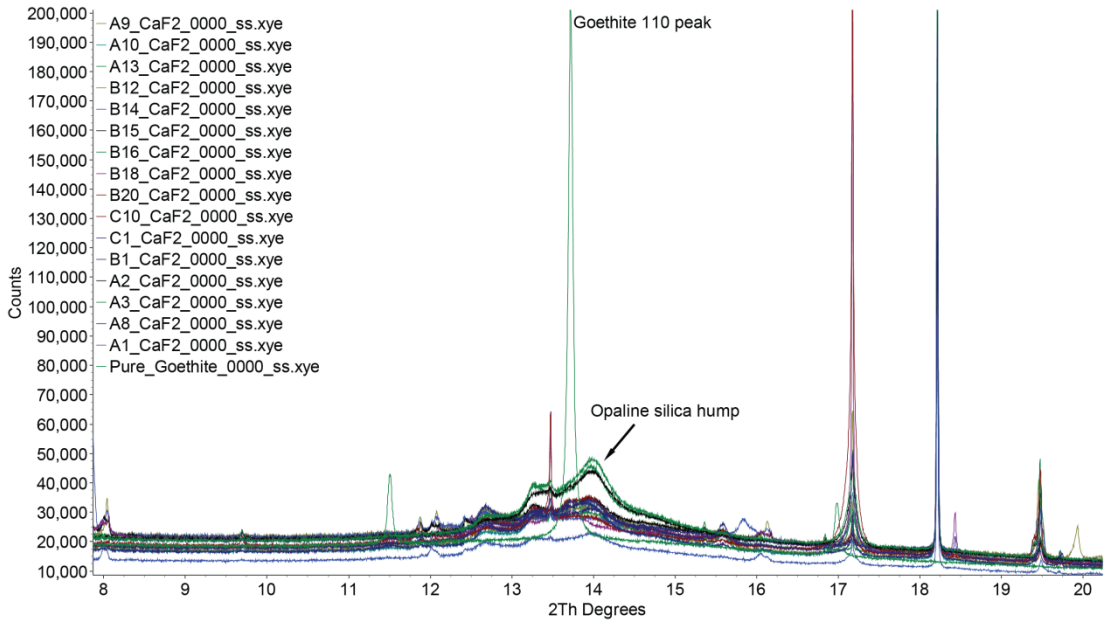

Figure 6-11 The XRD hump of opaline silica sitting on the shoulder of goethite 110 peak.

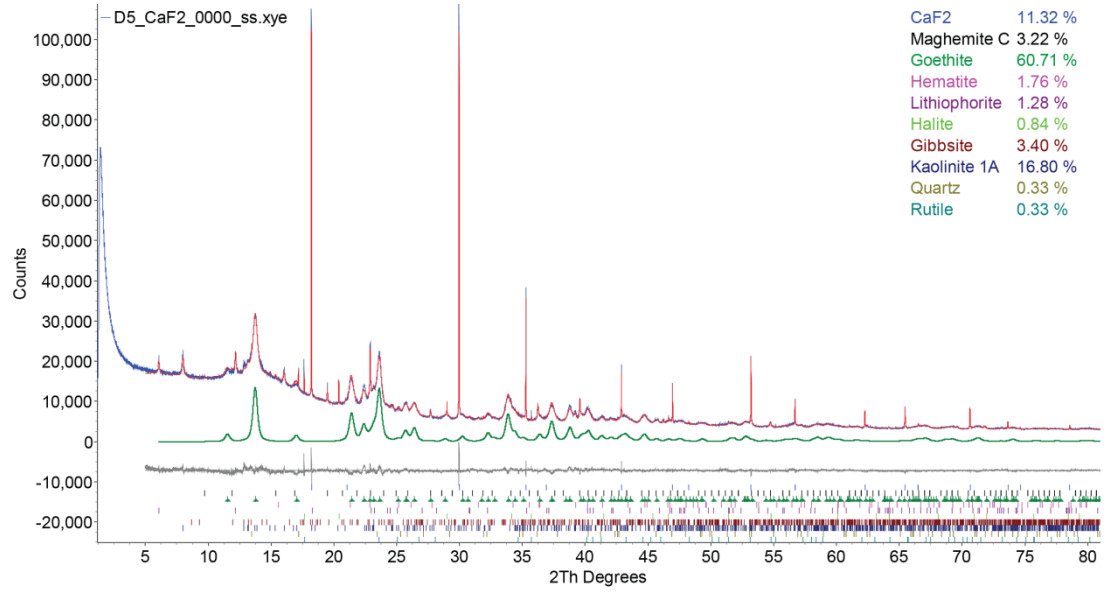

Figure 6-12 Typical Rietveld fitting of the synchrotron XRD pattern of nickel laterite ore samples used to extract goethite lattice parameters

The correlations between the lattice parameters of goethite in these laterite ore samples and their corresponding Kabai rate constant *k* for iron leaching from iron oxides are shown in Figure 6-13. The figures suggest that goethite with smaller unit cells tend to leach slower, although not exclusively.

The oxide type laterite samples identified in the dashed box of Figure 6-8 generally demonstrate increasing leaching rate with increasing lattice dimensions, except samples A15 (red dots in Figure 6-13). The correlation coefficients R, t-statistic, P-value, F-value[4] considering only this group of samples (A4, A6, A15, A16, A17, B11, C6, D1, D2, D3, D4, D5) are calculated (Table 6-6) using the Regression tool in Data Analysis in Microsoft® Excel. All the t-statistics are larger than 2.228 ($t_{0.05,10}$); F-values are larger than 4.965 ($F_{0.05,10}$) for lattice parameters except the CSD value (LVol-IB). The P-values for all the lattice parameters are smaller than 0.05, which suggest the positive correlation between the leaching rates and the goethite unit cell dimensions is statistically significant at the 95% confidence level. Although the goethite lattice parameters can be determined relatively precisely, the goethite LVol-IB sizes (crystallite size) derived from their synchrotron patterns have larger standard deviations which prevent any correlation between the goethite LVol-IB sizes and the laterite ore leaching rates from being obtained for the data in Figure 6-13d.

6.7 Guest metal substitutions in goethite in laterites ores

The variation of goethite lattice parameters is normally due to guest metal substitution (Section 2.6.5). In order to test whether there is any correlation between guest metal substitution and goethite leaching rate, the guest metal level in goethite of the group of nickel laterite ore samples identified in Figure 6-8 were examined by TEM/EDS (Section 3.2.4.1). The chemical compositions of 20 - 40 iron oxide crystals from each sample were averaged based on the weighting of the FeKα peak areas in the EDS spectra. As iron is mostly located in goethite in these samples, these iron oxide particles were assumed to be goethite. The averaged chemical compositions of iron oxides in each sample are listed in Table 6-7. From the range of elements present, aluminium, chromium, manganese, and nickel are previously observed to substitute for iron in goethite crystal structure and change goethite leachability (Section 2.6.5). Other elements may be

[4] The correlation coefficients R, t-statistic, P-value, and F-value are statistic indicators evaluating the validity of regression model (Field, 2007, p204). $F = t^2 = (n-k-1)R^2/(1-R^2)$, where n = number of observations, k = number of regressions. P-value describe the probability that the generated model is not valid.

adsorbed on the surface of goethite crystals or from other phases adjacent to the electron beam during TEM analysis.

The correlations between the goethite lattice parameters and the metal substitutions are plotted in Figure 6-14. Although the unit cell dimensions of goethite in natural laterite ore samples are the average effect of multiple metal substitutions, the effects of single metal substituted goethite (Section 2.6.5.9) are presented for these natural goethite crystals (Figure 6-14): aluminium and chromium substitutions tend to shrink and nickel substitution tends to expand the goethite unit cell; manganese substitution expands the *b*-axis but shrinks the *a*-axis and *c*-axis of the goethite lattice. The statistical indicators summarised in Table 6-8 suggest all these linear regressions are statistically significant except Figure 6-14f.

The selected laterite ore samples with most of iron located in goethite (as indicated in Figure 6-8) demonstrate a positive correlation between iron leaching rates and the goethite lattice dimensions (Figure 6-13). Goethite lattice dimensions also change with aluminium, chromium, manganese, and nickel substitution levels (Figure 6-14). It is therefore plausible to investigate the correlations between the iron leaching rate constants *k* from iron oxides versus the aluminium, chromium, and nickel substitution levels (Figure 6-15). The corresponding statistical indicators for the linear regressions of Figure 6-15 listed in Table 6-9 suggest the iron leaching rates are positively correlated with nickel substitution level in goethite at the 95% confidence level (Figure 6-15a). Although the correlations between the iron leaching rates and aluminium or chromium substitutions are not statistically significant at the 95% confidence level, a general decreasing trend can be observed (Figure 6-15b and Figure 6-15c) which is consistent with the literature summarised in Table 2-3. If the iron leaching rates are plotted with the sum of aluminium and chromium substitutions, a better correlation with P-value slightly higher than 0.05 can be observed, although still not statistically significant at the 95% confidence level. This suggests the goethite leaching rate is not solely controlled by the guest metal substitution. Other factors also influencing goethite leaching rate will be investigated in next chapter.

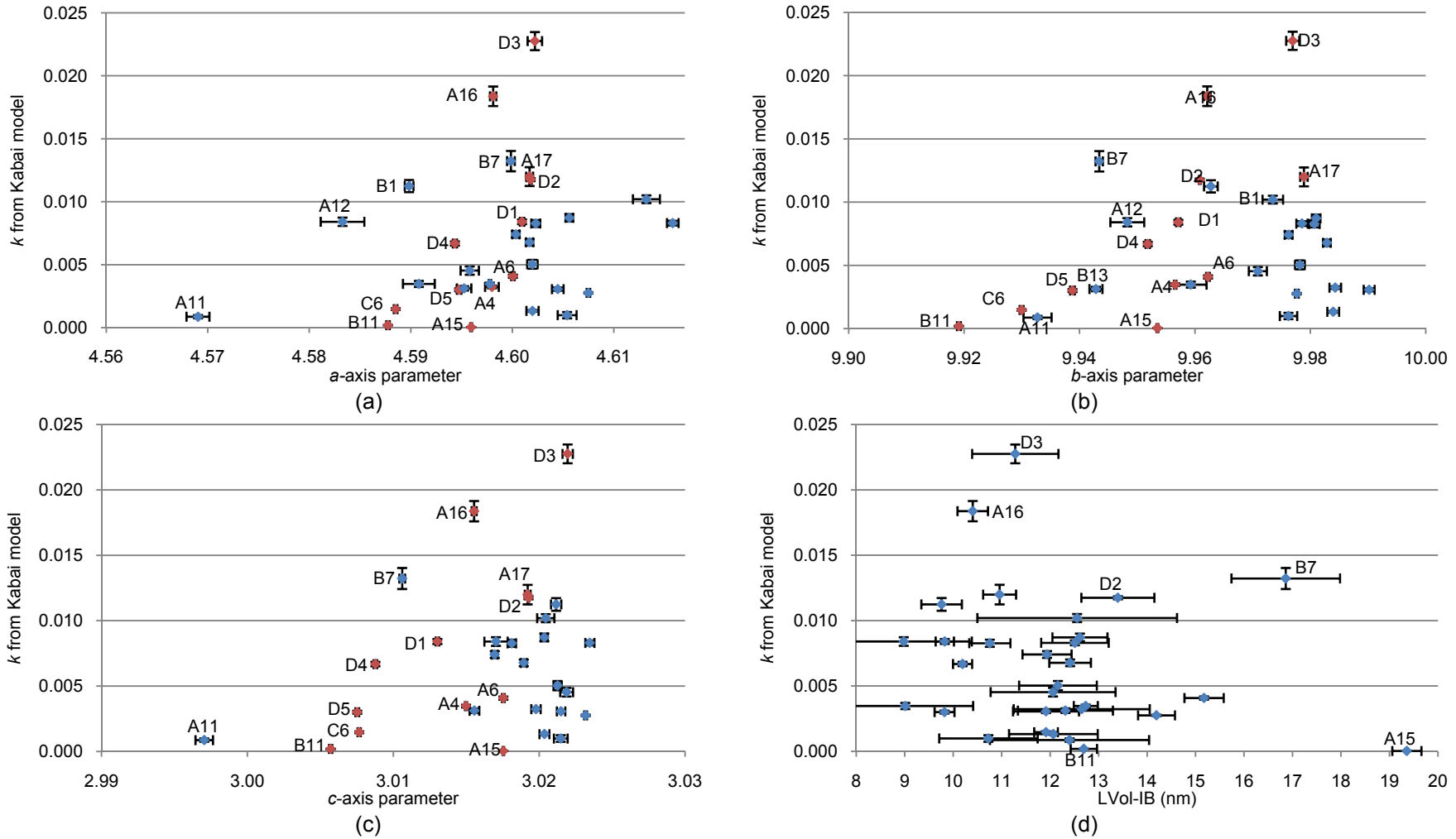

Figure 6-13 The correlation between laterite ore column leaching rates (Appendix 8) and goethite lattice parameters and CSD size. Samples highlighted in red are in the dashed box of Figure 6-8 as well.

Table 6-6 Correlation coefficients for data presented in Figure 6-13 for the group of samples identified in Figure 6-8 only.

Independent variables	Correlation coefficient R	t-statistic	P-value	F-value
a-axis parameter	0.660	2.777	0.020	7.714
b-axis parameter	0.725	3.326	0.008	11.060
c-axis parameter	0.625	2.532	0.030	6.409
Lvol-IB	0.417	1.452	0.177	2.107

Table 6-7 Averaged chemical compositions of iron rich crystals in each nickel laterite samples. The figures in brackets are errors for the last decimal propagated from the errors of each spectrum determined by the INCA-Analysis software.

sample	Na	Mg	Al	Si	P	S	Cl	K	Ca	Ti	Cr	Mn	Fe	Ni	Zn	O
A4			0.50(2)	1.30(3)		0.039(6)	0.2(1)	0.066(7)	0.14(1)		3.71(5)		69.0(1)	1.22(4)	0.019(4)	23.8(1)
A6			0.86(2)	2.89(3)		0.11(1)	0.28(1)	0.25(1)			1.78(3)	0.02(1)	67.13(8)	1.85(3)		24.8(1)
A15	0.51(2)	0.092(7)	2.12(3)	4.93(3)		0.010(2)	0.524(9)	0.305(8)	0.088(4)		1.92(2)		62.34(6)	0.44(1)		26.72(8)
A16		0.064(9)	2.12(4)	4.66(5)			0.113(8)	0.032(5)	0.055(6)		1.42(3)	0.26(1)	63.17(9)	1.57(3)		26.5(1)
A17		0.49(2)	0.97(2)	4.05(3)	0.022(5)	0.203(9)	0.013(2)		0.010(2)		0.52(2)	1.90(2)	63.52(7)	2.47(2)		25.81(9)
B11	0.28(1)	0.092(6)	4.86(3)	7.50(4)	0.053(4)		0.53(1)	0.540(9)	0.016(1)		1.27(2)	0.11(1)	54.80(6)	0.33(1)		29.62(8)
C6	2.97(3)	0.36(1)	4.53(3)	5.35(3)	0.67(2)	0.36(1)	0.30(1)	0.44(1)	0.29(1)		1.36(2)	0.02(1)	52.68(6)	1.37(2)	0.17(1)	29.14(9)
D1		0.49(1)	2.25(3)	4.63(4)	0.39(2)			0.04(1)		0.016(4)	1.56(2)	0.24(1)	62.00(8)	1.45(2)		26.9(1)
D2	0.034(9)	1.17(3)	2.62(4)	12.51(7)	0.24(2)		0.067(7)				2.18(3)		47.24(9)	1.38(3)		32.6(1)
D3	0.38(3)	1.66(3)	1.89(4)	11.93(6)		0.56(2)	0.50(1)	0.133(9)	0.086(5)		0.25(2)		48.55(9)	2.09(3)		32.0(1)
D4	1.56(3)	0.018(4)	3.38(3)	3.75(3)	1.73(3)	1.49(3)		2.67(2)	0.012(2)		3.29(3)		51.05(7)	1.62(2)		29.4(1)
D5		0.086(6)	3.37(3)	4.08(3)	0.11(1)			0.015(2)			2.17(2)	0.149(7)	61.81(6)	1.28(2)		26.94(8)

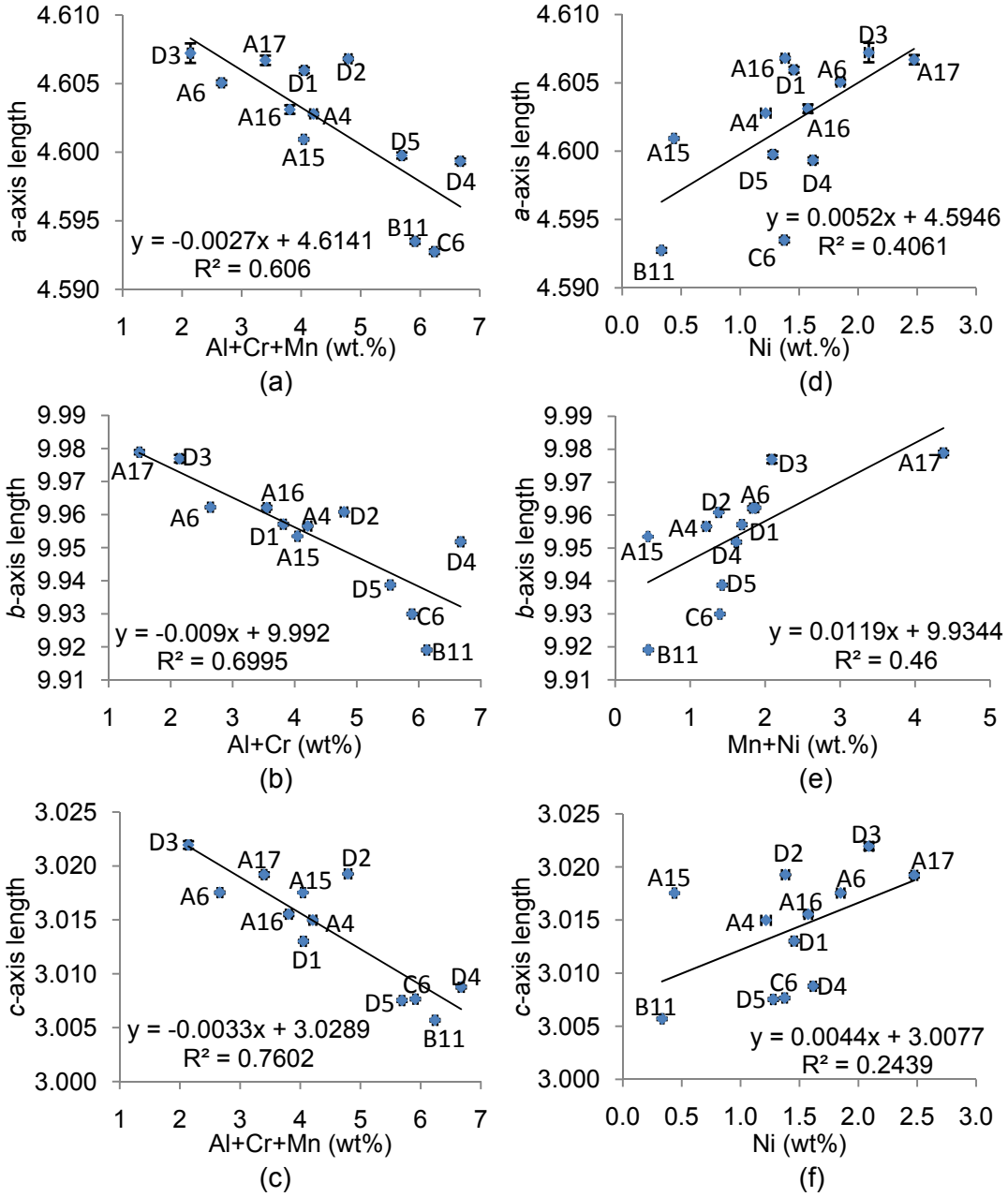

Figure 6-14 Plots of the goethite lattice parameters and the guest metal levels associated with goethite crystals in the oxide type nickel laterite ore samples.

Table 6-8 Statistical indicators of fitting in Figure 6-14

Fitting in Figure 6-14	Correlation coefficient R	t-statistic	P-value	F-value
(a)	0.778	-3.922	0.003	15.379
(b)	0.836	-4.825	0.0007	23.280
(c)	0.872	-5.630	0.0002	31.701
(d)	0.637	2.615	0.026	6.839
(e)	0.678	2.918	0.015	8.518
(f)	0.493	1.796	0.103	3.225

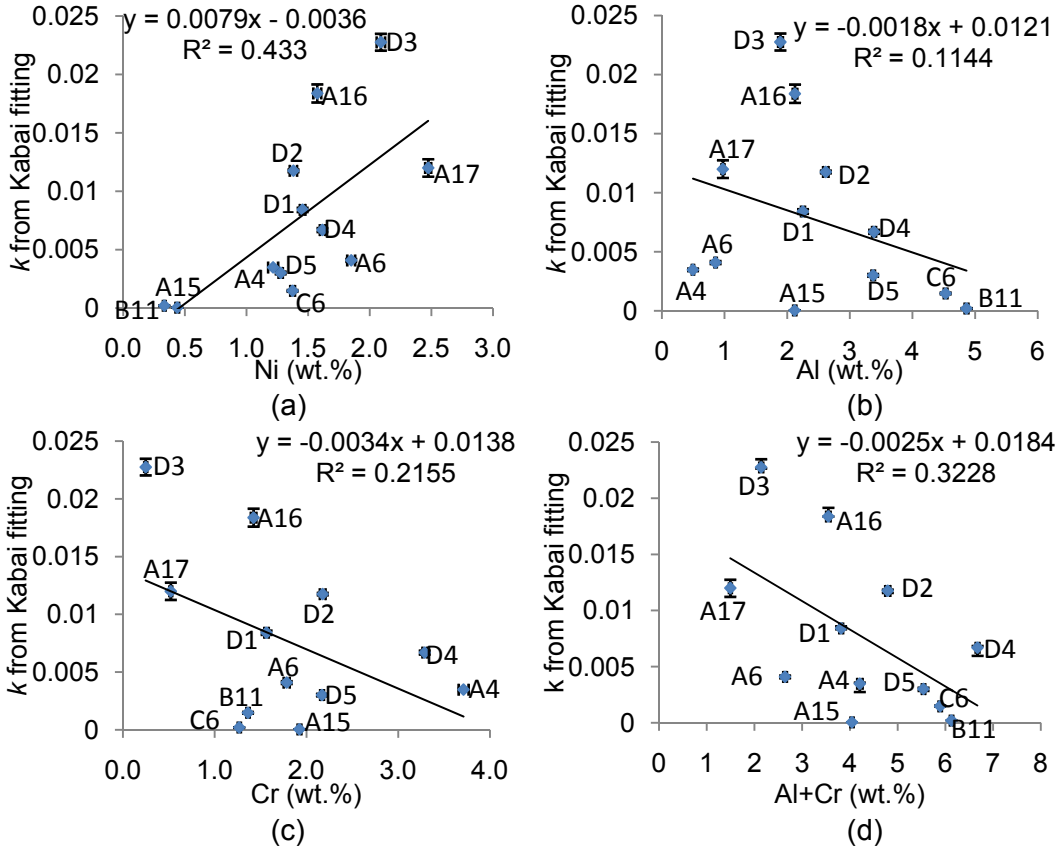

Figure 6-15 Plots of guest metal levels associated with goethite crystals in the oxide type nickel laterite ore samples and their leaching rates.

Table 6-9 Statistical indicators of fitting in Figure 6-15

Fitting in Figure 6-15	Correlation coefficient R	t-statistic	P-value	F-value
(a)	0.658	2.763	0.020	7.636
(b)	0.338	-1.137	0.282	1.292
(c)	0.464	-1.658	0.128	2.748
(d)	0.568	-2.183	0.053	4.766

6.8 Summary

Rather than only consider the metal final extractions from the suite of nickel laterite ores which frequently occurred over different leaching times, the leaching rates of iron oxides in the column leaching experiment were extracted by fitting the iron leaching data with the Kabai model. The incongruent iron leaching from different ferruginous phases of these laterite ores was revealed by plotting the iron leaching data using the linear form of the Kabai model. The use of a two-line fitting method (Schwertmann & Latham, 1986) was discussed and the iron extraction rate from the iron

oxides was separated from the influence of nontronite dissolution by translating and fitting the subsequent iron leaching data in a separate coordinate system.

The mineralogy of the nickel laterite ore samples was derived from the quantitative phase analysis of their laboratory XRD patterns. The parameter “Proportion of Fe in goethite” was introduced to correlate with the iron extraction rates. This parameter replaced the absolute goethite phase percentage in the ore samples to remove the dilution effect of nonferrous phases in iron leaching correlation plots.

A subset of oxide type laterite ore samples, which exhibits the widest leaching variations, demonstrates positive correlations between iron leaching rates and goethite lattice parameters. Correlations between goethite lattice parameters and aluminium, chromium, manganese, and nickel substitution levels were also observed. This suggests that the variable iron leaching rates of the oxide type laterite ore samples can be partially attributed to the effects of metal substitutions into the goethite crystal structure. The positive correlation between the iron leaching rates and nickel substitution levels is significant at the 95% confidence level, while the negative correlations with aluminium and chromium substitution levels cannot be confirmed for the limited number of observations. Guest metal substitution cannot fully explain the variation in iron leaching rate of goethite in these laterite ores.

The rate constants of iron leaching from iron oxides of high goethite ores are extremely variable, which suggest that goethite in different samples dissolves differently. Beside guest metal substitutions, other factors contributing to the variation of goethite leaching rate will be discussed in the following chapters, which report the investigations of the microstructures of goethite in the different laterite ore samples.

Chapter 7 Micro-morphology of goethite in laterite ores and their leaching performances

7.1 Introduction

According to the mineralogical analyses and leaching rate calculations in the previous chapter, the leaching rates of laterite samples where the iron is mainly associated with goethite are extremely variable. This suggests that the goethite component in different samples dissolves at different rates. In order to understand the reason for variable dissolution performance, the micro-morphologies of goethite crystals in these laterite ore samples were investigated.

This chapter is based on the paper:

Wang, X., McDonald, R. G., Hart, R. D., Li, J., & van Riessen, A., (2013). Acid resistance of goethite in nickel laterite ore from Western Australia. Part I. The relationship between goethite morphologies and acid leaching performance. Hydrometallurgy, DOI: 10.1016/j.hydromet.2013.09.005.

7.2 Goethite morphologies of samples with iron mainly in goethite

TEM images of the twelve laterite ore samples with iron mainly located in goethite (Figure 6-8) are discussed in this section. The descriptions below follow the order of samples with decreasing iron leaching rate.

Samples D3 and A16 are fast leaching. The typical goethite micro-morphologies in these samples are shown in Figure 7-1 and Figure 7-2. The typical goethite morphology in the fast leaching laterite ore sample D3 and A16 are long multidomain needles. Each domain has a different length so the tip of the crystal appears serrated. Differentiating goethite crystals and dissociated domains may not be easy, as shown in Figure 7-1b, as a separated domain could be regarded as an individual goethite crystal. This makes the measurement of crystal length and width challenging. To address this challenge, these goethite morphological characteristics were quantified by averaging the dimensions of more than 80 goethite crystals and this is shown in Figure 7-3 for sample D3 and Figure 7-4 for sample A16.

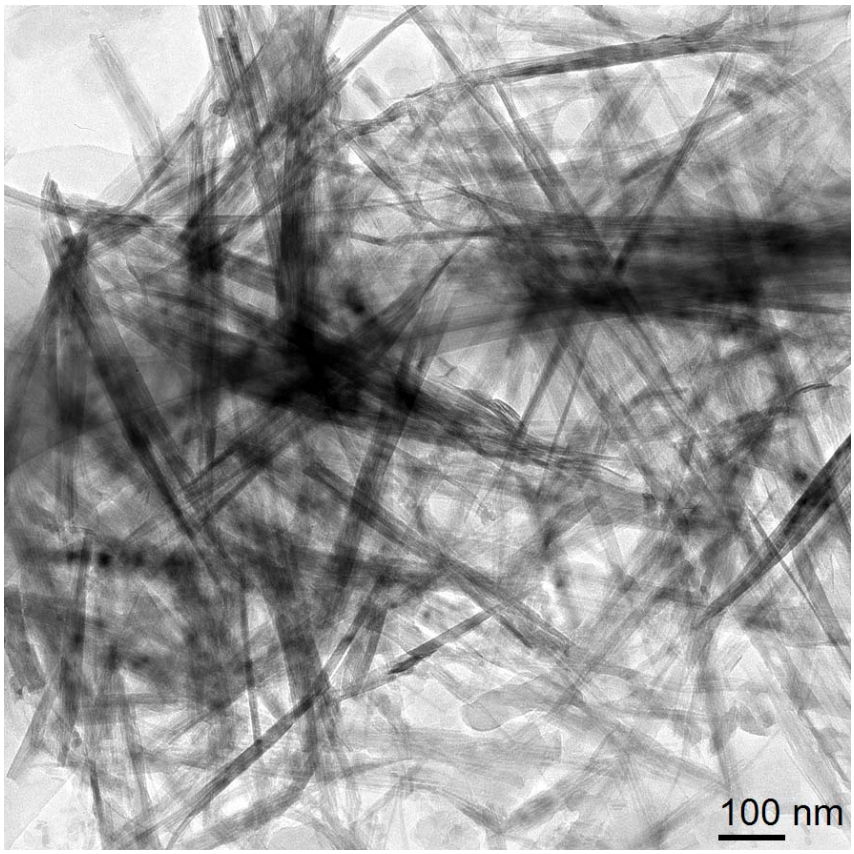

(a)

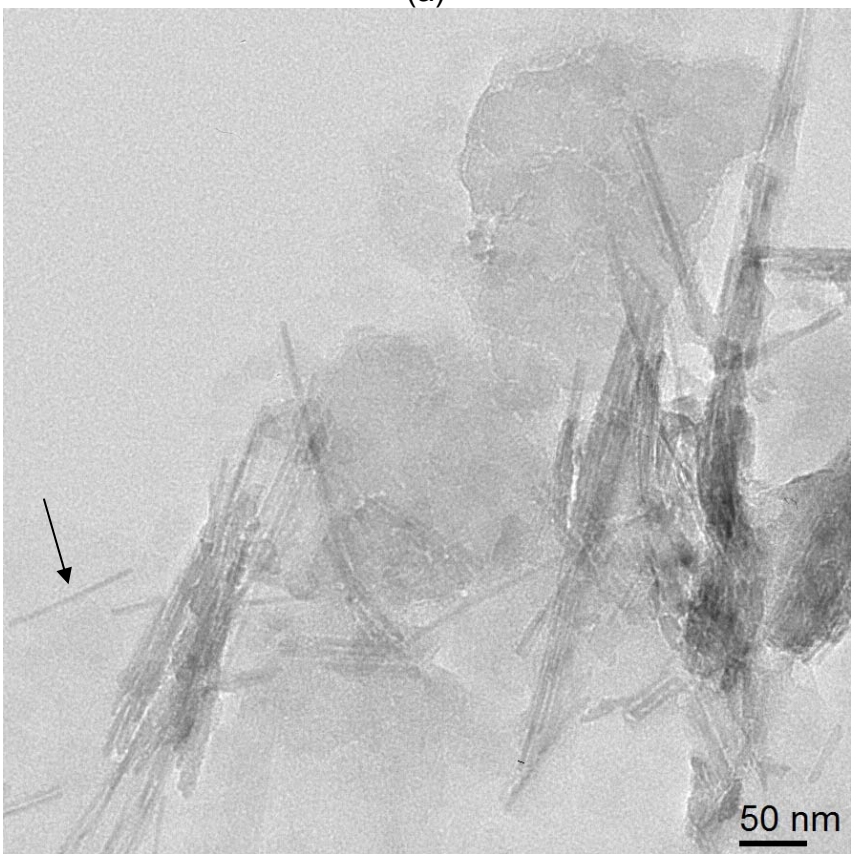

(b)

Figure 7-1 The goethite morphology in sample D3. (a) Goethite is typically present as needles; (b) the arrow points to an isolated goethite domain.

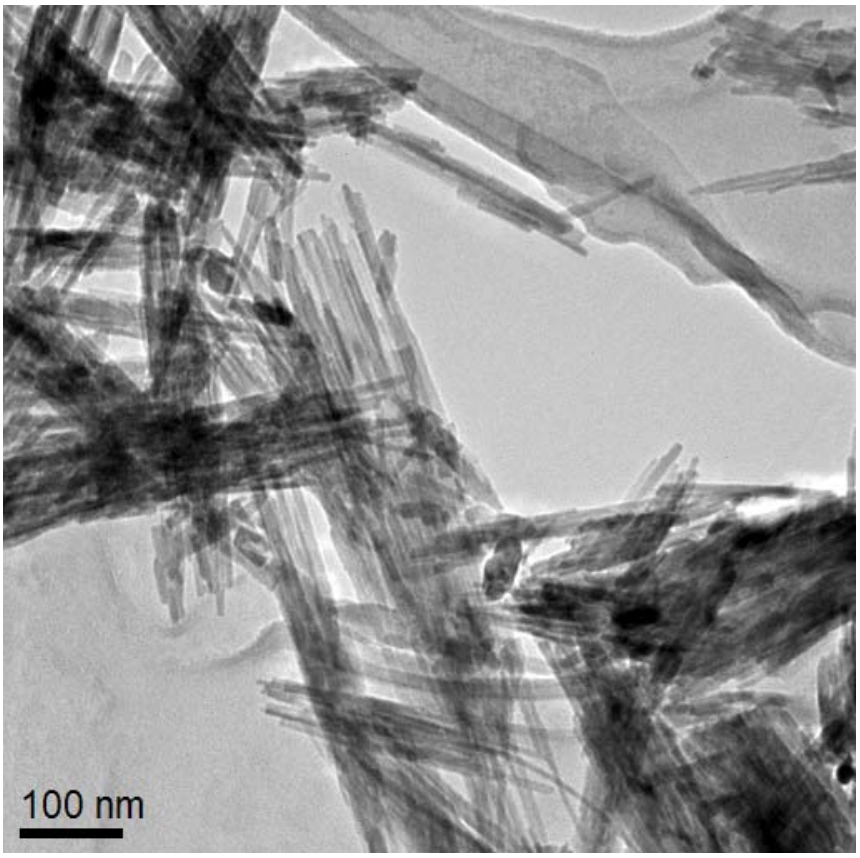

(a)

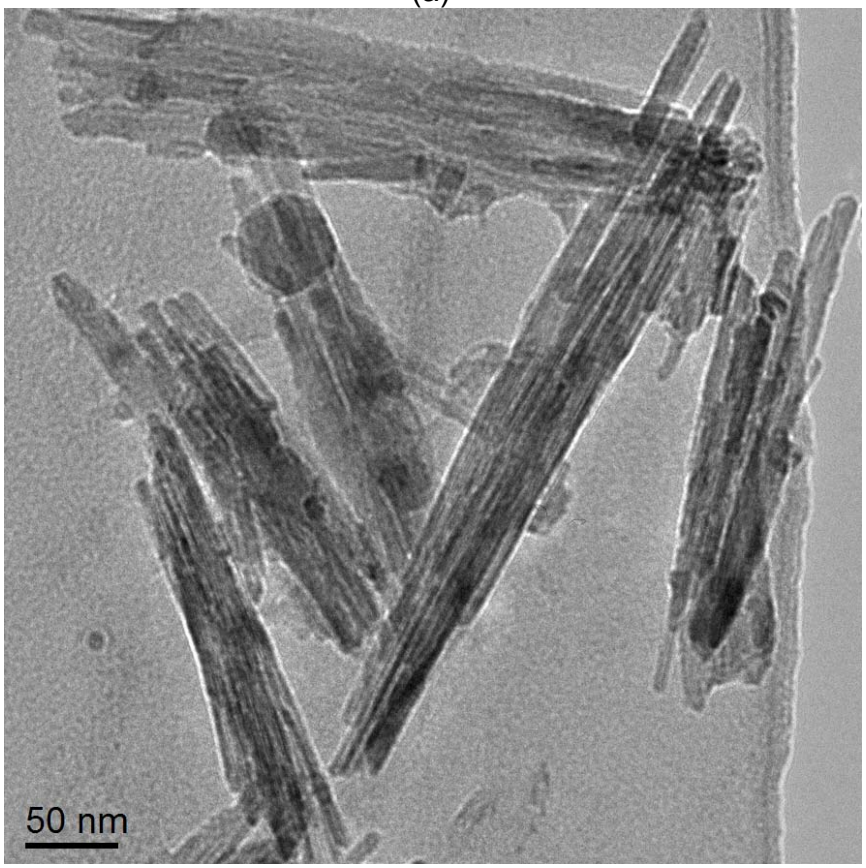

(b)

Figure 7-2 The goethite morphology in sample A16. (a) Goethite is in needle shape; (b) multidomain needle goethite is the typical morphology.

The acicular goethite crystals in sample A16 are generally wider than those in sample D3, as shown in Figure 7-3b and Figure 7-4b. The aspect ratio of goethite in sample A16 (Figure 7-4d) is slightly smaller than that in sample D3 (Figure 7-3d). The domain width in multidomain needle goethite in sample A16 (Figure 7-4c) is larger than that in sample D3 (Figure 7-3c). With this information, it may be assumed that the specific surface area of goethite crystals in sample D3 is larger than that in sample A16, and this partly explains the higher iron leaching rate for sample D3 than sample A16. Separating goethite from other phases is difficult hence the direct measurement of powder samples surface areas using gas adsorption techniques, such as the Brunauer-Emmett-Teller (BET) method is not deemed to be a suitable option.

The sample A16 has a simple phase composition (Table 6-2), therefore the acicular iron rich particles observed under TEM were assumed to be goethite. The acicular goethite crystals can be randomly aggregated on carbon film for presentation in TEM micrographs, *e.g.* Figure 7-1a. However, two different forms of needle organisations were frequently observed (Figure 7-5) suggesting that these goethite needle crystals organisations are grown in this way and are less likely to be a result from particle aggregation. The parallel needle morphology in Figure 7-5a can be regarded as a single crystal having multiple domains, which may be formed if goethite nucleation is favoured over goethite growth along the needle axis. If this particle subsequently breaks up, it will produce multiple needles. The 3-fold rotational texture of goethite needles (Figure 7-5b) may be formed via the 120° goethite twinning mechanism discussed in Section 2.6.3.2.

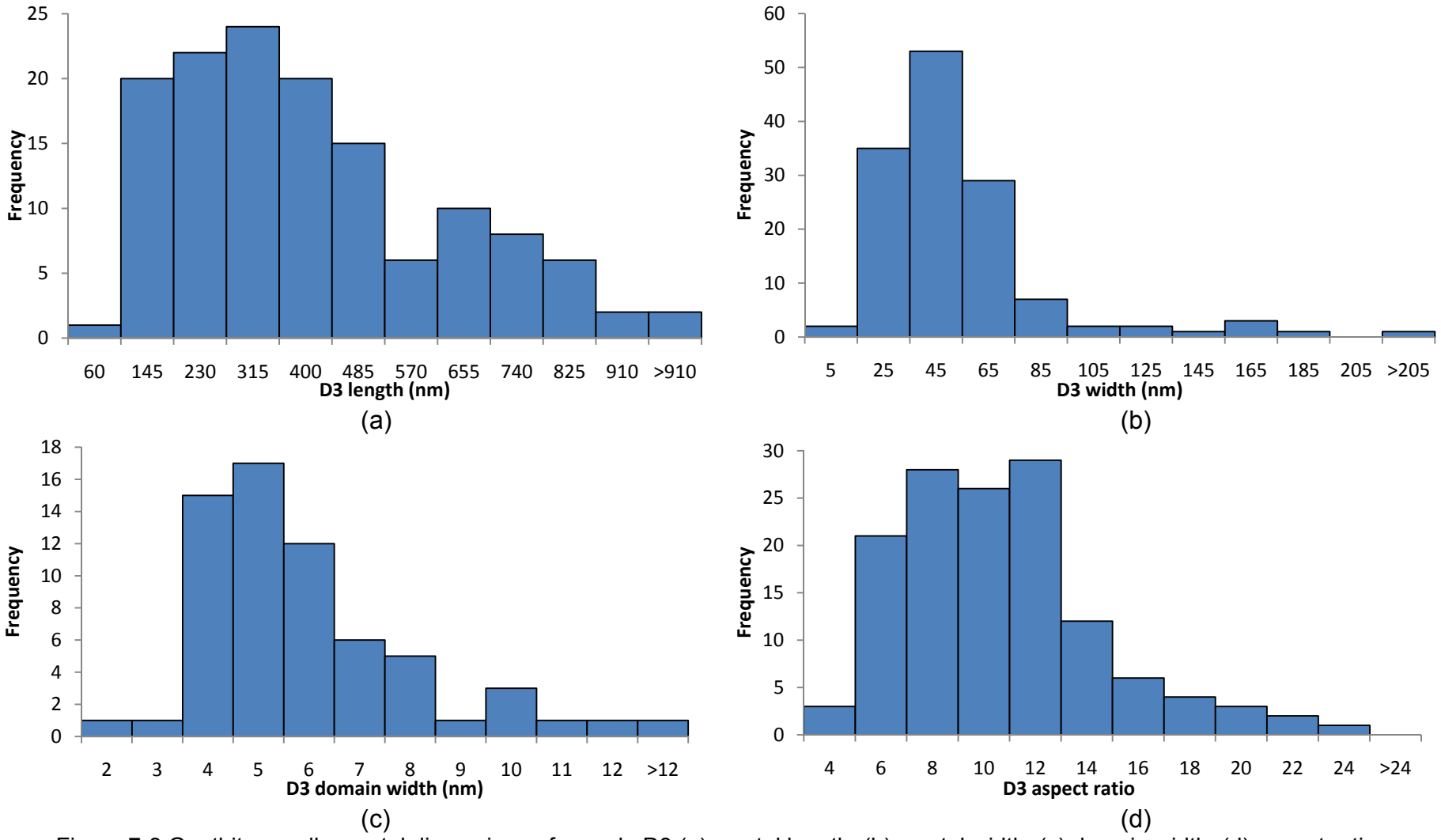

Figure 7-3 Goethite needle crystal dimensions of sample D3 (a) crystal length; (b) crystal width; (c) domain width; (d) aspect ratio.

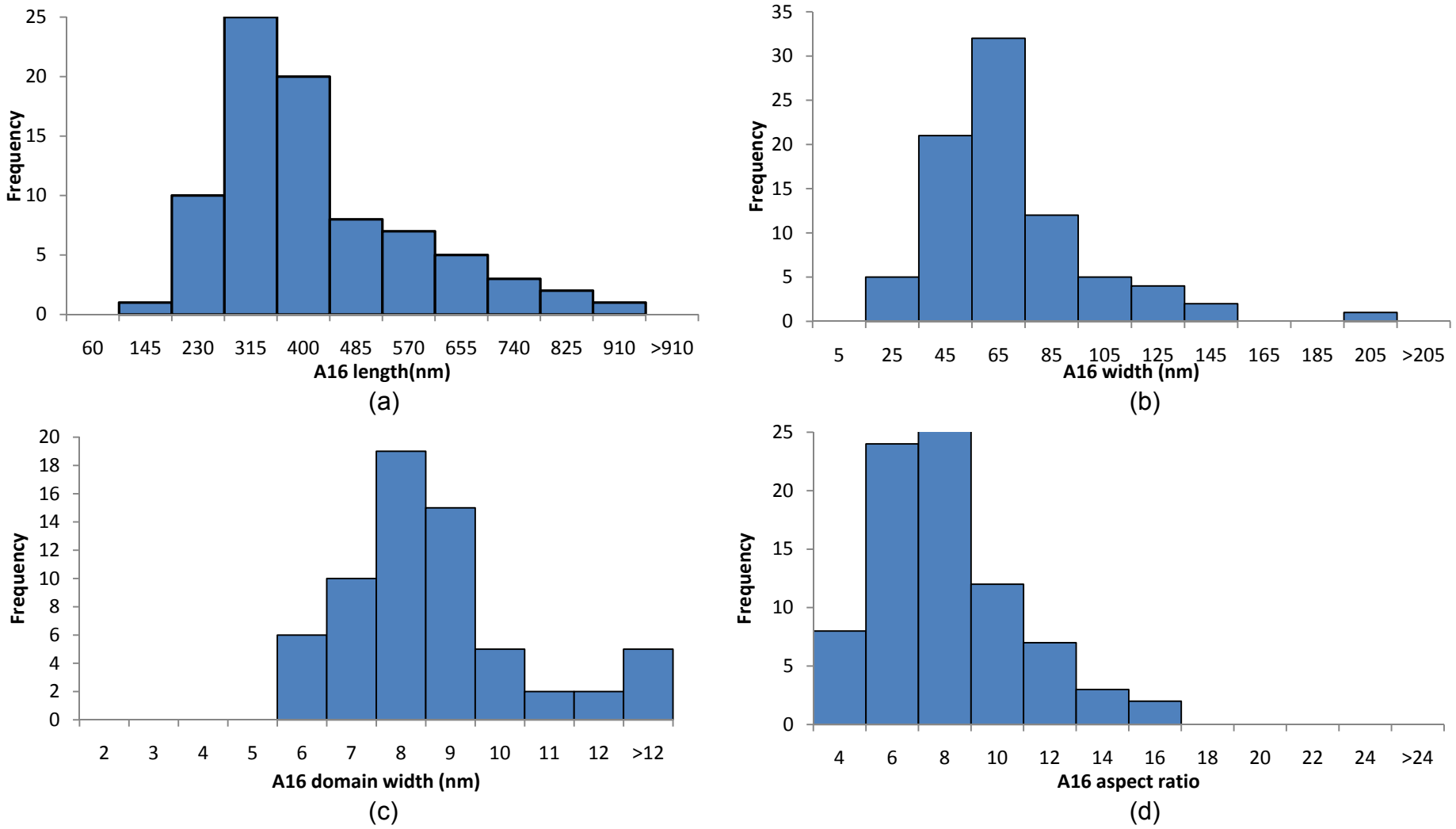

Figure 7-4 Goethite needle crystal dimensions of sample A16 (a) crystal length; (b) crystal width; (c) domain width; (d) aspect ratio.

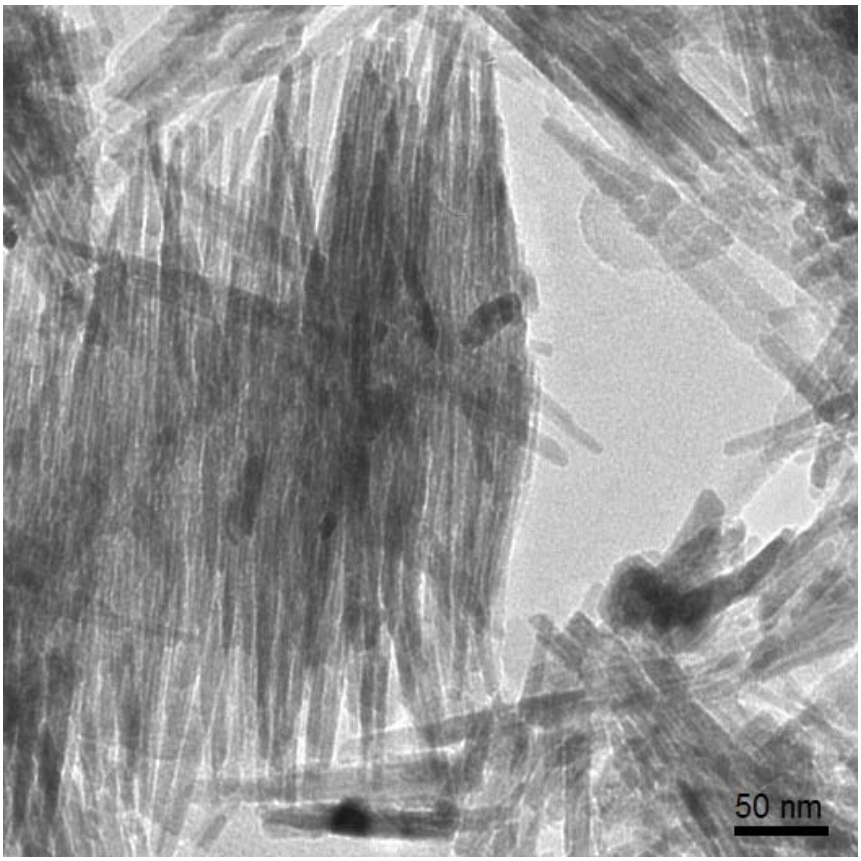

(a)

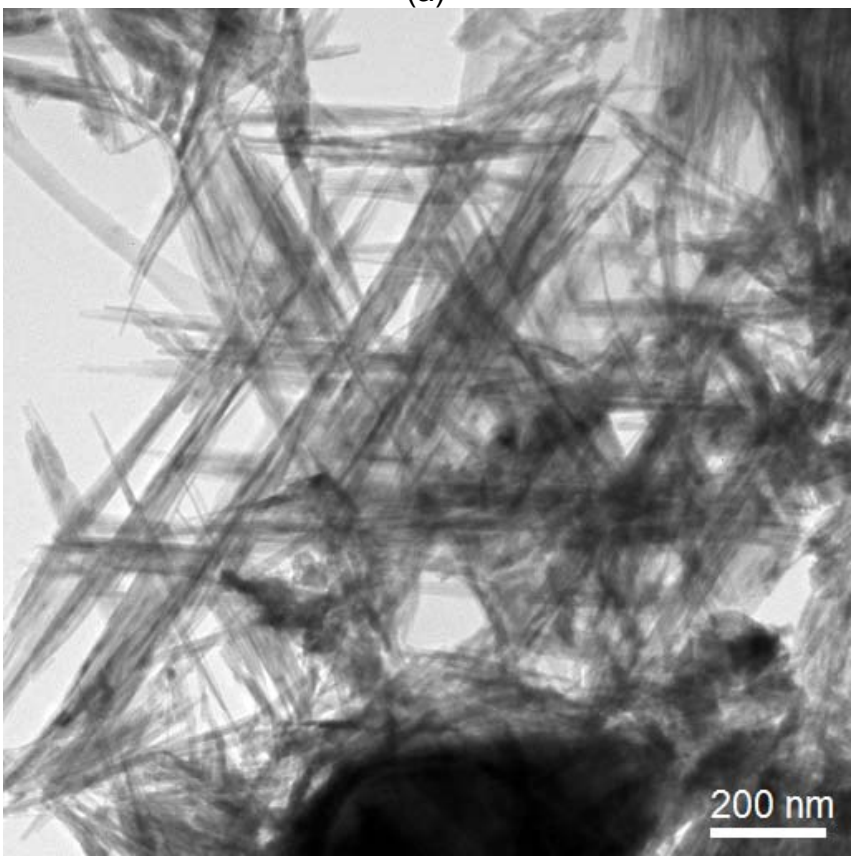

(b)

Figure 7-5 The organisation of acicular goethite crystals in laterite ore sample A16.
(a) Parallel textured needles; (b) 3-fold rotational texture.

The typical goethite morphologies in the moderately slower leaching laterite samples A17 and D2 are shown in Figure 7-6 and Figure 7-7. The histograms of goethite crystal dimensions in these samples are also shown in Figure 7-8 and Figure 7-9, based on the measurement of more than 90 goethite crystals in both samples. The length and width of goethite crystals in sample A17 may not be directly comparable with goethite in other samples as these (Figure 7-6) appear to be incompletely liberated parallel needles, similar to that shown in Figure 7-5a. The goethite crystals in samples A17 and D2 are still needle like but have a lower aspect ratio compared with the goethite morphologies in samples D3 (Figure 7-1) and A16 (Figure 7-2). The goethite domain widths of the four samples are less variable than their length and crystal width.

Textured goethite crystal assemblies become more common in slower leaching samples D1 (Figure 7-10), D4 (Figure 7-11), and A4 (Figure 7-12). It is difficult to measure the dimensions of needle crystals inside these textures. The 3-fold rotational texture of goethite crystals is unlikely to be achieved by aggregation of goethite needles but instead to form during crystal growth in soil environments. These goethite crystal textures were not dissociated by ultrasound. This texture could lead to low specific surface area which may be partly responsible for the relatively slow dissolution of sample D1, D4 and A4.

The goethite morphology of slower leaching samples D5, A6, and A5 are shown in Figure 7-13, Figure 7-14, and Figure 7-15, respectively. Electron-dense cementations (terminology after Schwertmann (1988, p240) and Schwertmann & Taylor (1989, p416)) in these samples are more common than that in the preceding samples. Acicular goethite crystals are fewer and become the minority. The goethite needle cementations in sample D5 (Figure 7-13) maybe consist of several layers of 3-fold rotational textures. Acicular goethite crystals could not be distinguished from the cementations in sample A6 (Figure 7-14). Other than goethite cementations, sample A5 (Figure 7-15) also contains acicular goethite crystals and kaolinite flakes, confirmed by their corresponding EDS data in Table 7-1.

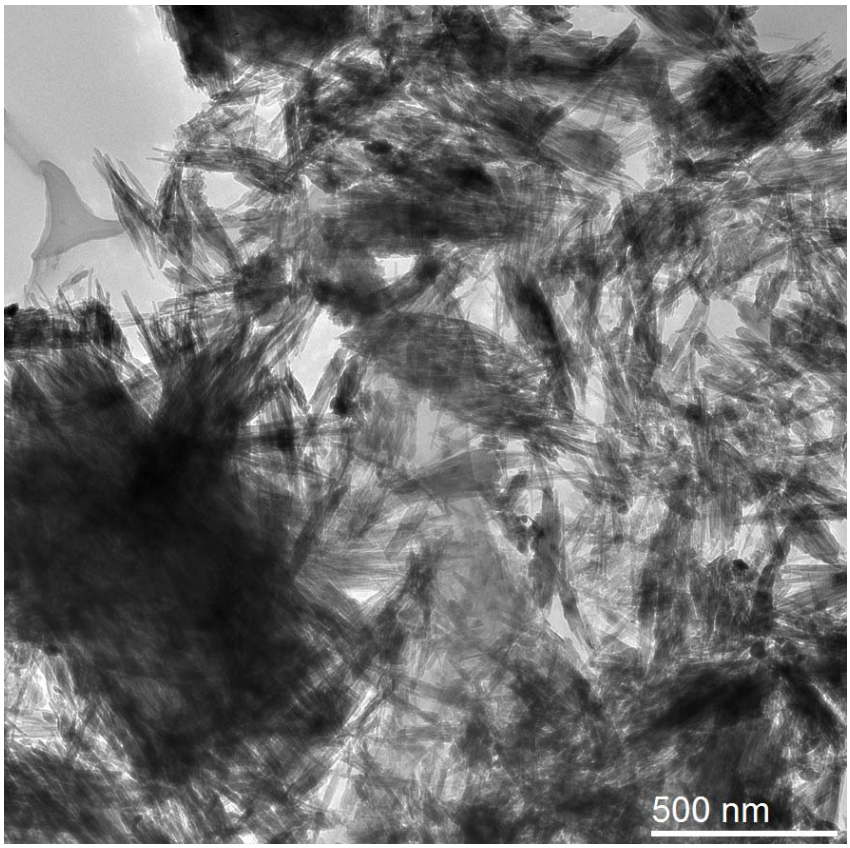

(a)

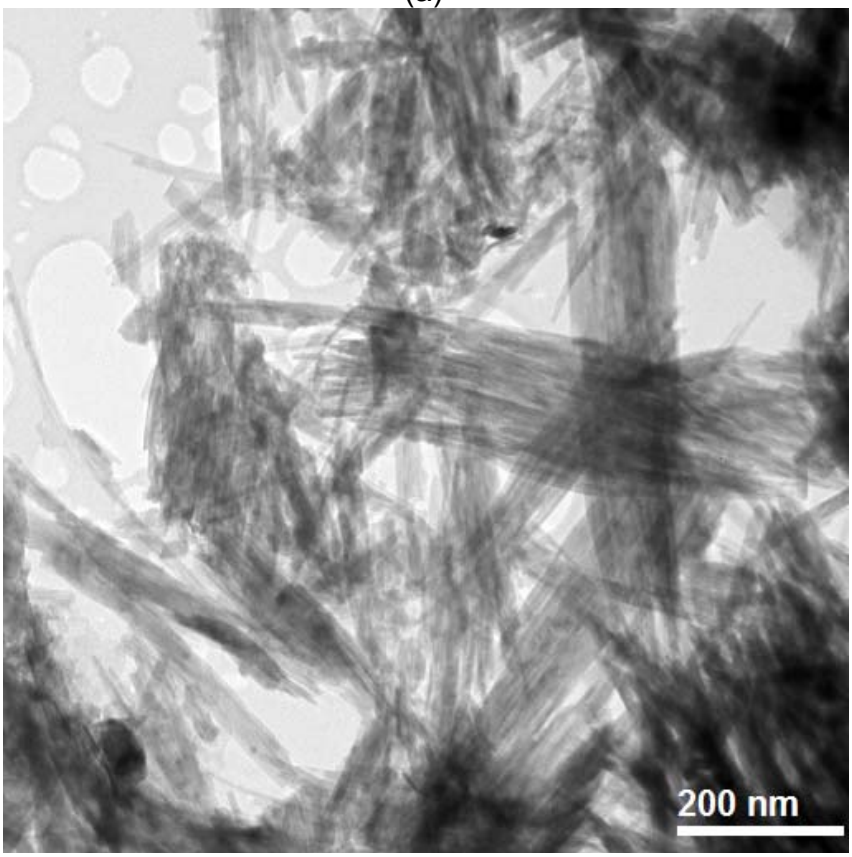

(b)

Figure 7-6 The goethite morphology in sample A17. (a) Goethite needles; (b) multidomain needle goethite.

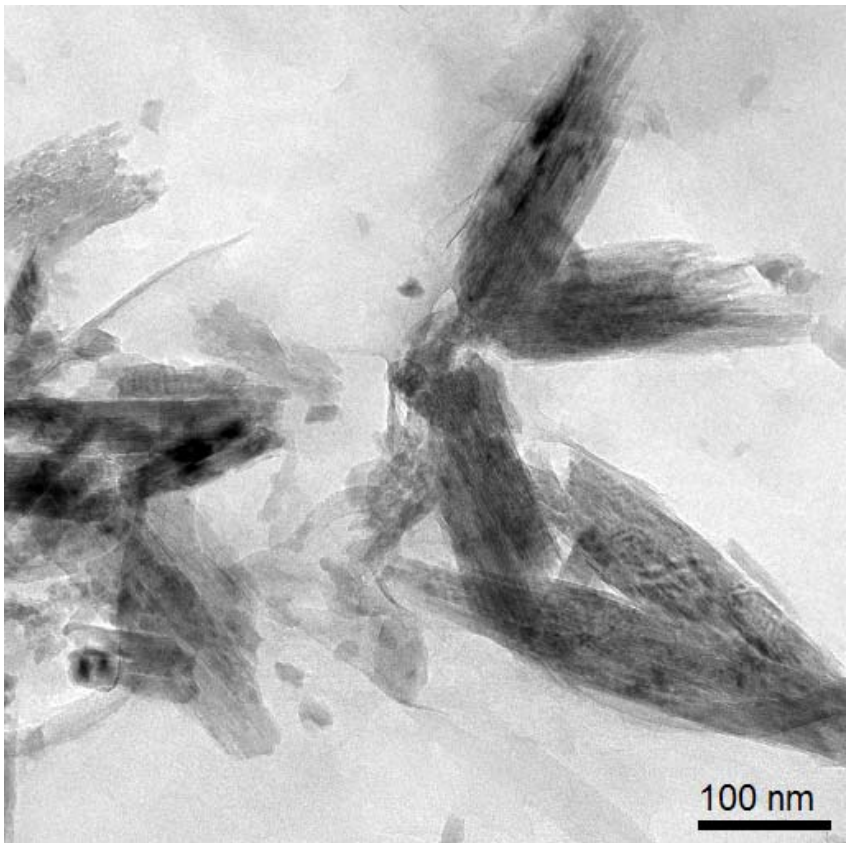

(a)

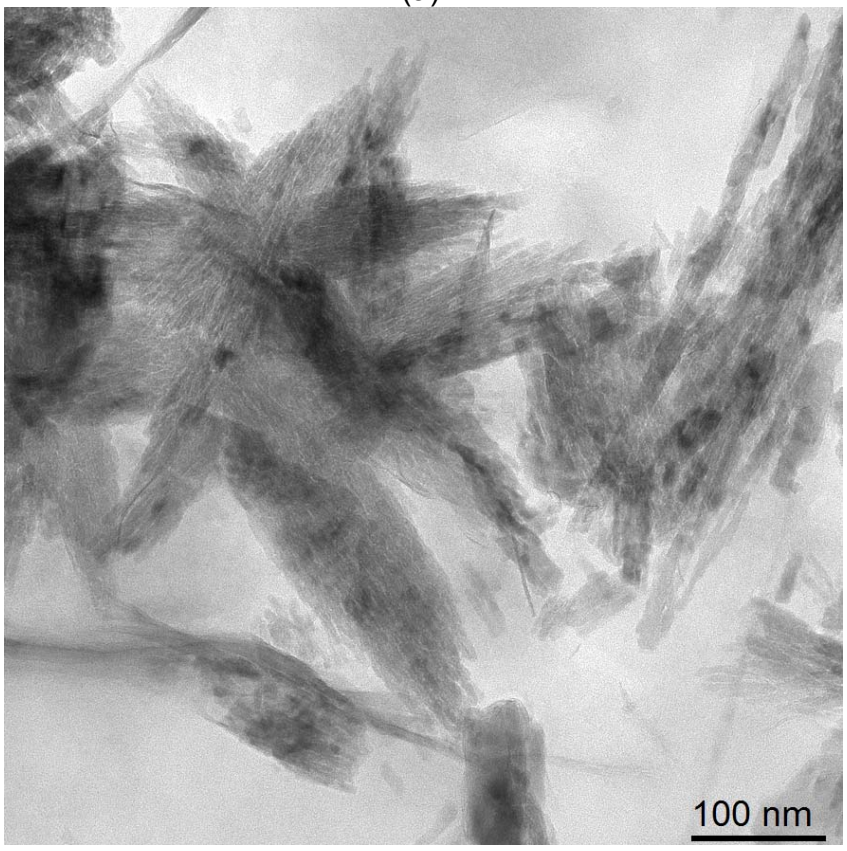

(b)

Figure 7-7 The goethite morphology in sample D2. (a) Goethite needles; (b) multidomain acicular goethite crystals with small aspect ratio.

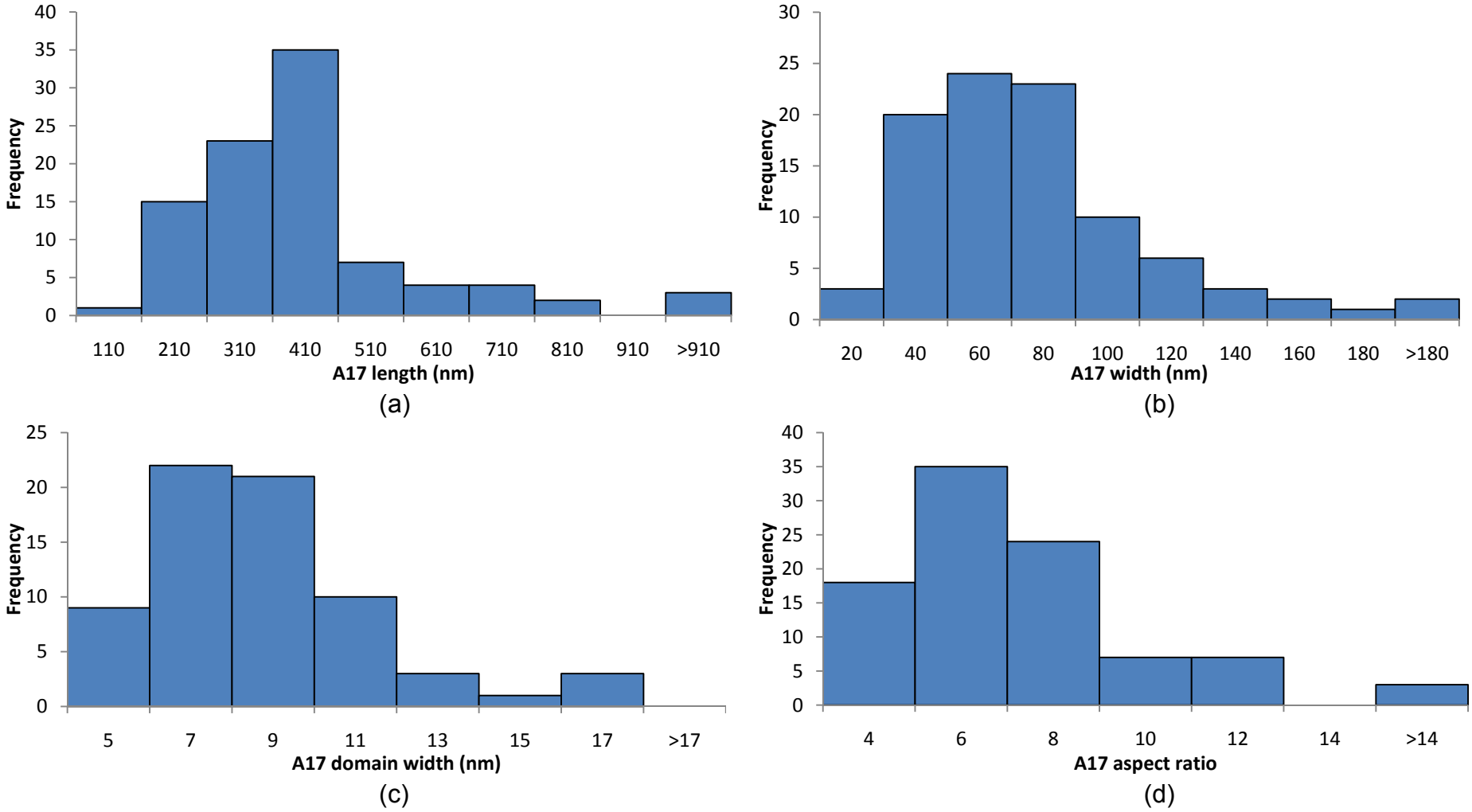

Figure 7-8 Goethite needle crystal dimensions of sample A17 (a) crystal length; (b) crystal width; (c) domain width; (d) aspect ratio.

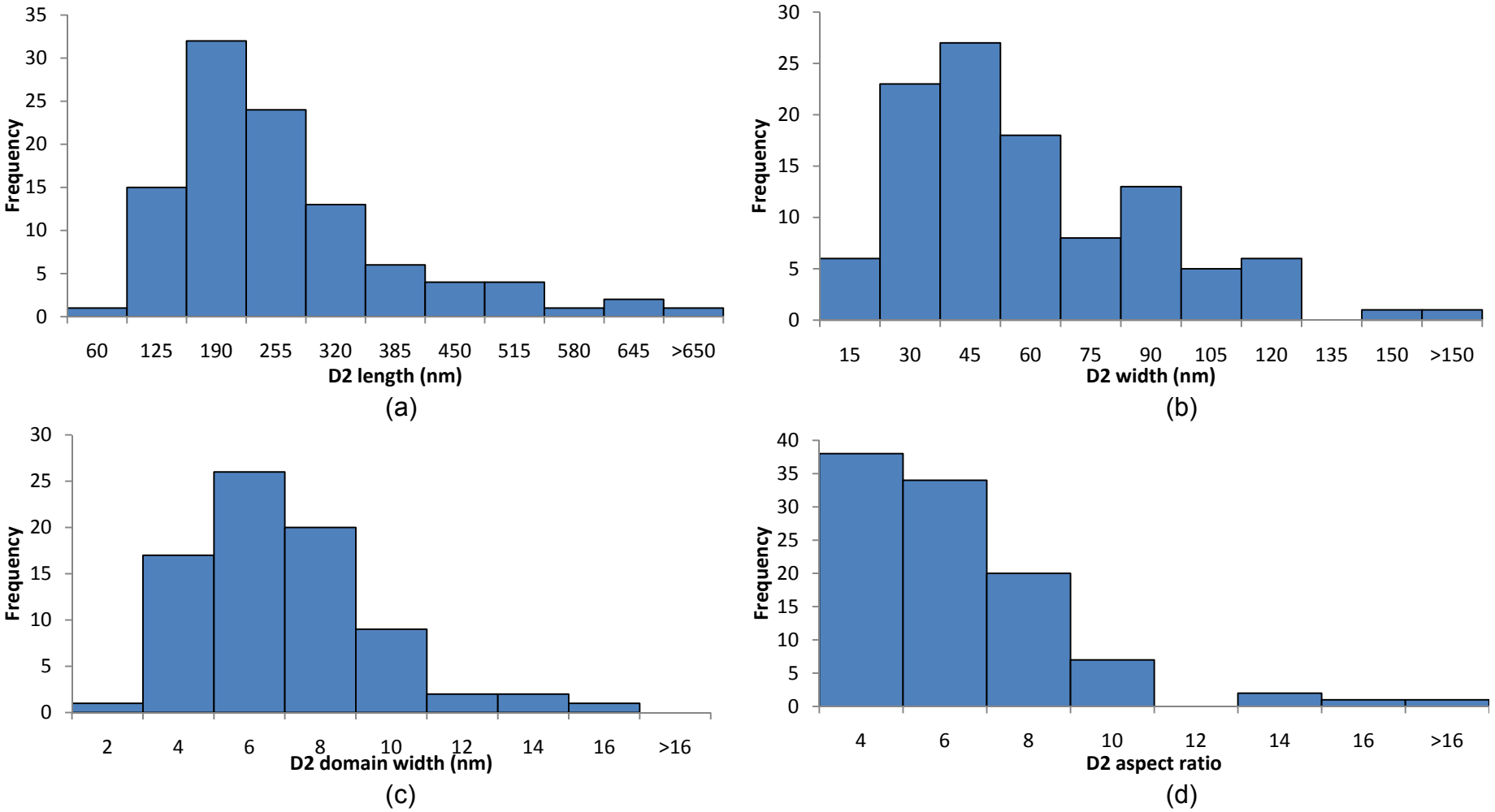

Figure 7-9 Goethite needle crystal dimensions of sample D2 (a) crystal length; (b) crystal width; (c) domain width; (d) aspect ratio.

Table 7-1 EDS results of selected particles studied in this chapter

Particle	Sample	Na	Mg	Al	Si	P	Cl	K	Ca	Cr	Mn	Fe	Ni	O
Figure 7-15b1	A5			8.6(2)	6.2(2)				5.95(17)			48.0(4)		31.2(5)
Figure 7-15b2	A5										1.24(4)	67.3(7)	1.7(4)	29.8(9)
Figure 7-15b3	A5			2.7(4)			2.3(4)					66.9(8)	3.8(4)	24(1)
Figure 7-16a	A15			1.74(3)	9.78(5)					2.69(4)		54.69(9)	1.19(3)	29.9(1)
Figure 7-16c	A15			2.02(4)	8.79(4)					2.34(3)		56.64(9)	0.87(2)	29.4(1)
Figure 7-16d	A15			5.56(6)	9.94(5)		0.45(1)		0.62(1)	2.96(5)		48.11(7)	0.55(1)	31.8(1)
Figure 7-17a	B11	0.4(1)		4.07(16)	9.4(2)		0.53(6)	0.46(5)		0.70(7)		53.1(3)	1.02(9)	30.3(5)
Figure 7-17b1	B11		0.59(2)	14.13(7)	25.86(9)	1.09(5)			0.54(1)	0.36(1)		10.26(2)		47.2(1)
Figure 7-17b2	B11		0.68(2)	8.8(2)	16.49(7)	0.66(2)				1.40(2)		33.26(4)	0.41(1)	38.25(6)
Figure 7-18a	B11			14.9(3)	15.3(3)					0.51(6)		26.3(3)	0.50(7)	42.4(5)
Figure 7-22a1	A15			0.69(12)	2.40(15)							65.4(3)		31.5(4)
Figure 7-22a2	A15			5.2(2)	31.4(4)					0.82(10)		15.3(3)		47.3(6)
Figure 7-22b	A15			0.58(6)	45.0(2)							1.89(5)		52.6(2)
Figure 7-23 1	A5				5.15(14)							62.2(2)		32.6(3)
Figure 7-23 2	A5		0.57(17)		12.2(4)							51.1(6)		36.2(7)
Figure 7-23 3	A5			0.52(16)	44.4(5)							2.90(17)		52.2(6)
Figure 7-24a1	B11			4.18(16)	3.16(15)					1.55(9)		57.1(3)	1.09(9)	32.9(4)
Figure 7-24a2	B11			4.40(19)	40.1(4)					1.7(1)		2.3(1)		51.4(4)
Figure 7-24b	B11			3.52(14)	43.2(3)							0.61(5)		52.6(3)
Figure 7-25	D5			16.0(3)	23.3(3)					0.65(8)	0.65(8)	12.6(2)	0.34(9)	46.5(5)
Figure 7-26a	A15			3.0(4)	7.4(5)					4.6(4)		50.2(8)		35(1)
Figure 7-26b	A15			4.0(1)	5.26(13)					4.34(10)		52.3(2)		34.1(3)
Figure 7-27a1	B11		1.62(2)	8.1(4)	21.4(5)					4.4(2)		20.8(4)		43.6(8)
Figure 7-27a2	B11			7.0(4)	7.8(4)					7.4(3)		41.4(6)		36.4(8)
Figure 7-27b	B11			6.7(4)	14.5(5)					3.1(3)		36.1(6)		39.5(9)
Figure 7-28	A15				3.8(3)							64.2(6)		31.9(7)

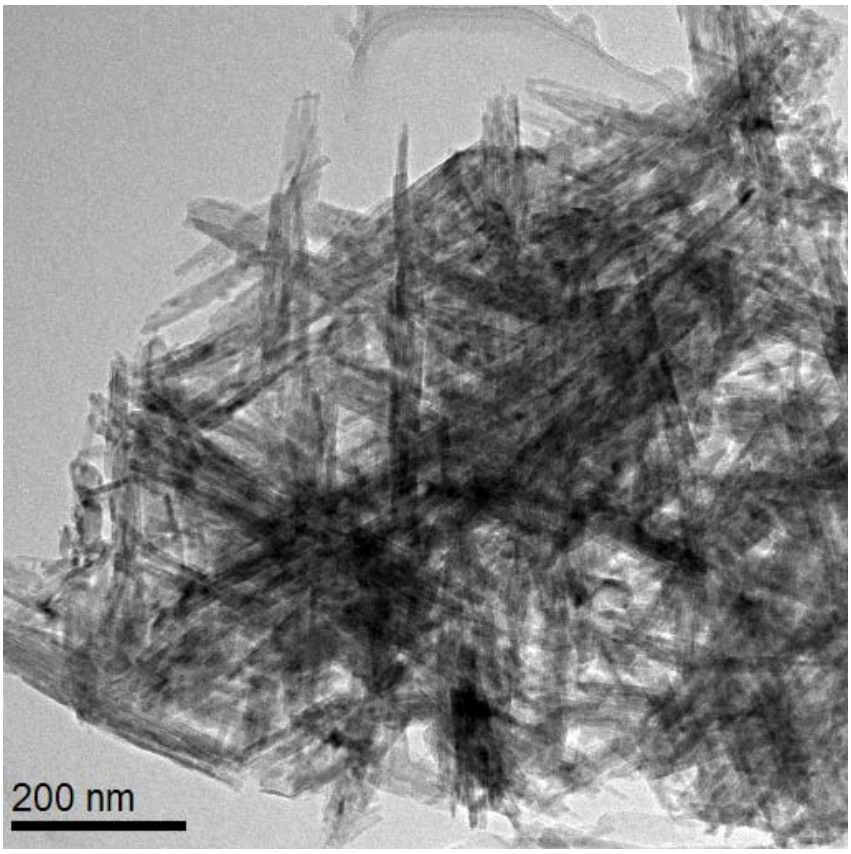

(a)

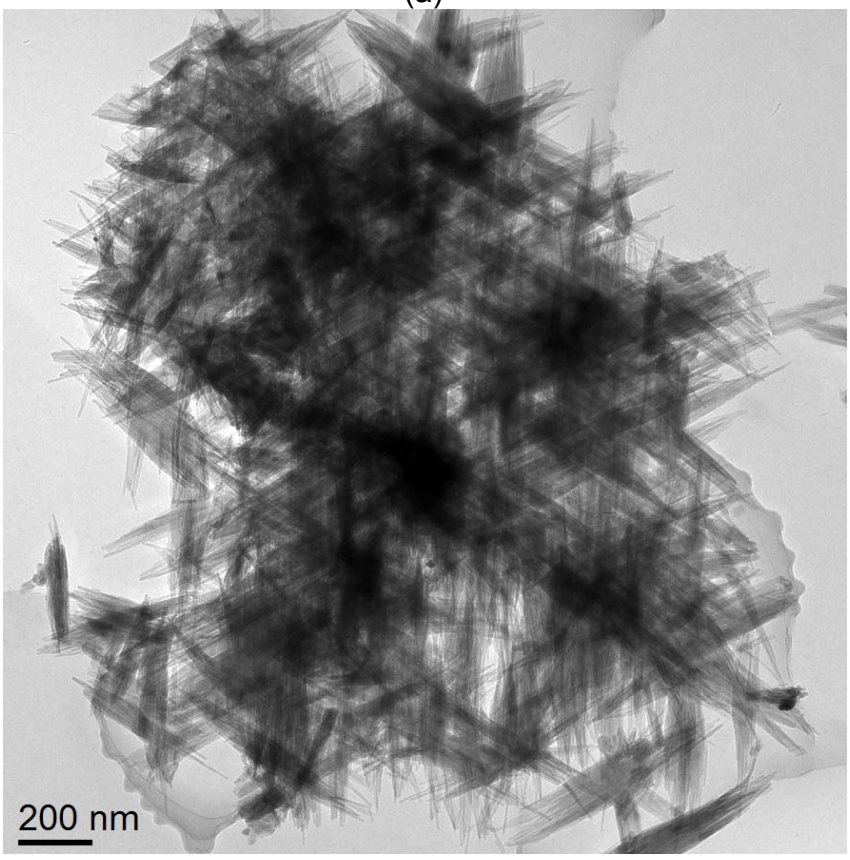

(b)

Figure 7-10 Goethite crystals with the 3-fold rotational texture in sample D1 (a, b).

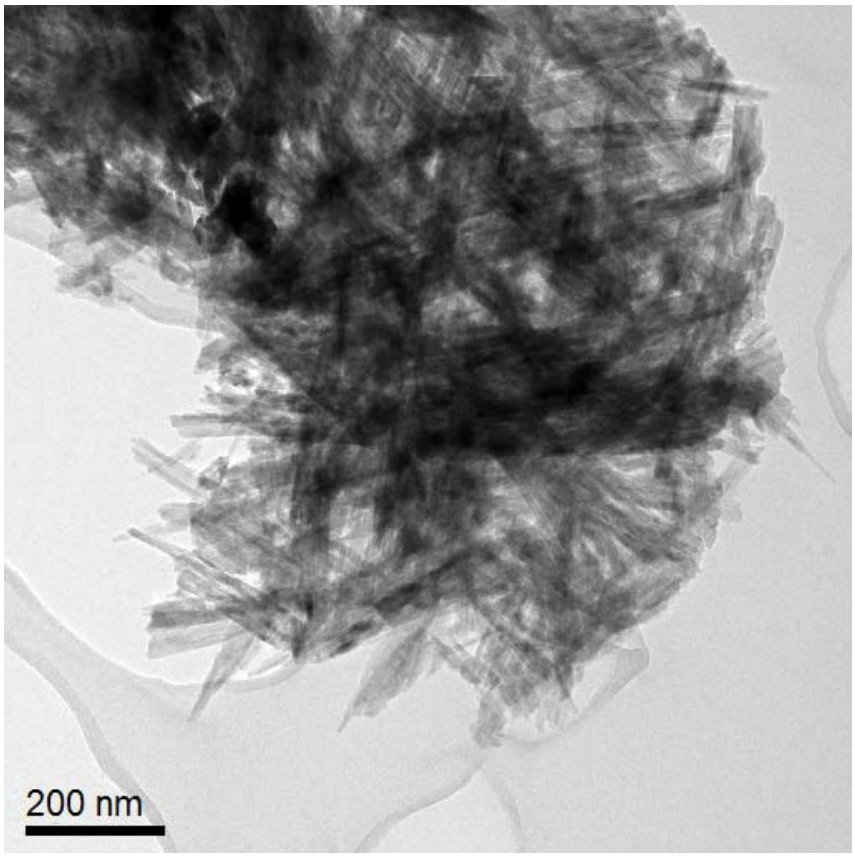

(a)

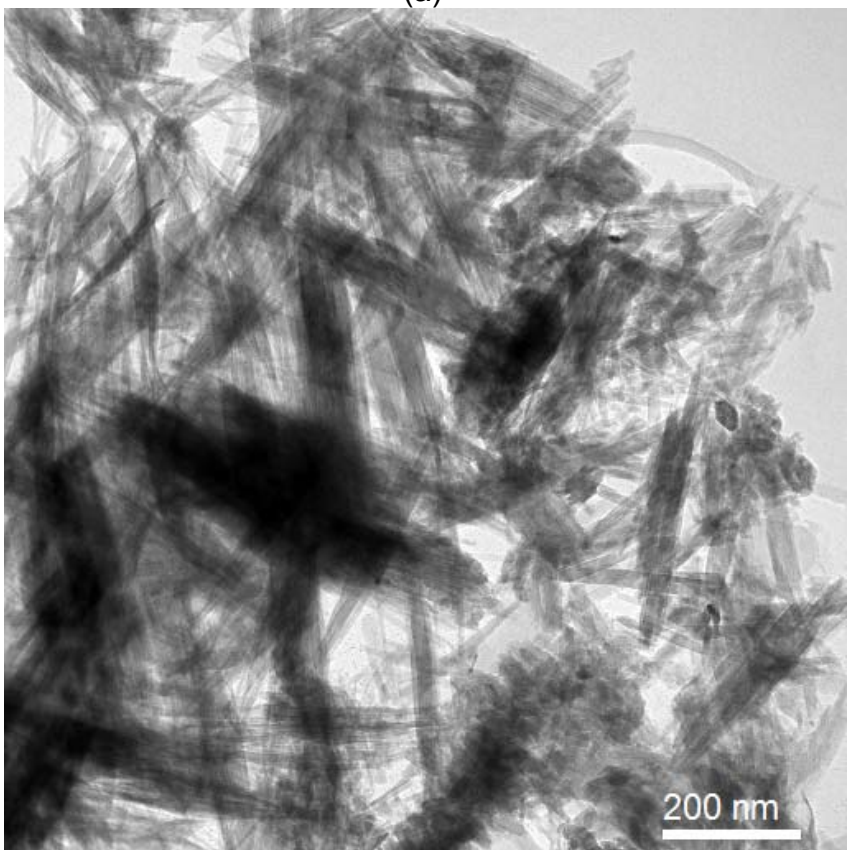

(b)

Figure 7-11 The morphology of goethite crystals in sample D4. (a) 3-fold rotational texture; (b) 3-fold rotational texture aggregated with acicular goethite crystals.

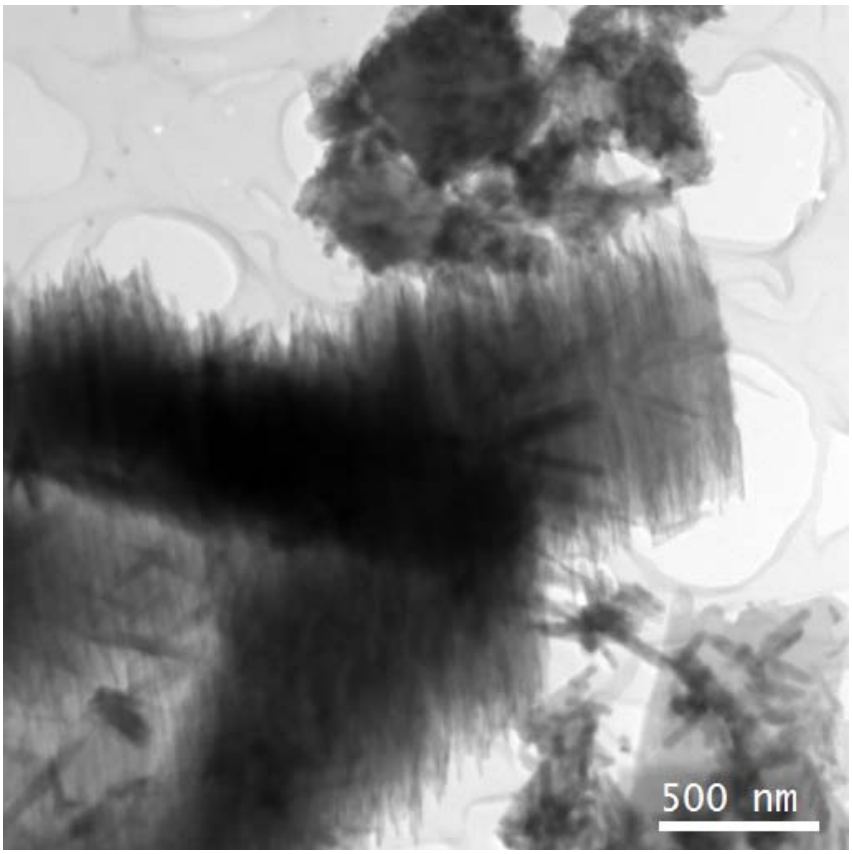

(a)

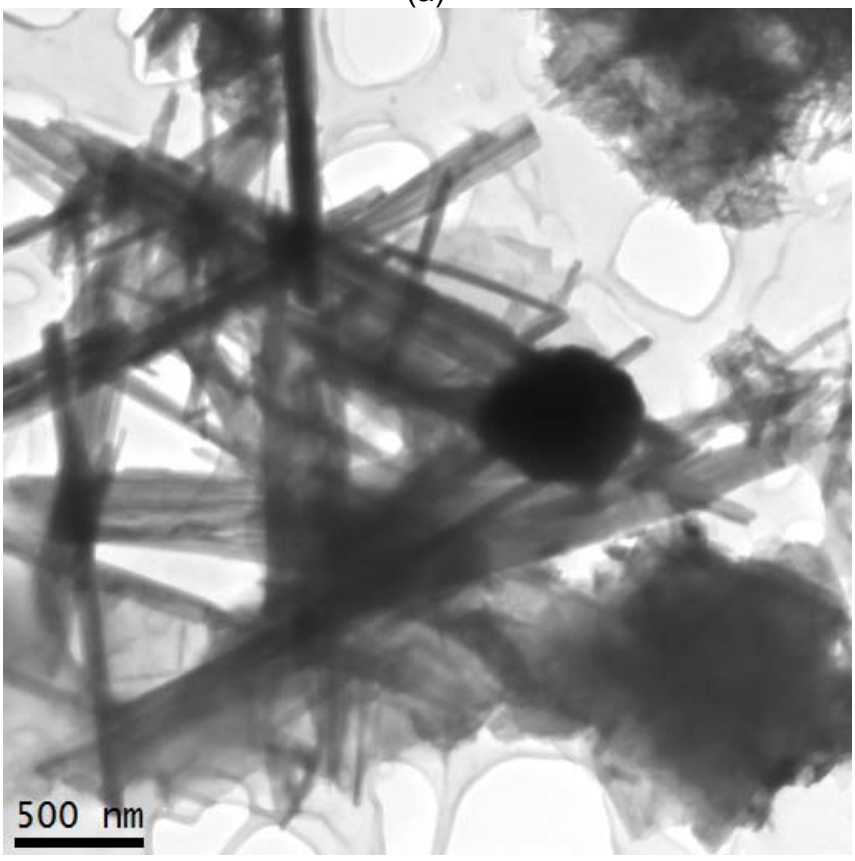

(b)

Figure 7-12 The morphology of goethite crystals in sample A4. (a) Parallel textured needles; (b) 3-fold rotational texture.

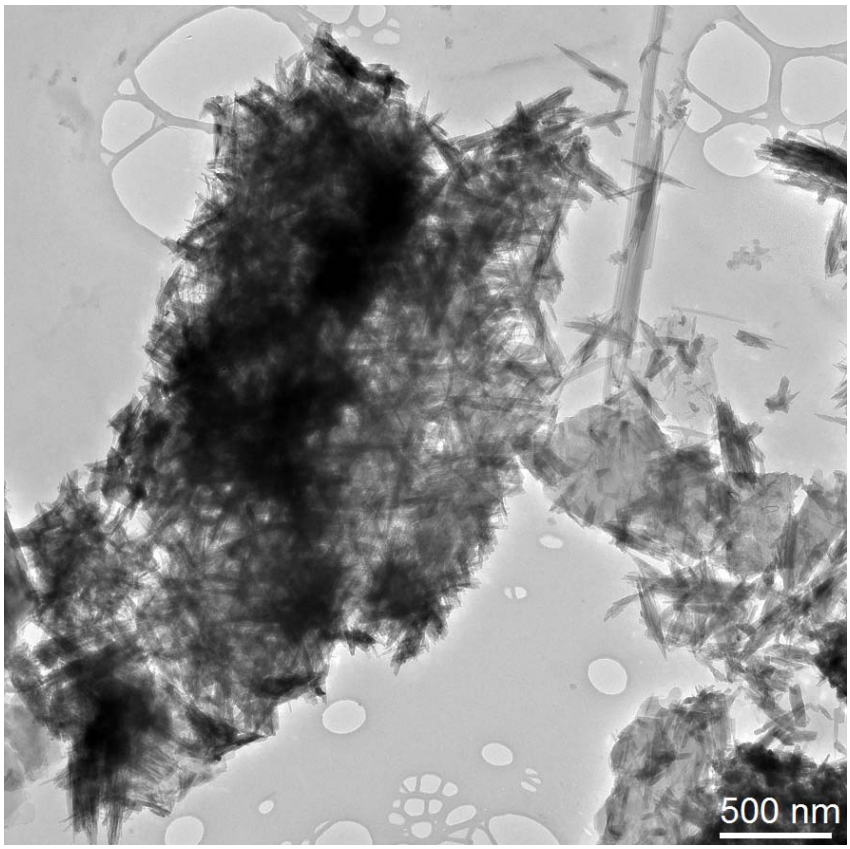

(a)

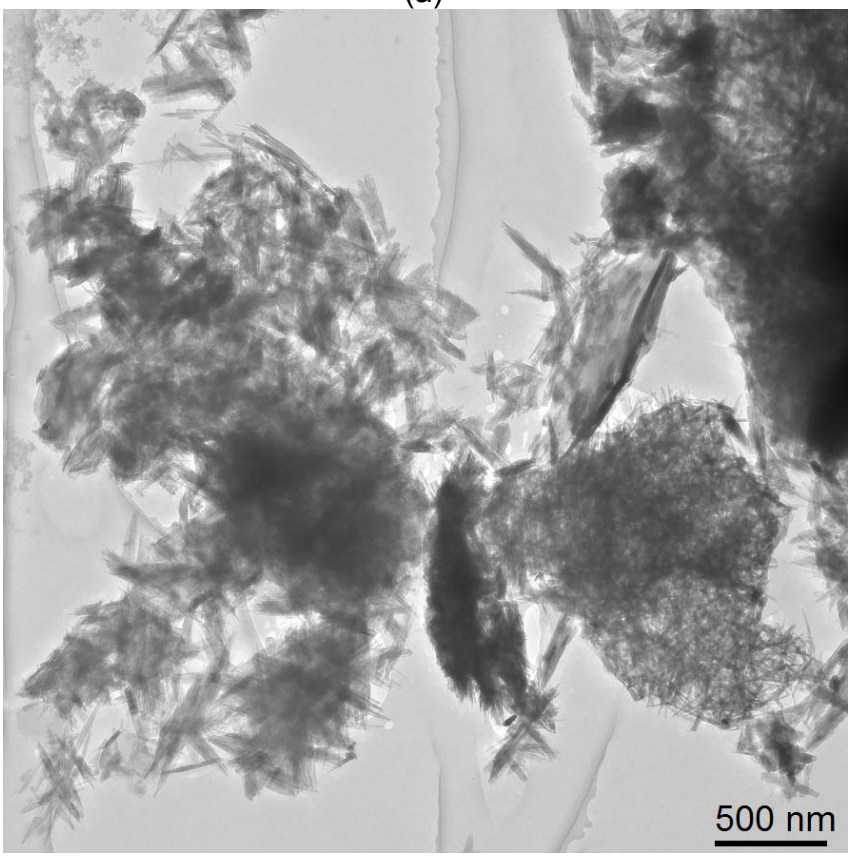

(b)

Figure 7-13 The morphology of goethite crystals in sample D5. (a, b) needle textured goethite cementations with small amount of acicular goethite crystals.

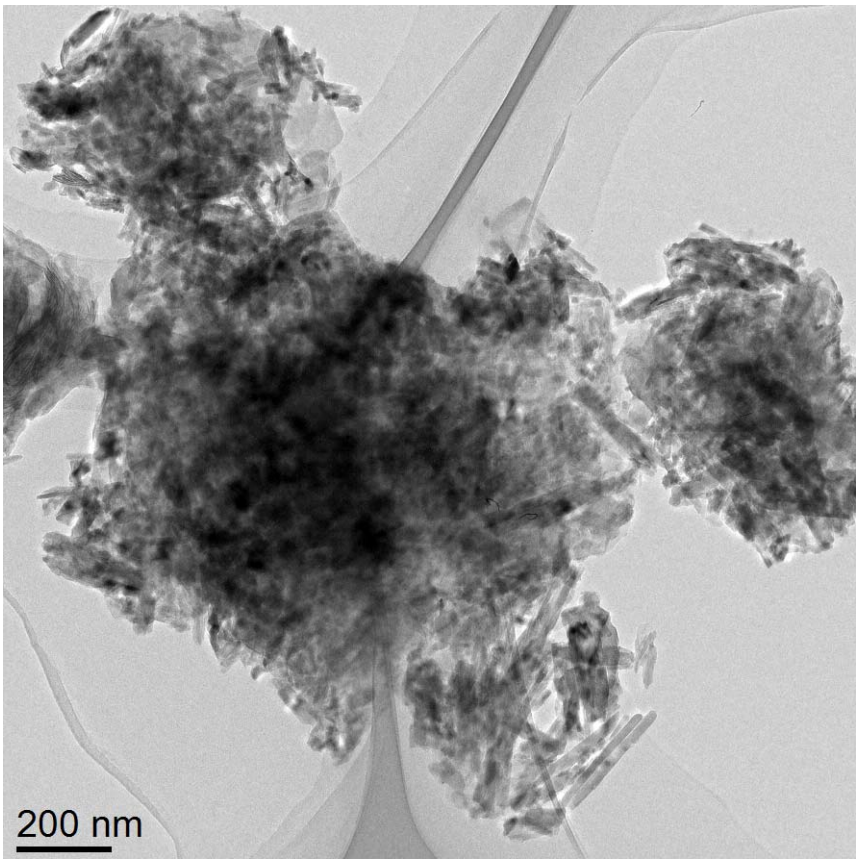

(a)

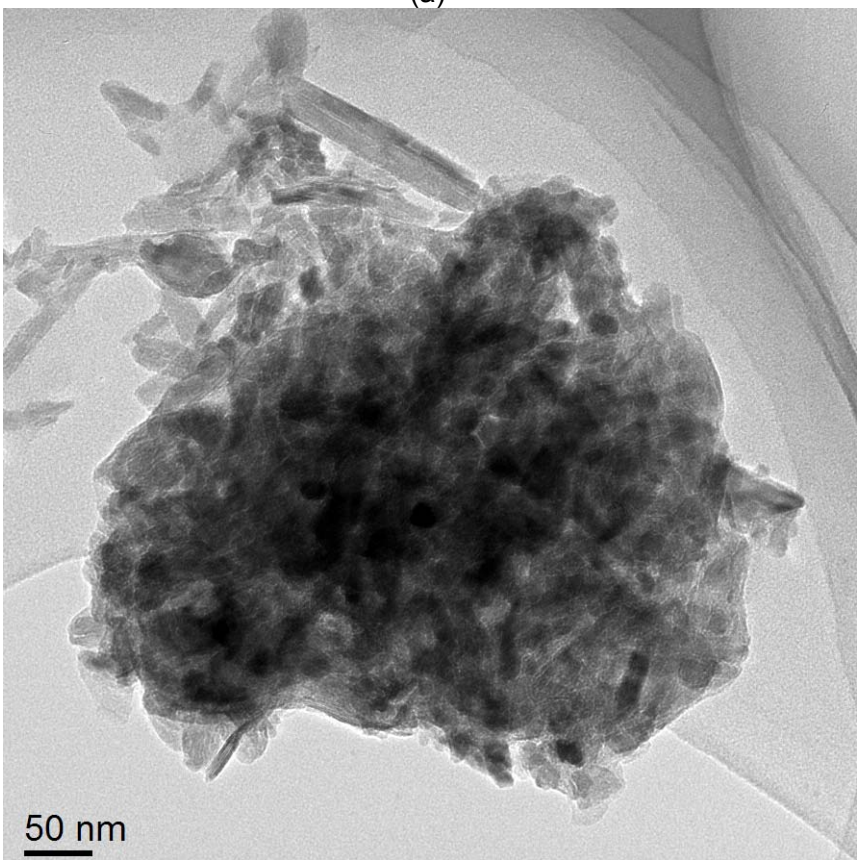

(b)

Figure 7-14 The morphology of goethite in sample A6. (a, b) goethite cementations.

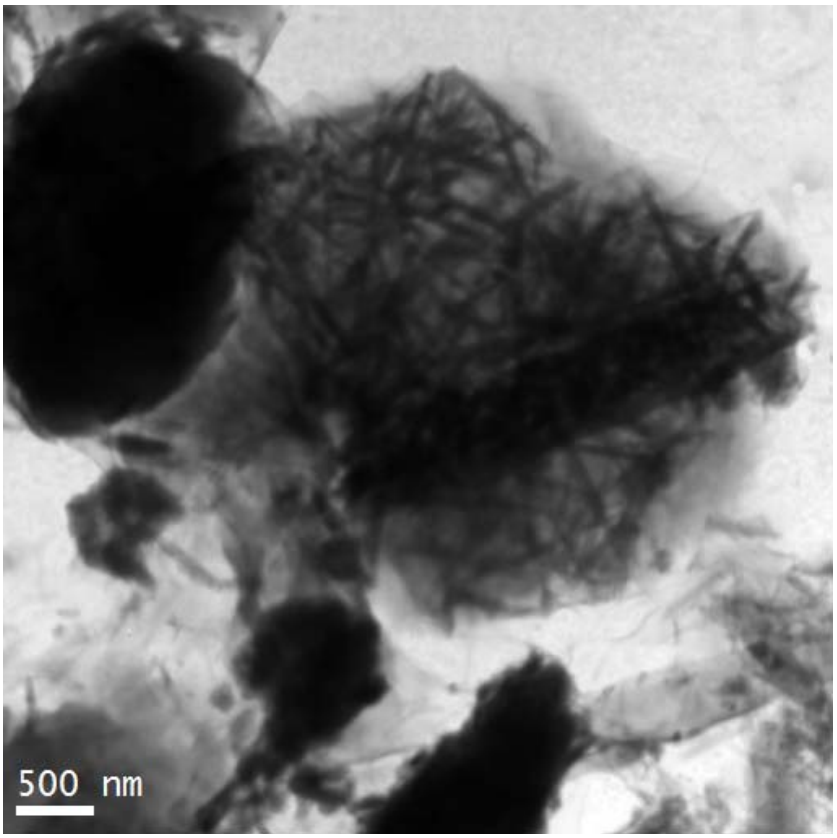

(a)

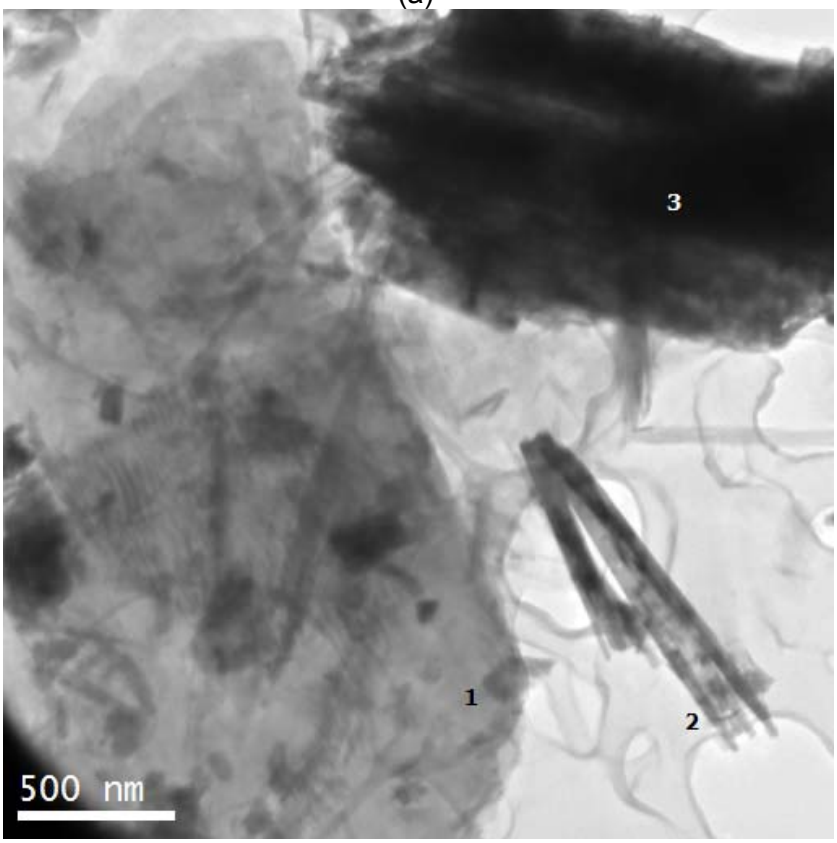

(b)

Figure 7-15 The morphologies of particles in sample A5. (a) Needle textured goethite cementation; (b1) kaolinite flake; (b2) acicular goethite crystal, and (b3) goethite cementation.

The goethite cementations observed in sample D5 (Figure 7-13), A6 (Figure 7-14) and A5 (Figure 7-15) represent common morphology observed in the two slowest leach sample A15 (Figure 7-16) and B11 (Figure 7-17). All types of goethite cementations observed in preceding samples, including the needle textured (Figure 7-16a), the 3-fold rotational textured (Figure 7-16b), the parallel textured (Figure 7-16c), and the goethite cementation without obvious texture (Figure 7-16d), are present in sample A15. Other than goethite cementations, goethite is also found to closely associate with kaolinite flakes in sample B11 (Figure 7-17b). Individual acicular goethite crystals are seldom seen in these two slow leach samples.

The goethite morphologies observed in the order of decreasing dissolution rate suggest that acicular goethite crystals are rich in fast iron leaching samples, while the goethite in slow iron leaching samples are mainly in the form of electron-dense cementations. These cementations may contain needles or in the form of either parallel aligned or 3-fold rotational textures. These cementation morphologies are likely to lead to low specific surface area which is a key factor determining goethite dissolution rate. Therefore it is important to investigate the microstructure and chemical composition of these cementations.

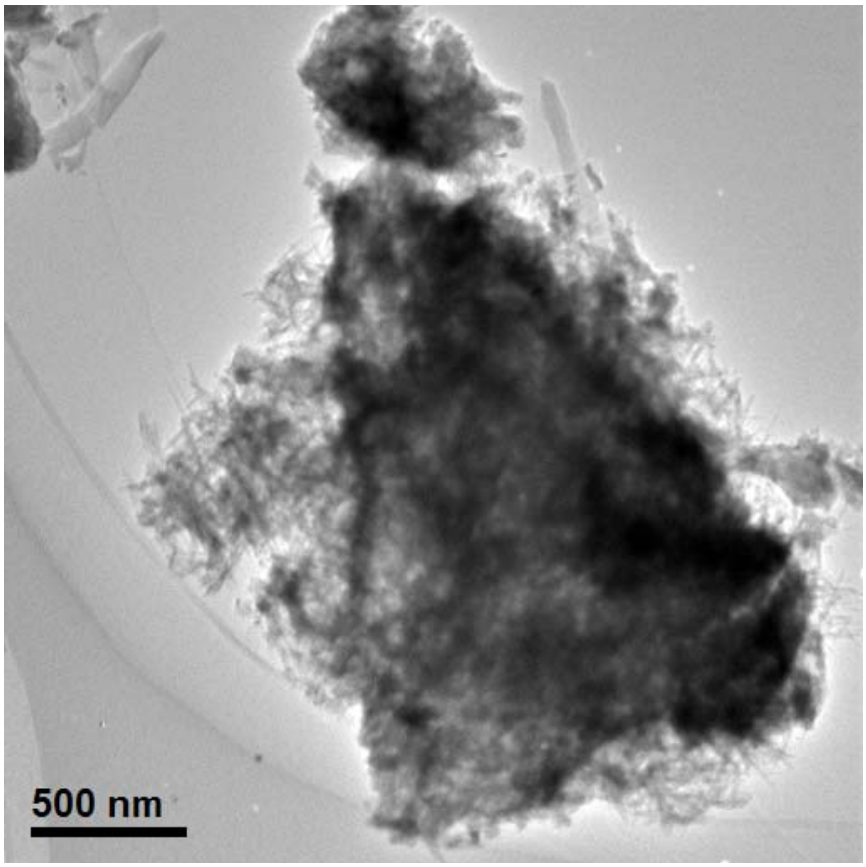

(a)

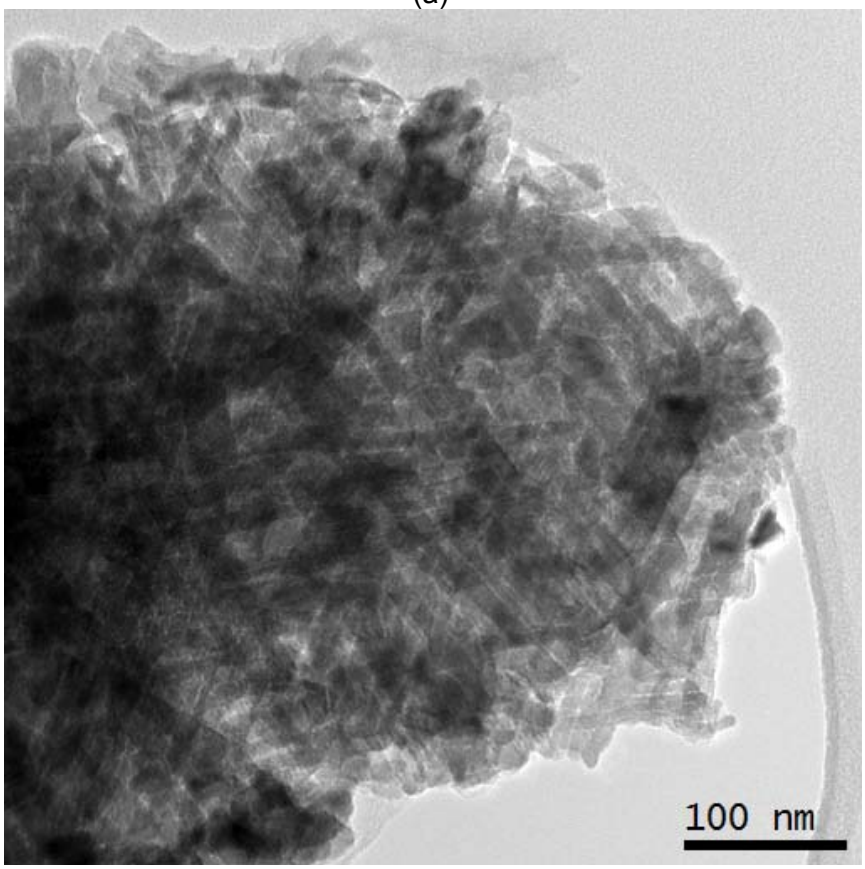

(b)

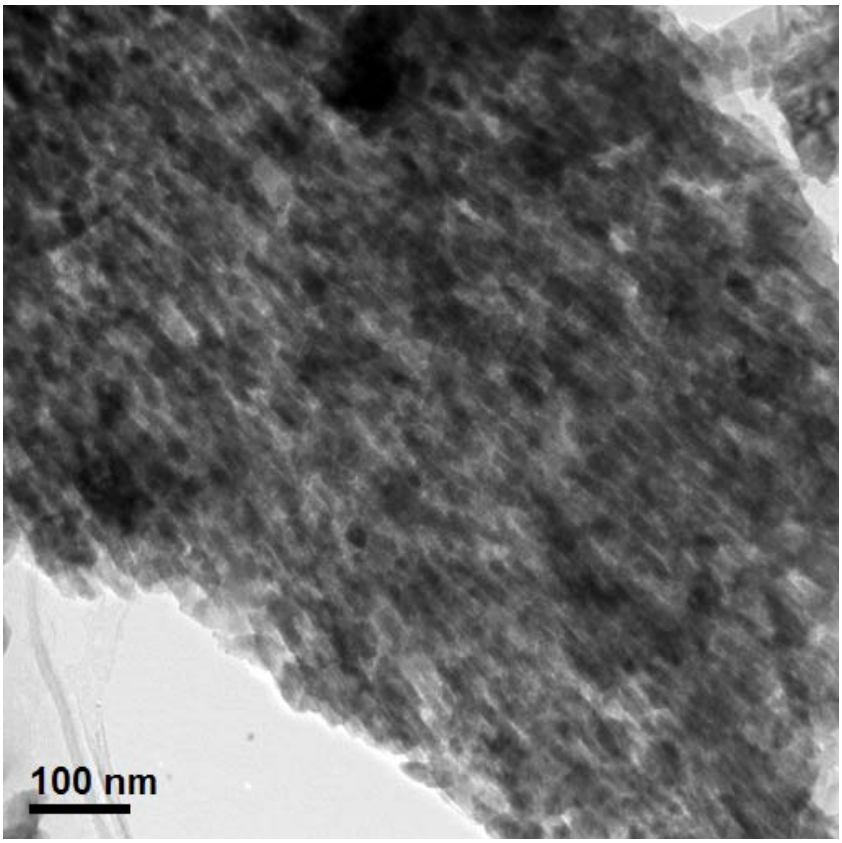

(c)

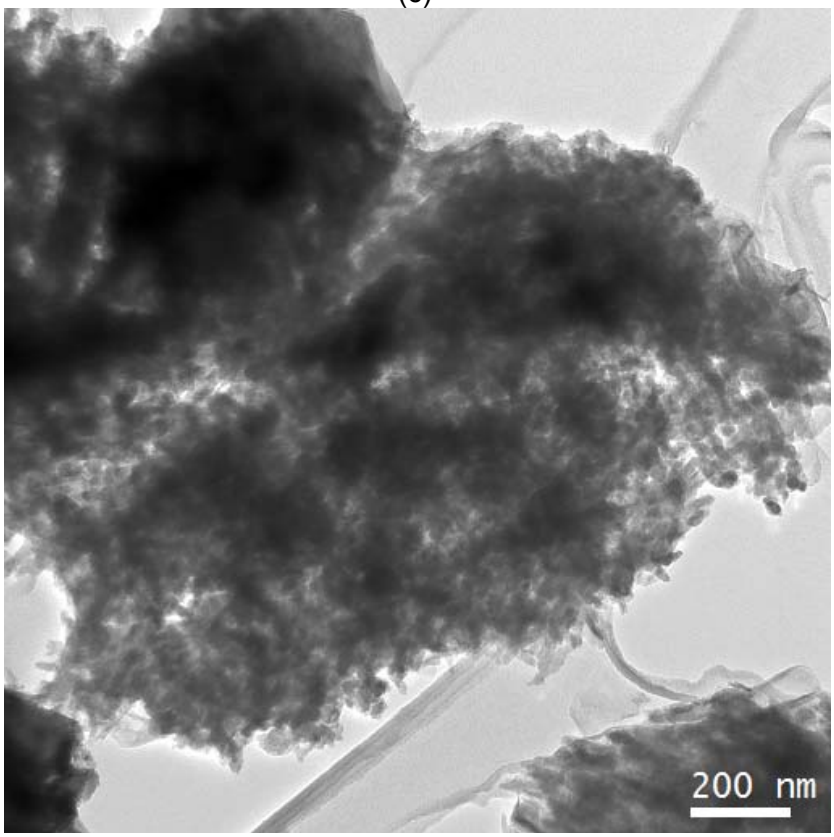

(d)

Figure 7-16 The morphology of goethite crystals in sample A15. (a) Needle textured goethite cementation; (b) 3-fold rotational goethite cementations; (c) parallel textured goethite cementation; (d) goethite cementation.

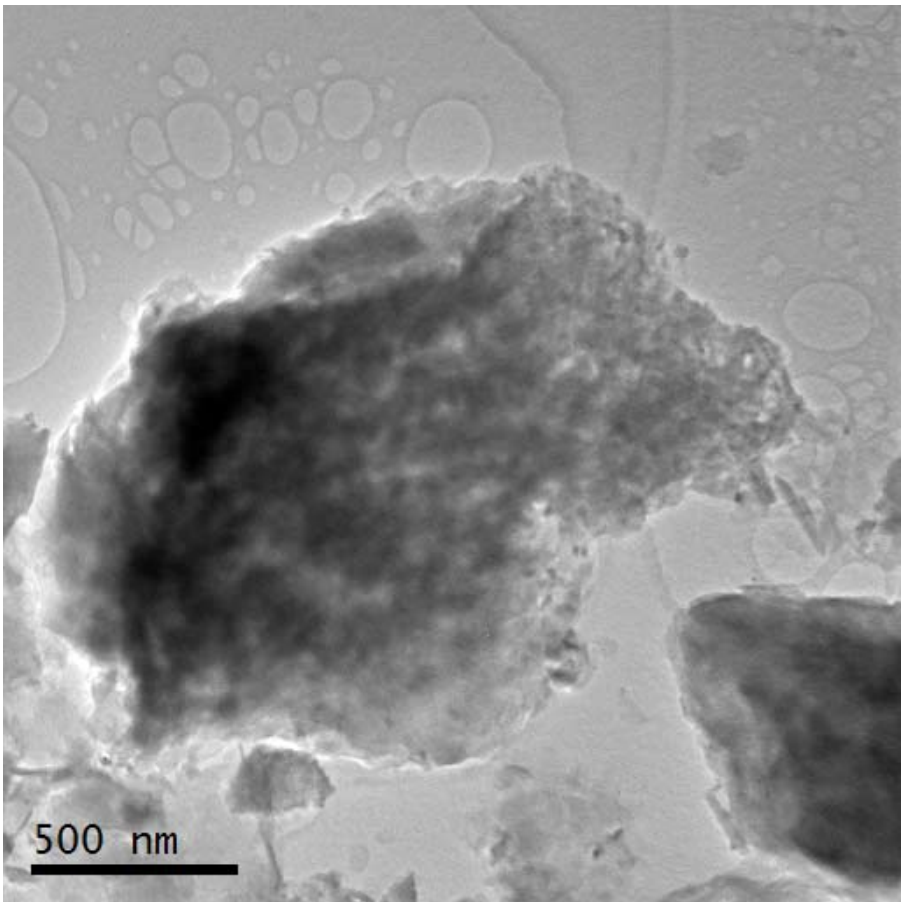

(a)

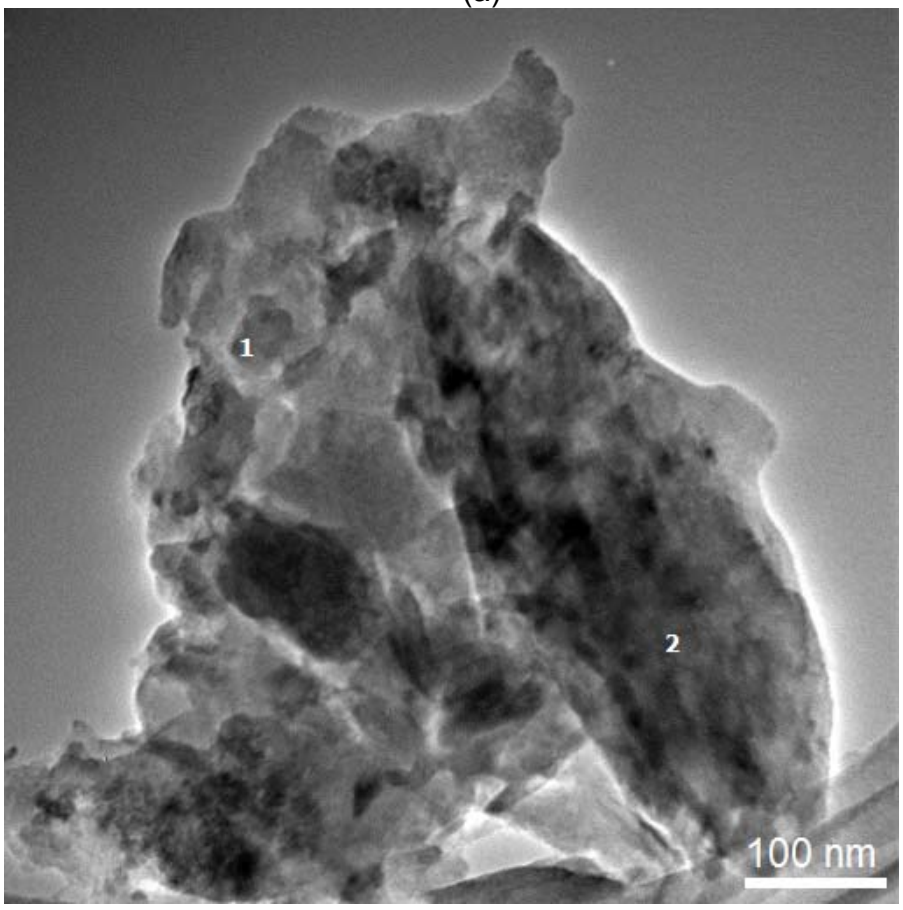

(b)

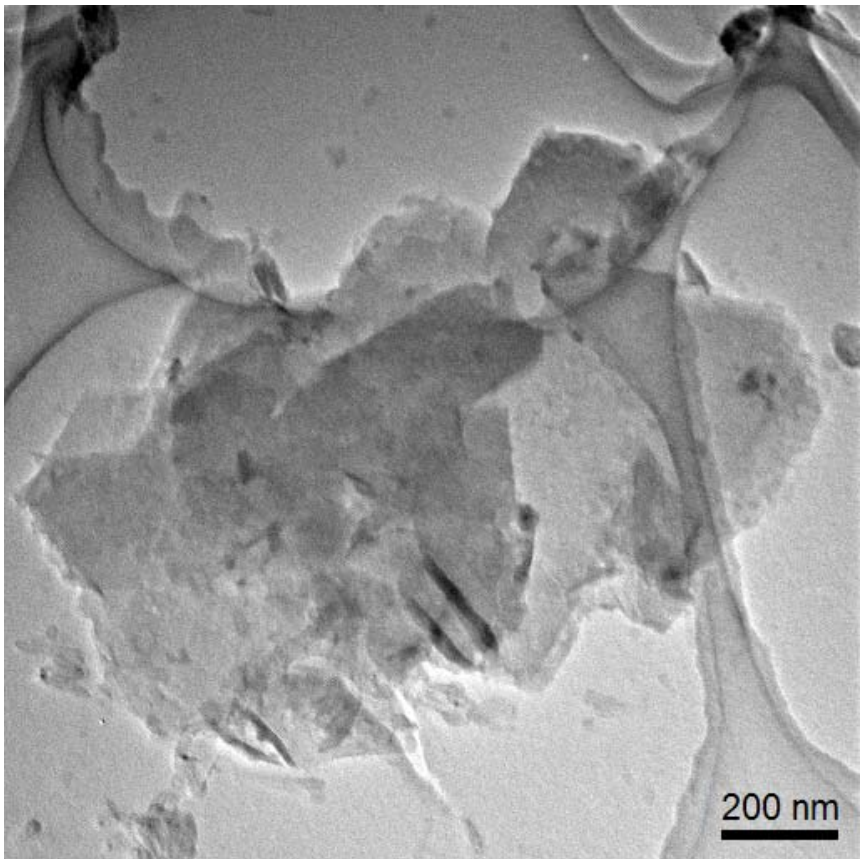

(c)

Figure 7-17 The morphology of particles in sample B11. (a) Goethite cementation; (b1) kaolinite and (b2) goethite formed close together; (c) kaolinite flakes.

7.3 The microstructure of goethite cementations in slow leach samples

Although sample A15 was subjected to extensive ultrasonic agitation to minimise particle aggregation prior to TEM imaging, the cemented clusters were the most commonly observed morphology in this sample (Figure 7-16), while acicular goethite needles were rarely observed. The cemented clusters prevented effective sizing of the goethite crystallites. According to the QXRD results (Table 6-2), sample A15 has a relatively simple phase composition with more than 95 wt.% of iron associated with goethite. Thus the iron rich particles (Table 7-1) observed in TEM (Figure 7-16) were assumed to be goethite as a Selected Area Electron Diffraction (SAED) pattern could not be obtained for these electron-dense particles. The EDS data of the particles observed in Figure 7-16 are presented in Table 7-1, and demonstrate high concentrations of silicon, aluminium, and chromium along with the major

elements iron and oxygen. As silicon was believed not to substitute into goethite structure (Section 2.6.5.8), silica or silicate (*e.g.* kaolinite, halloysite) may be cementing the goethite particles. When silica surrounds or encapsulates goethite it will create a barrier that hinders goethite acid leaching. The naturally formed 3-fold rotational textured (Figure 7-16b) and parallel textured (Figure 7-16c) goethite cementations maybe formed *in situ* through isovolumetric weathering from parent Fe-silicate, retaining the contour outline of the parent rock (Rozenson *et al.*, 1982).

The goethite particle in sample B11 (Figure 7-17b2) is intimately associated with kaolinite (Figure 7-17b1), and this is supported by the EDS data in Table 7-1. The 3-fold rotational textured goethite crystals in sample B11 (Figure 7-18a) are likely to have formed paragenetically with kaolinite, which is supported by the kaolinite SAED pattern (Figure 7-18b) and iron-rich EDS data (Table 7-1) obtained from this particle. The paragenetic goethite growth with kaolinite is similar to the goethite epitaxial growth on kaolinite reported by Boudeulle and Muller (1988).

STEM/EDS mapping was used to map the elemental distribution of the goethite cementations in slow leaching sample A15 (Figure 7-19). The elemental maps confirmed that silicon and iron occur in different locations but closely associated; chromium is more likely to associate with iron while aluminium is more likely to associate with silicon. Hence not all the aluminium detected by TEM/EDS from cementations is substituted into the goethite structure. The elemental maps suggest that goethite and silica or silicate (*e.g.* kaolinite, halloysite) are intimately interlaced.

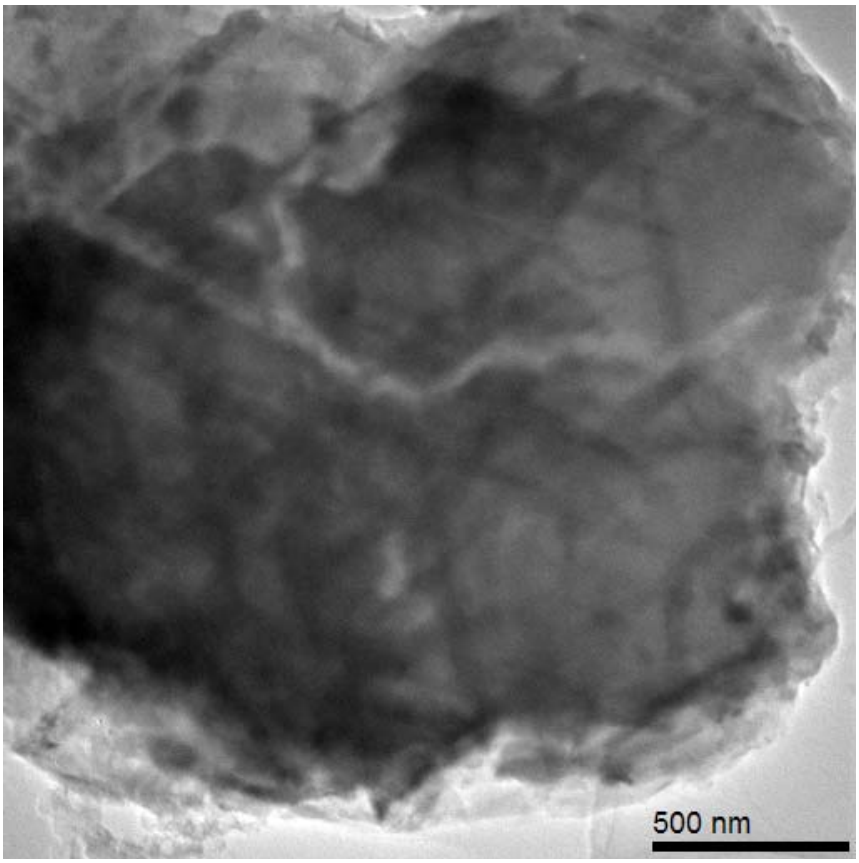

(a)

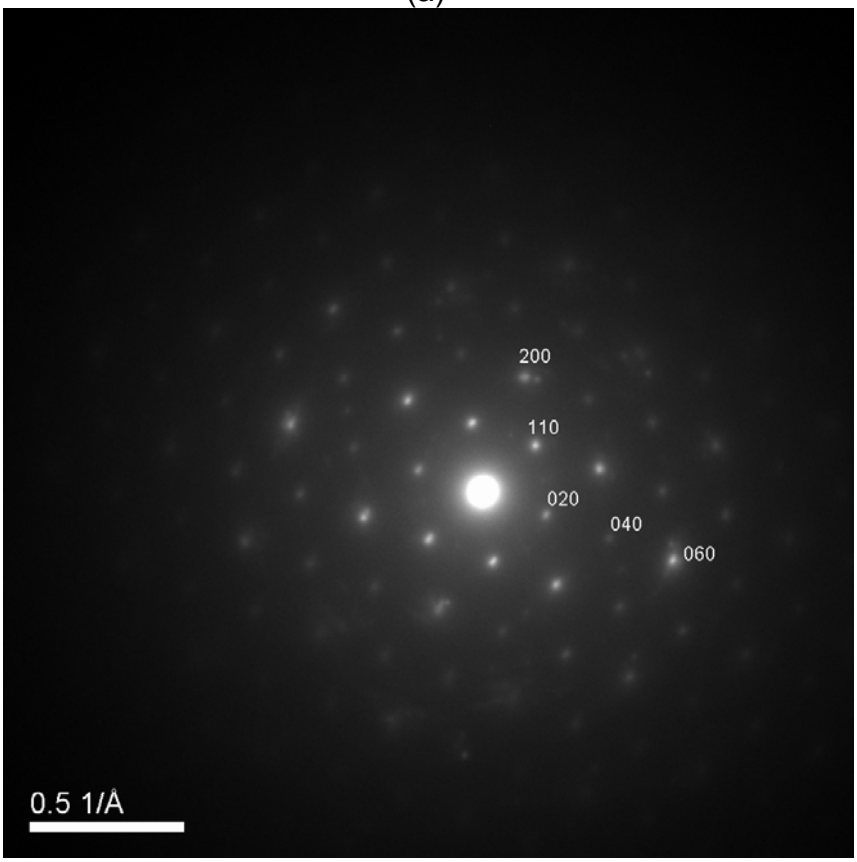

(b)

Figure 7-18 Paragenetic growth of goethite and kaolinite in sample B11. (a) 3-fold rotational textured goethite in kaolinite flake; (b) kaolinite SAED pattern from (a).

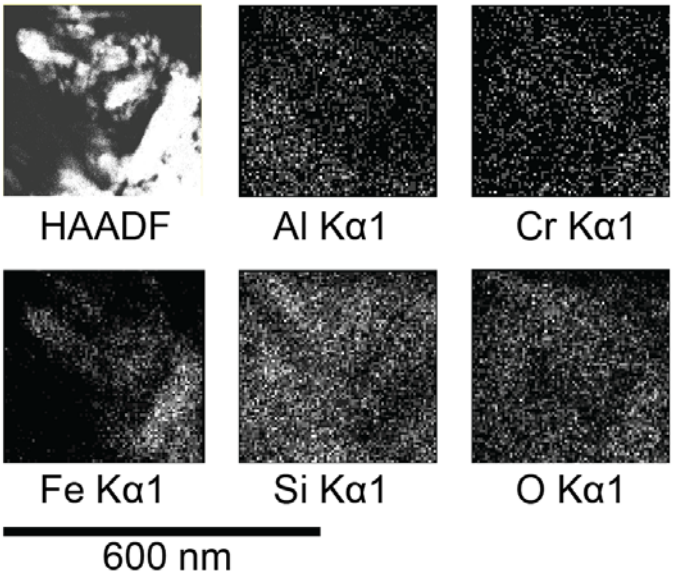

(a)

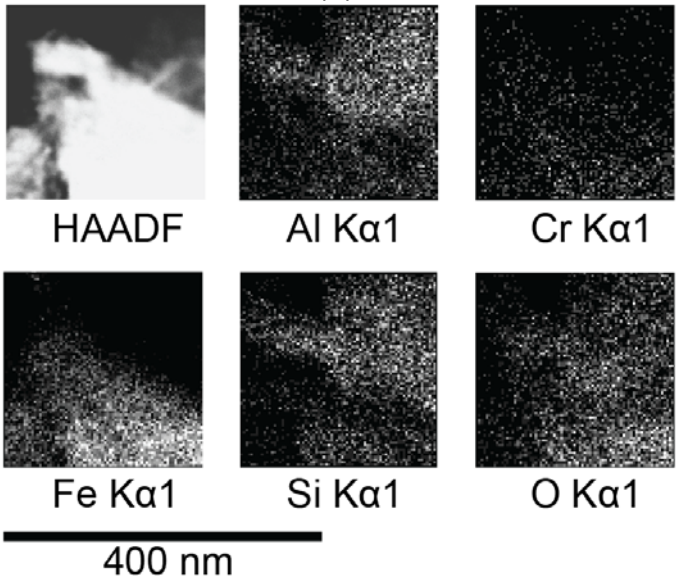

(b)

Figure 7-19 HAADF images with associated elemental maps of cementations in sample A15.

7.4 Accelerated acid leaching of acid-resistant laterite samples

In order to investigate the form of the silicon in goethite cementations, a chemical treatment was used to remove iron from the electron-dense goethite cementations in the slow leach samples. More aggressive leaching than column leaching should be used to effectively dissolve iron from the cementations in these slow leaching samples. Performing such a process at atmospheric pressure is essential to ensure that the process chemistry does not change significantly as found for HPAL (Whittington & Muir, 2000).

7.4.1 Materials and methods

Four limonitic nickel laterite ore samples A15, B11, A5, and D5 with low iron and nickel leaching rates determined by the column leaching experiment (Figure 6-8) were acid leached at 95 °C in a Parr 1 gallon titanium autoclave for either 16 hours (samples A15 and B11) or 9 hours (samples D5 and A5). Slurries consisting of 200 g solids and either 2000 kg/t sulphuric acid (samples A15 and B11) or 1000 kg/t sulphuric acid (samples D5 and A5) were leached at 9 % w/w solids, with approximately 2 L total volume. The more aggressive leaching conditions were used for samples A15 and B11 as these are the slowest leaching ore samples. The solid residues and filtrate were sampled at selected reaction times. Other details of the AL conditions are described in Section 3.2.7.

The washed and dried leaching residuals and the filtrates were analysed by ICP-OES to determine the leaching rates. The measurement conditions are provided in Section 3.2.2. The solids weight losses during acid leaching were calculated from the solid to liquid ratio derived from ICP assay of both solids and leachates. The solids were also examined by synchrotron X-ray diffraction (SXRD) (Section 3.2.3.4) for phase identification and laboratory X-ray diffraction (QXRD) using CoKα radiation (Section 3.2.3.2) for phase quantification. The phase identification and the quantitative phase analysis for each feed laterite ore sample were determined based on the synchrotron diffraction patterns. To assess the phase changes during acid leaching, the quantitative phase analysis of the leaching residues was based on laboratory XRD patterns, which examined a larger sample volume.

In order to concentrate the unleached iron oxides and break up the goethite-silica cementations, the AL leached residues from the slow leaching ore samples A15 and B11 were digested with potassium hydroxide (KOH) in a covered Teflon beaker (atmospheric pressure) placed in a boiling water bath for 1.5 hours. Other caustic digestion conditions were described in Section 3.2.8. The sub-samples of the feed ores, AL residues, and caustic digestion residues were imaged by TEM. Other TEM analysis conditions are presented in Section 3.2.4.

Sodium hydroxide caustic digestion is regarded as an efficient way to concentrate iron oxides by removing kaolinite, gibbsite and amorphous silica (Kämpf & Schwertmann, 1982; Singh & Gilkes, 1991; Xu *et al.*, 2009). The possibility of goethite crystallinity "healing" due to goethite recrystallisation in hot caustic solution reported by Schwertmann *et al.* (1985) was not applicable here, as the amorphous silica present in the samples (according to QXRD data) is sufficient to prevent goethite recrystallisation (Kämpf & Schwertmann, 1982). Potassium hydroxide rather than sodium hydroxide was used to prevent sodalite formation and improve silica removal from solids (Lowe, 2007, Chapter 4).

7.4.2 Phase changes of ore samples during acid leaching

The phase identification and quantitative phase analysis for the four feed laterite ore samples are shown in Table 7-2. The crystallographic information file entries for each mineral phase used in the Rietveld quantitative analyses are provided, except the nontronite phase for which a lattice model was developed using the modified PONKCS method (Chapter 4). Quartz is essentially inert under acidic conditions.

The phase concentration changes of these samples assessed by quantitative phase analysis of laboratory based XRD patterns of the leach residues are shown in Figure 7-20. The QPA result for the solids at "time zero" in Figure 7-20 can differ from the QPA result of the feed laterite ores (Table 7-2), because the solids sampled from autoclave at "time zero" may have partially dissolved during the heating period. A large difference, however, is more likely to indicate a sub-sampling difference between the feed and leached sub-samples.

The data in Figure 7-20 have been normalised taking into account the solids weight loss calculated from the solids to liquid ratio. Hence these curves represent the absolute solids phase percentage changes rather than the weight percentages in the XRD samples. No new phase (new reflections) were generated during the acid leaching. The slight increase in goethite content during the initial leaching of samples A15 and B11 is probably due to QPA error. It indicates that goethite dissolution from the cementations of the

two samples requires an activation time. Other minor iron oxide phases such as hematite, maghemite, and magnetite were present in low concentration and all dissolve relatively slowly compared to goethite. This contradicts previous work where hematite was reported to dissolve faster than goethite in both natural laterite (Schwertmann & Latham, 1986) and synthetic samples (Cornell & Giovanoli, 1993). This is not uncommon because the dissolution rate for iron oxides are more susceptible to particle micro-morphologies and micro-structures rather than to specific crystal structures (Schwertmann, 1988, p237).

The goethite dissolution curves of these four limonitic laterite ore samples compared in Figure 7-21 are very different. Goethite in samples A15 and B11 show the greatest acid resistance followed by the goethite in sample A5, while the goethite in sample D5 is the least acid-resistant in these four samples.

Table 7-2 Absolute phase compositions of the four laterite ore samples, determined by Rietveld quantitative phase analysis using the internal standard method. Uncertainties of 2σ (95% confidence level) are in brackets.

Phase entry #[a]	D5	A15	B11	A5
Quartz low ICSD 156198	0.28(7)	32.8(4)	7.5(1)	38.6(7)
Goethite ICSD 245057	55.6(7)	50.2(6)	51.0(6)	26.3(4)
Maghemite-C ICSD 87119	3.29(8)	1.13(6)	6.8(1)	5.31(14)
Hematite ICSD 56372	-	-	-	8.64(18)
Hematite ICSD 64599	1.8(1)	-	2.76(8)	-
Magnetite ICSD 75627	--	-	2.20(9)	0.31(7)
Chromian Spinel LPF 1212472		0.09(3)	-	0.09(2)
Lithiophorite ICSD 75283	2.3(2)	-	--	-
Kaolinite-1A ICSD 63192	-	-	14.0(4)	1.1(2)
Kaolinite-1A ICSD 31135	17.9(5)	4.2(4)	-	
Lizardite ICSD 87436	-	-	-	1.31(18)
Gibbsite ICSD 6162	1.0(2)	-	-	-
Rutile ICSD 93097	0.11(4)	-	-	-
Halite ICSD 18189	0.89(5)	-	-	-
Nontronite PONKCS[b]	-	-	5.6(3)	-
XRD amorphous	16.8(8)	11.5(9)	10.1(8)	18.3(10)

[a] The crystallographic information files were selected either from the Inorganic Crystal Structure Database (ICSD) or Linus Pauling File (LPF) database.

[b] The nontronite model was developed from enriched Bulong nontronite using the PONKCS method (Wang *et al.*, 2011).

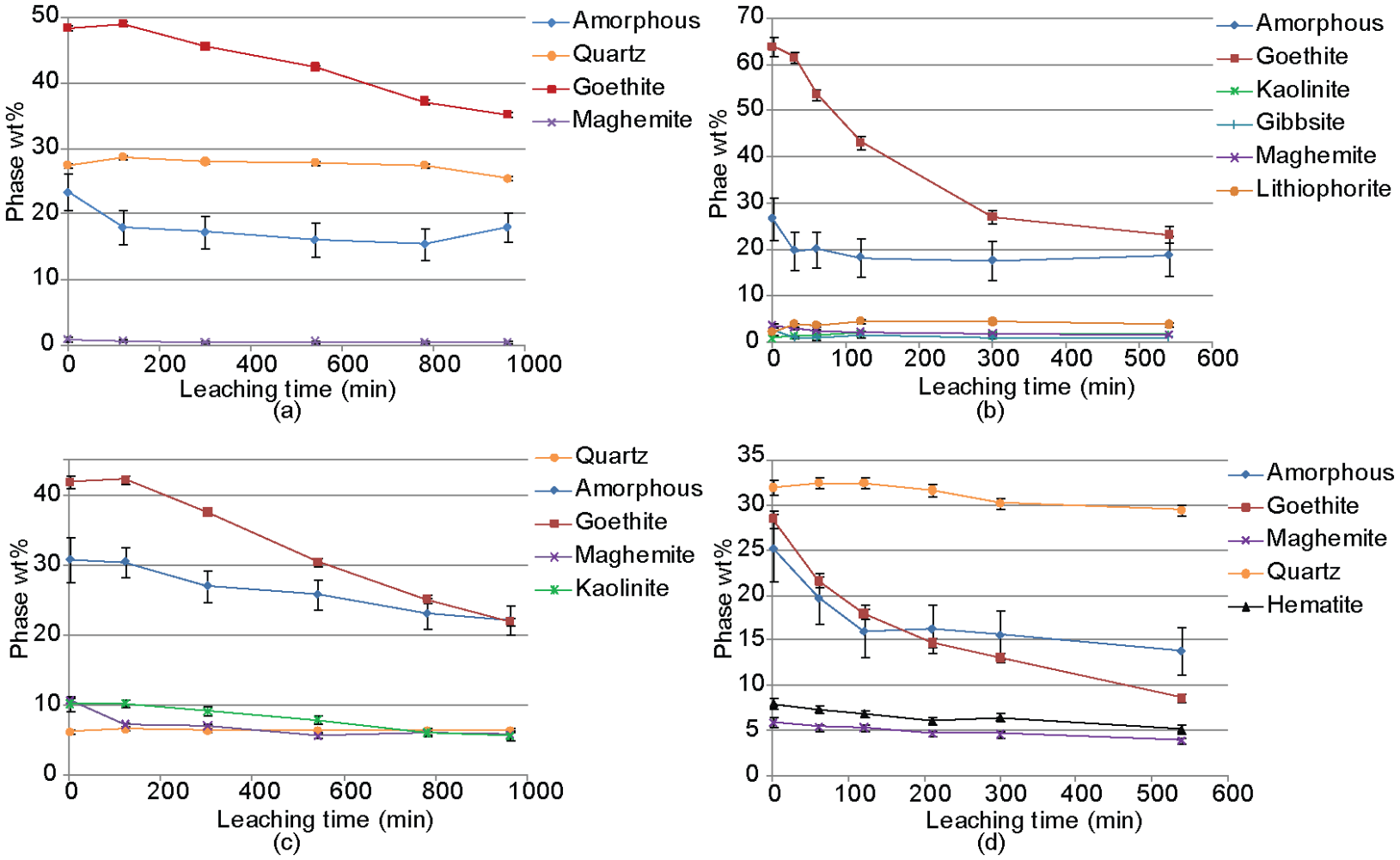

Figure 7-20 Phase concentration changes during the sulphuric acid AL of laterite ore samples (a) A15, (b) D5, (c) B11, and (d) A5. The 3σ error bars are larger for amorphous content than other crystalline phases due to uncertainty propagation.

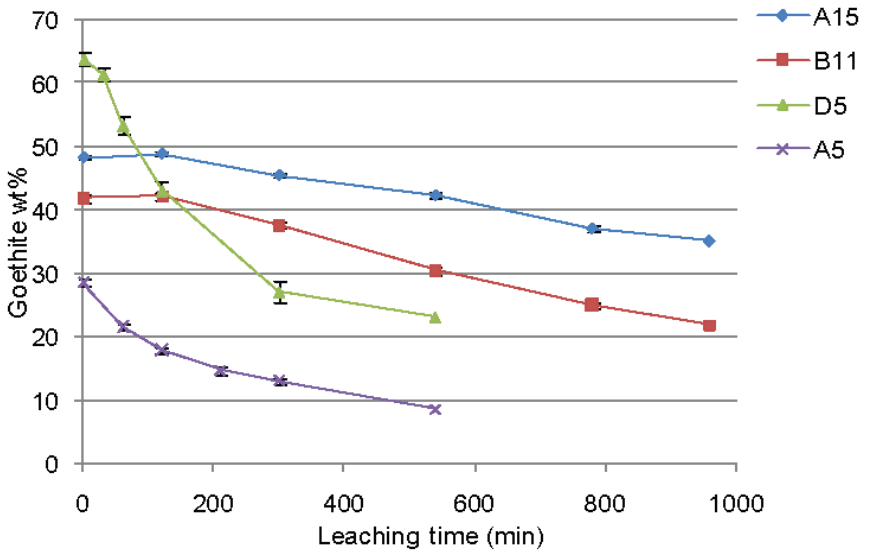

Figure 7-21 Comparison of goethite dissolution curves for four laterite samples.

Table 7-3 The dissolution rate constant *k* of iron oxide phase of the four laterite ore samples generated by non-linear Kabai fitting.

	Non-linear Kabai fitting		
sample	*k* (day^{-1})	a	R^2
A5	2.6(1)	0.65(3)	0.9987
A15	0.54(2)	0.80(2)	0.9994
B11	1.18(2)	1.05(2)	0.9996
D5	3.8(3)	0.65(5)	0.9966

The rate constants *k* for these four samples derived from the non-linear Kabai fitting of the iron leaching curves is given in Table 7-3. These indicate the sample leachability follows the order: D5 > A5 > B11 > A15. This is exactly the same order observed from the 9-month long column leaching experiment (Section 3.2.6). Comparing the rate constant '*k*' in Table 7-3 with the corresponding values of these four samples in Appendix 8, the high temperature AL increased the dissolution rate by factors of approximately 10^3 times for sample D5 and A5, 5×10^3 times for sample B11 and 10^4 times for sample A15, indicating that the high temperature AL can effectively distinguish the fast leach laterite ores from slow leach ores experimentally within a short time (16 hours in this case). The constant of average order '*a*' of both AL leaching (Table 7-3) and column leaching (Appendix 8) are the same order of magnitude, which is consistent with Kabai's finding that the constant of average order '*a*' is related to the nature of the solids and does

not vary with experimental conditions, such as temperature and acid concentration (Kabai, 1973).

7.4.3 Particle morphology changes due to acid leaching

The residues from the 16 hour acid leached sample A15 show distinctly separated, larger (~1 μm) single domain goethite particles (Figure 7-22a, particle 1) and goethite embedded in amorphous silica (Figure 7-22a, particle 2). The presence of large goethite particles suggests these were a slow dissolving component in the original laterite A15 sample. The EDS data of corresponding particles given in Table 7-1 indicates no nickel is present in the large single domain goethite. The mechanism for the formation of the goethite particles may involve high dissolved silica concentration conditions (Section 2.6.5.8).

Comparison of the morphology of interlaced silica and goethite cementations in the feed sample (Figure 7-16d) and the morphology of silica in the post-leached sample (Figure 7-22b) along with their corresponding EDS analysis (Table 7-1) suggests goethite has been removed from the silica framework. It should be noted that although iron oxides were leached, the framework of the cementation was preserved.

The TEM image of sample A5 shows a large single domain goethite particle aggregated with acicular needles in the leach residue (Figure 7-23) with corresponding EDS data shown in Table 7-1. The diamond shaped tip of the single domain goethite (particle “1” in Figure 7-23) may indicate the presence of a high silica concentration environment during goethite formation (Section 2.6.5.8). The smaller acicular particles (labelled “2” in Figure 7-23) were still partially encapsulated by amorphous silica (labelled “3” in Figure 7-23) which is believed to contribute to the acid resistance in this sample.

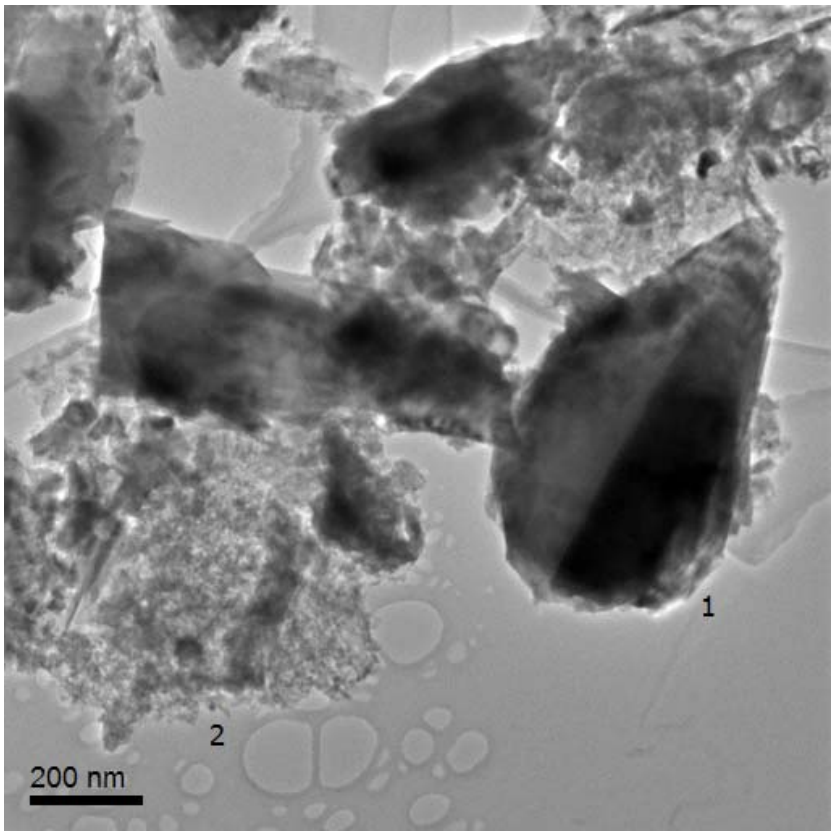

(a)

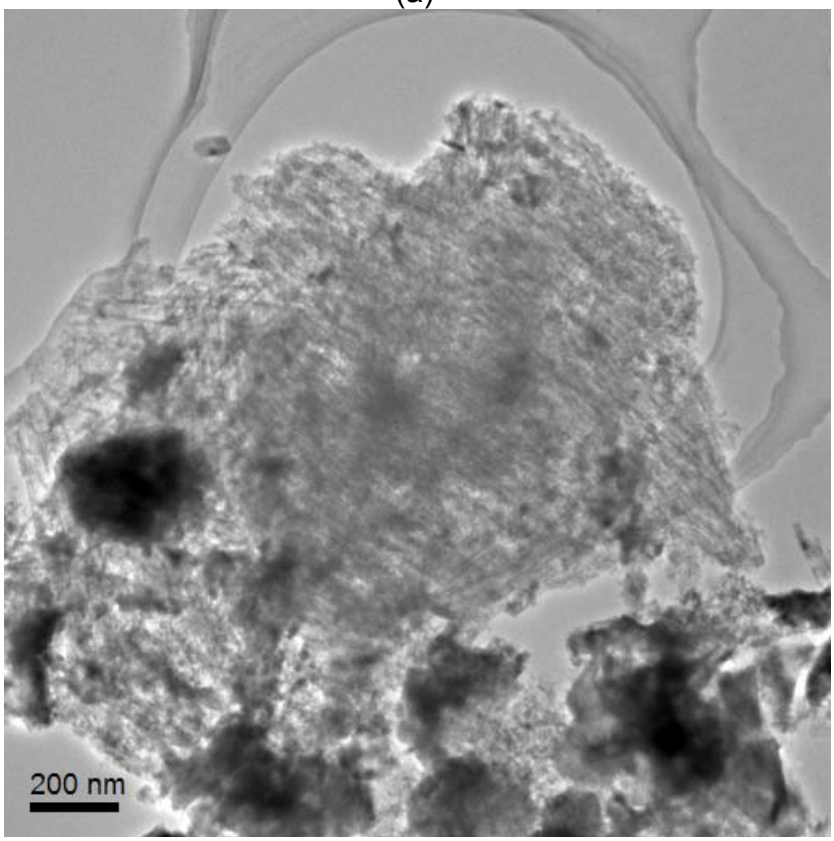

(b)

Figure 7-22 TEM images of the AL residues of sample A15 (a) a large single domain goethite particle labelled as “1” and small goethite labelled as “2” in amorphous silica; (b) amorphous silica with needle like texture;

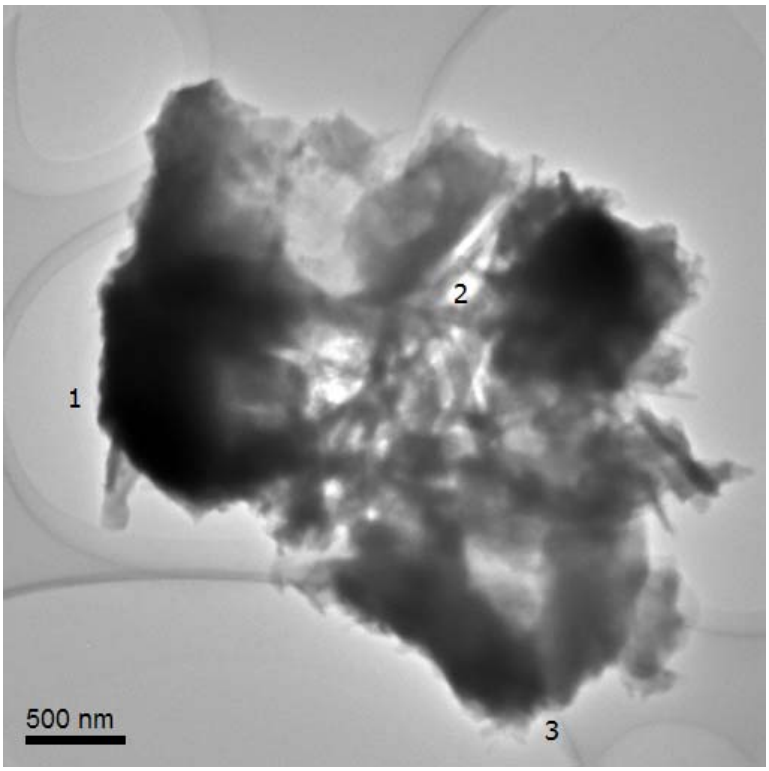

Figure 7-23 TEM images of the acid leached residues of sample A5. Single domain goethite labelled as “1”, acicular goethite crystals labelled as “2”, and amorphous silica labelled as “3”

From the corresponding EDS information in Table 7-1, the electron dense iron oxide residue (Figure 7-24a1) in the slow leaching sample B11 is closely associated with the surrounding granular amorphous silica (Figure 7-24a2), from which most of the iron had been leached. This again supports the proposal that iron oxide particles were interlaced with amorphous silica in the feed sample. The silica residue in the sample shown in Figure 7-24b did not produce a diffraction pattern indicating it is amorphous silica.

Needle shaped goethite particles were also noted to be embedded in kaolinite layers in the acid leached residue of fast leaching sample D5 (Figure 7-25), supported by the corresponding EDS information in Table 7-1. This morphology was not noted in the D5 feed sample. Once most of the acicular multidomain goethite was dissolved, this goethite-kaolinite association becomes dominant and is more likely to be captured by TEM observations. This also suggests the goethite-kaolinite association is acid resistant and explains why not all the goethite in sample D5 was dissolved.

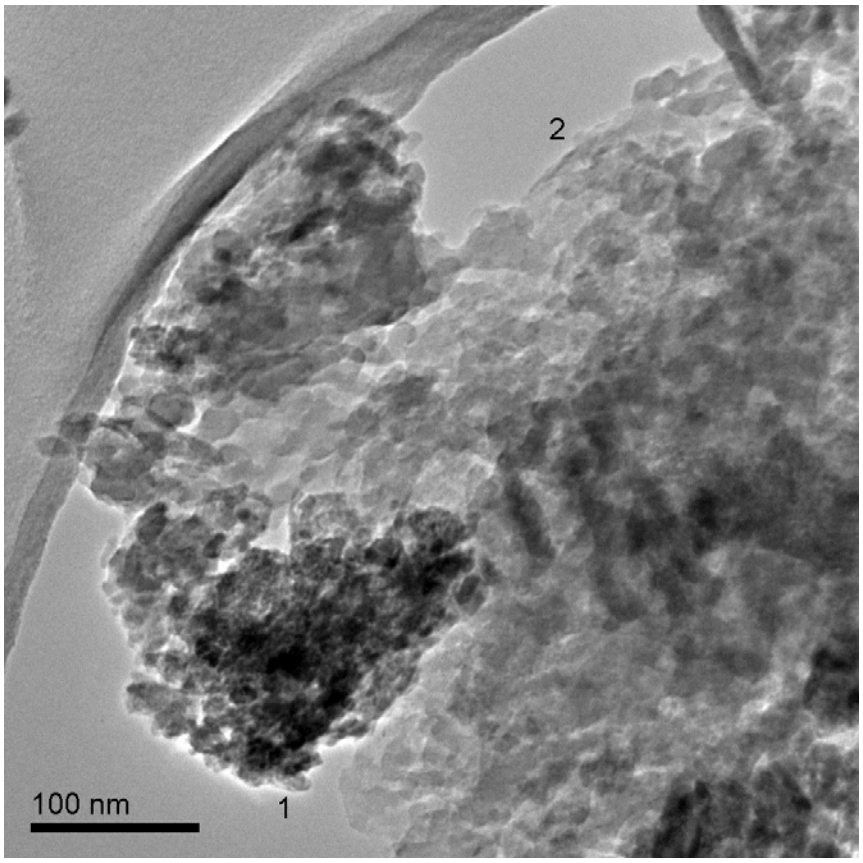

(a)

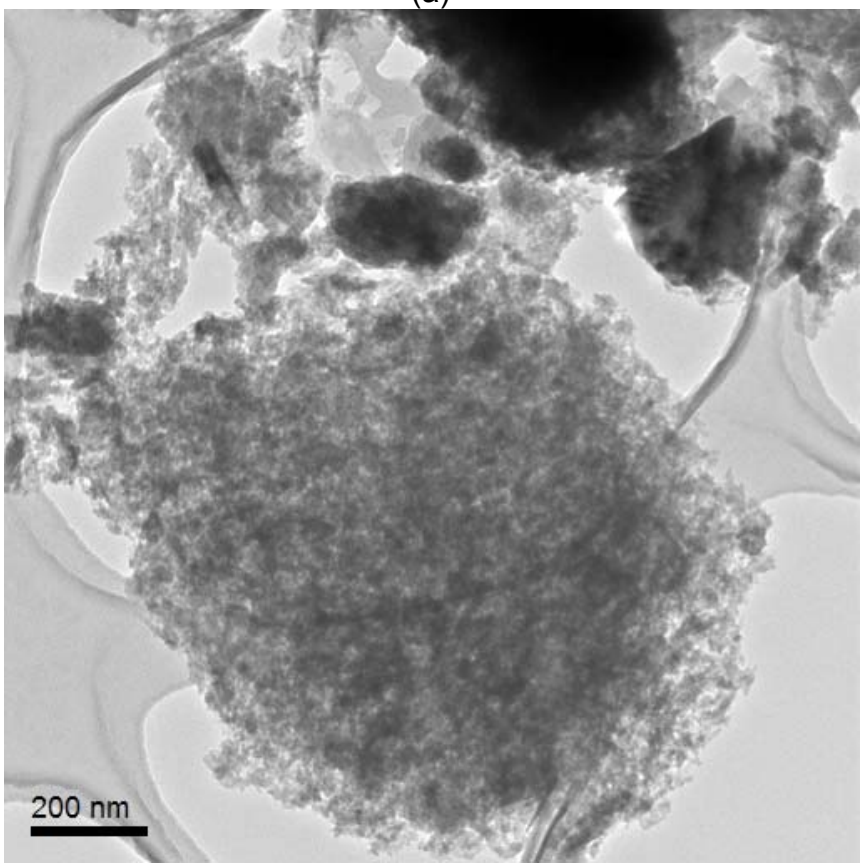

(b)

Figure 7-24 TEM images of the acid leached residues of sample B11 (a) residual goethite labelled as “1” and amorphous silica labelled as “2”; (b) amorphous silica;

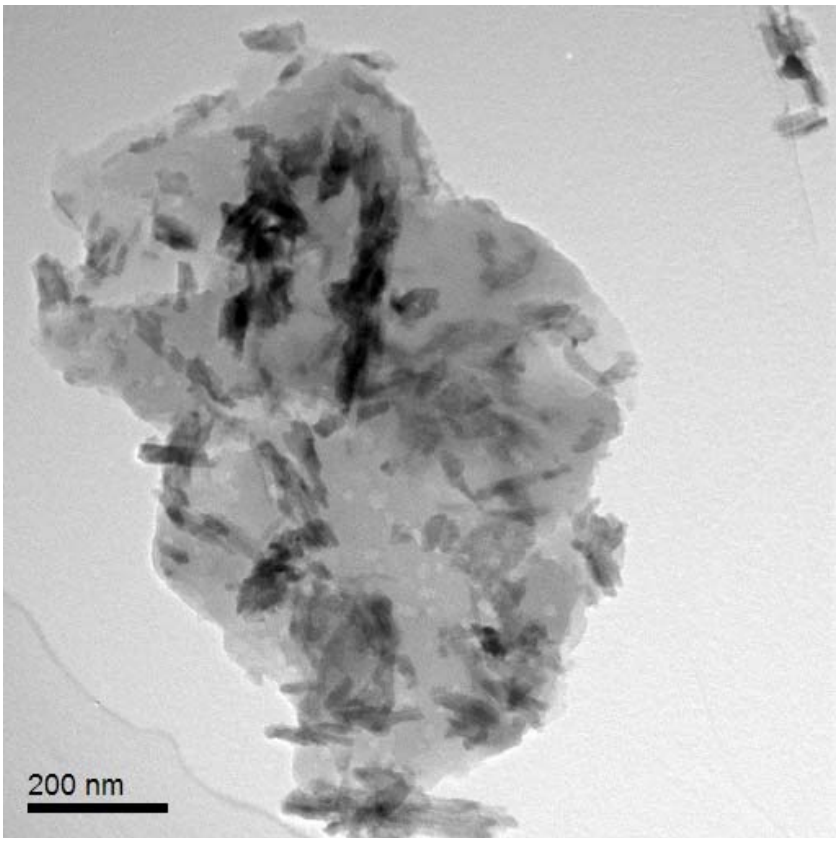

Figure 7-25 TEM images of the acid leached residues of sample D5. Goethite in kaolinite layers is still present in the leaching residue of fast leach sample D5

7.4.4 Particle morphology of sample after caustic digestion

The AL residues of slow leaching samples A15 and B11 were further digested in hot caustic liquor and the particle morphologies of the residue are shown in Figure 7-26 and Figure 7-27 respectively, with the corresponding EDS data reported in Table 7-1. Unlike the AL, which dissolved iron oxide but left the silica or the aluminosilicate framework intact, the caustic digestion broke up the cementations and released goethite particles. The EDS data (Table 7-1) of the released goethite particles in Figure 7-26 still show considerable levels of silicon and aluminium, which suggests the selected caustic digest conditions, while being able to liberate the goethite, were unable to completely dissolve all the silica and/or aluminosilicate. The morphologies of the caustic digested AL residue of sample B11 (Figure 7-27) shows similar features to sample A15. The cementations were collapsed, liberating both kaolinite residuals (Figure 7-27a1) and iron oxides particles (Figure 7-27a2).

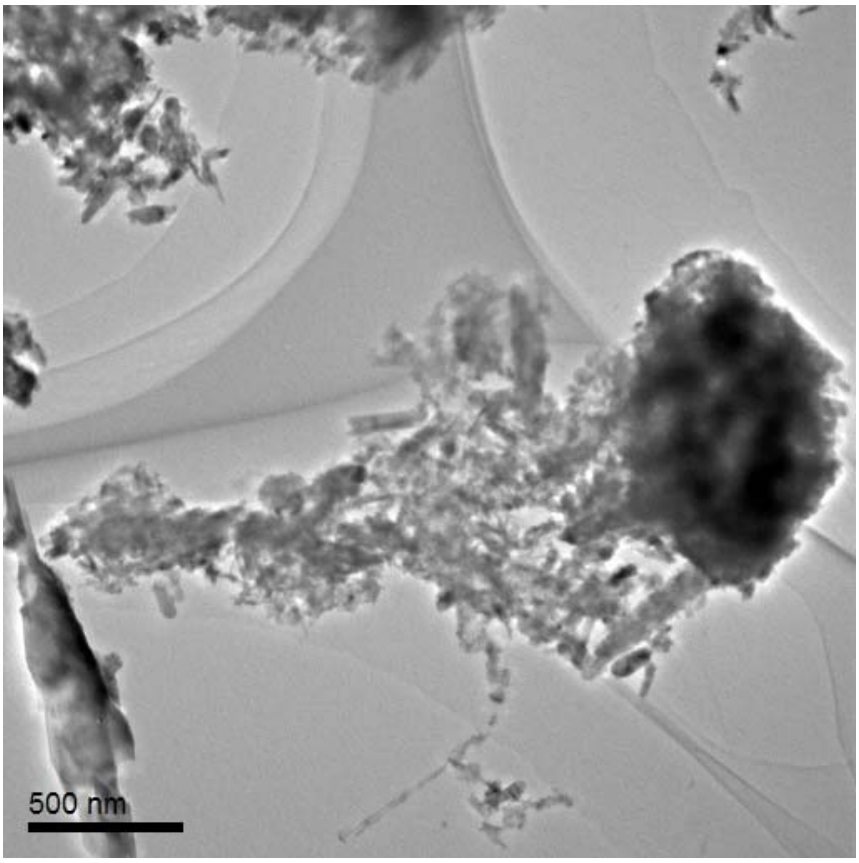

(a)

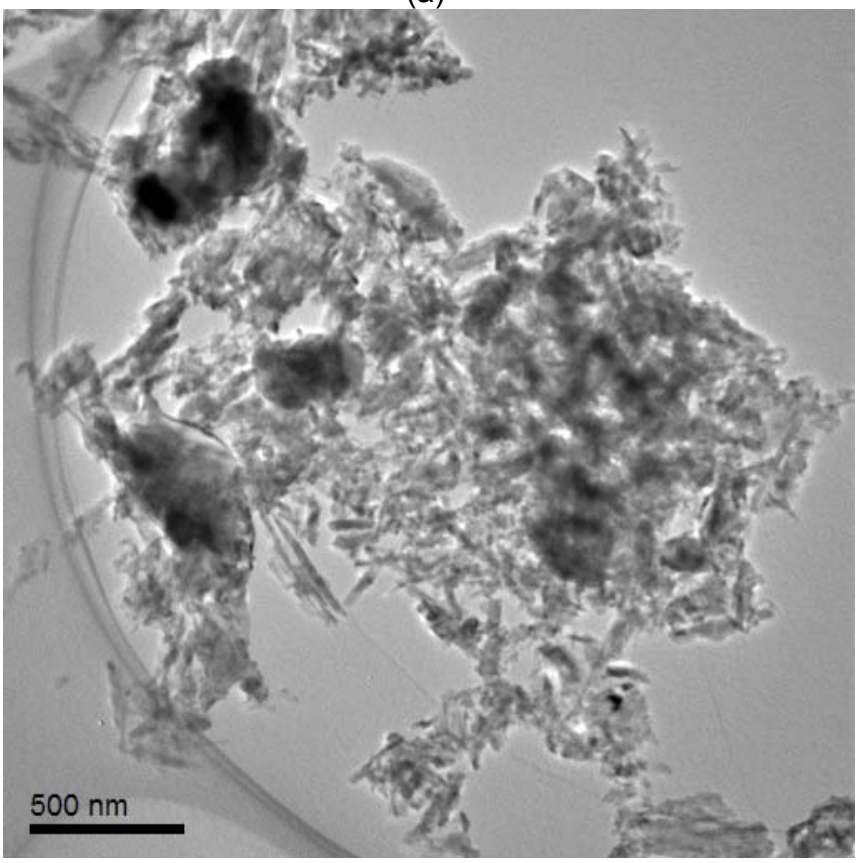

(b)

Figure 7-26 TEM images of the caustic digested residues showing liberated goethite particles from collapsed cementations in sample A15.

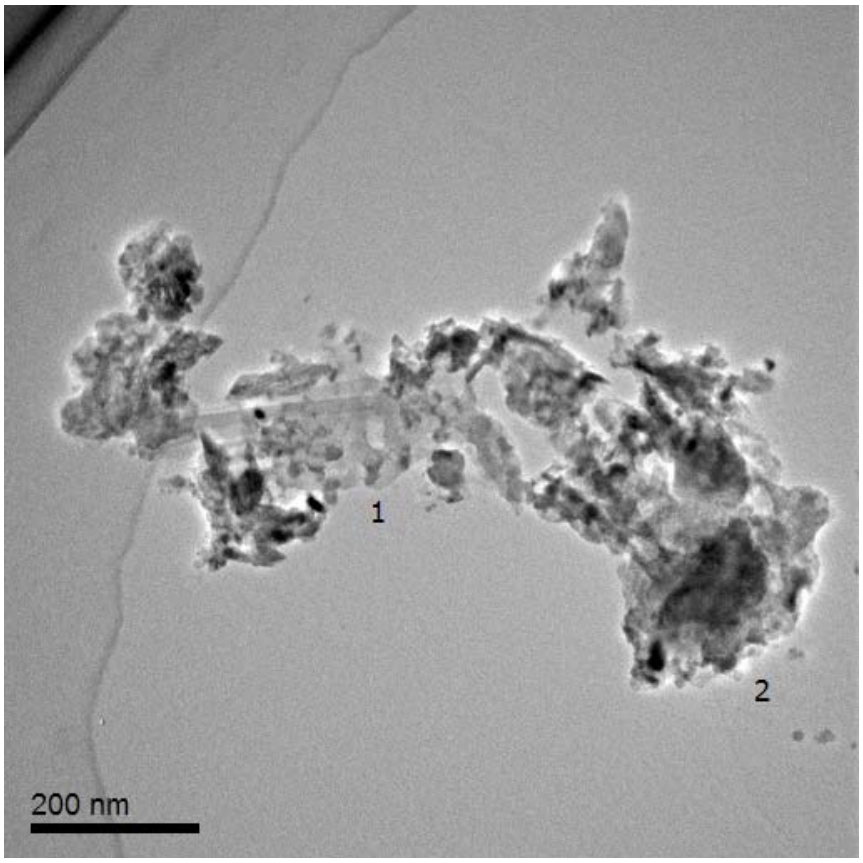

(a)

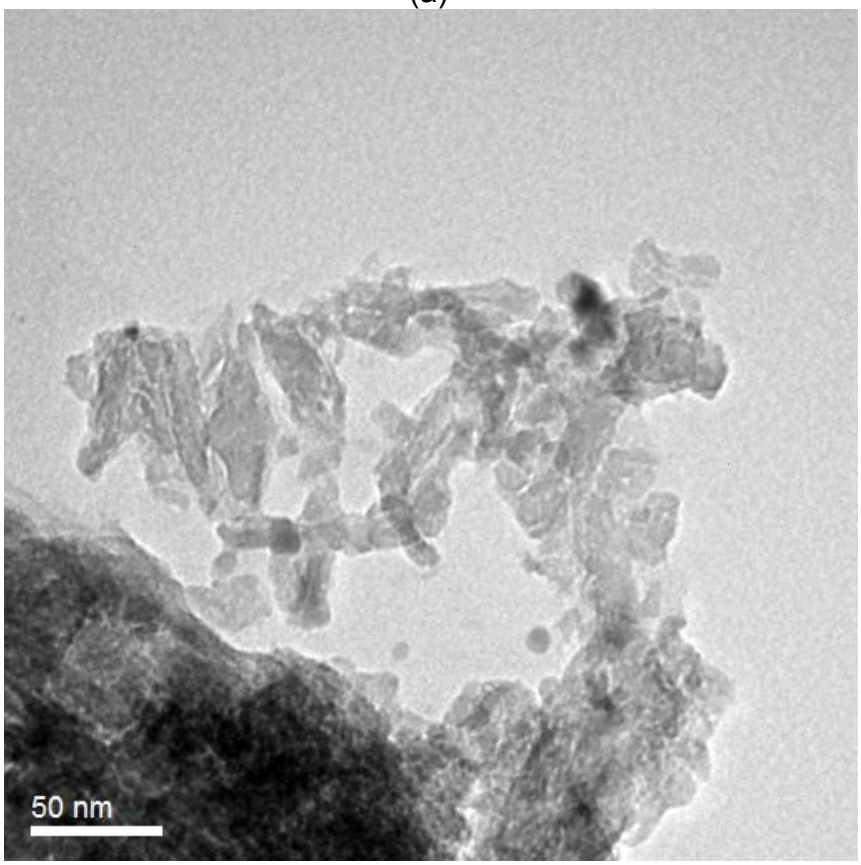

(b)

Figure 7-27 TEM images of the caustic digested residues showing liberated goethite particles from collapsed cementations in sample B11.

7.4.5 Effect of silicates on goethite formation

In contrast with fast leach samples (D3, A16, *etc.*), goethite in slow leach sample A15 does not have acicular morphology. This may be partly due to chromium structural substitution (Schwertmann *et al.*, 1989; Manjanna & Venkateswaran, 2002), as supported by the EDS data of the corresponding particles. The presence of the silica in the goethite growth environment may also account for the goethite morphologies and their acid leaching properties. For example, amorphous silica was reported to cement goethite due to the dehydration of $Si(OH)_4$ adsorbed on goethite surfaces, which provides the framework to mechanically immobilise clay minerals (Marsan & Torrent, 1989).

It is widely accepted that silicate species strongly hinder the nucleation of goethite and slows its growth rate. In laboratory experiments complete transformation of ferrihydrite and lepidocrocite to goethite in the presence of high concentration of silicate species can take many months (Schwertmann & Taylor, 1972a, b). Slow goethite growth results in the formation of large monodomain particles normally several hundreds of nanometers across in the direction perpendicular to [001] (Schwertmann & Taylor, 1972a, b; Cornell *et al.*, 1987; Glasauer *et al.*, 1999). These large goethite particles were less acicular than those normally observed as silicate species retard goethite growth in the [001] direction, resulting in a clear diamond tip, *i.e.* (021) crystal habit (Cornell & Giovanoli, 1987b; Cornell *et al.*, 1987; Glasauer *et al.*, 1999). Monodomain goethite is also observed in sample A15, as shown in Figure 7-22a1 as well as in Figure 7-28. The clear diamond shaped tip of goethite in sample A15 (Figure 7-28) indicates growth of the goethite in [001] direction may have been inhibited by preferential silicate species adsorption on the (001) face (Cornell & Giovanoli, 1987b; Quin *et al.*, 1988). Almost all of the large goethite particles investigated in slow leaching samples had low guest metal substitution based on EDS data in Table 7-1. From the view point of nickel extraction, leaching of these particles will not add economic value. In comparison, separation of the smaller goethite crystals, which do contain nickel from silica cementations, is a promising way of enhancing nickel extraction.

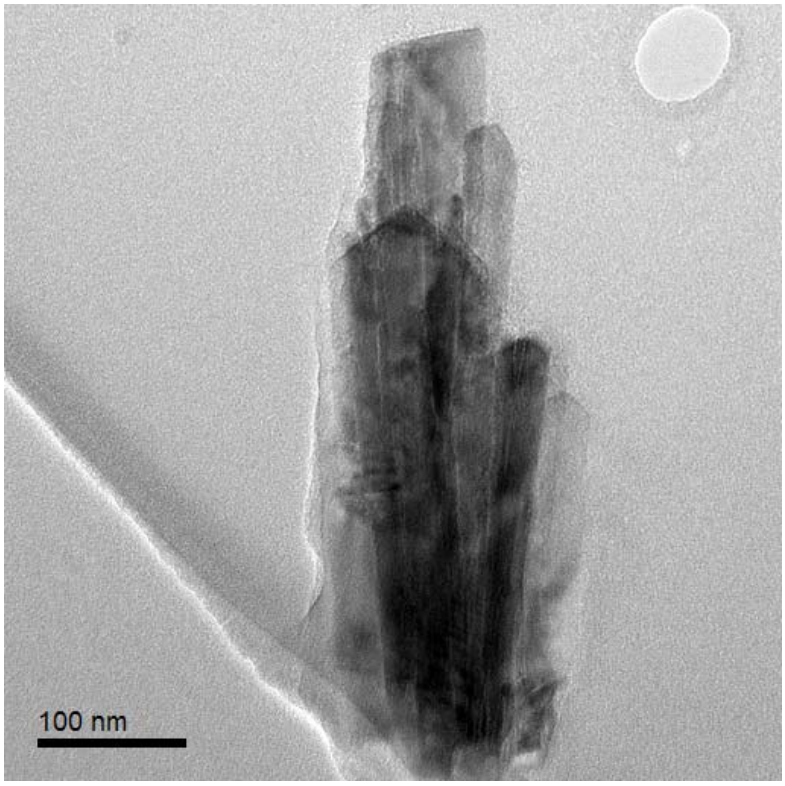

Figure 7-28 Goethite crystal with large domain and diamond shape tips in sample A15

As reviewed in Section 2.6.5.8, silicon is regarded as being difficult to incorporate into the goethite structure (Cornell *et al.*, 1987; Quin *et al.*, 1988; Mejía Gómez *et al.*, 2011). Goethite and silicate co-precipitation experiments (Glasauer *et al.*, 1999), silicon adsorption on goethite surface tests (Torrent *et al.*, 1992; Gerth *et al.*, 1993), and the characterisation of natural goethite morphologies (Smith & Eggleton, 1983) suggest that silicon is either adsorbed on the goethite surface or located at goethite domain boundaries. The present work indicates silica is closely associated with goethite in laterite samples but most of the silicon is not substituted into the goethite structure.

The epitaxial growth of goethite from kaolinite was reported for a laterite sample from Cameroon by Boudeulle & Muller (1988). Three of the successive goethite unit cells in the *c*-direction (space group Pbnm) are about the same size as two successive kaolinite unit cells in the *a*-direction (space group P1). As the kaolinite sheet presents a ternary symmetry, there are three possible epitaxial growth directions for goethite. The goethite

needles tend to position themselves with 120° separation angle. This was observed in sample B11 (Figure 7-18) of this study. The weathering of iron-kaolinite producing iron-free kaolinite and goethite in laterite from Israel was reported by Rozenson *et al.* (1982). As kaolinite is not easily dissolved in sulphuric acid, it also retards goethite dissolution. The sample B11 may come from a deeper zone of limonite in the profile in the early stages of weathering, while the fast leach samples with acicular goethite crystals might come from an upper zone where extensive weathering has been experienced and iron is better separated from other elements, such as silicon and aluminium.

7.5 Summary

To date, bulk chemical assay (ICP/XRF) and mineralogical phase quantitative analysis (QXRD) have not been able to predict nickel laterite ore leaching rates. In this chapter, STEM/TEM imaging and associated EDS elemental analysis and mapping are shown to be good techniques for distinguishing slow and fast leaching limonitic nickel laterite ores.

A detailed morphological characterisation of the fast and slow leach samples suggests the leachability of goethite in limonitic nickel laterite ores is distinguishable and predictable from the observations of goethite morphology and the physical association with other minerals, *i.e.* presence of silica or kaolinite cementations. Goethite crystals in fast leaching samples are normally acicular in shape, while goethite in slow leach sample tends to be locked in the goethite-silica cementations or paragenetically interlaced with kaolinite. STEM/EDS mapping was employed to demonstrate presence of silica networks within goethite cementations and, when kaolinite was present that most of the aluminium in the intergrowths is associated with silicon. The identification of these morphologies represents novel findings that explain the different leaching rates.

Atmospheric pressure leaching (AL) at elevated temperature is a fast tool to test the leachability of different laterite samples. Micrometer scale large goethite crystals were present in AL residues of slow leach sample A15. From the EDS data, these guest metal free large goethite crystals were more acid resistant than the small chromium substituted goethite crystals.

The amorphous silica co-present with goethite particles suggests these morphological features were slowly formed in a silicate rich environment. The paragenetic goethite growth with kaolinite results from weathering of the parent rock. This hypothesis is supported by the literature in Section 2.6.5.8 concerning the impact of silicate species on synthetic goethite morphology and natural goethite-kaolinite associations. Furthermore, these features probably arise from variations in the parent rock from which these materials and associated regolith have been formed.

Chapter 8 Verifying the inhibition effect of cementations on acid leaching

8.1 Introduction

In Chapter 7 it was demonstrated that the goethite-silica/silicate cementations might be responsible for the slow leaching of some laterite ores, and the follow on caustic digestion is effective in breaking up the cementation framework. This chapter describes a validation experiment to test the effect of a pre-treatment liberating goethite from cementations on the acid leaching rate of the slow leach laterite ores A15 and B11. The distributions of silicon, iron, and aluminium in cementations were further investigated using Energy Filtered Transmission Electron Microscopy (EFTEM) to acquire a better understanding of the cementation microstructure.

8.2 Experiment and materials

According to the AL leaching rates shown in Appendix 8, two slow leach laterite ore samples A15 and B11 (approximately 90 g of each original ore powder prepared in Section 3.2.1) were treated with 9 L of 5 M potassium hydroxide (KOH) liquor for 5.5 hours. The caustic digestion experiment conditions are detailed in Section 3.2.9. The pregnant liquors were analysed by ICP-OES. The solid residues were examined by ICP-OES, QXRD, TEM, and EFTEM to assess the mineralogy and morphology changes. A Bruker® D8 Discover with CoKα radiation (Section 3.2.3.2) was used to collect the XRD patterns. A JEOL® TEM 3000F equipped with a Gatan® image filter (Section 3.2.4.4) was employed to image the samples in EFTEM mode. The caustic digestion residues were then acid leached under the same AL conditions as used in Chapter 7 (detailed in Section 3.2.7) to test the leaching performance after liberation of the goethite crystals from goethite-silica/silicate cementations.

8.3 Mineralogy changes induced by caustic digestion

The mineralogical compositions of both laterite ore samples before and after KOH treatment are given in Table 8-1. It can be seen that the hot KOH

treatment dissolved kaolinite, and resulted in quartz and iron oxide phases being enriched in both samples. Nontronite previously present in the XRD pattern of B11 feed sample was not observed in the KOH treated residues (Figure 8-1). Smectite dissolution in hot caustic liquor has previously been reported (Bauer & Berger, 1998; Cama *et al.*, 2000).

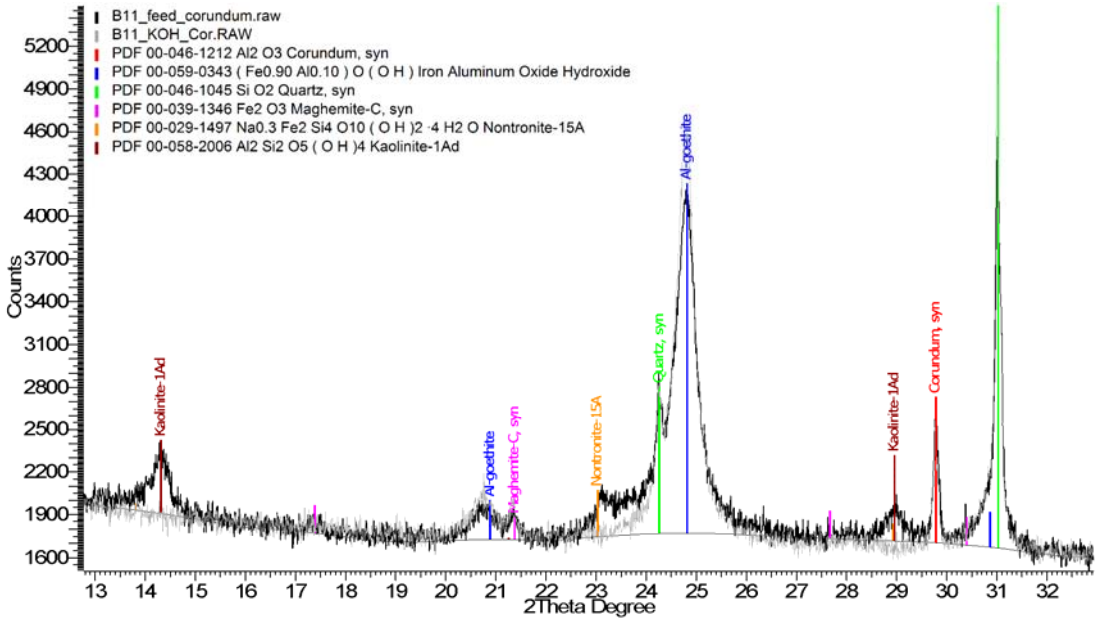

Figure 8-1 Comparison of the XRD patterns for sample B11 before (black) and after (gray) KOH treatment. Kaolinite and nontronite were removed by KOH treatment.

The ICP analysis results for the KOH digestion liquors from samples A15 and B11 (Table 8-2) suggest significant amounts of aluminium and silicon along with small amounts of sodium were dissolved. This can be explained by the dissolution of kaolinite and nontronite in KOH liquor. Sodium could also be dissolved from small amounts of soluble salt. Approximately 3 times more aluminium and silicon were digested from sample B11 than sample A15, which are consistent with the concentrations of kaolinite and nontronite in these feed ores (Table 8-1). Any nickel released from nontronite was not lost in KOH digestion liquor but was preserved in solids.

The ICP analyses of the solid samples pre- and post- KOH digestion are given in Table 8-3. The upgrade ratios for iron and nickel in both samples are similar to their sample mass loss ratios. Iron and nickel are better enriched in

sample B11 than in sample A15. The upgrade ratios for aluminium and silicon in both samples are less than unity, which is consistent with strong dissolution of these elements. That the upgrade ratio for silicon in sample A15 is much higher suggests it is more difficult to digest than in sample B11. This is because most of the silicon in sample A15 is present as quartz, which is essentially inert to the KOH treatment conditions used (Deleuze *et al.*, 1995). Furthermore when the absolute aluminium and silicon mass losses are compared, more silicon than aluminium is digested for both samples. Since kaolinite is expected to release approximately equal amounts of aluminium and silicon this means that other phases containing silicon were leached. For sample A15 this is probably amorphous silica, which is invisible to XRD analysis. For sample B11 nontronite dissolution in KOH treatment will release silicon. However amorphous silica is also likely to be present in the sample B11 as the amount nontronite in Table 8-1 would not release silicon more than twice as much as aluminium (Table 8-3).

Table 8-1 QPA results for samples A15 and B11 before and after KOH treatment based on the XRD patterns. The figures in brackets represent Rietveld calculated errors in the last decimal places.

Sample	Goethite	Quartz	Hematite	Maghemite	Kaolinite	Nontronite	Amorphous
A15 feed ore	49.07(23)	25.17(14)	-	0.845(95)	3.77(32)	-	21.1(10)
A15 digested	57.73(19)	29.09(13)	-	1.22(16)	-	-	12.0(13)
B11 feed ore	41.93(67)	5.89(11)	1.52(19)	8.44(19)	9.92(43)	4.88(33)	27.4(12)
B11 digested	56.75(21)	7.016(70)	1.92(18)	11.17(14)	-	-	23.1(11)

Table 8-2 Metal ion contents of KOH digestion liquors for sample A15 and B11.

	Concentration (mg/L)							
Sample	Ni	Al	Ca	Si	Fe	Mg	Na	K
A15	<0.2	122	3.79	265	3.03	<0.2	135	168341
B11	<0.2	389	4.82	762	4.42	<0.2	154	165576

Table 8-3 Metal contents for samples A15 and B11 before and after KOH treatment. The upgrade ratios for the solids mass and for Ni, Fe, Al, and Si are calculated.

Sample	Mass (g)	Concentration (wt.%)									
		Ni	Co	Mg	Mn	Fe	Al	Cr	Si	Ca	Na
A15 feed ore	89.3	0.423	0.025	0.196	0.065	31.9	2.12	1.60	17.0	0.002	0.042
A15 digested	77.2	0.536	0.032	0.371	0.092	38.9	1.10	1.77	14.2	0.161	0.013
Upgrade ratio	1.157	1.267	-	-	-	1.220	0.520	-	0.836	-	-
Absolute mass loss (g)	-	-	-	-	-	-	1.044	-	4.219	-	-
B11 feed ore	90.1	0.490	0.066	0.389	0.264	32.8	5.03	1.82	11.3	0.008	0.047
B11 digested	62.3	0.696	0.084	0.626	0.260	46.7	2.31	2.23	4.81	0.344	0.014
Upgrade ratio	1.446	1.421	-	-	-	1.423	0.458	-	0.426	-	-
Absolute mass loss (g)	-	-	-	-	-	-	3.093	-	7.185	-	-

8.4 Morphology of slow leach samples after caustic digestion

The TEM images of KOH treated sample A15 are shown in Figure 8-2. The EDS data of the corresponding particles are listed in Table 8-4. It can be seen that the acicular goethite crystals (Figure 8-2a1) and the anhedral electron dense iron oxide particles (Figure 8-2a2) were released from cementations. Figure 8-3 also shows that the needles of goethite and the anhedral iron oxide particles were released by the KOH treatment in sample A15, with the EDS data given in Table 8-4. The round and diamond shaped tips of goethite needles in Figure 8-2 and Figure 8-3 are similar to those observed in Figure 7-23 for sample A5 and Figure 7-28 for sample A15. These tip shapes suggest the goethite crystals were formed slowly in high silicon concentration conditions. The high chromium content in these goethite crystals may also contribute to their stumpy shape (Section 2.6.5.4).

The TEM images of KOH treated B11 shown in Figure 8-4 and the corresponding EDS data given in Table 8-4 also demonstrate the breakdown of silicate cementations and the release of iron oxide particles. The iron oxide particles were assumed to be goethite since it is the major phase in sample B11 (Table 8-1) as the electron dense particles preclude meaningful Selected Area Electron Diffraction (SAED) patterns being collected. The majority of these goethite crystals were irregularly shaped. Both large goethite crystals (>500 nm, Figure 8-5a3) and small goethite crystals (~ 100 nm, Figure 8-5a2) were observed. The size distributions of goethite crystals released from cementations in sample B11 shown in Figure 8-6 is skewed. About 50 % of the goethite crystals are smaller than 150 nm and nearly 20 % of the goethite crystals are larger than 450 nm, and this accounts for most of the goethite.

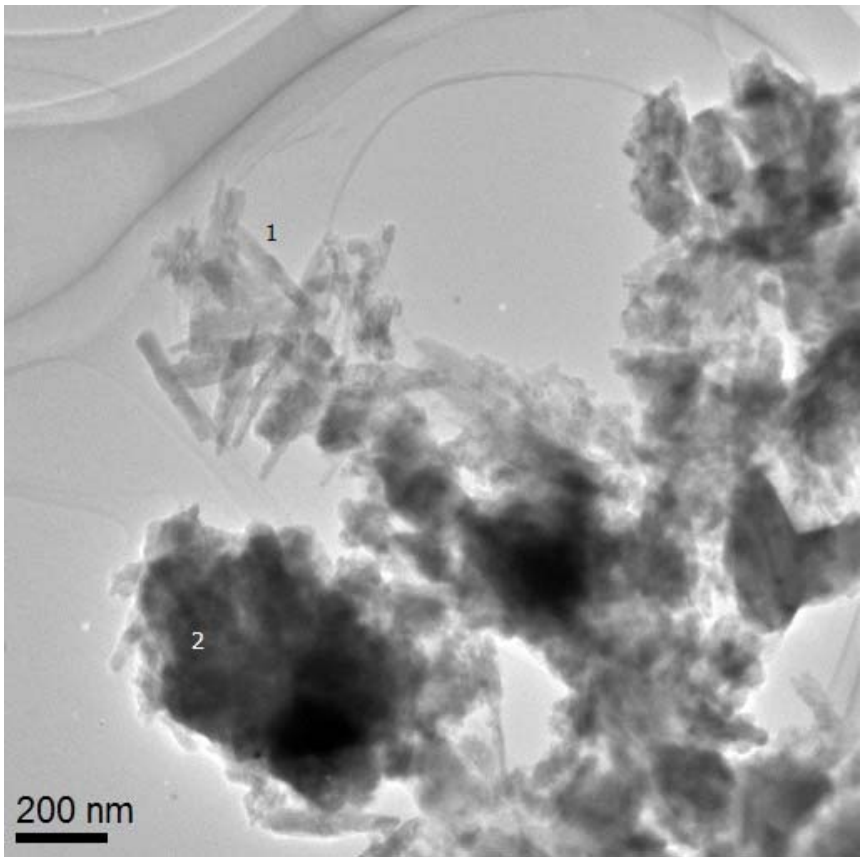

(a)

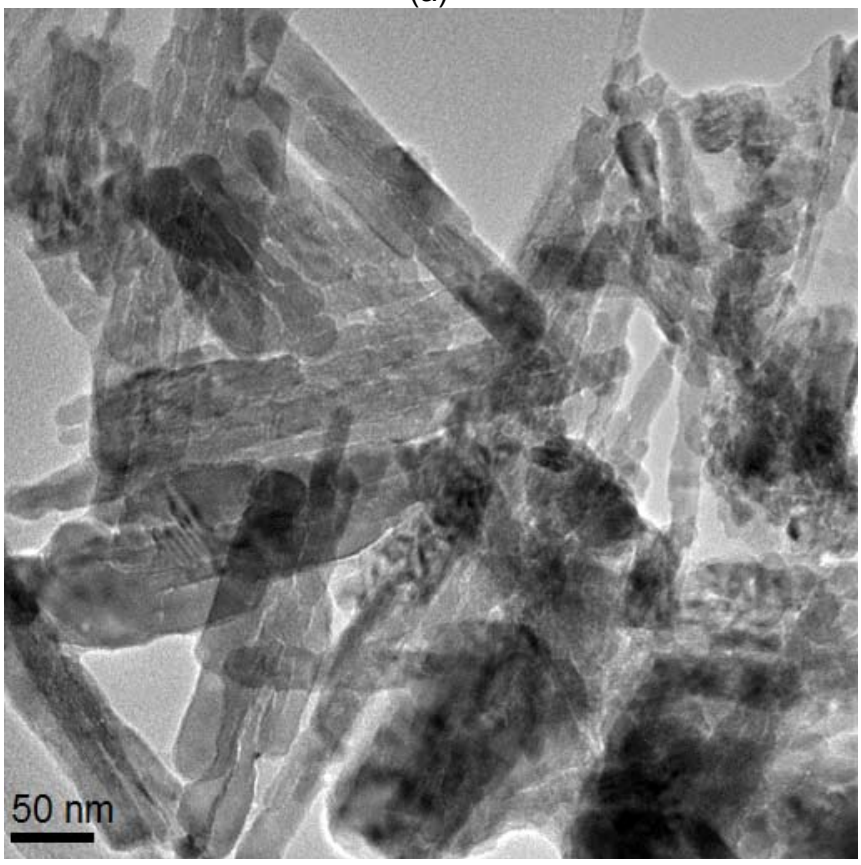

(b)

Figure 8-2 TEM images of KOH digested A15: (a) acicular goethite crystals released from cementations; (b) a1 at higher magnification: goethite needles with round tips.

Table 8-4 EDS results for selected particles shown in figures of this chapter

Particle	Sample	Mg	Al	Si	K	Ca	Cr	Fe	Ni	O
Figure 8-2a1	A15	0.49(2)	1.89(13)	5.20(14)			3.46(5)	61.4(4)	0.35(1)	27.2(1)
Figure 8-2a2	A15		1.76(13)	2.01(9)			1.88(2)	69.3(7)	0.34(2)	24.7(5)
Figure 8-3b1	A15	0.79(4)	4.14(16)	6.24(15)	0.21(2)	0.25(2)	3.71(5)	55.1(4)	0.45(3)	29.1(4)
Figure 8-3b2	A15	0.59(3)	5.79(16)	3.33(12)			4.10(8)	58.3(3)		27.9(1)
Figure 8-4a1	B11		2.65(14)	2.40(15)			1.27(2)	67.6(6)		25.5(3)
Figure 8-4a2	B11	1.11(4)	4.57(15)	4.36(13)			2.55(4)	58.7(5)	0.72(1)	28.0(1)
Figure 8-4a3	B11	0.75(3)	4.00(14)	3.35(12)			3.60(5)	60.9(4)	0.33(2)	27.1(2)
Figure 8-4a4	B11	4.51(12)	4.36(17)	22.5(3)	5.0(1)		1.44(2)	21.6(3)		40.4(4)
Figure 8-4b1	B11	4.14(12)	5.38(12)	14.2(2)			1.25(2)	35.2(5)	1.18(9)	35.5(4)
Figure 8-4b2	B11	5.06(12)	10.8(2)	24.0(3)	5.6(1)		0.86(2)	8.68(13)	0.65(7)	44.4(5)
Figure 8-4b3	B11		3.69(12)	3.06(11)			1.33(2)	64.1(5)	1.06(9)	26.3(3)
Figure 8-5a1	B11	5.07(14)	8.1(2)	19.7(2)	3.4(1)		3.64(5)	18.5(3)	0.87(8)	40.8(5)
Figure 8-5a2	B11	1.25(4)	4.20(11)	7.2(2)	0.49(4)		2.42(4)	53.7(5)	0.36(2)	29.8(2)
Figure 8-5a3	B11	0.73(3)	0.72(8)	1.38(4)			6.82(11)	65.3(5)	0.38(2)	24.7(5)

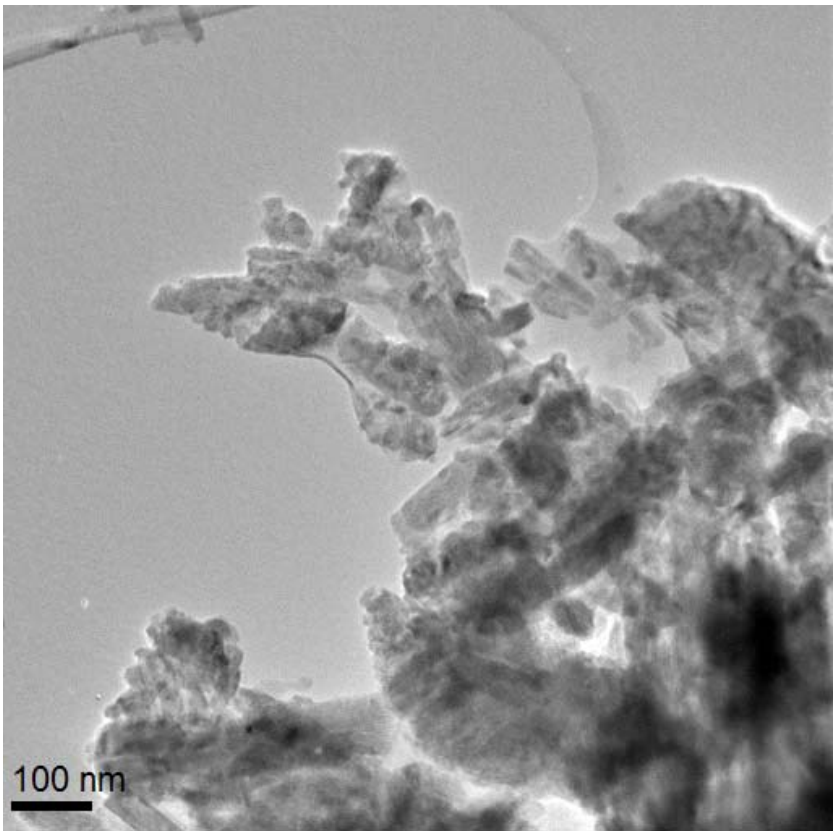

(a)

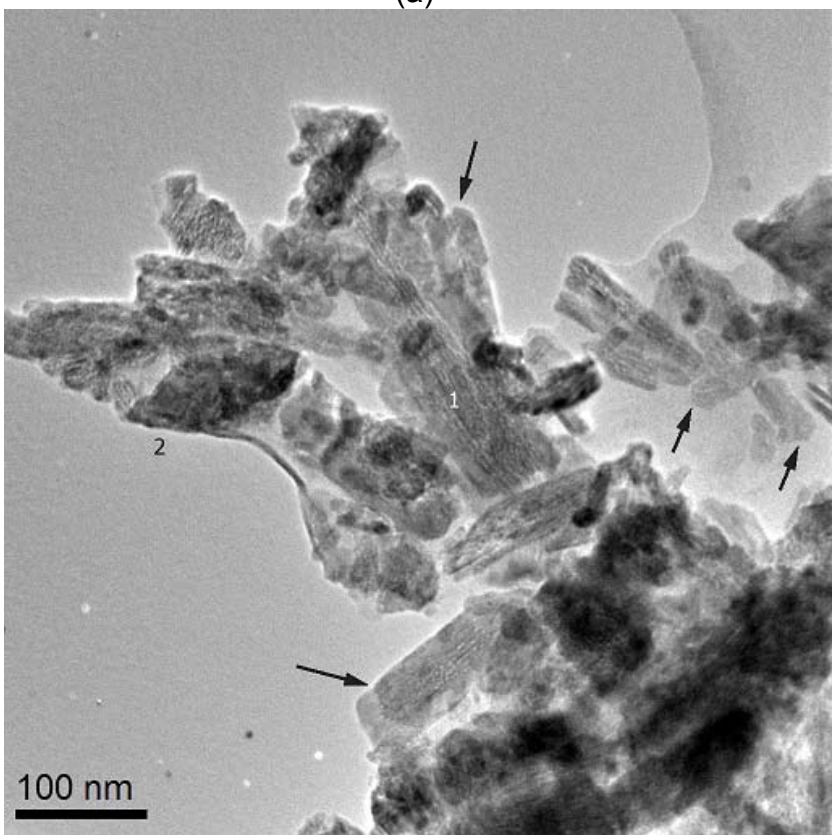

(b)

Figure 8-3 TEM images of KOH digested A15: (a) acicular goethite crystals released from cementations; (b) higher magnification image: goethite needles with round and diamond shape tips (arrows).

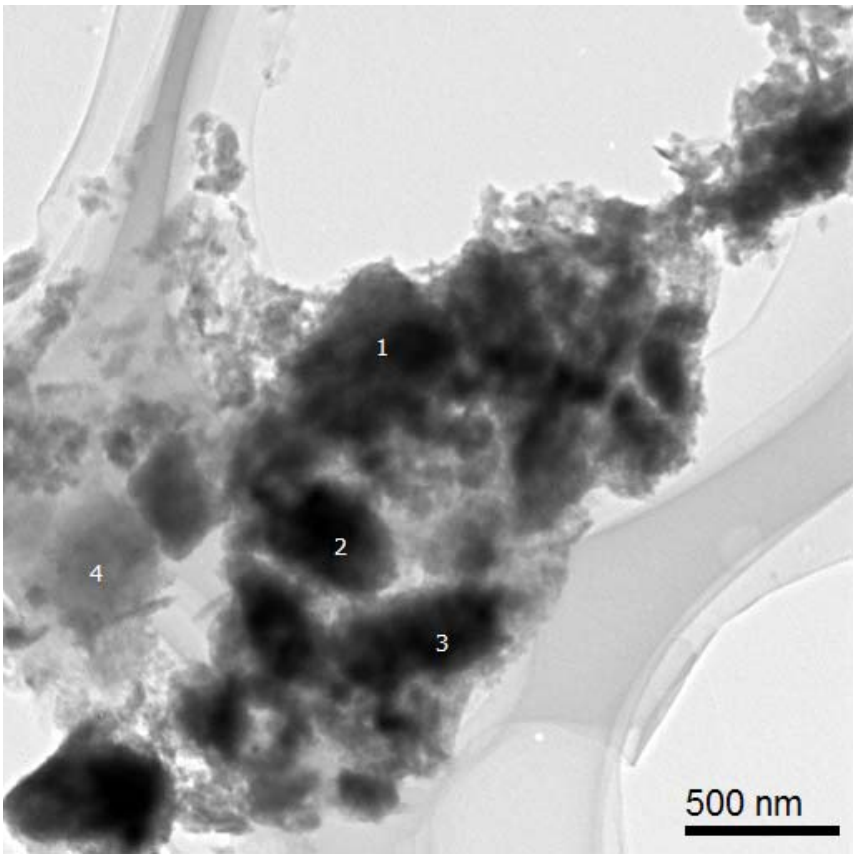

(a)

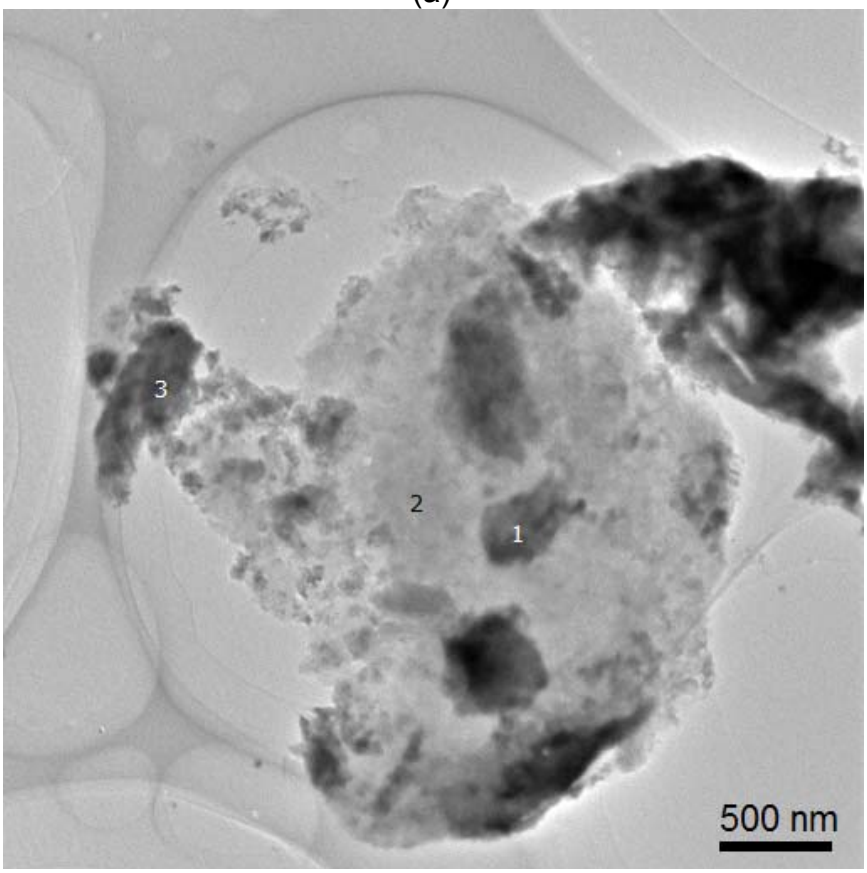

(b)

Figure 8-4 TEM images of KOH digested B11 showing collapsed cementations and the released iron oxide particles (a, b).

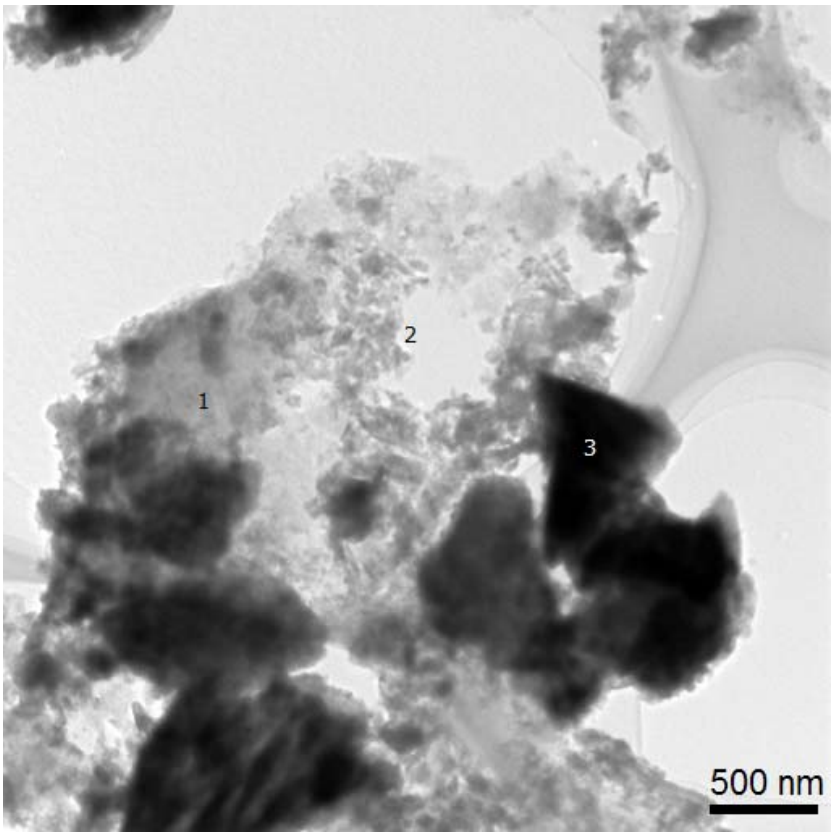

(a)

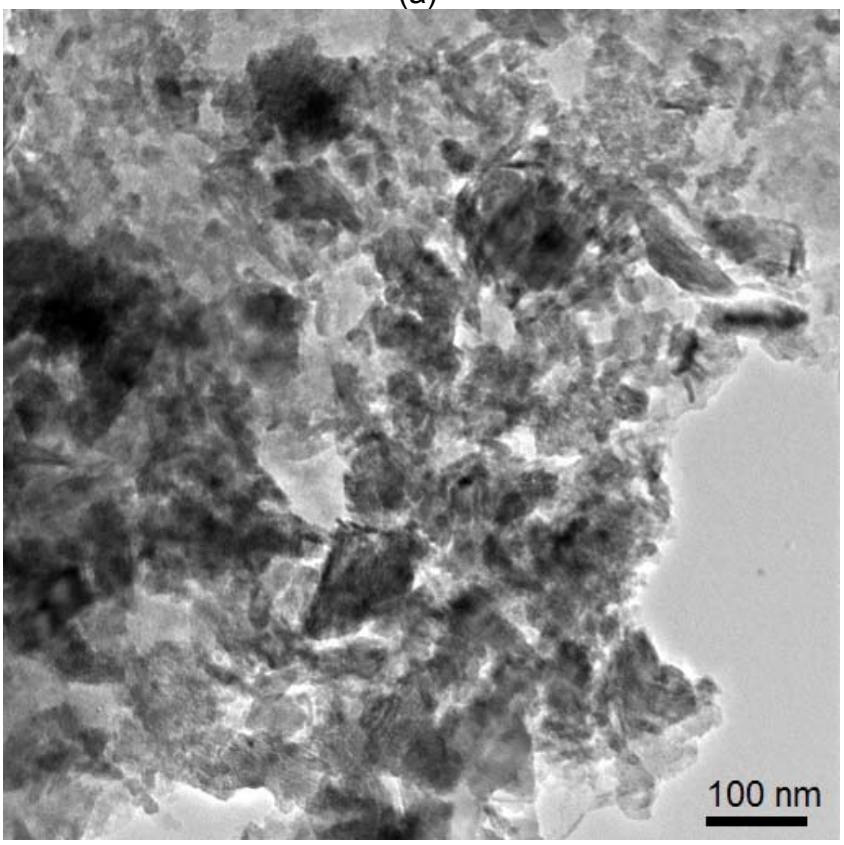

(b)

Figure 8-5 TEM images of KOH digested B11: (a) collapsed cementation and the released large iron oxide particles; (b) a2 at higher magnification: small goethite particles.

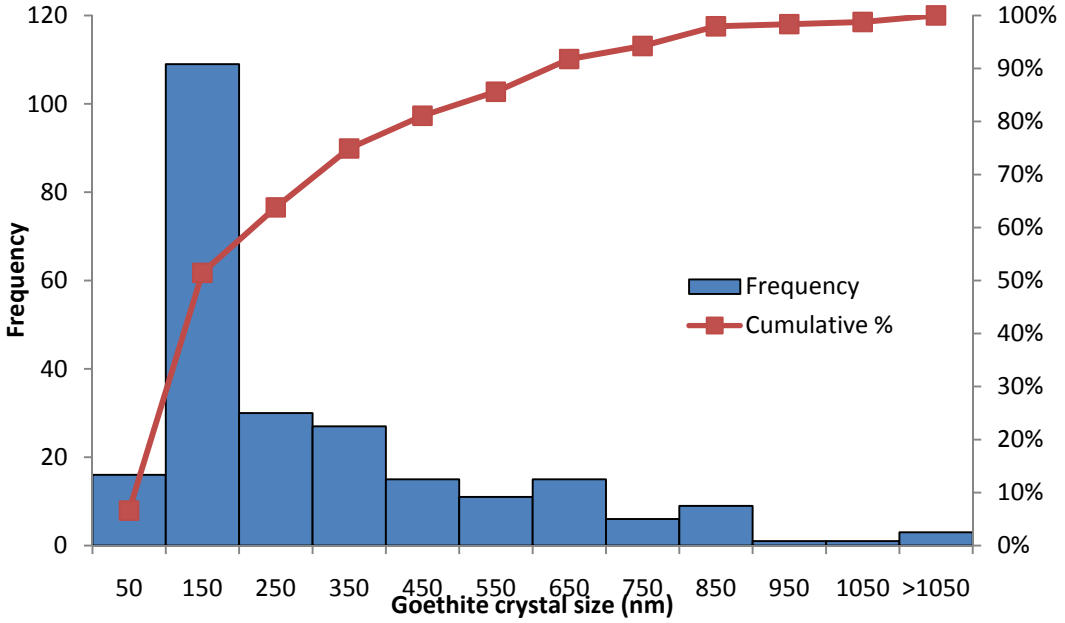

Figure 8-6 Size distribution of goethite crystals released from cementations in sample B11. This distribution is based on 242 goethite crystals measured from TEM images of KOH treated B11. The longest dimensions of goethite particles were measured.

8.5 Silicon, aluminium, and iron locations in released goethite

It is clear for the morphologies of KOH treated particles that the cementations previously holding goethite crystallites together had collapsed. However, certain levels of silicon and aluminium were still preserved in the KOH treated samples according to the EDS data in Table 8-4. In order to examine the relationship between silicon and iron, the laterite ore samples A15 and B11 before and after KOH treatment were imaged using the EFTEM technique (Section 3.2.4.4).

Rather than collecting the chemical information from a whole spectrum for each pixel in STEM/EDS mapping (Figure 7-19), EFTEM produces images using electrons with a specific energy loss. Therefore EELS addressing the chemical composition of the whole area of interest should be collected first so that the major elements to be mapped can be identified. A typical EELS of goethite particles in WA laterite ore samples D4 is shown in Figure 8-7.

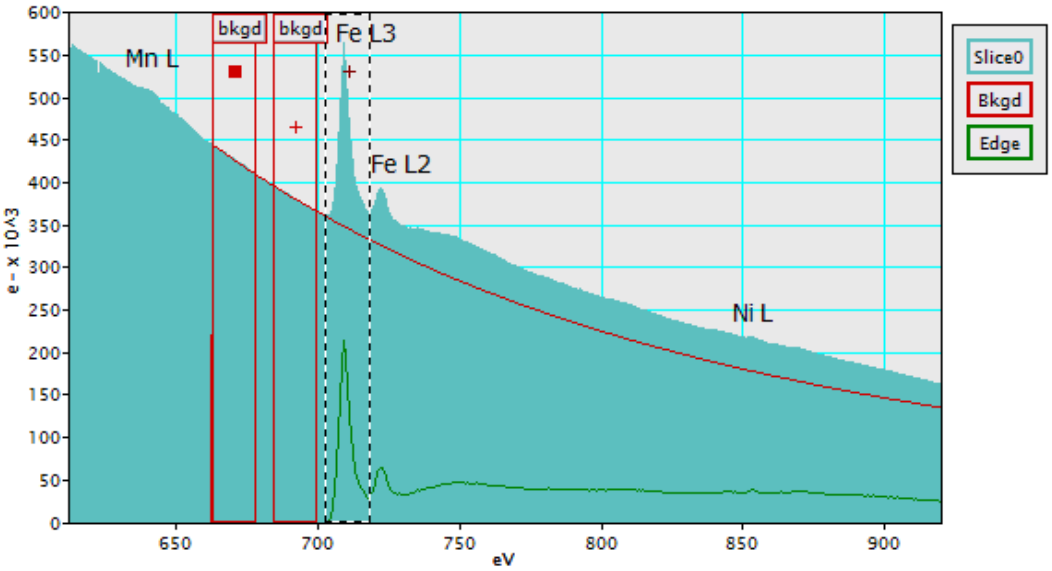

Figure 8-7 Part of the EELS (cyan) of the electron energy loss from 610 to 920 eV for goethite particles in sample D4 shown in Figure 8-8. The ionisation edges are superimposed on a slanting background due to the edge tails accumulated from lower energy losses. Electron counts in two energy windows (red) prior to the signal edge (Fe L_3) are fitted to a power law to extrapolate the background beneath the signal edge (Hofer & Warbichler, 2005, p62). The background (red) subtracted energy loss edge is given by the green line. The electrons with energy loss in the (dashed) window were used to generate an element map after background subtraction.

Mapping silicon in iron rich samples is difficult because the silicon L_3 edge (99 eV) is strongly affected by the adjacent iron M_1 edge (95 eV). Silicon mapping requires use of electrons with high energy loss at the silicon K edge (1839 eV). However, the intensity of electrons with this high energy loss is low, therefore a prolonged data collection time is required, which could induce goethite dehydration due to the high beam current. Particular care was taken to avoid data being taken from beam damaged or deformed goethite crystals by comparing the particle shapes before and after EFTEM mapping.

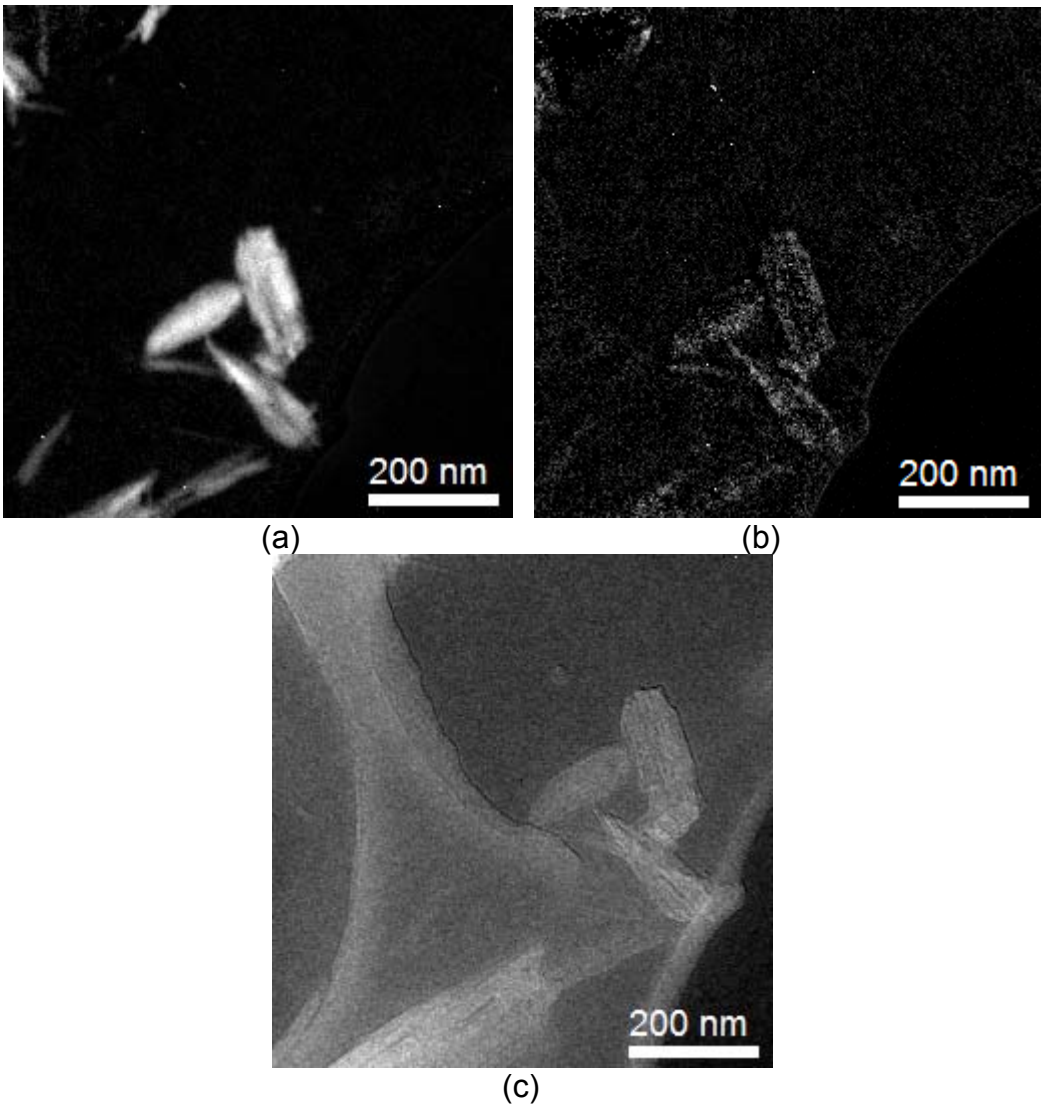

(a) (b)

(c)

Figure 8-8 Typical EFTEM element maps for selected element (a) Fe, (b) Ni, and (c) the thickness map for the area of interest consisting of three goethite crystals in sample D4. Ni is intimately associated with Fe. The thickness map (Figure 8-8c) derived from the image generated by zero loss electrons compared with that generated by unfiltered electrons (Malis *et al.*, 1988) gives a better idea of whether the positive signal is due to a thicker sample or due to real spatial distribution.

The EFTEM elemental maps for a cementation in sample A15 sitting on the edge of carbon film are shown in Figure 8-9. The unfiltered TEM image (Figure 8-9a) demonstrates that this is a parallel needle textured cementation similar to that observed in Figure 7-16c. The oxygen map and the iron map have similar contours within the cementation indicating this particle is predominantly iron oxide. Aluminium is rich in the central and left (iron rich) electron dense zones (Figure 8-9e), consistent with the thickness map

(Figure 8-9b). It is reasonable to assume that aluminium is substituted into the goethite structure. In contrast, the silicon map (Figure 8-9f) does not coincide with the aluminium map (Figure 8-9e) which indicates that kaolinite is not present within this cementation. Instead the silicon is spread out across the cementation but mostly rich in the left thinner zone and aggregated in discrete islands. It is therefore plausible to conclude that silica is cementing goethite needles. The EELS from 450 to 1950 eV shown in Figure 8-10 suggests no other element is present in this cementation except chromium. The low concentration of chromium and the overlap of the oxygen K edge tail (Figure 8-10a) prevented meaningful chromium mapping.

The EFTEM element maps of released acicular goethite crystals in the KOH digested sample A15 are shown in Figure 8-11. The goethite crystals have diamond shaped tips and internal domains along the long axis (Figure 8-11a). The coincidence of the iron map and the oxygen map confirms the needles are iron oxide particles. The internal domain structure can be also observed in the aluminium map (Figure 8-11e) which supports the contention that aluminium is substituted into the goethite crystal structure for sample A15. The silicon map (Figure 8-11f) neither coincides with the aluminium map nor with the iron map. It indicates the goethite diamond tip is covered by a layer containing silicon. It is also concluded that the goethite diamond tip is a result of silica adsorption, and this agrees with earlier reports summarised in Section 2.6.5.8, though it should be noted that the layer of silicon observed may have formed during and subsequent to the KOH treatment. However, at least two points can be drawn from the current observations for sample A15: 1) Silicon does not substitute into goethite structure; 2) the goethite tip (021) face readily adsorbs silica.

Figure 8-9 suggests silicon is spread across goethite-silica cementations; and Figure 8-11 suggests silicon is not substituted in goethite structure. It is highly probably that the cementations in sample A15 are silica cementing goethite.

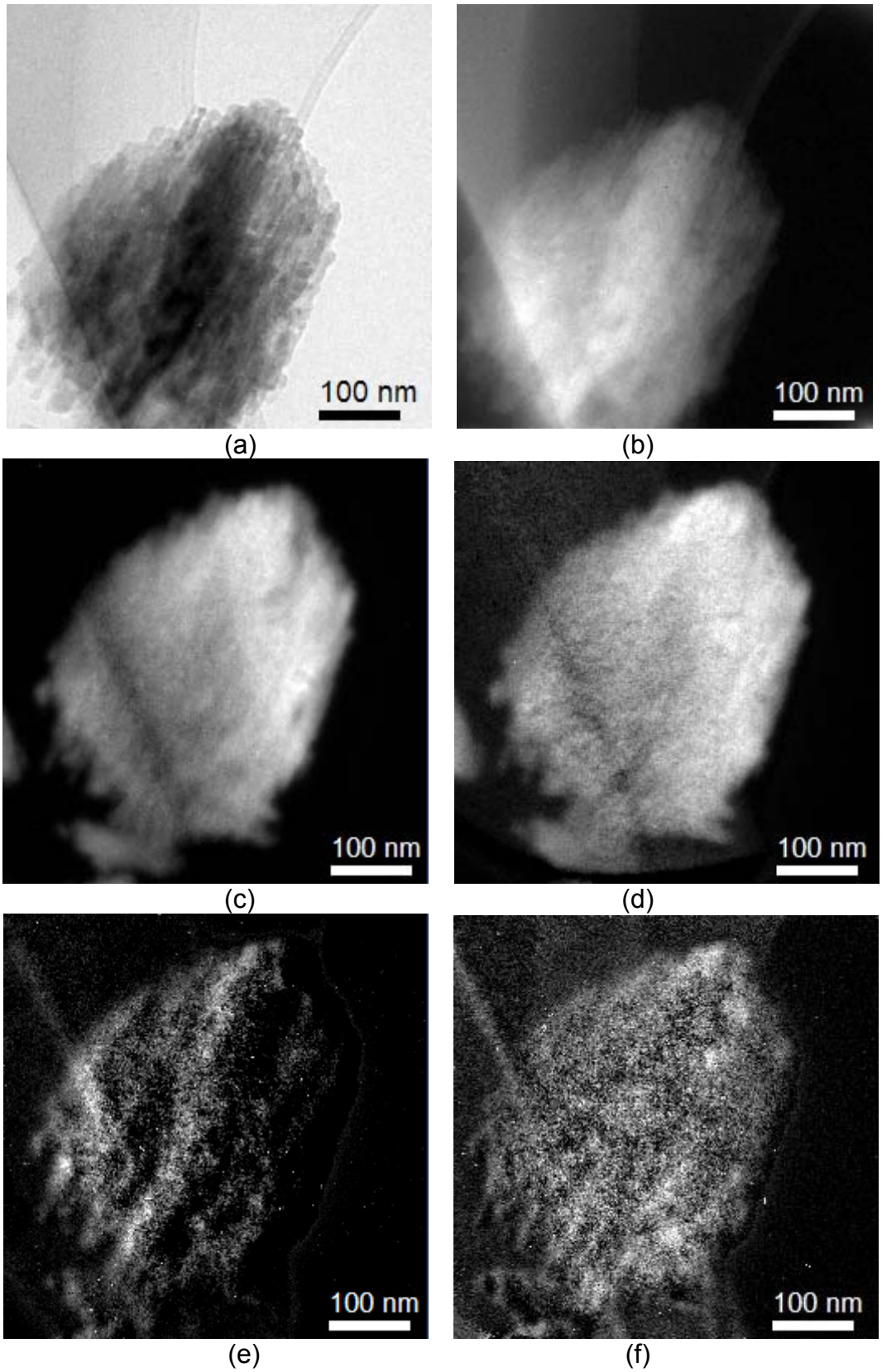

Figure 8-9 EFTEM element maps of a cementation sitting on the carbon film in sample A15. (a) Unfiltered TEM image; (b) thickness map; (c) Fe map; (d) O map; (e) Al map; and (f) Si map. All the images are dark field images except (a).

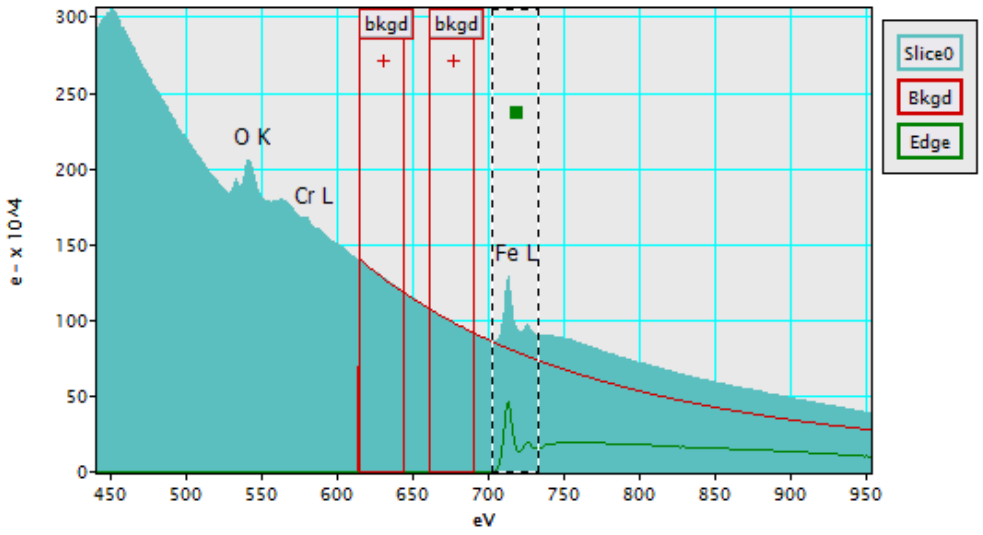

(a)

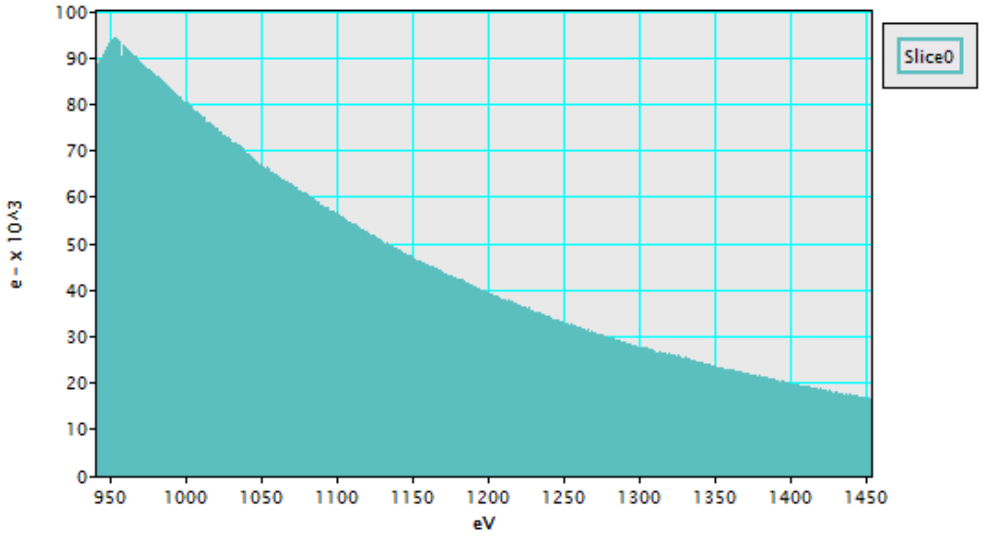

(b)

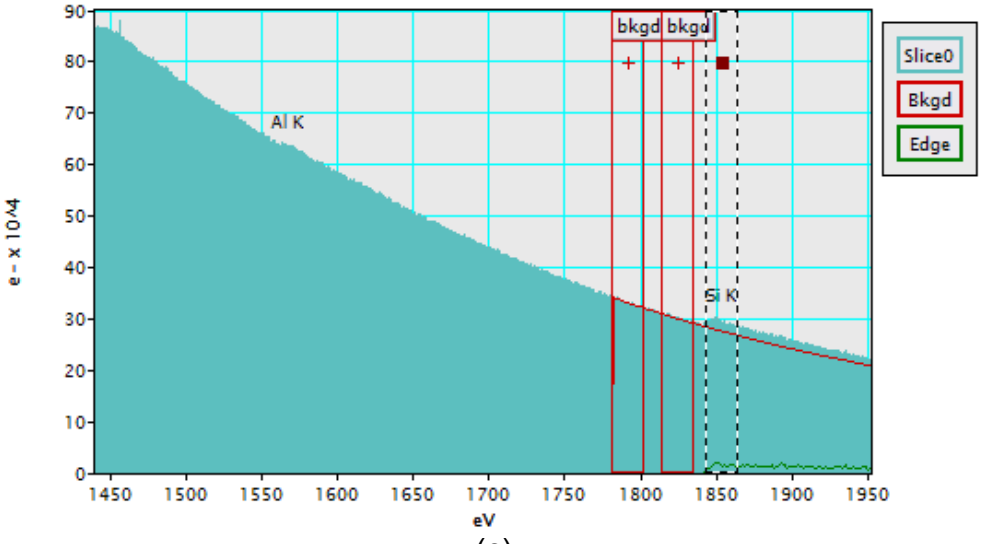

(c)

Figure 8-10 EELS of the cementation shown in Figure 8-9 at consecutive energy loss ranges (a), (b), (c) indicate only Fe, O, Si, Al, and Cr are detected. The two window background subtraction for EFTEM is similar to that employed in Figure 8-7.

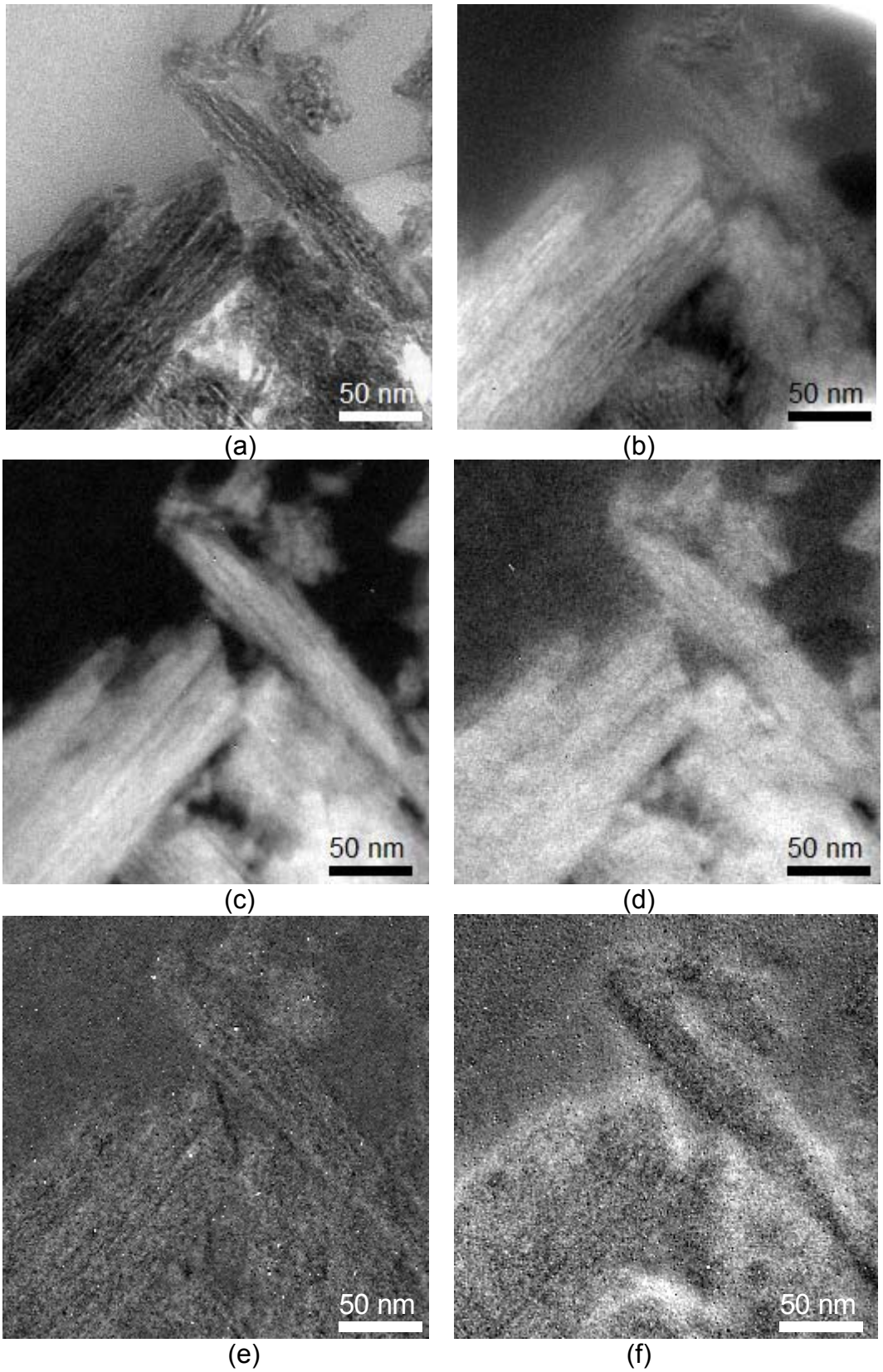

Figure 8-11 EFTEM element maps of the released acicular goethite crystals for KOH digested sample A15: (a) unfiltered TEM image; (b) thickness map; (c) Fe map; (d) O map; (e) Al map; and (f) Si map. All the images are dark field images except (a).

The EFTEM element maps of KOH digested sample B11 are shown in Figure 8-12. As also noted in Figure 8-5b, the goethite crystals released from sample B11 are not needle shaped. However, the internal domains could still been observed in these anhedral goethite crystals (Figure 8-12a). The iron map and oxygen map suggest that several particles in the central to left side of the image are iron oxide. The thickness, oxygen, aluminium, and silicon maps suggest the large thicker particle on the right side is aluminium silicate. According to the phase identification data for the B11 feed ores (Table 8-1), the several anhedral particles in the central to left side should be goethite and the large particles on the right side should be kaolinite. Although the amount of kaolinite is below the detection limit of laboratory XRD for KOH digested sample B11, it can be observed by TEM imaging. The aluminium map still indicates an appreciable amount of aluminium is hosted in goethite crystals, while most aluminium is in kaolinite of sample B11.

A similar morphology of the released goethite crystals for KOH digested sample B11 is shown in Figure 8-13. The iron and oxygen maps indicate several anhedral particles in the centre are iron oxide. These are assumed to be goethite as described previously. By analogy, the thickness, oxygen, aluminium, and silicon maps suggest a large thinner plate at the top of the image is aluminium silicate and is likely to be kaolinite. The iron map also shows several small iron oxide particles are co-located with the top right of the kaolinite flake. If these iron oxide particles were attached to the surface of the kaolinite flake, it should give a brighter signal in the thickness map. However, the thickness map (Figure 8-13b) of the top kaolinite flake is quite homogeneous. This suggests the iron oxide particles are intergrown with the kaolinite flake rather than attached to the flake surface.

Figure 8-12 and Figure 8-13 demonstrate the close association of goethite and kaolinite in sample B11. This is consistent with the Bulong laterite profile (Figure 2-2) in which goethite and kaolinite are the major phases in the limonite zone. EFTEM elemental maps indicate these phases were formed paragenetically, as described in Section 2.6.3. This might be the reason for the slow leach of sample B11. The KOH treatment removed most of the kaolinite and successfully released goethite crystals from sample B11.

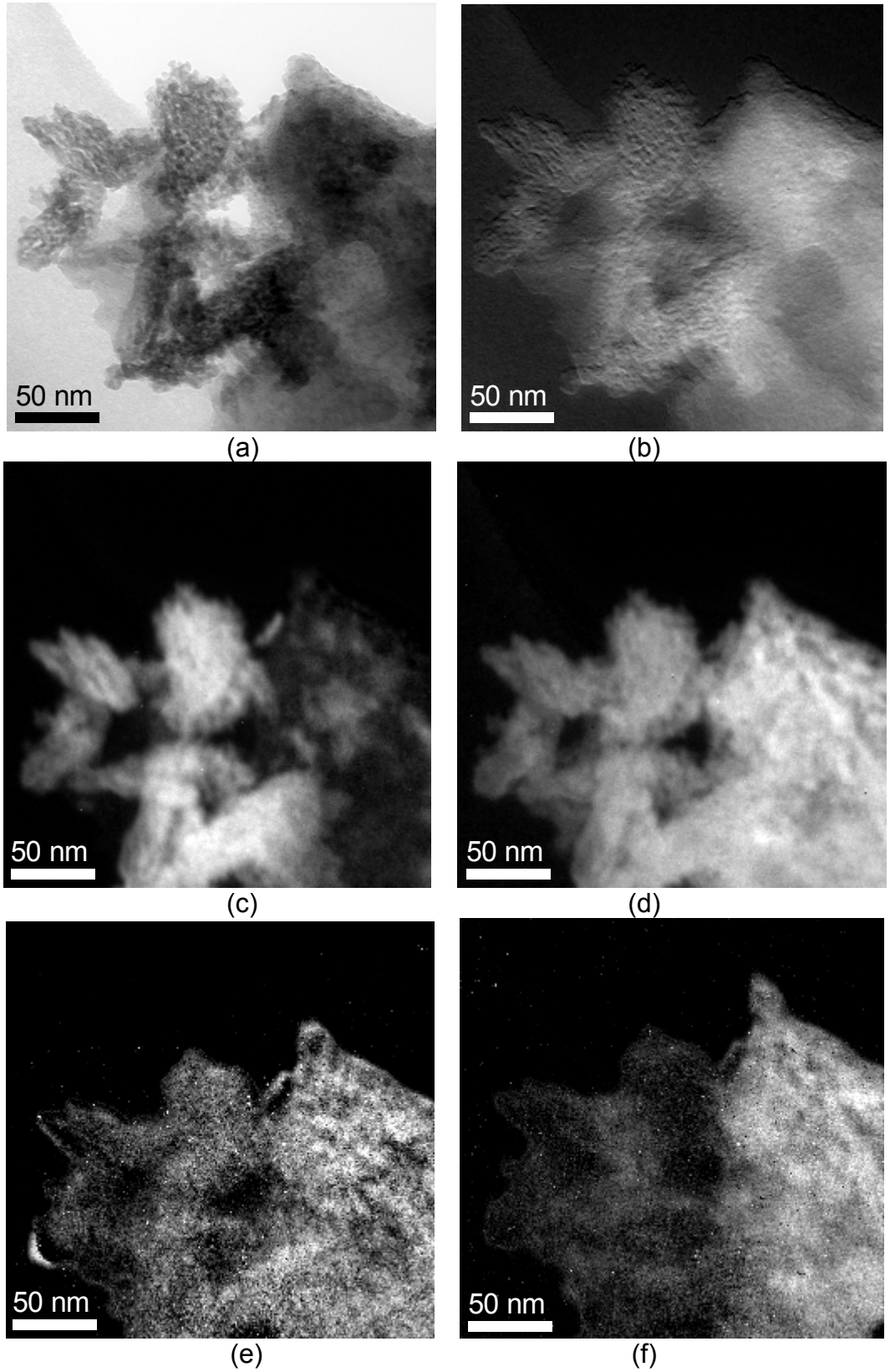

Figure 8-12 EFTEM images of released goethite crystals for KOH digested sample B11: (a) unfiltered TEM image; (b) thickness map; (c) Fe map; (d) O map; (e) Al map; and (f) Si map. All the images are dark field images except (a).

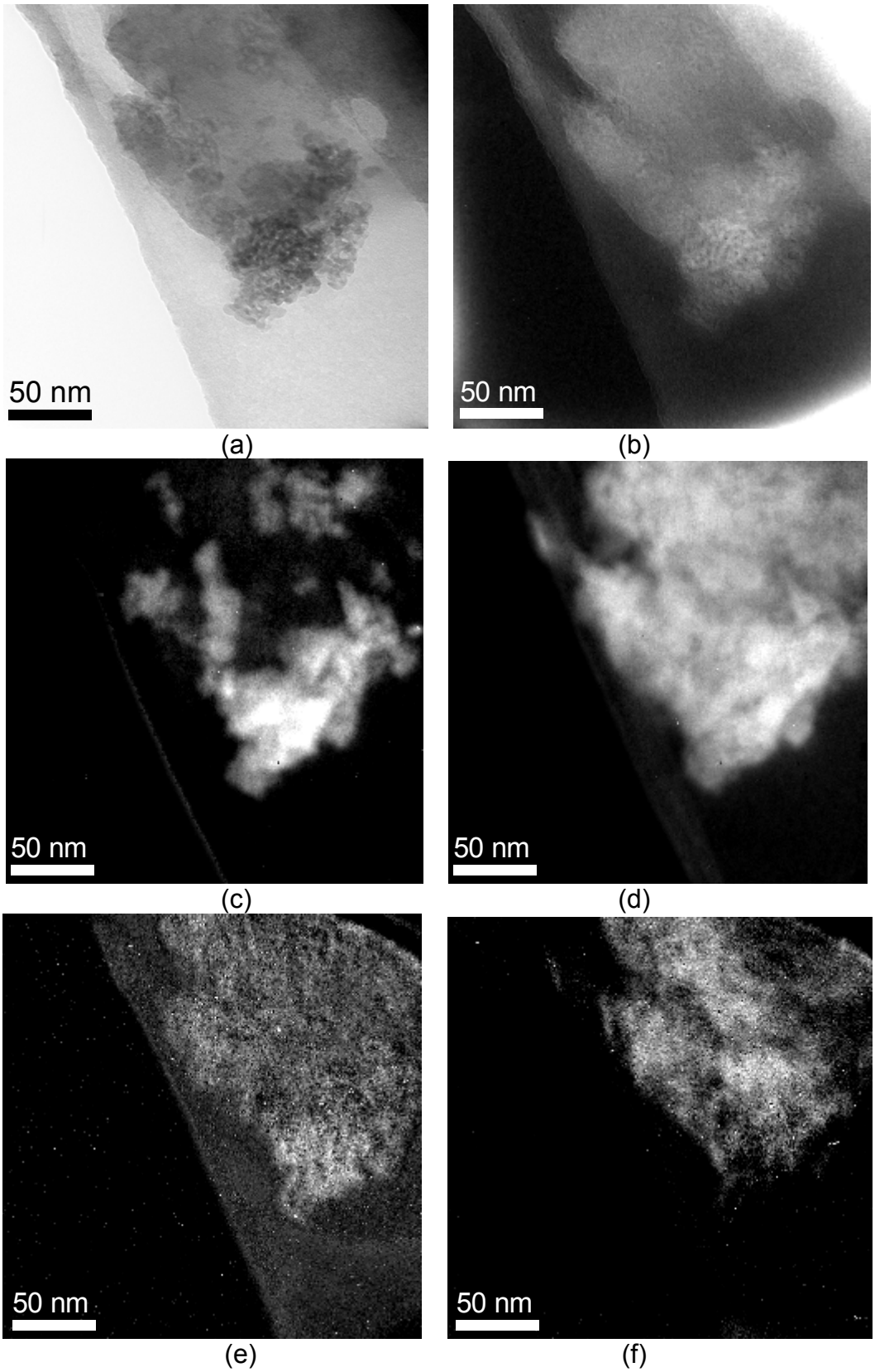

Figure 8-13 EFTEM images of released goethite crystals for KOH digested sample B11: (a) unfiltered TEM image; (b) thickness map; (c) Fe map; (d) O map; (e) Al map; and (f) Si map. All the images are dark field images except (a).

8.6 The effect of caustic digestion on AL performance

Caustic digestion successfully broke up the goethite-silica/silicate cementations and liberated goethite crystals for slow leach samples A15 and B11. This pre-treatment should facilitate the acid leaching of goethite in these ores. The digested ore samples were leached under similar AL conditions (Section 3.2.7) used in Chapter 7 to enable comparison of the leaching rate before and after caustic digestion treatment. The leached pulps were sampled at prescribed leaching times and both solids and leachate were analysed by ICP-OES to determine the elemental contents. The phase compositions of solids were determined from laboratory XRD patterns using CoKα radiation (Section 3.2.3.2).

8.6.1 Phases change during dissolution

The phase composition changes during AL leaching of the KOH treated samples A15 and B11 based on QXRD results are shown in Figure 8-14. No new phase (new reflections) was generated during acid leaching. The data in Figure 8-14 have been normalised to take into account the solids weight loss calculated from the solids to liquid ratio. Hence these curves represent the absolute solids phase percentage changes rather than the weight percentages in the XRD samples. Other minor iron oxide phases such as hematite, maghemite, and magnetite were present in low concentrations and all dissolve relatively slowly.

The phase change curves for goethite in samples A15 and B11 with and without KOH treatment are compared in Figure 8-15. It is clear that KOH treatment increased the goethite dissolution rate for both samples. If goethite crystals were not encapsulated by silica or kaolinite, removing these two phases by KOH treatment would not affect goethite acid dissolution rate. The surface of the goethite in the KOH treated samples is more readily accessible and is rapidly leached from time zero, as there is now good contact with the sulphuric acid.

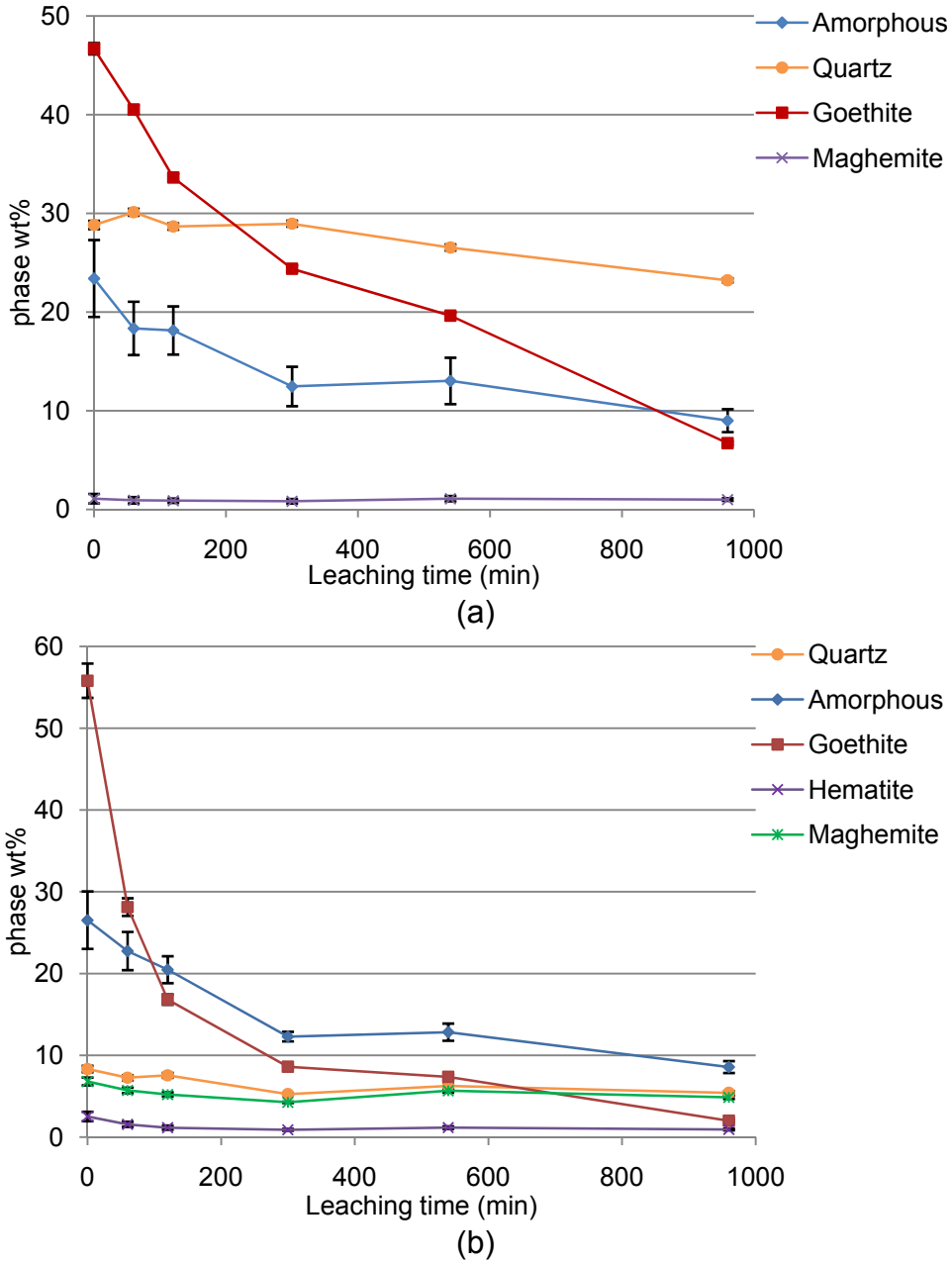

Figure 8-14 Phase composition changes during the sulphuric acid leach of KOH treated samples (a) A15 and (b) B11. The 3σ error bars are larger for the amorphous content than other crystalline phases due to uncertainty propagation.

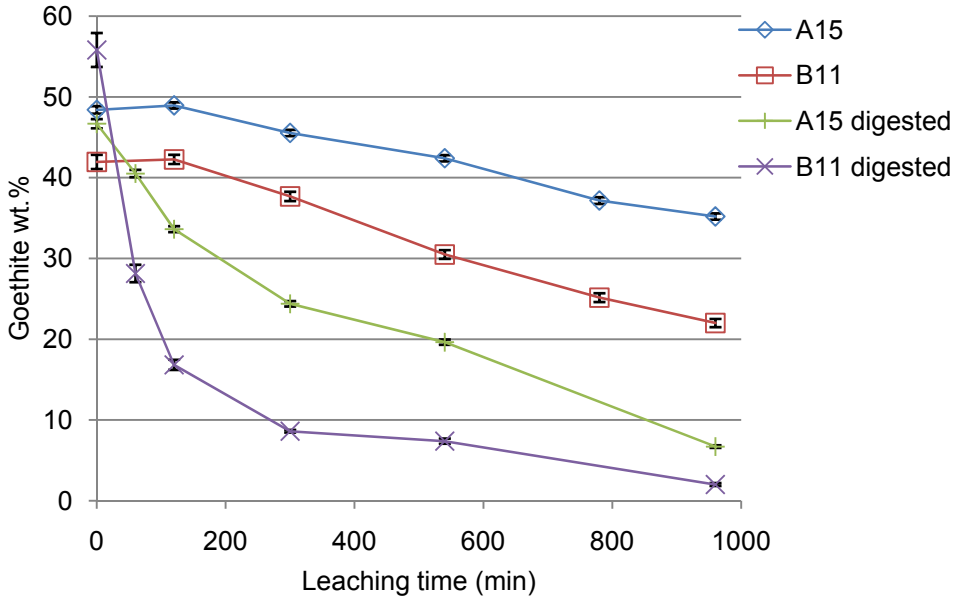

Figure 8-15 Comparison of goethite dissolution curves for laterite ore samples before (A15; B11) and after (A15 digested; B11 digested) KOH treatment.

8.6.2 Iron and nickel leaching curves

The iron and nickel leaching curves for both samples before and after KOH digestion are shown in Figure 8-16. The KOH treated samples gave higher iron and nickel final extractions (above 85 %), while the untreated ore samples released around half or less of the iron and nickel under the same AL conditions after 16 hours of leaching. Higher iron and nickel leaching rates were also obtained from the KOH treated ore samples.

Compared with the AL experiments described in Chapter 7, where 200 g ore samples were leached by approximately 2 L acid solutions, the initial solids mass of the KOH treated ore samples is much lower (77.2 g for A15 and 62.3 g for B11, as described in Section 8.3). To keep the leaching conditions (acid concentrations) unchanged, the volume of the leaching pulps are also only one third of the volume used in the previous AL experiment. This means less pulp could be sampled each time and for samples taken after time zero the sample line was not flushed beforehand so the residual material in sample line might contaminate the next sample. Therefore the metal extractions tend to be slightly underestimated except for the final sample (960 min.) which was taken from the reaction vessel at the

conclusion of the experiment. This, however, is not expected to change the interpretation of the data given by the curves shown in Figure 8-16.

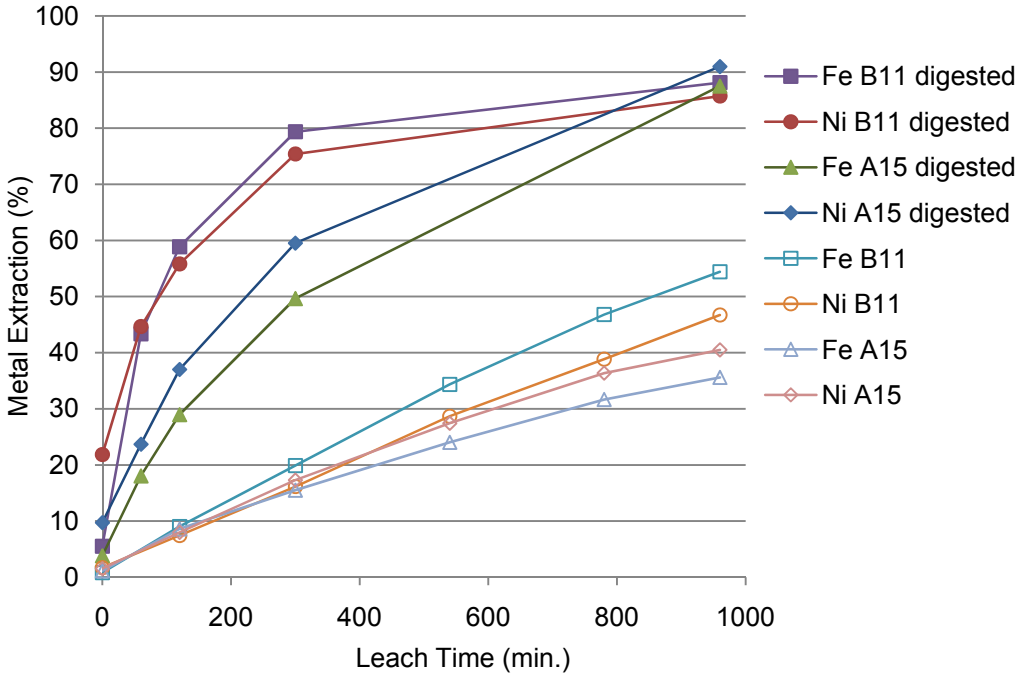

Figure 8-16 Fe and Ni extraction curves of sample A15 and B11 before and after caustic digestion.

For the same reason, the leaching rate constants for both KOH treated samples calculated from the iron extraction values (Figure 8-16) will also be slightly underestimated. These are compared with the leaching rate constants for the untreated laterite ore samples (reported in Table 7-3) in Table 8-5. The KOH treatment increased the iron leaching rates for samples A15 and B11 by more than 6 times.

Table 8-5 The dissolution rate constant 'k' for Fe in samples A15 and B11 before and after caustic digestion. The errors for the last decimal in brackets are generated by non-linear Kabai fittings.

	Non-linear Kabai fitting		
Sample	k (day^{-1})	a	R^2
A15	0.54(2)	0.80(2)	0.9994
A15 digested	3.3(2)	0.85(5)	0.9984
B11	1.18(2)	1.05(2)	0.9996
B11 digested	9(1)	0.55(6)	0.9977

It is also noted that the nickel extraction curve for sample A15 is above the iron extraction curves (Figure 8-16). This is more apparent in the KOH treated sample A15. This may be because nickel is primarily richer in smaller, more readily leached goethite crystals rather than in larger, slower leaching goethite crystals, as discussed in Section 7.4.3.

8.7 Summary

Potassium hydroxide treatment markedly accelerates the acid leaching rates of the laterite ores discussed in this chapter by more than six times by breaking up the microstructure ascribed to goethite-silica/silicate cementations. The slow atmospheric leaching for sample A15 is believed to be due to a microstructure in which silica cements goethite crystals. In comparison the primary reason for the slow leaching of sample B11 is thought to be due to goethite-kaolinite cementations which are formed paragenetically. The associated microstructures were inferred by TEM imaging of the liberated goethite crystal morphologies and EFTEM maps at iron, silicon, aluminium, and oxygen absorption edges for these crystals. The kaolinite phase in sample B11 appears to have been removed more completely than the silica framework of goethite-silica cementations in sample A15 by KOH treatment, and this may explain a faster acid leaching rate for sample B11. The liberated goethite crystals after KOH treatment in sample A15 were found to have two distinct morphologies, the smaller acicular crystals usually with round or diamond tips and the larger electron dense anhedral crystals. These morphologies agree with those of synthetic goethite grown from high silicate conditions (Section 2.6.5.8). Half of the goethite crystals released from B11 cementations have dimensions smaller than 150 nm, while most of the goethite mass is in larger crystals (>450 nm). The use of KOH treatment followed by acid leaching is not expected be cost-efficient in nickel laterite heap leaching operations. However, it allows verification that a physical envelope of silica and/or silicates hinders the contact between goethite surfaces and acid leach liquor. Ultimately this information can be used to decide if certain ores are economically viable for heap leaching.

Chapter 9 Conclusions

9.1 Summary

Research on the acid leaching properties of nickel laterite ore samples is intrinsically challenging due to the complexity of these multiphase regolith samples. The variation in the acid leaching properties of individual phases leads to a complex overall leaching performance of the ore samples. This thesis demonstrates a further level of complexity by showing that the way these phases are organised and associated also influences the acid leaching performance of such ores. The characterisation of the micromorphology and microstructure for the sub-micrometer scale particles was undertaken using TEM imaging, although this technique has poor sampling statistics when applied to unknown multiphase natural ore samples. Notwithstanding such difficulties, useful information was obtained by careful analysis and detailed characterisation of the morphology of dozens of ore samples before and after acid leaching.

Turbostratically disordered nontronite, one of the major nickel containing phases in nickel laterite ores from Western Australia, is difficult to quantify from XRD measurements by conventional Rietveld-based methods. A modification was made to the existing PONKCS method by incorporating anisotropic peak width and asymmetric peak shape so that both fitting of the complex XRD pattern and the accuracy of quantitative analysis data for turbostratic disordered nontronite were improved. Furthermore, the supercell model approach, which was translated into TOPAS symbolic computation system for the first time, produced further improvement to the quantitative analysis data of turbostratically disordered nontronite. With these developments in the quantitative phase analysis methodology, the phases in nickel laterite ore samples could be characterised more accurately.

Both the iron and nickel column leaching data for almost half of the nickel laterite ore samples studied exhibited dual extraction rate behaviour when plotted using the linear Kabai equation. This indicated these two metals were extracted from different phases with distinctly different leaching rates. The iron leaching rate from the slow leaching iron oxides were derived from

the second half of the leaching data for these samples. This approach approximately removed the influence of nontronite dissolution on the iron and nickel leaching rates. The previous practice of assessing the mineralogical commonality of laterite ore samples by plotting the final metal extractions against phase abundance was replaced by correlating the metal dissolution rate with the fraction of this metal present in a target phase. This approach eliminated the dilution effect of inert phases on the abundance of target phases. Oxide type laterite samples, in which goethite is the main nickel containing phase, were found to have the most variable iron and nickel final extraction and leaching rates within the sample suite studied.

Distinctly different goethite morphologies between fast and slow leaching oxide type laterite samples were revealed by TEM imaging and EDS analysis. The goethite crystals in the fast leaching ores have acicular shapes, while acicular shape goethite crystals are scarce in slow leaching ores. Instead, the goethite particles in slow leaching ores are encapsulated in electron-optical dense cementations. The STEM/EDS mapping and EFTEM imaging of these cementations before and after KOH treatment and after sulphuric acid leaching confirmed the goethite crystals are cemented by silica or silicates. It is plausible to conclude the microstructure of goethite-silica/silicate cementations in some laterite ores is responsible for the slow leaching rates and low final extractions. This was verified by an experiment that showed the acid leaching rate of the slow leaching ores increased six times after liberating the goethite crystals from their cementations by KOH treatment.

9.2 Conclusions

(a) The description of anisotropic peak width and asymmetric peak shapes can be incorporated into the PONCKS method to improve the fitting of XRD patterns for turbostratically disordered nontronite. The deviations of the calculated nontronite weight fraction from the true values were reduced to within 5 wt.% in the synthetic laterite samples.

(b) Further improvement was achieved by a supercell model which successfully modelled the asymmetric non-basal reflection bands of the turbostratically disordered nontronite and reduced the deviation of the

calculated nontronite weight fraction to within 1 wt.% in the synthetic laterite samples.

(c) The oxide type laterite ore samples demonstrate much more variable final extractions and leaching rates than the samples with clay type laterite ores. The lattice parameters of goethite in the oxide type laterite ore samples positively correlated with the iron leaching rate. The effects of Al^{3+}, Cr^{3+}, Mn^{3+} and Ni^{2+} substitution for Fe^{3+} on goethite lattice dimensions reported in literature are also observed in multi-element substituted natural goethite. The leaching rate tends to decrease with Al^{3+} and Cr^{3+} substitution but increase with Ni^{2+} substitution level.

(d) The goethite crystals in the fast leaching ores are acicular in shape, while the goethite particles in slow leaching ores are in electron-optical dense particles. The direct iron, silicon, aluminium, oxygen mapping by STEM/EDS and EFTEM confirmed that these particles are goethite-silica/silicate cementations.

(e) Atmospheric pressure acid leaching at elevated temperature can effectively accelerate the dissolution rate of nickel laterite ore samples more than 10^3 times compare to heap leach conditions, while keeping the order of sample leachability preserved. Micrometer scale large goethite crystals and paragenetic goethite in silica or kaolinite are still present in extensively sulphuric acid leached samples. The silica framework is not broken down by acid leaching. The characteristics of goethite diamond shaped tips are consistent with the morphology of synthetic goethite grown in high silicate conditions as reported in the literature.

(f) KOH digestion effectively disintegrates the cementation structure and liberates the goethite crystals within. The acid leaching rate for same ore samples increased by more than six times after KOH leaching. The microstructure of goethite-silica/silicate cementations was identified as the main reason for the low leaching rates for some oxide type nickel laterite ores.

9.3 Recommendations for future work

Although this research reveals the main reason of the large variation in nickel laterite ore acid leaching performance which is the microstructure of

goethite-silica/silicate cementation in oxide type laterite ores, other factors affecting the acid dissolution of laterite ore should be examined.

(a) The variation in the acid dissolution properties of other nickel containing minerals, *e.g.* serpentine group and chlorite group, should be examined, although it is less variable than goethite leaching properties.

(b) Redox Potential (Eh) should be monitored even for non-reductive leaching as Eh can be influenced by the mineral compositions leached.

(c) The laterite ore samples should be related to their parent geology, which is not available due to the confidentiality IP agreements in this research. Once the geological attributes of laterite ores were linked to a predictable leaching performance, mining for laterite ores could be more efficient.

(d) A way of incorporating a description for preferred orientation in the supercell model should be developed to allow this model be used for laboratory XRD patterns collected from conventional front loaded nontronite samples.

(e) Principal Component Analysis (PCA) would also be a useful way to assess correlations among large data sets. This tool is recommend for the future work of investigating the links between laterite properties and its leaching performance.

(f) The acceleration of acid leaching at elevated temperature should be studied for a range of laterite ores to develop a model that could allow column leaching performance to be predicted from a simple accelerated leaching experiment at elevated temperature. Assessing ore leaching performance with shorter test periods is distinctly advantageous.

(g) Other metallurgical processes aimed at disintegrating the goethite-silica/silicate cementations should be developed to benefit heap leaching performance of nickel laterite ores in Western Australia.

(h) Use X-ray Absorption Spectroscopy to examine the atomic environment of the majority of nickel atoms, which will shed light on the distribution of nickel in laterite ore samples.

Reference

Agatzini-Leonardou, S., & Dimaki, D. (1994). Heap leaching of poor nickel laterites by sulphuric acid at ambient temperature. Paper presented at the Hydrometallurgy '94, Cambridge, United Kingdom.

Agatzini-Leonardou, S., Tsakiridis, P. E., Oustadakis, P., Karidakis, T., & Katsiapi, A. (2009). Hydrometallurgical process for the separation and recovery of nickel from sulphate heap leach liquor of nickeliferrous laterite ores. *Minerals Engineering, 22*, 1181–1192.

Agatzini-Leonardou, S., & Zafiratos, I. G. (2004). Beneficiation of a Greek serpentinic nickeliferous ore Part II. Sulphuric acid heap and agitation leaching. *Hydrometallurgy, 74*(3–4), 267–275.

Allmann, R. (2008). General data reduction. In Dinnebier, Robert E. & Billinge, Simon J. L. (Eds.), *Powder Diffraction: Theory and Practice*. Cambridge, U.K.: RSC Publishing.

Alvarez, M., Rueda, E. H., & Sileo, E. E. (2006). Structural characterization and chemical reactivity of synthetic Mn-goethites and hematites. *Chemical Geology, 231*(4), 288–299.

Alvarez, M., Rueda, E. H., & Sileo, E. E. (2007). Simultaneous incorporation of Mn and Al in the goethite structure. *Geochimica et Cosmochimica Acta, 71*(4), 1009–1020.

Alvarez, M., Sileo, E. E., & Rueda, E. H. (2005). Effect of Mn(II) incorporation on the transformation of ferrihydrite to goethite. *Chemical Geology, 216*(1–2), 89–97.

Alvarez, M., Sileo, E. E., & Rueda, E. H. (2008). Structure and reactivity of synthetic Co-substituted goethites. *American Mineralogist, 93*(4), 584–590.

Anand, R. R., & Gilkes, R. J. (1987a). Iron oxides in lateritic soils from Western Australia. *Journal of Soil Science, 38*(4), 607-622.

Anand, R. R., & Gilkes, R. J. (1987b). Variations in the properties of iron oxides within individual specimens of lateritic duricrust. *Australian Journal of Soil Research, 25*(3), 287–302.

Andersen, J. C. Ø., Rollinson, G. K., Snook, B., Herrington, R., & Fairhurst, R. J. (2009). Use of QEMSCAN® for the characterization of Ni-rich and Ni-poor goethite in laterite ores. *Minerals Engineering, 22*(13), 1119–1129.

Andreazza, J. J. (2007) Processing of laterite ore. World Patent No. WO 2007/092994 A1.

Arroyo, J. C., & Neudorf, D. A. (2004) Atmospheric leach process for the recovery of nickel and cobalt from limonite and saprolite ores. United States Patent No. US 6,680,035.

Atkins, P. W., & Shriver, D. F. (2006). Inorganic chemistry (4th ed.). New York: W.H. Freeman.

Atkinson, R. J., Posner, A. M., & Quirk, J. P. (1968). Crystal nucleation in Fe(III) solutions and hydroxide gels. *Journal of Inorganic Nuclear Chemistry, 30*(9), 2371–2381.

Avrami, M. (1939). Kinetics of phase change. I. General theory. *The Journal of Chemical Physics, 7*(12), 1103–1112.

Avrami, M. (1940). Kinetics of phase change. II. Transformation-time relations for random distribution of nuclei. *The Journal of Chemical Physics, 8*(2), 212–224.

Avrami, M. (1941). Kinetics of phase change. III. Granulation, phase change, and microstructure. *The Journal of Chemical Physics, 9*(2), 177–184.

Balasubramanian, R., Cook, D. C., & Yamashita, M. (2002). Magnetic relaxation in nano-phase chromium substituted goethite. *Hyperfine Interactions, 139–140*(1–4), 167–173.

Barrón, V., Gálvez, N., Hochella Jr., M. F., & Torrent, J. (1997). Epitaxial overgrowth of goethite on hematite synthesized in phosphate media: A scanning force and transmission electron microscopy study. *American Mineralogist, 82*(11–12), 1091–1100.

Barrón, V., & Torrent, J. (1996). Surface hydroxyl configuration of various crystal faces of hematite and goethite. *Journal of Colloid and Interface Science, 177*(2), 407–410.

Barthelmy, D. (1997-2009, 12/31/2009). Online Mineralogy Database Retrieved 21st February, 2010, from http://webmineral.com/data/Goethite.shtml

Bauer, A., & Berger, G. (1998). Kaolinite and smectite dissolution rate in high molar KOH solutions at 35° and 80°C. *Applied Geochemistry, 13*(7), 905–916.

Bayliss, P. (1989). Unit-cell dimensions of two dimensional clay minerals. *Powder Diffraction, 4*(1), 19–20.

Bergmann, J., & Kleeberg, R. (1998). Rietveld analysis of disordered layer silicates. *Materials Science Forum, 278–281*, 300–305.

Besson, G., Bookin, A. S., Dainyak, L. G., Rautureau, M., Tsipursky, S. I., Tchoubar, C., & Drits, V. A. (1983). Use of diffraction and Mössbauer methods for the structural and crystailochemical characterization of nontronites. *Journal of Applied Crystallography, 16*(4), 374–383.

Beukes, J. P., Giesekke, E. W., & Elliott, W. (2000). Nickel retention by goethite and hematite. *Minerals Engineering, 13*(14–15), 1573–1579.

Bibak, A., Gerth, J., & Borggaard, O. K. (1995). Retention of cobalt by pure and foreign-element associated goethites. *Clays and Clay Minerals, 43*(2), 141–149.

Bish, D. L., & Howard, S. A. (1988). Quantitative phase analysis using the Rietveld method. *Journal of Applied Crystallography, 21*(2), 86–91.

Bodine, M. W. (1987). CLAYFORM: a Fortran 77 computer program apportioning the constituents in the chemical analysis of a clay or other silicate mineral into a structural formula. *Computers & Geosciences, 13*(1), 77–88.

Bonetto, R. D., Zalba, P. E., Conconi, M. S., & Manassero, M. (2003). The Rietveld method applied to quantitative phase analysis of minerals containing disordered structures. *Revista geológica de Chile, 30*(1), 103–115.

Boudeulle, M., & Muller, J.-P. (1988). Structural characteristics of hematite and goethite and their relationships with kaolinite in a laterite from Cameroon. A TEM study. *Mineral Bulletin, 111*(2), 149–166.

Boudreau, B. P., & Ruddick, B. R. (1991). On a reactive continuum representation of organic matter diagenesis. *American Journal of Science, 291*(5), 507–538.

Bousserrhine, N., Gasser, U., Jeanroy, E., & Berthelin, J. (1998). Effect of aluminium substitution on ferri-reducing bacterial activity and dissolution of goethites. *Comptes Rendus de l'Académie des Sciences - Series IIA - Earth and Planetary Science, 326*(9), 617–624.

Bousserrhine, N., Gasser, U. G., Jeanroy, E., & Berthelin, J. (1999). Bacterial and chemical reductive dissolution of Mn-, Co-, Cr-, and Al-substituted goethites. *Geomicrobiology Journal, 16*(3), 245–258.

Brand, N. W., Butt, C. R. M., & Elias, M. (1998). Nickel laterites: Classification and features. *AGSO Jounal of Australian Geology & Geophysics, 17*(4), 81–88.

Brenner, I. B., & Zander, A. T. (2000). Axially and radially viewed inductively coupled plasmas — a critical review. *Spectrochimica Acta Part B: Atomic Spectroscopy, 55*(8), 1195–1240.

Brindley, G. W. (1945). XLV. The effect of grain or particle size on X-ray reflections from mixed powders and alloys, considered in relation to the quantitative determination of crystalline substances by X-ray methods. *Philosophical Magazine Series 7, 36*(256), 347–369.

Bronevoi, V. A., & Furmakova, L. N. (1975). The formation conditions of alumogoethite in bauxites. *Proceedings of the Russian Mineralogical Society, 104*(4), 461–466.

Brown, W. E., Dollimore, D., & Galway, A. K. (1980). Theory of solid state reaction kinetics. In Bamford, C. H. & Tipper, C. F. H. (Eds.), *Comprehensive Chemical Kinetics* (Vol. 22, pp. 41–113). Amsterdam: Elsevier.

Bruker AXS. (2009). DIFFRAC^{plus} TOPAS 4.2 technical reference. Karlsruhe, Germany: Bruker AXS GmbH.

Burns, R. G. (1976). The uptake of cobalt into ferromanganese nodules, soils, and synthetic manganese (IV) oxides. *Geochimica et Cosmochimica Acta, 40*(1), 95–102.

Byerley, J. J., Rempel, G. L., & Garrido, G. F. (1979). Copper catalysed leaching of magnetite in aqueous sulfur dioxide. *Hydrometallurgy, 4*(4), 317–336.

Cama, J., Ganor, J., Ayora, C., & Lasaga, C. A. (2000). Smectite dissolution kinetics at 80°C and pH 8.8. *Geochimica et Cosmochimica Acta, 64*(15), 2701–2717.

Campo, B. C., Rosseler, O., Alvarez, M., Rueda, E. H., & Volpe, M. A. (2008). On the nature of goethite, Mn-goethite and Co-goethite as supports for gold nanoparticles. *Materials Chemistry and Physics, 109*(2–3), 448–454.

Carvalho-e-Silva, M. L., Ramos, A. Y., Tolentino, H. C. N., Enzweiler, J., Netto, S. M., & Alves, M. d. C. M. (2003). Incorporation of Ni into natural goethite: An investigation by X-ray absorption spectroscopy. *American Mineralogist, 88*(5–6), 876–882.

Casey, W. H., & Ludwig, C. (1996). The mechanism of dissolution of oxide minerals. *Nature, 381*(6582), 506–509.

Chander, S., & Sharma, V. N. (1981). Reduction roasting/ammonia leaching of nickeliferous laterites. *Hydrometallurgy, 7*(4), 315–327.

Chateigner, D., Blanchart, P., Deniel, S., Lutterotti, L., & Wenk, H.-R. (2010). Characterization of microstructure and crystallographic texture of silicate and phyllosilicate ceramics. *Advances in Science and Technology, 68*(1), 13–22.

Cheary, R. W., & Coelho, A. (1992). A fundamental parameters approach to X-ray line-profile fitting. *Journal of Applied Crystallography, 25*(2), 109–121.

Cheary, R. W., Coelho, A. A., & Cline, J. P. (2004). Fundamental parameters line profile fitting in laboratory diffractometers. *Journal of Research of the National Institute of Standards and Technology, 109*(1), 1–25.

Cheng, C. Y., Misra, V. N., Clough, J., & Mun, R. (1999). Dephosphorisation of western australian iron ore by hydrometallurgical process. *Minerals Engineering, 12*(9), 1083–1092.

Chiarizia, R., & Horwitz, E. P. (1991). New formulations for iron oxides dissolution. *Hydrometallurgy, 27*(3), 339–360.

Christoffersen, J., & Christoffersen, M. R. (1976). The kinetics of dissolution of calcium sulphate dihydrate in water. *Journal of Crystal Growth, 35*(1), 79–88.

Cliff, G., & Lorimer, G. W. (1975). The quantitative analysis of thin specimens. *Journal of Microscopy, 103*(2), 203–207.

Coelho, A. A., Evans, J., Evans, I., Kern, A., & Parsons, S. (2011). The TOPAS symbolic computation system. *Powder Diffraction, 26*(S1), S22–S25.

Cook, D. C. (2004). Application of Mössbauer spectroscopy to the study of corrosion. *Hyperfine Interactions, 153*(1–4), 61–82.

Cook, D. C., Oh, S. J., & Balasubramanian, R. Y., M. (1999). the role of goethite in the formation of the protective corrosion layers on steels. *Hyperfine Interactions, 122*(1–2), 59–70.

Cornell, R. M. (1988). The influence of some divalent cations on the transformation of ferrihydrite to more crystalline products. *Clay Minerals, 23*(3), 329–332.

Cornell, R. M., & Giovanoli, R. (1985). Effect of solution conditions on the proportion and morphology of goethite formed from ferrihydrite. *Clays and Clay Minerals, 33*(5), 424–432.

Cornell, R. M., & Giovanoli, R. (1986). Factors that govern the formation of multi-domainic goethites. *Clays and Clay Minerals, 34*(1), 557–564.

Cornell, R. M., & Giovanoli, R. (1987a). Effect of manganese on the transformation of ferrihydrite into goethite and jacobsite in alkaline media. *Clays and Clay Minerals, 35*(1), 11–20.

Cornell, R. M., & Giovanoli, R. (1987b). The influence of silicate species on the morphology of goethite (α-FeOOH) grown from ferrihydrite ($5Fe_2O_3 \cdot 9H_2O$). *Journal of the Chemical Society, Chemical Communications, 16*(6), 413–414.

Cornell, R. M., & Giovanoli, R. (1989). Effect of cobalt on the formation of crystalline iron oxides from ferrihydrite in alkaline media. *Clays and Clay Minerals, 37*(1), 65–70.

Cornell, R. M., & Giovanoli, R. (1993). Acid dissolution of hematites of different morphologies. *Clay Minerals, 28*(2), 223–232.

Cornell, R. M., Giovanoli, R., & Schindler, P. W. (1987). Effect of silicate species on the transformation of ferrihydrite into goethite and hematite in alkaline media. *Clays and Clay Minerals, 35*(1), 21–28.

Cornell, R. M., Giovanoli, R., & Schneider, W. (1992). The effect of nickel on the conversion of amorphous iron(III) hydroxide into more crystalline iron

oxides in alkaline media. *Journal of Chemical Technology & Biotechnology, 53*(1), 73–79.

Cornell, R. M., Mann, S., & Skarnulis, A. J. (1983). A high-resolution electron microscopy examination of domain boundaries in crystals of synthetic goethite. *Journal of Chemical Society. Faraday Transactions, 79*(11), 2679–2684.

Cornell, R. M., Posner, A. M., & Quirk, J. P. (1974). Crystal morphology and the dissolution of goethite. *Journal of Inorganic and Nuclear Chemistry, 36*(9), 1937–1946.

Cornell, R. M., Posner, A. M., & Quirk, J. P. (1975). The complete dissolution of goethite. *Journal of Applied Chemistry and Biotechnology, 25*(9), 701–706.

Cornell, R. M., Posner, A. M., & Quirk, J. P. (1976). Kinetics and mechanisms of the acid dissolution of goethite (α-FeOOH). *Journal of Inorganic and Nuclear Chemistry, 38*(3), 563–567.

Cornell, R. M., & Schwertmann, U. (1996). The iron oxides: structure, properties, reactions, occurrence and uses (1st ed.). Weinheim, Germany: VCH.

Cornell, R. M., & Schwertmann, U. (2003). The iron oxides: structure, properties, reactions, occurences and uses (2nd ed.). Weinheim, Germany: Wiley-Vch Verlag GmbH & Co. KGaA.

Crundwell, F. K., Moats, M. S., Ramachandran, V., Robinson, T. G., & Davenport, W. G. (2011). Upgrading of laterite ores. *Extractive Metallurgy of Nickel, Cobalt and Platinum Group Metals* (1st ed., pp. 39–47). Oxford: Elsevier.

Dąbrowski, W., Gryboś, P., Hottowy, P., Świentek, K., & Wiącek, P. (2003). Integrated readout of silicon strip detectors for position sensitive measurement of X-rays. *Nuclear Instruments and Methods in Physics Research Section A: Accelerators, Spectrometers, Detectors and Associated Equipment, 512*(1–2), 213–219.

Dalvi, A. D., Bacon, W. G., & Osborne, R. C. (2004). The Past and the Future of Nickel Laterites. Paper presented at the PDAC 2004 International Convention, Canada. www.pdac.ca/pdac/publications/papers/2004/techprgm-dalvi-bacon.pdf

Das, S. K., Das, B., Sakthivel, R., & Mishra, B. K. (2010). Mineralogy, microstructure, and chemical composition of goethites in some iron ore deposits of Orissa, India. *Mineral Processing and Extractive Metallurgy Review, 31*(2), 97–110.

David, W. I. F., Leoni, M., & Scardi, P. (2010). Domain size analysis in the Rietveld method. *Materials Science Forum, 651*(1), 187–200.

de Carvalho-e-Silva, M. L. M., Partiti, C. S. M., Enzweiler, J., Petit, S., Netto, S. M., & de Oliveira, S. M. B. (2002). Characterization of Ni-containing goethites by Mössbauer spectroscopy and other techniques. *Hyperfine Interactions, 142*(3–4), 559–576.

de Graaf, J. E. (1980). The treatment of lateritic nickel ores — A further study of the Caron process and other possible improvements: Part II. Leaching studies. *Hydrometallurgy, 5*(2–3), 255–271.

Decarreau, A., Petit, S., Martin, F., Farges, F., Vieillard, P., & Joussein, E. (2008). Hydrothermal synthesis, between 75 and 150°C, of high-charge, ferric nontronites. *Clays and Clay Minerals, 56*(3), 322–337.

Dekov, V. M., Kamenov, G. D., Stummeyer, J., Thiry, M., Savelli, C., Shanks, W. C., Fortin, D., Kuzmann, E., & Vértes, A. (2007). Hydrothermal nontronite formation at Eolo Seamount (Aeolian volcanic arc, Tyrrhenian Sea). *Chemical Geology, 245*(1–2), 103–119.

Deleuze, M., Goiffon, A., Ibanez, A., & Philippot, E. (1995). Solvent Influence on Kinetics and Dissolution Mechanism of Quartz in Concentrated Basic Media (NaOH, KOH, LiOH). *Journal of Solid State Chemistry, 118*(2), 254–260.

Drits, V. A., McCarty, D. K., & Zviagina, B. B. (2006). Crystal-chemical factors responsible for the distribution of octahedral cations over trans- and cis-sites in dioctahedral 2:1 layer silicates. *Clays and Clay Minerals, 54*(2), 131–152.

Dutrizac, J. E., & Jambor, J. L. (2000). Jarosites and their application in hydrometallurgy. *Reviews in Mineralogy and Geochemistry, 40*(1), 405–452.

Duyvesteyn, W., P., C., Liu, H., & Davis, M. J. (2001) Heap leaching of nickel containing ore. World Patent No. WO 01/75184 A2.

Dyson, N. F., & Scott, T. R. (1976). Acid leaching of nickel sulphide concentrates. *Hydrometallurgy, 1*(4), 361–372.

Ebinger, M. H., & Schulze, D. G. (1989). Mn-substituted goethite and Fe-substituted groutite synthesized at acid pH. *Clays and Clay Minerals, 37*(2), 151–156.

Ebinger, M. H., & Schulze, D. G. (1990). The Influence of pH on the synthesis of mixed Fe-Mn oxide minerals. *Clay Minerals, 25*(4), 507–518.

Eggleton, R. A. (1977). Nontronite: chemistry and X-ray diffraction. *Clay Minerals, 12*(3), 181–194.

Elias, M., Donaldson, M. J., & Giorgetta, N. E. (1981). Geology, mineralogy, and chemistry of lateritic nickel-cobalt deposits near Kalgoorlie, Western Australia. *Economic Geology, 76*(6), 1775–1783.

Elliot, A., Fletcher, H., Li, J., Watling, H., & Robinson, D. J. (2009). Heap leaching of nickel laterites - A challenge and an opportunity. Paper presented at the 39th Annual Hydrometallurgy Meeting & 48th Annual Conference of Metallurgists of CIM, Sudbury, Ontario, Canada.

Fan, R., & Gerson, A. R. (2011). Nickel geochemistry of a Philippine laterite examined by bulk and microprobe synchrotron analyses. *Geochimica et Cosmochimica Acta, 75*(21), 6400–6415.

Fazey, P. G., O'Connor, B. H., & Hammond, L. C. (1991). X-ray powder diffraction Rietveld characterization of synthetic aluminum-substituted goethite. *Clays and Clay Minerals, 39*(3), 248–253.

Fey, M. V., & Dixon, J. B. (1981). Synthesis and propertise of poorly crystalline hydrated aluminous goethites. *Clays and Clay Minerals, 29*(2), 91–100.

Field, A. (2007). Discovering statistics using SPSS (3rd ed.): SAGE Publications.

First Quantum Minerals Ltd. (2011). Ravensthorpe nickel mine Retrieved 6th Oct 2012, from http://www.first-quantum.com/Our-Business/operating-mines/Ravensthorpe/default.aspx

Fischer, W. R. (1987). Standard potentials (Eo) of iron(III) oxides under reducing conditions. *Zeitschrift für Pflanzenernährung und Bodenkunde, 150*(5), 286–289.

Fitzpatrick, R. W., & Schwertmann, U. (1982). Al-substituted goethite — An indicator of pedogenic and other weathering environments in South Africa. *Geoderma, 27*(4), 335–347.

Ford, R. G., Bertsch, P. M., & Farley, K. J. (1997). Changes in transition and heavy metal partitioning during hydrous iron oxide aging. *Environmental Science & Technology, 31*(7), 2028–2033.

Ford, R. G., Kemner, K. M., & Bertsch, P. M. (1999). Influence of sorbate-sorbent interactions on the crystallization kinetics of nickel- and lead-ferrihydrite coprecipitates. *Geochimica et Cosmochimica Acta, 63*(1), 39–48.

Fordham, A. W., & Norrish, K. (1979). Electron microprobe and electron microscope studies of soil clay particles. *Australian Journal of Soil Research, 17*(2), 283–306.

Fordham, A. W., & Norrish, K. (1983). The nature of soil particles particularly those reacting with arsenate in a series of chemically treated samples. *Australian Journal of Soil Research, 21*(4), 455–477.

Freyssinet, P., Butt, C. R. M., Morris, R. C., & Piantone, P. (2005). Ore-forming processes related to lateritic weathering. *Economic Geology 100th Anniversary Volume, 1*, 681–722.

Gálvez, N., Barrón, V., & Torrent, J. (1999). Effect of phosphate on the crystallization of hematite, goethite, and lepidocrocite from ferrihydrite. *Clays and Clay Minerals, 47*(3), 304–311.

Ganor, J., Mogollón, J. L., & Lasaga, A. C. (1995). The effect of pH on kaolinite dissolution rates and on activation energy. *Geochimica et Cosmochimica Acta, 59*(6), 1037–1052.

Gasser, U. G., Jeanroy, E., Mustin, C., Barres, O., Nuesch, R., Berthelin, J., & Herbillon, A. J. (1996). Properties of synthetic goethites with Co for Fe substitution. *Clay Minerals, 31*(4), 465–476.

Gasser, U. G., Nueesch, R., Singer, M. J., & Jeanroy, E. (1999). Distribution of manganese in synthetic goethite. *Clay Minerals, 34*(2), 291–299.

Gates, W. P., Slade, P. G., Manceau, A., & Lanson, B. (2002). Site occupancies by iron in nontronite. *Clays and Clay Minerals, 50*(2), 223–239.

Gaudin, A., Decarreau, A., Noack, Y., & Grauby, O. (2005). Clay mineralogy of the nickel laterite ore developed from serpentinised peridotites at Murrin Murrin, Western Australia. *Australian Journal of Earth Sciences, 52*(2), 231–241.

Gaudin, A., Grauby, O., Noack, Y., Decarreau, A., & Petit, S. (2004). Accurate crystal chemistry of ferric smectites from the lateritic nickel ore of Murrin Murrin (Western Australia). I. XRD and multi-scale chemical approaches. *Clay Minerals, 39*(3), 301–315.

Georgiou, D., & Papangelakis, V. G. (1998). Sulphuric acid pressure leaching of a limonitic laterite: chemistry and kinetics. *Hydrometallurgy, 49*(1–2), 23–46.

Georgiou, D., & Papangelakis, V. G. (2004). Characterization of limonitic laterite and solids during sulfuric acid pressure leaching using transmission electron microscopy. *Minerals Engineering, 17*(3), 461–463.

Gerth, J. (1990). Unit-cell dimensions of pure and trace metal-associated goethites. *Geochimica et Cosmochimica Acta, 54*(2), 363–371.

Gerth, J., Brümmer, G. W., & Tiller, K. G. (1993). Retention of Ni, Zn and Cd by Si-associated goethite. *Zeitschrift für Pflanzenernährung und Bodenkunde, 156*(2), 123–129.

Ginstling, A. M., & Brounshtein, B. I. (1950). The diffusion kinetics of reactions in spherical particles. *Russian Journal of Applied Chemistry, 23*, 1327–1338.

Giovanoli, R., & Brütsch, R. (1975). Kinetics and mechanism of the dehydration of γ-FeOOH. *Thermochimica Acta, 13*(1), 15–36.

Glasauer, S., Friedl, J., & Schwertmann, U. (1999). Properties of goethites prepared under acidic and basic conditions in the presence of silicate. *Journal of Colloid and Interface Science, 216*(1), 106–115.

Glasser, L. S. D., & Ingram, L. (1968). Refinement of the crystal structure of groutite – MnOOH. *Acta Crystallographica Section B, 24*(9), 1233–1236.

Gleeson, S. A., Butt, C. R. M., & Elias, M. (2003). Nickel laterites: A review. *Society of Economic Geologists Newsletter, 2003*(54), 9–16.

Golightly, J. P. (1979). Nickeliferous laterites: A general description. Paper presented at the International Laterite Symposium, New Orleans, U. S.

Goodman, B. A., & Lewis, D. G. (1981). Mössbauer spectra of aluminous gaoethites (α-FeOOH). *European Journal of Soil Science, 32*(3), 351–363.

Gorichev, I. G., & Kipriyanov, N. A. (1984). Regular kinetic features of the dissolution of metal oxides in acidic media. *Russian Chemical Reviews, 53*(11), 1039–1061.

Goss, C. J. (1987). The kinetics and reaction mechanism of the goethite to hematite transformation. *Mineralogical Magazine, 51*, 437–451.

Gu, Q. (2011). DataPro (Version 2.7). Melbourne, Australia: Australian Synchrotron. Retrieved from http://www.synchrotron.org.au/images/stories/beamline/powder/Datapro2.7.zip.

Guggenheim, S., Adams, J. M., Bain, D. C., Bergaya, F., Brigatti, M. F., Drits, V. A., Formoso, M. L. L., Galán, E., Kogure, T., & Stanjek, H. (2006). Summary of recommendations of nomenclature committees relevant to clay mineralogy: report of the Association Internationale pour l'Etude des Argiles (AIPEA) Nomenclature Committee for 2006. *Clay Minerals, 41*(4), 863–877.

Guy, C., & Schott, J. (1989). Multisite surface reaction versus transport control during the hydrolysis of a complex oxide. *Chemical Geology, 78*(3–4), 181–204.

Hölzer, G., Fritsch, M., Deutsch, M., Härtwig, J., & Förster, E. (1997). $K\alpha_{1,2}$ and $K\beta_{1,3}$ x-ray emission lines of the 3d transition metals. *Physical Review A, 56*(6), 4554–4568.

Habashi, F. (1970). Princiles of extractive metallurgy (1st ed. Vol. 1 General Principles). New York: Gordon and Breach Science Publishers.

Hammersley, A. P. (1997). FIT2D: An introduction and overview. Grenoble, France: ESRF.

Hammersley, A. P. (1998). FIT2D V9.129 reference manual V3.1. Grenoble, France: ESRF.

Hanawalt, J. D. (1986). Manual search/match methods for powder diffraction in 1986. *Powder Diffraction, 1*(1), 7–13.

Hanawalt, J. D., & Rinn, H. W. (1986). Identification of crystalline materials - classification and use of X-ray diffraction patterns. *Powder Diffraction, 1*(1), 2–6.

Hanawalt, J. D., Rinn, H. W., & Frevel, L. K. (1986). Chemical analysis by X-ray diffraction - classification and use of X-ray diffraction patterns. *Powder Diffraction, 1*(2), 2–14.

Harris, B., White, C., Jansen, M., & Pursell, D. (2006a). A new approach to the high concentration chloride leaching of nickel laterites. Paper presented at the ALTA 2006, Perth, WA.

Harris, G. B., White, C. W., & Demopoulos, G. P. (2006b). Iron control in high concentration chloride leach processes. Paper presented at the The Third International Symposium on Iron Control in Hydrometallurgy, Montreal, Canada.

Harrison, L. G. (1969). The theory of solid phase kinetics. In Bamford, C. H. & Tipper, C. F. H. (Eds.), *Comprehensive Chemical Kinetics* (Vol. 2, pp. 377–462). Amsterdam: Elsevier.

Hart, R. D., St Pierre, T. G., Gilkes, R. J., Mckinley, A. J., Siradz, S., & Singh, B. (2002). Iron in soil kaolins from Indonesia and Western Australia. *Clay Minerals, 37*(4), 671–685.

Helgren, D. M., & Butzer, K. W. (1977). Paleosols of the Southern Cape coast, South Africa: Implications for laterite definition, genesis, and age. *Geographical Review, 67*(4), 430–445.

Hiemstra, T., Barnett, M. O., & van Riemsdijk, W. H. (2007). Interaction of silicic acid with goethite. *Journal of Colloid and Interface Science, 310*(1), 8–17.

Hill, R. J., & Howard, C. J. (1987). Quantitative phase analysis from neutron powder diffraction data using the Rietveld method. *Journal of Applied Crystallography, 20*(6), 467–474.

Hixson, A. W., & Crowell, J. H. (1931). Dependence of reaction velocity upon surface and agitation. I.Theoretical consideration. *Industrial and Engineering Chemistry, 23*(8), 923–931.

Hofer, F., & Warbichler, P. (2005). Elemental mapping using energy filtered imaging. In Ahn, Channing C. (Ed.), *Transmission Electron Energy Loss Spectrometry in Materials Science and The EELS Atlas* (2nd ed., pp. 159–222). Weinheim, Germany: Wiley-VCH Verlag GmbH & Co. KGaA.

Holt, J. B., Cutler, I. B., & Wadsworth, M. E. (1962). Rate of thermal dehydration of kaolinite in vacuum. *Journal of the American Ceramic Society, 45*(3), 133–136.

Houben, G. J. (2003). Iron oxide incrustations in wells. Part 2: chemical dissolution and modeling. *Applied Geochemistry, 18*(6), 941–954.

Inouye, K., Ishii, S., Kaneko, K., & Ishikawa, T. (1972). The effect of copper(II) on the crystallization of α-FeOOH. *Zeitschrift für Anorganische und Allgemeine Chemie, 391*(1), 86–96.

International Stainless Steel Forum. (2012). Stainless Steel in Figures 2012. Retrieved from worldstainless.org website: http://www.worldstainless.org/

Iwasaki, K., & Yamamura, T. (2002). Whisker-like goethite nanoparticies containing cobalt synthesized in a wet process. *Materials Transactions, 43*(8), 2097–2103.

Jónás, K., & Solymár, K. (1970). Preparation, X-ray, derivatographic and infrared study of aluminum-substituted goethites. *Acta Chimica Academiae Scientiarum Hungaricae, 66*(4), 383–394.

Järvinen, M. (1993). Application of symmetrized harmonics expansion to correction of the preferred orientation effect. *Journal of Applied Crystallography, 26*(4), 525–531.

Jander, W. (1927). Reaktionen im festen Zustande bei höheren Temperaturen. Reaktionsgeschwindigkeiten endotherm verlaufender Umsetzungen. *Zeitschrift für anorganische und allgemeine Chemie, 163*(1), 1–30.

Jeanroy, E., Rajot, J. L., Pillon, P., & Herbillon, A. J. (1991). Differential dissolution of hematite and goethite in dithionite and its implication on soil yellowing. *Geoderma, 50*(1–2), 79–94.

Jepson, W. B., & Rowse, J. B. (1975). The composition of kaolinite — An electron microscope microprobe study. *Clays and Clay Minerals, 23*(4), 310–317.

Jordan, B., O'Connor, B. H., & Li, D. (1990). Use of Rietveld pattern fitting to determine the weight fraction of crystalline material in natural low quartz specimens. *Powder Diffraction, 5*(2), 64–69.

Kämpf, N., & Schwertmann, U. (1982). The 5-M-NaOH concentration treatment for iron oxides in soils. *Clays and Clay Minerals, 30*(6), 401–408.

Kabai, J. (1973). Determination of specific activation energies of metal oxides and metal oxide hydrates by measurement of the rate of dissolution. *Acta Chimica Academiae Scientiarum Hungaricae, 78*(1), 57–73.

Kandori, K., Uchida, S., Kataoka, S., & Ishikawa, T. (1992). Effects of silicate and phosphate ions on the formation of ferric oxide hydroxide particles. *Journal of Materials Science, 27*(3), 719–728.

Karim, Z. (1984). Characteristics of ferrihydrites formed by oxidation of $FeCl_2$ solutions containing different amounts of silica. *Clays and Clay Minerals, 32*(3), 181–184.

Kaur, N., Grafe, M., Singh, B., & Kennedy, B. J. (2009a). Simultaneous incorporation of Cr, Zn, Cd and Pb in the goethite structure. *Clays and Clay Minerals, 57*(2), 234–250.

Kaur, N., Singh, B., & Kennedy, B. J. (2009b). Copper substitution alone and in the presence of chromium, zinc, cadmium and lead in goethite (α-FeOOH). *Clay Minerals, 44*(3), 293–310.

Kaur, N., Singh, B., & Kennedy, B. J. (2010). Dissolution of Cr, Zn, Cd, and Pb single- and multi-metal-substituted goethite: relationship to structural, morphological, and dehydroxylation properties. *Clays and Clay Minerals, 58*(3), 415–430.

Keeling, J. L., Raven, M. D., & Gates, W. P. (2000). Geology and characterization of two hydrothermal nontronites from weathered metamorphic rocks at the Uley graphite mine, south Australia. *Clays and Clay Minerals, 48*(5), 537–548.

Kerfoot, D. G. E. (2000). Nickel. *Ullmann's Encyclopedia of Industrial Chemistry*: Wiley-VCH Verlag GmbH & Co. KGaA.

Kern, A. (2011). TOPAS PONKCS Walkthrough. Paper presented at the 7th TOPAS Bruker Users' Meeting, Sydney, Australia.

Khalafalla, S. E., & Pahlman, J. E. (1981). *Selective extraction of metals from pacific sea nodules with dissolved sulfur dioxide*. (RI 8518). Washington D. C.: United States Bureau of Mines.

Kim, J., Dong, H., Seabaugh, J., Newell, S. W., & Eberl, D. D. (2004). Role of microbes in the smectite-to-illite reaction. *Science, 303*(5659), 830–832.

Kittelty, D. A. (2008) Low Eh leach with sulfur recycle. World Patent No. WO 2008/138038 A1.

Kleeberg, R., Monecke, T., & Hillier, S. (2008). Preferred orientation of mineral grains in sample mounts for quantitative XRD measurements. How random are powder samples? *Clays and Clay Minerals, 56*(4), 404–415.

Klein, C., Dutrow, B., & Dana, J. D. (2008). The 23rd edition of the manual of mineral science: (after James D. Dana): J. Wiley.

Klug, H. P., & Alexander, L. E. (1974). X-ray diffraction procedures for polycrystalline and amorphous materials (2nd ed.): Wiley.

Koga, Y., & Harrison, L. G. (1984). Reactions of solids with gases other than oxygen. In Bamford, C. H., Tipper, C. F. H. & Compton, R. G. (Eds.), *Comprehensive Chemical Kinetics* (Vol. 21, pp. 119–149). Amsterdam: Elsevier.

Krehula, S., & Musić, S. (2006). Influence of Mn-dopant on the properties of α-FeOOH particles precipitated in highly alkaline media. *Journal of Alloys and Compounds, 426*(1–2), 327–334.

Krehula, S., & Musić, S. (2007). Influence of copper ions on the precipitation of goethite and hematite in highly alkaline media. *Journal of Molecular Structure, 834–836*(1), 154–161.

Krehula, S., & Musić, S. (2008). Influence of cobalt ions on the precipitation of goethite in highly alkaline media. *Clay Minerals, 43*(1), 95–105.

Krehula, S., & Musić, S. (2009). The influence of a Cr-dopant on the properties of α-FeOOH particles precipitated in highly alkaline media. *Journal of Alloys and Compounds, 469*(1–2), 336–342.

Krehula, S., Musić, S., & Popović, S. (2005). Influence of Ni-dopant on the properties of synthetic goethite. *Journal of Alloys and Compounds, 403*(1–2), 368–375.

Kumar, R., Das, S., Ray, R. K., & Biswas, A. K. (1993). Leaching of pure and cobalt bearing goethites in sulphurous acid: kinetics and mechanisms. *Hydrometallurgy, 32*(1), 39–59.

Kumar, R., Ray, R. K., & Biswas, A. K. (1990). Physico-chemical nature and leaching behaviour of goethites containing Ni, Co and Cu in the sorption and coprecipitation mode. *Hydrometallurgy, 25*(1), 61–83.

Kwon, S.-K., Kimijima, K. i., Kanie, K., Suzuki, S., Muramatsu, A., Saito, M., Shinoda, K., & Waseda, Y. (2007a). Influence of silicate ions on the formation of goethite from green rust in aqueous solution. *Corrosion Science, 49*(7), 2946–2961.

Kwon, S.-K., Shinoda, K., Suzuki, S., & Waseda, Y. (2007b). Influence of silicon on local structure and morphology of γ-FeOOH and α-FeOOH particles. *Corrosion Science, 49*(3), 1513–1526.

Laird, D. A. (2006). Influence of layer charge on swelling of smectites. *Applied Clay Science, 34*(1–4), 74–87.

Landers, M. (2010). The crystal chemistry, dissolution kinetics and dehydroxylation of oxide-type lateritic Ni ore. Doctor of Philosophy, University of Western Australia, Perth.

Landers, M., & Gilkes, R. J. (2007). Dehydroxylation and dissolution of nickeliferous goethite in New Caledonian lateritic Ni ore. *Applied Clay Science, 35*(3–4), 162–172.

Landers, M., Gilkes, R. J., & Wells, M. A. (2009a). Dissolution kinetics of dehydroxylated nickeliferous goethite from limonitic lateritic nickel ore. *Applied Clay Science, 42*(3–4), 615–624.

Landers, M., Gilkes, R. J., & Wells, M. A. (2009b). Rapid dehydroxylation of nickeliferous goethite in lateritic nickel ore: X-ray diffraction and TEM investigation. *Clays and Clay Minerals, 57*(6), 751–770.

Landers, M., Gräfe, M., Gilkes, R. J., Saunders, M., & Wells, M. A. (2011). Nickel distribution and speciation in rapidly dehydroxylated goethite in oxide-type lateritic nickel ores: XAS and TEM spectroscopic (EELS and EFTEM) investigation. *Australian Journal of Earth Sciences, 58*(7), 745–765.

Larsen, O., & Postma, D. (2001). Kinetics of reductive bulk dissolution of lepidocrocite, ferrihydrite, and goethite. *Geochimica et Cosmochimica Acta, 65*(9), 1367–1379.

Larsen, O., Postma, D., & Jakobsen, R. (2006). The reactivity of iron oxides towards reductive dissolution with ascorbic acid in a shallow sandy aquifer (Rømø, Denmark). *Geochimica et Cosmochimica Acta, 70*(19), 4827–4835.

Levenspiel, O. (1999). Chemical Reaction Engineering (3rd ed.). New York: Wiley.

Lewis, D. G., & Schwertmann, U. (1979a). The influence of Al on iron oxides. III. Preparation of Al goethite in 1 M KOH. *Clay Minerals, 14*(2), 115–126.

Lewis, D. G., & Schwertmann, U. (1979b). The influence of aluminium on the formation of iron oxides. IV. The influence of [Al], [OH], and temperature. *Clays and Clay Minerals, 27*(3), 195–200.

Li, D., O'Connor, B. H., Low, I.-M., van Riessen, A., & Toby, B. H. (2006). Mineralogy of Al-substituted goethites. *Powder Diffraction, 21*(4), 289–299.

Li, D. Y., O'Connor, B. H., Chen, Q. T., & Zadnik, M. G. (1994). Quantitative powder X-ray diffractometry phase analysis of silicon nitride materials by a multiline, Mean-Normalized-Intensity method. *Journal of the American Ceramic Society, 77*(8), 2195–2198.

Li, S. (1999). Study of nickeliferrous laterite reduction. Master of Engineering, McMaster University, Hamilton, Ontario. Retrieved from http://digitalcommons.mcmaster.ca/opendissertations/6745

Li, Y., Li, H., Wang, H., Qing, S., Hu, J., Hou, Y., Li, H., & Li, L. (2011). Smelting potential of HIsmelt technology for high-phosphorus iron ore and ilmenite. Paper presented at the 2011 International Conference on Computer Distributed Control and Intelligent Environmental Monitoring, Changsha, China.

Lim-Nunez, R., & Gilkes, R. J. (1987). Acid dissolution of synthetic metal-containing goethites and hematites. Paper presented at the Proceedings of the International Clay Conference, Denver.

Liu, H. (2006) An improved process for heap leaching of nickeliferous oxidic ores. World Patent No. WO 2006/119559 A1.

Liu, H., & Reynolds, G. A. (2009) A process for atmospheric leaching of laterite ores using hypersaline leach solution. World Patent No. WO 2009/114904 A1.

Liu, K., Chen, Q., & Hu, H. (2009). Comparative leaching of minerals by sulphuric acid in a Chinese ferruginous nickel laterite ore. *Hydrometallurgy, 98*(3–4), 281–286.

Liu, K., Chen, Q., Hu, H., & Yin, Z. (2010a). Characterization and leaching behaviour of lizardite in Yuanjiang laterite ore. *Applied Clay Science, 47*(3–4), 311–316.

Liu, K., Chen, Q., Hu, H., Yin, Z., & Wu, B. (2010b). Pressure acid leaching of a Chinese laterite ore containing mainly maghemite and magnetite. *Hydrometallurgy, 104*(1), 32–38.

Lowe, J. L. (2007). DSP in the Bayer process: A fundamental study of its precipitation and role in impurity removal. Doctor of Philosophy, Curtin University, Perth.

Ludwig, C., & Casey, W. H. (1996). On the mechanisms of dissolution of bunsenite [NiO(s)] and other simple oxide minerals. *Journal of Colloid and Interface Science, 178*(1), 176–185.

Lutterotti, L., Matthies, S., & Wenk, H.-R. (1999). MAUD: A friendly Java program for material analysis using diffraction. *Newsletter of the CPD, 21*, 14–15.

Lutterotti, L., Voltolini, M., Wenk, H.-R., Bandyopadhyay, K., & Vanorio, T. (2009). Texture analysis of a turbostratically disordered Ca-montmorillonite. *American Mineralogist, 95*(1), 98–103.

MacRae, C. M., Wilson, N. C., Pownceby, M. I., & Miller, P. R. (2011). The occurence of phosphorus and other impurities in Australian iron ores. Paper presented at the Iron Ore 2011, Perth, Australia.

Madsen, I. C. (1999). IUCr CPD round robin on Quantitative Phase Analysis, standard powder X-ray diffraction data sets — Data analysis kit. from IUCr CPD http://www.mx.iucr.org/iucr-top/comm/cpd/QARR/data-kit.htm

Madsen, I. C., & Scarlett, N. V. Y. (2008). Quantitative phase analysis. In Dinnebier, Robert E. & Billinge, Simon J. L. (Eds.), *Powder Diffraction: Theory and Practice* (1 ed., Vol. 1, pp. 298–331). Cambridge: The Royal Society of Chemistry.

Madsen, I. C., Scarlett, N. V. Y., Cranswick, L. M. D., & Lwin, T. (2001). Outcomes of the International Union of Crystallography Commission on Powder Diffraction round robin on Quantitative Phase Analysis: samples 1a to 1h. *Journal of Applied Crystallography, 34*(4), 409–426.

Madsen, I. C., Scarlett, N. V. Y., & Kern, A. (2011). Description and survey of methodologies for the determination of amorphous content via X-ray powder diffraction. *Zeitschrift für Kristallographie, 226*(12), 944–955.

Madsen, I. C., Scarlett, N. V. Y., Riley, D. P., & Raven, M. D. (2013). Quantitative phase analysis using the Rietveld method. In Mittemeijer, E.J. & Welzel, U. (Eds.), *Modern Diffraction Methods* (1st ed., Vol. 1, pp. 285–320). Singapore: Wiley.

Malis, T., Cheng, S. C., & Egerton, R. F. (1988). EELS log-ratio technique for specimen-thickness measurement in the TEM. *Journal of Electron Microscopy Technique, 8*(2), 193–200.

Manceau, A., Chateigner, D., & Gates, W. P. (1998). Polarized EXAFS, distance-valence least-squares modeling (DVLS), and quantitative texture

analysis approaches to the structural refinement of Garfield nontronite. *Physics and Chemistry of Minerals, 25*(5), 347–365.

Manceau, A., Schlegel, M. L., Musso, M., Sole, V. A., Gauthier, C., Petit, P. E., & Trolard, F. (2000). Crystal chemistry of trace elements in natural and synthetic goethite. *Geochimica et Cosmochimica Acta, 64*(21), 3643–3661.

Manjanna, J., & Venkateswaran, G. (2002). Preparation and kinetic considerations for the dissolution of Cr-substituted iron oxides in reductive-complexing formulations. *The Canadian Journal of Chemical Engineering, 80*(5), 882–896.

Mann, S., Cornell, R. M., & Schwertmann, U. (1985). The influence of aluminium on iron oxides. Part XII High-Resolution Transmission Electron Microscopic (HRTEM) study of aluminous goethites. *Clay Minerals, 20*(2), 255–262.

Marsan, F. A., & Torrent, J. (1989). Fragipan bonding by silica and iron oxides in a soil from northwestern Italy. *Soil Science Society of America Journal, 53*(4), 1140–1145.

McCusker, L. B., Von Dreele, R. B., Cox, D. E., Louër, D., & Scardi, P. (1999). Rietveld refinement guidelines. *Journal of Applied Crystallography, 32*(1), 36–50.

McDonald, R. G., & Whittington, B. I. (2008a). Atmospheric acid leaching of nickel laterites review. Part I. Sulphuric acid technologies. *Hydrometallurgy, 91*(1–4), 35–55.

McDonald, R. G., & Whittington, B. I. (2008b). Atmospheric acid leaching of nickel laterites review. Part II. Chloride and bio-technologies. *Hydrometallurgy, 91*(1–4), 56–69.

Mejía Gómez, J. A., de Resende, V. G., Antonissen, J., & De Grave, E. (2011). Characterization of the effects of silicon on the formation of goethite. *Corrosion Science, 53*(5), 1756–1761.

Mejía Gómez, J. A., Resende, V. G., Antonissen, J., & Grave, E. (2009). Influence of Mn-for-Fe substitution on structural properties of synthetic goethite. *Hyperfine Interactions, 189*(1–3), 143–149.

Milton, C., Appleman, D. E., Appleman, M. H., Chao, E. C. T., Cuttita, F., Dinnin, J. I., Dwornik, E. J., Ingram, B. L., & Rose, H. J. (1976). *Merumite, a complex assemblage of chromium minerals from Guyana*. Washington, D.C.: U.S. Government Printing Office.

Moore, D. M., & Reynolds, R. C. (1997). X-Ray diffraction and the identification and analysis of clay minerals (2nd ed.). Oxford: Oxford University Press.

Moroney, A. S. (2007) Laterite heap leaching with ferrous lixiviants. World Patent No. WO 2009/079716 A1.

Moroney, A. S., Hernandez, O. Y. C., & Liu, H. (2009) Limonite and saprolite heap leach process. World Patent No. WO 2009/033227 A1.

Morris, R. C. (1998). BIF -hosted iron ore deposits-Hamersley style. *AGSO Journal of Australian Geology & Geophysics, 17*(4), 207–211.

Mudd, G. M. (2010). Global trends and environmental issues in nickel mining: Sulfides versus laterites. *Ore Geology Reviews, 38*(1–2), 9–26.

Núñez, N. O., Tartaj, P., Morales, M. P., Pozas, R., Ocaña, M., & Serna, C. J. (2003). Preparation, characterization, and magnetic properties of Fe-based alloy particles with elongated morphology. *Chemistry of Materials, 15*(18), 3558–3563.

Nahon, D. B., & Colin, F. (1982). Chemical weathering of orthopyroxenes under lateritic conditions. *American Journal of Science, 282*(8), 1232–1243.

Nazemi, M. K., Rashchi, F., & Mostoufi, N. (2011). A new approach for identifying the rate controlling step applied to the leaching of nickel from spent catalyst. *International Journal of Mineral Processing, 100*(1–2), 21–26.

Nesse, W. D. (2000). Introduction to mineralogy (1st ed.). New York: Oxford University Press.

Neudorf, D., & Huggins, D. A. (2006) Method for nickel and cobalt recovery from laterite ores by combination of atmospheric and moderate pressure leaching. U.S.A. Patent No. US 2006/0024224 A1.

New, R. (2011). Nickel. *Australian commodities, 18*(2), 125–131.

Norrish, K., & Taylor, R. M. (1961). The isomorphous replacement of iron by aluminium in soil goethites. *European Journal of Soil Science, 12*(2), 294–306.

Noyes, A. A., & Whitney, W. R. (1897). The rate of solution of solid substances in their own solutions. *Journal of the American Chemical Society, 19*(12), 930–934.

O'Connor, B. H., & Raven, M. D. (1988). Application of the Rietveld refinement procedure in assaying powdered mixtures. *Powder Diffraction, 3*(1), 2–6.

O'Reilly, S. E., Furukawa, Y., & Newell, S. (2006). Dissolution and microbial Fe(III) reduction of nontronite (NAu-1). *Chemical Geology, 235*(1–2), 1–11.

Pabst, A. (1976). A note on choice of end members in representing certain systems and on a possible alternative to Vegard's rule. *The Canadian Mineralogist, 14*(4), 503–507.

Parfitt, R. L., & Atkinson, R. J. (1976). Phosphate adsorption on goethite (α-FeOOH). *Nature, 264*(5588), 740–742.

Park, K.-H., Mohapatra, D., Reddy, B. R., & Nam, C.-W. (2007). A study on the oxidative ammonia/ammonium sulphate leaching of a complex (Cu-Ni-Co-Fe) matte. *Hydrometallurgy, 86*(3–4), 164–171.

Postma, D. (1993). The reactivity of iron oxides in sediments: A kinetic approach. *Geochimica et Cosmochimica Acta, 57*(21–22), 5027–5034.

Pozas, R., Cristina Rojas, T., Ocana, M., & Serna, C. J. (2004a). The nature of Co in synthetic Co-substituted goethites. *Clays and Clay Minerals, 52*(6), 760–766.

Pozas, R., Ocaña, M., Morales, M. P., Tartaj, P., Nuñez, N. O., & Serna, C. J. (2004b). Synthesis of acicular Fe-Co nanoparticles and the effect of Al addition on their magnetic properties. *Nanotechnology, 15*(4), S190–S196.

Purkiss, S. A. R. (2004) Heap leaching base metals from oxide ores. World Patent No. WO 2004/031422 A1.

Quin, T. G., Long, G. J., Benson, C. G., Mann, S., & Williams, R. J. P. (1988). Influence of silicon and phosphorus on structural and magnetic properties of dynthetic goethite and related oxides. *Clays and Clay Minerals, 36*(2), 165–175.

Rao, G. V., & Sastri, S. R. S. (1996). Novel approach for enriching nickel content in lean lateritic chromite overburden. *Minerals and Metallurgical Processing, 13*, 77–81.

Rawle, A. (2008). Basic principles of particle size analysis. Retrieved from http://www.atascientific.com.au/publications/wp-content/uploads/2012/07/Basic_principles_of_particle_size_analysis_MRK034-low_res.pdf

Rietveld, H. M. (1967). Line profiles of neutron powder-diffraction peaks for structure refinement. *Acta Crystallographica, 22*(1), 151–152.

Rietveld, H. M. (1969). A profile refinement method for nuclear and magnetic structures. *Journal of Applied Crystallography, 2*(2), 65–71.

Robertson, S. W., & van Staden, P. J. (2009). The progression of metallurgical testwork during heap leach design. Paper presented at the The SAIMM Southern African Hydrometallurgy Conference 2009, Gauteng, South Africa.

Roche, E. G., & Prasad, J. (2009) Acid recovery from metal sulfates. World Patent No. WO 2009/039579 A1.

Rodríguez-Carvajal, J. (1993). Recent advances in magnetic structure determination by neutron powder diffraction. *Physica B: Condensed Matter, 192*(1–2), 55–69.

Rodriguez, M. (2008) Improved hydrometallurgical method for the extraction of nickel from laterite ores. Australia Patent No. WO 2008/022395 A1.

Rodriguez, M., & Wedderburn, B. J. (2007) Hydrometallurgical method for the extraction of nickel and cobalt from laterite ores. Australia Patent No. WO 2007/016737 A1.

Rozenson, I., Spiro, B., & Zak, I. (1982). Transformation of iron-bearing kaolinite to iron-free kaolinite, goethite, and hematite. *Clays and Clay Minerals, 30*(3), 207–214.

Ruan, H. D., & Gilkes, R. J. (1995a). Acid dissolution of synthetic aluminous goethite before and after transformation to hematite by heating. *Clay Minerals, 30*(1), 55–65.

Ruan, H. D., & Gilkes, R. J. (1995b). Dehydroxylation of aluminous goethite: Unit cell dimensions, crystal size and surface area. *Clays and Clay Minerals, 43*(2), 196–211.

Russell, J. D., Parfitt, R. L., Fraser, A. R., & Farmer, V. C. (1974). Surface structures of gibbsite goethite and phosphated goethite. *Nature, 248*(5445), 220–221.

Scarlett, N. V. Y., & Madsen, I. C. (2006). Quantification of phases with partial or no known crystal structures. *Powder Diffraction, 21*(4), 278–284.

Scarlett, N. V. Y., Madsen, I. C., Cranswick, L. M. D., Lwin, T., Groleau, E., Stephenson, G., Aylmore, M., & Agron-Olshina, N. (2002). Outcomes of the International Union of Crystallography Commission on Powder Diffraction round robin on Quantitative Phase Analysis: samples 2, 3, 4, synthetic bauxite, natural granodiorite and pharmaceuticals. *Journal of Applied Crystallography, 35*(4), 383–400.

Scarlett, N. V. Y., Madsen, I. C., & Whittington, B. I. (2008). Time-resolved diffraction studies into the pressure acid leaching of nickel laterite ores: A comparison of laboratory and synchrotron X-ray experiments. *Journal of Applied Crystallography, 41*(1), 572–583.

Scarlett, N. V. Y., Raven, M., & Madsen, I. (2011). Powder X-ray diffraction study of the hydration and leaching behavior of nontronite. *Clays and Clay Minerals, 59*(6), 560–567.

Scheinost, A. C., Schulze, D. G., & Schwertmann, U. (1999). Diffuse reflectance spectra of Al substituted goethite: A ligand field approach. *Clays and Clay Minerals, 47*(2), 156–164.

Scheinost, A. C., Stanjek, H., Schulze, D. G., Gasser, U., & Sparks, D. L. (2001). Structural environment and oxidation state of Mn in goethite-groutite solid-solutions. *American Mineralogist, 86*(1), 139–146.

Schellmann, W. (1983). Geochemical principles of lateritic nickel ore formation. Paper presented at the The 2rd International Seminar on Lateritisation Process, Sao Paulo, Brazil.

Schmitt, B., Brönnimann, C., Eikenberry, E. F., Gozzo, F., Hörmann, C., Horisberger, R., & Patterson, B. (2003). Mythen detector system. *Nuclear Instruments and Methods in Physics Research Section A: Accelerators, Spectrometers, Detectors and Associated Equipment, 501*(1), 267–272.

Schott, J., Brantley, S., Crerar, D., Guy, C., Borcsik, M., & Willaime, C. (1989). Dissolution kinetics of strained calcite. *Geochimica et Cosmochimica Acta, 53*(2), 373–382.

Schulze, D. G. (1984). The influence of aluminium on iron oxides. VIII. Unit-cell dimensions of Al-substituted goethites and estimation of Al from them. *Clays and Clay Minerals, 32*(1), 36–44.

Schulze, D. G., & Schwertmann, U. (1984). The influence of aluminium on iron oxides. X. Properties of Al-substituted goethites. *Clay Minerals, 19*(4), 521–539.

Schulze, D. G., & Schwertmann, U. (1987). The influence of aluminium on iron oxides. XIII. Properties of goethite synthesised in 0.3 M KOH at 25°C. *Clay Minerals, 22*(1), 83–92.

Schwertmann, U. (1966). Inhibitory effect of soil organic matter on the crystallization of amorphous ferric hydroxide. *Nature, 212*(5062), 645–646.

Schwertmann, U. (1984a). The double dehydroxylation peak of goethite. *Thermochimica Acta, 78*(1–3), 39–46.

Schwertmann, U. (1984b). The influence of aluminium on iron oxides. IX. Dissolution of Al-goethites in 6 M HCl. *Clay Minerals, 19*(1), 9–19.

Schwertmann, U. (1988). Some properties of soil and synthetic iron oxides. In Stucki, J. W., Goodman, B. A. & Schwertmann, Udo (Eds.), *Iron in Soils and Clay Minerals* (pp. 203–250). Dordrecht, Holland: D. Reidel Publishing Company.

Schwertmann, U. (1991). Solubility and dissolution of iron oxides. *Plant and Soil, 130*(1), 1–25.

Schwertmann, U., Cambier, P., & Murad, E. (1985). Properties of goethites of varying crystallinity. *Clays and Clay Minerals, 33*(5), 369–378.

Schwertmann, U., & Carlson, L. (1994). Aluminum influence on iron oxides: XVII. Unit-cell parameters and aluminum substitution of natural goethites. *Soil Science Society of America Journal, 58*(1), 256–261.

Schwertmann, U., Carlson, L., & Murad, E. (1987). Properties of iron oxides in two Finnish lakes in relation to the environment of their formation. *Clays and Clay Minerals, 35*(4), 297–304.

Schwertmann, U., Gasser, U., & Sticher, H. (1989). Chromium-for-iron substitution in synthetic goethites. *Geochimica et Cosmochimica Acta, 53*(6), 1293–1297.

Schwertmann, U., & Latham, M. (1986). Properties of iron oxides in some new caledonian oxisols. *Geoderma, 39*(2), 105–123.

Schwertmann, U., & Murad, E. (1983). Effect of pH on the formation of goethite and hematite from ferrihydrite. *Clays and Clay Minerals, 31*(4), 277–284.

Schwertmann, U., & Taylor, R. M. (1972a). The influence of silicate on the transformation of lepidocrocite to goethite. *Clays and Clay Minerals, 20*(3), 159–164.

Schwertmann, U., & Taylor, R. M. (1972b). The transformation of lepidocrocite to goethite. *Clays and Clay Minerals, 20*, 151–158.

Schwertmann, U., & Taylor, R. M. (1989). Iron oxides. In Dixon, J. B. & Weed, S. B. (Eds.), *Minerals in Soil Enviroments* (1st ed., pp. 379–438). Madison, Wisconsin: Soil Science Society of America.

Senanayake, G. (2009). A review of chloride assisted copper sulfide leaching by oxygenated sulfuric acid and mechanistic considerations. *Hydrometallurgy, 98*(1–2), 21–32.

Senanayake, G., Childs, J., Akerstrom, B. D., & Pugaev, D. (2011). Reductive acid leaching of laterite and metal oxides — A review with new data for Fe(Ni,Co)OOH and a limonitic ore. *Hydrometallurgy, 110*(1–4), 13–32.

Senanayake, G., Senaputra, A., & Nicol, M. J. (2010). Effect of thiosulfate, sulfide, copper(II), cobalt(II)/(III) and iron oxides on the ammoniacal carbonate leaching of nickel and ferronickel in the Caron process. *Hydrometallurgy, 105*(1–2), 60–68.

Senaputra, A., Senanayake, G., Nicol, M. J., & Nikoloski, A. (2008). Leaching nickel and nickel sulfides in ammonia/ammonium carbonate solutions. Paper presented at the Hydrometallurgy 2008 The sixth international symposium, Phoenix, Arizona.

Shannon, R. D. (1976). Revised effective ionic radii and systematic studies of interatomic distances in halides and chalcogenides. *Acta Crystallographica Section A, 32*(5), 751–767.

Shaw, S., Pepper, S. E., Bryan, N. D., & Livens, F. R. (2005). The kinetics and mechanisms of goethite and hematite crystallization under alkaline conditions, and in the presence of phosphate. *American Mineralogist, 90*(11–12), 1852–1860.

Sidhu, P. S., Gilkes, R. J., Cornell, R. M., Posner, A. M., & Quirk, J. P. (1981). Dissolution of iron oxides and oxyhydroxides in hydrochloric and perchloric acids. *Clays and Clay Minerals, 29*(4), 269–276.

Sileo, E. E., Alvarez, M., & Rueda, E. H. (2001). Structural studies on the manganese for iron substitution in the synthetic goethite-jacobsite system. *International Journal of Inorganic Materials, 3*(4–5), 271–279.

Sileo, E. E., Ramos, A. Y., Magaz, G. E., & Blesa, M. A. (2004). Long-range vs. short-range ordering in synthetic Cr-substituted goethites. *Geochimica et Cosmochimica Acta, 68*(14), 3053–3063.

Singh, B., & Gilkes, R. J. (1991). Concentration of iron oxides from soil clays by 5M NaOH treatment: The complete removal of sodalite and kaolinite. *Clay Minerals, 26*(4), 463–472.

Singh, B., & Gilkes, R. J. (1992). Properties and distribution of iron oxides and their association with minor elements in the soils of south-western Australia. *European Journal of Soil Science, 43*(1), 77–98.

Singh, B., Sherman, D. M., Gilkes, R. J., Wells, M. A., & Mosselmans, J. F. W. (2002). Incorporation of Cr, Mn and Ni into goethite (α-FeOOH):

mechanism from extended X-ray absorption fine structure spectroscopy. *Clay Minerals, 37*(4), 639–649.

Smith, K. L., & Eggleton, R. A. (1983). Botryoidal goethite: A Transmission Electron Microscope study. *Clays and Clay Minerals 31*(5), 392–396.

Steemson, M. L., & Smith, M. E. (2009). The development of nickel laterite heap leach projects. Paper presented at the ALTA 2009 conference, Perth, Western Australia.

Steyl, J. D. T., Pelser, M., & Smit, J. T. (2008). Atomospheric leach process for nickel laterites ores. Paper presented at the Hydrometallurgy 2008 The sixth international symposium, Phoenix, Arizona.

Stiers, W., & Schwertmann, U. (1985). Evidence for manganese substitution in synthetic goethite. *Geochimica et Cosmochimica Acta, 49*(9), 1909–1911.

Stinton, G. W., & Evans, J. S. O. (2007). Parametric Rietveld refinement. *Journal of Applied Crystallography, 40*(1), 87–95.

Stumm, W., & Wollast, R. (1990). Coordination chemistry of weathering: Kinetics of the surface-controlled dissolution of oxide minerals. *Reviews of Geophysics, 28*(1), 53–69.

Sudakar, C., Subbanna, G. N., & Kutty, T. R. N. (2004). Effect of cationic substituents on particle morphology of goethite and the magnetic properties of maghemite derived from substituted goethite. *Journal of Materials Science, 39*(13), 4271–4286.

Sudol, S. (2005). The thunder from down under: Everything you wanted to know about laterites but were afraid to ask. *Canadian Mining Journal, 126*(5), 8–11.

Surana, V. S., & Warren, I. H. (1969). The leaching of goethite. *Transactions of the Institution of Mining and Metallurgy, 78*, C133–C139.

Suzuki, S., Takahashi, Y., Kamimura, T., Miyuki, H., Shinoda, K., Tohji, K., & Waseda, Y. (2004). Influence of chromium on the local structure and morphology of ferric oxyhydroxides. *Corrosion Science, 46*(7), 1751–1763.

Tang, H., Guo, Z., & Zhao, Z. (2010). Phosphorus removal of high phosphorus iron ore by gas-based reduction and melt separation. *Journal of Iron and Steel Research, International, 17*(9), 1–6.

Tardy, Y. (1997). Petrology of Laterites and Tropical Soils: Taylor & Francis.

Taylor, A. (2007). Nickel processing technology 10 years on from Cawse, Bulong and Murrin Murrin. Paper presented at the ALTA Ni/Co 2007–12th Nickel/Cobalt Conference, Perth.

Taylor, A. (2009). Trends in Nickel-Cobalt Processing. Paper presented at the ALTA 2009 Conference, Perth, Western Australia.

Taylor, J. C. (1991). Computer programs for the standardless quantitative analysis of minerals using the full powder diffraction profile. *Powder Diffraction, 6*(1), 2–9.

Taylor, J. C., & Matulis, C. E. (1994). A new method for Rietveld clay analysis. Part I. Use of a universal measured standard profile for Rietveld quantification of montmorillonites. *Powder Diffraction, 9*(2), 119–123.

Thiel, R. (1963). Zum system α-FeOOH–α-AlOOH. *Zeitschrift für Anorganische und Allgemeine Chemie, 326*(1), 70–78.

Thurston, E. (1913). The Madras Presidency, With Mysore, Coorg and the Associated States. Cambridge: Cambridge University Press.

Torrent, J., & Barrón, V. (1990). Phosphate adsorption and desorption by goethites differing in crystal morphology. *Soil Science Society of America Journal, 54*(7–8), 1007–1012.

Torrent, J., Barron, V., & Schwertmann, U. (1987). The reductive dissolution of synthetic goethite and hematite in dithionite. *Clay Minerals, 22*(3), 329–337.

Torrent, J., Schwertmann, U., & Barrón, V. (1992). Fast and slow phosphate sorption by goethite-rich natural materials. *Clays and Clay Minerals, 40*(1), 14–21.

Trolard, F., Bourrie, G., Jeanroy, E., Herbillon, A. J., & Martin, H. (1995). Trace metals in natural iron oxides from laterites: A study using selective kinetic extraction. *Geochimica et Cosmochimica Acta, 59*(7), 1285–1297.

Tsipursky, S. I., & Drits, V. A. (1984). The distribution of octahedral cations in the 2:1 layers of dioctahedral smectites studied by oblique-texture electron diffraction. *Clay Minerals, 19*(2), 177–193.

Ufer, K., Roth, G., Kleeberg, R., Stanjek, H., Dohrmann, R., & Bergmann, J. (2004). Description of X-ray powder pattern of turbostratically disordered layer structures with a Rietveld compatible approach. *Zeitschrift für Kristallographie, 219*(9), 519–527.

Ufer, K., Stanjek, H., Roth, G., Dohrmann, R., Kleeberg, R., & Kaufhold, S. (2008). Quantitative phase analysis of Bentonites by the Rietveld method. *Clays and Clay Minerals, 56*(2), 272–282.

van der Woude, J. H. A., de Bruyn, P. L., & Pieters, J. (1984). Formation of colloidal dispersions from supersaturated iron(III) nitrate solutions. III. Development of goethite at room temperature. *Colloids and Surfaces, 9*(2), 173–188.

van Staden, P. J., Robertson, S. W., Gericke, M., Neale, J. W., & Seyedbagheri, A. (2009). Maximising the value derived from laboratory testwork towards heap leaching design. Paper presented at the 5th Base Metals Conference, Kasane, Botswana.

Vandenberghe, R. E., Verbeeck, A. E., De Grave, E., & Stiers, W. (1986). ^{57}Fe Mössbauer effect study of Mn-substituted goethite and hematite. *Hyperfine Interactions, 29*(1–4), 1157–1160.

Vegard, L., & Dale, H. (1928). Untersuchungen üeber mischkristalle und Legierungen. *Zeitschrift für Kristallographie, 67*, 148–162.

Vempati, R. K., Morris, R. V., Lauer, H. V., & Helmke, P. A. (1995). Reflectivity and other physicochemical properties of Mn-substituted goethites and hematites. *Journal of Geophysical Research: Planets, 100*(E2), 3285–3295.

Venema, P., Hiemstra, T., & van Riemsdijk, W. H. (1996). Multisite adsorption of cadmium on goethite. *Journal of Colloid and Interface Science, 183*(2), 515–527.

Wadsworth, M. E. (1979). Hydrometallurgical Process. In Sohn, Hong Yong & Wadsworth, Milton E. (Eds.), *Rate processes of extractive metallurgy* (1st ed.). New York: Plenum Press.

Wagner, C. (1933). Beitrag zur Theorie des Anlaufvorgangs. *Zeitschrift für Physikalische Chemie B, 21*, 25–41.

Wallwork, K. S., Kennedy, B. J., & Wang, D. (2007). The high resolution powder diffraction beamline for the Australian Synchrotron. Paper presented at the AIP Conference.

http://direct.bl.uk/bld/PlaceOrder.do?UIN=210058720&ETOC=RN&from=searchengine

Walter, D., Buxbaum, G., & Laqua, W. (2001). The mechanism of the thermal transformation from goethite to hematite. *Journal of Thermal Analysis and Calorimetry, 63*(3), 733–748.

Wang, J., Shen, S., Kang, J., Li, H., & Guo, Z. (2010). Effect of ore solid concentration on the bioleaching of phosphorus from high-phosphorus iron ores using indigenous sulfur-oxidizing bacteria from municipal wastewater. *Process Biochemistry, 45*(10), 1624–1631.

Wang, X., Hart, R. D., Li, J., McDonald, R. G., & van Riessen, A. (2012). Quantitative analysis of turbostratically disordered nontronite with a supercell model calibrated by the PONKCS method. *Journal of Applied Crystallography 45*(6), 1295–1302.

Wang, X., Li, J., Hart, R. D., van Riessen, A., & McDonald, R. (2011). Quantitative X-ray diffraction phase analysis of poorly ordered nontronite clay in nickel laterites. *Journal of Applied Crystallography, 44*(5), 902–910.

Warren, B. E. (1941). X-ray diffraction in random layer lattices. *The Physical Review, 59*(9), 693–698.

Warren, B. E., & Bodenstein, P. (1965). The diffraction pattern of fine particle carbon blacks. *Acta Crystallographica, 18*(2), 282–286.

Warren, B. E., & Bodenstein, P. (1966). The shape of two-dimensional carbon black reflections. *Acta Crystallographica, 20*(5), 602–605.

Warren, I. H., & Hay, M. G. (1975). Leaching of iron oxides with aqueous solutions of sulphur dioxide. *Transactions of the Institution of Mining and Metallurgy. Section C, Mineral processing and extractive metallurgy, 84*, C49–C53.

Warren, I. H., & Roach, G. I. D. (1971). Physical aspects of the leaching of goethite and hematite. *Transactions of the Institution of Mining and Metallurgy, 80*, C152–C155.

Watling, H. R. (2006). The bioleaching of sulphide minerals with emphasis on copper sulphides — A review. *Hydrometallurgy, 84*(1–2), 81–108.

Watling, H. R., Elliot, A. D., Fletcher, H. M., Robinson, D. J., & Sully, D. M. (2011). Ore mineralogy of nickel laterites: Controls on processing characteristics under simulated heap-leach conditions. *Australian Journal of Earth Sciences, 58*(7), 725–744.

Wedderburn, B. (2009). Nickel laterite processing — A shift towards heap leaching. Paper presented at the ALTA 2009 Conference, Kalgoorlie, Western Australia.

Wedderburn, B. (2010). Nickel heap leaching study. Paper presented at the INSG Meeting April 2010, Lisbon, Portugal.

Weidler, P. G., Schwinn, T., & Gaub, H. E. (1996). Vicinal faces on synthetic goethite observed by atomic force microscopy. *Clays and Clay Minerals, 44*(4), 437–442.

Wells, M. A., Fitzpatrick, R. W., & Gilkes, R. J. (2006). Thermal and mineral properties of Al-, Cr-, Mn-, Ni- and Ti-substituted goethite. *Clays and Clay Minerals, 54*(2), 176–194.

Wells, M. A., & Gilkes, R. J. (1998). Synthetic Ni goethite and hematite: reproducing hosts for nickel mineralization in Ni-laterites. Paper presented at the 3rd Australian Regolith Conference, Kalgoorlie, Western Australia.

Whittington, B. I., & Johnson, J. (2005). Pressure acid leaching of arid-region nickel laterite ore Part III: Effect of process water on nickel losses in the residue. *Hydrometallurgy, 78*(3–4), 256–263.

Whittington, B. I., Johnson, J. A., Quan, L. P., McDonald, R. G., & Muir, D. M. (2003a). Pressure acid leaching of arid-region nickel laterite ore Part II: Effect of ore type. *Hydrometallurgy, 70*(1–3), 47–62.

Whittington, B. I., McDonald, R. G., Johnson, J. A., & Muir, D. M. (2003b). Pressure acid leaching of arid-region nickel laterite ore Part I: Effect of water quality. *Hydrometallurgy, 70*(1–3), 31–46.

Whittington, B. I., & Muir, D. (2000). Pressure acid leaching of nickel laterites: A review. *Mineral Processing and Extractive Metallurgy Review, 21*(6), 527–599.

Wieland, E., Wehrli, B., & Stumm, W. (1988). The coordination chemistry of weathering: III. A generalization on the dissolution rates of minerals. *Geochimica et Cosmochimica Acta, 52*(8), 1969–1981.

Williams, D. B., & Carter, C. B. (2009). Transmission Electron Microscopy. A textbook for Materials Science (2 ed.). New York: New York Plenum Press 2009.

Wu, F. (2012). Aluminous goethite in the Bayer process and its impact on alumina recovery and settling. Doctoral of Philosophy, Curtin University, Perth, Australia.

Xu, B., Wingate, C., & Smith, P. (2009). The effect of surface area on the modelling of quartz dissolution under conditions relevant to the Bayer process. *Hydrometallurgy, 98*(1–2), 108–115.

Yang, D., & Frindt, R. F. (1996). Powder x-ray diffraction of turbostratically stacked layer systems. *Journal of Materials Research, 11*(7), 1733–1738.

Yongue-Fouateu, R., Ghogomu, R. T., Penaye, J., Ekodeck, G. E., Stendal, H., & Colin, F. (2006). Nickel and cobalt distribution in the laterites of the Lomié region, south-east Cameroon. *Journal of African Earth Sciences, 45*(1), 33–47.

Young, R. A. (1995). The Rietveld method: Oxford University Press.

Zhai, Y., Mu, W., Liu, Y., & Xu, Q. (2010). A green process for recovering nickel from nickeliferous laterite ores. *Transactions of Nonferrous Metals Society of China, 20*(Supplement 1), s65–s70.

Zhang, Y., & Muhammed, M. (1989). The removal of phosphorus from iron ore by leaching with nitric acid. *Hydrometallurgy, 21*(3), 255–275.

Zinder, B., Furrer, G., & Stumm, W. (1986). The coordination chemistry of weathering: II. Dissolution of Fe(III) oxides. *Geochimica et Cosmochimica Acta, 50*(9), 1861–1869.

Zuniga, M., Parada L, F., & Asselin, E. (2010). Leaching of a limonitic laterite in ammoniacal solutions with metallic iron. *Hydrometallurgy, 104*(2), 260–267.

Appendix 1. Comment on the kinetic fitting of Cornell's 1993 study

Both the monograph "Iron oxides" (Cornell & Schwertmann, 1996; Cornell & Schwertmann, 2003) and the Cornell's 1993 paper (Cornell & Giovanoli, 1993) claim that the Avrami-Erofejev model fits the experimental acid dissolution of goethite data better than the Kabai model did. This cannot be true because the Avrami-Erofejev model is a special case of the Kabai model when a=2.

Avrami-Erofejev model: (only *k* is adjustable during fitting)

$$\left(-\mathrm{Ln}(1-\alpha)\right)^{\frac{1}{2}} = kt$$

Kabai model: (both a and *k* are adjustable during fitting)

$$\left(-\mathrm{Ln}(1-\alpha)\right)^{\frac{1}{a}} = kt$$

To check this claim, the hematite acid dissolution data in Cornel's 1993 paper was digitised from the chart of the original publication, as shown in Figure A1-1.

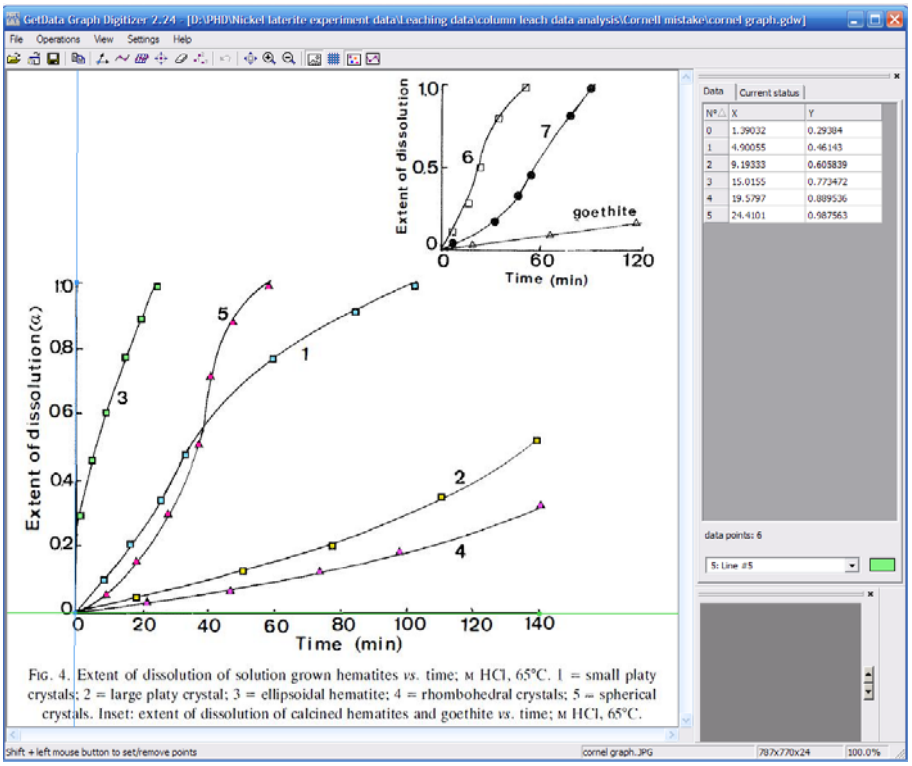

Figure A1-1 The seven leaching curves were digitised from the graphs.

Both Kabai fitting and Avrami-Erofejev fitting for the digitised data were conducted in Wolfram® *Mathematica* v8.0.4. The results are compared in Table A1-1 with the refined model parameters shown in Table A1-2.

Table A1-1 Comparison of the fittings of Kabai model and Avrami-Erofejev model on the same leaching curves.

Sample	Kabai fitting	Avrami-Erofejev fitting
1	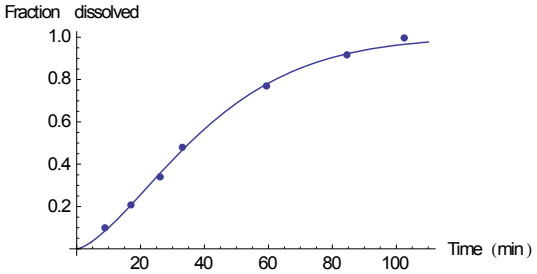	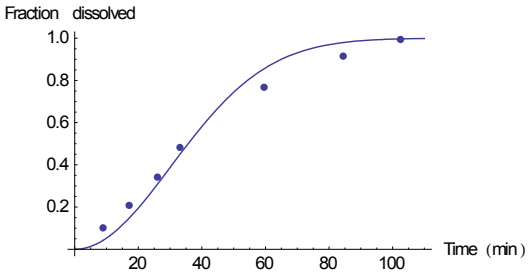
2	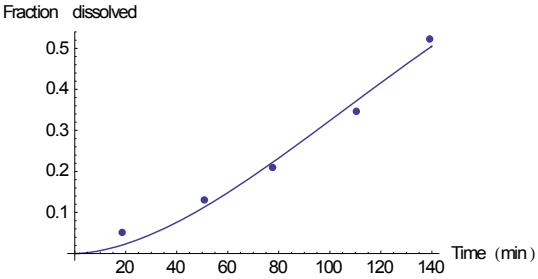	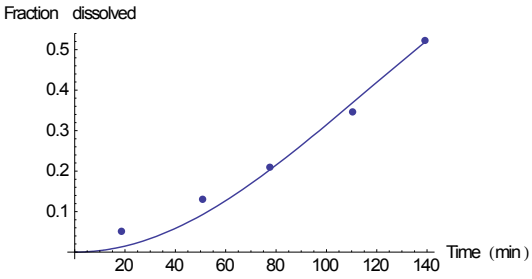
3	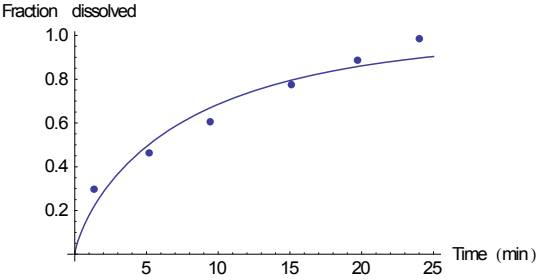	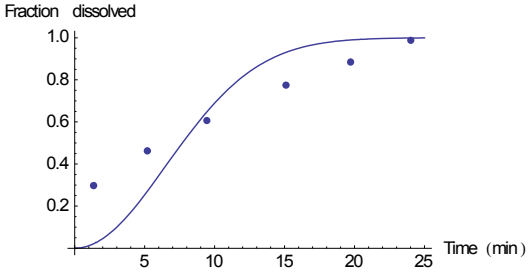
4	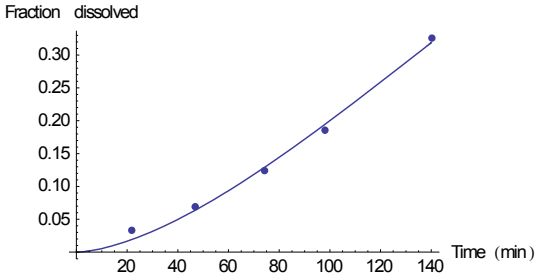	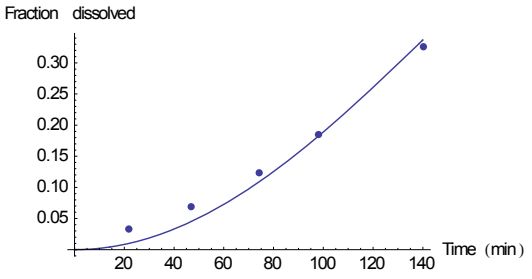
5	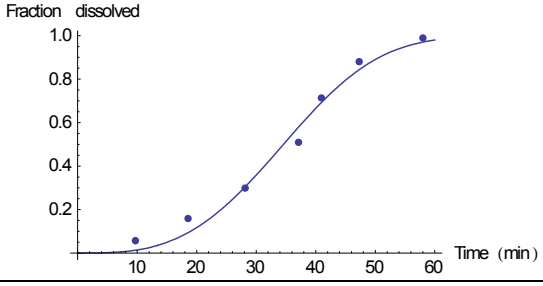	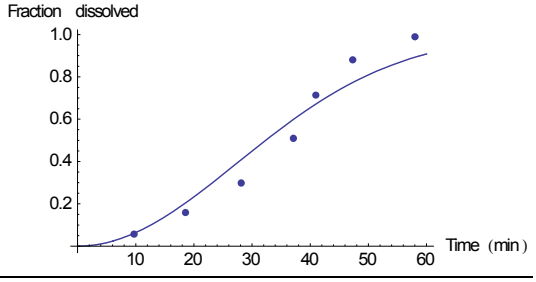

Sample	Kabai fitting	Avrami-Erofejev fitting
6	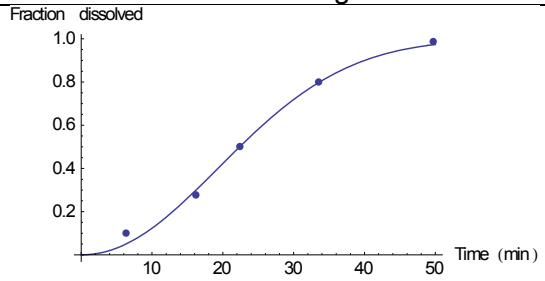	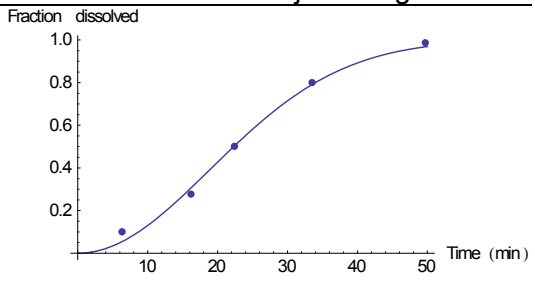
7	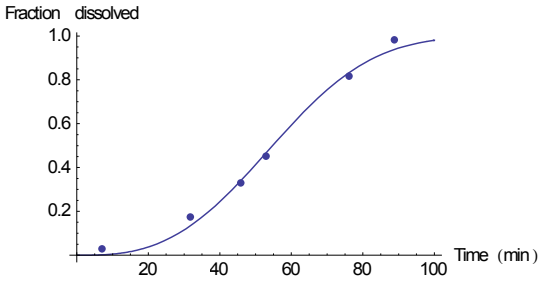	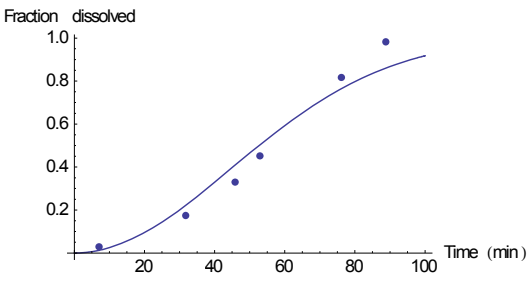

Table A1-2 Refined parameters and goodness of fitting R^2 of both "Kabai" and "Avrami-Erofejev" model

	Kabai			Avrami-Erofejev	
Sample	k 10^{-3}(min^{-1})	a	R^2	k 10^{-3}(min^{-1})	R^2
1	22.2(4)	1.49(5)	0.999	23(1)	0.993
2	5.8(3)	1.8(2)	0.995	6.1(2)	0.993
3	120(20)	0.8(1)	0.993	110(20)	0.950
4	4.0(2)	1.6(1)	0.998	4.6(1)	0.991
5	25.7(6)	3.1(4)	0.995	26(1)	0.983
6	37(1)	2.1(2)	0.998	37(1)	0.998
7	16.1(4)	2.9(2)	0.997	15.8(9)	0.985

It is clear from the fittings in Table A1-1 and the R^2 figures in Table A1-2, that none of Avrami-Erofejev fittings are better than the Kabai fittings, which suggest Cornell's comments in above publications were not correct. The Wolfram® *Mathematica* notebook file containing these fittings is available upon request.

Appendix 2. X-ray diffractometer characterisation

The accuracy and stability of a measuring instrument is vital to the quality and precision of the result generated from it. It is imperative to understand and characterise the X-ray diffractometer to be used prior to data collection. The following parameters were assessed for the Bruker® D8 Advance and D8 Discover as part of the data analysis undertaken for this thesis; zero error, K_β residual, and their stability, especially when the X-ray tube was replaced and beam path was realigned. Variation of sample holder location has been identified as a contributor to changes in sample height.

A2.1 Angular accuracy

The Bruker® supplied NIST 1976 corundum ceramic plate was used as a standard reference material to check the angular accuracy of the D8 Advance goniometer. Eleven standard patterns scanned from 12th Dec 2011 to 30th Dec 2011 were analysed to check the instrumental stability.

In order to extract accurate peak positions, each peak was treated as independent, *i.e.* no peak position constraint was used and the 5th order Chebyshev background coefficients were refined. Both Split Pseudo-Voigt (SPV) and Split Pearson VII (SPVII) peak profile fittings were tested since they gave better fit than the symmetric peak profiles (PV or PVII). No sample displacement error and zero error shift correction were used at this stage to extract the apparent peak positions. Data lower than 8^o 2θ were ignored to minimise air scattering interference. As no monochromator was used in the beam path the polarisation factor was fixed to 0. Instrumental parameters, cobalt radiation wavelength values as well as the starting value of SPV peak profile are shown in Figure A2-1.

The fitted peak positions of each pattern were recorded and compared to the calculated peak position for each corundum hkl reflection based on the wavelength EMREF[5] and certified lattice parameter of NIST SRM 1976. The deviations of the measured peak position from the certified peak positions are plotted against the certified peak positions in Figure A2-2. All but one

[5] The reference wavelength with largest area in the radiation family (Hölzer *et al.*, 1997) was used in Bragg equation to calculate peak position (Bruker AXS, 2009).

measurement was positive. After removal of two outliers from data collected on the 19th and 29th December the maximum deviations span from 0.006 to 0.018° 2θ.

```
Rp 250
Rs 250
lpsd_th2_angular_range_degrees  3
   lpsd_equitorial_divergence_degrees  0.3
   lpsd_equitorial_sample_length_mm  20
      lpsd_beam_spill_correct_intensity 0
axial_conv
   filament_length  12
   sample_length  25
   receiving_slit_length  17
   primary_soller_angle  2.5
   secondary_soller_angle  2.5
   axial_n_beta  30
lam
   ymin_on_ymax  0.0001
   la  0.5981 lo  1.78896 lh  0.47
   la  0.0503 lo  1.789879 lh  0.3357
   la  0.3516 lo  1.79285 lh  0.8052
xo_ls
   xo @ 29.79268109
   l @ 733.7
   peak_type spv
      spv_h1 @ 0.05
      spv_h2 @ 0.05
      spv_l1 @ 0.5
      spv_l2 @ 0.5
…
```

Figure A2-1 The beam path settings used in Bruker® D8 Advance and the starting values of the first SPV peak.

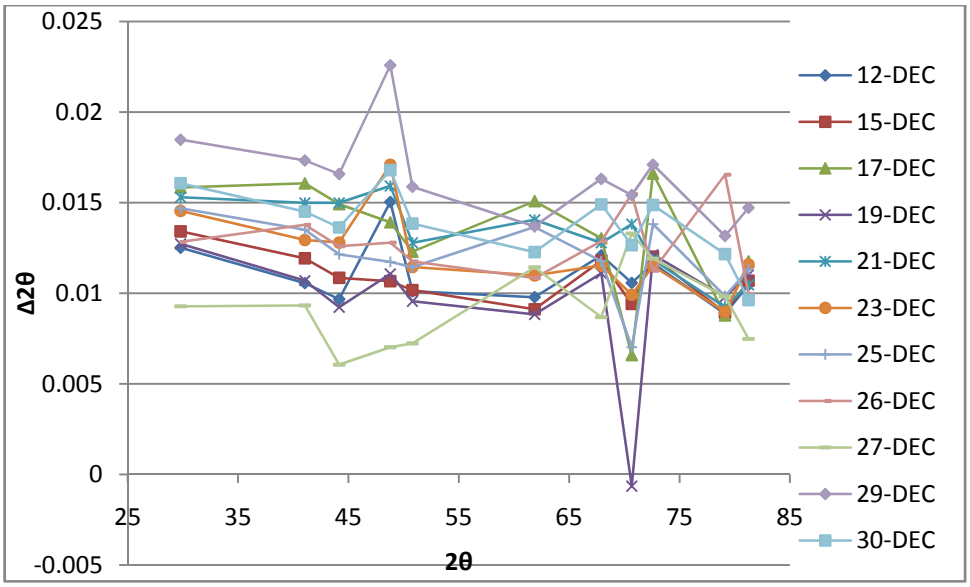

Figure A2-2 Angular dependency of the SPV peak position deviations of all the scanned patterns

A2.2 Zero error determination

The goniometer zero error should be calculated from all the peak positions in the pattern, hence peak position constraint should be used in the model of the standard material. The peak intensities may not be constrained by crystallographic structure as it is not helpful in refining peak positions. Hence a corundum lattice model (hkl_Is phase) was used to calculate the goniometer zero error from the 11 NIST 1976 patterns collected above. All the settings, including instrumental parameters and radiation files, were the same as those described in Figure A2-1 except the hkl_Is phase with the certified NIST 1976 lattice parameters were used (Figure A2-3). Peak profiles were fitted with “Double Voigt” method with Fundamental Parameter Approach. Sample displacement shift was initially not used because the NIST 1976 corundum ceramics plate is aligned and mounted permanently to the metal holder.

```
hkl_ls
  LVol_FWHM_CS_G_L(1, 238.775, 0.89, 266.405, cscorg,  392.832, cscorl, 749.430)
  r_bragg  0.8933012933
  phase_name "hkl_corundum"
  MVW( 611.7675635,@ 254.827, 100)
  scale @ 0.0903313346
  space_group R-3cH
  Trigonal(!acor 4.758846,!ccor 12.99306)
```

Figure A2-3 The hkl_ls phase model of the NIST SRM 1976 used in zero_error determination

The trend of calculated zero error is shown in Figure A2-4. The turbulent trend may lead one to believe the goniometer is unstable. A closer examination of Figure A2-2 indicates that the difference of angular deviation between pattern scanned on 27th Dec and pattern scanned on 29th Dec is larger at low angle and smaller at higher angle. This observation implies that the difference of angular deviation might come from the difference of sample displacement error which has a cos(θ) dependency. Since the low angle peak positions are more vulnerable to sample displacement error induced shift, the zero error determined from patterns below 90 °2θ can be affected by the sample displacement error if it was ignored. This highlighted the fact that the sample displacement error was varying even though the corundum plate is securely fixed to the metal holder. The remaining factor that can lead to the observed variance must be attributed to the sample load and unload operation of the D8 Advance robot hand. A careful observation on the behaviour of the robot hand revealed the root cause: when the sample holder is unloaded and returned back to the holder magazine, the holder position is not centred and fitted into the correct position, as shown in Figure A2-5. When this sample (normally only the standard will be scanned repeatedly) is rescanned, the sample surface is no longer straight up when it is grabbed again by the robot hand and this sample will be slightly tilted when it is dropped into the sample spinner slot, which in turn introduce sample displacement error. When this sample holder positioning problem was recognised, another pattern of NIST 1976 standard was collected on 30th Dec after the sample holder was centred in the holder magazine and the zero error went back to the average value. If the two patterns suspected to have

sample displacement error are ignored, the remaining 9 zero errors in Figure A2-4 show the correct instrument zero error would be around 0.008 °2θ.

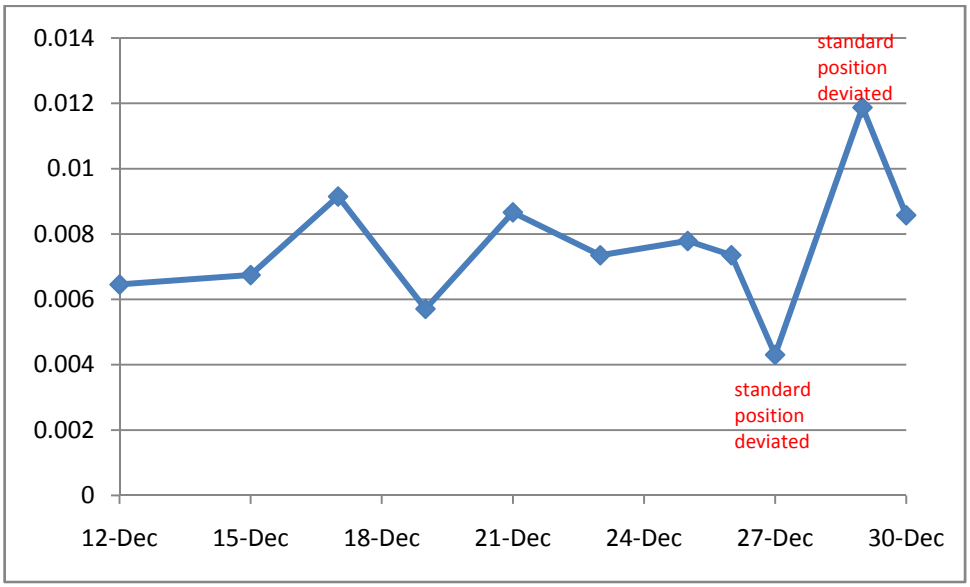

Figure A2-4 Zero error trend from 12th Dec to 30th Dec. The zero errors were calculated without using sample displacement error. Patterns scanned on 27th Dec and on 29th Dec are outliers with sample holder positioning problem.

Usually in Bragg-Brentano geometry, the zero error of a goniometer is relative stable and the sample displacement error changes from sample to sample. The standard patterns can be jointly used to determine the goniometer zero error and the individual sample displacement errors. All the NIST 1976 patterns were then fitted simultaneously with zero error refinable but linked across patterns and the individual sample displacement errors were refined. The Gaussian and Lorentzian size broadening parameters were linked across the patterns as well as the patterns are collected on the same sample. Simultaneous refining multiple patterns has shown to be a good way to stabilising parameters against random error and generating physically meaningful results by averaging parameters from multiple measurements within the Rietveld iterative process (Stinton & Evans, 2007; Wang *et al.*, 2011; Madsen *et al.*, 2013, p291). The final zero error calculated from these patterns is 0.0096(2) 2θ°, as shown in Figure A2-6. The zero error should then be fixed as the characterised value of this goniometer.

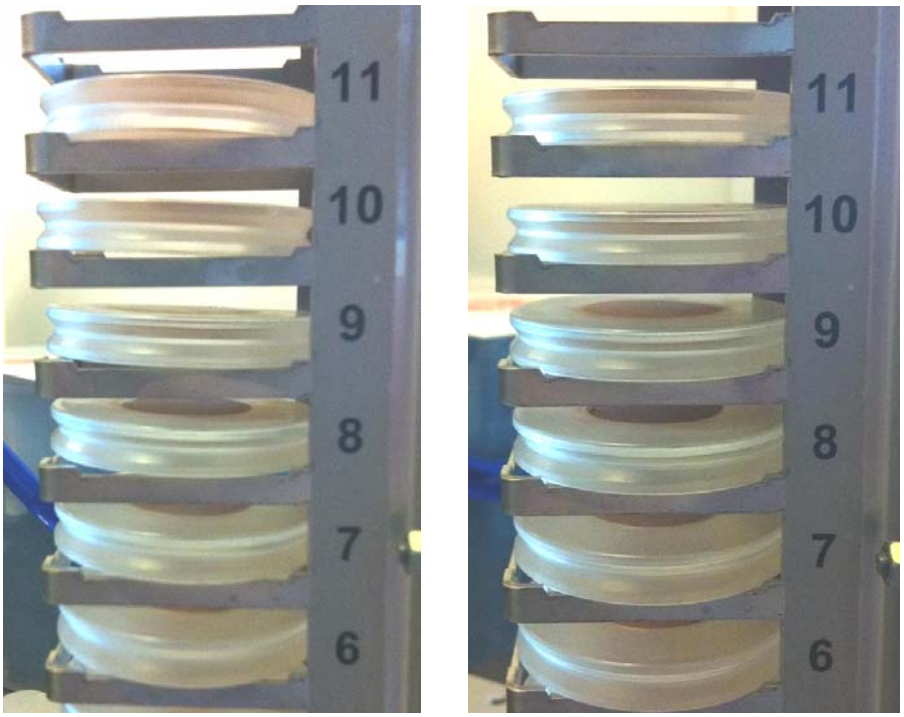

(a) (b)

Figure A2-5 Robot returns sample holders to a tilted position (a) compared to the correct holder position (b)

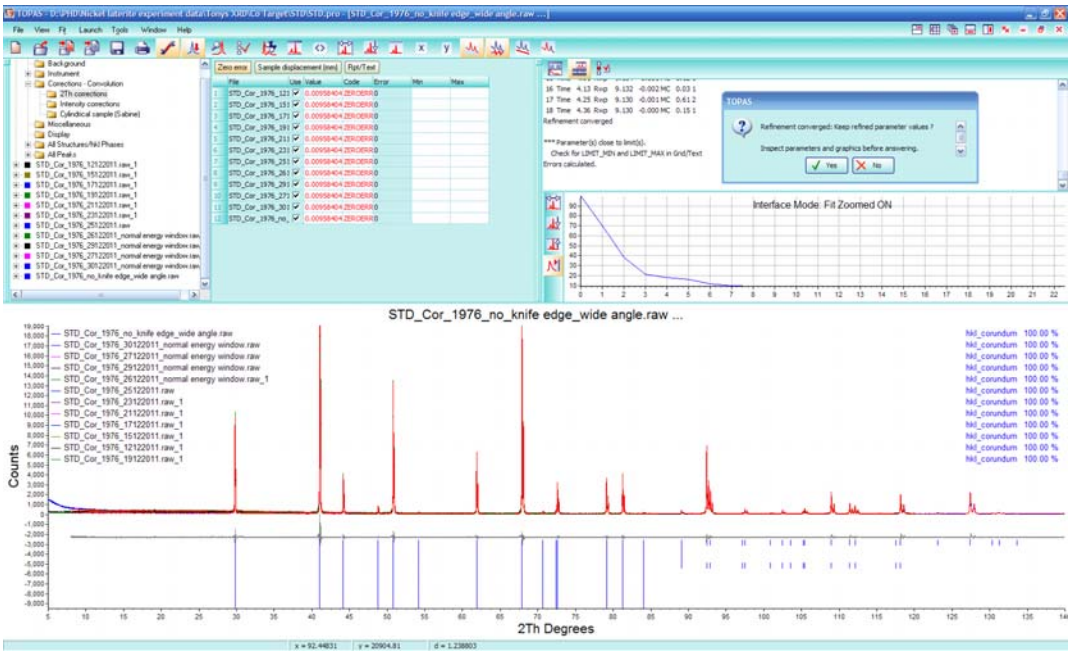

Figure A2-6 Multiple NIST SRM 1976 patterns jointly determine the zero error of the goniometer

A2.3 CoK_β residual characterisation

As no monochromator was used in the beam path, iron filters were installed on both primary arm and secondary arm to attenuate the CoK_β photons. However, residual CoK_β photons are still transmitted and contribute to the pattern (the energy window of LynxEye detector cannot differentiate this from the CoK_α), which is more apparent for high intensity peaks, as shown in Figure A2-7. The CoK_α and CoK_β radiation files can be weighted and combined to describe this polychromatic photon source. The standard pattern was initially fitted with a corundum lattice model (hkl_Is phase) to obtain a correct peak profile before refining the intensity or area of the CoK_β radiation components. The final X-ray source file is listed in Figure A2-8.

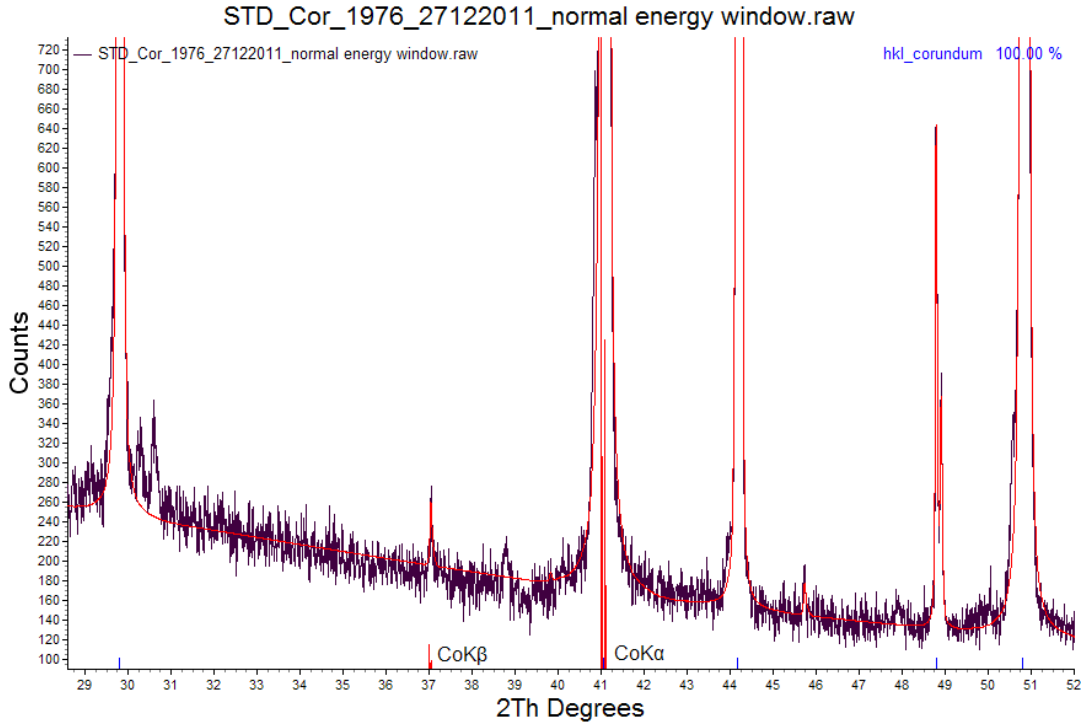

Figure A2-7 Residual CoK_β photons contributing to pattern signal can be identified and modelled. Three lower peaks at 30.2, 30.6, 38.8 2θ° belong to mullite (PDF# 00-015-0776) impurity in the NIST 1976 standard

```
lam
ymin_on_ymax  0.0001
        la  0.378 lo  1.7889847 lh  0.4633522
        la  0.144 lo  1.7892524 lh  0.6958819
        la  0.127 lo  1.7896946 lh  1.176738
        la  0.088 lo  1.7888515 lh  0.208542
        la  0.197 lo  1.7927905 lh  0.6237179
        la  0.095 lo  1.7930637 lh  0.7190761
        la  0.05 lo  1.7934738 lh  1.1578452
        la !Kbeta_area 0.001522140797 min=0; max=0.005; lo 1.6207938 lh 0.6462327
        la =Kbeta_area 0.420935; :  0.0006407223364 lo  1.6211689 lh  0.75888
        la =Kbeta_area 0.340757; :  0.0005186801316 lo  1.622858 lh  2.0774644
        la =Kbeta_area 0.229399; :  0.0003491775767 lo  1.6216651 lh  1.0372054
        la =Kbeta_area 0.182628; :  0.0002779855295 lo  1.6236359 lh  2.8895524
        la =Kbeta_area 0.055679; :  8.475127744e-005 lo  1.6198346 lh  0.8020733
```

Figure A2-8 X-ray source file including both CoK_{α} and CoK_{β} components.

A2.4 Summary

The goniometer zero error is calculated as 0.0096(2) °2θ. High angle data are preferred for zero error determination; low angle peak positions are easily affected by sample displacement error, which is a random variable if sample holder loading and unloading by the robot hand are taken into account. To minimise this variation, careful examination should be made to make sure all sample holders are centred in the magazine slot before robot hand operation. A CoK_{α} and CoK_{β} combined lam file was generated to describe the polychromatic photon source of the iron filtered Co radiation.

Appendix 3. Characterisation of the wavelength and instrumental broadening of synchrotron XRD

The instrumental contributions to the peak profile and the wavelength employed in the Australian Synchrotron Powder Diffraction Beamline were determined according to the standard pattern of the NIST SRM 660b LaB_6 powders diluted with diamond powder with 1:9 weight ratio, collected in a 0.3 mm borosilicate glass capillary.

A3.1 Instrumental convolutions determined by peaks phase

The instrumental convolutions on the LaB_6 lines profiles were determined using an FP type peaks phase (size broadening constrained to isotropic). The diamond peaks were excluded. An 8^{th} order Chebyshev background was refined. The X-ray wavelength, although not affecting the peaks phase positions, was set as a close value of 1 Å. The polarisation factor was set to 90°. The calculation step for variable step size patterns was set as 0.002, which is close to the step size of the Mythen detector. The goniometer radius used in this beamline was fixed at 761.2 mm. No zero error correction or sample displacement error correction was applied. The instrumental convolutions were tested one by one and five most effective convolutions (those reduced R_{wp} most) were accepted. They are shown in Figure A3-1. These should be fixed to represent the instrument induced line broadening in other refinements. The final fitting of the peaks phase to the LaB_6 line profiles is shown in Figure A3-2.

```
User_Defined_Dependence_Convolution(gauss_fwhm, 1/Cos(Th) , @, 0.01144311248 min =0.0001; max =0.05;)
User_Defined_Dependence_Convolution(gauss_fwhm, Tan(Th) , @, 0.01154093578 min =0.0001; max =0.05;)
User_Defined_Dependence_Convolution(gauss_fwhm, Sin(2 Th) , @, 0.01092638219 min =0.0001; max =0.05;)
User_Defined_Dependence_Convolution(lor_fwhm, Tan(Th) , @, 0.005592507985 min =0.0001; max =0.05;)
User_Defined_Dependence_Convolution(circles_conv, 1/Cos(Th) , @, -0.01403950676 min =-0.1; max =0;)
```

Figure A3-1 The five instrumental convolutions adopted that gave the best fit to the NIST SRM 660b LaB_6 profile.

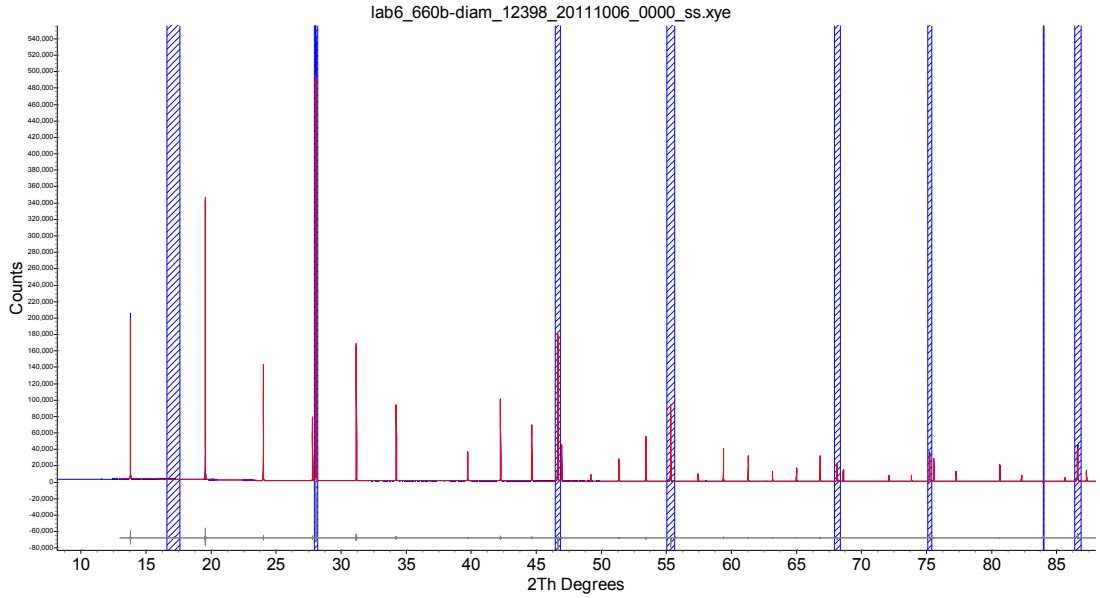

Figure A3-2 The fitting of the peaks phase to the LaB_6 line profiles with instrumental convolutions. The excluded regions contain peaks of diamond and other impurities. Final R_{wp} 3.45.

A3.2 X-ray wavelength determined with certified LaB_6 lattice parameter

The peaks phase was replaced with a LaB_6 structure model in which the NIST certified lattice parameter value 4.15689 Å was fixed. The sample induced broadening determined from previous peaks phase was adopted in the LaB_6 structure model. The initial scale factor for LaB_6 phase was determined from several refinements. After a close fit was achieved, the wavelength and the zero error are refined in the “Continue after convergence” and “Randomize as a function of errors” mode within a defined interval. By doing this, the TOPAS program searches combinations of every refined parameter value within a given interval to achieve the best fit to the standard pattern. The refinement could be stopped if it began to diverge and the parameter combination of the best fitting was stored and accepted. The final parameter set describing the instrumental parameters of the setting used in ASPD was shown in Figure A3-3. These values were fixed in the refinement for real samples. The final fitting is shown in Figure A3-4.

```
LP_Factor( 90)
Zero_Error( -0.001772470927 min =-0.01; max =0.01;)
Rp 761.2
Rs 761.2
User_Defined_Dependence_Convolution(gauss_fwhm,1/Cos(Th),,0.01144311248)
User_Defined_Dependence_Convolution(gauss_fwhm,Tan(Th),,0.01154093578)
User_Defined_Dependence_Convolution(gauss_fwhm,Sin(2 Th),,0.01092638219)
User_Defined_Dependence_Convolution(lor_fwhm,Tan(Th),,0.005592507985)
User_Defined_Dependence_Convolution(circles_conv,1/Cos(Th),,-0.01403950676)
lam
ymin_on_ymax  0.001
la  1 lo  0.999047433 min =0.999; max =1; lh  0.0001
x_calculation_step 0.002
```

Figure A3-3 Final parameter set describing the instrumental settings employed in this study

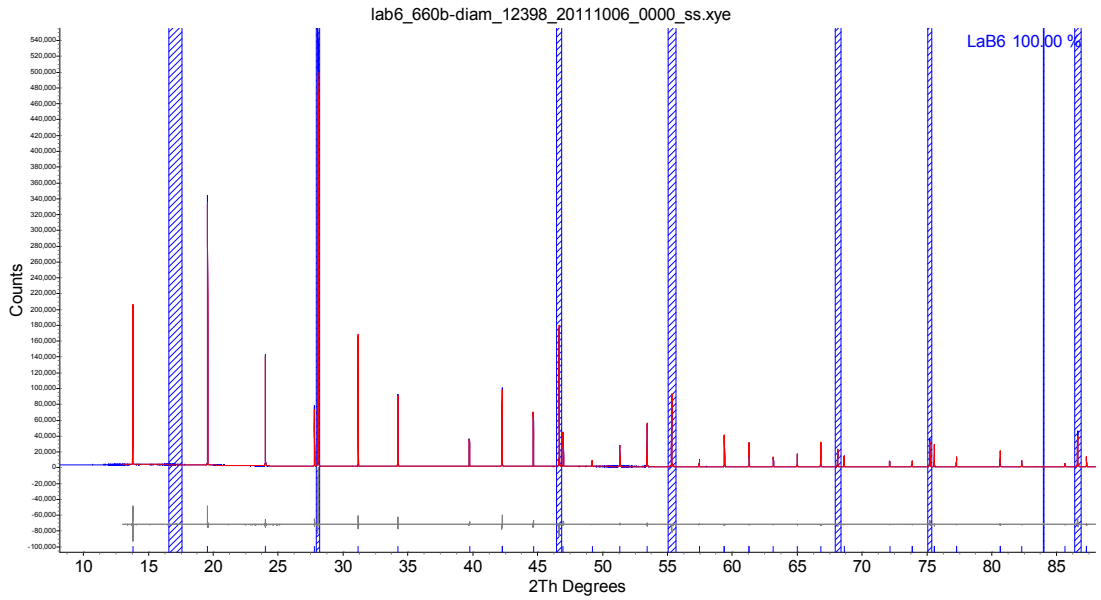

Figure A3-4 The fitting of the LaB_6 structure model with NIST certified lattice parameters to determine the accurate wavelength and the zero error. The excluded regions contain peaks of diamond and other impurities. Final R_{wp} 4.69.

Appendix 4. Synchrotron XRD pattern background modelling

A4.1 Capillary background

The synchrotron powder diffraction data were collected in Debye-Scherrer geometry. The powder samples were placed in 0.3 mm OD low background borosilicate glass capillaries (Charles Supper, Massachusetts, USA). However, the glass material of capillaries still gave appreciable background shown in Figure A4-1. Due to the variation of capillary wall thickness, the contribution of capillary background is expected to be different but not angularly dependent, *i.e.* the shape of the capillary background should be preserved.

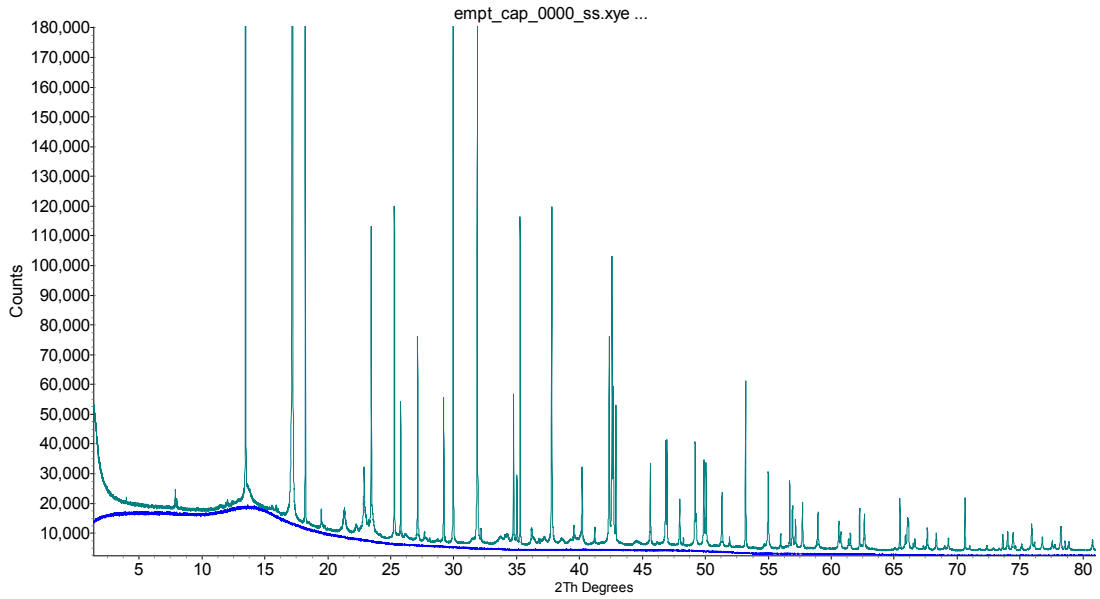

Figure A4-1 Typical synchrotron XRD pattern of powder sample in a capillary and the pattern of an empty capillary at the bottom.

To model this background, two approaches were developed. The first one comes from the PONKCS method which is good at modelling reflections of an unknown phase. The capillary glass can also be regarded as an unknown phase in the sample which does not count in the phase quantification. Five Split Pseudo-Voigt (SPV) peaks (*xo_ls*) were used as a group to model the capillary background with same refinable scale factor. The parameters of the individual peak shape (*spv_h1*, *spv_h2*, *spv_l1*, *spv_l2*) for each SPV peak were predetermined by fitting the empty capillary pattern

(Figure A4-2) and then fixed, leaving the overall scale factor refinable when they were used to model capillary background in other patterns. The TOPAS syntax of the five peaks phase group is shown in Figure A4-3. With these peak phases modelling the capillary contribution, only zero order Chebyshev background was used.

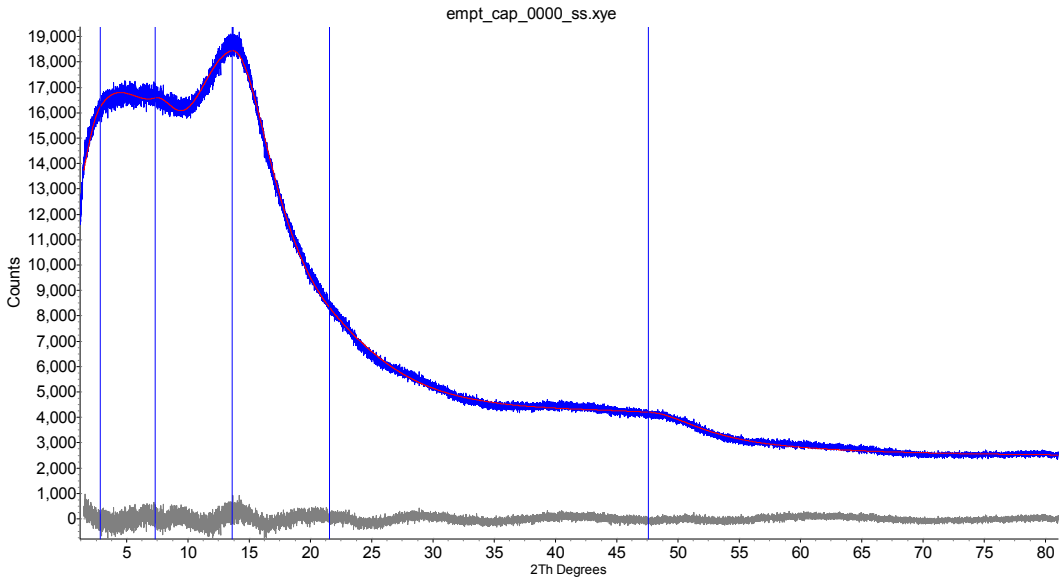

Figure A4-2 Five SPV peaks modelling the capillary background.

```
'5 peak phases fitting the capillary background
xo_Is  xo  2.854029748 I  26.5143566  scale capbkg 0.656022319_0.00318
    peak_type spv
      spv_h1  2.150160328        spv_h2  3.828048142
      spv_l1  0.06458609229      spv_l2  0.1047932461
xo_Is  xo  7.294149323 I  152.1496774 scale capbkg 0.656022319_0.00318
    peak_type spv
      spv_h1  10.59803694        spv_h2  1.753650569
      spv_l1  0.3684495515       spv_l2  7.450466912e-009
xo_Is  xo  13.60002472 I  3635.365672 scale capbkg 0.656022319_0.00318
    peak_type spv
      spv_h1  7.123272992        spv_h2  4.490810609
      spv_l1  1                  spv_l2  0.9999999995
xo_Is  xo  21.55970801 I  2107.581707 scale capbkg 0.656022319_0.00318
    peak_type spv
      spv_h1  13.19446629        spv_h2  7.380904926
      spv_l1  1                  spv_l2  0.9999998868
xo_Is  xo  47.57206105 I  7183.709164 scale capbkg 0.656022319_0.00318
    peak_type spv
      spv_h1  22.51810784        spv_h2  5.439230789
      spv_l1  0.1647704458       spv_l2  0.9999992216
```

Figure A4-3 The five peaks phase used to model capillary background. The peak shape parameter values were determined by fitting an empty capillary pattern. The scale factors of each peak phase were linked to the same refinable value.

The second approach is to use a polynomial function to fit the empty capillary background. This was achieved using a mathematical software Wolfram® *Mathematica* v8.0.4. To simplify the polynomial function calculated, the capillary pattern was divided into two parts, a part before 35° 2θ and a part after this angle, as shown in Figure A4-4. Hence a piecewise polynomial function was used to simulate the capillary background. This function was written in TOPAS syntax using keyword "*fit_obj*" (Figure A4-5) and achieved good fitting to capillary background (Figure A4-6). A coefficient 's' of this piecewise polynomial function is refined when it is used to model capillary background in other patterns (Figure A4-5). The second approach has wider application since it can be used in TOPAS versions without the GUI *e.g.* TOPAS R or TOPAS Academic.

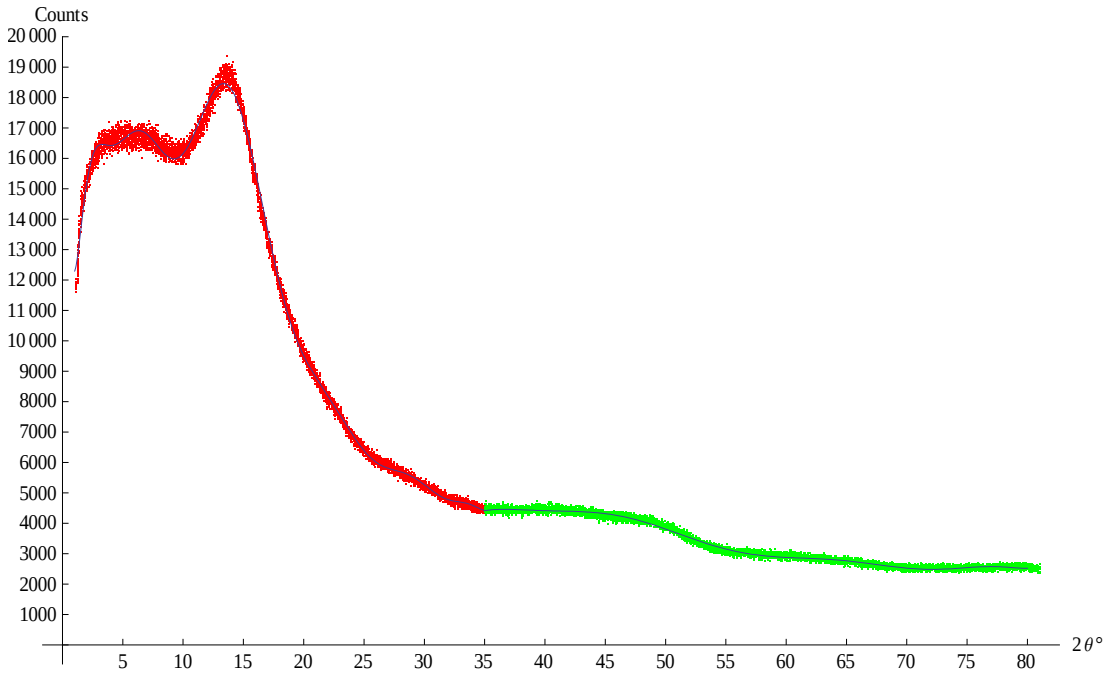

If (x < 35, 27743.639853559627` - 46549.61223211559` X + 52098.28536982045` X^2 - 28546.30947252649` X^3 + 9230.117955328415` X^4 - 1927.3020096113044` X^5 + 273.9874659917117` X^6 - 27.423852367037316` X^7 + 1.973407285926008` X^8 - 0.10318465820317267` X^9 + 0.003923128516695164` X^10 - 0.00010730757212999851` X^11 + 2.05675327389832 e - 6 X^12 - 2.6214714968398083 e - 8 X^13 + 1.9954696734261587 e - 10 X^14 - 6.86394951633631 e - 13 X^15,

3.526103033661559 e7 - 7.339497875640113 e6 X + 675194.6656418281` X^2 - 36171.573758643055` X^3 + 1250.4017368526625` X^4 - 29.16011068159462` X^5 + 0.46486017292988907` X^6 - 0.0050050362144683815` X^7 + 0.00003485247898178806` X^8 - 1.4182742459633872 e - 7 X^9 + 2.562819571799154 e - 10 X^10);

Figure A4-4 A piecewise polynomial function calculated by Wolfram® *Mathematica* v8.0.4 was used to model the capillary background.

```
prm s 0.99963`_0.00013
fit_obj = s If (X < 35,
  27743.639853559627      -      46549.61223211559      X      +
52098.28536982045     X^2     -     28546.30947252649     X^3     +
9230.117955328415     X^4     -     1927.3020096113044     X^5     +
273.9874659917117     X^6     -     27.423852367037316     X^7     +
1.973407285926008     X^8     -     0.10318465820317267     X^9     +
0.003923128516695164  X^10  -  0.00010730757212999851  X^11  +
2.05675327389832e-6   X^12   -   2.6214714968398083e-8   X^13   +
1.9954696734261587e-10 X^14 - 6.86394951633631e-13 X^15,
  3.526103033661559e7      -      7.339497875640113e6      X      +
675194.6656418281     X^2     -     36171.573758643055     X^3     +
1250.4017368526625     X^4     -     29.16011068159462     X^5     +
0.46486017292988907   X^6   -   0.0050050362144683815   X^7   +
0.00003485247898178806  X^8  -  1.4182742459633872e-7  X^9  +
2.562819571799154e-10 X^10);
```

Figure A4-5 The TOPAS syntax of a piecewise polynomial function to model the capillary background in Synchrotron XRD pattern. An overall scale factor 's' was used to scale the whole piecewise polynomial function if this syntax is used to model capillary background in other patterns.

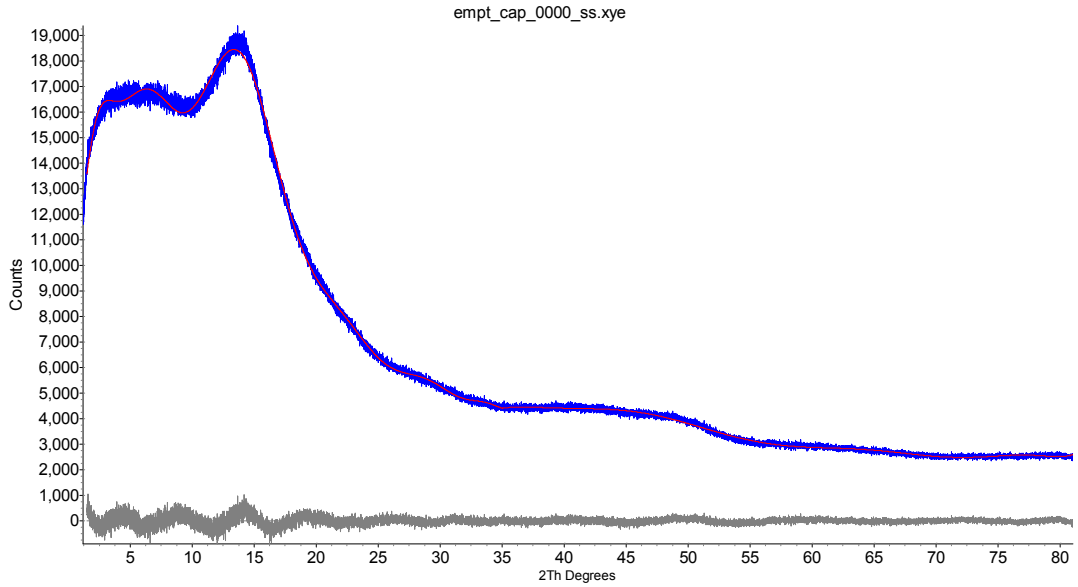

Figure A4-6 The fitting of the capillary background with a piecewise polynomial function calculated from Wolfram® *Mathematica*.

A4.2 Low angle high background

As with XRD patterns collected using laboratory Bragg-Brentano geometry, a high background below 5° 2θ is obvious. Previously this high background was ignored if the Bragg peaks of crystalline phases were far from low angle area, as the case shown in Figure A4-1. However, if the

sample contains clay minerals, *e.g.* nontronite, with the major basal reflection close to the low angle region, this basal reflection usually sits on the shoulder of the low angle high background. In this case, the low angle high background has to be appropriately fitted as well to minimise its impact on modelling the clay basal reflection.

Conventionally, the low angle high background in TOPAS is modelled by the *One_on_X* macro which essentially uses an inverse proportional function *fit_obj=a/X* (*a* refinable). However, sometimes this function does not give as much curvature as the experimental data has (Figure A4-7a). The function *fit_obj=a/(X-b)* (*a*, *b* refinable) was used instead as it fits the low angle high background much better than the *One_on_X* macro (Figure A4-7b).

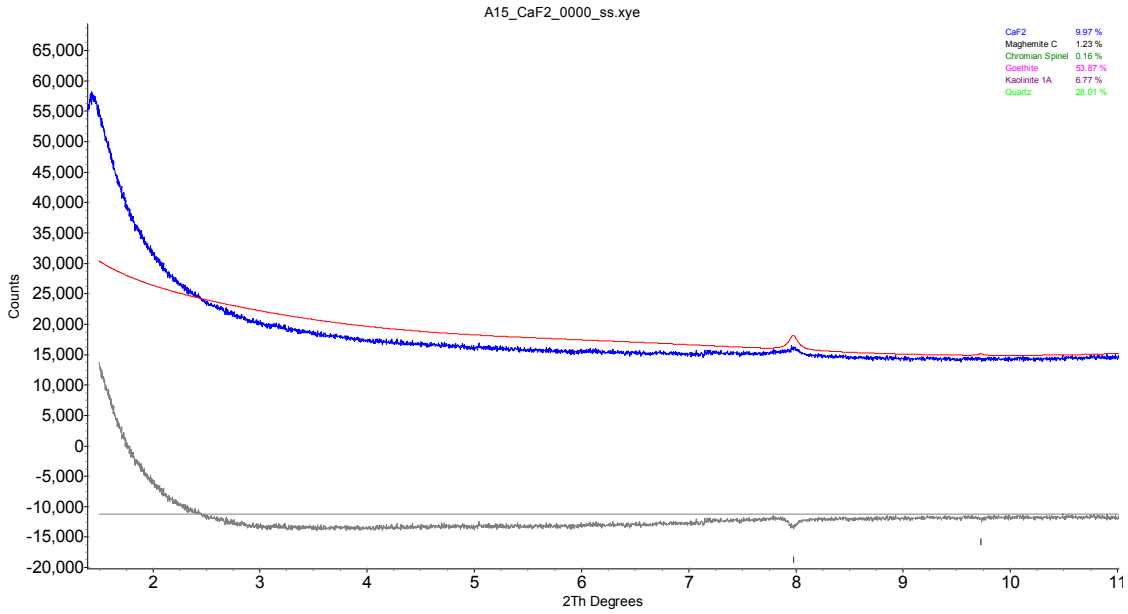

(a)

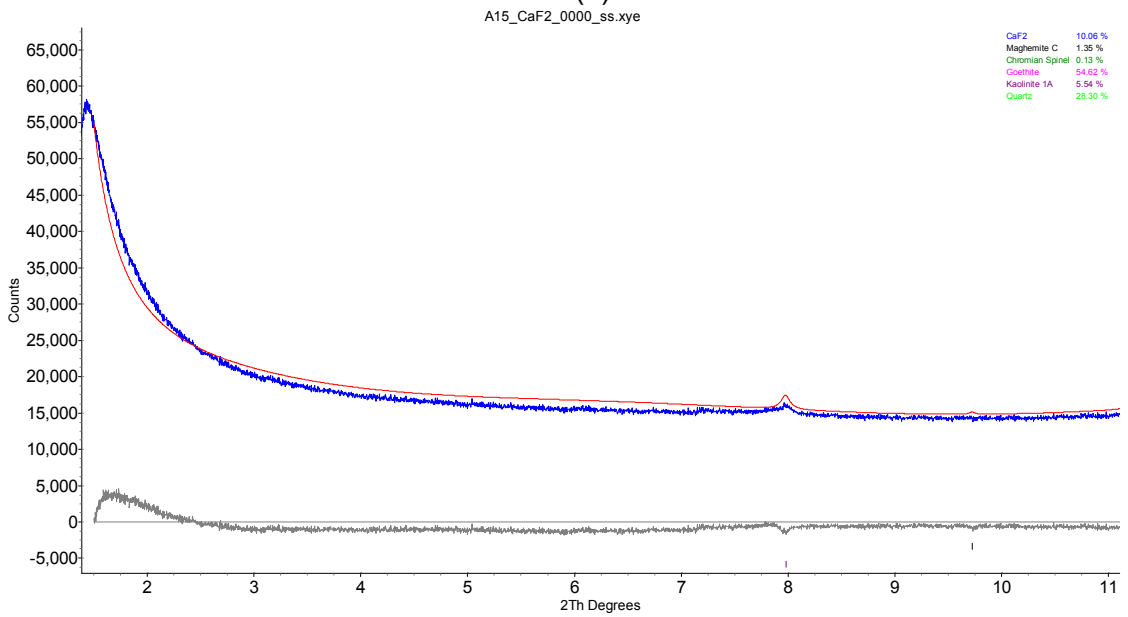

(b)

Figure A4-7 Comparison of the fitting of (a) the a/x background come with TOPAS One_on_X macro and (b) the customised a/(x-b) function used in this study.

Appendix 5. Capillary displacement correction in Debye-Scherrer geometry

The capillary displacement correction in Debye-Scherrer geometry used in this study is modified[†] from the macro published by Dr. Pamela Whitfield in TOPAS wiki: http://topas.dur.ac.uk/topaswiki/doku.php?id=ds_capillary_sd

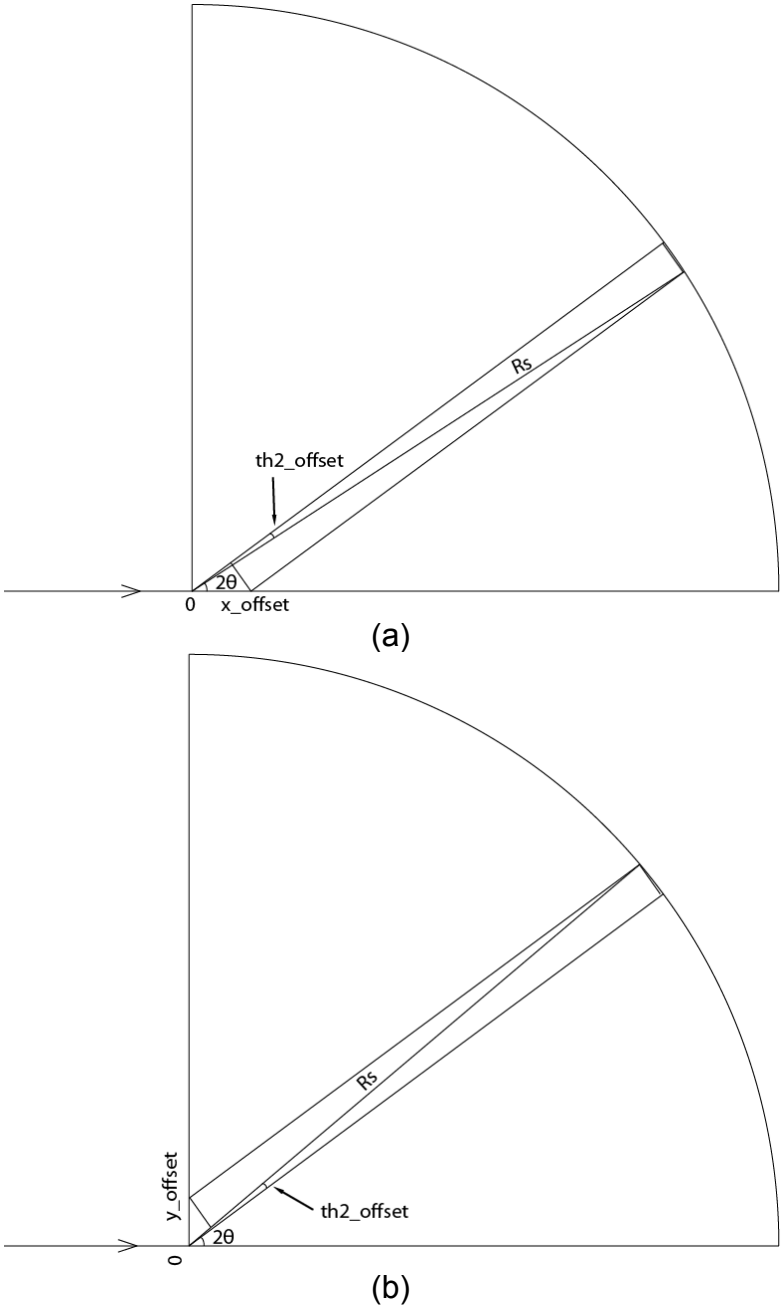

Figure A5-1 The capillary displacement from the centre of goniometer in (a) horizontal direction and in (b) vertical direction.

The 2θ peak shift in Figure A5-1a can be described as Eq. A5-1.

$$\mathrm{th2\_offset} = -\mathrm{ArcSin}\left(\frac{\mathrm{x\_offset}}{\mathrm{R_S}} \cdot \sin(2\theta)\right) \qquad \text{Eq. A5-1}$$

The 2θ peak shift in Figure A5-1b can be described as Eq. A5-2.

$$\mathrm{th2\_offset} = \mathrm{ArcSin}\left(\frac{\mathrm{y\_offset}}{\mathrm{R_S}} \cdot \cos(2\theta)\right) \qquad \text{Eq. A5-2}$$

where:

$\mathrm{R_S}$ = goniometer radius,

$\mathrm{x\_offset}$: capillary displacement in horizontal direction,

$\mathrm{y\_offset}$: capillary displacement in vertical direction,

2θ: Bragg angle.

The TOPAS syntax used in .inp files to correct capillary displacement is shown below:

```
prm hd_h 0 min=-Rs/1000; max=Rs/1000;
th2_offset = -ArcSin(hd_h Sin(2 Th) / Rs ) Rad;
prm hd_v 0 min=-Rs/1000; max=Rs/1000;
th2_offset = ArcSin(hd_v Cos(2 Th) / Rs ) Rad;
```

† Madsen, Ian (2012) personal communication.

Appendix 6. Supercell model describing turbostratic disordered nontronite

A6.1 Original supercell model written in BGMN syntax
(http://www.bgmn.de/download-structures.html)

```
// turbostratically disordered smectite, d(001) approx. 15 A
// structure of TOT layer (cis-vacant): Tsipurski et al., Clay Minerals 19(1984), 177-193 (modified)
// model for turbostratic disorder: Ufer et al., Z. Kristallogr. 219(2004), 519-527

PHASE=nontronite15a  SpacegroupNo=5 HermannMauguin=C121          // S.G.
PARAM=A=0.53_0.525^0.535 PARAM=B=0.915_0.91^0.92
PARAM=c0=1.5_1.4^1.58 BETA=100.2       // refine lattice parameters (nm),

pi==2*acos(0)
RP=4   //reflection profile, use both Lorentzian size B1 and squared Lorentzian strain B2 (Default)

layer==9         // layer: factor for elongation in c direction
C=c0*layer      // C: lattice parameter C for supercell

PARAM=b10=0.002_0^0.015           // isotropic broadening of hkl reflections
PARAM=b1l=0.03_0^0.1                 // separate broadening of 00l reflections
B1=ifthenelse(and(eq(h,0),eq(k,0)), b10+b1l, b10)   // broader 00l peaks

PARAM=K20=0.000026_0.00001^0.0001  //K20: hkl lines strain broadening
PARAM=K2l=0_0^0.002                              // K2l: 00l lines strain broadening

PARAM=GEWICHT=0_0                              // refine scale factor
GOAL: nontronite=GEWICHT*ifthenelse(ifdef(d),exp(my*d*3/4),1)  //Brindley correction, my = Leaner Absorption Coefficient (µm-1)

breit2=1/sqr(C)          // additional l-dependent broadening to avoid "ripples"
B2=cat(R2==sqr(h/A)+sqr(k/B), Z2==max(sqr(sk)-R2,0), orientierung2==Z2/sqr(sk), ifthenelse(and(eq(h,0),eq(k,0)), K2l*sqr(sk),K20*sqr(sk)+breit2*orientierung2))     // squared lorentzian (Gauss-like) broadening

GEWICHT[1]=GEWICHT*ifthenelse(and(eq(h,0),eq(k,0)), ifthenelse(mod(l,layer),0,layer),1)      // scaling of classes (00l and hkl) and removal of redundant 00l reflections

// === octahedral occupancies ====
pMG=0.02 PARAM=pFE=0.7_0.5^1 pAL=(1-pMG-pFE)
PARAM=ptrans=0.5_0.0^1.0   // ratio of cis and trans vacancy; 0 for trans-vacant.

// === tetrahedral occupancies ====
sitet=(1-fetet-altet) PARAM=fetet=0.01_0^0.5 altet=0.05

// === interlayer occupancies ====
PARAM=pCA=0.1_0.0^0.3
pOZ=pCA
```

```
//==== rigid body of the interlayer cation coordinated by 6 oxygen (water)
dCAO=0.241              //distance of cation - oxygen
set(ECA,0,0,0)
set(EOZ1,0,0,dCAO)
set(EOZ2,0,0,-dCAO)
set(EOZ3,dCAO,0,0)
set(EOZ4,-dCAO,0,0)
set(EOZ5,0,dCAO,0)
set(EOZ6,0,-dCAO,0)
T(0.6892,0.2092,0.5*c0*sin(pi*BETA/180),45,180*acos(1/sqrt(3))/pi,-
18.42,ECA,EOZ1,EOZ2,EOZ3,EOZ4,EOZ5,EOZ6) //shift and rotate rigid body

// --- isotropic temperature factors (nm^2) ---
tdsint=0.008
tdsoct=0.005
tdstet=0.004
tdso=0.008
tdsH2O=0.025

// --- positions of oxygen in TOT layer, use absolute positions in c [nm]
zT=0.271350
zO11=0.10955
zO12=0.10553
zO2=0.33668

// ------TOT layer atom position------
E=(AL+3(ptrans*pAL),MG+2(ptrans*pMG),FE+3(ptrans*pFE)) Wyckoff=a y=0.0
TDS=tdsoct                      // octahedral trans site
E=(AL+3((1-ptrans)*pAL),MG+2((1-ptrans)*pMG),FE+3((1-ptrans)*pFE)) Wyckoff=a
y=0.6540 TDS=tdsoct             // octahedral cis site
E=(AL+3(pAL),MG+2(pMG),FE+3(pFE)) Wyckoff=a y=0.3210 TDS=tdsoct
// octahedral cis site, always occupied
E=(SI+4(sitet),AL+3(altet),FE+3(fetet)) Wyckoff=c x=0.4320 y=0.3330
z=zT/(layer*c0) TDS=tdstet    // tetrahedral
E=(SI+4(sitet),AL+3(altet),FE+3(fetet)) Wyckoff=c x=0.4320 y=0.6620
z=zT/(layer*c0) TDS=tdstet    // tetrahedral
E=O Wyckoff=c x=0.1730 y=0.7250 z=zO2/(layer*c0) TDS=tdso
// z is in absolute coordinate
E=O Wyckoff=c x=0.1700 y=0.2680 z=zO2/(layer*c0) TDS=tdso
E=O Wyckoff=c x=0.4170 y=0.6560 z=zO11/(layer*c0) TDS=tdso
E=O Wyckoff=c x=0.3430 y=0.3470 z=zO11/(layer*c0) TDS=tdso
E=O Wyckoff=c x=0.3340 y=0.9760 z=zO12/(layer*c0) TDS=tdso
E=O Wyckoff=c x=0.4890 y=0.4960 z=zO2/(layer*c0) TDS=tdso

// ------interlayer positions ------
E=CA+2(pCA) Wyckoff=c x=X(ECA) y=Y(ECA) z=Z(ECA)   TDS=tdsint
E=O-2(pOZ)  Wyckoff=c x=X(EOZ1) y=Y(EOZ1) z=Z(EOZ1)   TDS=tdsH2O
E=O-2(pOZ)  Wyckoff=c x=X(EOZ2) y=Y(EOZ2) z=Z(EOZ2)   TDS=tdsH2O
E=O-2(pOZ)  Wyckoff=c x=X(EOZ3) y=Y(EOZ3) z=Z(EOZ3)   TDS=tdsH2O
E=O-2(pOZ)  Wyckoff=c x=X(EOZ4) y=Y(EOZ4) z=Z(EOZ4)   TDS=tdsH2O
E=O-2(pOZ)  Wyckoff=c x=X(EOZ5) y=Y(EOZ5) z=Z(EOZ5)   TDS=tdsH2O
E=O-2(pOZ)  Wyckoff=c x=X(EOZ6) y=Y(EOZ6) z=Z(EOZ6)   TDS=tdsH2O
```

A6.2 Supercell model in TOPAS symbolic computation system

```
'turbostratically disordered smectite, d(001) approx. 15 A
```

```
'structure of TOT layer (cis-vacant): Tsipurski et al., Clay Minerals 19(1984), 177-
193 (modified)
'model for turbostratic disorder: Ufer et al., Z. Kristallogr. 219(2004), 519-527

str
prm !interlayer 0.5
local scnon  0.00041 min 0.000001 max 1 'scale factor
prm mshkl  0.01999 min 0.00005 max 0.02 'strain of non-basal reflection
prm ms00l  6.73911 min 0.001 max 10 'strain of basal reflection
prm cshkl  15.63019 min 10 max 1000 'size of non-basal reflections
prm cs00l  9.20520 min 1 max 20 'size of basal reflections
'occupancies of cations
prm !pMg 0.065 min 0 max 1
prm !pNi 0.065 min 0 max 1
prm !pFe 0.6 min 0 max 1
prm !pAl 0.2375 min 0 max 1 'octahedral position, Mg + Fe + Al +Ni <= 1.
prm !ptrans 1 min 0 max 1 'ratio of cis and trans vacancy, 0 => trans-vacant.
prm !altet 0.08375 min 0 max 1
prm sitet =1-altet;:0.91625 'tetrahedral site: Al + Si = 1.
prm pNa = interlayer 0.717;:0.31488 min 0
prm pMgI = interlayer 0.287;:0.12604 min 0
prm pH2O = pNa+pMgI;:0.44092 min 0 'interlayer H2O

'atom absolute position in c direction
prm !zT 2.7135
prm !zO11 1.0955
prm !zO12 1.0553
prm !zO2 3.3668
prm !layer 9 'layer: supercell factor for elongation in c direction
prm cnon 15.61679 min 14 max 15.8 'subcell c

lor_fwhm = If(And(H==0,K==0), 0.1 Rad Lam/(Cos(Th) cs00l), 0.1 Rad Lam/(Cos(Th)
cshkl)); 'thinner in 00l direction
lor_fwhm = If(And(H==0,K==0), ms00l Tan(Th), Sqrt((mshkl Tan(Th))^2 +
L^2/(Get(c)^2 L^2 + Get(c)^4 ((H/Get(a))^2+(K/Get(b))^2))) ); 'aniso strain and
additional l-dependent broadening to avoid "ripples"
scale_pks = If(And(H==0,K==0),If(Mod(L,layer),0,layer),1); 'scaling of classes (00l
and hkl) and removal of redundant 00l reflections
scale =scnon;
'scale = cmCaF2 cvCaF2 scCaF2/Get(cell_mass)/Get(cell_volume)/0.1*0.9;

r_bragg  2.35613318
phase_name "Bulong supercell"
MVW( 999.686, 6620.83728, 98.741)
'corrected_weight_percent  42.9984672
space_group 5
Phase_LAC_1_on_cm(6.48560)
Phase_Density_g_on_cm3(0.25073)
a anon  5.25575 min 5.25 max 5.35
b !bnon  9.09592434 min 9.1 max 9.2
c =layer*cnon; 'supercell c
be benon  99.81479

'Na+0.716Mg2+0.287[Si4+7.33Al3+0.67][Al3+0.95Fe3+2.40Ni2+0.26Co2+0.01Mg2
+0.26Cr3+0.09]O20(OH)4  'Bulong Nontronite Chemical Formula
```

```
'octahedral trans
site Al1 num_posns 2 x =0; y =0; z =0; occ Al+3 =ptrans*pAl; beq 0.5
site Mg1 num_posns 2 x =0; y =0; z =0; occ Mg+2 =ptrans*pMg; beq 0.5
site Fe1 num_posns 2 x =0; y =0; z =0; occ Fe+3 =ptrans*pFe; beq 0.5
site Ni1 num_posns 2 x =0; y =0; z =0; occ Ni+2 =ptrans*pNi; beq 0.5
'octahedral cis
site Al2 num_posns 2 x=0; y 0.6540 z=0; occ Al+3 =(1-ptrans)*pAl; beq 0.5
site Mg2 num_posns 2 x=0; y 0.6540 z=0; occ Mg+2 =(1-ptrans)*pMg; beq  0.5
site Fe2 num_posns 2 x =0; y 0.6540 z =0; occ Fe+3 =(1-ptrans)*pFe; beq  0.5
site Ni2 num_posns 2 x =0; y 0.6540 z =0; occ Ni+2 =(1-ptrans)*pNi; beq 0.5
site Al3 num_posns 2 x =0; y 0.3210 z =0; occ Al+3 =pAl; beq 0.5
site Mg3 num_posns 2 x =0; y 0.3210 z =0; occ Mg+2 =pMg;         beq 0.5
site Fe3 num_posns 2 x =0; y 0.3210 z =0; occ Fe+3 =pFe; beq 0.5
site Ni3 num_posns 2 x =0; y 0.3210 z =0; occ Ni+2 =pNi; beq  0.5
'tetrahedral
site Si1 num_posns 4 x 0.4320 y =1/3; z =zT/(layer*cnon); occ Si+4  =sitet; beq 0.4
site Al4 num_posns 4 x 0.4320 y =1/3; z =zT/(layer*cnon); occ Al+3  =altet; beq  0.4
site Si2 num_posns 4 x 0.4320 y =2/3; z =zT/(layer*cnon); occ Si+4  =sitet; beq  0.4
site Al5 num_posns 4 x 0.4320 y =2/3; z =zT/(layer*cnon); occ Al+3  =altet; beq  0.4

site O7 num_posns 4 x 0.1730 y 0.7250 z =zO2/(layer*cnon); occ O-2 1 beq  0.8
site O8 num_posns 4 x 0.1700 y 0.2680 z =zO2/(layer*cnon); occ O-2 1 beq  0.8
site O9 num_posns 4 x 0.4170 y 0.6560 z =zO11/(layer*cnon); occ O-2 1 beq  0.8
site O10 num_posns 4 x 0.3430 y 0.3470 z =zO11/(layer*cnon); occ O-2 1 beq  0.8
site O11 num_posns 4 x 0.3340 y -0.0240 z =zO12/(layer*cnon); occ O-2 1 beq  0.8
site O12 num_posns 4 x 0.4890 y 0.4960 z =zO2/(layer*cnon); occ O-2 1 beq  0.8
site Mg num_posns 4 x 0.50000 y 0.25000 z 0.05556 occ Mg+2 =pMgI; beq 0.8
site Na num_posns 4 x 0.50000 y 0.25000 z 0.05556 occ Na+1=pNa; beq 0.8
site O1 num_posns 4 x 0.35860 y 0.43735 z 0.06560 occ O-2  =pH2O; beq 2.5
site O2 num_posns 4 x 0.64140 y 0.06265 z 0.04551 occ O-2 =pH2O; beq 2.5
site O3 num_posns 4 x 0.07980 y 0.25000 z 0.04551 occ O-2 =pH2O; beq 2.5
site O4 num_posns 4 x 0.92020 y 0.25000 z 0.06560 occ O-2 =pH2O; beq 2.5
site O5 num_posns 4 x 0.35860 y 0.06265 z 0.06560 occ O-2 =pH2O; beq 2.5
site O6 num_posns  4 x  0.64140 y  0.43735 z  0.04551 occ O-2  =pH2O;  beq 2.5

'rigid body of the interlayer complex
local !dMgO 2.41
rigid
point_for_site Mg
point_for_site Na
point_for_site O1 uz = dMgO;
point_for_site O2 uz =-dMgO;
point_for_site O3 ux = dMgO;
point_for_site O4 ux =-dMgO;
point_for_site O5 uy = dMgO;
point_for_site O6 uy =-dMgO;

rotate 45 qx 1 operate_on_points "O*"
rotate =180/Pi*ArcSin(1/Sqrt(3)); qy 1 operate_on_points "O*"
rotate 180 qz 1 operate_on_points "O*"
translate tx =0.5*anon+0.5*cnon*Cos(benon Deg); ty =0.25*bnon; tz
=0.5*cnon*Sin(benon Deg); operate_on_points "O* K Ca Mg Na"
```

Appendix 7. Linear fittings of the column leaching data of the laterite samples

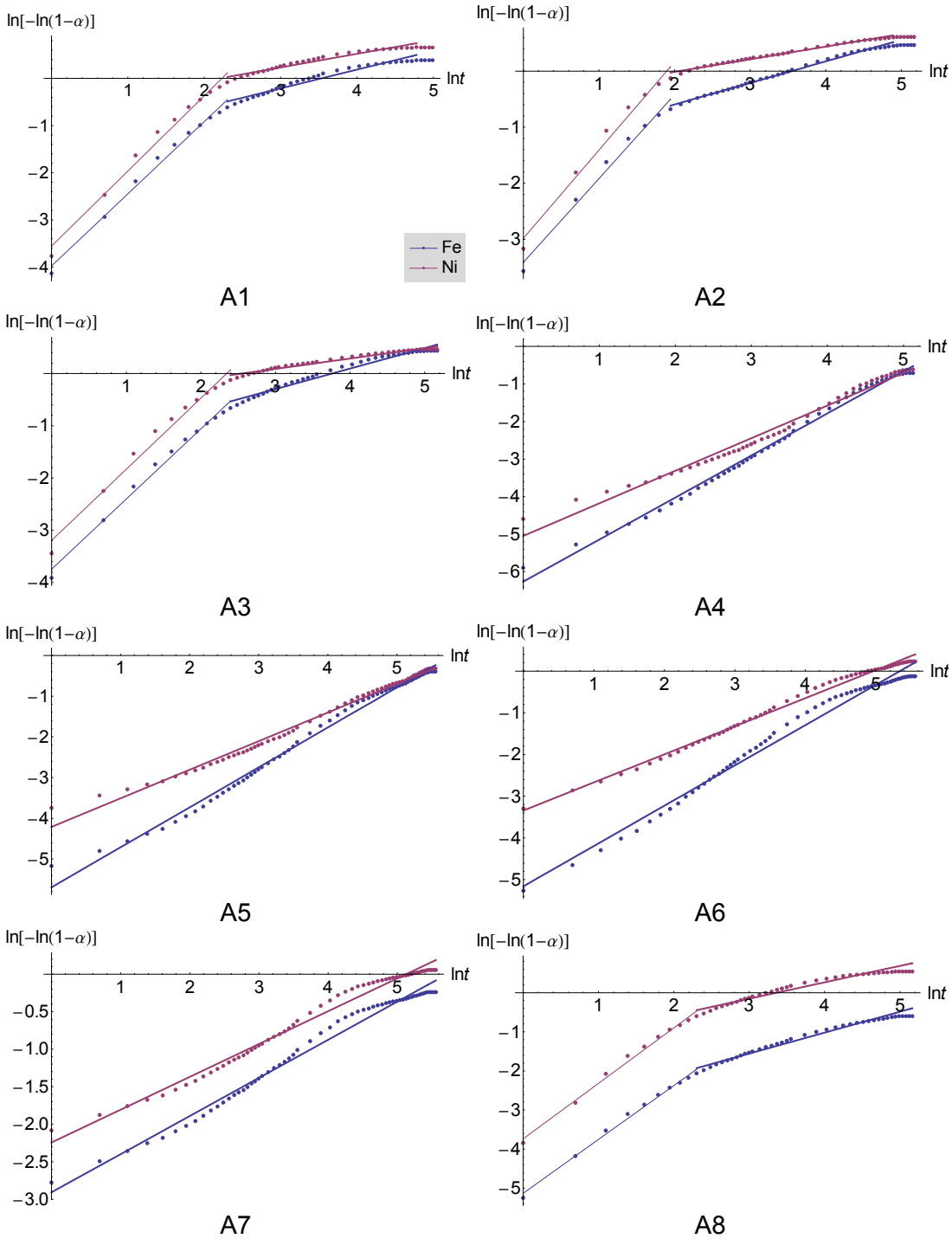

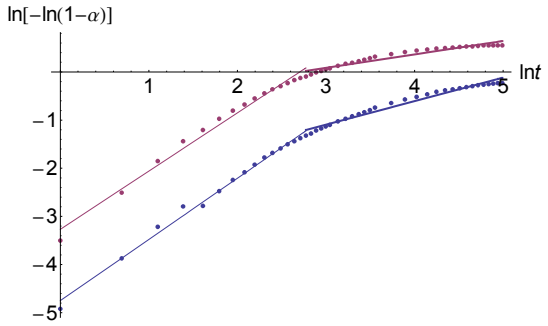

A9

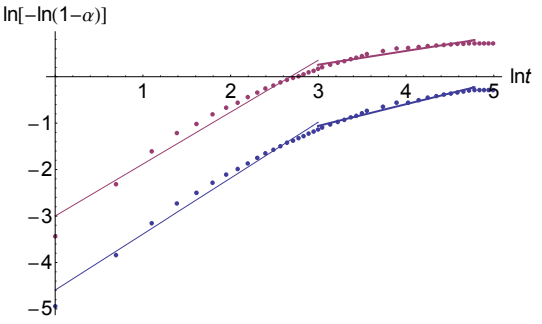

A10

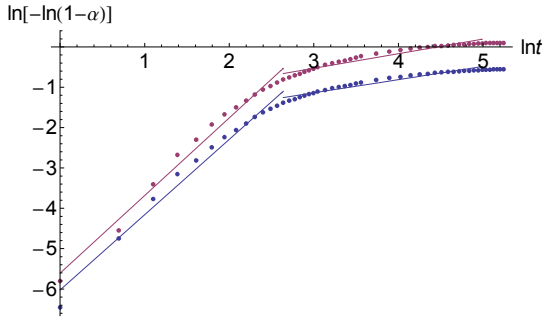

A11

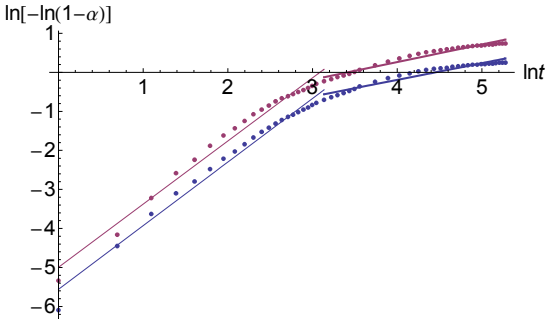

A12

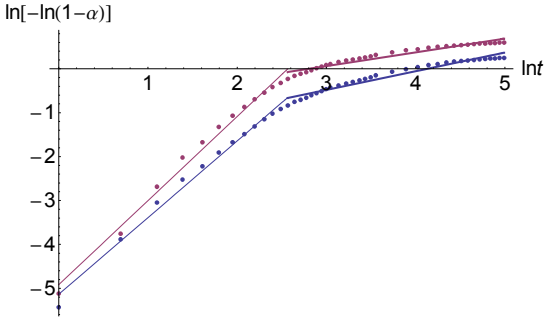

A13

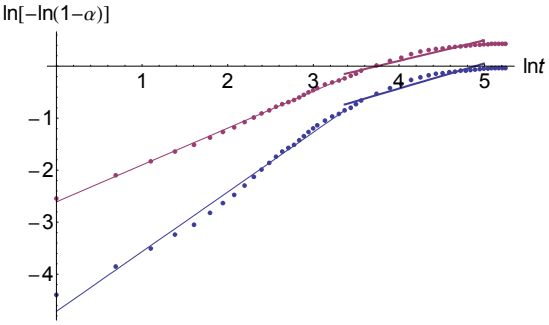

A14

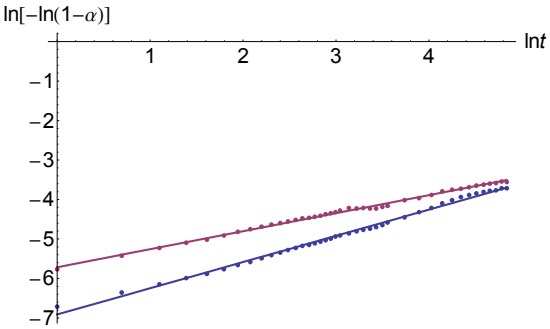

A15

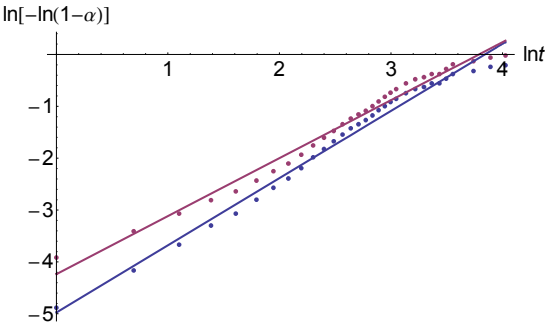

A16

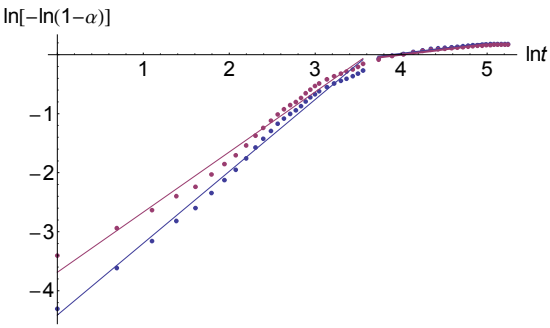

A17

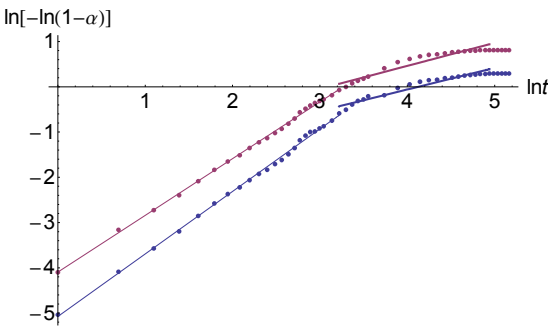

B1

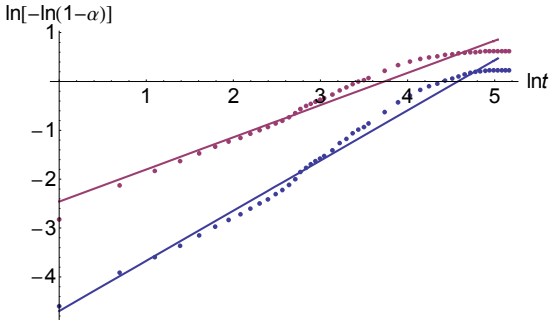

B2

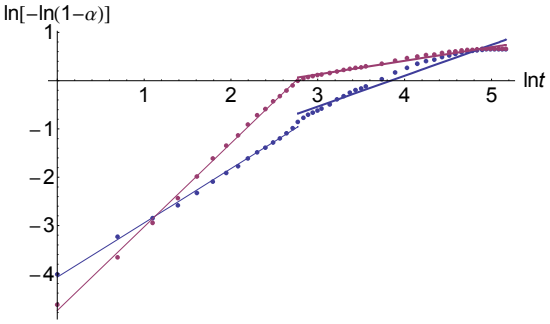

B3

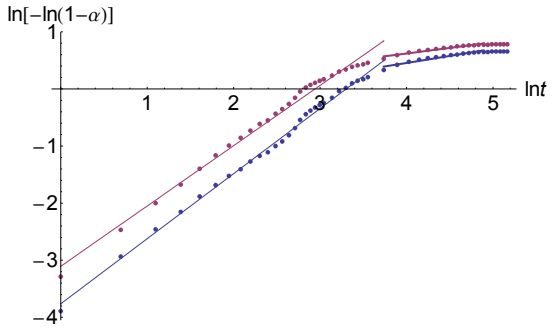

B4

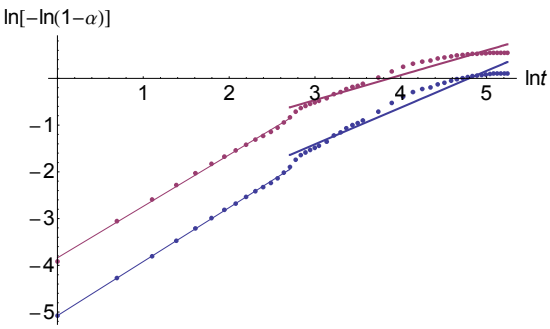

B5

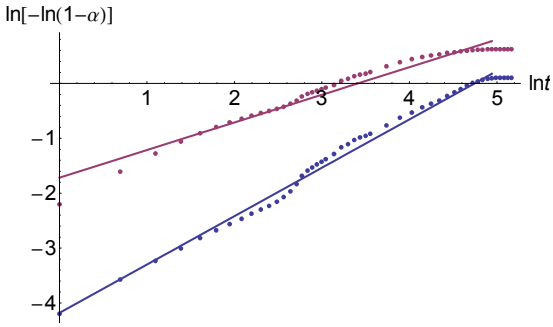

B6

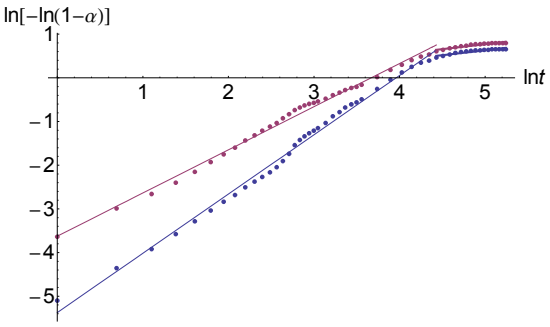

B7

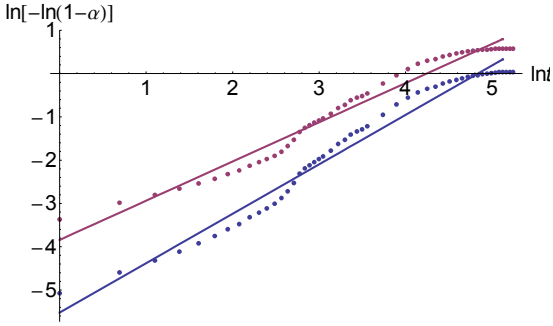

B8

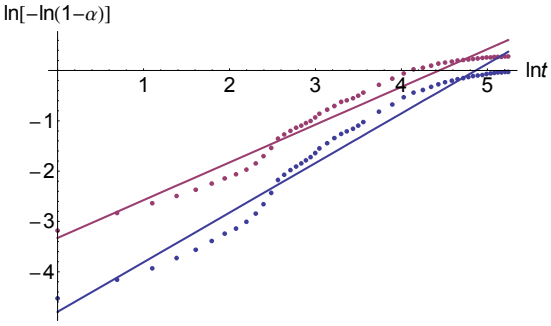

B9

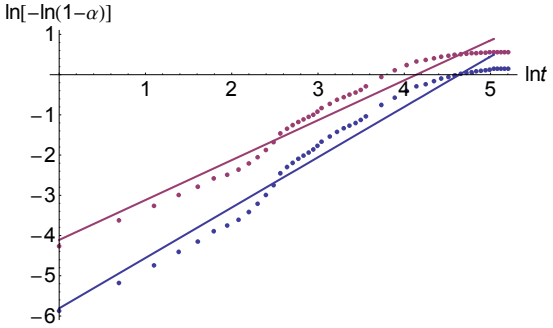

B10

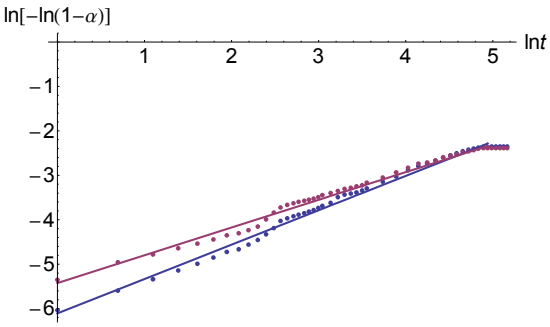

B11

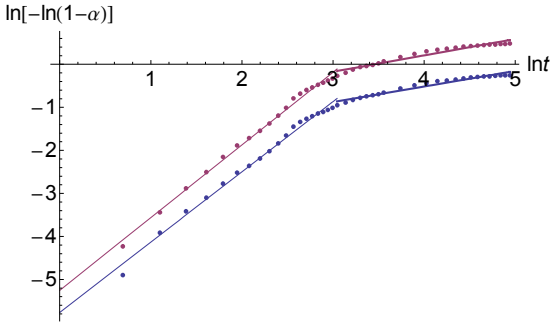

B12

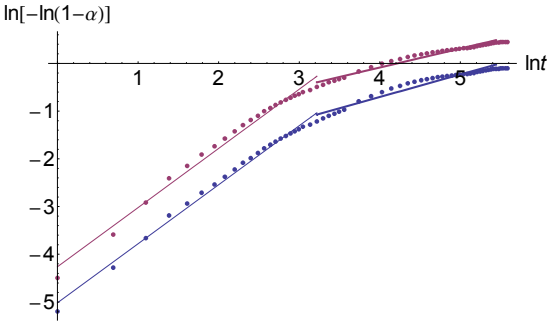

B13

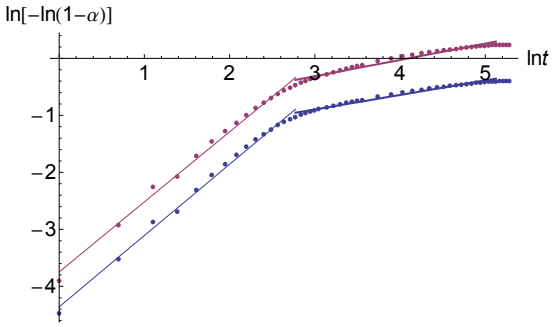

B14

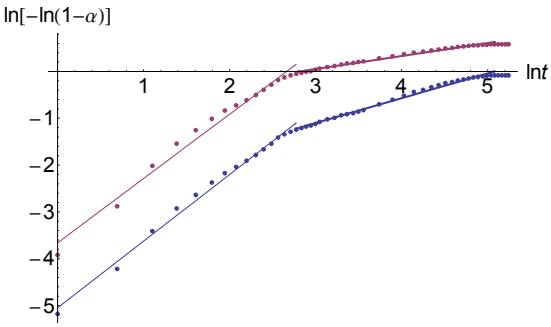

B15

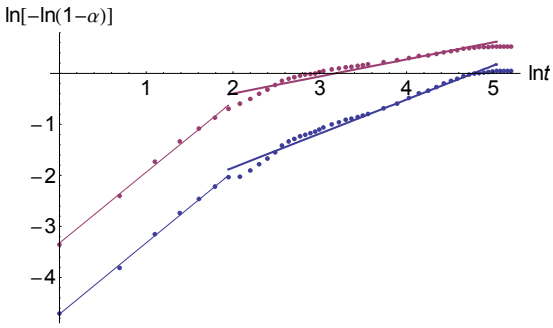

B16

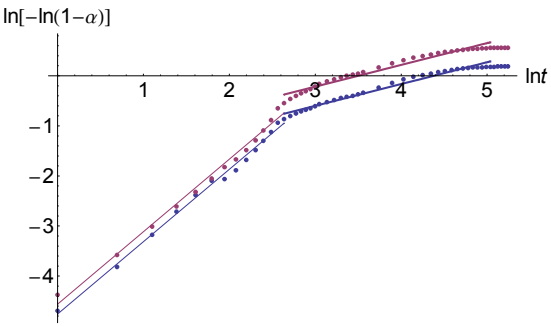

B17

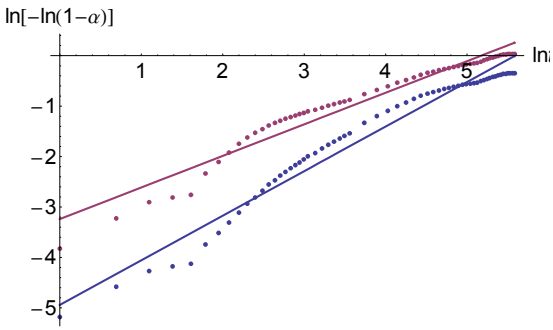

B18

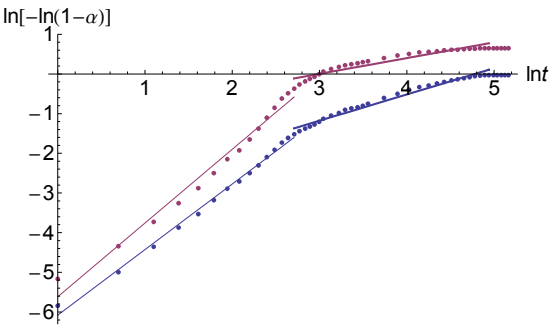

B19

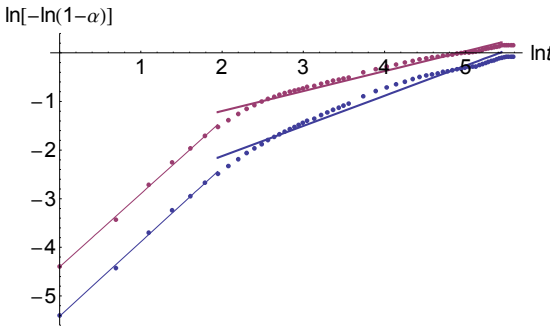

B20

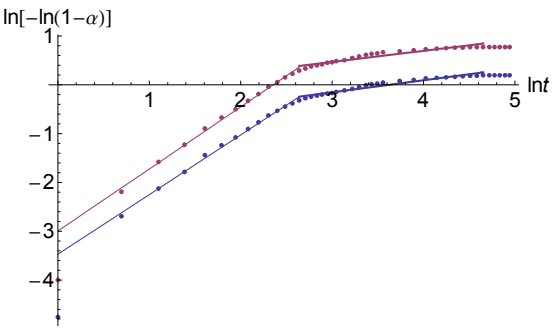

C1

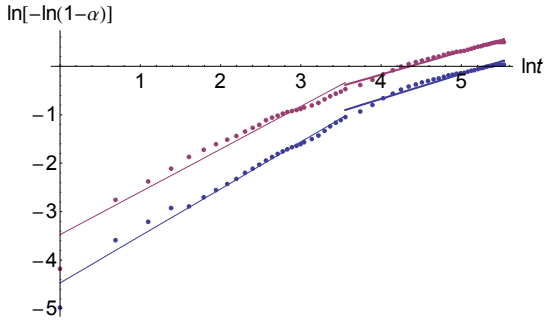

C2

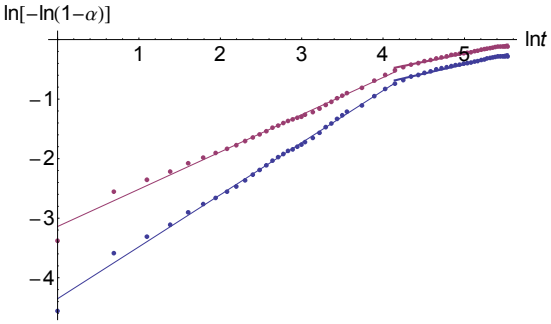

C3

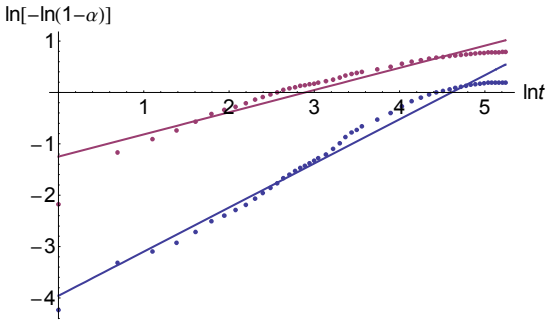

C4

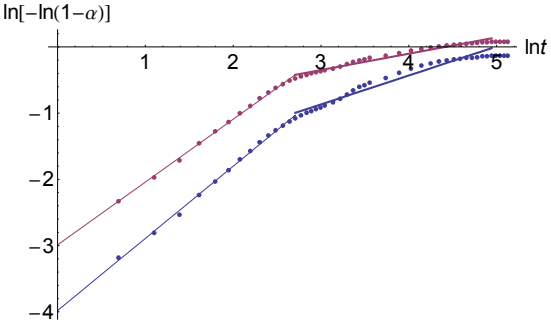

C5

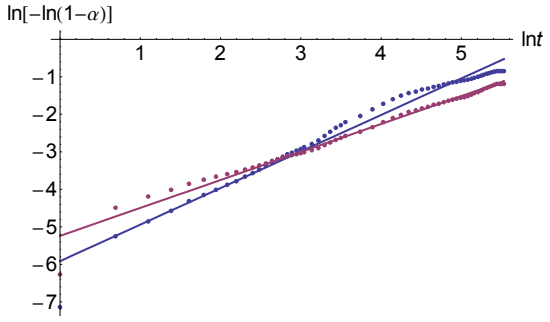

C6

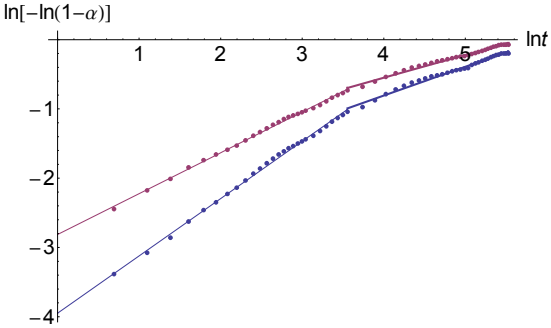

C7

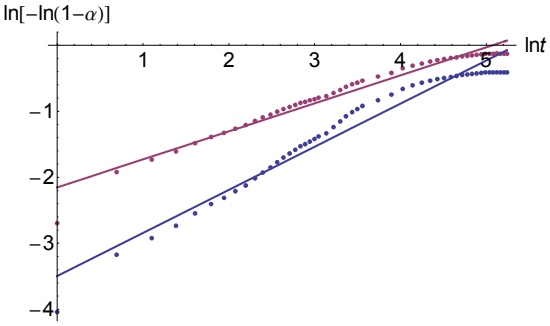

C8

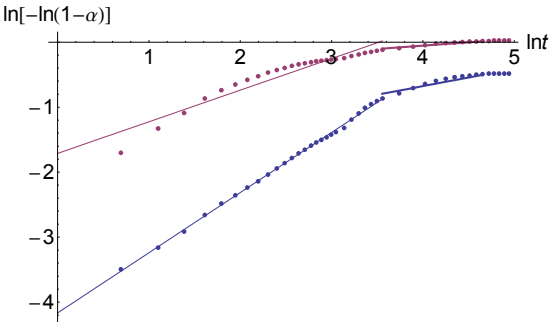

C9

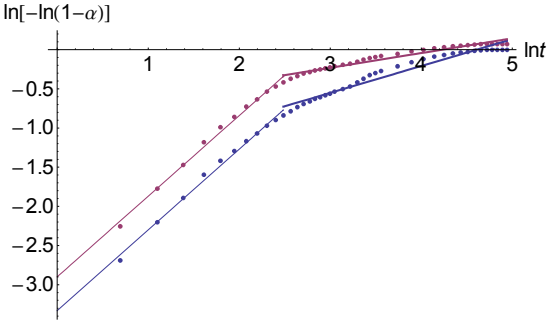

C10

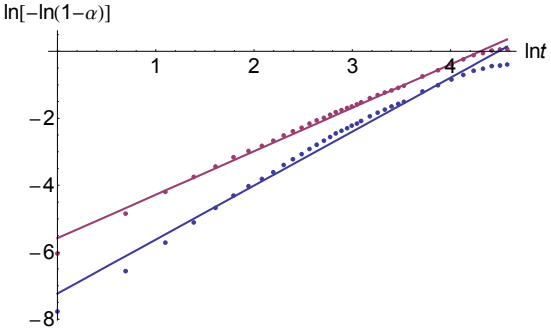

D1

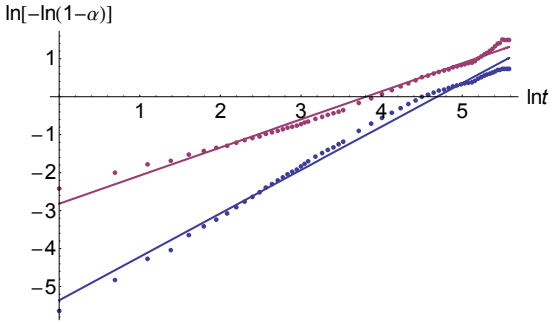

D2

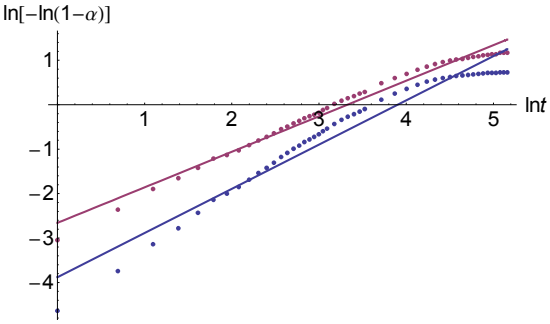

D3

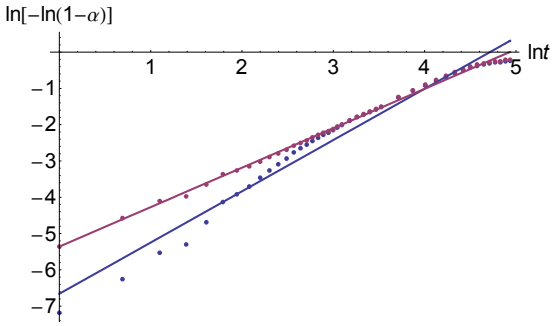

D4

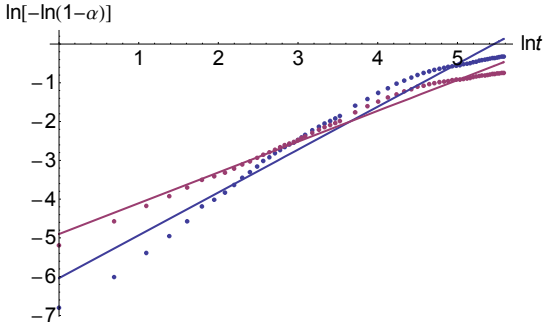

D5

Appendix 8. Fittings of the empirical dissolution models to the leaching curves

A8.1 Linear fitting of adapted data to test congruency.

Following are Wolfram® *Mathematica* calculation record of the linear Kabai fitting for the iron column leaching data of sample C3:

```
In:= {tC3,pC3}=Transpose[ReadList["D:\\PHD\\Nickel laterite experiment
data\\leaching data\\column leach data analysis\\Kabai&CC1976
fitting\\C3.txt",{Number,Number}]];
In:= C3L=Transpose[{Log[tC3],Log[-Log[1-pC3/100]]}]
Out:= {{0,-4.56055},{Log[2],-3.58341},{Log[3],-3.30601},{Log[4],-3.10694},{Log[5],-
2.90286},{Log[6],-2.7607},{Log[7],-2.65659},{Log[8],-2.55518},{Log[9],-
2.47017},{Log[10],-2.3606},{Log[11],-2.27076},{Log[12],-2.19404},{Log[13],-
2.1156},{Log[14],-2.03873},{Log[15],-1.9761},{Log[16],-1.91807},{Log[17],-
1.86844},{Log[18],-1.84207},{Log[19],-1.79992},{Log[20],-1.76544},{Log[21],-
1.72223},{Log[23],-1.65609},{Log[25],-1.56957},{Log[27],-1.47215},{Log[29],-
1.40695},{Log[31],-1.32875},{Log[33],-1.27151},{Log[35],-1.21486},{Log[42],-
1.10269},{Log[49],-0.949406},{Log[56],-0.828227},{Log[63],-0.742321},{Log[70],-
0.67877},{Log[77],-0.624801},{Log[84],-0.59249},{Log[91],-0.559553},{Log[98],-
0.533311},{Log[105],-0.503112},{Log[112],-0.485535},{Log[119],-
0.465211},{Log[126],-0.443324},{Log[133],-0.429536},{Log[140],-
0.417124},{Log[147],-0.407637},{Log[154],-0.397315},{Log[161],-
0.388146},{Log[168],-0.371207},{Log[175],-0.359158},{Log[182],-
0.344842},{Log[189],-0.333063},{Log[196],-0.32132},{Log[203],-
0.311022},{Log[210],-0.301031},{Log[217],-0.291246},{Log[224],-
0.282223},{Log[231],-0.279129},{Log[238],-0.279158},{Log[245],-
0.279187},{Log[252],-0.279191}}
In:= ListPlot[C3L, PlotRange->All, AxesOrigin->{0,0}]
```

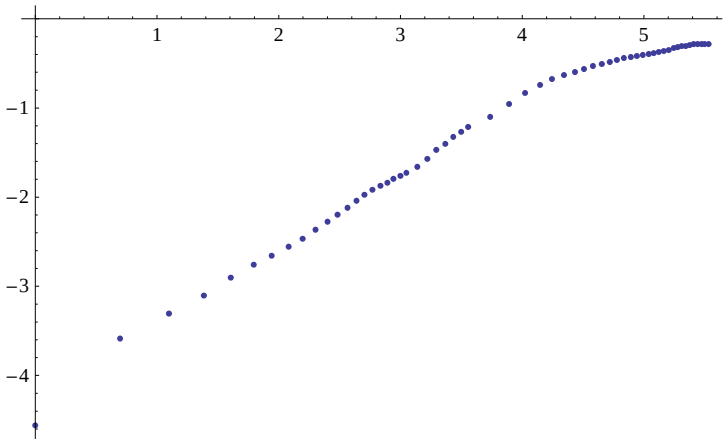

Out:=

In:= Take[C3L,32]

Out:= {{0,-4.56055},{Log[2],-3.58341},{Log[3],-3.30601},{Log[4],-3.10694},{Log[5],-2.90286},{Log[6],-2.7607},{Log[7],-2.65659},{Log[8],-2.55518},{Log[9],-2.47017},{Log[10],-2.3606},{Log[11],-2.27076},{Log[12],-2.19404},{Log[13],-2.1156},{Log[14],-2.03873},{Log[15],-1.9761},{Log[16],-1.91807},{Log[17],-1.86844},{Log[18],-1.84207},{Log[19],-1.79992},{Log[20],-1.76544},{Log[21],-1.72223},{Log[23],-1.65609},{Log[25],-1.56957},{Log[27],-1.47215},{Log[29],-1.40695},{Log[31],-1.32875},{Log[33],-1.27151},{Log[35],-1.21486},{Log[42],-1.10269},{Log[49],-0.949406},{Log[56],-0.828227},{Log[63],-0.742321}}

In:= Take[C3L,{32,59}]

Out:= {{Log[63],-0.742321},{Log[70],-0.67877},{Log[77],-0.624801},{Log[84],-0.59249},{Log[91],-0.559553},{Log[98],-0.533311},{Log[105],-0.503112},{Log[112],-0.485535},{Log[119],-0.465211},{Log[126],-0.443324},{Log[133],-0.429536},{Log[140],-0.417124},{Log[147],-0.407637},{Log[154],-0.397315},{Log[161],-0.388146},{Log[168],-0.371207},{Log[175],-0.359158},{Log[182],-0.344842},{Log[189],-0.333063},{Log[196],-0.32132},{Log[203],-0.311022},{Log[210],-0.301031},{Log[217],-0.291246},{Log[224],-0.282223},{Log[231],-0.279129},{Log[238],-0.279158},{Log[245],-0.279187},{Log[252],-0.279191}}

In:= C3N=LinearModelFit[Take[C3L,32],x,x]

Out:= FittedModel[$-4.35482 + 0.874305\ x$]

In:= C3N[{"BestFit","ParameterTable","RSquared"}]

Out:= {-4.35482+0.874305 x,{
 {, Estimate, Standard Error, t-Statistic, P-Value},
 {1, -4.35482, 0.0289677, -150.334, 9.91948×10^{-45}},
 {x, 0.874305, 0.0103027, 84.8614, 2.68554×10^{-37}}
},0.995851}

In:= C3M=LinearModelFit[Take[C3L,{32,59}],x,x]

Out:= FittedModel[$-2.00463 + 0.318262\,x$]

In:= C3M[{"BestFit","ParameterTable","RSquared"}]

Out:= {-2.00463+0.318262 x,{

{, Estimate, Standard Error, t-Statistic, P-Value},

{1, -2.00463, 0.0428181, -46.8173, 1.23072×10^{-26}},

{x, 0.318262, 0.00856073, 37.177, 4.53245×10^{-24}}

},0.981536}

In:= k1=Exp[-4.354823729803352`/0.8743050656020991`]

Out:= 0.0068679

In:= k2=Exp[-2.004627208520826`/0.3182623062097577`]

Out:= 0.00183876

In:= line1= Fit[Take[C3L,32], {1,x},x]

Out:= -4.35482+0.874305 x

In:= line2= Fit[Take[C3L,{32,59}], {1,x},x]

Out:= -2.00463+0.318262 x

In:= Show[ListPlot[C3L, PlotRange All,AxesLabel {"lnt","ln[-ln(1-α)]"},BaseStyle->{FontFamily->"Arial",FontSize->20},PlotStyle->PointSize[0.01],AxesOrigin->{0,0}],Plot[line1,{x,0,Log[63]}],Plot[line2,{x,Log[63],Log[252]},PlotStyle->Thick]]

Out=

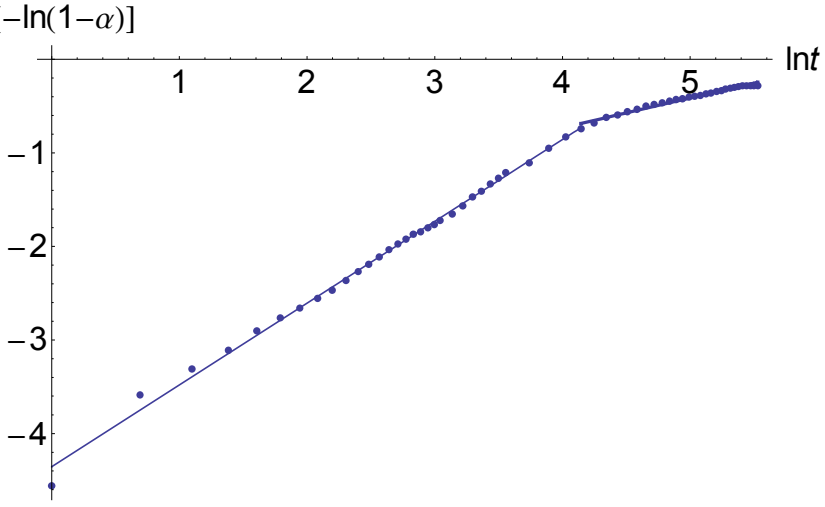

In:= 1-Exp[-Exp[-2.004627208520826`]]

Out:= 0.126031

A8.2 Backend non-linear fitting

Following are Wolfram® *Mathematica* calculation record of the non-linear Kabai fitting for the iron column leaching data on the second fitting line of sample C3:

In:= {tC3,pC3}=Transpose[ReadList["D:\\PHD\\Nickel laterite experiment data\\leaching data\\column leach data analysis\\Kabai&CC1976 fitting\\C3.txt",{Number,Number}]];
C3B=Take[Transpose[{tC3,(pC3/100-0.12603111553991397`)/(1-0.12603111553991397`)}],{32,59}]
Out:=
{{63,0.289152},{70,0.311011},{77,0.330121},{84,0.341794},{91,0.35387},{98,0.363613},{105,0.374957},{112,0.381623},{119,0.389387},{126,0.397814},{133,0.403157},{140,0.407988},{147,0.411695},{154,0.415742},{161,0.419348},{168,0.426037},{175,0.430817},{182,0.436519},{189,0.441229},{196,0.445939},{203,0.450083},{210,0.454114},{217,0.458072},{224,0.46173},{231,0.462987},{238,0.462975},{245,0.462963},{252,0.462961}}
In:= ListPlot[C3B, PlotRange->All,AxesOrigin->{0,0}]
Out:=

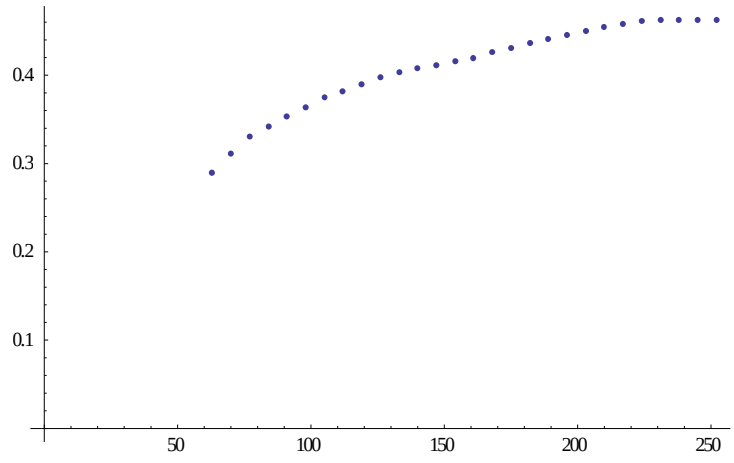

In:= fitkabaiC3B=FindFit[C3B,Kabai,{{k,0.0002},{a,0.3}},t]
Out:= {k->0.00133275,a->0.396933}
In:= modelkabaiC3B=Function[{t},Evaluate[Kabai/.fitkabaiC3B]]
Out:= Function[{t},1-$e^{-0.0722301\,t^{0.396933}}$]
In:= C3BK=NonlinearModelFit[C3B,Kabai,{{k,0.0002},{a, 0.3}},t]
Out:= FittedModel[$1-e^{-0.0722301\,t}$ «19»]
In:= C3BK[{"BestFit","ParameterTable","RSquared"}]

Out:= {1- $e^{-0.0722301\, t^{0.396933}}$,{

{, Estimate, Standard Error, t-Statistic, P-Value},

{k, 0.00133275, 0.0000649693, 20.5136, 1.39777×10^{-17}},

{a, 0.396933, 0.0119391, 33.2464, 7.81621×10^{-23}}

},0.999698}

In:= Show[ListPlot[C3B, PlotRange->All,AxesOrigin->{0,0}],Plot[modelkabaiC3B[t],{t,0,252}]]

Out:=

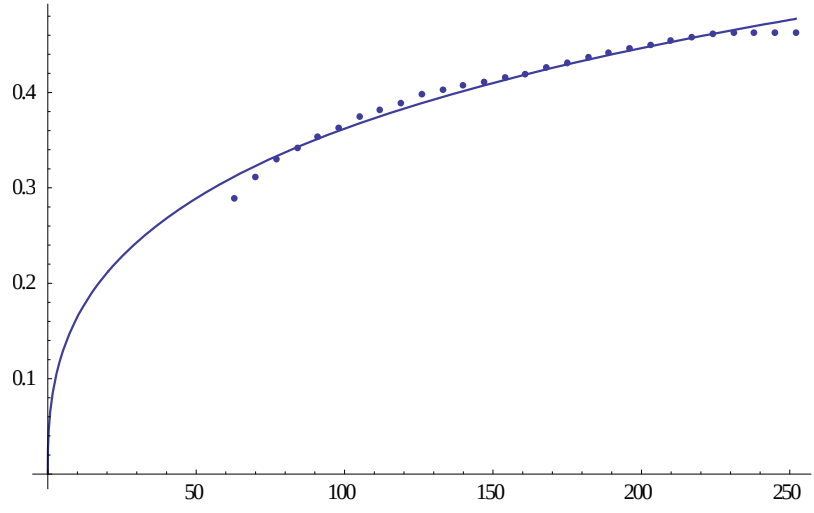

A8.3 Kabai rate constants for iron and nickel leaching from all the laterite samples

Table A8-1 The dissolution rate constant *k*, a and R^2 of iron oxide phases of all the ore samples generated by non-linear Kabai fitting.

sample	Fe leaching rate			Ni leaching rate		
	$k\ 10^{-3}(day^{-1})$	a	R^2	$k\ 10^{-3}(day^{-1})$	a	R^2
A1†	15.2(7)	0.47(2)	0.995	23(1)	0.42(2)	0.996
A2†	14.4(4)	0.48(1)	0.998	13.1(5)	0.38(1)	0.998
A3†	14.1(5)	0.49(2)	0.997	8.0(4)	0.36(1)	0.997
A4	3.5(1)	1.03(3)	0.994	3.53(9)	0.94(2)	0.996
A5	2.76(5)	0.88(2)	0.997	2.71(3)	0.736(6)	0.999
A6	4.1(1)	0.77(2)	0.992	6.9(1)	0.64(1)	0.997
A7	3.1(1)	0.48(1)	0.996	5.9(2)	0.43(1)	0.997
A8†	2.0(1)	0.54(2)	0.996	19.1(8)	0.49(2)	0.996
A9†	4.5(3)	0.54(2)	0.997	16.6(8)	0.43(3)	0.997
A10†	3.7(2)	0.49(2)	0.998	27(2)	0.40(3)	0.998
A11†	0.9(1)	0.38(2)	0.994	5.8(4)	0.41(2)	0.994
A12†	8.4(3)	0.50(3)	0.997	21.0(7)	0.55(2)	0.999
A13†	11.0(5)	0.52(2)	0.996	19.5(9)	0.46(3)	0.996
A14†	5.0(4)	0.45(3)	0.996	13.3(6)	0.42(3)	0.998

sample	Fe leaching rate			Ni leaching rate		
	k 10^{-3}(day^{-1})	a	R^2	k 10^{-3}(day^{-1})	a	R^2
A15	0.041(3)	0.694(9)	0.999	0.0031(3)	0.448(5)	0.999
A16	18.4(8)	1.04(5)	0.990	22.1(7)	1.04(4)	0.993
A17†	12.0(7)	0.58(3)	0.983	12.4(8)	0.52(3)	0.983
B1†	11.2(5)	0.48(3)	0.997	31(2)	0.55(4)	0.998
B2	10.2(3)	0.91(3)	0.990	25.9(8)	0.64(2)	0.996
B3	11.9(6)	0.62(4)	0.990	18.4(5)	0.43(1)	0.999
B4†	18(1)	0.30(3)	0.999	20(1)	0.28(2)	1.000
B5	7.9(3)	0.75(3)	0.993	16.7(6)	0.61(3)	0.996
B6	8.3(2)	0.80(2)	0.996	36(1)	0.49(2)	0.997
B7	13.2(8)	0.34(3)	0.999	20(2)	0.35(3)	1.000
B8	7.4(3)	0.92(4)	0.986	15.7(5)	0.90(3)	0.993
B9	6.8(3)	0.78(3)	0.989	11.9(5)	0.67(3)	0.991
B10	8.7(3)	0.93(4)	0.987	17.3(6)	0.87(4)	0.990
B11	0.20(2)	0.66(2)	0.993	0.10(1)	0.56(1)	0.995
B12†	2.4(3)	0.40(2)	0.997	15.8(6)	0.43(3)	0.998
B13†	3.1(2)	0.47(2)	0.996	9.2(2)	0.46(2)	0.998
B14†	0.87(9)	0.36(1)	0.998	6.1(3)	0.39(2)	0.998
B15†	5.1(2)	0.56(2)	0.998	14.5(4)	0.40(1)	0.999
B16†	7.1(2)	0.65(2)	0.996	15.7(9)	0.44(2)	0.993
B17†	8.3(3)	0.49(2)	0.997	18.2(7)	0.51(2)	0.997
B18	2.7(1)	0.67(2)	0.993	4.8(1)	0.51(1)	0.997
B19†	6.7(3)	0.61(3)	0.995	24(1)	0.47(3)	0.994
B20†	3.7(1)	0.59(2)	0.995	5.1(2)	0.47(1)	0.996
C1†	5.5(5)	0.35(2)	0.996	26(2)	0.35(3)	0.996
C2	4.3(1)	0.54(2)	0.999	9.9(2)	0.54(2)	0.999
C3	1.33(6)	0.40(1)	0.999	1.68(7)	0.37(1)	1.000
C4	9.6(3)	0.75(3)	0.992	63(3)	0.43(2)	0.997
C5†	4.5(3)	0.47(2)	0.995	3.5(3)	0.37(2)	0.997
C6	1.48(7)	0.75(2)	0.994	0.76(1)	0.718(6)	0.999
C7	2.2(1)	0.53(1)	0.996	2.33(6)	0.414(9)	1.000
C8	3.5(2)	0.53(2)	0.990	5.4(2)	0.38(1)	0.997
C9†	1.0(2)	0.33(3)	0.999	0.3(1)	0.28(3)	0.999
C10†	4.9(4)	0.40(2)	0.997	1.8(2)	0.34(2)	0.998
D1	8.4(2)	1.22(3)	0.995	12.3(1)	1.16(2)	0.998
D2	11.8(1)	1.14(1)	0.999	26.8(8)	0.87(3)	0.996
D3	22.8(7)	0.88(3)	0.994	40.2(5)	0.85(2)	0.999
D4	6.7(2)	1.03(3)	0.994	6.8(1)	1.01(2)	0.996
D5	3.0(1)	0.77(3)	0.990	1.44(8)	0.64(2)	0.991

†The Fe and Ni leaching data of these samples show “two lines features”, the dissolution rate constant ‘*k*’ of iron oxides were reported with the separation method described Chapter 6. The figures in brackets are the errors for the last decimal place, which are generated from the nonlinear Kabai fitting.

The nickel extraction rates from iron oxides are generally larger than the iron extraction rates. This is not uncommon based on previous reports summarised in Section 2.6.5.6. Most of the conclusions drawn from the leaching experiments of synthetic Ni-goethite attribute the preferential nickel leaching over iron to the surface adsorption of nickel on goethite crystals. However, another possibility is that nickel may be present in higher concentrations in smaller (fast leaching) goethite crystals and less abundant in larger (slow leaching) goethite crystals, which is confirmed by the TEM/EDS analysis in Chapter 7.

Appendix 9. Plots of goethite peak FWHMs and the iron leaching rates from iron oxides

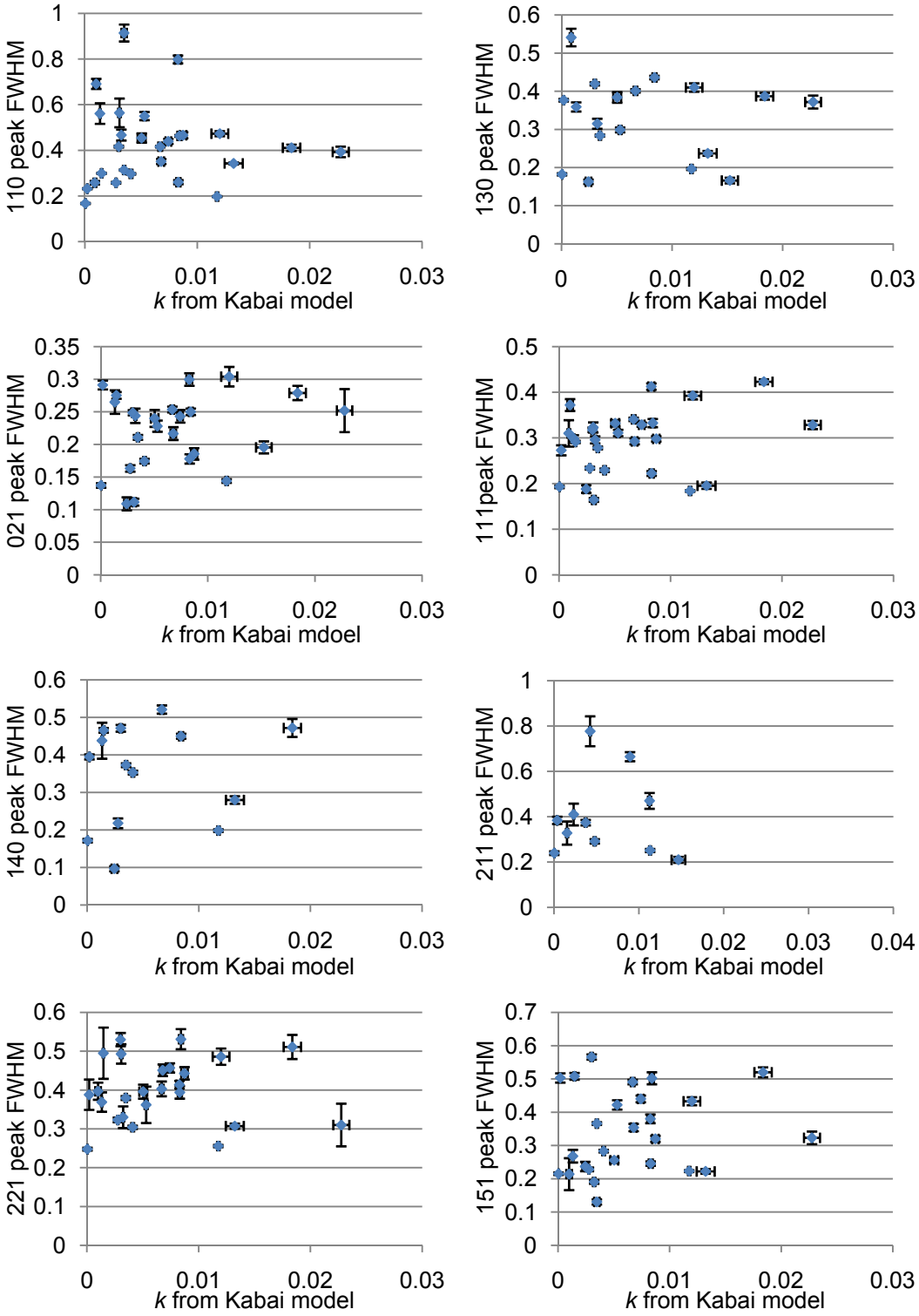

Figure A9-1 Plots of goethite peak FWHMs and the rate constants of Fe leaching from iron oxides

Table A9-1 Correlation coefficients of the Figure A9-1 generated from Microsoft® Excel Correlation Tool.

hkl reflections	Correlation coefficient R	t-statistic	P-value	F-value
110	-0.014	-0.070	0.944	0.005
130	-0.074	-0.295	0.772	0.087
021	0.215	1.057	0.302	1.117
111	0.279	1.481	0.151	2.194
140	0.132	0.460	0.653	0.212
211	-0.165	-0.503	0.627	0.253
221	0.020	0.096	0.924	0.009
151	0.145	0.718	0.479	0.516

The plots of goethite peak FWHMs (Figure A9-1) do not provide any obvious trends. The correlation coefficients of these plots shown in Table A9-1 are close to zero; the statistical indicatiors shown in Table A9-1 suggest these fittings are not significant at 95 % confidence level (P-value > 0.05). This suggests no correlation between goethite peak FWHMs and the rate constants of iron extraction from iron oxides.

Appendix 10. Copyright clearance

The Figure 2-2 was originally published in the journal article “Elias, M., Donaldson, M.J. and Giorgetta, N.E., 1981. Geology, mineralogy, and chemistry of lateritic nickel-cobalt deposits near Kalgoorlie, Western Australia. Economic Geology, 76(6): 1775-1783.”, whose copyright is held by the Society of Economic Geologists. The usage of this Figure in this thesis falls under the Fair Use Permission of the Society of Economic Geologists: http://www.segweb.org/SEG/Publications/Copyright_Information/SEG/_Publications/Copyright_Information.aspx?hkey=cf314016-0732-4fb6-86d0-e63bbf52a0f6

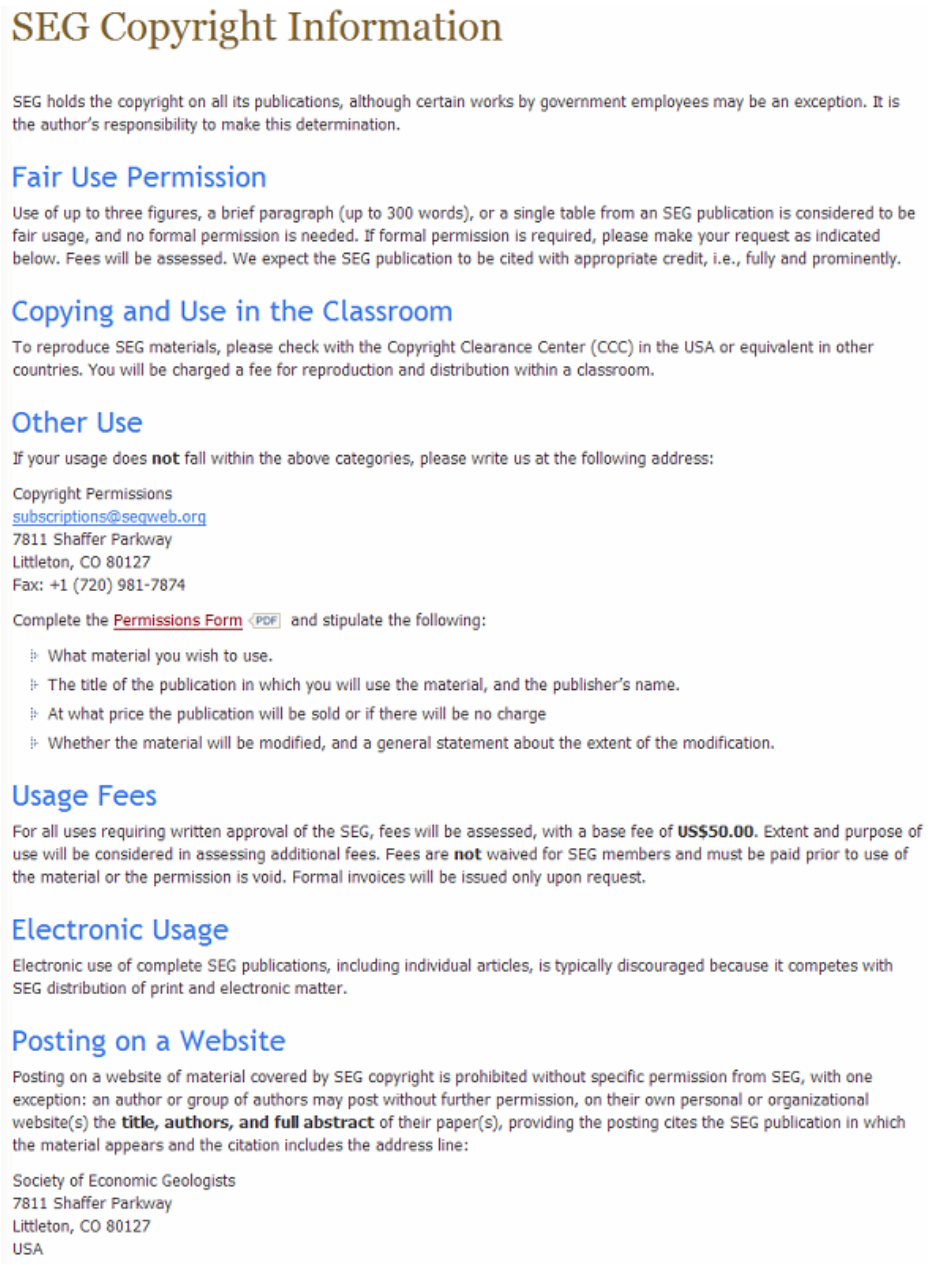

SEG Copyright Information

SEG holds the copyright on all its publications, although certain works by government employees may be an exception. It is the author's responsibility to make this determination.

Fair Use Permission

Use of up to three figures, a brief paragraph (up to 300 words), or a single table from an SEG publication is considered to be fair usage, and no formal permission is needed. If formal permission is required, please make your request as indicated below. Fees will be assessed. We expect the SEG publication to be cited with appropriate credit, i.e., fully and prominently.

Copying and Use in the Classroom

To reproduce SEG materials, please check with the Copyright Clearance Center (CCC) in the USA or equivalent in other countries. You will be charged a fee for reproduction and distribution within a classroom.

Other Use

If your usage does **not** fall within the above categories, please write us at the following address:

Copyright Permissions
subscriptions@segweb.org
7811 Shaffer Parkway
Littleton, CO 80127
Fax: +1 (720) 981-7874

Complete the Permissions Form (PDF) and stipulate the following:

- What material you wish to use.
- The title of the publication in which you will use the material, and the publisher's name.
- At what price the publication will be sold or if there will be no charge
- Whether the material will be modified, and a general statement about the extent of the modification.

Usage Fees

For all uses requiring written approval of the SEG, fees will be assessed, with a base fee of **US$50.00**. Extent and purpose of use will be considered in assessing additional fees. Fees are **not** waived for SEG members and must be paid prior to use of the material or the permission is void. Formal invoices will be issued only upon request.

Electronic Usage

Electronic use of complete SEG publications, including individual articles, is typically discouraged because it competes with SEG distribution of print and electronic matter.

Posting on a Website

Posting on a website of material covered by SEG copyright is prohibited without specific permission from SEG, with one exception: an author or group of authors may post without further permission, on their own personal or organizational website(s) the **title, authors, and full abstract** of their paper(s), providing the posting cites the SEG publication in which the material appears and the citation includes the address line:

Society of Economic Geologists
7811 Shaffer Parkway
Littleton, CO 80127
USA

Appendix 11. Publications resulting from this research at the time of printing

Wang, X., Li, J., Hart, R. D., van Riessen, A., & McDonald, R. (2011). Quantitative X-ray diffraction phase analysis of poorly ordered nontronite clay in nickel laterites. *Journal of Applied Crystallography, 44*(5), 902-910.

Wang, X., Hart, R. D., Li, J., McDonald, R. G., & Van Riessen, A. (2012). Quantitative analysis of turbostratically disordered nontronite with a supercell model calibrated by the PONKCS method. *Journal of Applied Crystallography 45*, 1295-1302.

Wang, X., McDonald, R. G., Hart, R. D., Li, J., & van Riessen, A., (2013). Acid resistance of goethite in nickel laterite ore from Western Australia. Part I. The relationship between goethite morphologies and acid leaching performance. Hydrometallurgy, DOI: 10.1016/j.hydromet.2013.09.005.

Wang, X., Li, J., Hart, R. D., McDonald, R., & van Riessen, A. (2011). Quantitative XRD analysis of poorly crystalline nontronite clay in nickel laterites. Presented at the Australian X-ray Analytical Association (AXAA) Conference 2011, Sydney, Australia.

Wang, X., McDonald, R. G., Hart, R. D., Li, J., & van Riessen, A. (2012). Morphology of acid resistant goethite in nickel laterite ore from Western Australia. Presented at the 10th Asia-Pacific Microscopy Conference & 2012 International Conference on Nanoscience and Nanotechnology & 22nd Australian Conference on Microscopy and Microanalysis, Perth, Australia.

Wang, X., Hart, R. D., Li, J., McDonald, R. G., & van Riessen, A. (2012). Calibration based models for turbostratic disordered nontronite quantification. Presented at the 13th European Powder Diffraction Conference, Grenoble, France.

Wang, X. (2012). Use of Knife Edge and Variable Divergence Slit Simultaneously. Presented at the 10th TOPAS User Meeting, Adelaide, Australia.

Wang, X., van Riessen, A., Hart, R. D., Li, J., & McDonald, R. G. (2013). Calibration based QPA models for turbostratically disordered nontronite quantification. Presented at the 11th TOPAS User Meeting, Gaithersburg, MD, USA.

Wang, X., van Riessen, A., Li, J., McDonald, R. G., & Hart, R. D. (2013). Incorporating preferred orientation correction into nontronite supercell model. Presented at the 4th Accuracy in Powder Diffraction Conference, Gaithersburg, MD, USA.